

PROCEEDINGS OF SPIE



SPIE—The International Society for Optical Engineering

Display Technologies III

**I-Wei Wu
Heiju Uchiike**
Chairs/Editors

**26-27 July 2000
Taipei, Taiwan**

Sponsored by
SPIE—The International Society for Optical Engineering
National Science Council (Taiwan)
PIDA—Photonics Industry Development Association



Volume 4079

REPORT DOCUMENTATION PAGE

Form Approved OMB No. 0704-0188

Public reporting burden for this collection of information is estimated to average 1 hour per response, including the time for reviewing instructions, searching existing data sources, gathering and maintaining the data needed, and completing and reviewing the collection of information. Send comments regarding this burden estimate or any other aspect of this collection of information, including suggestions for reducing this burden to Washington Headquarters Services, Directorate for Information Operations and Reports, 1215 Jefferson Davis Highway, Suite 1204, Arlington, VA 22202-4302, and to the Office of Management and Budget, Paperwork Reduction Project (0704-0188), Washington, DC 20503.

1. AGENCY USE ONLY (Leave blank)	2. REPORT DATE	3. REPORT TYPE AND DATES COVERED	
	July 2000	26-27 July 2001 Conference Proceedings - Final Report	
4. TITLE AND SUBTITLE		5. FUNDING NUMBERS	
Display Technologies III Held in Taipei, Taiwan on 26-27 July 2000.			
6. AUTHOR(S)			
I-Wei Wu and Heiju Uchiike, Editors			
7. PERFORMING ORGANIZATION NAME(S) AND ADDRESS(ES)		8. PERFORMING ORGANIZATION REPORT NUMBER	
Industrial Technology Research Institute Taipei, Taiwan		ISSN 0277-786X	
9. SPONSORING/MONITORING AGENCY NAME(S) AND ADDRESS(ES)		10. SPONSORING/MONITORING AGENCY REPORT NUMBER	
US Department of the Air Force Asian Office of Aerospace Research and Development (AOARD) Unit 45002 APO AP 96337-5002			
11. SUPPLEMENTARY NOTES			
Proceedings of SPIE, Vol. 4079. Published by: SPIE-The International Society for Optical Engineering, P.O. Box 10, Bellingham, Washington 98227-0010. This work relates to Department of the Air Force grant issued by the Asian Aerospace Office of Research and Development. The United States has a royalty free license throughout the world in all copyrightable material contained herein.			
12a. DISTRIBUTION/AVAILABILITY STATEMENT		12b. DISTRIBUTION CODE	
Approved for Public Release. U.S. Government Rights License. All other rights reserved by the copyright holder. (Code 1, 20)		A	
12. ABSTRACT (Maximum 200 words)			
<p>This third conference on Display Technologies, was part of the International Optoelectronics Symposium Held in Taipei, Taiwan on 26-28 July 2001 in conjunction with Photonics Taiwan 2000 (See http://www.spie.org/web/meetings/programs/pt00/pt00_home.html). This year's focus was on photonic technologies in the 21st century and included sessions on: LTPS and LCoS, LTPS TFT, PDP and CNT_FED, LED/OLED, LCD, and TFT/LCM.</p>			
13. SUBJECT TERMS		15. NUMBER OF PAGES	
AOARD, Foreign reports, Photonics, Electronics			
		16. PRICE CODE	
17. SECURITY CLASSIFICATION OF REPORT	18. SECURITY CLASSIFICATION OF THIS PAGE	19. SECURITY CLASSIFICATION OF ABSTRACT	20. LIMITATION OF ABSTRACT
UNCLASSIFIED	UNCLASSIFIED	UNCLASSIFIED	UL

NSN 7540-01-280-5500

Standard Form 298 (Rev. 2-89)
Prescribed by ANSI Std. Z39-18
298-102

PROCEEDINGS OF SPIE



SPIE—The International Society for Optical Engineering

Display Technologies III

I-Wei Wu
Heiju Uchiike
Chairs/Editors

26-27 July 2000
Taipei, Taiwan

Sponsored by
SPIE—The International Society for Optical Engineering
National Science Council (Taiwan)
PIDA—Photonics Industry Development Association

Published by
SPIE—The International Society for Optical Engineering



20011130 083

Volume 4079

SPIE is an international technical society dedicated to advancing engineering and scientific applications of optical, photonic, imaging, electronic, and optoelectronic technologies.

AQ F02-02-0299



The papers appearing in this book compose the proceedings of the technical conference cited on the cover and title page of this volume. They reflect the authors' opinions and are published as presented, in the interests of timely dissemination. Their inclusion in this publication does not necessarily constitute endorsement by the editors or by SPIE. Papers were selected by the conference program committee to be presented in oral or poster format, and were subject to review by volume editors or program committees.

Please use the following format to cite material from this book:

Author(s), "Title of paper," in *Display Technologies III*, I-Wei Wu, Heiju Uchiike, Editors, Proceedings of SPIE Vol. 4079, page numbers (2000).

ISSN 0277-786X
ISBN 0-8194-3718-2

Published by
SPIE—The International Society for Optical Engineering
P.O. Box 10, Bellingham, Washington 98227-0010 USA
Telephone 1 360/676-3290 (Pacific Time) • Fax 1 360/647-1445
<http://www.spie.org/>

Copyright ©2000, The Society of Photo-Optical Instrumentation Engineers.

Copying of material in this book for internal or personal use, or for the internal or personal use of specific clients, beyond the fair use provisions granted by the U.S. Copyright Law is authorized by SPIE subject to payment of copying fees. The Transactional Reporting Service base fee for this volume is \$15.00 per article (or portion thereof), which should be paid directly to the Copyright Clearance Center (CCC), 222 Rosewood Drive, Danvers, MA 01923 USA. Payment may also be made electronically through CCC Online at <http://www.directory.net/copyright/>. Other copying for republication, resale, advertising or promotion, or any form of systematic or multiple reproduction of any material in this book is prohibited except with permission in writing from the publisher. The CCC fee code is 0277-786X/00/\$15.00.

Printed in the United States of America.

Contents

vii Conference Committee

KEYNOTE PAPER

-
- 2 **Photonic technologies in the 21st century: creation of new industries [4079-201]**
T. Hiruma, Hamamatsu Photonics K.K. (Japan)

SESSION 1 LTPS and LCoS

- 8 **High-performance thin film transistors using Ni silicide for liquid-crystal displays (Invited Paper) [4079-01]**
J. Jang, J. I. Ryu, K. S. Cho, Kyung Hee Univ. (Korea)
- 17 **High-contrast SXGA silicon light valves for high-definition video projectors (Invited Paper) [4079-02]**
H. C. Huang, P. W. Cheng, H. S. Kwok, Hong Kong Univ. of Science and Technology

SESSION 2 LTPS TFT

- 28 **Metal-induced laterally crystallized polycrystalline silicon: technology, material, and devices (Invited Paper) [4079-03]**
M. Wong, Hong Kong Univ. of Science and Engineering
- 43 **Low-temperature poly-Si TFT characteristics in the overlapped area of excimer laser long-axis scans [4079-04]**
S.-C. Chang, C.-J. Shih, I-M. Lu, I-W. Wu, Industrial Technology Research Institute (Taiwan)
- 47 **Characteristics of single-pulse excimer laser beam profile on the low-temperature poly-Si TFTs [4079-05]**
C.-J. Shih, L.-M. Wang, S.-C. Chang, I-M. Lu, I-W. Wu, Industrial Technology Research Institute (Taiwan)
- 51 **Novel device structure for low-temperature polysilicon TFTs with controlled grain growth in channel regions [4079-06]**
L.-J. Cheng, Y.-L. Lu, C.-W. Lin, T.-K. Chang, H.-C. Cheng, National Chiao Tung Univ. (Taiwan)
- 55 **Comparison of the mechanisms of hydrogenation by rf plasma and SiNx [4079-07]**
L.-M. Wang, H.-J. Sung, I-M. Lu, I-W. Wu, Industrial Technology Research Institute (Taiwan)
- 59 **VGS compensation source follower for the LTPS TFT LCD data driver output buffer [4079-08]**
J.-R. Shih, S.-L. Chen, B. Wang, Industrial Technology Research Institute (Taiwan)

SESSION 3 PDP AND CNT_FED

- 70 **Advanced manufacturing technologies on color plasma displays (Invited Paper) [4079-09]**
K. Betsui, Fujitsu Labs. Ltd. (Japan)
- 79 **Recent advances of color plasma displays (Invited Paper) [4079-10]**
H. Uchiike, Saga Univ. (Japan)
- 82 **Gas discharge and experiments for plasma display panel [4079-11]**
P.-C. Chen, Y.-T. Chien, Acer Display Technology Inc. (Taiwan)
- 94 **Field emission display using carbon nanotubes as emitters [4079-12]**
F.-Y. Chuang, C.-C. Lee, J.-D. Lin, J.-H. Liao, H.-C. Cheng, C.-X. Han, Industrial Technology Research Institute (Taiwan); J.-L. Kwo, National Cheng Kung Univ. (Taiwan); W.-C. Wang, Industrial Technology Research Institute (Taiwan)
- 101 **Field emission characteristics of carbon nanotube emitters using screen-printing technique [4079-13]**
C.-C. Lee, F.-Y. Chuang, J.-D. Lin, J.-H. Liao, H.-C. Cheng, J.-R. Sheu, Y.-Y. Chang, C.-C. Tsou, W.-C. Wang, Industrial Technology Research Institute (Taiwan)

SESSION 4 LED/OLED

- 112 **White illumination characteristics of ZnS-based phosphor materials excited by InGaN-based ultraviolet light-emitting diode [4079-15]**
K. Murakami, T. Taguchi, Yamaguchi Univ. (Japan); M. Yoshino, Kasei Optonics (Japan)
- 120 **Characteristics of high-efficiency InGaN-based white LED lighting [4079-16]**
Y. Uchida, T. Setomoto, T. Taguchi, Yamaguchi Univ. (Japan); Y. Nakagawa, K. Miyazaki, Nichia Corp. (Japan)
- 127 **Multicolor organic LEDs processed by integration of screen printing and thermal transfer printing [4079-18]**
H. Chang, National Central Univ. (Taiwan); C. Wu, C. Yang, C.-W. Chen, National Taiwan Univ.; C.-C. Lee, National Central Univ. (Taiwan)
- 135 **Thermal transfer approach for the doping of organic LEDs [4079-19]**
C. Yang, C. Wu, National Taiwan Univ.; H. Chang, National Central Univ. (Taiwan); C.-W. Chen, National Taiwan Univ.
- 143 **Luminescence of the InGaN/GaN blue light-emitting diodes [4079-43]**
J. K. Sheu, T. W. Yeh, G. C. Chi, National Central Univ. (Taiwan); M. J. Jou, Epistar Corp. (Taiwan)

SESSION 5 LCD

- 152 **Recent trends in wide-viewing-angle color TFT-LCDs (Invited Paper) [4079-20]**
Y. Nagae, Hitachi, Ltd. (Japan)
- 160 **New two-domain TN/LCD with identical, symmetrical, and ± 80 -deg. viewing cone in left-, right-, up-, and down-viewing zones (Invited Paper) [4079-21]**
H. L. Ong, Kopin Corp. (USA); Y.-H. Wu, Unipac Optoelectronics Corp. (Taiwan)

-
- 176 **Overview of wide-viewing-angle LCD using interdigital electrodes [4079-22]**
L. Chuang, W.-F. Bair, C.-C. Chang, Industrial Technology Research Institute (Taiwan)
- 184 **Studies of polymer-stabilized cholesteric texture films [4079-23]**
A. Y.-G. Fuh, C.-Y. Huang, C.-H. Lin, T.-C. Ko, National Cheng Kung Univ. (Taiwan)
- 191 **Comparison between reflective LCDs with diffusive micro slant reflector (DMSR) and bump reflector [4079-24]**
C.-J. Wen, D.-L. Ting, C.-Y. Chen, L. Chuang, C.-C. Chang, Y.-J. Wong, Industrial Technology Research Institute (Taiwan)
- 201 **Intensive optical field improves the photopolymerization-induced alignment quality of liquid crystals [4079-25]**
L. Sun, Yantai Univ. (China); S. Wang, Changchun Institute of Physics (China)

SESSION 6 TFT/LCM

- 210 **Study of 5-mask TFT array process with low-cost high-yield high-performance characteristics [4079-26]**
J.-H. Chen, Industrial Technology Research Institute (Taiwan); T.-H. Huang, Quanta Display Inc. (Taiwan); I.-M. Lu, P.-F. Chen, D.-I Chen, Industrial Technology Research Institute (Taiwan)
- 217 **Amorphous-silicon thin film transistor with two-step exposure process [4079-27]**
P.-F. Chen, J.-H. Chen, D.-I. Chen, H.-J. Sung, J.-W. Hwang, I.-M. Lu, Industrial Technology Research Institute (Taiwan)
- 221 **Mismatch analysis of TAB-on-glass connection with ACF [4079-30]**
W.-F. Hou, T.-Y. Kam, National Chiao Tung Univ. (Taiwan); A. Hsieh, J.-C. Chen, S.-M. Chang, Industrial Technology Research Institute (Taiwan)
- 228 **Characteristic study of chip-on-film interconnection [4079-31]**
S.-M. Chang, Industrial Technology Research Institute (Taiwan) and National Tsing-Hua Univ. (Taiwan); J.-H. Jou, National Tsing-Hua Univ. (Taiwan); A. Hsieh, T.-H. Chen, Industrial Technology Research Institute (Taiwan); C.-Y. Chang, Y.-H. Wang, Wintek Corp. (Taiwan); H.-Y. Lin, Industrial Technology Research Institute (Taiwan); C.-M. Huang, Wintek Corp. (Taiwan)

POSTER SESSION

- 242 **Multibubble sonofluorescence display [4079-32]**
H.-M. Li, JI-AN Teachers College (China)
- 247 **Method and theory of turn back point error [4079-33]**
Y.-N. Liu, J.-K. Zeng, J.-Q. Liu, Xi'an Institute of Optics and Precision Mechanics (China); T. Wu, Northwestern Polytechnical Univ. (China)
- 251 **Partial plane level of terrace and its test [4079-34]**
Y.-N. Liu, J.-K. Zeng, J.-Q. Liu, Xi'an Institute of Optics and Precision Mechanics (China); T. Wu, Northwestern Polytechnical Univ. (China)
- 255 **Simulation of geometric effects on double-gate field emission devices [4079-35]**
C.-W. Wang, C.-L. Chen, Y.-H. Yang, T.-Y. Yang, I-Shou Univ. (Taiwan)

- 264 **Improve product aperture ratio by controlling magnitude of reverse tilt domain** [4079-37]
W. H. Ho, C. J. Pan, H. H. Wu, Prime View International Co., Ltd. (Taiwan)
- 268 **To evaluate the LC pretilt angles of the alignment layer polyamide using the Taguchi method**
[4079-38]
C. J. Pan, H. R. Lin, H. H. Wu, Prime View International Co., Ltd. (Taiwan)
- 271 **Are the color gamuts of CRT and LCD triangular? An experimental study** [4079-41]
G. Lee, National Tsing Hua Univ. (Taiwan); C. Wen, Industrial Technology Research Institute
(Taiwan)
- 279 **Field emission performances of diamond complex ceramic thin film** [4079-44]
W. Wang, J. Liang, G. Yuan, H. Zhao, C. Zhang, X. Yin, Changchun Institute of Physics (China)
- 288 *Author Index*

Conference Committee

Conference Chairs

I-Wei Wu, Industrial Technology Research Institute (Taiwan)
Heiju Uchiike, Saga University (Japan)

Program Committee

Chern-Lin Chen, National Taiwan University
Huang-Chung Cheng, National Chiao Tung University (Taiwan)
Gou Chung Chi, National Central University (Taiwan)
Shen-Li Fu, I-Shou University (Taiwan)
Andy Ying-Guey Fuh, National Cheng Kung University (Taiwan)
Chain-Shu Hsu, National Chiao Tung University (Taiwan)
Dyi-Chung Hu, HannStar Display Corporation (Taiwan)
Hideaki Kawakami, Hitachi, Ltd. (Japan)
Chen-Lung Kuo, Chi Mei Optoelectronics Corporation (Taiwan)
Kelvin Lee, Acer Display Technology, Inc. (Taiwan)
Jonq-Min Liu, Industrial Technology Research Institute (Taiwan)
Shigeo Mikoshiba, University of Electro-Communications (Japan)
Feng-Cheng Su, Unipac Optoelectronics Corporation (Taiwan)
Tai-Kang Wu, Prime View International Company, Ltd. (Taiwan)

Session Chairs

- 1 LTPS and LCoS
Heiju Uchiike, Saga University (Japan)
- 2 LTPS TFT
Jin Jang, Kyung Hee University (Korea)
Huang-Chung Cheng, National Chiao Tung University (Taiwan)
- 3 PDP and CNT_FED
Gou Chung Chi, National Central University (Taiwan)
Kelvin Lee, Acer Display Technology, Inc. (Taiwan)
- 4 LED/OLED
Jonq-Min Liu, Industrial Technology Research Institute (Taiwan)
Chern-Lin Chen, National Taiwan University
- 5 LCD
Tai-Kang Wu, Prime View International Company, Ltd. (Taiwan)
Chen-Lung Kuo, Chi Mei Optoelectronics Corporation (Taiwan)

- 6 TFT/LCM
Dyi-Chung Hu, HannStar Display Corporation (Taiwan)
Shen-Li Fu, I-Shou University (Taiwan)
- Poster Session
Andy Ying-Guey Fuh, National Cheng Kung University (Taiwan)
Feng-Cheng Su, Unipac Optoelectronics Corporation (Taiwan)

Keynote Paper

Photonic Technologies in the 21st Century : Creation of New Industries *

Teruo Hiruma
Hamamatsu Photonics KK
Hamamatsu, Japan

ABSTRACT

As we approach the new millennium, the ongoing aim of human society is not only for promoting scientific technology but also creating new industries. To achieve this goal, each person in industry must recognize anew that the real meaning of science is to explore the absolute truth. It is also important that people recognize that there are unlimited matters which we humans do now yet know.

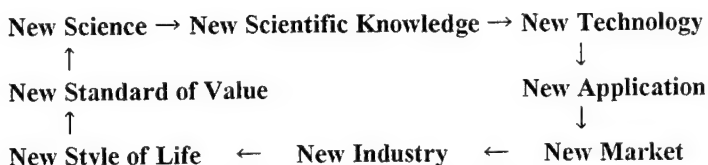
1. INTRODUCTION

The 20th century was one that witnessed many great discoveries and our knowledge increased many times during the last one hundred years. Yet even with such an explosion of knowledge and information there is much more that we do not yet understand. Our present knowledge represents only a fraction of what there is to know. For example, there have been major breakthroughs in understanding cell structure by studying individual components or systems such as the role of calcium ions in signal transduction. However very little is known about how all of these components work in concert. It is very much like trying to understand an orchestra by studying the individual instruments. In the future we will develop methods to study the function of the entire cell not just individual systems. On the molecular level we are just beginning to study the details of molecular dynamics during a chemical reaction. The work of this year's Nobel Prize winner in chemistry, Dr Zewail shows how it is possible to use photonics to study the intimate detail of a chemical reaction. Once we gain such detailed information about more complex systems it will be possible to more efficiently produce the chemicals we need and to destroy those that we no longer require.

At Hamamatsu Photonics it is our corporate mission to provide photonics technology that will help us to gain new knowledge of the world we live in. Photonic technologies are very unique in that they let us observe the parts of the world that are very far away (thousands of light years), very small (nanometers) or happen very quickly (in femtoseconds). The roots of our company can be found in the pioneering spirit of Professor Kenjiro Takayanagi who independently developed the technology of television despite the fact those around believed it could not be done because it had never been done. Professor Takayanagi hoped to develop a new way for people to experience the world. We inherited his spirit and continue this idea by using photonics to gain knowledge as well as improve the quality of life for all people.

In the twenty first century it will be possible that we could make all of mankind healthy. Not just in a physical sense but in the definition of the World Health Organization where "Health is a state of complete physical, mental and social well-being and not merely the absence of disease or infirmity." Photonics has the potential for creating the knowledge and industry that could make this possible. It is our hope that this new century sees the beginning of a new economic cycle shown in Figure 1. While industry is designed to generate profit, the purpose of industrialization is for all of mankind to share a common understanding of the New Life Style and to benefit from the New Standard of value, namely Health as defined above.

Figure 1:



*Also published in Proceedings of SPIE Volumes 4078, 4080, 4081, and 4082

Through the application of photonics we are now beginning to develop the New Science that will lead to the cycle illustrated in Figure 1. In this cycle, mankind is constantly improving its status by using new technologies to discover new knowledge. The application of this new knowledge leads first to new industries and then to a change in the social fabric of society. We understand that this is a very long-term goal. But mankind needs to dream in order to progress. Only by trying to see over the horizon can we discover something that will radically improve all of our lives. Thus while Hamamatsu Photonics' short-term goal is to generate profits, these profits are to be used in the quest for new knowledge which is our long-term target.

2. TECHNOLOGIES

This paper will discuss several technologies that are key to the development of new knowledge which will eventually produce new industries. Application of these technologies will be also discussed.

A. The Ultimate Laser Photon (Photon Factory)

The light emitted by a laser is unique in that it is monochromatic, coherent and directional. These properties have made laser-generated photons vital to all types of research ranging from biology to high-energy physics. We need to obtain a better understanding of exactly what is a photon and how it interacts with the world. By better understanding the photon on a fundamental level we will be able to use it more effectively. Phenomena such as the particle wave duality and teleportation must be better understood through a study of the photon.

The development of very small terawatt and pedawatt laser systems give many researchers access to inexpensive ultra high power. New physical phenomena are being discovered when such intense laser beams interact with matter because these lasers create electric fields much greater than those seen in any other experiment do.

B. Ultra Fast Measurement Technology

By continuing to push the speed at which we make measurements we will discover greater detail of how our world operates. We now have lasers that are capable of measuring the individual motion of atoms in molecules. Newer and faster methods will help get even greater detail of how molecules react. Even faster methods will allow us to follow the motion of electrons during important chemical reactions such as photosynthesis or vision.

C. Optical Correlation Technology

Even though we have discovered only a small fraction of our knowledge, we are severely limited in using it because even this limited amount of knowledge is too great to process with conventional computer systems. We must learn how to process information in parallel with optical processors such as spatial light modulators. Ultimately our goal is to process information in 3 or more dimensions using technology that must still be invented.

D. Forecast Simulators

With time not only has our information become too complex, but also the questions we need to answer become more difficult. As our planet's population increases and our technology becomes more complex, the risk of answering a question incorrectly grows exponentially. For example, the consequences of incorrectly predicting the outcome of global warming will be severe if we either under estimate or over estimate the significance of burning fossil fuels. Premature curtailing of fossil fuels will severely curtail the growth of developing countries leading to unnecessary pain and suffering. Failure to prevent global

warming will have even worse consequences. We need better methods to simulate events or conditions so we can better guide environmental, economic, technical, political, and military decisions.

Ultimately nations will never again fight a war on the battlefield but instead will use simulations to replace them. The simulations will simultaneously decide the output as well as convince the parties that physical conflict is too costly.

E. High Power Lasers

Photons are capable of doing many important things such as curing cancer, printing this manuscript or repairing an integrated circuit. At very high photon densities there are many new things that photons can do. At present, it is expensive to generate a lot of photons because the photon sources are expensive. Semiconductor laser diodes hold the promise of being able to reliably and inexpensively generate photons for many new and exciting applications. Just like the replacement of the vacuum tube with the transistor and then to the integrated circuit, so too will the semiconductor laser evolve and result in important technologies and new industries that we cannot even imagine today.

F. New Photochemistry

Much of our planet's energy is wasted in creating chemicals that we need to live or to improve our lives. Lasers are capable of creating specific excited states. Finding ways to selectively excite molecules so that they can be moved along specific reaction pathways will lead to huge savings in cost, energy and pollution. New knowledge on how to perform pathway specific photochemistry is vital to the goal of making everyone healthy according to the World Health Organization's definition of health.

3. APPLICATIONS

We can only speculate on what the full effect of such new photonic technologies will have in the long term. However over a short period of time we can easily imagine some of the benefits we might enjoy from these as well as other photonic technologies. Some of these benefits are discussed below.

A. Measurement of Physiological Functions

The pulse oximeter has already found an important role in guaranteeing that the oxygen concentration of the blood is maintained at as close to optimum as possible. Countless lives have been saved and others have had severe injury prevented by this simple optical device. Not very far away are devices that will permit rapid and painless screening for diabetes. Noninvasive cancer diagnosis is already being tested in clinical trials.

Ultimately a device will be available that checks your body's functions on a daily basis. It screens for potential problems before they cause disease. Adjustments to exercise, diet or even administration of drugs can be performed before the individual is aware of a problem. Such an advanced detection system would save costs, pain and anxiety. It would go as long way to attaining the goal of making people truly healthy.

B. Optical Medicine

In the past few years, photodynamic therapy has been shown to be a valuable treatment for some forms of cancer. In some cases it is far more useful than other techniques such as surgery because it leaves the effected organ in tact. Therefore for young women, cancer of the cervix no longer means that it is the end of their dream to have a family. For older people suffering from the wet form of macula degeneration, photodynamic therapy will soon be used to prevent the blindness caused by this disease.

New chemicals are being developed that are absorbed faster by the cancer cells and discharged more rapidly by the body. This will make treatment simpler and more effective. Patients may not even need to stay overnight in a hospital. Presently PDT can only be used on cancers that are found on a surface. Techniques are being developed that will be used in the treatment of cancers that are deep inside an organ.

Cosmetic uses of photons for hair removal, port wine stain removal or tattoo removal make it easier for a person to be accepted by society. These applications are far from superficial since they greatly improve the quality of life for those that need them.

Other applications of photonics to medical practice will certainly emerge in the near future for things such as the treatment of stroke, heart disease, healing of wounds and reducing or relieving pain.

C. Early Detection of Disease

Cancer screening using Positron Emission Tomography (PET) holds the promise of early detection and cure of this terrible affliction. Injection of fluorodeoxyglucose into the blood stream is currently used to uncover cells that are metabolizing at rates faster than those of their neighbors. These cells are then analyzed to determine if they are malignant. Such a screening method could in the near future make an entire city cancer death free.

Light CT uses nonionizing infrared photons to take a three dimensional image of the body. Work is under way in many places around the world to use light CT as a method for detecting breast cancer. This technique could be less expensive than x-ray methods and used safely on all individuals including pregnant women. Other uses of the light CT would be to quickly determine if a stroke is caused by ischemia or a hematoma. Such information is vital in determining the correct treatment. Rapid treatment of stroke can greatly reduce the damage to the brain resulting in a patient that can lead a normal life even after such a severe trauma.

In the future we hope to quantify the health of a person, not just the presence of disease.

D. Fiberless Optical Communication

Information is the most important commodity in our society. We are constructing very large and expensive infrastructures to move information from one location to the other. Fiber optics is one of the key technologies for information transport because of the very high capacity available due to wavelength division multiplexing. This technique suffers from the fact that fibers must be placed between locations. At Hamamatsu Photonics we have developed a series of fiberless optical communications systems. These operate by transmitting the optical signals through air. They have the capability to send data, or video without the need for government licenses or owning a right of way. One such a fiberless system is used at sporting events such as golf tournaments to transmit the video camera output to the broadcaster's trailer or even back to a studio. Such a system was used at the Atlanta Olympics and is now being tested in Hamamatsu City. In our hometown it is being used to connect elementary schools with the city hall. It could also be used to connect remote clinics with the medical school for telemedicine.

E. Health Industry for Successful Aging

Many countries will soon suffer from an increase in their average age. In the past such an increase in age would greatly burden society in terms of medical expenses and the cost of financially supporting an aging population. We believe that it is possible to completely eliminate the impact of a graying population by finding ways to reduce the pace and effect of the aging process. At Hamamatsu Photonics we are using photonic technology to understand how locomotion is effected as a person ages. We hope to develop exercises that will prevent the loss of mobility and greatly reduce the probability of an older person falling. While just a small step, it will have a big impact on the quality of life of our seniors.

F. Disposal of Industrial Waste

High power lasers and controlled photochemistry hold the promise of being able to safely dispose of dangerous waste products. It will do this by selective destruction of the dangerous ingredients into less danger or even harmless smaller molecules. These smaller molecules can then be recycled into new products.

G. Search for New Energy Sources

Perhaps the biggest impact that photonics can have on mankind is the development of clean and inexpensive energy. For once this is available; the quality of life of the entire world can be improved without damaging the planet. We must continue our search for a way to harness laser fusion and solar energy for they are needed to make the world a better place to live for all of us.

Photonics holds the promise of creating New Science and New Technology which will lead to New Industrial and of course to a world population that is truly healthy.

SESSION 1

LTPS and LCoS

High-performance thin-film transistors using Ni silicide for liquid-crystal displays

Jin Jang, Jai Il Ryu, and Kyu Sik Cho

Department of Physics, Kyung Hee University, Dongdaemoon-ku, Seoul 130-701, Korea

ABSTRACT

The Ni-silicide of a sheet resistance of $7 \Omega/\square$ can be formed at 230°C on n^+ a-Si:H and thus can be applied to gate and source/drain contacts for high performance TFTs. Because of its low resistance it is possible to make a self-alignment between gate and source/drain, which lead to a coplanar a-Si:H TFT having a low parasitic capacitance between them. The NiSi_2 precipitates can be formed on a-Si:H at around 350°C and needlelike Si crystallites are grown as a result of the migration of the NiSi_2 precipitates through a-Si:H network. Amorphous silicon can be crystallized at 500°C in 10 minutes in a modest electric field. The low temperature poly-Si TFT with a field effect mobility of $120 \text{ cm}^2/\text{Vs}$ has been demonstrated using the low temperature poly-Si.

Keywords: Silicide, Parasitic resistance, SMC poly-Si TFT

1. INTRODUCTION

To achieve small contact resistance and self-alignment of source/drain (S/D) to gate, silicide electrode is considered as a good candidate. Ni-silicide, mainly NiSi phase, can be formed at as low as 230°C on a-Si:H. Recently we have developed Ni-silicide S/D contacts for a-Si:H inverted staggered thin-film transistor (TFT)¹⁻², a-Si:H coplanar TFT³⁻⁴, and poly-Si coplanar TFT⁵⁻⁷.

The performance of a-Si:H TFT depend strongly on the S/D parasitic resistance⁸⁻⁹. In our previous work it was reduced by using the Ni-silicides on a-Si:H. To reduce the parasitic series resistance, Ching-Fa Yeh et al. performed a plasma ion implantation¹⁰ and G. K. Guist et al. did a gas immersion laser doping¹¹. The Ni-silicide formed at 230°C on n^+ a-Si:H has a sheet resistance of $7 \Omega/\square$, which is at least two orders of magnitude lower than that of n^+ -doped poly-Si. This significantly low sheet resistance of Ni-silicide enables us to lower the contact resistance in the form of silicide-metal interface, resulting in the reduction in the parasitic resistance. The NiSi_2 precipitates can be formed at around 350°C on a-Si which induces a silicide-mediated-crystallization (SMC). The a-Si having an average Ni concentration of order of 10^{13} cm^{-2} can be crystallized in 10 minutes at 500°C in an electric field¹². A SMC poly-Si TFT with a field effect of $120 \text{ cm}^2/\text{Vs}$ has been developed.

2. NI SILICIDE FORMATION

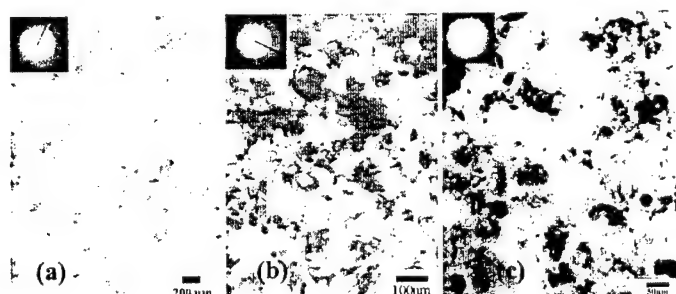


Figure 1. TEM bright-field images and their electron diffraction patterns of the Ni-silicides on a-Si:H formed at (a) 150°C , (b) 240°C and (c) 350°C .

J. Jang is with the Department of Physics, Kyung Hee University, Seoul 130-701, Korea. E-mail : jjjang@khu.ac.kr, URL : <http://tftlcd.khu.ac.kr>, Tel : +82-2-961-0270, Fax : +82-2-968-6924.

TABLE 1. Properties of the Ni-silicides on a-Si:H formed at various temperatures

	Ni ₂ Si	NiSi	NiSi ₂
Formation temperature (°C)	~ 150	240 ~ 390	325 ~ 480
Phase	Orthorhombic Ni-rich	Orthorhombic	Cubic Si-rich
Sheet resistance (Ω/\square)	Below 580	2.8 ~ 2.95	4.0 ~ 5.5
Crystal direction	(112), (103), (202), (020)	(211), (102)	(100), (110), (111)
Remarks		Lowest sheet resistance	Nuclei for SMC

Formation of Ni-silicides on a-Si depends strongly on the Ni/Si ratio and annealing temperature. As shown in the electron diffraction patterns shown in Fig. 1, the structure of Ni-silicide changes from amorphous to polycrystalline with increasing annealing temperature. The phase of Ni-silicide is changed as follows; Ni₂Si \rightarrow NiSi \rightarrow NiSi₂. The dependence of sheet resistance as a function of ion energy for various annealing temperatures is plotted in Fig. 2. Table 1 summarizes the structural and electrical properties of Ni-silicides. The sheet resistance of the Ni-silicide formed at 210 °C is about 7 Ω/\square , and increases to about 13 Ω/\square at 270 °C. This increase appears to be due to the change in the Ni-silicide phase to silicon-rich silicide. Figure 3 shows the plot of Ni and Si binding energy as a function of the sputtering time, i.e., film depth. Note that there is a silicide layer of about 20nm on the a-Si:H.

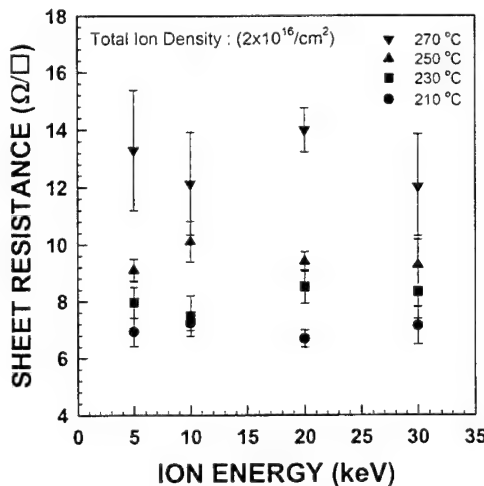


Figure 2. Sheet resistance of Ni-silicides on a-Si:H as a function of ion acceleration voltage for various annealing temperatures (total ion dose: $2 \times 10^{16} \text{ cm}^{-2}$).

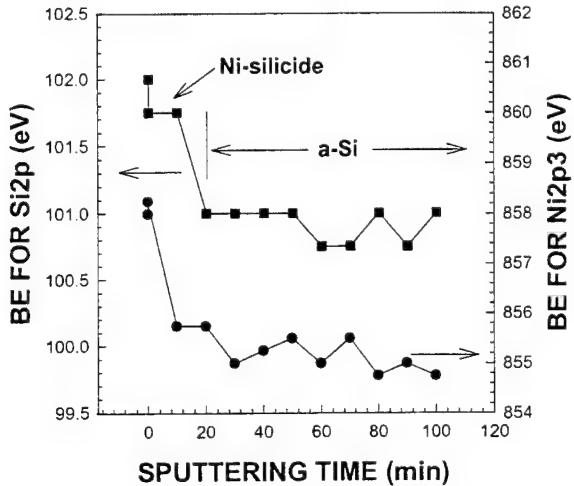


Figure 3. Variation of Ni and Si binding energy as a function of sputtering time.

3. A-Si:H TFT WITH NI SILICIDE

We fabricated a-Si:H TFTs with 3 different structures. Figure 4-(a) depicts the a-Si:H coplanar TFT in which Ni-silicide S/D is self-aligned to the gate. In the case of a-Si:H coplanar TFT⁴, conventional coplanar structures employing contact windows can not be accepted because of the high resistance ($\sim 10^6 \Omega/\square$) of n⁺-doped a-Si:H, even if a process margin of $\pm 1 \mu\text{m}$ was considered. The Ni-silicide S/D was self-aligned to a gate with a 120-nm offset³ when the gate insulator was wet-etched in a 10%-buffered HF solution. Thus, the series resistance could be minimized. We applied this low resistance Ni-silicide to the fabrication of a-Si:H TFTs with an etch stopper (ES) (b) and a back-channel etched (BCE) (c).

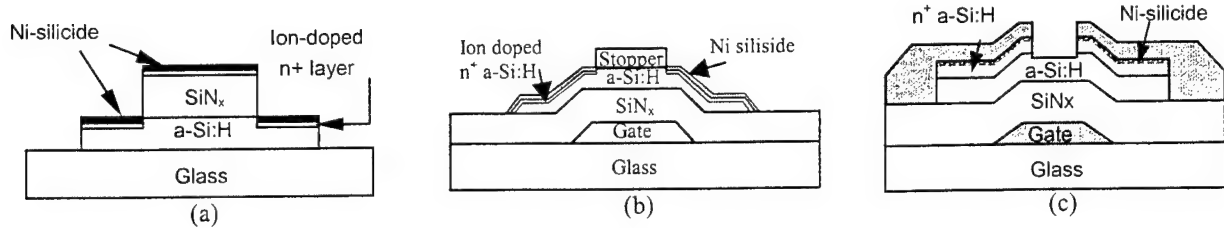


Figure 4. Cross-sectional views of the fabricated TFTs: coplanar a-Si:H (a), ES a-Si:H(b), BCE a-Si:H (c).

3.1. N⁺ contact

Figure 5 shows the field effect mobility (μ_{fe}) for the a-Si:H TFT with different (Al and Ni) S/D contact materials. The field effect mobility was obtained in the saturation region. The field effect mobility increases with annealing temperature. The field effect mobility of the TFTs using Ni and Al S/D contacts increases with the same rate until 150°C annealing. This is due to the improvement in the contact resistance for the two a-Si:H TFTs¹³. However, at 200 °C annealing, the TFT mobility with Ni S/D contacts increases from 1.0 cm²/Vs to 1.22 cm²/Vs, while the Al contact showed a saturation in the mobility as shown in Fig. 5. This can be explained by lowering of contact resistance by the Ni-silicide formation. By measuring the drain current, I_D , in the linear region for the TFTs with different channel lengths, the Ni-silicide/n⁺ a-Si:H contact resistance was obtained¹⁴. It decreases from $1.45 \times 10^5 \Omega$ to $2.75 \times 10^4 \Omega$ by increasing the annealing temperature from 150 °C to 240 °C. The Al-contacted TFT shows an increase in mobility at 220 °C in Fig. 5. But this is due to a hillock formation¹⁵ and Al penetration into n⁺ a-Si:H degrades the off-state leakage current.

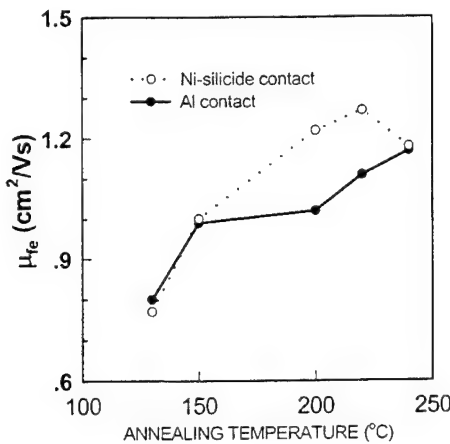


Figure 5. Changes in the field effect mobility of the a-Si:H TFTs with Ni-silicide and Al S/D contacts. W/L = 12 μm/6 μm.

3.2. Coplanar a-Si:H TFT

Figure 6 shows the field effect mobility and transfer characteristics of the coplanar, self-aligned a-Si:H TFT at $V_d = 0.1$ V. The coplanar a-Si:H TFT exhibits a field effect mobility of 0.6 cm²/Vs and a threshold voltage of 2 V. The field effect mobility and the threshold voltage were determined using the following expression for trans-conductance, g_m , in the linear region:

$$g_m = \left. \frac{\partial I_d}{\partial V_g} \right|_{V_d \approx 0.1} = \mu_{fe} C_i \frac{W}{L} V_d \quad (2)$$

where, W/L , C_i , μ_{fe} are the ratio of channel width to length, gate insulator capacitance, and field effect mobility, respectively. The transfer characteristics in linear scale at $V_d = 0.1V$ are inserted in Fig. 6. The field effect mobility and threshold voltage obtained from the inset of Fig. 6 are $0.58 \text{ cm}^2/\text{Vs}$ and 2.5 V , respectively, using the relation in linear region at $V_d = 0.1 \text{ V}$.

$$I_d = \mu_{fe} C_i \frac{W}{L} (V_g - V_T) V_d \Big|_{V_d \approx 0.1} \quad (3)$$

The major advantage of the new process is that in our TFT, gate and S/D Ni-silicide layers were formed simultaneously, resulting in a self-aligned structure. There is no overlap capacitance between gate and S/D, leading to a zero feed-through voltage. This is of interest since a LCD panel increases in size, making it more difficult to obtain a good quality LCD panel. The field effect mobility obtained from the trans-conductance and from the transfer characteristics at $V_d = 0.1 \text{ V}$ are almost the same. The field effect mobility, threshold voltage and the on/off current ratio of the coplanar a-Si:H TFT obtained from the present work are almost the same as those of typical inverted staggered a-Si:H TFTs. However, the present TFT has an advantage of small parasitic capacitance which is important for high performance large-area liquid crystal displays⁴.

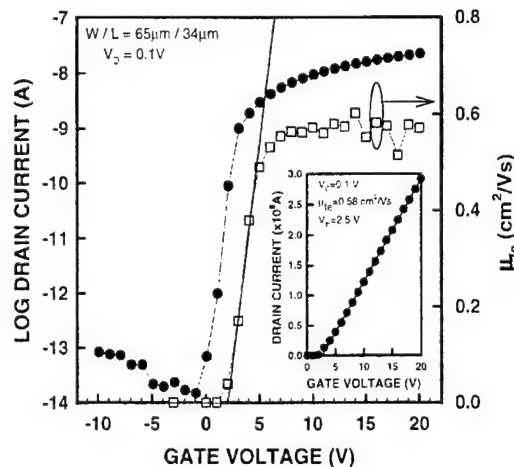


Figure 6. Plot of square root of the drain current versus gate voltage for an a-Si:H TFT using Ni-silicide and ion doped n⁺ a-Si:H layers.

3.3. 4-mask process for a-Si:H TFT array

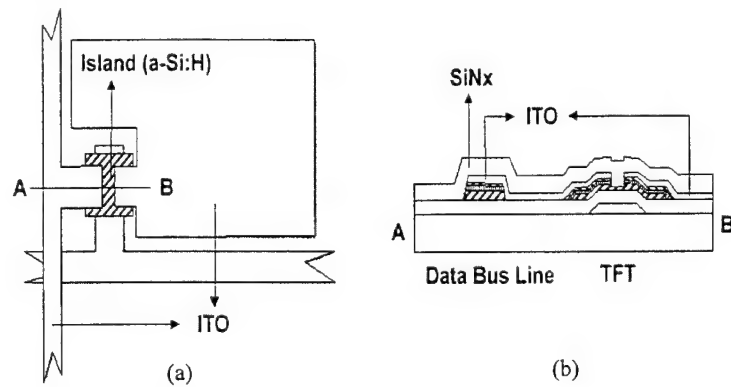


Figure 7. Schematic diagram of 4-mask TFT-arrays using Ni silicide: plan view (a), and cross-sectional view (b).

We developed a high performance, inverted staggered a-Si:H TFT, in which a thin Ni-silicide layer is inserted between an n⁺ a-Si:H and an ITO. The Ni-silicide can be formed at as low as 230 °C. The fabricated TFT exhibited a field-effect mobility of 1.48 cm²/Vs, a threshold voltage of 5.9 V, a subthreshold slope of 0.54 V/dec, an on/off current ratio of ~10⁸ and an off-state leakage current of 3×10^{-14} A at the drain voltage of 5 V and the gate voltage of -5 V.

A 4 - mask TFT array process can be possible using the Ni-silicide. The fabrication procedure as follows: First, a metal film is deposited on the glass substrate (Corning 1737), then patterned for the gate bus lines (1st mask). Then, SiN_x, a-Si:H, n⁺ a-Si:H are consecutively deposited by PECVD without breaking the vacuum and then the Ni layer is deposited on the top of n⁺ a-Si:H and then patterned (2nd mask) for the islands and the data bus lines. The ITO was deposited by sputtering and then patterned for TFT channel and the data bus lines (3rd mask). Finally, a passivation layer of SiN_x was deposited and then it is patterned for the contact (4th mask) for the driver connections.

3.4. Self-aligned a-Si:H TFT using a SiOF etch stopper

We used the low resistance Ni-silicide to the fabrication of a completely self-aligned a-Si:H TFT. Figure 8 shows the log I_d–V_g characteristic of the a-Si:H TFTs with different ion-stoppers, SiOF and SiN_x. The TFT with a SiOF ion-stopper has a field effect mobility of 0.52 cm²/Vs and a threshold voltage of 4.72 V, while the TFT with a SiN_x ion-stopper has a field effect mobility of 0.42 cm²/Vs and a threshold voltage of 4.30V. The better performance of the SiOF TFT appears to be due to the fluorine incorporation at the a-Si:H/SiN_x interface and the defect passivation by fluorine incorporation².

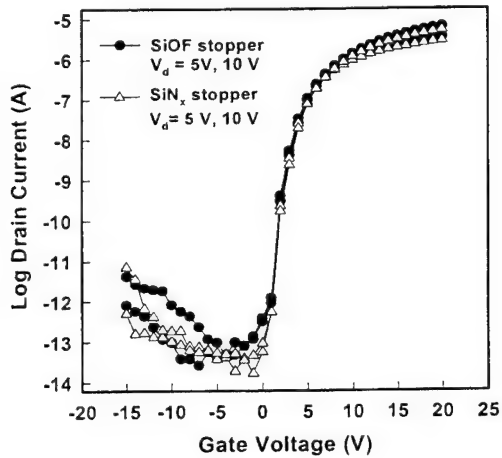


Figure 8. Transfer characteristics of the completely self-aligned TFTs.

Figure 9 shows the top and cross-sectional views of the pixel structure using a SiOF-ES. The SiOF acts as an interlayer also. The SiOF islands are formed in the TFT-regions and line-crossover regions for improving the TFT performance and reducing the line-capacitance, respectively.

The UXGA (1600×3×1200) and XGA (1024×3×768)-resolution TFT-arrays were simulated for the 3-different TFT structures of SiOF-ES, SiN_x-ES, and BCE types to compare the gate-pulse delay and the results were plotted in Fig. 9. Equivalent circuit models for a TFT-LCD can be found in the literatures¹⁶⁻¹⁷. The inset in Fig. 9 shows the simulated signal delays for the 3-different structures. The SiN_x thickness of the gate insulator was fixed at 300 nm. And the crossover area of the gate/data line was 10 μm × 8 μm. The dielectric constants of the SiN_x and SiOF were 7.4 and 3.4, respectively. The signal delay (99%-charging) for the SiOF-ES, SiN_x-ES, and BCE structures were 1.8 μs, 2.1 μs, and 2.6 μs in XGA array, and 2.2 μs, 2.6 μs, and 3.5 μs in UXGA array, respectively.

Thinning the gate insulator is important to decrease the threshold voltage of TFT and thus the driving voltage of TFT-LCD can be reduced. For bottom-gate a-Si:H TFTs, however, a thin gate insulator is unacceptable because thinning gate insulator leads to an increase in capacitance between the gate and data lines. In this case, a low dielectric constant SiOF layer that acts

as both the stopper and the line-interlayer can be much more appropriate for reducing the capacitance and thus the RC delay.

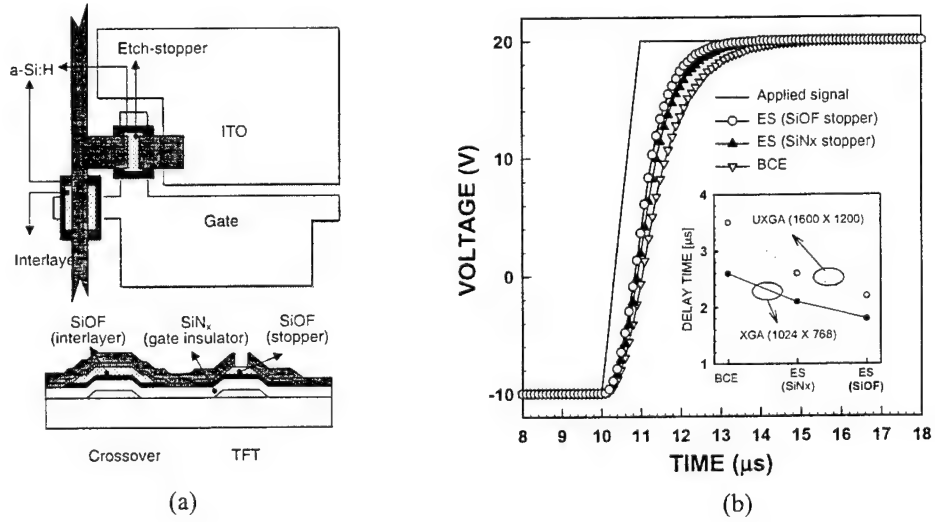


Figure 9. The plan and cross-sectional views of the pixel structure of a TFT-LCD for the application of a SiOF etch stopper (a), and the charging behavior of a pixel during gate pulse and the delay signal waveform for the three-different structures (b). A resolution of UXGA was used.

4. LOW TEMPERATURE POLY-SI TFT BY NI SMC IN AN ELECTRIC FIELD

4.1. Low temperature activation of S/D region

Figure 10 shows the Raman spectroscopy of a ELA poly-Si before (a) and after (b) an ion shower doping. The ion doping damages the lattice structure and thus an amorphous phase centered at 490 cm^{-1} appears after ion doping. Note that the Ni-silicide can be easily formed on a-Si:H than on poly-Si¹⁸. In our experiment, the poly-Si is amorphized after ion shower and this enhances the silicide formation. By using this method, S/D contact resistance can be reduced and thus a high performance ELA poly-Si TFT can be obtained without an addition activation of n⁺ layer after ion doping.

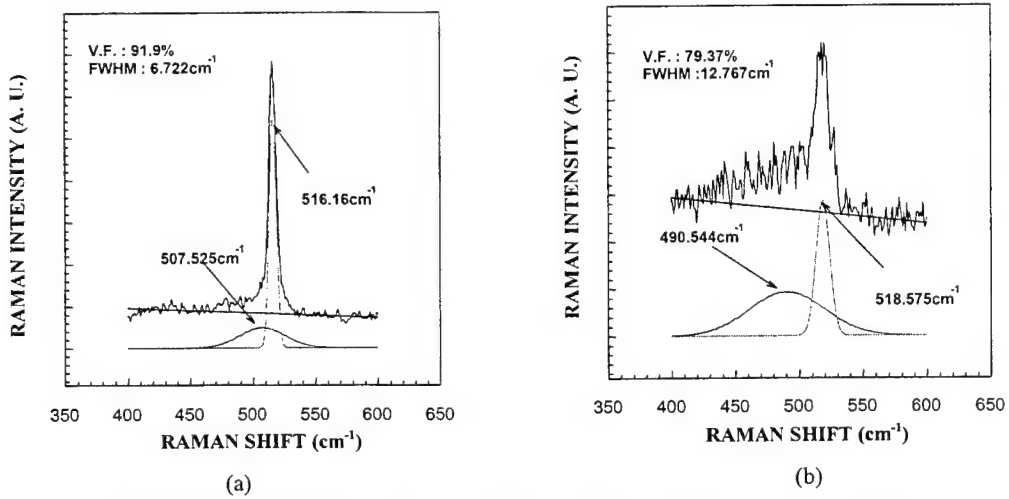


Figure 10. Raman spectra of the poly-Si before (a) and after ion shower doping (b).

4.2. High performance SMC poly-Si TFT

Poly-Si TFTs on glass substrate are of interest for active matrix liquid crystal displays (AMLCD's) and active matrix organic light emitting diodes (AMOLED's). The high field effect mobility ($100 \text{ cm}^2/\text{Vs}$) of poly-Si TFT enables the integration of peripheral drive circuits on glass substrate and decreases the TFT area for display, thus realizing higher resolution and more compact display. A key step for a low temperature poly-Si TFT is to make a high mobility, uniform poly-Si film on glass substrate.

Recently, we developed a new crystallization method^{12, 19} called a SMC. A-Si with Ni area density of $2 \times 10^{13} \text{ cm}^{-2}$ can be crystallized by heating it for 10 minutes in a modest electric field²⁰. It was found that the TFT performance improves with decreasing Ni density on the a-Si:H. But we need a critical density to make a complete crystallization over whole area²⁰. Figure 11 shows the transfer characteristics of a SMC poly-Si TFT using an average Ni thickness of 0.15 Å. The off-state leakage current is $1.1 \times 10^{-11} \text{ A}/\mu\text{m}$ at the drain voltage of 5 V and the gate voltage of -6 V. The on-off current ratio is $> 7 \times 10^5$ at the drain voltage of 5 V. The TFT exhibited a field effect mobility of $120 \text{ cm}^2/\text{Vs}$, a threshold voltage of -1.5 V and a sub-threshold slope of 0.5 V/dec.

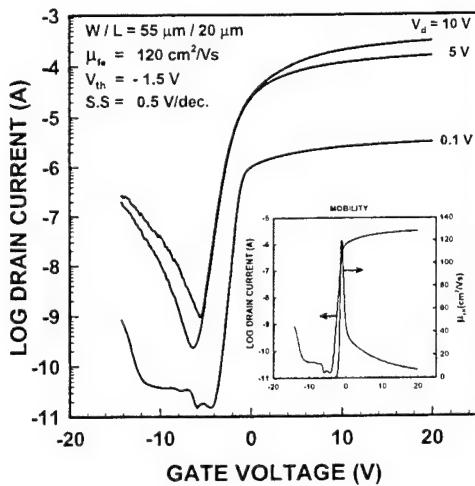


Figure 11. Transfer characteristics of a SMC poly-Si TFT using average Ni thickness of 0.15 Å. The inset shows its field effect mobility.

4.3. A comparison of a SMC poly-Si TFT with an ELA poly-Si TFT

The SMC in an electric field, a technique more compatible with batch processing than ELA, was developed for the low temperature poly-Si TFT-LCD²¹.

Figure 12 shows the transfer characteristics for the poly-Si TFTs with a Ni-SMC poly-Si and an ELA poly-Si with a self-aligned coplanar structure. Both ELA and SMC poly-Si TFTs were fabricated by using the same process except for the crystallization method. The grain size of the ELA poly-Si was 400 nm, which was obtained through the optimization of laser intensity. The Ni-SMC poly-Si TFT exhibited a subthreshold slope of 0.6 V/dec and on/off current ratio of $\sim 1.1 \times 10^6$ at $V_d = 0.1 \text{ V}$. The ELA poly-Si TFT exhibited a subthreshold slope of 0.5 V/dec and on/off current ratio of $\sim 2.8 \times 10^4$ at $V_d = 0.1 \text{ V}$. The off-state leakage current of the SMC poly-Si TFT is $\sim 7 \times 10^{-12} \text{ A}/\mu\text{m}$ at $V_d = 5 \text{ V}$ and $V_g = -6 \text{ V}$ and higher than that ($2 \times 10^{-12} \text{ A}/\mu\text{m}$) of an ELA poly-Si TFT. Both TFTs show similar tendency in subthreshold region and on region.

It is well known that poly-Si has many trap states in grain boundaries and these states take charge carriers and build up potential barriers to the flow of carriers. The presence of a potential barrier at a grain boundary and thus additional scattering leads to a field effect mobility degradation. The high density of trap states deteriorates a subthreshold slope, increases threshold voltage and leakage current. It is believed that the leakage current by the field-enhanced tunneling of electron from the valence band to the conduction band via grain boundary traps. But in the Ni MILC poly-Si TFT it is found

that the leakage does not depend on the Ni contamination in the poly-Si if it is not very high²². The Ni impurity on the off-state leakage current of the SMC poly-Si TFT is being studied in our lab and will be published.

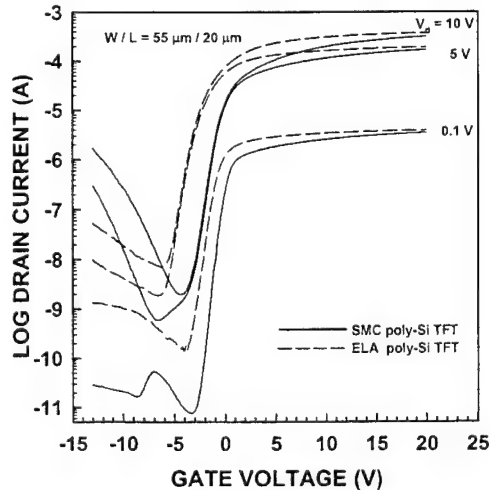


Figure 12. A comparison of a SMC poly-Si TFT with an ELA poly-Si TFT.

5. CONCLUSION

Low resistance Ni-silicides can be formed on a-Si:H at low temperatures less than 250°C and thus applied for high performance a-Si:H and poly-Si TFTs in various forms. The high field effect mobility a-Si:H TFT of $> 1.4 \text{ cm}^2/\text{Vs}$ has been obtained by using the low resistance Ni-silicide as contacts. We found that ion shower promotes the silicide formation for a TFT contact because the poly-Si was amorphized by an ion shower. In addition the NiSi_2 , having the same lattice structure as Si with only 0.4 % lattice constant difference, can be formed on a-Si at 350°C. The crystallization proceeds from these NiSi_2 precipitates. The crystallization of a-Si can be done at 500°C in 10 minutes in an electric field. A SMC poly-Si TFT having a similar TFT performance with an ELA-poly-Si TFT, has been developed.

REFERENCES

1. S.Y. Yoon, J. H. Choi, H. C. Kim, J.Y. Oh, C. S. Kim, S. M. Pietruszko, C. O. Kim, and J. Jang, "Low temperature Ni silicide formation and its application to source/drain contacts for a-Si:H TFTs," *AMLCD '97 Digest*, pp. 223-226, 1997.
2. K. W. Kim, K. S. Cho, J. I. Ryu, K. H. Yoo, and J. Jang, "Amorphous silicon thin film-transistor with a fluorinated silicon oxide ion stopper," *IEEE Electron. Device. Lett.*, to be published.
3. S. K. Kim, Y. J. Choi, K. S. Cho, and J. Jang, "Coplanar amorphous silicon thin film transistor fabricated by inductively coupled plasma chemical vapor deposition," *J. Appl. Phys.* **84**, pp. 4006-4012, 1998.
4. S. K. Kim, Y. J. Choi, W. K. Kwak, K. S. Cho, and J. Jang, "A novel coplanar amorphous silicon thin-film transistor using silicide layers," *IEEE Electron Device Lett.* **20**, pp. 33-35, 1999.
5. J. I. Ryu, H. C. Kim, S. K. Kim, and J. Jang, "A novel self-aligned polycrystalline silicon thin-film transistor using silicide layers," *IEEE Electron Device Lett.* **18**, pp. 272-274, 1997.
6. K. H. Lee, J. K. Park, and J. Jang, "A high-performance polycrystalline silicon thin film transistor with a silicon nitride gate insulator," *IEEE Trans. Electron Devices* **45**, pp. 2548-2551, 1998.
7. H. J. Lim, B. Y. Ryu, J. Jang, "N-channel polycrystalline silicon thin film transistors using as-deposited polycrystalline silicon and ion doping," *Appl. Phys. Lett.* **66**, pp. 2888-2890, 1995.
8. C. Y. Chen, and J. Kanicki, "Origin of series resistances in a-Si:H TFTs," *Solid -States Electronics* **42**, pp. 705-713, 1998.
9. S. Luan, and G. W. Neudeck, "An experimental study of the source/drain parasitic resistance effects in amorphous silicon thin film transistors," *J. Appl. Phys.* **72**, pp. 766-772, 1992.

10. C. F. Yeh, T. J. Chen, C. Liu, J. Shao, and N. W. Cheung, " Application of plasma immersion ion implantation doping to low-temperature processed poly-Si TFT's," *IEEE Electron Device Lett.* **19**, pp. 432-434, 1998.
11. G. K. Giust and T. W. Sigmon, " Self-aligned aluminum top-gate polysilicon thin-film transistors fabricated using laser recrystallization and gas-immersion laser doping," *IEEE Electron Device Lett.* **18**, pp. 394-396, 1997.
12. J. Jang, J. Y. Oh, S. K. Kim, Y. J. Choi, S. Y. Yoon, and C. O. Kim, "Electric-field-enhanced crystallization of amorphous silicon," *Nature*, **395**, pp. 481-483, 1998.
13. J. Jang, K. W. Kim, "Silicide electrode technologies for high-performance poly-Si TFTs," *AMLCD '99 Digest*, pp. 235-238, 1999.
14. C-S Chiang, C-Y. Chen, and J. Kanicki, "Gate-four-probe a-Si:H TFT structure : a new technique to measure the intrinsic performance of a-Si:H TFT," *AMLCD '97 Digest*, pp. 67-70, 1997.
15. M. Ikeda, "TFT-LCD gate and data bus-line design and process technology," *SID '95 Digest*, pp. 11-15, 1995.
16. K. Khakzar and E. H. Lueder, "Modeling of amorphous-silicon thin-film transistors for circuit simulations with SPICE," *IEEE Trans. Electron Devices*, **39**, pp. 1428-1434, 1992.
17. H. Aoki, "Dynamic characterization of a-Si TFT-LCD pixels," *IEEE Trans. Electron Devices*, **43**, pp. 31-39, 1996.
18. C. Calandra, O. Bisi and G. Ottaviani, "Electronic properties of silicon-transition metal interface compounds," *Surface Science Reports*, **4**, 271-364, 1985.
19. Y. J. Choi, W. K. Kwak, S. J. Park, J. Jang, S. Y. Yoon and C. O. Kim, "A low-temperature poly-Si TFT with a SMC poly-Si crystallized at 420 °C," *SID 99 Digest*, pp.508-511, 1999.
20. J. Jang, S. J. Park, K. H. Kim, B. R. Cho, W. K. Kwak, "Polycrystalline silicon produced by Ni-silicide mediated crystallization of amorphous silicon in an electric field," *J. Appl. Phys.* **88**, 2000, to be published.
21. S. Y. Yoon, K. S. Cho, S. J. Park, B. R. Cho, "High Quality Poly-Si Crystallized at 400 °C by Field Enhanced SMC," *SID '00 Digest*, to be published.
22. D. Murley, N. Young, M Trainor and D. McCulloch, "Laser annealed-metal induced lateral crystallization (L-MILC) poly-Si TFT," *AM-LCD 2000 Digest*, to be published.

High Contrast SXGA Silicon Light Valves for High Definition Video Projectors

H. C. Huang*, P. W. Cheng and H. S. Kwok

Department of Electrical and Electronic Engineering

The Hong Kong University of Science and Technology, Clear Water Bay, Hong Kong

ABSTRACT

We have developed a highly integrated liquid-crystal-on-silicon light valve for three-panel color projector. The silicon panel was designed and fabricated by a $0.35\mu m$, 3-metal and dual-voltage CMOS process with a spatial resolution of 1280×1024 pixels. The pixel pitch was $12\mu m$, the fill factor was 90% and the display area was 0.77" in diagonal. Eight-bit digital data drivers and gamma-correction circuitry were integrated into the silicon panel for true gray scale and full color representation. The display panel was assembled with a mixed twisted nematic and birefringence liquid crystal cell for high contrast at CMOS compatible voltage. Contrast ratio was typically 200:1 at $5.5V_{rms}$. In addition, silicon surface layers, liquid crystal materials, pixel structures and driving schemes were carefully optimized for the minimization of visual flicker. Flicker ratio of less than 3% was achieved at 60Hz frame rate. The optical sub-system utilized a trichroic prism assembly for both color separation and recombination. With this trichroic prism assembly incorporating three silicon light valves, a compact and high-contrast SXGA video projector was demonstrated.

Keywords: Silicon light valve, video projector

1. INTRODUCTION

Current liquid crystal video projectors mainly rely on transmissive thin film transistor liquid crystal display (TFT-LCD) for image generation. The major drawback of this kind of projector is low aperture ratio of the TFT-LCD and hence, low light efficiency of the projector system. The aperture ratio of a high-resolution XGA TFT-LCD, which has 1024×768 pixels, is only 0.5 [1]. In addition to low light efficiency, the low aperture ratio also introduces black grids or pixelation. Depixelization is often necessary through microlens, and adds complexity to the optical system design.

Reflective-mode silicon light valve based on liquid-crystal-on-silicon technology can overcome this drawback of the TFT-LCD projector. The aperture ratio of the silicon light valve can be as high as 90%, since all the electronics are hidden beneath reflective mirrors of pixel [2]. As a result, the light efficiency and quality of projected image are greatly improved. Moreover, fabrication process of the silicon light valve is consistent with standard silicon VLSI technology. Display drivers and other electronic functions can be fully integrated onto the silicon light valve, and makes a whole display system on a chip possible.

In our previous work, we have developed a highly integrated liquid-crystal-on-silicon XGA video projector [3]. In this paper, we describe the development of another highly integrated liquid-crystal-on-silicon SXGA video projector of higher resolution, higher contrast and better performance. The silicon panel of 1280×1024 spatial resolution was designed with sub-micron design rules and fabricated by a custom CMOS technology emphasizing on back-end planarization. Very advanced display driver and very fine pixel were integrated together as a self-contained and high-resolution display panel. The silicon panel has low-voltage devices for logic control and data inputs. The silicon panel has also high-voltage devices for efficiently driving liquid crystal (LC) cell. We chose to assemble a reflective mixed twisted nematic and birefringence (MTB) LC cell on the panel. The MTB mode has advantages of high reflectance and high contrast at CMOS compatible voltage. Silicon surface layers, liquid crystal materials, pixel structures and driving schemes were carefully optimized for the minimization of visual flicker. In order to incorporate three silicon light valves in a compact manner, a trichroic prism assembly (TPA) of high fidelity was developed. This TPA can efficiently separate and recombine three primary colors for three silicon light valves, and lead to a compact and high definition SXGA video projector.

*Correspondence: Email: eehuang@ust.hk

2. THE SILICON PANEL

The heart of this high-definition video projector is the silicon panel, which integrates display drivers and fine pixel array together. Figure 1 shows a functional block diagram of the SXGA silicon panel. The display is easy to be interfaced with only two control signals, one pixel clock and one scan clock. The control signals are responsible for display data manipulation and signal synchronization. Whereas, FLM marks the first row of data and DISP points to the first pixel of each active row. The data drivers have 8-bit resolution and are divided into odd and even columns for ease of layout. The partition of the pixel array into odd and even columns also reduces the pixel clock by one half.

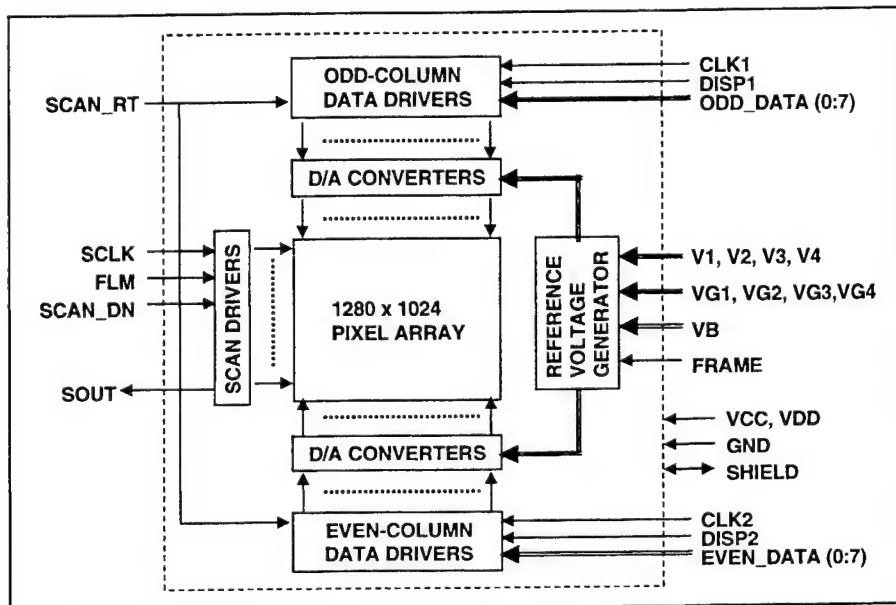


Figure 1 Functional block diagram of the SXGA silicon panel.

Pixel data are shifted in series to the data drivers and transferred in parallel to the D/A converters where D/A conversions are performed. Gamma-correction circuitry is integrated onto the silicon panel in order to generate reference voltages for the D/A conversions. Fine tune of the reference voltages is possible through the external gamma correction voltages VG1, VG2, VG3 and VG4 for red, green and blue light illuminations.

The silicon panel can accept standard 3.3V digital logic input at a pixel rate of 108MHz for the SXGA signal. The panel can further raise the voltage level up to 5.5Vrms through built-in level shifters for efficiently driving the LC cell. Bi-directional scanning feature was included for both the horizontal data drivers and vertical scan driver. The display panel had 1280 x 1024 spatial resolution in mosaic arrangement. The pixel pitch was 12 μ m and the fill factor was 90% as a result of 0.35 μ m layout rules. The display area is 0.77" in diagonal and the die size is 1.0" in diagonal. Figure 2 shows photograph of a packaged SXGA silicon light valve. The data drivers are on the top and bottom, the scan driver is on the right, and the pixel array is the center.

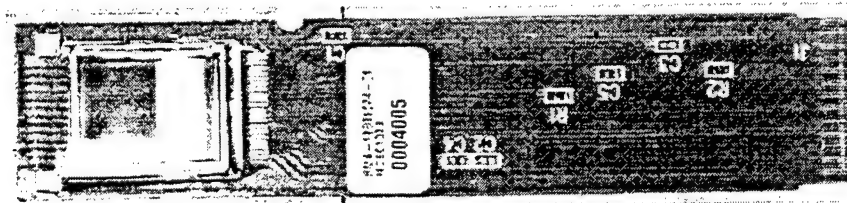


Figure 2 Photograph of a packaged SXGA silicon light valve.

Because the silicon panel is used as back plane for the silicon light valve, surface finish is very important. The CMOS fabrication process employs a back-end planarization process to ensure an optically flat silicon surface. Local topographic variation of less than 100Å within the pixels and global topographic variation of less than 500Å among pixels were achieved. With this back-end planarization process, optical performance of the silicon light valve was greatly improved. The improvements were three folds. Firstly, the flat surface improved mirror quality of the pixel metal, and hence, the optical reflectance was increased. Secondly, the flat surface improved liquid crystal alignment in the LC cell fabrication at a later stage. Reliability and performance of the LC cell were got better. Finally, a dielectric mirror was coated onto the pixel metal for further improvement of the metal reflectivity. The reflectivity of the pixel metal was expanded from 86% of bulk metal to more than 95% within the visible spectrum. In addition, there was a light shield beneath gaps of the pixels for light leakage protection. Light leakage into the silicon substrate could generate photocurrent and preclude proper circuit operation. The light shield could absorb most of the penetrated light and reflect only a small portion of the incident light back to the LC cell. Figure 3 shows reflectivity of the bare metal, the dielectric mirror and the black matrix.

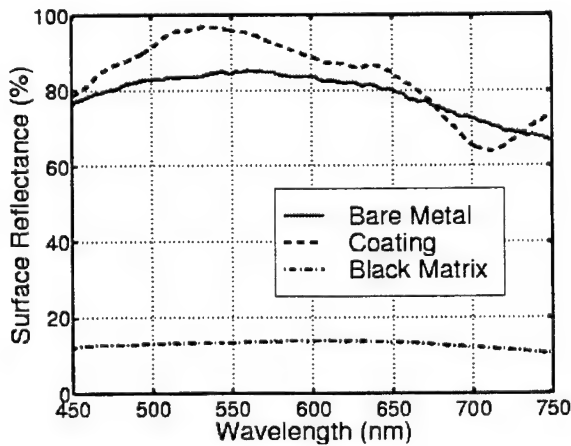


Figure 3 The reflectivity of the pixel metal, the dielectric mirror and the light shield.

3. REFLECTIVE LCD MODES

The silicon panel can accept and generate electronic image on the panel. The reflective LC cell on top of the silicon panel is to convert the electronic image into the optical image through optical modulation. One important criterion for the LC cell is to do efficient conversion at CMOS compatible voltage. The LC cell should also be able to give the best optical reflectance. Wavelength dispersion is usually not a concern since narrow-band red, green and blue lights will be used in the projector. In addition, the cell gap should be in the range of 3 to 4μm for ease of cell assembly and to maintain a good aspect ratio with the pixel pitch of 12μm. For these requirements, the normally white (NW) mode operated with a polarizing beam splitter (PBS) is preferred [4].

The common NW modes are the ECB, TN-ECB [5], MTN [6] and the SCTN [7] modes. All these LCD modes can be characterized by three parameters; twist angle, ϕ , retardation, $d\Delta n$, and polarizer angle, α . Here, d is the cell gap, Δn is the LC birefringence and α is the angle between the polarizer axis and the input director of the LC cell. By searching parameter space of ϕ , $d\Delta n$ and α , we have identified a set of LCD modes with 100% reflectance. These are called the mixed twisted nematic and birefringence (MTB) modes. The advantage of the MTB mode is the combination of twisted nematic and birefringence effects for optical modulation. As a result, high contrast can be achieved at low voltage.

We assembled a MTB mode onto the silicon substrate and performed reflectance-vs-voltage characterization with a DMS machine. A narrow-band PBS was used to direct the incident light onto the MTB LC cell and reflect the modulated light back to the DMS machine. Figure 4 shows characterized reflectance-vs-voltage curves of the MTB LC cell under red, green and blue light illuminations. The contrast ratios were 270:1, 190:1 and 150:1, respectively, for the red, green and blue light illuminations. The contrast ratio was typically 200:1 for the white light illumination.

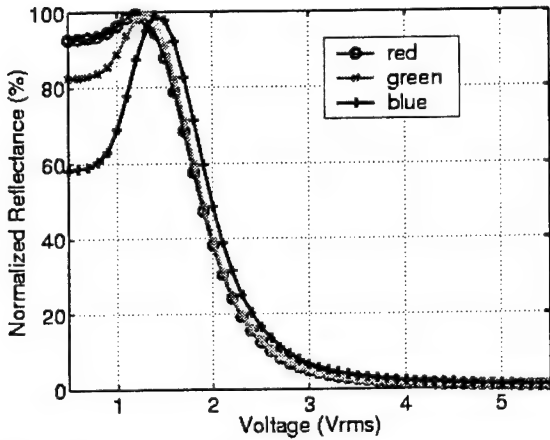


Figure 4 The characterized reflectance-vs-voltage curves of the MTB LC cell on the SXGA silicon panel.

With polynomial curve fitting of the reflectance-vs-voltage curve of the green, we proceeded to obtain gamma-correction network of the green in order to generate gamma-correction reference voltages for the green silicon light valve. This gamma-correction network of the green was integrated onto the silicon panel. The reflectance-vs-voltage curves of the red, green and blue have a similar shape, but appears in different voltage ranges. Whereas, the red curve appears to the left of the green curve and the blue curve appears to the right of the green curve. The gamma corrections of the red and blue could be obtained through the same gamma-correction network of the green by tuning four external gamma correction voltages. Whereas, VG1, VG2, VG3 and VG4 defined 100%, 75%, 25% and 0% reflectance of the reflectance-vs-voltage curves, respectively. A shift of these four voltages to the left defined the red reflectance-vs-voltage curve, while a shift to the right defined the blue curve, as shown in Figure 5. In this arrangement, we were able to obtain linear gray scales for the red, green and blue images on the same silicon light valve. The gamma corrections are deemed required in order to implement a full-color video projector.

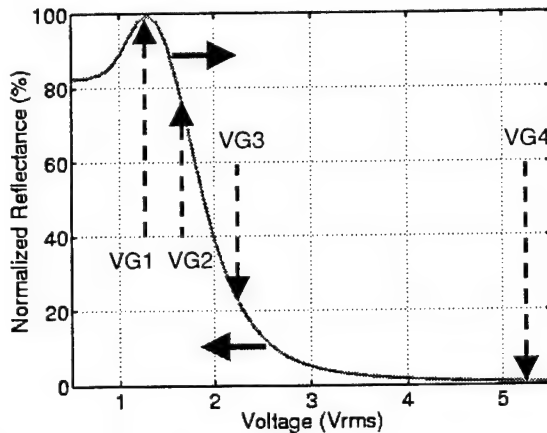


Figure 5 Fine tune of the green curve of the MTB cell through four gamma correction voltages.

4. OPTICAL SYSTEM

The optical projector requires an optical sub-system to separate the three primary colors from the input white light source, and another sub-system to recombine the three primary colors after modulation by the reflective silicon light valves. The former color separator and the color recombiner can be the same piece of optics or they can be physically different. The former uses one PBS for all the three LCD panels while the latter employs three PBS for 3 LCD panels.

For a compact optical projector design, we used a trichroic prism assembly (TPA) for both the color separator and recombiner. The optical system using the PTA and one PBS for all the three LCD panels are shown in Figure 6. In this optical system, a PBS first polarizes the light beam from the metal halide lamp. The *s*-polarization light after the polarization then enters the TPA in which the blue part of the light beam is reflected by surface BC. Thereafter, this blue light is totally internally reflected by surface AB, and illuminates the blue LCD panel. The reflected light from the blue LCD panel after modulation will be *p*-polarized. This reflected *p*-polarized light beam retraces the same light path of the incident *s*-polarized beam.

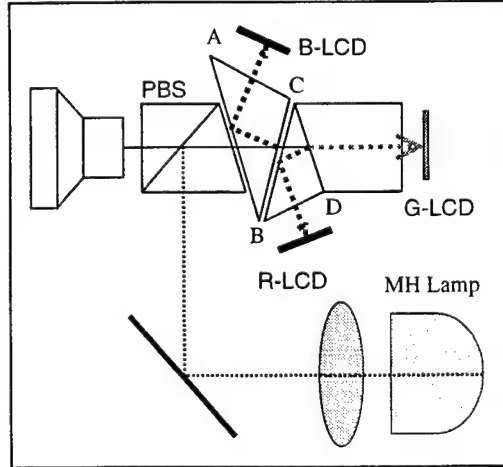


Figure 6 Layout of the compact optical projector with one PTA and one PBS.

The same is true for the other two primary colors. Whereas, the red part of the light beam is reflected by surface CD, totally internally reflected by surface BC, and illuminates the red LCD panel. The green part of the light beam goes through surfaces BC and CD and illuminates the green LCD panel. Both the reflected red and green *p*-polarized light beams also retrace the same paths of the incident *s*-polarized beams. As a result, the TPA acts as both a color separator for *s*-polarized light, and as a color recombiner for *p*-polarized light. We used a collimated Oriel metal halide lamp with grating as light source to characterize color fidelity of the TPA. Figure 7 shows measured red, green and blue reflectance spectra for this TPA. From the results, it can be seen that there is negligible *s*-*p* polarization split. The spectra for both *s*-polarized and *p*-polarized light are very sharp and identical. Hence, this TPA is good for a compact color projector application.

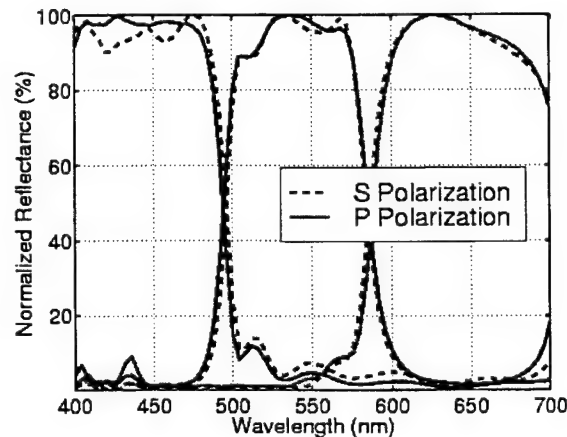


Figure 7 Measured red, green and blue reflectance spectra of the TPA.

5. ON THE MINIMIZATION OF VISUAL FLICKER

Flicker is the major visual defect of the silicon light valves. The silicon light valve depends on active devices to apply driving voltages to the pixels during address time and ability of the pixels to conserve the voltage for the rest of frame time. To avoid chemical degradation of the LC material, an alternating voltage waveform has to be applied to the LC cell. For this purpose, several modes of polarity inversion including frame, column, row and dot inversions are adopted. Each mode has its advantages and disadvantages. The frame inversion is commonly used in the silicon light valve for the purpose of minimizing lateral electric field in small pixels. The lateral electric field can result in an undesired reverse tilt domain in each pixel and lead to poor contrast ratio of the display [8]. While the frame inversion is good for minimizing the lateral field effect, it also produces higher degree of flicker and image retention compared with other modes of polarity inversion.

5.1. FLICKER MODEL

Flicker and image retention can be characterized by monitoring luminance of the same image on the display in alternative frames. A larger luminance difference corresponds to a higher degree of flicker. We defined the flicker as the ratio the AC root-mean-squared luminance over the DC root-mean-squared luminance. Since the luminance is controlled by pixel voltage, the flicker can also be characterized through monitoring of the pixel voltage. The voltage retention capability of the pixel is described by an equivalent circuit consisting of a storage capacitor connected to ground and a LC cell capacitor with a parallel leakage resistance connected to a common electrode on the glass plate.

The voltage holding ratio (VHR) is defined as the ratio of the root-mean-squared voltage divided by the applied voltage pulse on a pixel electrode. The value is mainly determined by the RC time constant of the LC pixel and auxiliary storage capacitor. The RC time constant can be calculated from resistivity and dielectric constant of the LC material and geometry of the pixel. There are two causes for the decrease of the VHR. One is leakage current through the pixel transistor. The other is existence of a depolarization field caused by the accumulation of extra charges on the surface of the LC cell. In addition, there are different conduction mechanisms in polar liquids in combination with other dielectric layers in the silicon light valve. The conduction mechanism can perturb charge distribution within the LC element and enhance the flicker and image retention. This conduction mechanism can be represented by a residual DC (R-DC) charge on the pixel.

In addition to the LC cell and pixel transistor, word and bit line voltages can also contribute to the flicker. The word line turns on the pixel transistor for charging. But the pixel voltage is dropped slightly through parasitic capacitor coupling when the word line turns off. The bit line voltage varies randomly and perturbs the pixel voltage randomly. But the perturbation becomes coherent when the polarity of the inversion is changed. These two couplings can be represented by two parasitic capacitors connected from the pixel to the word and bit lines, respectively. A flicker model of the pixel is illustrated in Figure 8.

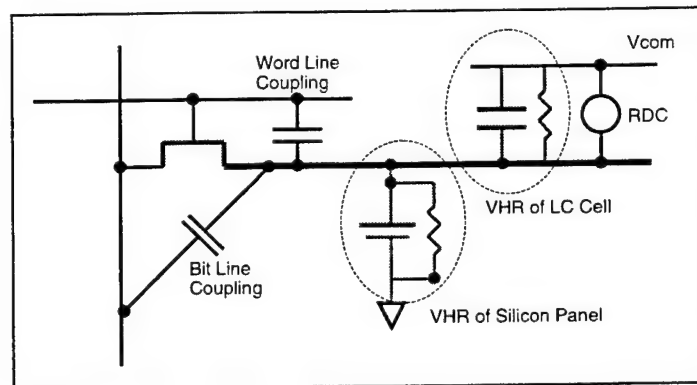


Figure 8 Flicker model of the pixel in silicon light valve.

5.2. FLICKER CHARACTERIZATIONS

For these four flicker mechanisms, we have designed four experiments to investigate causes of flicker and determine parameters of the flicker model. The first one was a capacitance-voltage (CV) measurement of the LC cell in order to determine the cell capacitance and parallel leakage resistance. The second one was an R-DC measurement of the LC cell in

order to determine extra charge accumulation on the surface of the LC cell. The third one was a VHR measurement of a pixel made by the LC cell, an external transistor and a storage capacitor. A short pulse of voltage was applied to the pixel during the address time and the charge was held by the pixel during the rest of frame time. Pixel voltage was buffered and amplified by a high-impedance operational amplifier and monitored by a digital oscilloscope. Voltage holding capability of the pixel was recorded.

The last one was a direct measurement of the flicker due to both the LC cell and silicon panel. The light valve was placed on a hot chuck and illuminated by different light intensities. A video pattern generator was used to drive the silicon light valve at different frame rates and different polarities of inversion. A photo detector in connection with a digital oscilloscope was used to monitor luminance of the projected image. Flicker was recorded and a DC offset voltage was increased on the common electrode until the flicker was minimized. Different driving schemes can also be applied to compensate for the flicker for different causes.

Figure 9 shows the flicker measurements of a XGA silicon light valve. There were three flicker mechanisms observed in the luminance curve. One was the hot-state R-DC voltage caused by the passivation layer. The second was the bit line coupling which occurred when the polarity of frame inversion is reversed. The third was insufficient VHR of the pixel transistor and storage capacitor. Through the temperature characterization, it was found that the insufficient VHR of the silicon panel was mainly due to the temperature, which increased the saturation current of the transistor and caused the pixel voltage to decay. Light leakage also reduced the VHR of the storage capacitor.

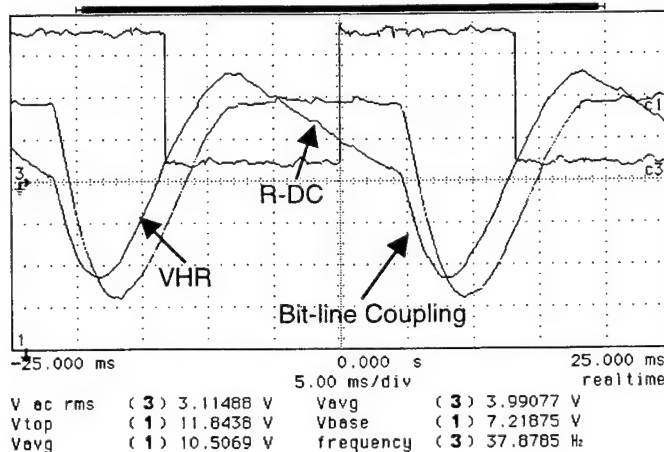


Figure 10 Flicker measurement of the SXGA light valve.

5.3. SOLUTIONS FOR FLICKER MINIMIZATION

Through these flicker characterizations, we have identified causes of flicker and proceeded to find solutions for the minimization of flicker. The R-DC charge accumulation was mainly caused by of different work functions of the ITO glass plate and silicon surface. Different passivation schemes have different work functions and affect the R-DC. From the R-DC measurements, we found that the bare metal had the smallest R-DC voltage, while the multi-layer passivation had the worst R-DC voltage. It was also found that the R-DC charge could be reduced by Vcom compensation.

The VHR of the LC cell was mainly determined by the specific resistivity of the LC mixture. A higher resistivity favored low VHR. It was found that the specific resistivity of the LC mixture had to be larger than $5 \times 10^{12} \Omega\text{cm}$ in order to achieve more than 97% VHR of the LC cell according to the VHR measurements.

The VHR of the silicon panel was determined by the temperature and light leakage. Whereas, the temperature increased exponentially the saturation current of the pixel transistor, and the light leakage drained the pixel charge through the storage capacitor. It was found that a good light shield protection is required to prevent from the light leakage. It was also found the temperature of silicon panel had to be reduced to room temperature in order to improve the VHR of the silicon panel.

The parasitic capacitor coupling was determined by magnitudes of parasitic capacitance and storage capacitance. A larger ratio of the storage and parasitic capacitance could reduce the coupling. It was found that a minimal ratio of 20 was required to minimize the coupling. However, a ratio of larger than 20 could not be achieved when the pixel was reduced to $10 \mu\text{m}$ pitch. It was found that imbalance driving was useful to compensate for the charge deviation caused by the word line coupling.

With all these optimizations on silicon surface layers, liquid crystal materials, pixel designs and driving schemes, we have reduced the visual flicker to an extent. Flicker ratio of less than 3% at 60 Hz frame rate was achieved for the SXGA silicon light valve under 150W light illumination.

6. SXGA VIDEO PROJECTOR PROTOTYPE

6.1 VIDEO INTERFACE CONTROLLER

We used a video interface controller to interface digital video inputs with three silicon light valves. The video interface controller consists of analog and digital parts. The digital part extracts digital video data and synchronization signals by a Paneling receiver. The synchronization signals are used to generate pixel clock through a phase-locked-loop frequency synthesizer. The analog part fine tunes gamma correction voltages for red, green and blue light valves.

The extracted 8-bit digital video data and synchronization signals are fed directly into the digital-input SXGA light valves. With the high bandwidth of the integrated digital data drivers and the better noise immunity of the digital drive scheme, we are able to display extremely stable image of SXGA resolution. Figure 10 show a microscope picture of stable image and fine pixels on the display.

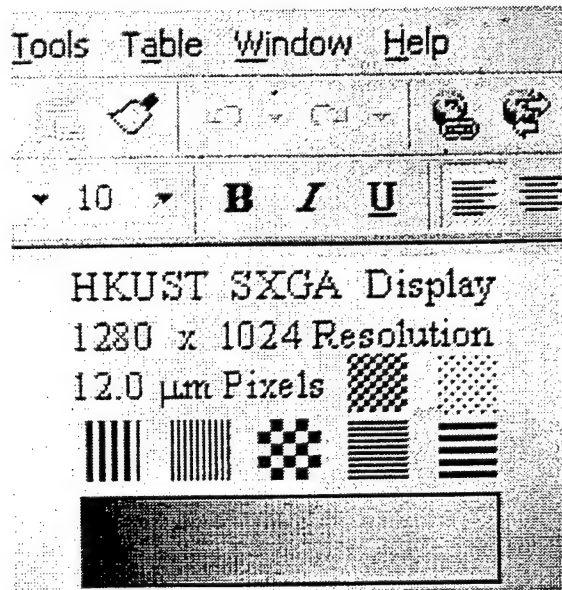


Figure 10 The microscope picture of the silicon light valve showing fine and resolvable pixels.

6.2 VIDEO PROJECTOR PROTOTYPE

Figure 11 shows the appearance of our silicon-based liquid crystal video projector prototype. A 50W metal halide lamp is used as the white light source. A band-pass mirror is used to filter out infrared and ultra-violet parts of the light beam. The optical system which consists of TPA and one PBS for all the three SXGA silicon light valves is used to color separation and recombination and then projects the image to the screen through the projection lens. The measured brightness is about 100 lumens with reasonable color saturation.

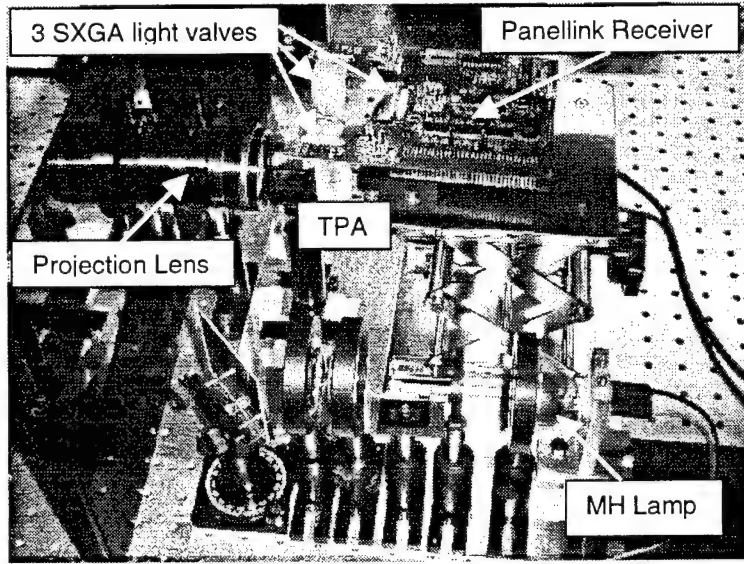


Figure 11 A compact video projector prototype employs one TPA and three SXGA silicon light valves.

With the integrated gamma-correction resistor network for reference voltage generation, we are also able to drive the LC cell accordingly and obtained linear gray scales. We further tuned gamma corrections for three primary colors through external gamma correction voltages and obtained images of good color saturation. Figure 12(a) shows a projected image of linear gray scales and good color saturation. Figure 12(b) shows color coordinates of the SXGA projector prototype. NTSC standard is also included for comparison.

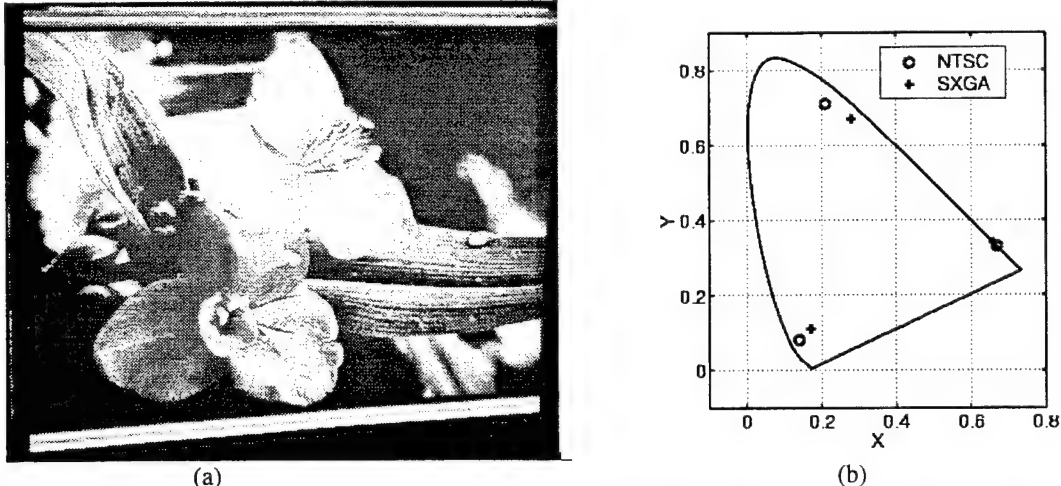


Figure 12 (a) A projected image and (b) color coordinates of the SXGA video projector prototype.

7. CONCLUSION

In conclusion, we have developed a compact and high-resolution SXGA video projector based on silicon light valves. The silicon panel was designed and fabricated by a custom CMOS technology in order to make electronic devices suitable for optical applications. Very advanced display driver and very fine pixels were integrated together as a self-contained and high-resolution display panel. The LC cell configuration was an optimized MTB mode, which can achieve high reflectance and contrast at CMOS compatible voltage. We have also developed a compact optical system, which employed a trichroic prism assembly to incorporate three silicon light valves. The color separation and recombination was conducted through

this compact prism assembly. With integrated high-bandwidth digital data drivers, we have demonstrated stable images and fine pixels of SXGA resolution. With integrated gamma-correction feature, we have also demonstrated projected images of linear gray scales and good color saturation. In addition, silicon surface layers, liquid crystal materials, pixel structures and driving schemes were carefully optimized for the minimization of visual flicker. Flicker ratio of less than 3% was achieved at 60Hz frame rate. We believe this compact and high-resolution video projector is useful for both the high-definition television (HDTV) and PC monitor applications.

ACKNOWLEDGMENT

This work was partially sponsored by Grants from the Research Grant Council and Industry Department of the Hong Kong Government. The silicon light valves were assembled at Varitronix, Hong Kong.

REFERENCES

1. N.Okamoto, and Y.Itoh and J.Ito, "High brightness technology of p-Si TFT-LCD front projector", Proc. of the 5th Int'l Display Workshop, pp. 813-816, 1998.
2. R.L. Melcher, M.Ohhata and K.Enami, "High-information content Projection Display Based on reflective LC on silicon light valves", Digest of Technical papers, Society for Informational Display, pp. 25-29, 1998.
3. P W Cheng, H C Huang and H S Kwok, "A high-resolution projection display based on silicon light valves ", Proc. of the 19th Int'l Display Research Conf., pp. 497-500, 1999.
4. F. H. Yu, J. Chen, S. T. Tang and H. S. Kwok, "A new TN-ECB mode Reflective LCD with Large Cell Gap and Low Operating Voltage", Proc. of 17th Int'l. Display Research Conf., pp. 155-158, 1997.
5. T. Sonehara, "Photo-addressed liquid crystal SLM with twisted nematic ECB (TN-ECB) mode", Jap. J. Appl. Phys., **29**(7), pp. L1231, 1990.
6. S. T. Wu and C. S. Wu, "Mixed-mode twisted nematic liquid crystal cells for reflective displays, " Appl. Phys. Lett., **68**(11), pp. 1455, 1996.
7. K. H. Yang, "A self-compensated twisted nematic mode for reflective light valve, ", Proc. of the 16th Int'l. Display Research Conf., pp. 449-452, 1996.
8. H C Huang, D D Huang and J Chen, "Optical modeling of small pixels in reflective mixed-mode twisted nematic cells", Digest of Technical papers, Society for Informational Display, pp. 742-745, 1999.

SESSION 2

LTPS TFT

Metal-Induced Laterally Crystallized Polycrystalline Silicon: Technology, Material and Devices

Man Wong*

Department of Electrical and Electronic Engineering
The Hong Kong University of Science and Engineering
Clear Water Bay, Kowloon, Hong Kong

ABSTRACT

Polycrystalline silicon (poly-Si) has been obtained by low-temperature ($< 500^{\circ}\text{C}$), nickel-based, metal-induced crystallization (MIC) of amorphous silicon. Because crystallization outside of the nickel-covered regions is not only possible but also commonly utilized, the technique is more often called metal-induced lateral crystallization (MILC). Based on studies on the crystallization kinetics and material characteristics, a unified mechanism is proposed for MIC both under and outside of the nickel coverage. Conduction in MILC poly-Si is found to be anisotropic with respect to the MILC direction. While the material quality of MILC poly-Si is significantly better than that of solid-phase crystallized poly-Si, the performance of MILC poly-Si thin-film transistors (TFTs) is quite sensitive to and degraded by the inclusion of MIC/MILC interfaces in the device channel regions. When such interfaces are eliminated, excellent TFTs are obtained that can be used to realize high performance systems-on-pieces, including sophisticated displays based on liquid crystals or organic light-emitting diodes. The application of MILC poly-Si is not limited to low-temperature electronics, it is found that high-temperature re-crystallization results in MILC poly-Si with material quality approaching that of single-crystal Si. Re-crystallized MILC poly-Si has been used to realize high performance piezo-resistors and TFTs for integrated sensor applications.

Keywords: Nickel, metal-induced crystallization, polysilicon, thin-film transistor, displays, low-temperature electronics.

1. INTRODUCTION

The mobile computing and communications market would not have been viable without the availability of portable, low power liquid crystal displays (LCDs). The demand for higher information content has been driving the switch from passive to active matrix LCDs. Low-cost production of such displays requires low-temperature (low- T) thin-film transistor (TFT) technologies that are compatible with the constraints imposed by the inexpensive but commonly used LCD glass substrates. Traditionally, this requirement has been fulfilled by using the low- T amorphous silicon (a-Si) TFT technology. However, the low field-effect mobility (μ_{FE}) of a-Si TFTs limits their applications to pixel switches within a display matrix. Clearly, a low- T polycrystalline silicon (poly-Si) technology for making TFTs with high mobility and low leakage current would be desirable for the realization of systems-on-pieces (SOPs), integrating driver and other functional circuit blocks with the pixel transistors on the same glass panel.

Poly-Si with large crystallite grains has been obtained using a variety of techniques: rapid-thermal annealing (RTA) [1], Excimer laser crystallization (LC) [2], and solid-phase crystallization (SPC) [3]. RTA is a high temperature ($>600^{\circ}\text{C}$) process, resulting in films containing high densities of defects. By localizing the high temperature to the silicon layer, LC can be considered a “low- T ” process. While it is capable of producing poly-Si films with low defect densities, it suffers from high initial setup cost and high process complexity. Conventional SPC is a relatively inexpensive batch process, though at around 600°C , the process temperature is still considered high.

Metal-induced crystallization (MIC) of a-Si has been proposed as a low- T crystallization technique for making high performance poly-Si TFTs [4]. MIC is superior compared to other low- T poly-Si technologies such as LC and SPC because unlike LC, it is a low-cost batch process and unlike SPC, better quality poly-Si thin films can be obtained.

* Correspondence: Email: milc@ieee.org; Telephone: +852 2358 7057; Facsimile: +852 2358 1485.

2. METAL INDUCED CRYSTALLIZATION

MIC of a-Si, amorphous germanium (a-Ge) or amorphous SiGe has been investigated with either double layers of metal and the amorphous semiconducting material or metal species implanted into Si or Ge. Studies showed that MIC could dramatically decrease the temperature necessary for the crystallization of a-Si and a-Ge. Recently, selective deposition of palladium or nickel (Ni) on a-Si thin films was found to induce crystallization of a-Si outside of the metal coverage (Fig. 1). This phenomenon is called metal-induced lateral crystallization (MILC) [5].

Thin a-Si films were deposited on oxidized Si wafers by low-pressure chemical vapor deposition (LPCVD) at 550°C. Silane (SiH_4) was used as the Si source gas. The deposition pressure was about 300mTorr. Ni films with thickness ranging from 5 to 10nm were deposited in a high-vacuum electron beam evaporator. Prior to loading the wafers into the evaporator, the native oxide on the a-Si films was removed by dipping the wafers in dilute HF. For patterned Ni samples, a lift-off process using photoresist was employed. The photoresist was patterned to expose selected regions of the a-Si thin film before the Ni evaporation. Ni deposited on the photoresist was removed together with the photoresist while Ni deposited on the a-Si was left behind. Crystallization heat treatment was done in N_2 in a conventional atmospheric pressure horizontal furnace.

The optical micro-graph of a sample heat-treated for 16 hours at 500°C is displayed in Figure 1A. Three distinct regions are visible: that with the darkest contrast (Area 1) was originally covered by Ni. This is surrounded by a region (Area 2) with the brightest contrast, which is in turn embedded in a gray region labeled Area 3. Typical Raman spectra obtained in regions equivalent to Areas 1, 2 and 3 in a sample heat-treated for 6 hours are presented in Figure 1B. The broad structure near 480cm^{-1} in the spectrum (Trace a) obtained in Area 3 indicates the film remained amorphous. Instead of the broad structure, sharp peaks near 520cm^{-1} were detected in the spectra obtained in Areas 1 (Trace b) and 2 (Trace c), indicating the a-Si in these two regions has been crystallized. This provides direct evidence that MILC and MIC have occurred in Areas 2 and 1, respectively [5]. The FWHM of the Raman peak obtained in Area 2 (MILC) is about 7.8cm^{-1} , smaller than the 8.3cm^{-1} obtained in Area 1 (MIC), indicating the average grain size in the MILC region is larger than that in the MIC region.

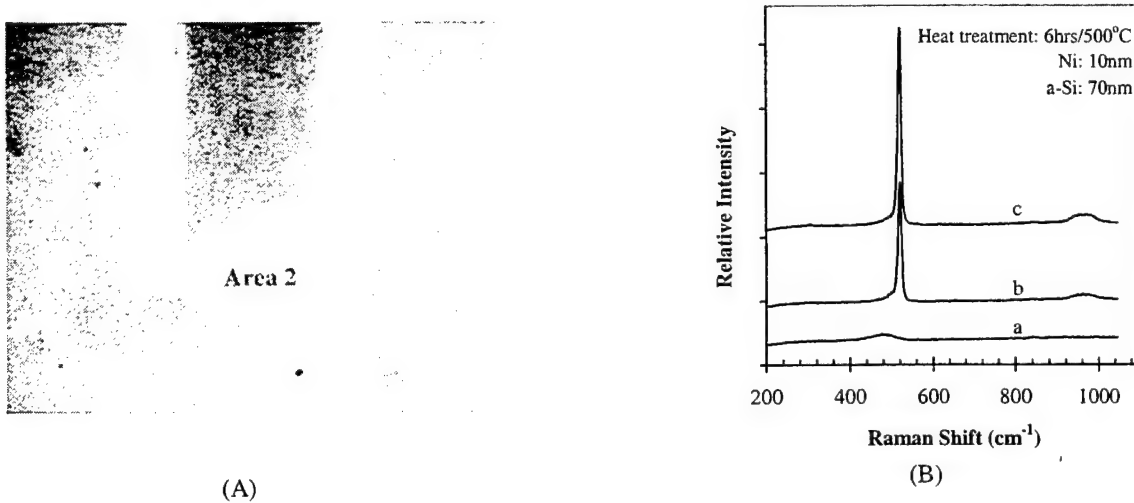


Figure 1. A) Optical micrograph of a sample with selectively deposited Ni on a-Si after heat treatment for 16 hours at 500°C. The $50\mu\text{m}$ wide Ni-covered region (Area 1) is surrounded by a bright MILC region (Area 2). Area 3 is a-Si. B) The equivalent Raman spectra - Trace a: the a-Si region (Area 3), Trace c: the MILC region (Area 2) and Trace b: the Ni-covered region (Area 1).

The MILC rate, estimated by dividing the total MILC length by the total heat treatment time, is plotted in Figure 2 as a function of the reciprocal of the product of the absolute crystallization temperature and the Boltzmann constant. For a given temperature, a slightly lower MILC rate has been obtained on low-temperature oxide (LTO) coated glass than on oxidized silicon, with activation energy (E_a) of 1.97eV and 2.06eV [6], respectively.

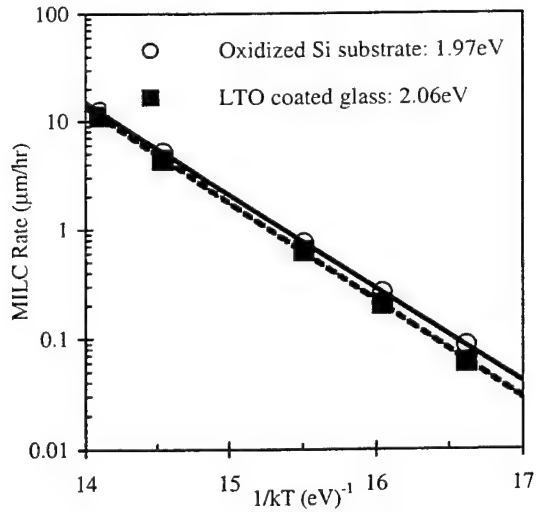


Figure 2. Dependence of the MILC rate on the reciprocal of “ kT ”, where “ k ” is the Boltzmann constant in eV/K and “ T ” is the heat-treatment temperature in K.

The MILC rate is shown in Figure 3 to decrease upon extended heat treatment. The continuous microscopic rearrangement of the atoms in the a-Si during the extended heat treatment is partially responsible for this downward drift of the MILC rate [7]. This is verified by the decrease in MILC rate (Fig. 3A) upon extended heat treatment of a-Si samples which have been pre-annealed for 70 hours at 500°C prior to the Ni deposition. Furthermore, it can be seen that the MILC rate (~1 μm/hr) after 70 hours of extended heat treatment of the samples and without the pre-annealing is about 20% slower than the initial MILC rate (~1.2 μm/hr) of the samples with the 70-hour pre-annealing. This indicates other mechanisms, in addition to the changing state of the a-Si, are needed to fully account for the decrease of the MILC rate upon extended heat treatment. It is shown in Figure 3B that after the removal of the original Ni coverage, the MILC rate became much smaller and decreased much faster upon extended heat treatment. This implies there is a supply of Ni to the crystallization front, possibly via a diffusion mechanism. In the absence of a source of Ni, Ni is gradually depleted from the crystallization front and eventually slows down the MILC rate.

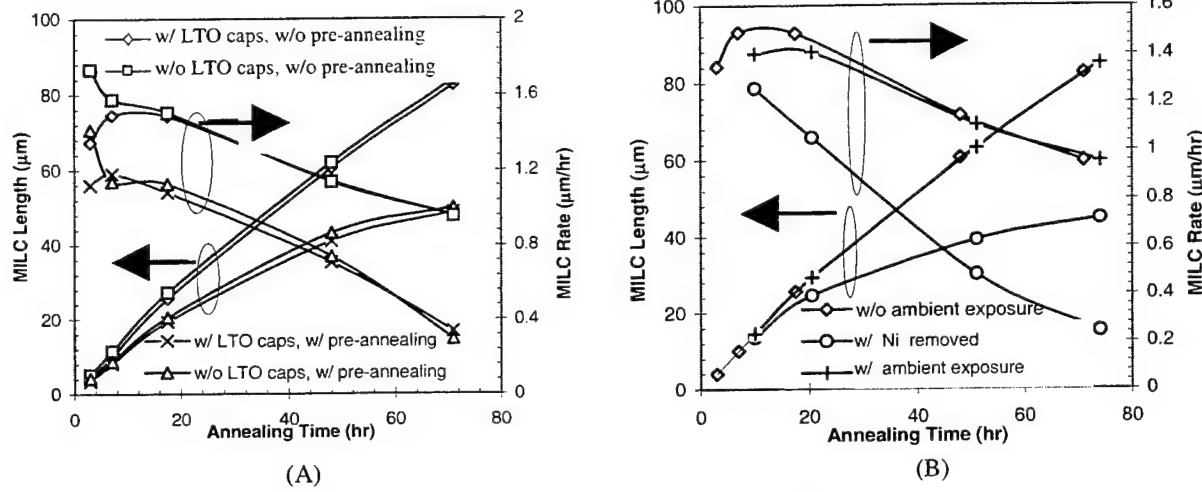


Figure 3. A) MILC length and rate with or without pre-annealing of a-Si. B) The dependence of the MILC length and rate on the heat treatment time, with or without the Ni source removed.

Ni distribution in the MIC, the MILC and the a-Si regions has been obtained using scanning secondary ion mass spectrometry (SIMS) [6]. A two-dimensional distribution of the integrated secondary Ni ion yield, expressed as brightness intensity, is plotted in Figure 4. As expected, the MIC region is the brightest, indicating the highest Ni concentration. Low

levels of Ni, as indicated by the scattered bright spots, have been detected in the MILC region. A dense population of bright spots also has been detected along the interface of the a-Si and the MILC regions, thus proving the MILC front is rich in Ni.

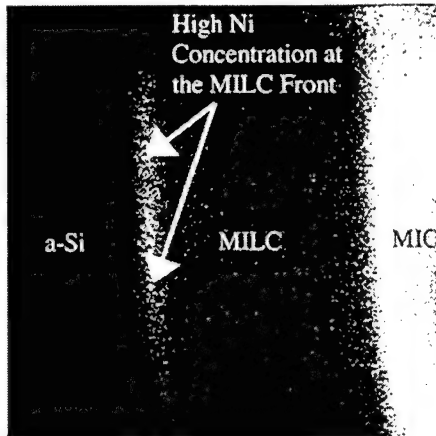


Figure 4. Two-dimensional distribution of Ni obtained by scanning micro-SIMS analysis of the MIC, the MILC and the a-Si regions. The Ni concentration is proportional to the brightness and the density of the spots. A high concentration of Ni, about 0.4 atom %, is observed at the MILC front.

The secondary Ni ion count across a line-scan is shown in Figure 5A [6]. It should be noted that the shape of this lateral Ni distribution is almost identical to that in the vertical direction shown in Figure 5B [5], obtained using x-ray photo-electron spectroscopy (XPS) in the MIC region.

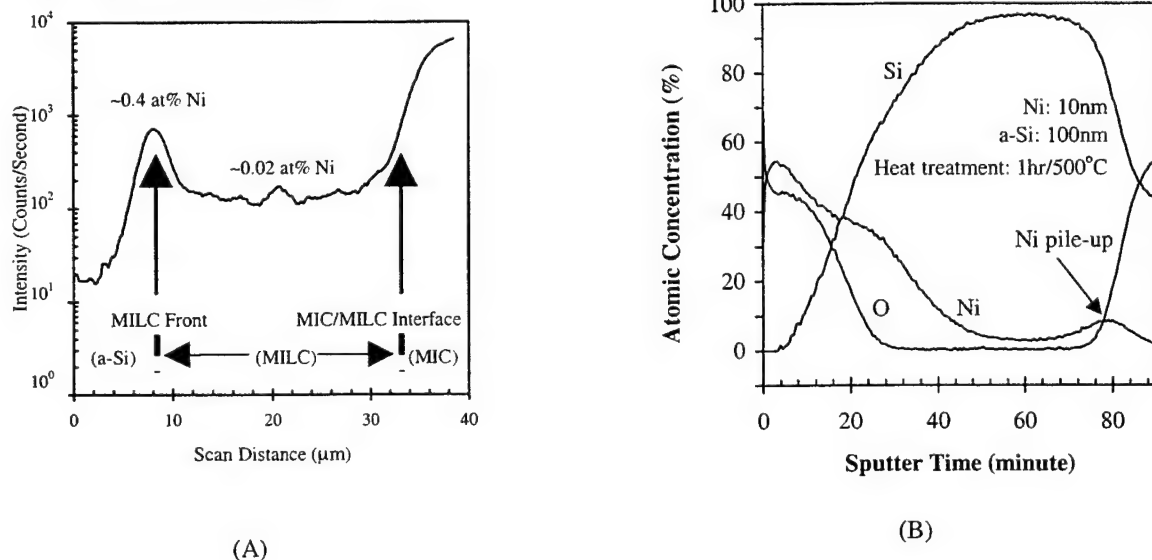


Figure 5. A) Distribution of Ni across the MIC, the MILC- and the a-Si regions obtained by SIMS and B) XPS depth profiles of Si, Ni and O concentrations across an MIC region.

3. MECHANISM OF MIC

Ni induced MIC of a-Si occurs via a three-step process [5]: silicide formation, breakup of the silicide layer into small nodules, and transport of the silicide nodules through the a-Si film.

At the early stage of the MIC heat treatment, Ni readily reacts with the a-Si and converts itself into NiSi_2 . Nucleation and growth of small grains of Si crystal then take place randomly along the interface between the NiSi_2 and the underlying a-Si.

It would not be surprising that the nucleation was aided by the small lattice mismatch between NiSi_2 and crystalline Si. Further growth of the crystalline grains eventually leads to the puncturing and break up of the NiSi_2 layer. Subsequent to the break up, small nodules of NiSi_2 move away from the crystallized top region of the a-Si film. The diffusion of Ni through the nodules is responsible for the movement of the nodules away from the crystallized regions of Si into the a-Si region [8]. In the case of MIC, the fastest moving nodules will be found at the crystallization front, which is the interface between the crystallized Si and the a-Si. The slower moving nodules will be trapped inside the crystallized region, giving rise to the weak Ni XPS signal detected in the bulk of the film. Once the crystallization front reaches the bottom buried oxide, all remaining moving nodules are stopped, thus contributing to the small peak of Ni XPS signal (Fig. 5B) at the bottom interface of the crystallized silicon thin film.

Based on this model of MIC, MILC is easily explained. At the edges of a Ni covered region, certain number of the break-away NiSi_2 nodules will move laterally into the a-Si region not originally covered by Ni. As the nodules move laterally, any a-Si along the path of the moving nodules will be crystallized. As in MIC, slowly moving nodules will be trapped in the bulk of the MILC region, leaving only the fast moving nodules at the MILC crystallization front. The source of the secondary Ni ions detected by SIMS in the MILC region (Fig. 5A) is the Ni containing nodules trapped in the grain boundaries.

4. ANISOTROPIC CONDUCTION

Shown in Figure 6 are the transmission electron microscopy (TEM) and transmission electron diffraction (TED) micrographs of an MILC poly-Si region, in which elongated grains (Fig. 6B), separated by low-angle grain boundaries (GBs), are primarily aligned to the MILC direction. This relatively ordered and anisotropic micro-structure is very different from those in SPC, LPCVD and MIC poly-Si, in which random nucleation and homogenous grain growth lead to isotropic micro-structures. The TED micro-graph in Figure 6A taken in the MILC area indicates the grains are primarily {110}-oriented, while that in Figure 6C taken in the MIC area indicates a nearly random distribution of grain orientations [5].

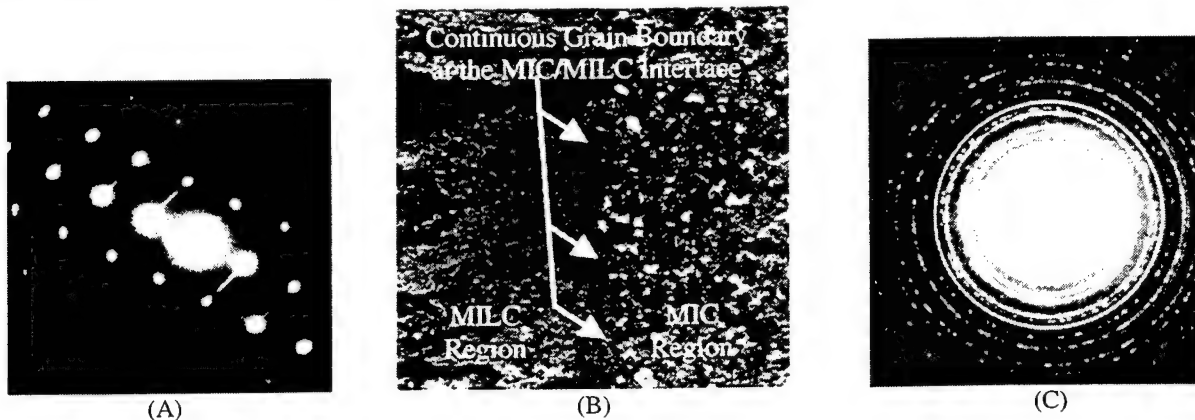


Figure 6. A) TED micro-graph in the MILC area, showing predominantly {110} orientation, B) TEM micro-graph showing elongated grains in the MILC region. A distinct grain boundary (MMGB) separates the MIC and the MILC regions, and C) TED micro-graph in the MIC area.

Arrhenius plots of ρ_t and ρ_p are shown in Figure 7B, where ρ_t and ρ_p denotes, respectively, the resistivity values for conduction parallel and transverse to the MILC direction. While linear fits can be obtained for both ρ_t and ρ_p for the lightly doped resistors, the distribution of the data for the more highly doped ones exhibits much increased influence of defect and/or GB scattering. Only in the low T range can approximate linear fits be obtained. Nevertheless, the extracted E_a is found to be inversely proportional to the doping concentration, agreeing with the GB trapping model. However, for both implant doses, higher E_a is obtained for ρ_t than for ρ_p , which is largely responsible to the observed resistivity anisotropy in MILC poly-Si [9].

The T -dependence of the resistivity anisotropy ratios (ρ_t/ρ_p) for the resistors is plotted in Figure 7A. For lightly doped resistors, ρ_t/ρ_p is quite large and consistently decreases with increasing T . Extrapolating the trend to high T yields a limiting value of 1.22. For heavily doped ones, ρ_t/ρ_p becomes relatively insensitive to T and slowly decreases from 1.25 to 1.19 with increasing T . In other words, for resistors operated at sufficiently high T , ρ_t/ρ_p approaches a similar value which is slightly larger than unity.

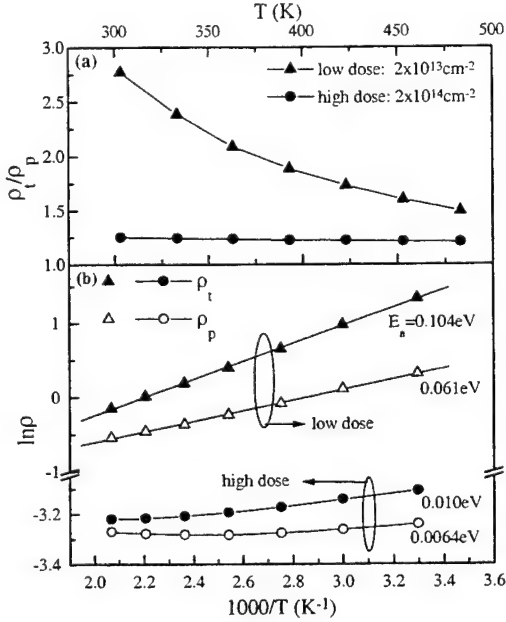


Figure 7. A) Temperature dependence of the resistivity anisotropy ratio, ρ_t/ρ_p , of MILC poly-Si at two different implant doses of 2×10^{13} (low) and $2 \times 10^{14} \text{ cm}^{-2}$ (high). B) Arrhenius plots of the corresponding ρ_t and ρ_p of the MILC poly-Si resistors. E_a of ρ_t and ρ_p for the low-dose resistors are, respectively, 0.104eV and 0.061eV . For high-dose resistors, the values extracted in the low T range are 0.010eV and 0.0064eV , respectively.

5. THIN-FILM TRANSISTORS

5.1 Device Types

Shown in Figure 8 is a micro-graph of two collided MILC regions obtained using secondary electron microscopy (SEM) in the orientation imaging mode. Also labeled in the Figure are the three major grain boundaries transverse to the MILC direction. Two of these are the MMGBs, located at the intersections of the MIC and the MILC regions. The remaining one, dubbed LLGB, is located at the intersection of the two MILC regions. SIMS (Fig. 5A) reveals that while the Ni concentration is relatively low within the MILC region, it is higher in the LLGB and still higher in the MMGBs [6].

Depending on which of these GBs are included in the channel region of a device, five different kinds of MILC TFTs can be implemented [10]. In the nomenclature used in Figure 8, each type of MILC TFT is uniquely identified by a preceding “nml” triplet. Each n, m or l takes on the value of either 1 or 0, indicating respectively the presence or absence of the corresponding transverse grain boundary. Using this nomenclature, a “111”-MILC TFT is a device with an LLGB in the middle of the channel and the MMGBs self-aligned to the edges of the gate electrode. A “110”-MILC TFT is an offset MILC-TFT [11] with one MMGB separated from the drain metallurgical junction and a “000”-MILC TFT [10] is a device without any of the three transverse grain boundaries and with the lowest concentration of Ni remaining in the active channels.

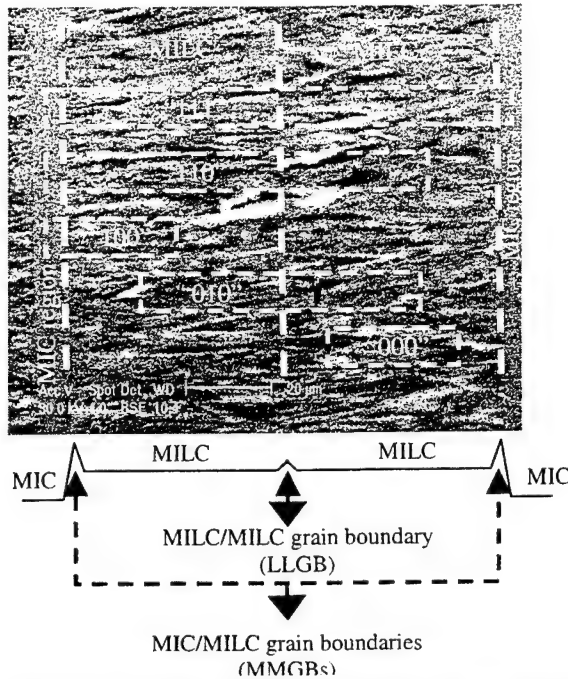


Figure 8. SEM micro-graph showing both MIC and MILC regions. A total of three GBs (two MMGBs and one LLGB) transverse to the MILC direction can be identified. The active areas of the five possible MILC TFTs are delineated by the five rectangular boxes superimposed on the micro-graph.

5.2 “111”-MILC and SPC TFTs

Compared to the processing of SPC TFTs, an additional masking step for Ni deposition is required for the realization of all but the “111”-MILC TFTs. Consequently, SPC and “111”-MILC TFTs, requiring similar process complexities, are compared. The threshold voltages (V_{th}) of the devices are defined as the gate voltages (V_g) required to achieve a normalized drain current (I_d) of $(W/L) \times 10\text{nA}$ at a specified drain voltage (V_{ds}), where W and L are the channel width and length, respectively. μ_{FE} was extracted from the maximum trans-conductance (g_{max}). As verified by the current-voltage (IV) characteristics presented in Figure 9, the performance of the MILC-TFTs is indeed superior to that of the SPC-TFTs.

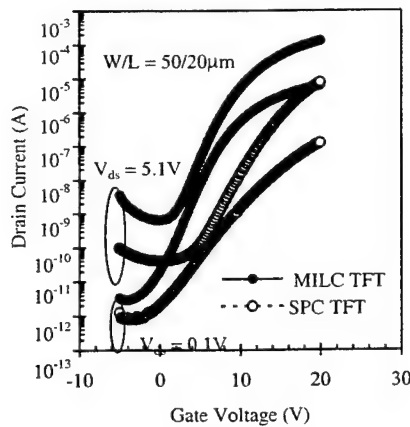


Figure 9. Transfer characteristics of “111”-MILC and SPC TFTs.

A comparison of the relevant device parameters of the two kinds of devices is summarized in Table I. Clearly, the MILC-TFTs have lower V_{th} , smaller sub-threshold slope (S), and higher μ_{FE} . However, the minimum current (I_{min}), which is a measure of the TFT leakage current, is higher for “111”-MILC [12].

Table I. Comparison of the relevant device parameters of “111”-MILC and SPC TFTs.

	V_{th} (V)	S (V/dec)	μ_{FE} (cm^2/Vs)	I_{min} (pA)
“111”-MILC TFT	6.2	1.2	74	2.9
SPC-TFT	15.6	3.3	5	0.8

5.3 Effects of MIC/MILC Interface on the Performance of “111”-MILC TFTs

Because MIC, instead of MILC, occurs in the source and drain (S/D) regions of “111”-MILC TFTs, continuous MMGBs [3] are formed which are “self-aligned” to the edges of the gate electrode. For TFTs employing self-aligned S/D doping, these MMGBs overlap the S/D metallurgical junctions (Fig. 10A) and fall within the corresponding depletion regions. Because of the overlap of the MMGBs and the S/D junctions at both ends of the channel, the MMGB traps are readily filled with charge carriers supplied by the S/D. The resulting MMGB energy barriers, the height of which is a function of the trap densities, extend into the channel region. This is depicted in Figure 10B. Since a higher V_g is required to achieve surface inversion in the regions with the MMGB barriers, it is equivalent to adding two high- V_{th} MMGB “transistors”, in series, to both sides of the intrinsic MILC transistor. This is depicted in Figure 10C.

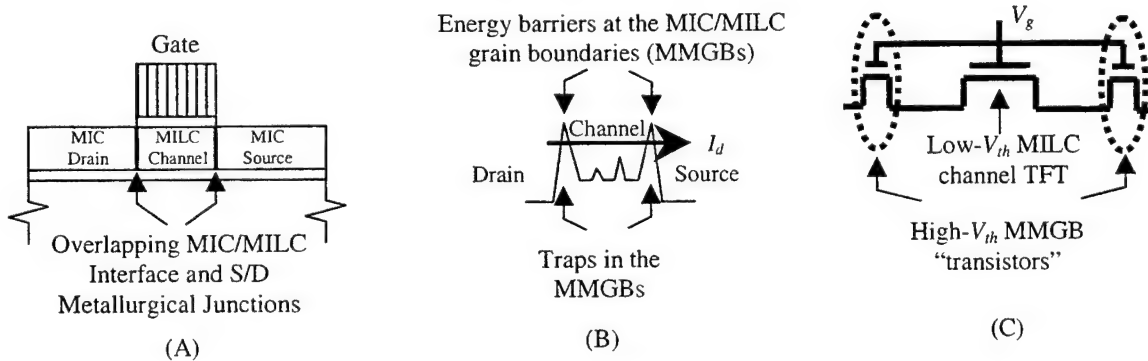


Figure 10. A) Schematic cross section of a “111”-MILC TFT showing the MMGBs self-aligned to the S/D metallurgical junctions, B) the energy barriers near the S/D metallurgical junctions and C) the device model at low V_{ds} .

While “111”-MILC TFTs are better than their SPC counterparts in many device performance measures, they suffer from higher leakage current [12], higher effective V_{th} [13], reverse short channel effect (R-SCE) [14] and lower drain breakdown voltage (kink effect) [15]. The cause of the degradation has been traced to the superposition of the MMGB, with its high densities of defects, and the depletion region of the drain junction, with its high electric field.

The leakage current and its sensitivity to L have been measured for both “111”-MILC and SPC TFTs. The leakage current of “111”-MILC TFTs is not only higher (Fig. 9) but also more sensitive to L scaling (Fig. 11A) than that of SPC-TFTs [12].

When an MMGB coincides with any one of the metallurgical junctions, it becomes part of the channel. The high density of grain boundary trap states effectively raises the local, hence also the overall, V_{th} of the device. Only by removing the MMGBs from both junctions can one effectively reduce the V_{th} . Shown in Figure 11B is the dependence of I_d on V_g of a) a “111”-MILC TFT, b) a “110”-MILC TFT with the MMGB offset from the drain-junction and c) a “010”-MILC TFT with the MMGBs offset from both source and the drain junctions. Clearly, the I_d - V_g characteristics and the apparent V_{th} values of the first two devices are almost identical, while the V_{th} value of the last device, with the double-sided offset, is clearly smaller [13].

However, it should be noted that the difference in this V_{th} is only apparent and does not lead to an increase in I_d at sufficiently high V_g . This is because an MMGB has a very small lateral extent, hence can be considered as a device with a

very short channel length, albeit with a higher V_{th} . While conduction at low V_g is limited by the high- V_{th} MMGB TFT, it is limited at high V_g by the resistance of the intrinsic MILC channel TFT, which is common to all three device structures.

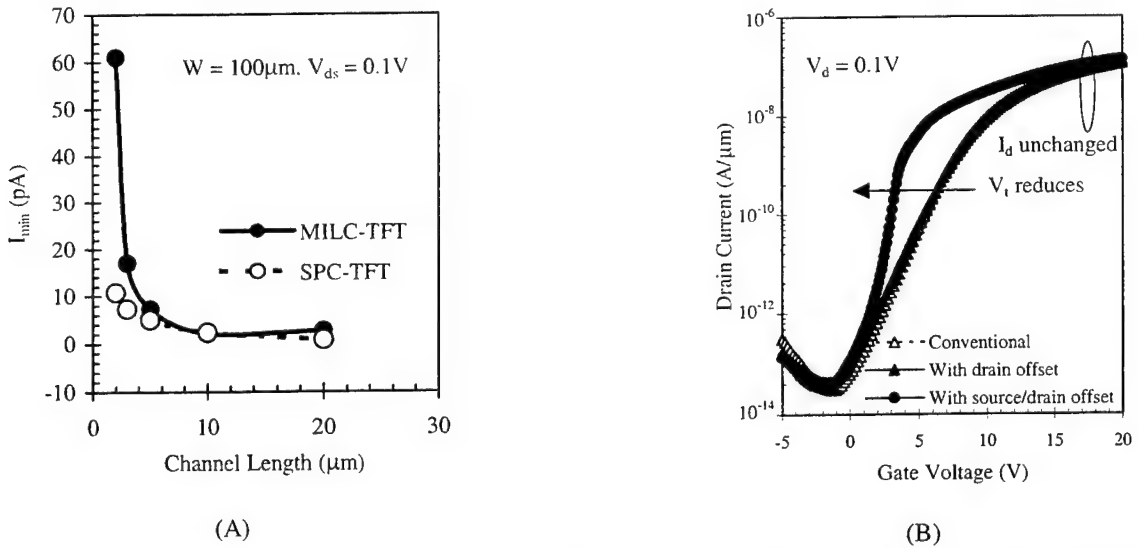


Figure 11. A) I_{min} vs L for N-channel “111”-MILC and SPC TFTs. B) I_d - V_g characteristics of the three different kinds of MILC TFTs: conventional, drain offset, and source/drain offset denote, respectively, “111”, “110” and “010”-MILC TFTs.

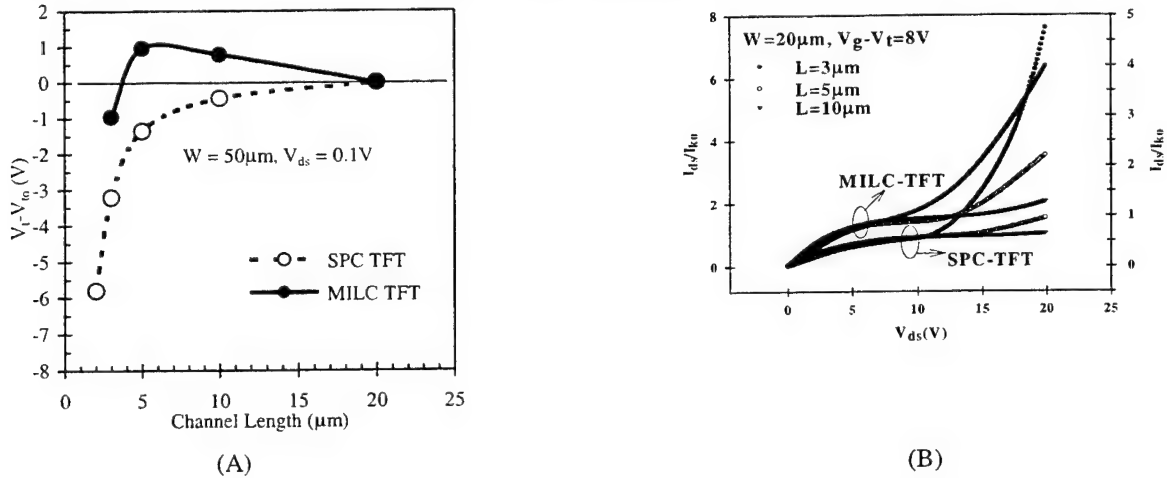


Figure 12. A) Comparison of the V_{th} scaling behavior of “111”-MILC and SPC TFTs. R-SCE is evident in the “111”-MILC TFTs. Only changes in V_{th} are plotted, with V_{th0} denoting the threshold voltage measured on the transistors with the longest channel lengths. B) Normalized output current characteristics of “111”-MILC and SPC TFTs at common gate drive. ‘ I_{k0} ’ is the drain current at the onset of soft drain breakdown (kink effect).

Shown in Figure 12A is a comparison of the L dependence of the V_{th} of “111”-MILC and SPC TFTs. It can be observed that while V_{th} of SPC TFTs decreases monotonically with L , that of “111”-MILC TFTs initially increases with L before rolling off at $L \approx 5\mu\text{m}$, thus manifesting R-SCE [14]. When L of the intrinsic MILC transistor is reduced, a larger fraction of the channel region comes under the influence of the MMGB energy barriers, thus raising the V_{th} . Further reduction of L leads to drain-induced barrier lowering (DIBL) and conventional SCE takes over, resulting in a reduction in V_{th} with L .

Substrate current resulting from a sufficiently large V_{ds} is known to lower V_{th} via a modulated body potential. This is manifested as current kinks in the I_d - V_{ds} curves. In Figure 12B, I_d normalized by the drain current at the kink (I_k) is plotted

against V_{ds} . Because of the overlap of the defective MMGB and the high-field junction, V_{ds} at which the “kink” occurs, denoted by V_k , is lower in “111”-MILC than in SPC TFTs [15].

5.3 Metal-Induced Unilaterally Crystallized Polycrystalline Silicon

Employing metal-induced unilateral crystallization (MIUC) results in the formation of “000”-MILC TFTs (also denoted as MIUC TFTs) with the removal from the edges of and within the channel all major grain boundaries - including the MMGBs - transverse to the drain current flow [10]. Schematics of the “000”-MILC TFT, showing the associated channel potential variation in the sub-threshold regime, are shown in Figures 13A. For comparison, similar schematics for “111”-MILC TFTs are shown in Figure 13B.

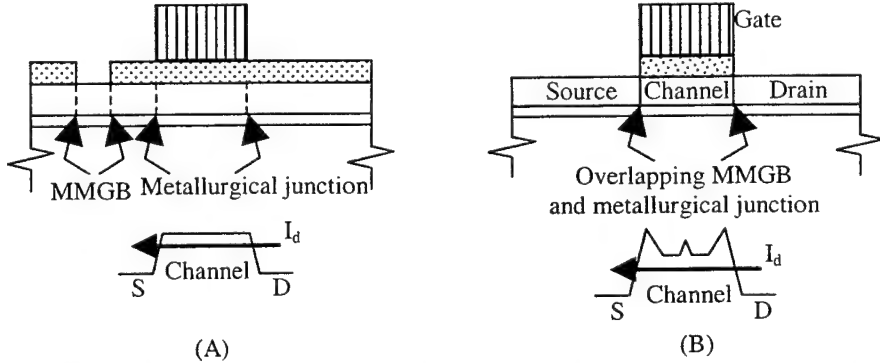


Figure 13. Schematics of the channel potential profiles of (A) a “000”-MILC TFT showing the MMGBs offset from the metallurgical junctions and (B) a “111”-MILC TFT showing the MMGBs overlapping the metallurgical junctions.

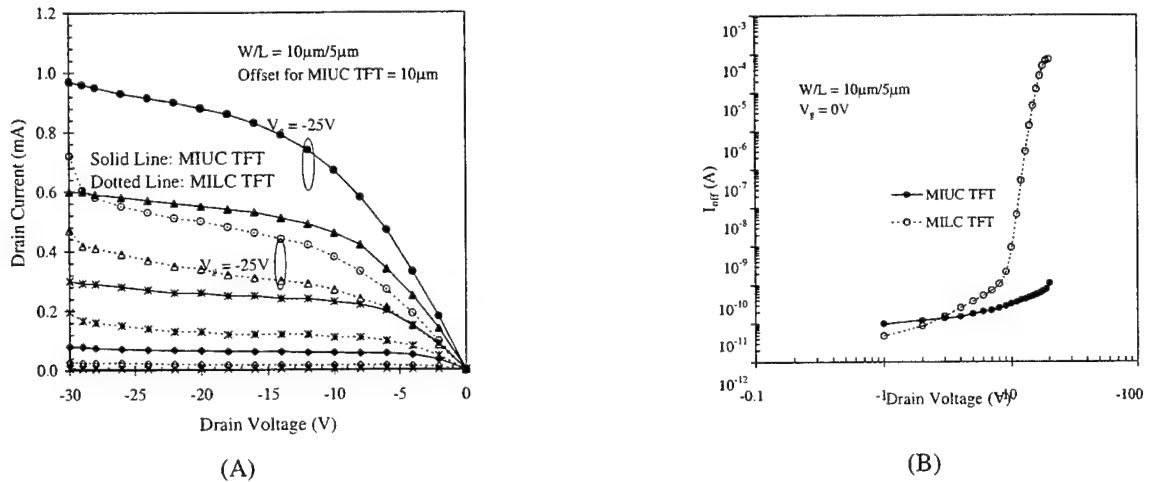


Figure 14. A) I_d dependence on V_{ds} from $V_g = -5\text{V}$ to -25V at -5V interval for p-channel MIUC (solid lines) and “111”-MILC (dotted lines) TFTs. Earlier drain breakdown can be clearly observed in the conventional MILC TFTs. B) Leakage current (I_{off}) dependence on V_{ds} .

Compared to the conventional bilaterally crystallized “111”-MILC TFTs, “000”-MILC TFTs are shown to have higher electron and hole μ_{EF} (Table II), higher drive current and better immunity to early drain breakdown (Fig. 14A), significantly reduced leakage current (Fig. 14B), as well as much improved spatial uniformity of device parameters (Fig. 15). All of these positive attributes make “000”-MILC TFTs particularly suitable for SOP applications requiring low-temperature processed TFTs over a large area.

Table II. Comparison of the device parameters of both n- and p-type MIUC (“000”-MILC) and MILC TFTs.

	N-type		P-type	
	“000”-MILC	“111”-MILC	“000”-MILC	“111”-MILC
μ_{EF} (cm ² /Vs)	78	70	98	75
V_{th} (V) @ $ V_d = 5V$	3.0	3.8	-4.2	-5.7
S (V/decade)	1.1	1.4	1.0	1.5
I_{off} (pA/ μ m) ($ V_{ds} = 5V$)	1.8	17	0.8	470
I_{on}/I_{off} ($ V_{ds} = 5V$)	1.4×10^{-7}	9.3×10^{-5}	3.4×10^{-7}	3.6×10^{-4}

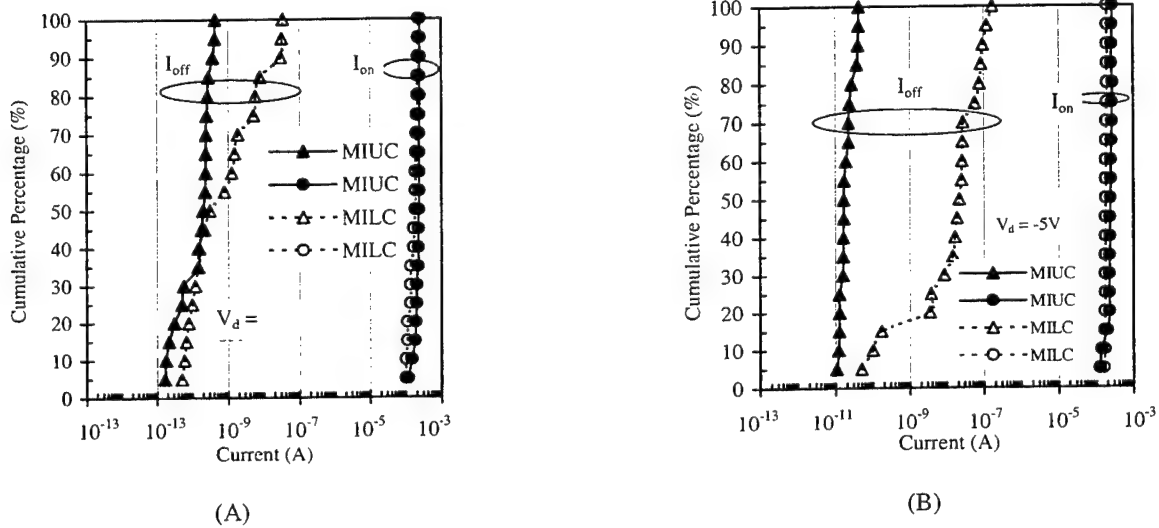


Figure 15. Statistical distributions of I_{on} and I_{off} for (A) n-type and (B) p-type MIUC (“000”-MILC) and “111”-MILC TFTs with $W/L = 10/5\mu m$.

6. RE-CRYSTALLIZED MILC POLYCRYSTALLINE SILICON

Outside of flat-panel displays, hence free from the low temperature constraint, high temperature processed poly-Si devices have been employed in other important applications such as micro-electro-mechanical systems (MEMS) [16] and 3-dimensional (3D) integrated circuits (ICs) [17]. Early work on the re-crystallization (RC) of conventional low-pressure chemical vapor deposited (LPCVD) poly-Si thin films showed that high temperature processing generally led to a small amount of grain growth and limited improvement in the crystallinity of poly-Si. This occurs because poly-Si has a higher free energy than single-crystal Si, and heating provides the necessary thermal activation energy required for the micro-structure transformation.

Compared to the micro-structure of conventional poly-Si with random fine grains, that of MILC poly-Si consists of relatively ordered elongated grains separated by low-angle grain boundaries (GBs) [5]. A high- T anneal leads to RC of MILC poly-Si and significant material enhancement [18]. The improvement can be traced to the evolution of the unique grain structure of MILC poly-Si during the high- T anneal. The longitudinal grains (Fig. 6B) are no longer discernable in the TEM micro-graph (Fig. 16) of the RC-MILC poly-Si.

Shown in Figure 17A is the dependence of the room temperature resistivity (ρ) on the doping concentration (N_A) of MILC poly-Si, LPCVD poly-Si and single-crystal Si. With a slope ($\delta\rho/\delta N_A$) of -5.4 decades/decade, ρ of the conventional fine-grain poly-Si exhibits the most sensitive dependence on N_A . At -3.0 decades/decade, the slope for low- T MILC poly-Si is significantly reduced, thus reflecting a reduced trap density and a considerable improvement in the material quality relative

to conventional poly-Si. After a high- T anneal, the slope of -1.0 decade/decade for high- T MILC poly-Si is only slightly larger than the -0.77 decade/decade reported for single-crystal Si [19]. This result is consistent with the TEM observation that the material quality of high- T MILC poly-Si approaches that of single-crystal Si.



Figure 16. Typical TEM micro-graph of RC-MILC poly-Si. Distinct elongated grains are no longer discernable, leaving only long-range stress-induced and short-range micro-defect induced contrast variations.

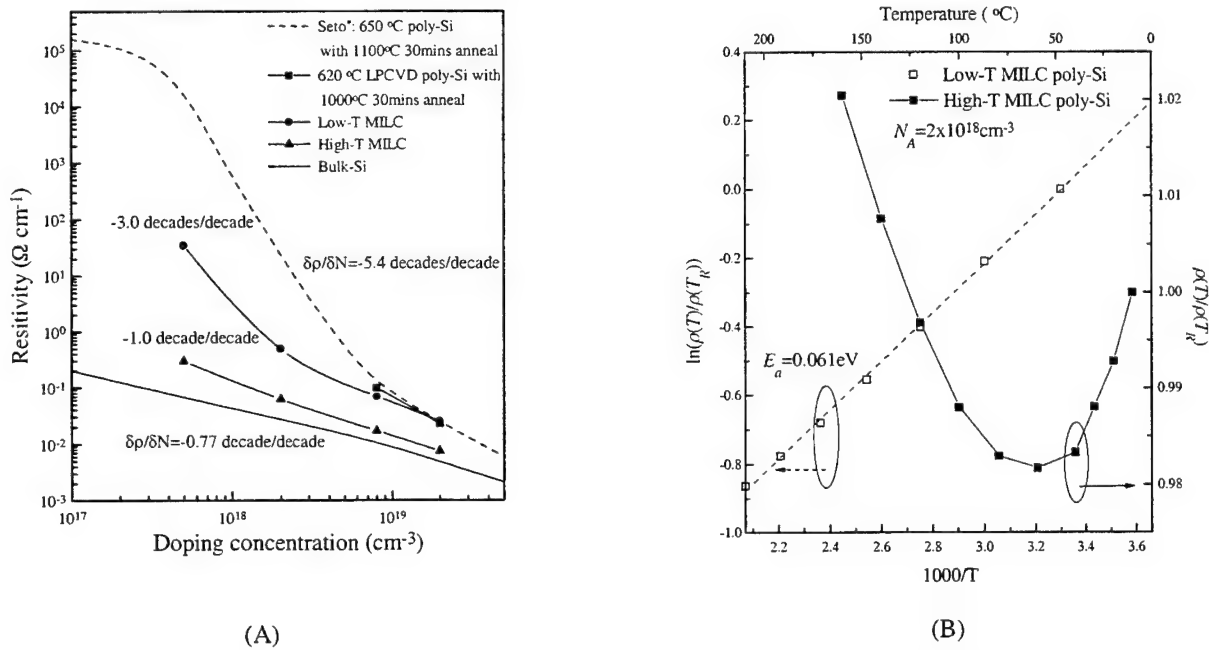


Figure 17. A) The dependence of the room temperature resistivity on doping concentration for LPCVD poly-Si, bulk Si and low- and high- T MILC poly-Si. B) The temperature dependence of ρ of both low- and high- T MILC poly-Si with the same doping concentration of $2 \times 10^{18} \text{ cm}^{-3}$.

Additional evidence of the good crystallinity of high- T MILC poly-Si was obtained by studying the T dependence of ρ . The data are presented in Figure 17B for both low- and high- T MILC poly-Si resistors, implanted with the same boron dose of $8 \times 10^{13} \text{ cm}^{-2}$. Clearly, ρ for low- T MILC poly-Si exhibits an exponential dependence on $1/T$, with E_a of 0.061eV. This behavior is consistent with the mechanism of thermionic emission over GBs, commonly used to model conduction in

conventional poly-Si. On the other hand, the behavior of the high- T MILC poly-Si resistor is rather more complicated. In the low T range, ρ still depends weakly exponentially on $1/T$ as in low- T MILC poly-Si, though with a significantly reduced E_a of 0.0043eV. However, as T is increased beyond $\sim 60^\circ\text{C}$, the dependence is reversed, with ρ increases with increasing T . This turn-around indicates that instead of thermionic emission over the GBs, intra-grain phonon scattering, which controls the conduction behavior in bulk-Si at elevated T , also appears to dominate that of high- T MILC poly-Si.

The piezo-resistive effect of boron-doped RC-MILC poly-Si [20] has been characterized and the longitudinal gauge factor (k) compared to those of LPCVD and LC poly-Si (Figure 18). In the N_A range from 5×10^{17} to $2\times 10^{19} \text{ cm}^{-3}$, k of RC-MILC poly-Si typically varies from 43 to 55. Not only are these values significantly larger than those measured in conventional LPCVD poly-Si (30-40 [21], 24-20 [22] and 20-26 for the control samples), they are even better than the 50-35 [22] reported for LC poly-Si.

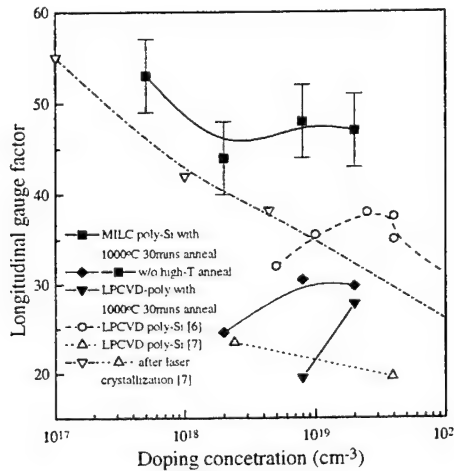


Figure 18. Longitudinal gauge factor vs. doping concentration for boron-doped MILC poly-Si. Results of conventional LPCVD poly-Si, the control samples and LC poly-Si are included for comparison.

The greatly improved material and electrical properties also make it possible to fabricate high performance active electronic devices. Typical TFT parameters of low- and high- T MILC TFTs, including μ_{FE} , V_{th} , S , minimum I_{off} , I_{on}/I_{off} are summarized and compared in Table III. It is worth noting that while the maximum I_{on}/I_{off} of both low- and high- T MILC TFTs exceed 10^7 , only for the high- T devices can this ratio still exceed 10^7 at more practical biased conditions, such as $|V_{ds}| = 5\text{V}$ and $|V_g| = 5\text{V}$.

Table III. Comparison of typical TFT parameters of low- and high- T MILC devices.

	N-type		P-type	
	Low- T	High- T	Low- T	High- T
μ_{FE} (cm^2/Vs)	70	150	90	100
V_{th} (V) ($ V_{ds} = 0.1\text{V}$)	5.0	3.4	-6.0	-3.8
S (V/decade)	0.35	0.33	0.40	0.28
Min. I_{off} ($\text{pA}/\mu\text{m}$) ($ V_{ds} = 5\text{V}$)	2.0	1.7	1.6	1.6
Max. I_{on}/I_{off} ($ V_{ds} = 5\text{V}$)	1.3×10^7	3.4×10^7	1.6×10^7	2.3×10^7
I_{on}/I_{off} @ ($ V_{ds} = 5\text{V}$, $ V_g = 5\text{V}$)	5×10^6	3.2×10^7	1.0×10^6	1.5×10^7

7. CONCLUSION

Polycrystalline silicon (poly-Si) has been obtained by low-temperature (< 500°C), nickel-based, metal-induced lateral crystallization (MILC) of amorphous silicon. MILC is superior compared to other low-temperature poly-Si technologies such as laser crystallization (LC) and solid-phase crystallization (SPC) because unlike LC, it is a low-cost batch process and unlike SPC, better quality poly-Si thin films can be obtained. Anisotropic grain growth in MILC poly-Si leads to anisotropic conduction with respect to the MILC direction. While the material quality of MILC poly-Si is significantly better than that of SPC poly-Si, the performance of MILC poly-Si thin-film transistors (TFTs) is quite sensitive to and degraded by the inclusion of MIC/MILC interfaces in the device channel regions. When such interfaces are eliminated using metal-induced unilateral crystallization, excellent TFTs are obtained that can be used to realize high performance systems-on-pieces, including sophisticated displays based on liquid crystals or organic light-emitting diodes. The application of MILC poly-Si is not limited to low-temperature electronics, it is found that high-temperature re-crystallization (RC) results in MILC poly-Si with material quality approaching that of single-crystal Si. RC-MILC poly-Si has been used to realize high performance piezo-resistors and TFTs for integrated sensor applications.

ACKNOWLEDGMENT

This work was supported by grants from the Hong Kong Research Grants Council.

REFERENCES

1. R. Kakkad, J. Smith, W. S. Lau, S. J. Fonash, R. Kerns, "Crystallized Si films by low-temperature rapid thermal annealing of amorphous silicon," *J. Appl. Phys.*, Vol. 65, No. 5, 1 March 1989, p2069-2072.
2. N. Kubo, N. Kusumoto, T. Inushima, and S. Yamazaki, "Characterization of polycrystalline-Si thin film transistors fabricated by excimer laser annealing method," *IEEE Transactions on Electron Devices*, Vol. 4, No. 10, Oct. 1994, p1876-1879.
3. E. Ibok, S. Garg, "A Characterization of the effect of deposition temperature on polysilicon properties," *J. Electrochem. Soc.*, Vol. 140, No. 10, Oct. 1993, p2927-2937.
4. S. W. Lee, S. K. Joo, "Low temperature poly-Si thin-film transistor fabrication by metal-induced lateral crystallization," *IEEE Electron Devices Letters*, Vol. 17, No. 4, 1996, p160-162.
5. Z. Jin, G. A. Bhat, M. Yeung, H. S. Kwok, M. Wong, "Nickel induced crystallization of amorphous silicon thin films," *J. Appl. Phys.*, Vol 84, No 1, 1 July 1998, p194-200.
6. M. Wong, Z. Jin, G. A. Bhat, P. Wong, H. S. Kwok, "Characterization of the MIC/MILC interface and its effects on the performance of MILC thin film transistors," to be published in the May/2000 issue of the *IEEE Transactions on Electron Devices*.
7. Z. Jin, H. S. Kwok, M. Wong, "The effects of extended heat treatment on Ni induced lateral crystallization of amorphous silicon films," *the IEEE Trans. on Electron Devices*, Vol. 46, No. 1, January 1999. p78-82.
8. C. Hayzelden, J. L. Batstone, "Silicide formation and silicide-mediated crystallization of nickel-implanted amorphous silicon thin films," *J. Appl. Phys.* 73(12), 1993. p8279-8289.
9. M. Wang, Z. Meng, M. Wong, "Anisotropic conduction behavior in metal-induced laterally crystallized polycrystalline silicon thin films," *Applied Physics Letters*, Vol. 76(4), Jan/24/00, p448-450.
10. Z. Meng, M. Wang, M. Wong, "High performance offset metal-induced unilaterally crystallized polycrystalline silicon thin film transistors for system-on-panel applications," *The IEEE Transactions on Electron Devices*, Vol. 47(2), Feb/2000. p404-409.
11. G. A. Bhat, Z. Jin, H. S. Kwok, and M. Wong, "Analysis and reduction of kink effect in MILC-TFTs," in *Proceedings of the 18th International Display Research Conference*, Sept/28-Oct/1, 1998, Seoul, Korea, p433-436.
12. G. A. Bhat, Z. Jin, H. S. Kwok, M. Wong, "Effects of longitudinal grains on the performance of MILC TFTs," *The IEEE Electron Device Letters*, Vol. 20(2), Feb/1999, p97-99.
13. M. Wong, G. A. Bhat, H. S. Kwok, "Reduction of threshold voltage in metal-induced laterally crystallized thin film transistors," in *Proceedings of the Asia Region Society for Information Display Symposium and Workshop*. Mar/17-19/1999, Hsinchu, Taiwan, p281-285.
14. M. Wong, G. A. Bhat, H. S. Kwok, "Reverse short-channel effect in metal-induced laterally crystallized polysilicon thin-film transistors," *The IEEE Electron Device Letters*, Vol. 20(11), Nov/1999, p566-568.
15. G. A. Bhat, Z. Jin, H. S. Kwok, M. Wong, "The effects of MIC/MILC interface on the performance of MILC-TFTs," in *Digest of the 56th Annual Device Research Conference*, Jun/22/98, Virginia, USA, p110-111.

16. J. M. Bustillo, R. T. Howe, R. S. Muller, "Surface micromachining for microelectromechanical systems," in Proceedings of the IEEE, 86, 1998, p1552.
17. T. Yamanaka, T. Hashimoto, N. Hasegawa, T. Tanaka, N. Hashimoto, A. Shimizu, N. Ohki, K. Ishibashi, K. Sasaki, T. Nishida, T. Mine, E. Takeda, T. Nagano, "Advanced TFT SRAM cell technology using a phase-shift lithography," IEEE Trans. Electron Devices, 42, 1995, p1305.
18. Z. Meng, M. Wang, H. S. Kwok, M. Wong, "Re-crystallized metal-induced laterally crystallized polycrystalline silicon for system-on-panel applications," to be presented at the SID International Symposium, Seminar and Exhibition, May/14-19/2000. Long Beach, CA, USA.
19. M. Wang, Z. Meng, Y. Zohar, M. Wong, "A new polycrystalline silicon technology for integrated sensor applications," in Proc. of IEEE MEMS'00 Conference, Miyazaki, Japan, Jan/23-27/2000, p114-119.
20. X. Li, Y. Zohar, M. Wong, "Improved piezo-resistive sensor using novel nickel-induced laterally crystallized polycrystalline silicon," in Proc. of Transducers'99, Vol. 1, Sendai, Japan, 1999, p266-269.
21. P. J. French, A. G. R. Evans, "Piezoresistance in polysilicon and its applications to strain gauges," Solid-State Electron., 32, 1989, p1.
22. A. Druzhinin, E. Lavitska, I. Maryamova, V. Voronin, "Mechanical sensors based on laser-recrystallized SOI structures," Sensors and actuators A, 61, 1997, p400.

Low temperature poly-si TFT characteristics in the overlapped area of excimer laser long-axis scans

Shih-Chang Chang, Chu-Jung Shih, I-Min Lu and I-Wei Wu

ERSO/ITRI
195-4, Sec. 4, Chung Hsing Rd.,
Hsinchu, Taiwan, R.O.C.

ABSTRACT

We have investigated the laser crystallized LT poly-Si TFT characteristics in the overlapped area of excimer laser scans in the long axis direction. Continuous TFTs located at the edges of single scan and overlaps of two scans were used. Different laser energy densities were dual-scanned to study the characteristics of the TFTs in overlapped area. It was found that the laser with higher energy density dominates the TFT characteristics, and their characteristics in the overlapped area can be as good as those in the non-overlapped area. Based on these results, large uniform LT poly-Si panel can be fabricated by overlapping the laser scans in the long axis direction.

Keywords: Low Temperature Poly-Si TFT, Excimer Laser, Long Axis

1. INTRODUCTION

Because of the capability of implanting CMOS driver on cheap glass substrate, low temperature poly silicon (LTPS) crystallized by excimer laser was studied for many years. Several critical processes are needed to achieve high performance TFT like laser crystallization [1]~[9]. At this moment, scanning mode excimer laser annealing is the most popular method for mass production of LTPS panel, however, the length of laser beam generally limited the panel sizes.

In this study, we overlapped two laser scans in the long axis direction and characterized the TFTs located at the overlapped area. It was found that the laser with higher energy density dominates the TFT characteristics, and their characteristics in the overlapped area can be as good as the non-overlapped area. Based on these results, large uniform LT poly-Si panel can be fabricated by overlapping the laser scans in the long axis direction

2. EXPERIMENTS AND RESULTS

Figure 1 shows the typical transfer characteristics of our n-type single-gate TFT with W/L of 20/20um. Its high mobility and low leakage current are sufficient for driver and pixel applications.

Figure 2 shows the continuous TFTs design in this study. The pitch of poly-Si islands is 25um and the spacing is 5um to detail sampling of the TFT characteristics in the concerned area. The total length is 3.6mm and contains 144 individual TFTs.

The edge of the Excimer laser beam ($L_x \times W = 60\text{mm} \times 2\text{mm}$) was parallel irradiated on these TFTs by 255mJ/cm^2 , 98% overlap in scanning direction (shot to shot advance equals 40um) and 150 Hz repetition rate. Figure 3 illustrates geometry of these continuous TFTs in the scanned area.

2.1. TFT Characteristics in the Edge of Laser Beam

In Figure 4, the TFT characteristics of each edge of the laser beam were shown. Each parameter was normalized with the parameters characterized from the TFTs in the central of the laser beam. The threshold voltage (V_{th}) and sub-threshold swing (SS) were increased and the mobility (μ) and the minimum leakage current (I_{min} , $V_d=10V$) were degraded at the beam edge, because of the trapezoidal slope of the laser energy density at the beam edge. At the beam edge, the lower energy density gives lower mobility, higher threshold voltage and poorer sub-threshold swing that represents smaller poly silicon grains and worse crystallinity. The unbalanced beam energy also can be found in this figure, the energy density in the right beam edge is higher, inversely, in the left is lower respect to the central of the laser beam. Therefore the better TFT characteristics were obtained in the right beam region. The slope region of beam is different in the left and right beam edge, however, it was believed caused by the non-uniformity of the homogenizer of laser system.

2.2. TFT Characteristics in the Overlapped Area of Laser Beam

Two scans of laser with the same energy density were irradiated and side-by-side overlapped by 2mm as illustrated in Figure 3. The overlap area was precisely irradiated on the continuous TFTs. Characteristics of one set of continuous TFTs in which two laser scans overlapped were shown in Figure 5.

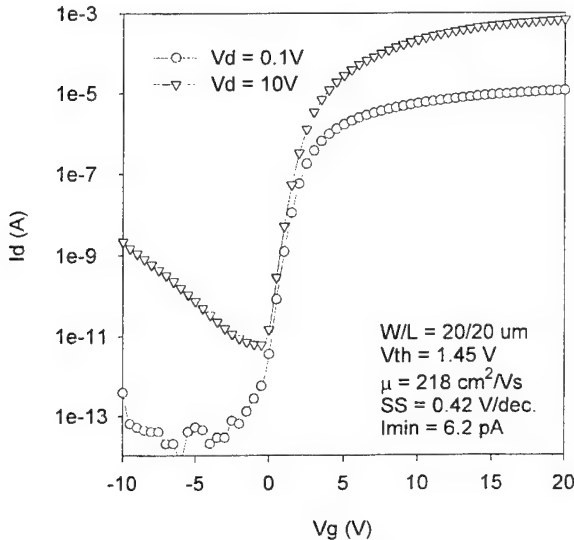


Figure 1. Typical TFT Id-Vg curves.

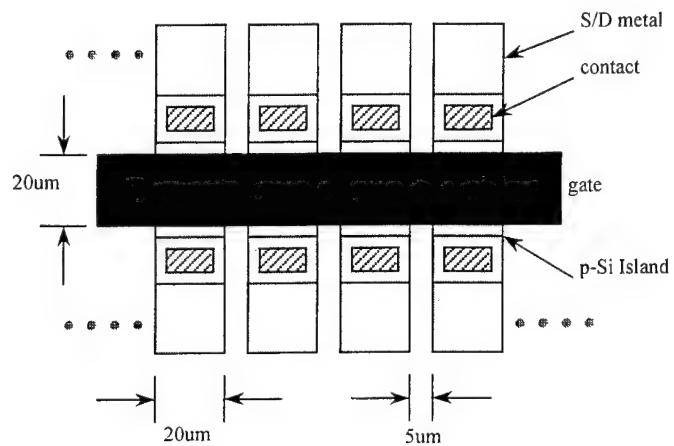


Figure 2. Design of continuous TFTs.

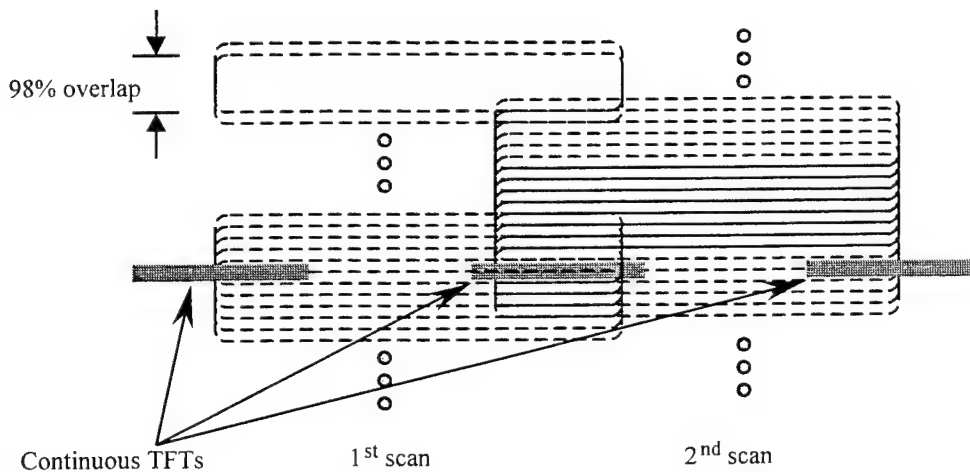


Figure 3. Geometry of TFTs in the scanned area.

The parameters like V_{th} , μ , SS and I_{min} are almost the same as the TFTs in the central of laser beam. The slope region of laser beam in the first scan was disappeared by irradiating the second scan, on the other hand, the TFT characteristics were not effected by the slope region of the second scan. The result indicates the TFT characteristics were dominated by the higher energy density of laser, and the latter lower energy density of laser irradiated on the crystallized poly silicon film did not affect the TFT characteristics.

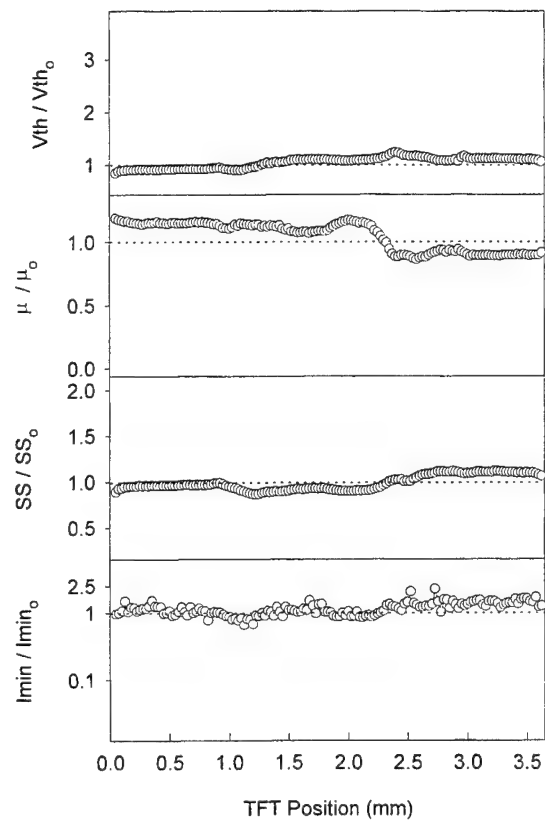
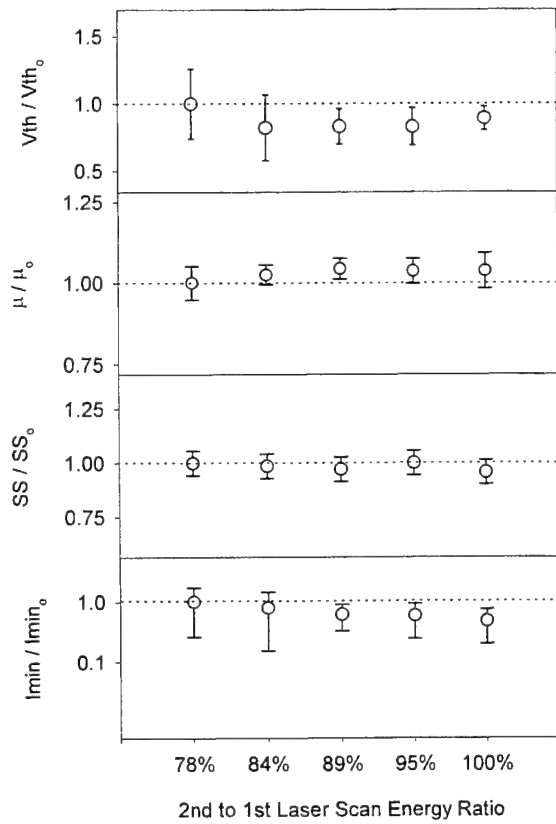
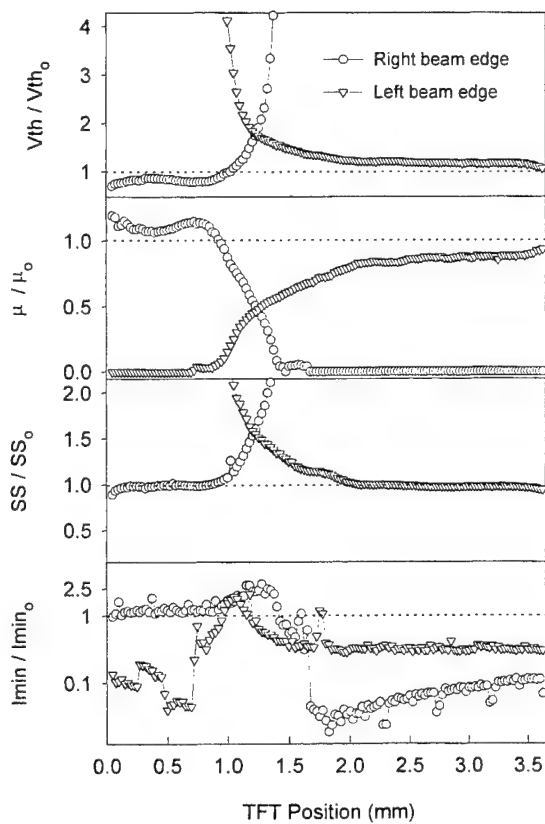


Figure 4. | **Figure 5.**

Figure 6.

Figure 4. TFT characteristics at beam edge.

Figure 5. T TFT characteristics at overlapped area.

Figure 6. TFT characteristics in dual-scanned area with different 2nd scan energy densities.

2.3. Characteristics of Dual-Scanned TFTs

To verify that the TFT characteristics were not effected by latter lower laser energy density, poly silicon films crystallized by the same laser energy density were irradiated again by different lower laser energy densities and the dual-scanned results were shown in Figure 6. Etch parameter was normalized by the parameter that extracted form the single-scanned TFTs. From this figure, the dual-scanned TFT characteristics are almost the same comparing with single-scanned TFTs', i.e., the TFT characteristics are dominated by higher laser energy density.

3. CONCLUSION

According the discussed results, the TFT characteristics in the overlapped area can be as good as non-overlapped area, and large uniform LT poly-Si panel can be fabricated by overlapping the laser scans in the long axis direction.

REFERENCES

1. T. Sameshima, Applied Surface Science 96-98 (1996) pp. 352-358.
2. H. Watanabe et al., Jpn. J. Appl. Phys. Vol 33 (1994) Pt. 1, No. 8, pp. 4491-4498.
3. S. D. Brotherton, et al., J. Appl. Phys. 82 (8), 1997, pp. 4086-4094.
4. K. Sera, et al., IEEE Transactions on Electron Devices, Vol. 36, No. 12, 1989, pp. 2868-2872.
5. J. S. Im, et al., Appl. Phys. Lett. 63 (14), 1993, pp. 1969-1971.
6. K. Yoneda, IDW '97, pp. 231-234.
7. D. Pribat, et al., Flat Panel Display Materials II, MRS Vol. 424, p. 127.
8. S.C. Chang, et al., IDW '99, pp. 151-154.
9. S.C. Chang, et al., ASID '99, pp. 293-296.

The Characteristics of Single-pulse Excimer laser beam profile on the Low Temperature Poly-Si TFTs

Chu-Jung Shih, Li-Ming Wang, Shih-Chang Chang, I-Min Lu, I-Wei Wu

Electronics Research and Service Organization / Industrial Technology Research Institute (ERSO/ITRI)
Taiwan
195-4, Sec. 4, Chung Hsing Rd., Hsinchu, Taiwan, R.O.C.

ABSTRACT

Laser crystallization has been the most promising technology to manufacture low temperature poly-silicon (LTPS) thin film transistors (TFTs), since LTPS technology can make LCD panels with integrated drivers. Higher mobility and lower leakage current than the solid-phase crystallization (SPC) counterparts can be obtained by laser crystallization. [1] Excimer laser emit in the UV region with a short pulse duration (10~30ns), and high temperature can be developed in the Si-surface region, causing melting, without appreciate heating (400°C) with the glass substrate. [2] Laser processes should provide uniform and stable laser beam profiles to obtain uniform distribution of electrical characteristics of TFTs.

In this study, the effects of laser beam profiles were investigated on the crystallization of poly-Si films. "One Pulse" laser crystallized poly-Si was analyzed by SEM and alpha-step to distinguish the effects of non-uniform laser beam profiles. Surface smoothness of poly-Si films with various laser-overlapping ratios was also measured to investigate the effects of laser beam profiles. Then the relationships of TFT characteristics and laser overlapping ratios will be discussed.

Keywords: Single-pulse excimer laser beam profile, Laser overlapping ratio

1. INTRODUCTION

We developed a methodology to investigate the effects of laser beam profiles on the crystallization of poly-silicon. By the analysis of "one pulse" laser crystallized poly-silicon films, the laser overlapping ratios can be related to the film qualities of poly-Si. Especially for the high energy densities at the two edges of a single-pulse laser beam, a high laser-overlapping ratio should be employed to manufacture high performance TFTs.

2. EXPERIMENTS AND RESULTS

Excimer laser beam passes through a homogenizer and irradiates on the glass substrate. In general, the optical module converts the laser beam from a quasi-gaussian intensity profile to a spatially uniform "top hat" profile with a beam uniformity of about less than $\pm 5\%$. In order to obtain uniform characteristics of TFTs, the laser beam profiles should be analyzed. Therefore, we set up a measuring system to monitor the beam profile, and discussed the effects on the crystallization of poly-Si. The dehydrogenated a-Si films were irradiated by excimer laser (253 mJ/cm^2 , beam size = $60.0 \times 1.73 \text{ mm}^2$) with various overlapping ratios. The repetition rate of laser used in this study is 150 Hz.

2.1. The Characteristics of Single-pulse Excimer Laser Beam Profile

Figure 1 shows the laser beam profile of excimer laser system used in this study. The uniformity of top-hat is $\pm 7\%$, and FWHM is 1.73 mm. Before the amorphization occurring, the grain size of laser crystallized poly-Si increases as the increasing laser energy densities.

Figure 2 shows SEM image of single-pulse excimer laser crystallized poly-silicon. **Figure 3** shows the SEM photograph of the square region in figure 2 in a larger size. Very large grains and micro-crystalline grains can be seen in this region. As shown in this figure, $2\text{-}3 \mu\text{m}$ grains and micro-crystalline grains are due to the effects of super-lateral growth

(SLG) phenomena and amorphization phenomena, respectively. So it is hard to control the qualities of laser crystallized poly-silicon films by the non-uniform laser beam profiles, especially at the two edges of laser beam.

Figure 4 shows the surface topography of single-pulse excimer laser crystallized poly-Si film, which is measured by alpha-step. The RMS (root-mean square) surface roughness of SLG region and amorphization region are about 200Å and 30Å, respectively. In figure 4, the laser beam profile can correspond with the SEM photograph in the figure 2.

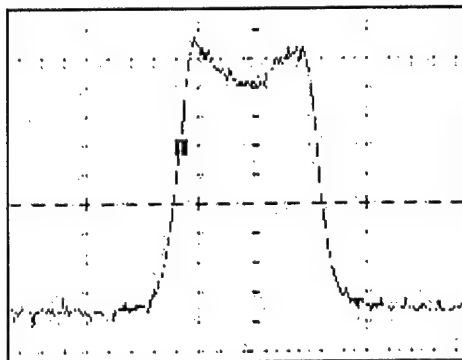


Figure 1 The laser beam profile of excimer laser system used in this study. The uniformity of top-hat is $\pm 7\%$, and FWHM is 1.73 mm.

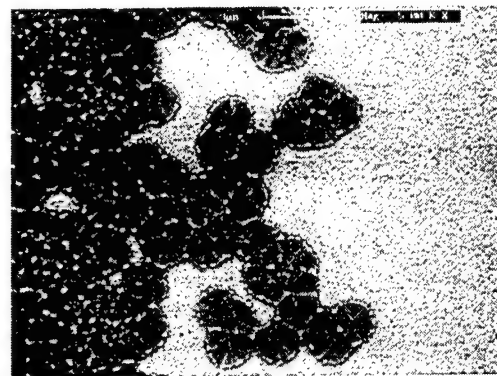


Figure 3 The SEM photograph of the square region in figure 2 in a larger size.

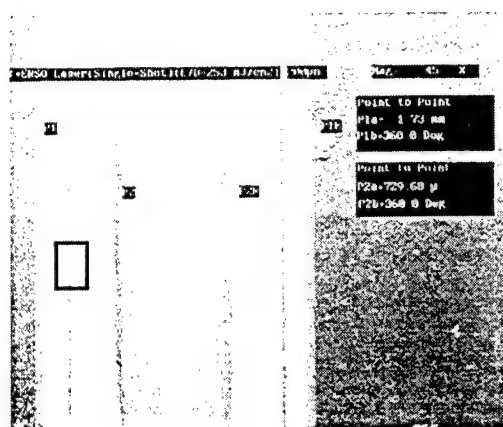


Figure 2 The SEM photograph of single-pulse excimer laser crystallized poly-silicon.

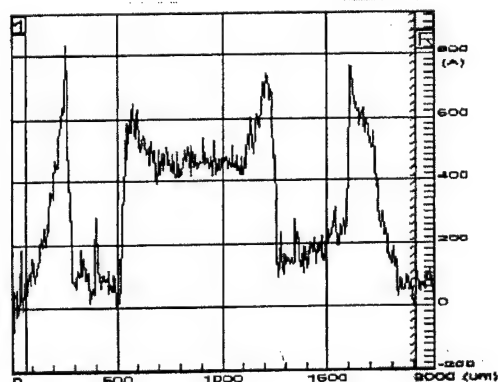


Figure 4 The surface topography of single pulse excimer laser crystallized poly-Si film.

2.2. SEM photographs of poly-Si film with various laser-overlapping ratios

Figure 5~Figure 7 show SEM photographs of the laser crystallized poly-Si film with various laser-overlapping ratios of 75%, 90%, and 99%. The overlapping ratio means the percentage of the overlapping distance between one laser pulse and its next pulse along the direction of the laser beam scanning.

From the observations of SEM photographs, the SLG and amorphization regions will not disappear until the overlapping ratio is higher than 90%. If the dehydrogenated a-Si films are irradiated by a higher energy density, which is at the two edges

of the laser beam, the SLG and amorphization phenomena will occur. This is the reason why the overlapping ratio of laser scanning should be larger than 90% for the manufacturing of uniform laser crystallized film.

2.3. Alpha-step Analysis of excimer laser crystallized poly-Si film

Figure 8 shows the surface topography of the poly-Si films when the overlapping ratio is 75%. There are 4 peaks with-in the distance of 1600 μm due to the higher energy densities at the edges of the laser beam. The 4 peaks are caused due to the SLG and amorphization regions when the overlapping ratio is 75%.

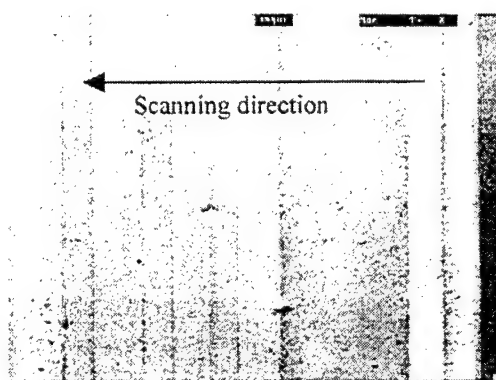


Figure 5 The SEM photograph of the laser crystallized poly-Si film with 75% laser overlapping ratio.

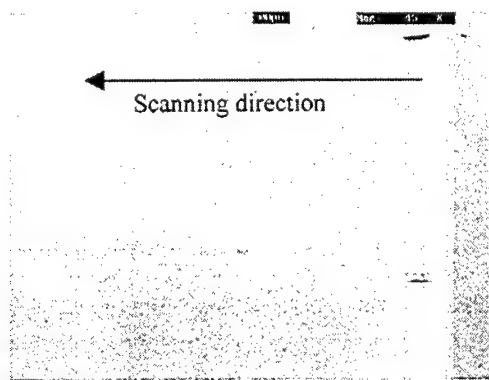


Figure 7 The SEM photograph of the laser crystallized poly-Si film with 99% laser overlapping ratio.

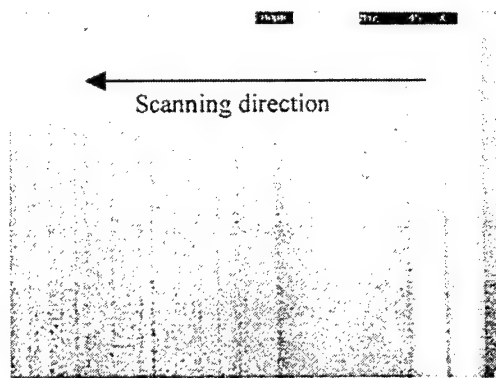


Figure 6 The SEM photograph of the laser crystallized poly-Si film with 90% laser overlapping ratio.

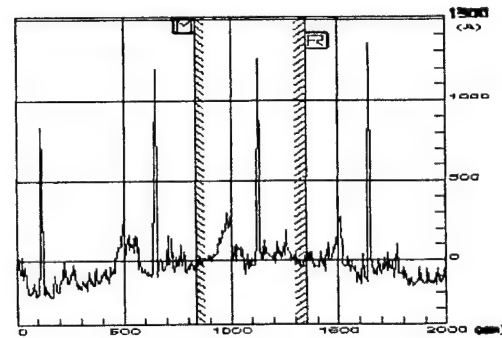


Figure 8 The surface topography of the poly-Si films when the overlapping ratio is 75%.

2.4. TFT Characteristics with various laser overlapping ratios

Figure 9 shows the typical $\text{Id}-\text{Vg}$ curves ($\text{Vd}=0.1\text{volt}, 10\text{volt}$) of our n-type single-gate TFT ($\text{W/L}=50/20\mu\text{m}$) with various laser overlapping ratios (96%~99%). Table 1 shows the relationships of the mobility (μ), the threshold voltage (Vth), the sub-threshold swing (SS), and the minimum leakage current (Imin , $\text{Vd}=10\text{V}$) with laser overlapping ratios. It is obvious that the characteristics of TFTs with higher overlapping ratios are better.

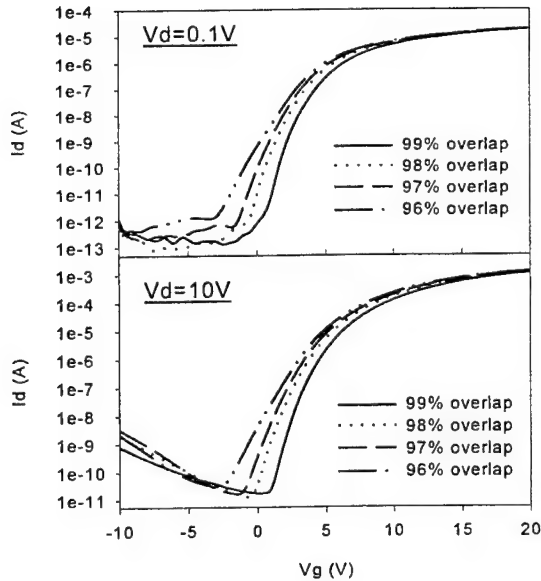


Figure 9 The typical I_d - V_g curves ($V_d=0.1$ and 10 volt) of n-type single-gate TFT ($W/L = 50/20\mu m$) with various laser overlapping ratios (96%~99%).

overlap	μ (cm^2/Vs)	V_{th} (Volt)	SS (V/dec.)	I_{min} (pA)
99%	156	3.78	0.64	17.4
98%	148	3.06	0.73	13.7
97%	148	2.65	0.82	16.3
96%	148	2.20	1.11	30.2

Table 1 The TFT characteristics with various laser-overlapping ratios.

CONCLUSION

In this study, we investigated the effects of laser beam profiles on the crystallization of poly-Si films. “One Pulse” laser crystallized poly-Si was analyzed by SEM and alpha-step to distinguish the effects of non-uniform laser beam profiles. Surface smoothness of poly-Si films with various laser-overlapping ratios was also measured to investigate the effects of laser beam profiles. By the analysis of “one pulse” laser crystallized poly-silicon films, the laser overlapping ratios can be related to the film qualities of poly-Si. It is obvious that the characteristics of TFTs with higher overlapping ratios are better for the relationships of the mobility (μ), the threshold voltage (V_{th}), the sub-threshold swing (SS), and the minimum leakage current (I_{min} , $V_d=10V$). It is very important to prevent from the highest energy density area of the single-pulse laser shot to emit to amorphous-Si film. Therefore, it is useful to overcome this problem with higher overlapping ratios. Especially for the high energy densities at the two edges of a single-pulse laser beam, a high laser-overlapping ratio should be employed to manufacture high performance TFTs.

REFERENCES

1. I-Wei Wu, Mat. Res. Soc. Symp. Proc. Vol.471, pp.125 (1997)
2. G. Fortunato, Thin Solid Films, Vol. 296, pp.82 (1997)

A Novel Device Structure for Low-Temperature Polysilicon TFTs with Controlled Grain Growth in Channel Regions

Li-Jing Cheng, Yin-Lung Lu, Ching-Wei Lin, Ting-Kuo Chang and Huang-Chung Cheng

Institute of Electronics, National Chiao Tung University, Hsinchu, 300 Taiwan

ABSTRACT

In this paper, we demonstrate a novel device structure of low-temperature polysilicon thin-film transistors (LTPS TFTs) for AMLCD applications with using excimer-laser crystallization (ELC). The device structure consists of a thin channel and a thick source/drain. This structure has its merit in the process of ELC and is capable of improving TFTs' electrical characteristics. During excimer laser irradiation, this kind of recessed structure is able to build up localized lateral thermal gradients in the regions near the steps and entice crystallization from the chiller thick source/drain regions toward the hotter thin channels. Because of the development of crystallization process, the average field-effect mobility of the devices can be increased to about $350 \text{ cm}^2/\text{V.s}$, and the on/off current ratios exceed eight orders. In addition to improvement of device performance, the process window of ELC is broadened with the recessed structure.

Keywords: low-temperature polysilicon thin-film transistors (LTPS TFTs), excimer-laser crystallization (ELC), recessed channel, localized lateral thermal gradient

INTRODUCTION

Low-temperature polycrystalline silicon thin-film transistors (LTPS TFTs) have been studied because of their potential application in high-performance active matrix thin-film displays on glass substrate. Development of high-performance LTPS TFTs will benefit the cost-effective manufacturing of large-area active matrix liquid-crystal displays (AMLCD) by replacing the off-board driver circuits, thereby paving the way for future "system on glass" (SOG) or even "3-D integration" applications. Excimer-laser crystallization (ELC) is a powerful technology to produce high-quality polycrystalline silicon film with low thermal budget. However, as many prior literatures have shown, the grain size of the ELC polysilicon film is significantly dependent on energy density of laser irradiation. In addition, the energy for producing super-large grains is too critical to hit it right. In order to broaden the process window of ELC and improve crystal uniformity or even control the large grains in specific locations, especially in channels, we should apply some auxiliary method to reduce the sensibility of crystallized grain size to laser energy density and to direct grain growth. Lots of techniques on this issue have been discussed, such as ELC with pre-patterned Si films, with anti-reflective capping patterns or with shield masks. In this work, we have developed an alternative approach to control grain growth by using different thicknesses of α -Si silicon film. When pulsed laser irradiates the α -Si thin film with different thicknesses, the temperature in thin regions will ramp and quench more swiftly than the thick will do. Consequently, the lag of solidification in thin regions generates lateral thermal gradients and obliging grains to grow from the thick films to the thin. Here we tailor the thick silicon regions for source/drain and the thin for channels in order to make grains grow from the source/drain to the channel. Because stronger thermal gradients exist in the films with greater difference in thickness, the grains in the channel regions with thicker source/drain can extend longer. The grain configuration makes devices have low leakage current and high mobility. Importantly, the recessed-channel structure can be used to blunt the sensibility of grain size to applied laser energy, especially in small-dimensional devices.

EXPERIMENTAL

The process, illustrated in Fig. 1, starts with forming α -Si silicon films of 500\AA and 1000\AA individually on two oxidized wafers by LPCVD at 550°C with silane source. Next, we remove the α -Si silicon films at the channel regions and then deposit another 500\AA α -Si silicon films to form recessed-channel structures. The recessed structures consist of 500\AA channel regions and 1000 or 1500\AA sources/drains. After excimer laser irradiation at 400°C , the crystallized silicon films are used to fabricate general self-aligned four-masked TFTs with 1000\AA TEOS gate oxide. The maximum temperature of all

processes is 600°C. Finally, some devices are passivated by NH₃ plasma treatment at 300°C for four hours. In order to prove our prediction, we have observed the results of grain growth at the channels by SEM micrographs and compared the electrical characteristics of ELC recessed-channel TFTs with that of the conventional structure in different laser energy densities.

RESULTS AND DISCUSSIONS

Narrow process window of ELC harms the uniformity of TFTs' electrical characteristics. We ascribe this poor result to super lateral growth (SLG) phenomenon [1] appearing at a critical laser energy density irradiation. Laser energy fluctuation makes grains randomly grow from the residual nucleation sites at the silicon-oxide interface. More importantly, if a laser source with fixed energy density is applied, the number of the residual nucleation sites is predominately dependent on the thickness of silicon films. So the uniformity of film thickness and laser energy density becomes a potent influence on the uniformity of device performance. However, if the different thicknesses of silicon film are fabricated artificially, lateral thermal gradients can be generated after laser irradiation. By doing so, the residual nucleation sites can be controlled in the thick regions if the laser energy exceeds a level that is able to completely melt the thin regions.

Fig. 2 shows a simulation result of temperature profile after 30ns-pulsed laser irradiation in a step silicon structure formed on an oxide substrate. We can find that lateral thermal gradient exists near the step region, while homogeneous nucleation resulting from completely melting dominates the crystallization process in the region far from the step. The result also tells us that the homogeneous grain growth will eventually hinder lateral growing grains if the recessed regions are too long. But if the solid-liquid interface laterally moves swifter, it is likely to overcome the homogeneous nucleating grains and stretch longer into the channels. Therefore, the strength of thermal gradient determinates the ability of lateral growth. By increasing the difference of film thickness, we can build up stronger lateral thermal gradients to enhance lateral grain growth. The SEM micrographs shown in Fig. 3 are good evidences to corroborate our idea to control grain growth in channel region with recessed structure. We observe that the grains can extend to about 0.9μm from the two sides, 1000 Å source/drain regions, toward the center of 500Å channel region, and the grains in recessed film with 1500Å source/drain can stretch to about 1.5μm.

Fig. 4 shows Id-Vg curves of recessed-channel and conventional TFTs with 2μm channel length before and after NH₃ plasma treatment. We can see that the device performance of ELC recessed-channel TFTs is superior to that of the conventional. The recessed-channel TFTs display greater on-current and field-effect mobility; furthermore, minimum-current and subthreshold swing are lower either after or before plasma treatment. In our opinion, the higher field-effect mobility and lower subthreshold swing result from better crystallinity and the longitudinal grain growth in the channel regions. Additionally, since the extending grains have less intra-grain defects near drain junctions, the leakage current, which results from thermionic field emission tunneling mechanism [2], can be suppressed in the recessed-channel TFTs. The typical electrical characteristics of recessed-channel (black) and conventional TFTs before and after plasma treatment are listed in Table 1.

Fig. 5 exhibits the influence of channel length on ELC recessed-channel TFTs. The recessed structure shows its merit in improving device performance especially when the channel length is getting shorter. Beside, it is thanks to lateral thermal gradients occurring in the recessed structure that we can insensate the effect of laser energy density upon grain size. Fig. 6 tells us that if the applied laser energy density is greater than a critical level that makes the 500Å channel regions completely melted (referring to the data of the conventional 500Å-thick TFTs), the device performance is about the same. The reason is that during higher-energy laser irradiation, all of the silicon residual nucleation sites disappear in the channel regions. When lateral grain growth can be artificially controlled in the process of crystallization, the process window of ELC will be broadened.

CONCLUSION

Recessed-channel TFTs fabricated by using ELC have shown superior device performance to the conventional. With this kind of structure for ELC, higher field effect mobility, lower subthreshold swing and lower minimum-current can be obtained. We attribute the results to longitudinal grain growth along the channels and lower intragrain defects near drain junctions. Furthermore, the process window can be broadened, because lateral grain growth is artificially controlled in the process of crystallization.

REFERENCE

- [1] James S. Im and H. J. Kin, *Appl. Phys. Lett.*, vol. 64, p. 2303, 1994.
- [2] I.-W Wu, A.G Lewis, T.-Y Huang, W.B Jackson, and A Chiang, *Electron Devices Meeting, 1990. Technical Digest., International*, p. 867 , 1990.

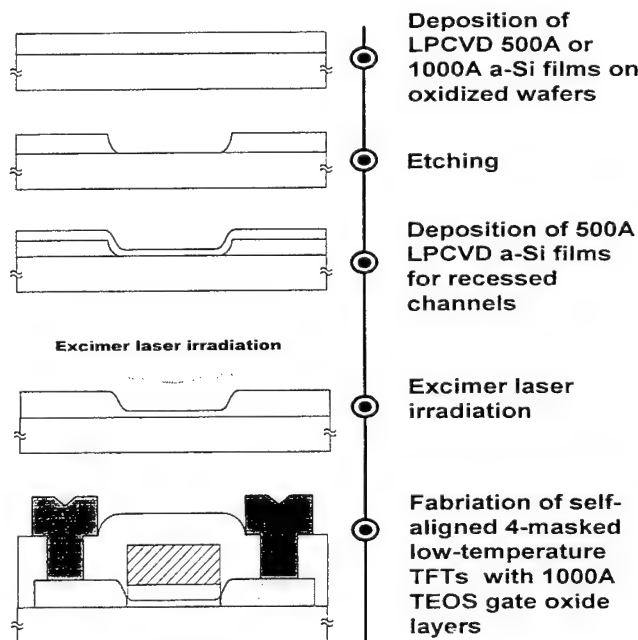


Fig. 1 The brief process flow of recessed TFTs.

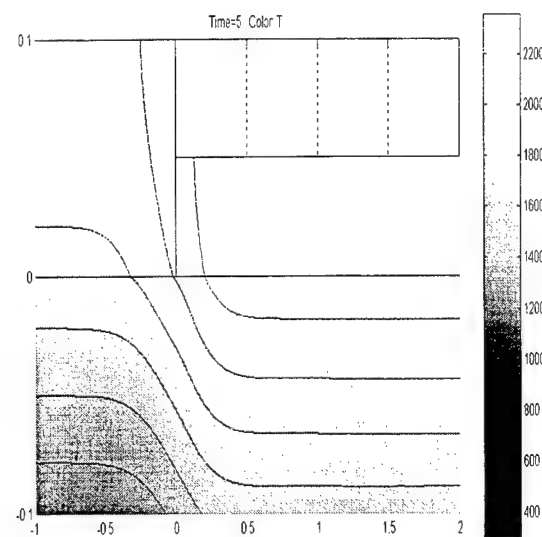


Fig. 2 Simulation of a temperature profile, in Kevine degree, at the edge of a recessed silicon film after laser irradiation. The upper region above zero is silicon and the bottom, silicon dioxide.

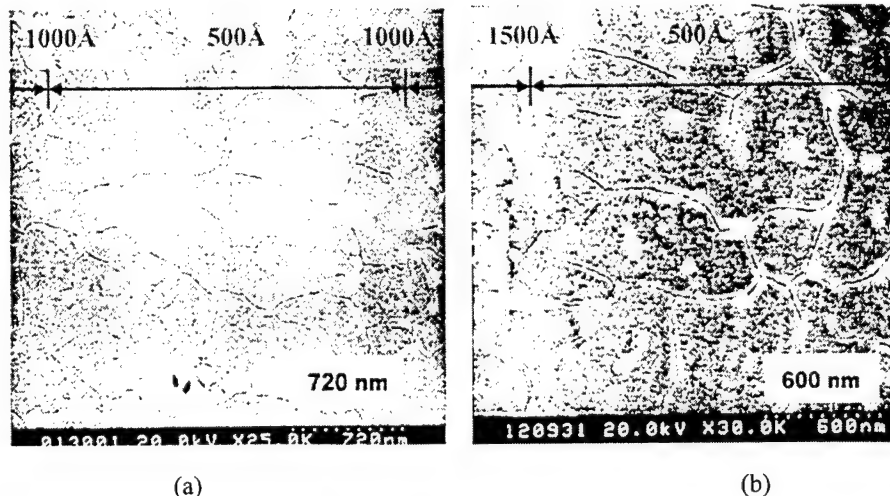


Fig. 3 The SEM micrographs of Secco etched ELC recessed-structure silicon films.

- (a) Grains extend about 0.9 μm from the two sides, 1000 \AA source/drain regions, toward the center of 500 \AA channel region.
- (b) Grains extend about 1.5 μm from the left side, 1500 \AA source/drain region, toward the right, 500 \AA channel region

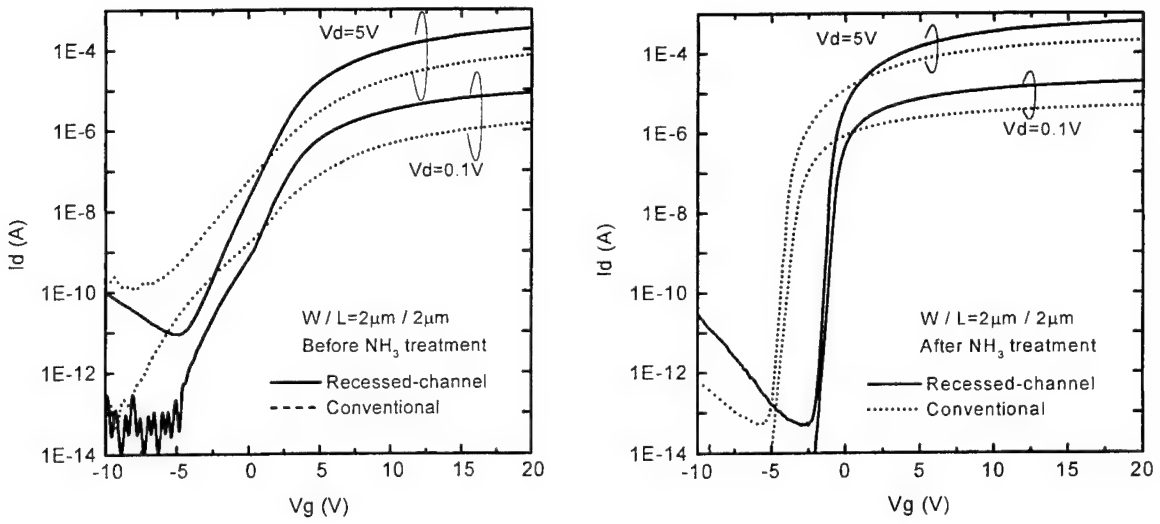


Fig. 4 Id-Vg curves of 2-μm recessed and conventional TFTs before (left) and after (right) NH₃ plasma treatment.

TABLE 1
Typical electrical characteristics of recessed-channel (black) and conventional TFTs before and after plasma treatment.

	μ_{FE} (cm ² /V.s)	on/off @Vd=5V	V _{th} (V)	SS (mV/dec)
With plasma treatment	2μ	432	3E10	-0.77
		158	8E8	-3.26
	5μ	276	9E8	-0.42
		156	3E8	-3.28
Without plasma treatment	2μ	239	4E7	0.74
		74.3	5E5	1.71
	5μ	125	2E7	3.42
		48.9	4E7	2.0

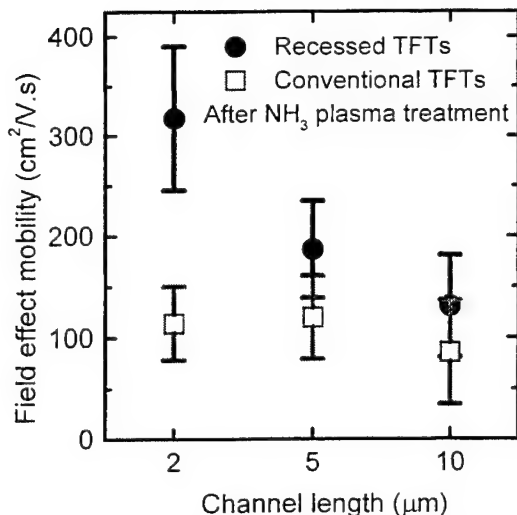


Fig. 5 The comparison of field-effect mobilities of recessed and conventional TFTs with different channel lengths.

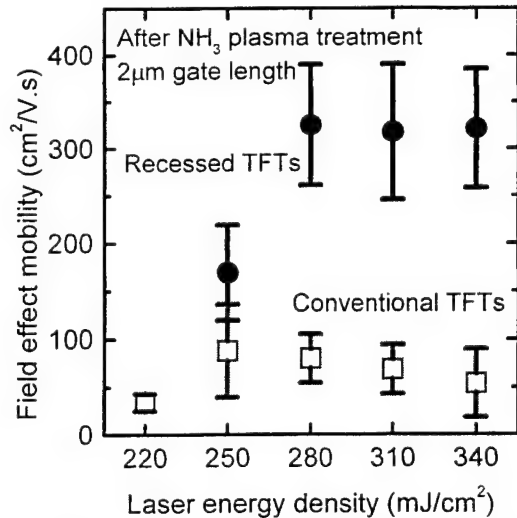


Fig. 6 The comparison of field-effect mobilities of recessed and conventional TFTs prepared with different laser energy densities.

Comparison of The Mechanisms of Hydrogenation by RF Plasma And SiNx

Li-Ming Wang, Hsia-Ju Sung, I-Min Lu and I-Wei Wu

Electronics Research and Service Organization / Industrial Technology Research Institute
E300, Bld. 15, 195-4, Sec. 4, Chung Hsing Rd., Hsinchu, Taiwan, R.O.C.

ABSTRACT

In low temperature poly-silicon (LTPS) TFT's, the electrical characteristics are controlled by the inter- and intra-grain defects in the poly-silicon films. Hydrogen passivation is an effective way to reduce the density of these defects and can improve TFT's characteristics. In this study we investigated the characteristics of TFT's as a function of the hydrogenation time for two different hydrogenation techniques: H₂/Ar plasma and PECVD silicon nitride film deposition. It was found that the characteristics of TFTs could be greatly improved after a very short period of time by both hydrogenation processes. In the H₂/Ar RF plasma hydrogenation process, the characteristic parameters would be apparently improved within 30 min., and with only limited improvement after that. In the nitride hydrogenation process, the electrical characteristics of TFTs would be optimized within 5 min. of annealing, but started to degrade with longer annealing time. From these result, we concluded that the hydrogenation mechanism of these two techniques are very much different from each other.

Keywords: Low Temperature Poly-Si TFT, Hydrogenation, RF Plasma, Silicon Nitride.

1. INTRODUCTION

Low temperature poly-silicon (LTPS) TFTs fabricated by excimer laser crystallization on glass substrate have received increasing attentions recently for their applications in driver-integrated liquid crystal display.¹⁻³ The electrical characteristics of LTPS TFTs are dominated by the inter- and intra-grain defects in the poly-silicon films.⁴⁻⁶ Hydrogen passivation is an effective way to reduce the density of these defects and improves TFT's characteristics. Hydrogen can be supplied by many methods, such as H₂ plasma,^{1,2} PECVD silicon nitride deposition followed by high temperature annealing,^{3,4} or hydrogen ion implantation.⁷

In this study we investigated the characteristics of TFTs as a function of the hydrogenation time for two different hydrogenation techniques: H₂/Ar plasma and PECVD silicon nitride deposition. And showed the difference of the mechanism of these two hydrogenation process.

2. EXPERIMENTS

The top-gate TFT's used in this hydrogenation experiment were fabricated on Corning 7059 glass. A 300 nm TEOS oxide was deposited by PECVD on the glass as the buffer layer to prevent contamination from surface of the glass. A 50 nm thick PECVD amorphous silicon (a-Si) film was then deposited at 450°C and subsequently annealed at 400°C for 2.5 hours under atmosphere to reduce the hydrogen content in the a-Si films. After the phosphorus doping to define the n-type region by photo resist as mask, this a-Si film was crystallized by excimer laser at 400°C and energy density 250 mJ/cm² which yielded a grain size of approximately 300 nm. The polycrystalline silicon island was defined by photolithography and dry etching process. A 100 nm TEOS oxide was deposited on the island as gate insulator and followed by gate metal deposition and patterning. Then 400 nm TEOS oxide was deposited as inter-layer, and the contact holes were patterned. Finally, a Cr/Al double-layer film was deposited and patterned as source/drain metal.

Figure 1 shows the cross-sectional structure of the top gate TFTs used in this study. The W/L is 50/20 μm. The devices were passivated by two hydrogenation techniques. The first one was based on directly immersing the whole devices in a H₂/Ar RF plasma. The second one used silicon nitride as a hydrogen source that was deposited on the devices by PECVD, and then the samples were baked at high temperature to out-diffuse the hydrogen.

3. RESULTS AND DISCUSSION

Figure 2 shows the typical Id-Vg curves of the TFTs before and after hydrogenation with drain voltages at 10 V and 0.1 V. The electrical characteristics of the TFTs had an apparent improvement after hydrogenation.

The electrical parameters (mobility, sub-threshold swing, threshold voltage and minimum leakage current) were extracted and presented as a function of the hydrogenation time in Figure 3. It was found that the characteristics of TFTs would be apparently improved after a very short period of hydrogenation. In the H₂/Ar RF plasma hydrogenation process, the characteristic parameters would be improved apparently in the first 30 min., and had further but limited improvement after that. And in the nitride hydrogenation process, the electrical characteristics of TFTs could be optimized in 5 min. of annealing, but the extended annealing time is detrimental to the TFTs.

In both techniques, hydrogen atoms have to diffuse through the interlayer oxide and gate oxide to reach the LTPS films. And these results indicate that the hydrogenation mechanism of RF plasma is different from that of PECVD silicon nitride. The density of monatomic hydrogen in the RF plasma remains at a constant level during the whole process, which makes a constant hydrogen concentration on the surface of the samples. The fast improvement of the characteristics of TFTs in the initial stage was due to the high hydrogen concentration gradient between RF plasma and the poly-silicon films. And as the hydrogen content in the devices increased with the hydrogenation time, the diffusion rate of hydrogen would gradually decrease by the Fick's law. This was reflected by the limited improvement of the electrical characteristics of TFTs after about 30 min. of hydrogenation. On the other hand, the monatomic hydrogen that PECVD silicon nitride can supply was limited by the hydrogen content of the nitride film. Although the electrical characteristics of TFTs could be optimized after 5 min. of annealing, it would degrade in the extended annealing process because of the hydrogen being trapped in the poly-silicon films would diffuse out, and with no further supplement of hydrogen atoms from the silicon nitride films. Therefore, the electrical characteristics of TFT's would gradually degrade.

4. CONCLUSION

In this work, we investigated the electrical characteristics of TFT's as a function of hydrogenation time by two different techniques: H₂/Ar plasma and PECVD silicon nitride film deposition. And it showed that the hydrogenation mechanism of these two techniques were very much different while both were very effective in improving the electrical characteristics of LTPS TFT's.

REFERENCES

1. W. B. Jackson, N. M. Johnson, C. C. Tsai, I.-W. Wu, A. Chiang and D. Smith, *Appl. Phys. Lett.*, **61** (1992) 1670.
2. K. Y. Choi, J. S. Yoo, M. K. Han and Y. S. Kim, *Jpn. J. Appl. Phys.*, **35** (1996) 915.
3. L. K. Lam, D. L. Chen and D. G. Ast, *Electrochem. Solid-State Lett.*, **2** (1999) 140.
4. G. P. Pollack, W. F. Richardson, S. D. S. Malhi, T. Bonifield, H. Shichijo, S. Banerjee, M. Elahy, A. H. Shah, R. Womack and P. K. Chartterjee, *IEEE Electron Device Lett.*, **EDL-5** (1984) 468.
5. D. R. Campbell, *Appl. Phys. Lett.*, **36** (1980) 604.
6. C. H. Seager and D. S. Ginley, *J. Appl. Phys.*, **52** (1981) 1050.
7. J. D. Bernstein, Shu Qin, Chung Chan and T.-J. King, *IEEE Trans. Electron Device*, **43** (1996) 1876.

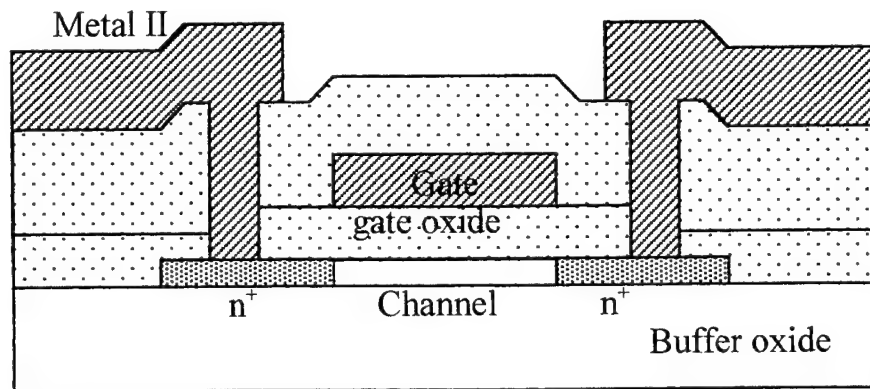


Figure 1. Cross-sectional structure of TFTs used for hydrogenation.

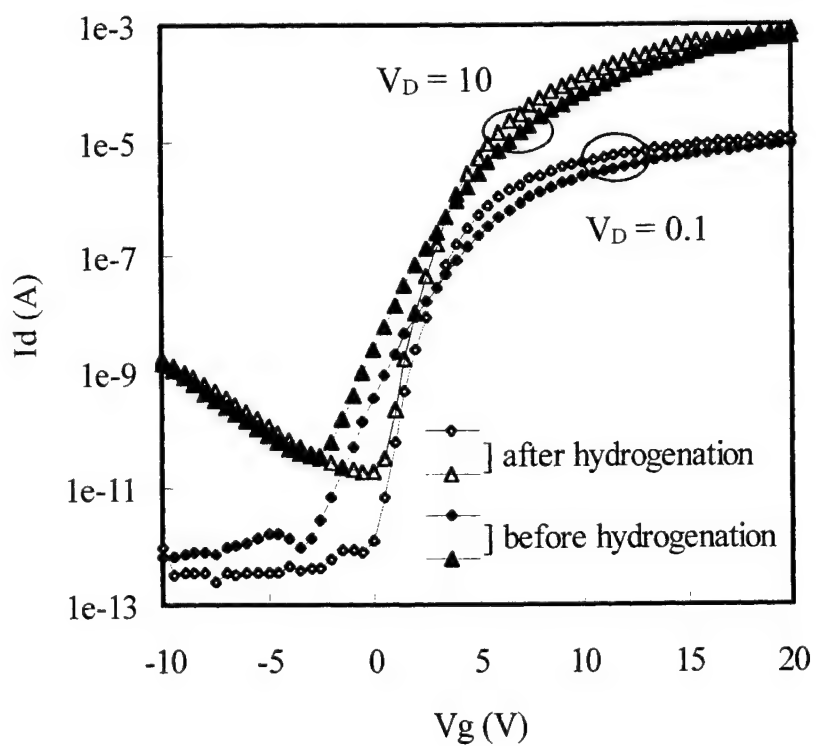


Figure 2. Typical I_d - V_g curve before and after hydrogenation.

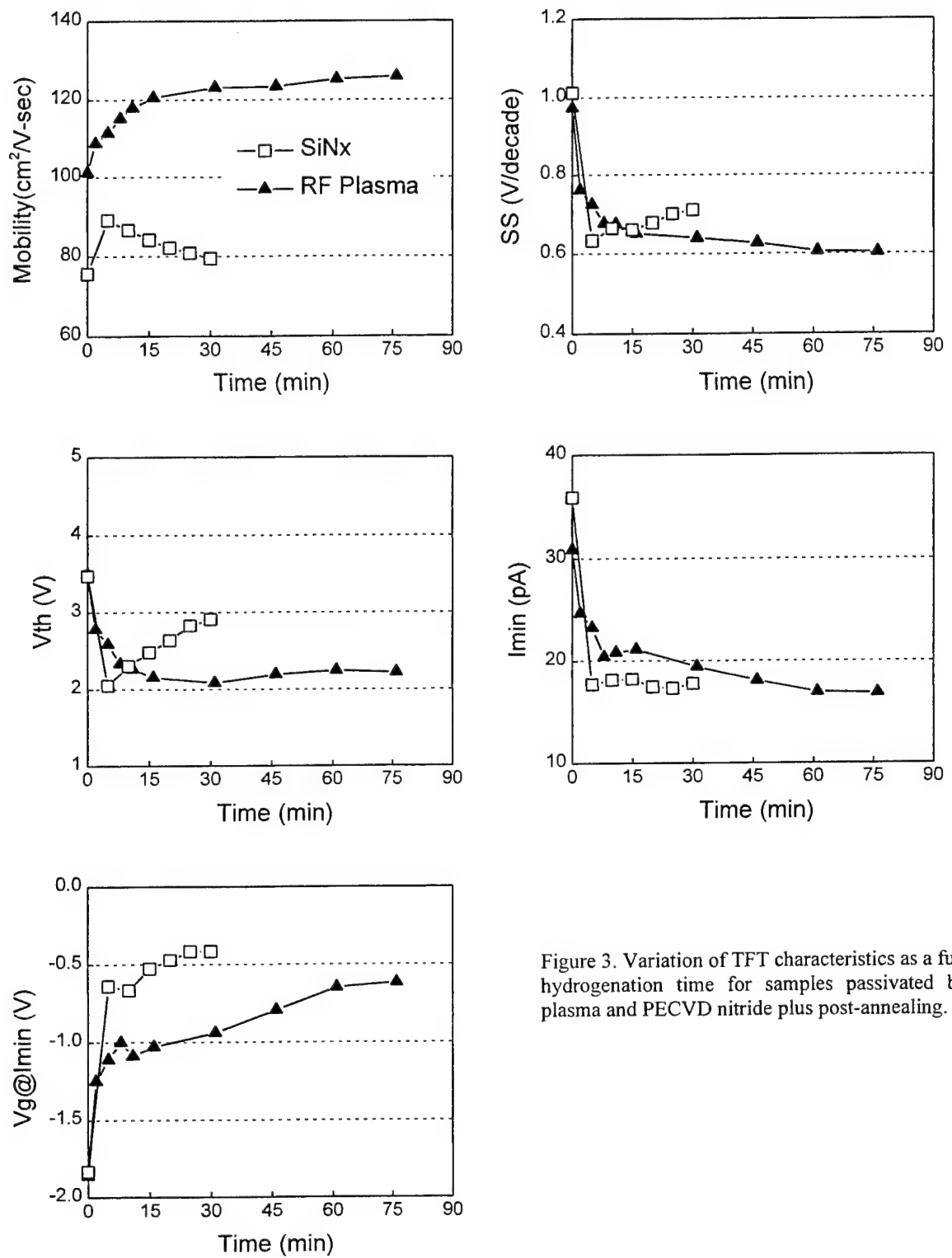


Figure 3. Variation of TFT characteristics as a function of hydrogenation time for samples passivated by H_2/Ar plasma and PECVD nitride plus post-annealing.

VGS Compensation Source Follower for the LTPS TFT LCD Data Driver Output Buffer

Jun-Ren Shih, Shang-Li Chen, Bowen Wang
Display System Design Dept., Electronics Research & Service Organization, Industrial Technology
Research Institute, Taiwan

ABSTRACT

Low Temperature Poly-Silicon (LTPS) TFT technology for LCD has been developed for a long time. Because of its higher mobility, scan driver and data driver could be fabricated on the glass panel to form a fully integrated display panel and reduce its cost. In this paper, new circuits for buffering the DAC in the data driver will be proposed. These circuits have the advantages of lower power and smaller area than the conventional ones. They all extend their full swing from 2 to 10 volts in 12us and have 6-bit resolution at least. Furthermore, the circuits have no feedback system as the operational amplifier (OP) does, which is hard to design in the current LTPS technology.

Keywords: Low Temperature Poly-Silicon TFT, source follower, output buffer, data driver

1. Introduction

Poly-silicon TFT (Thin Film Transistor) technology has been established for applications in active matrix liquid-crystal displays. In order to achieve finer gray scale for better image quality, data driver should be designed with lots of efforts. In the amorphous TFT technology, the scan driver and the data driver are fabricated on the silicon wafer, and then packaged and assembled with the glass panel with expensive and complicated process. Thus, the driver directly fabricated on the glass together with the pixel array is a trend in the future. This paper is focused on the design of the integrated data driver in the LTPS technology. The data driver we proposed in this paper contains a DAC and an analog buffer. The DAC in our circuit contains 2 capacitors and the switch circuit. It has no driving capabilities to drive the load of the data line. So we need a buffer to keep the converted analog voltage and provide enough driving capability. Conventionally the OP is configured as a unit gain buffer as the traditional analog buffer. However, in the LTPS technology, the TFT has much poor performance than the silicon MOS transistor. This makes the OP hard to design. We have proposed many other buffer circuits to take place of the OP in the data driver on the panel.

2. DEVICE CHARACTERISTICS

The i_d - v_d , i_d - v_g curve of our models is shown in figure 2.1(a) 2.1(b):

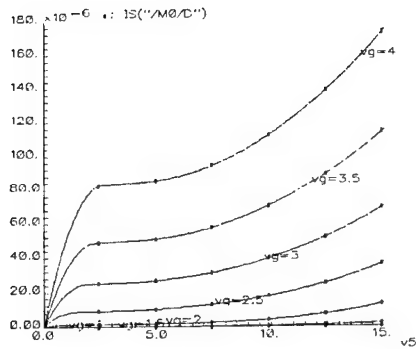


Figure 2.1(a) the i_d - v_d curve of the LTPS models.

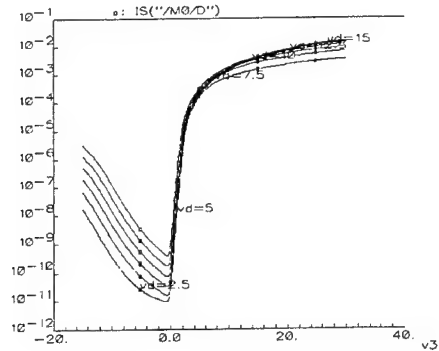


Figure 2.1(b) the i_d - v_g curve of the LTPS model.

From these curves, we can find many disadvantages for the LTPS TFT in the analog circuit. First, the mobility of the LTPS TFT is about 1/10 of the silicon MOS transistor. In order to get the enough current to drive the LCD panel, the size of the TFT must be at least 10 times of the silicon MOS transistor. Second, the threshold voltage of the LTPS TFT is larger than the silicon. This will make the output swing be limited. Third, there is leakage current when the MOS is in the cut-off region. Fourth, in the saturation region, the current of the TFT has greater variation than the MOS on the silicon. And finally, the kink effect makes smaller the saturation region of the TFT. All the above characteristics make the constant current source, which is very critical in analog circuits, has a very small swing.

New circuits are proposed in this paper to replace the operational amplifier as a unit gain buffer to save the area. In order to improve the output impedance of the biasing current sources in the proposed buffer circuits, cascaded structure of current source is necessary. Therefore, 15 volts of the power supply is applied to keep sufficient output range. In this way, the analog output buffer can be used in the driver on the panel. The details will be discussed in the following section.

3. DATA DRIVER STRUCTURE

The overall data driver structure is shown in figure 3.1:

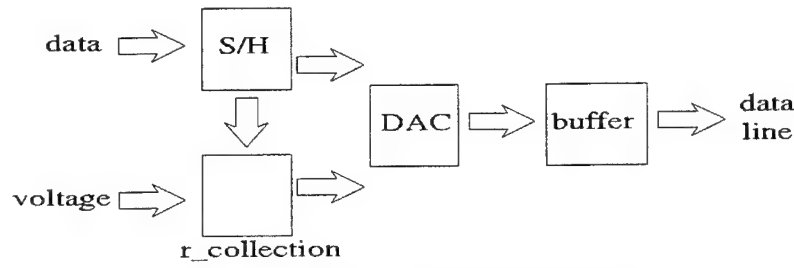


Figure 3.1 the data flow of the data driver in LTPS panel

Neglecting the circuit for sample and hold, the most important part of a data driver contains the gamma correction circuit, DAC, and the buffer. Our gamma correction circuit selects the reference voltages for the DAC according to the first 3 MSB of the digital input such that the converted analog output is a piecewise linear approximation to the transparency-to-voltage curve of the liquid crystal.

The DAC structure used in our data driver is shown in figure 3.2:

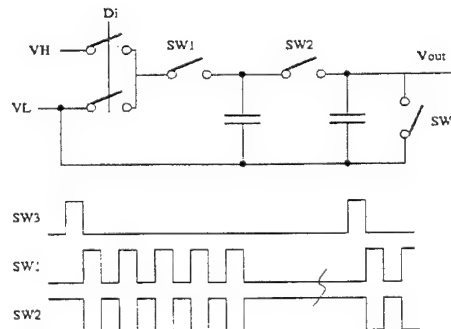


Figure 3.2 the DAC and the control signal in the data driver

The DAC contains 2 capacitors of the same size and several switches.

There are three steps before the output voltage is evaluated. In the first step SW3 is turned on to reset voltages on each node and capacitor. In the second step the non-overlap signals for SW1 and SW2 evaluate the output voltage on the node Vout according to the digital input Di, which is given serially with LSB first to choose VH or VL. The output voltage of the DAC, Vout, at the m-th time that SW2 is on is given by the following equation:

$$V_m = \frac{V_{m-1} + D_m(V_H - V_L)}{2}$$

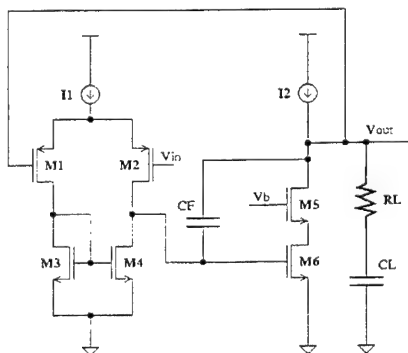
Since the reference voltage VH and VL are chosen by the first 3 MSB of the digital input, only 5 bits of the digital input has to be given serially as Di in the circuit. As SW2 is turned on at the 5th time, it enters the third step. All the switches are held still to keep the output voltage such that the buffer to be introduced later can drive

the data line according to the converted analog voltage in this step.

We can find that the DAC structure is very simple. The advantage of this DAC is that it has small area and consumes very low power. The control circuit will cost a little area but it won't be a problem since all DACs in the data driver can share the same control circuit. The major issue of this DAC on the LTPS technology is that it needs an output buffer to drive the large capacitor on the data line. This is what we are going to discuss in this paper. Some solutions are proposed under below.

Approach I

Traditional output buffer uses the operational amplifier that is configured as a unit-gain buffer. Here we also designed a two stage operational amplifier as the output buffer with the LTPS technology. The circuit and some device parameters are shown in figure 3.3:



component	M1	M2	M3	M4	M5	M6	CF	CL	RL
size	80/8	80/8	30/8	30/8	150/8	150/8	15p	10p	2k

Figure 3.3 the operational amplifier schematic and the size

Because the gain-bandwidth product is too small, we added M5 cascoded on M6. This makes the operational amplifier have higher gain and can have enough speed with reasonable size. The operational amplifier we designed has 66.2db DC gain and 400k unit gain frequency. It have 10-bits resolution and the slew rate reaches 0.9v/us. It can slew the voltage from 0v to 10v within 12usec. The drawback of this circuit is that the capacitor CF for compensation is too large to fit into the limited area of the driver integrated LTPS TFT LCD panel.

Approach II

The second approach is based on the source follower. Since the source follower output has a nearly constant voltage difference, slightly greater than the threshold voltage of the TFT, with the input, we tried to save the voltage difference in the capacitor and then add it back to the input such that the difference can be compensated. Suppose that only one stage of the source follower is used, the magnitude of the stored voltage difference is

about the range of the threshold voltage. While this voltage difference is added back to the gate of the TFT, the output voltage at the source of the TFT will shift by the same magnitude with some offset, which is again resulted from the channel length modulation and kink effect of the source follower itself. Therefore, we proposed new circuits using two stages of the source follower with different type of TFT. The stored voltage on the capacitor is the difference of the threshold voltage of the two TFT in this case. The offset of the new circuits will be greatly reduced because the gate and source of the TFT will have smaller shifting after the compensation. The circuits are shown in figure 3.4. The two switches labeled as SW1 are turned on in the first step such that the difference of the input and output are stored in the capacitor. Then in the second step these two switches are off and SW2 is turned on, so that the stored voltage difference is added back to the input and results in a compensated output.

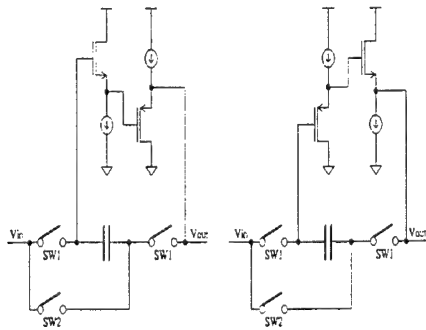


Figure 3.4 the circuit of the source follower with compensation capacitor

To be more specific, we use one p-type source follower and an n-type one to cancel the drop of the source followers in the first step. In this way, the voltage difference between the output and input will be $|V_{gspl}| - |V_{gsn}|$, which is much smaller than $|V_{gs}|$ in a single source follower. In this step, the voltage is also stored in the capacitor. In the second step it will be added back to the input and reflected to the output. This can compensate the offset left by the first step. The above source follower based unit gain buffer is of the class A buffer. The circuit we proposed had been simulated on smart-spice with the LTPS TFT models. The resolution of the DAC can achieve 6-bit. And the settling time (from 2v to 10v) can be within 10u. The DAC with this spec can be used in some low-end products.

The output current of the above class A buffer is the current of the constant current source minus the current provided by the TFT. This kind of the buffer has poor current efficiency. We further improved the circuit to be a class AB buffer structure which is shown in figure 3.5:

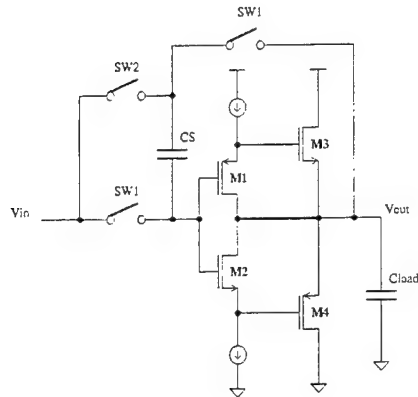


Figure 3.5 the improved circuit of the driver buffer

The basic function of the circuit is exactly the same as the class A ones. This kind of buffer has higher current efficiency. The dark line in the circuit is important since it makes M1 and M2 stay in the saturation region to keep V_{gs} constant. With this circuit, the DAC can reach 6-bit resolution with little current. The side effect of this circuit is that it has a little bit smaller range for operation.

The simulation result is shown in figure 3.6 (a) and 3.6 (b). The curve in figure 3.6 (a) is run in the UMC silicon models. The resolution can achieve 10-bit resolution in this model and the maximum speed can be up to 10Mhz. The curve in the figure 3.6 (b) is run in the LTPS models. The maximum error between the output and the input is 100mv in the output range 2v-10v. The result is worse than the UMC models, but it can achieve 6-bit resolution.

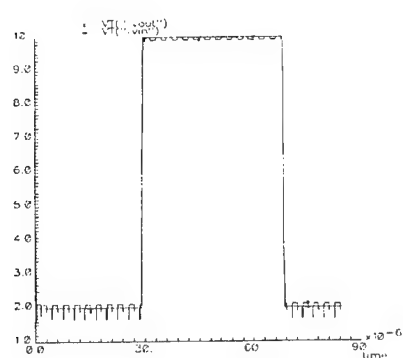


Figure 3.6 (a) the step response of the circuit
in UMC model

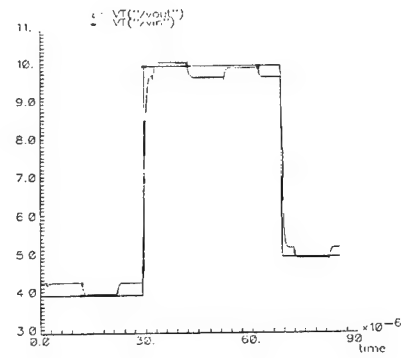


Figure 3.6 (b) the step response of the circuit
in LTPS models

Approach III

The circuit we designed in approach I have an additional capacitor that take a lot of area and add more complexity in the circuit design. In approach II, the capacitor for compensation in the second step will be a load to our DAC, which is composed of capacitors. This makes the resolution as low as 6-bit only. Furthermore, the switches in the circuit also affect the accuracy of the analog circuit by clock feed-through and charge injection effects. The third approach we propose here is going to remove the switches and the capacitor in approach II.

The circuit we design is shown in figure 3.7:

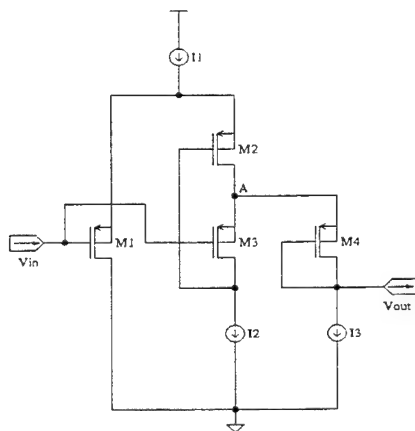


Figure 3.7 A new unit gain buffer

The basic idea of this circuit is also based on the source follower. A diode is used to compensate the voltage drop V_{gs} caused by the source follower. The basic component of these circuits is the two PMOS M3 and M4. M3 is the source follower that tracks the input voltage, and M4 is a diode with a constant voltage drop. The current flowing in M3 and M4 are fixed by current sources I_2 and I_3 . The configuration of M1, M2, and M3 is widely used in high swing cascoded bias circuits. This configuration guarantees that these three transistors are all in the saturation region. M4 is a diode with constant current so that V_{gs} of M4 is kept constant. We make M3 and M4 of the same size and the two current mirrors I_2 and I_3 exactly the same. Then we can find that $V_{gs1} = V_{gs2}$ and $V_{out} = V_{in}$.

For the concern of loading to the previous stage, which might be a DAC without strong driving capability, we can use two such buffers to transfer the load effect. We design the first buffer with smaller size connected to the DAC to lower the load of DAC. And the second buffer is designed with larger size in order to push the large load of the LCD panel.

This circuit has been simulated with our LTPS model. The advantage of the circuit is that the area is smaller than operational amplifier. The circuit doesn't have any capacitor and switch. Its resolution can be up to 8-bit. They

can charge or discharge 10pF of capacitor connected with 3K of resistor, which is a simplified model of the loading on a data line of the TFT LCD panel, within 10us. The simulation result is shown in figure 3.8 (a) and figure 3.8 (b). Figure 3.8 (a) is the sweep response of the circuit with Vin from 0v to 15v. The curve is the value of Vout-Vin. The error between Vout and Vin in the curve is +/-25mv when the input is 1.5v~10v. Figure 3.8 (b) is the step response of the circuit. We can see that the circuit can charge the load from 1v to 10v within 10usec.

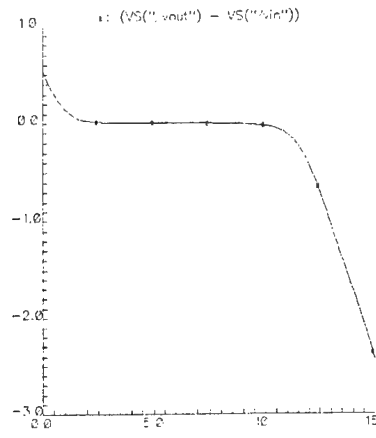


Figure 3.8 (a) the sweep response of the circuit,
Vin from 0v to 15v

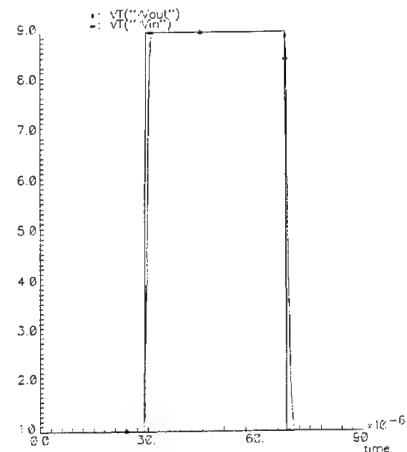


Figure 3.8 (b) the step response of the circuit

5. CONCLUSION

We have proposed various types of output buffer that could be implemented on the LTPS TFT LCD as part of the integrated data driver circuit. Since mobility of the LTPS technology is not as high as that of silicon, any circuit to be realized with the LTPS technology will take larger area than those to be implemented on silicon wafer. The output buffers we proposed have simple and realizable structure for the data driver such that they all have much smaller size than any conventional buffer configured with OP. On the other hand, these circuits also have higher speed than the OP. These circuits outperform the OP in many aspects except that they can only reach 6 to 8 bits of resolution. However, the resolution of these buffers can be improved easily as the processing technology is improved.

6. ACKNOWLEDGMENTS

We sincerely acknowledge the invaluable help of Yi and Rao, the advanced engineer in the erso, ITRI. Also, we want to thanks all of the engineers in Display System Design Dept.

7.REFERENCES

1. Seung-Woo Lee, Hoon-Ju Chung, Choong-Heon Lee, and Chul-Hi Han, "A Low-Power Poly-Si TFT-LCD with Integrated 8-bit Digital Data Drivers", 16.4, SID, 1998.
2. Seung-Woo Lee, Hoon-Ju Chung, Jin-Woo Lee, and Chul-Hi Han, "High Performance, Low-Power Integrated 8-bit Digital Data Driver for Poly-Si TFT-LCD's", SID, 1999.
3. Seung-Woo Lee, Hoon-Ju Chung, Jin-Woo Lee, and Chul-Hi Han, "A Novel Integrated Serial Digital Data Driver Poly-Si TFT-LCD's", ED, 1999.

SESSION 3

PDP and CNT_FED

Advanced manufacturing technologies on color plasma displays

Keiichi Betsui

Fujitsu Laboratories Ltd., 64 Nishiwaki Okubo-cho Akashi, 674-8555, Japan

ABSTRACT

The mass production of the color plasma display started from 1996. However, since the price of the panel is still expensive, PDPs are not in widespread use at home. It is necessary to develop the new and low-cost manufacturing technologies to reduce the price of the panel. This paper describes some of the features of new fabrication technologies of PDPs.

Keywords: PDP, fabrication, insulating film, rib, phosphor,

1. INTRODUCTION

Flat panel displays have always been essential to realizing wall-hanging TVs and space saving PCs, but for many years, severe size limitations seemed as though they would always keep the technology on the periphery and prevent it from becoming central to the AV and PC industries. By mass producing large plasma display panels, however, Fujitsu has opened up a new chapter in the history of this product. With the start of mass production of 42 inch PDPs in October 1996, at the same time as the announcement of the first commercial shipments to customers worldwide, PDPs are now well on their way to becoming the display of choice in large flat panels. Wall-hanging televisions have finally moved out of the realm of science fiction and into the reality and everyday life. This paper reports new fabrication technologies used in the formation of insulation film, barrier ribs, and phosphor layers.

2. STRUCTURE AND OPERATION PRINCIPLE OF AC-TYPE COLOR PDP

Figure 1 is a diagram showing the panel structure of a AC-type color PDP put into practical application. A plasma display consists of two parallel glass panels on which electrodes covered with a dielectric glass layer have been etched. The 0.1 mm wide gap between the two plates is then filled with a xenon/neon (XeNe) gas mixture. When voltage is applied between the electrodes, ionized gas collects at the surface layer according to the polarity. The collected charge is called the wall charge, and it produces an internal voltage difference (wall voltage). As a result of the surface discharge, ultraviolet ray radiation occurs. These ultraviolet rays activate phosphor dots, which then emit visible light. A color display is achieved by controlling the luminance from individual phosphors in the three prime colors. To maintain the discharge, the polarity of the external voltage is reversed. The applied voltage is lower than the initial voltage because the wall voltage remains inside the cells, so once discharging occurs, it continues unless it is stopped.

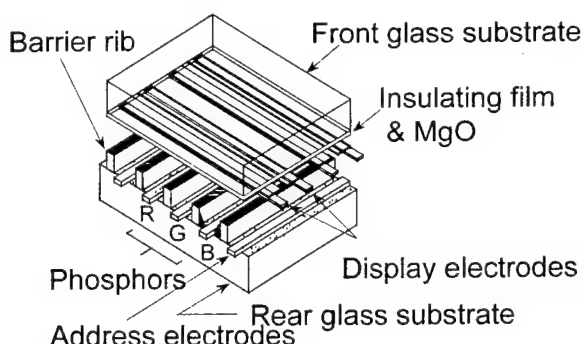


Fig.1 Structure of experimental panel

3. PDP FABRICATION PROCESS

PDP fabrication does not have an established process yet, so PDP fabrication processes differ depending on the panel makers. Figure 2 shows a typical fabrication process currently in operation. The front panel first goes through the patterning of transparent electrodes, followed by sputtering a film of chromium/copper/chromium (CrCuCr). The BUS electrodes (CrCuCr) are then patterned, a dielectric layer screen-printed and a final protective layer of Magnesium Oxide evaporated on. The back panel is processed a little differently: Address electrodes (CrCuCr) are first constructed, followed by printing of a dielectric layer and a rib pattern. The ribs are then sandblasted and a fluorescent layer is screen printed, with the sealant construction as the final step. The materials in PDP have several important characteristics. The materials have a low gas discharge rate and a tolerance against vacuum ultraviolet. They are also heatproof up to 350°C. Therefore, a glass material with a low melting point is usually used as material for insulation film and ribs. The low-melting-point glass and phosphor in this PDP fabrication process are powder, which is most remarkable because the fabrication process can use such powder material to form precise cell structure.

3.1 Insulating film formation process

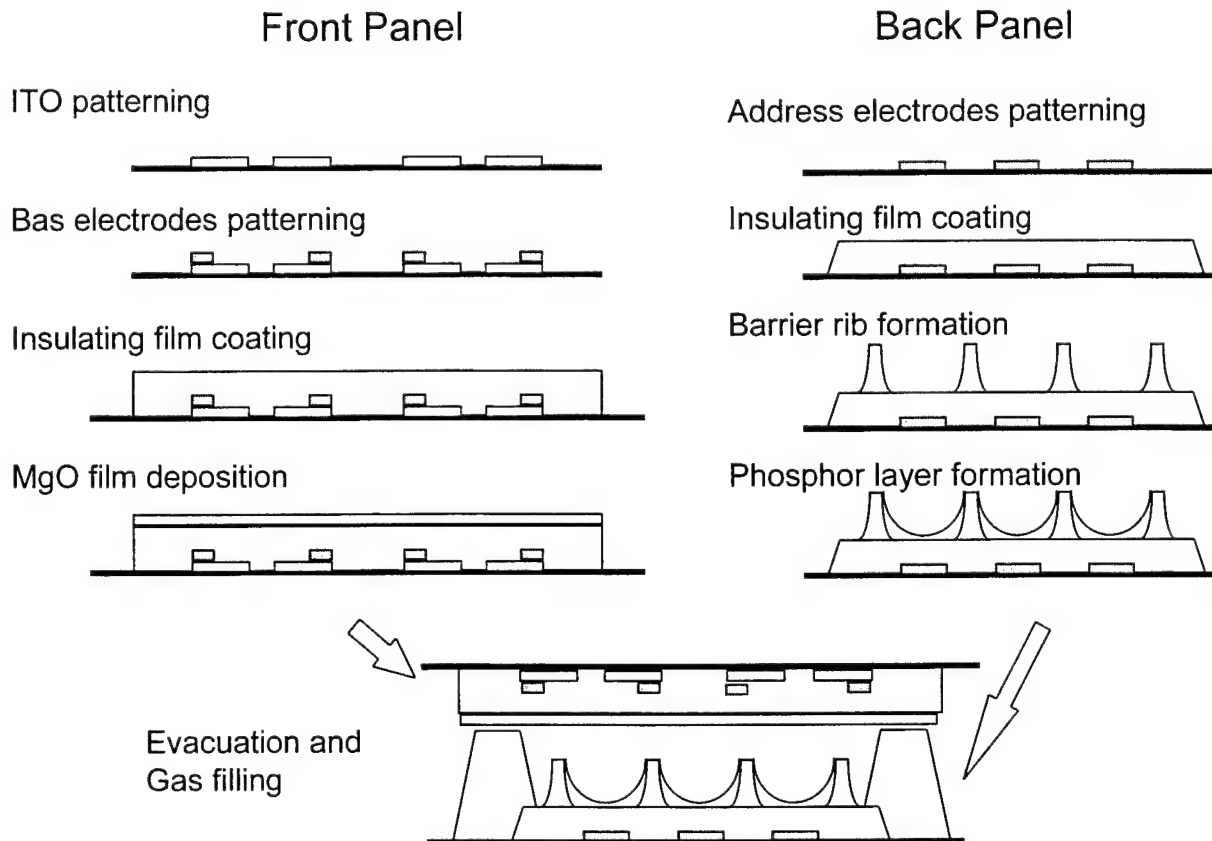


Figure 2. Panel fabrication process

The insulating film of front panels plays an important role in accumulating the wall charge and limiting the electrical discharge current. The inflator material of the PDP is low-melting-point glass with a softening point in a range from 450 °C to 580 °C. The thickness of the insulating film is about 30 µm. Since film thickness depends greatly on electrical discharge characteristics, high thickness uniformity without any defects is necessary. Good level of transparency is also necessary because the film is used in the a front panel, which must pass light from the phosphors. To obtain a good level of transparency, any bubbles in the film must be completely removed by high-temperature firing. However, to prevent a reaction between melting glass and electrode metal during the firing process, the material of the low-melting-point glass was

carefully selected. Screen-printing, slot die coating, roll courting, and sheet lamination are used for the coating of the insulation film.

Screen-printing method

Screen-printing is a method to coat the insulator with paste that comes from a squeegee through a screen mesh made of stainless-steel wires. The film thickness of the insulation layer can be controlled by selecting the mesh specifications (i.e., mesh wire diameter and pitch of meshes). The advantage of using this method is that shape and detailed patterns can be printed. However, immediately after printing, the film has mesh marks because of thickness variations. Since mesh marks cause irregularity in the display, sufficient smoothing is required. To obtain a smooth surface, a leveling time of ten minutes is required after printing.

Slot die coating method

Figure 4 is a schematic drawing of the slot coating method. Paste is dispensed on a glass substrate through a small gap in the feed head. The film thickness is adjusted by controlling the coating parameters, such as the moving velocity of the stage, slot gap of the die, and paste supply pressure. Basically, this method can coat only rectangular areas, whereas the screen-printing method can coat areas in a variety shapes.

Roll coating method

The roll coating method is widely used to coat such as photo resists. There are different kinds of roll coating methods, but the reverse roll coating method is described here because it can be applied to coat films in a wide range of thickness. Figure 5 is a schematic drawing of a roll coater. First, paste is applied onto two metal rolls (A roll and Comma roll), then paste on the A roll is transferred to a rubber roll(C roll). Paste on the C roll is transferred to a glass substrate. The advantage of this method is that the paste has a very wide range of the viscosity, enabling thick paste coating of ribs. Any swelling in the paste at the starting and terminating points of the coating area is controlled by changing the elevation of the C roll. The shape of the coating area is limited rectangles, similar to the slot coating method.

Sheet lamination method

Figure 6 is a schematic drawing of a sheet lamination method. The technology of the method is generally the same technology used for hybrid ICs. After removing the cover film, the sheet is laminated on the glass substrate between heated rolls, and the base film is removed. The sheet becomes a insulating film after firing. The advantage of this method is good thickness uniformity in the film and easy operation. However, film thickness cannot be adjusted during the process.

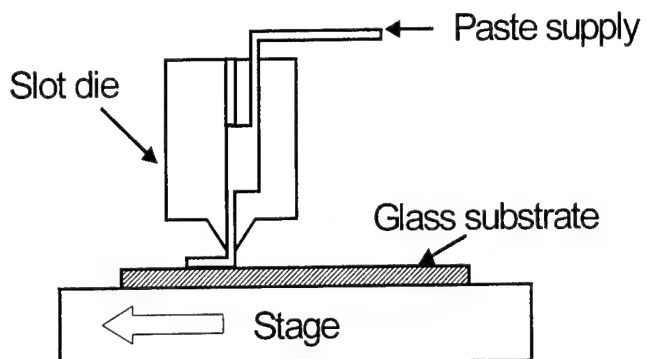


Figure 3. Slot Die Coating Method

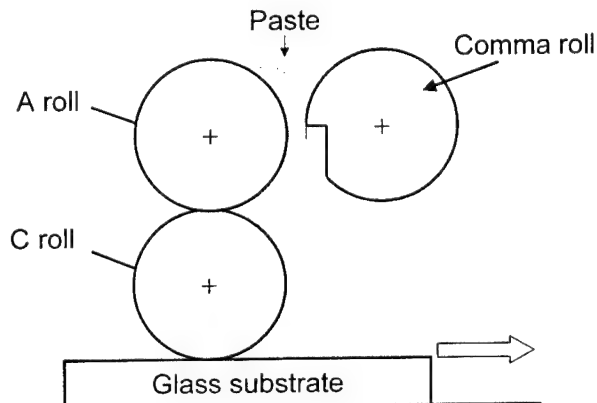


Figure 4. Roll Coating Method

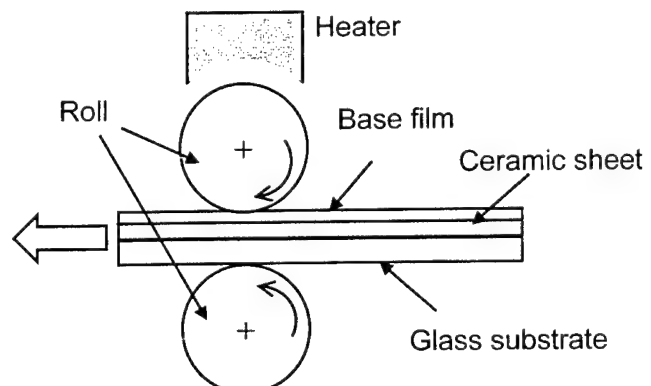


Figure 5. Sheet Lamination Method

3.2 Barrier rib formation process

Barrier ribs are formed on the back panel, and parallel ribs are usually used because they are easy to fabricate in AC-type PDPs. The ribs have a height of 140 μm , width of 70 μm , and pitch of 360 μm . The material in the ribs are frit glass containing ceramic filler. The fabrication method is a combination of different kinds of formation technologies. The following methods are proposed fabrication methods of barrier ribs.

- Screen-print method
- Sandblasting method
- Photo paste method
- Lift off method
- Mold method

Among these, Sandblasting, photo paste, lift off and mold methods are explained.

Sandblasting method

The sand blasting method has been the technology used for the mass production of large PDPs. Figure 6 shows a formation process using the sandblasting method. The sandblasting method is a newly developed process technology to fabricate barrier ribs, replacing the thick film printing method. First, rib material is coated all over a glass substrate by the paste coating method and then dried. Dry film is formed on the material to protect it during the sandblasting. Sand(powder) is sprayed on it by compressed air to cut the rib material except at areas where the dry film has formed. After that, the dry film is removed and the glass substrate is fired. Previously explained film coating methods (screen-printing, slot die coating, roll coating, and sheet lamination) can be used as the formation method of the rib material. Thickness uniformity and material homogeneity of coated thick film are important for ensuring a precise rib shape. In addition, since the sandblasting rate strongly depends on the amount of resin in the paste, drying conditions must be stabilized. Figure 7 are SEM photographs of ribs formed by the sandblasting method. The formation method using sandblasting with the photo exposure method provides sufficient accuracy for pattern formation. However, a lot of rib material is lost by this method during removal of paste by sandblasting.

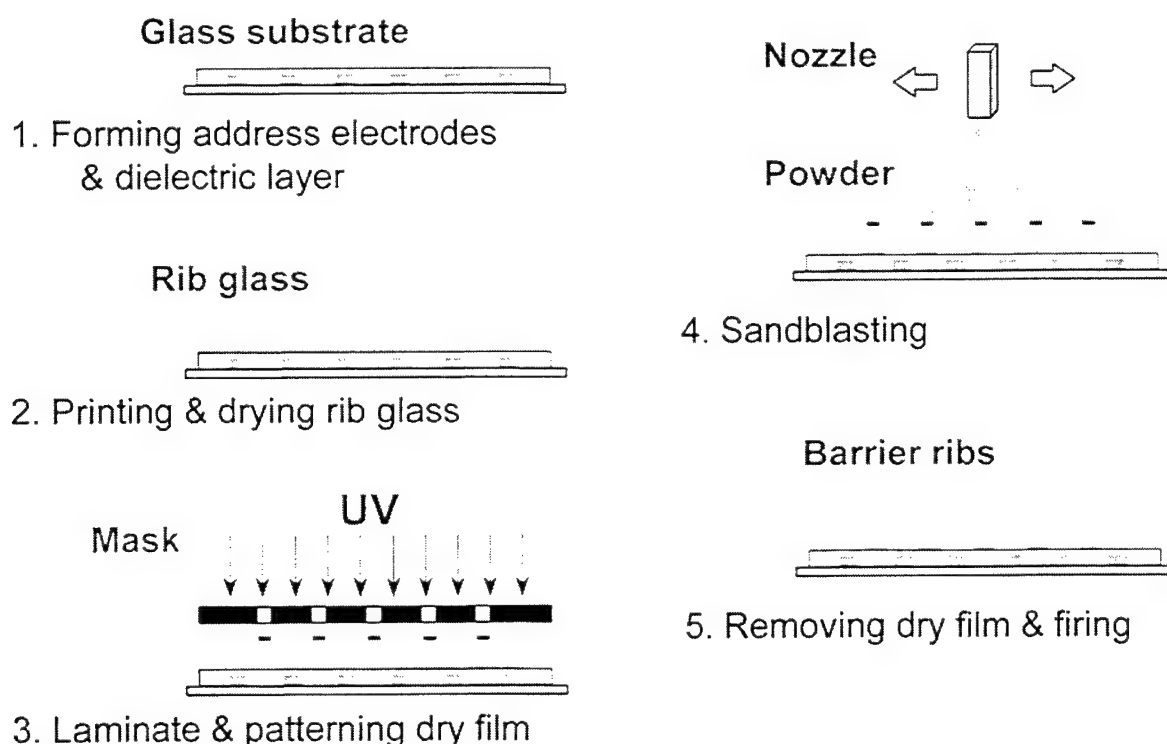


Figure 6. Sand Blasting Method



DeLTA Cell

25" SXGA Cell

Figure 7. SEM Images of Barrier Ribs made by sandblast^{1,2}

Lift off method

Figure 8 shows the formation process of ribs by the lift off method. First, in a lamination step, dry film is applied on the substrate where address electrodes are formed. Rib paste is then coated on the dry film, and channels in the dry film are filled with paste. After that, the dry film is removed. Finally, the rib material is fired. To obtain the desired section shape, exposure and development conditions are optimized. The optimization of the rib paste and dry film material is necessary to prevent the solvent from attacking the dry film in the coating process. The advantages of the lift off method is a low loss of rib material and a smooth surface on the side wall.

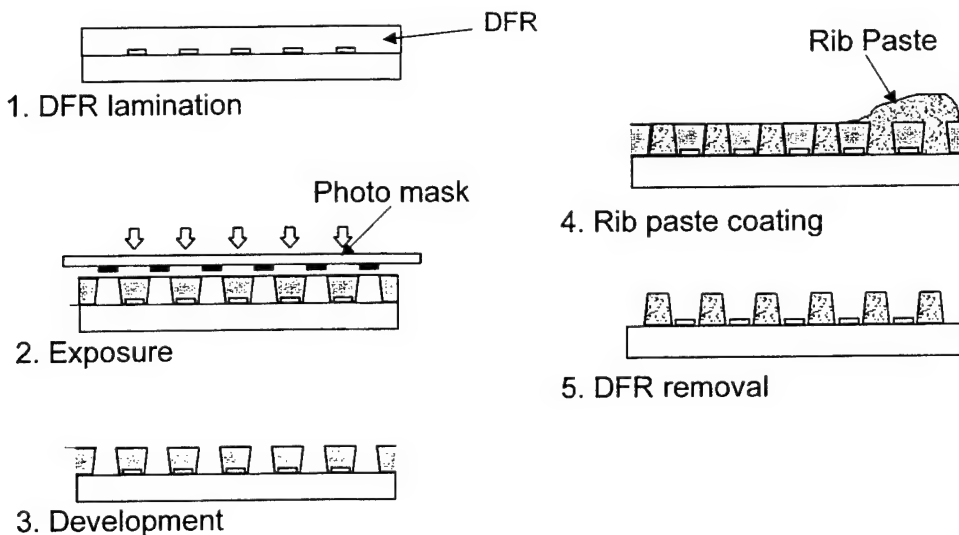


Figure 8. Lift Off Method

Photo paste method

Figure 9 shows the fabrication process of ribs by the photo paste method. Photo sensitive rib paste film is coated on the substrate where address electrodes are formed. After the paste is exposed, it is developed and rib paste in unexposed areas is removed. The advantage of photo paste method is that it is very simple since only exposure and development are done. However, because UV light is scattered by glass powder, exposing all of the film at one time is difficult.

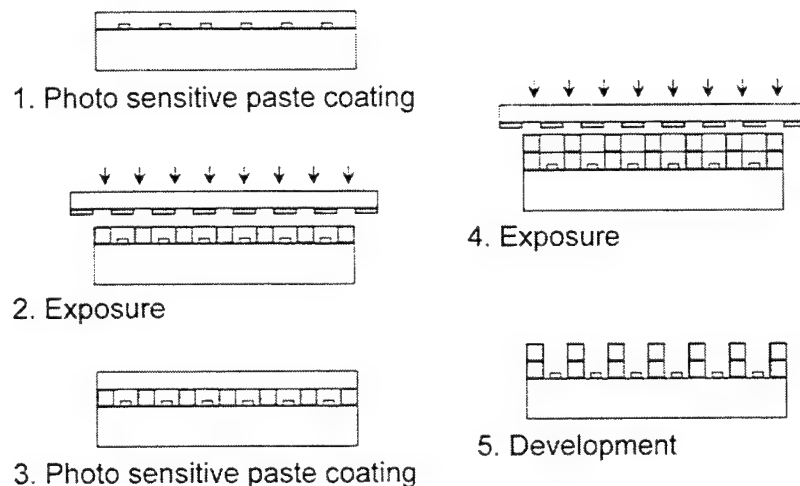


Figure 9. Photo Paste Method

Mold method

There are different mold methods and an example of one of them is shown in Figure 10. Rib paste is coated on a glass substrate. A mold is pressed on the paste film to modify the shape of the paste. The advantage of the mold method is a low fabrication cost due to its simple process.

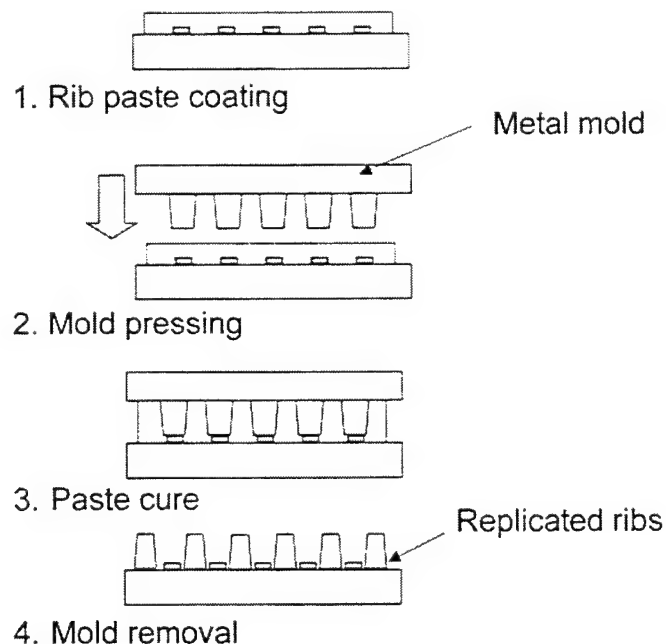
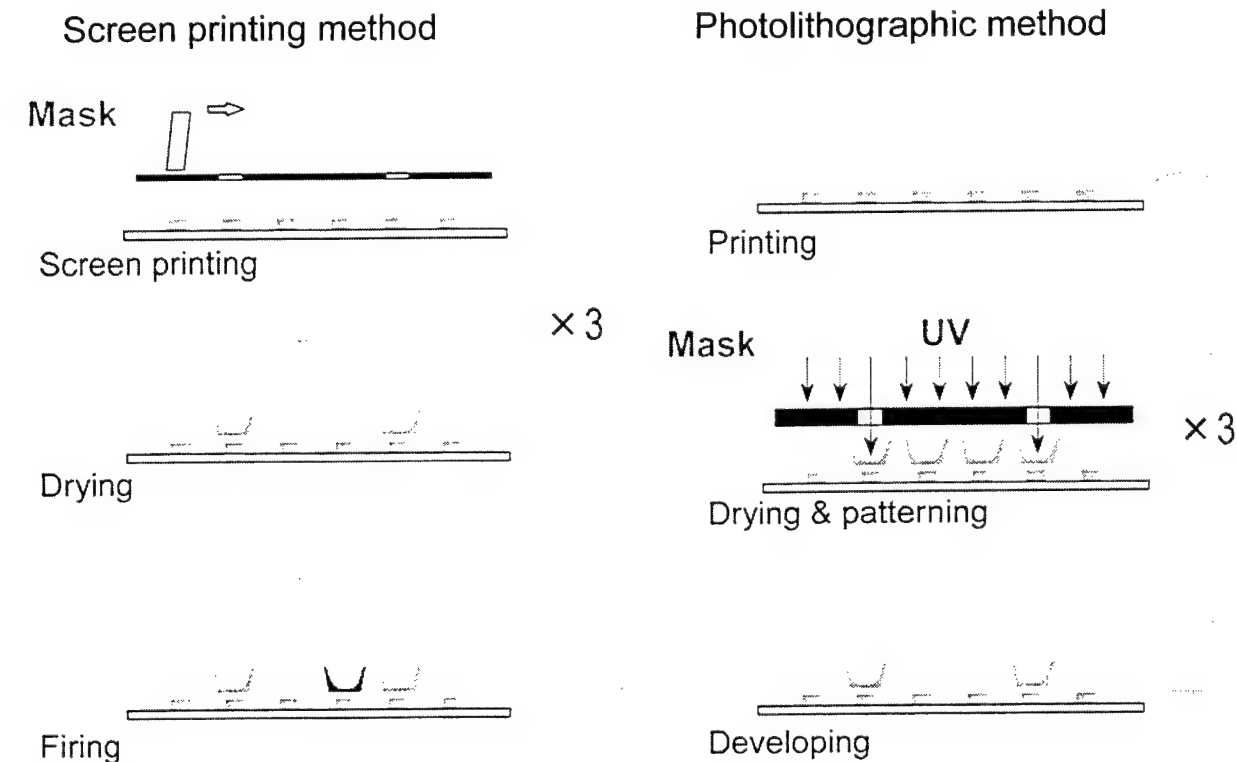


Figure 10. Mold Method

3.3 Phosphor formation process

The phosphor formation process of PDPs is explained in this section. To cover the surface of ribs on the back panel, phosphors of AC-type PDP are formed. The following methods are currently being developed as phosphor formation processes of PDPs.



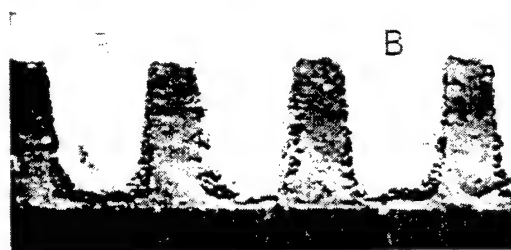
Screen-printing method

Figure 11 shows the phosphor formation process by the screen printing method.. The screen printing method is commonly used for forming phosphor layers. However, printing phosphors evenly between the fine-pitched ribs (130 μm pitch) requires high-quality technology and high-precision screen masking.

Photolithographic method

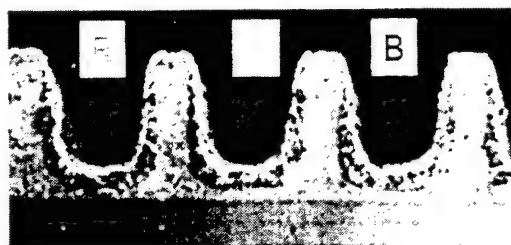
Figure 11 also shows the phosphor formation process by photolithographic method. Photosensitive phosphor paste is made of photo resists in which phosphor particle of specified colors are evenly dispersed. The prepared paste is coated to the entire surface of a rear substrate with barrier ribs. This substrate is then dried to evaporate the solvents in the paste at 100-120 °C. Any remaining paste on top of the barrier ribs does not cause any problems. Next, the dried film is exposed by UV light through a photo mask. The exposure and development of this paste produces a phosphor paste layers for the three primary colors. Finally, the substrate is fired to burn out all organic ingredients remaining in the phosphor paste layers and ensure that the phosphor layers consist of only phosphor particles. The primary issue of using this method this method is on the recycling of removed phosphor material. Figure 12 shows SEM images of phosphor layers made using screen printing method and photolithographic method.

Screen printing method



- Simple and established process
- High precision screen mask
- Short life time of screen mask

Photolithographic method



- Higher patterning accuracy
- Available for any shape
- More process steps

Figure 12. SEM Images of Phosphors

Dusting method

Figure 13 shows the phosphor formation method by the dusting method. Photo tacky material is coated on the rib surface. After UV light exposure, the part exposed UV light has tacky adhesion. Under such a condition, when the phosphor powder is sprinkled, the phosphor remains only in a cohesive part.

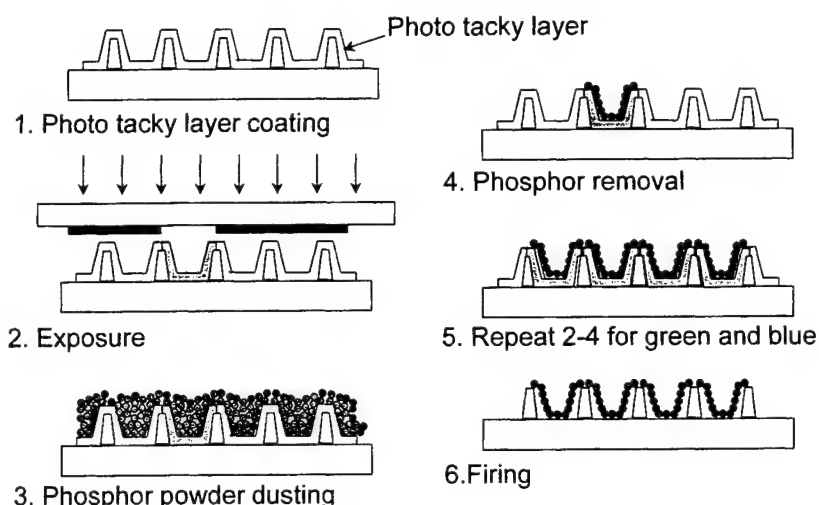
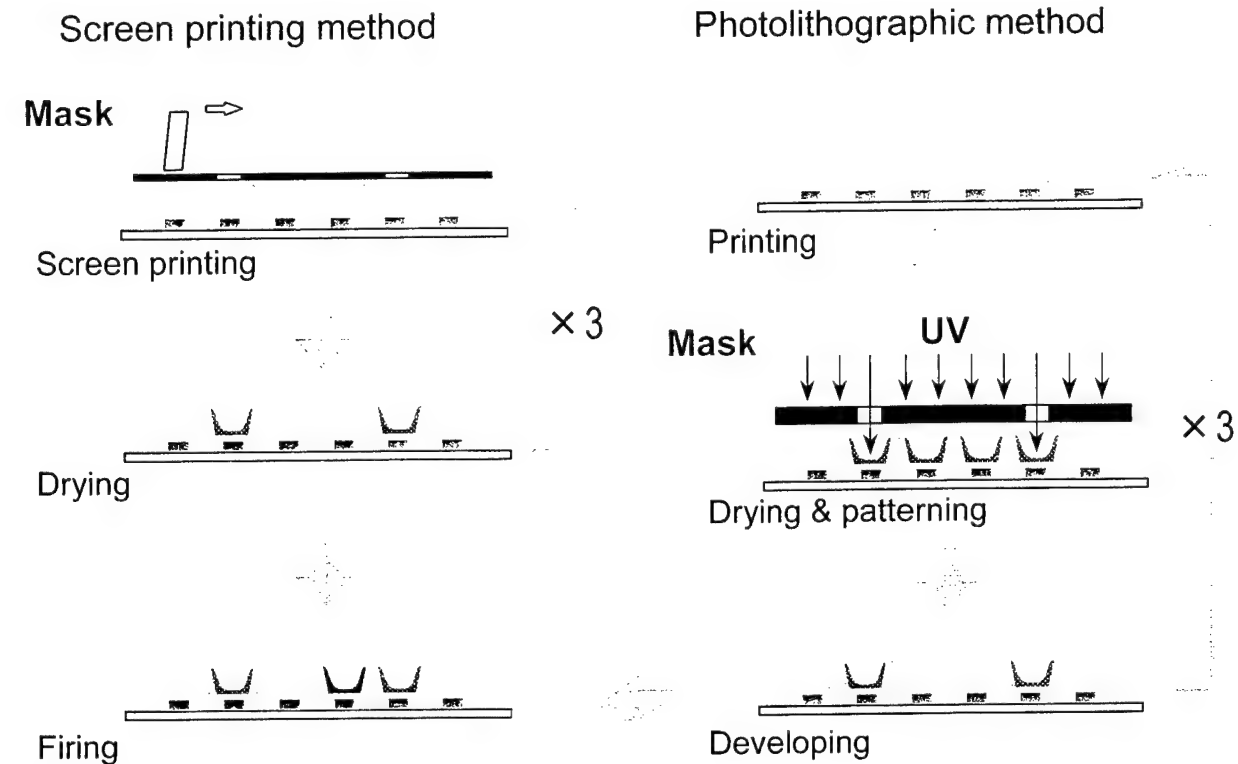


Figure 13. Dusting Method

3.3 Phosphor formation process

The phosphor formation process of PDPs is explained in this section. To cover the surface of ribs on the back panel, phosphors of AC-type PDP are formed. The following methods are currently being developed as phosphor formation processes of PDPs.



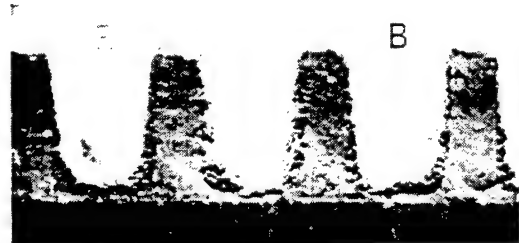
Screen-printing method

Figure 11 shows the phosphor formation process by the screen printing method.. The screen printing method is commonly used for forming phosphor layers. However, printing phosphors evenly between the fine-pitched ribs (130 µm pitch) requires high-quality technology and high-precision screen masking.

Photolithographic method

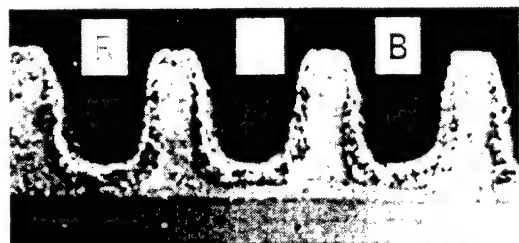
Figure 11 also shows the phosphor formation process by photolithographic method. Photosensitive phosphor paste is made of photo resists in which phosphor particle of specified colors are evenly dispersed. The prepared paste is coated to the entire surface of a rear substrate with barrier ribs. This substrate is then dried to evaporate the solvents in the paste at 100-120 °C. Any remaining paste on top of the barrier ribs does not cause any problems. Next, the dried film is exposed by UV light through a photo mask. The exposure and development of this paste produces a phosphor paste layers for the three primary colors. Finally, the substrate is fired to burn out all organic ingredients remaining in the phosphor paste layers and ensure that the phosphor layers consist of only phosphor particles. The primary issue of using this method this method is on the recycling of removed phosphor material. Figure 12 shows SEM images of phosphor layers made using screen printing method and photolithographic method.

Screen printing method



- Simple and established process
- High precision screen mask
- Short life time of screen mask

Photolithographic method



- Higher patterning accuracy
- Available for any shape
- More process steps

Figure 12. SEM Images of Phosphors

Dusting method

Figure 13 shows the phosphor formation method by the dusting method. Photo tacky material is coated on the rib surface. After UV light exposure, the part exposed UV light has tacky adhesion. Under such a condition, when the phosphor powder is sprinkled, the phosphor remains only in a cohesive part.

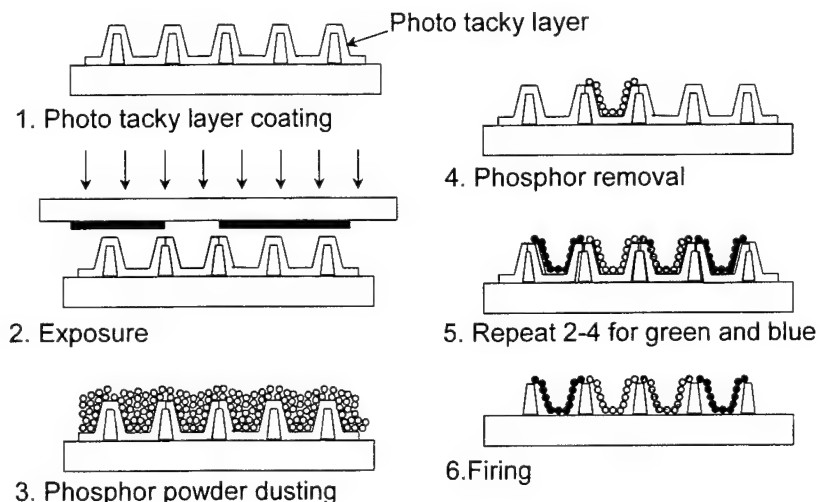


Figure 13. Dusting Method

4. SUMMARY

Advanced Color PDP manufacturing technologies have been reported. PDPs have been shown, step by step, to have qualities that make them the expected favorites for use in large screen displays. However, because the mass production of PDPs started relatively recently, the mass production technology currently in operation still has many problems. Moreover the manufacturing process must be developed to lower costs even further.

REFERENCES

1. F. Namiki, A.Tokai, T. Kosaka, K. Irie, O. Toyoda, N. Awaji, S. Kasahara, K. Betsui, H. Inoue, N. Matsui, M. Wakitani, "Characteristics of a High Resolution Full-Color Plasma Display Panel", *IDW'97 Digest*, pp.515-518, 1997.
2. O. Toyoda, T. Kosaka, F. Namiki, A.Tokai, H. Inoue, K. Betsui, "A High Performance Delta Arrangement Cell PDP with Meander Barrier Ribs", *IDW'99 Digest*, pp.599-602, 1999.

Recent Advances of Color Plasma Displays

Heiju Uchiike

Dept. of Electrical and Electronic Engineering, The SAGA University
Saga, 840-8502 Japan E-mail:uchiike@cc.saga-u.ac.jp

Abstract

Several kinds of color PDPs have been converged to a single group of the surface-discharge color ac PDPs of which the reason will be described on the basis of the recent advanced ultraviolet-rays measuring systems.

PDP Manufacturers completed to construct the first generation of mass production lines for color PDPs and now doing to accomplish the second generation of ones until 2001. Under the existing circumstances in Japanese PDP manufactures one of the most distinctive events in 1999 is amalgamating or cooperative motions between PDP manufacturers within or outside of Japan.

The present paper will also describe the latest information about the processes and materials of which composed the advanced color PDPs.

1. Introduction

During the past several years, 20-inch to 50-inch diagonal color PDPs have become available commercially and LG and Plasmaco tried to fabricate 60-inch diagonal ones to demonstrate them at the exhibition. On the basis of these accomplishments, manufacturers have now almost constructed the first generation of mass production of color PDPs and commercialized them, and recently *Fujitsu Hitachi Plasma Display (FHP)*, *NEC*, and *Pioneer* are constructing the second one, which are attracting a great deal of attention.

The system structure and design stage for the first generation of color PDPs are now over, and a mass production process, which can achieve a high yield and throughput, is being sought. As more manufacturers enter the color PDP production field and attempt to develop innovative technologies on the basis of new concepts for device materials and components, the manufacturing processes and the trend of color plasma display industry, in particular, in Japan are being reviewed.

Even though the surface-discharge electrode configuration has the excellent performance essentially, their performance must be improved to be used for the advanced computer monitors and the High-Definition TV. The recent distinctive results in the improvement of performance are ALIS by *Fujitsu*, Waffle structure and CLEAR (Hi-Contrast & Low Energy Address & Reduction of False Contour Sequence) operating scheme by *Pioneer*, and the full-scale High-Definition TV monitor by *Panasonic*, respectively. The specifications of Fujitsu are 500 cd/cm² and 250 W for 42-inch diagonal with 1,024 × 1,024 pixels. Those of Pioneer are 560 cd/cm² and high contrast ratio of 560:1. Those of Panasonic are very fine resolution of 1,920 × 1,080 pixels and very high contrast ratio of 300:1 for 42-inch diagonal one.

2. Color PDPs Market in Japan

It is pointed out that luminance of 500 cd/m² achieved by ALIS is evaluated to be acceptable value for home use TV. Sony will deliver color PDP TV receivers by purchasing ALIS from Fujitsu this year.

Under these circumstances, it is speculated that a maximum production volume of color PDPs in *Fujitsu*, *NEC*, and *Pioneer* in 1999 are 10,000, 10,000, and 4,000 units per a month, respectively. It is also speculated that total sales volume of color PDPs produced in Japan is a half of maximum production volume, that is, 12,000 units per a month. The selling amount of color PDPs in 1998 and 1999 are 500 and 1,500 million dollars, respectively and in 2002 it will be reached to 1 billion dollars after the present construction of the second stage manufacturing process lines will be completed. It is well known that a half volume of color PDPs are sold in Europe.

3. Current Status of Color PDP Developments

The 21-inch diagonal full-color ac-PDPs commercialized by *Fujitsu* in 1993 were the first to be used as television monitors. *Fujitsu*, *NEC*, *Pioneer*, *Mitsubishi Electric*, *Panasonic*, and *Hitachi* tried to be manufacturing or establishing to manufacture 40 to 50-inch diagonal full-color ac-PDPs.

Overseas, *Thomson CSF* is working on two-substrate electrode structure, while *Plasmaco* has adopted the surface-discharge electrode structure that is exactly identical to that of *Fujitsu* products. In the U.S. *Plasmaco* has developed 60-inch full-color ac-PDPs and demonstrated it at 1999 SID Symposium and Exhibition. In France, *Thomson CSF* has successfully developed high-definition PDPs with discharge cell pitches of 0.125 nm, and realized a 19-inch diagonal

XGA (1,024 ×RGB ×768 dot) display.

In the Asia region outside of Japan, *LG*, *Samsung*, and *Orion* and *Acer* and *CPT* are constructing mass production lines in Korea and Taiwan, respectively.

4. Operation Mechanisms of Color PDPs based on the Advanced Experiments using Ultraviolet Rays Measuring Systems

It has seemed to be very strange for us that luminance and luminous efficiency of color PDPs are larger than those of monochrome PDPs. The advanced experiments solved this strangeness based on the measured results that the ultraviolet rays emitted from Xe and Xe dimers are distributed simultaneously around both the cathodes and the anodes; neon orange color emission from Ne is limited around only the cathodes. Based on these experimental results, roughly speaking, luminance and luminous efficiency of color PDPs is two times larger than those of monochrome ones.

The computer simulation confirms the recent experimental results of simultaneous ultraviolet rays emission from both the cathodes and the anodes. The studies on the experimental and simulated results make remarkable progress on understanding the basic gas discharge phenomena generated in color PDPs. It is also expected that the experimental and simulated results contribute to improve performance of color PDPs, in particular, luminance and luminous efficiency.

5. Future Issues of Color PDPs Including Production of PDP Barrier Ribs and Phosphors

To understand the issues of color PDPs to be solved in the future, the electrode structure full-color ac-PDP is described below. On the rear glass substrate, address electrodes and barrier ribs are formed by baking, providing a discharge space for the prevention of optical cross talks.

The barrier ribs are approximately 50 μm wide and about 100 μm tall. RGB phosphors are printed on the address electrodes and rib sides, forming one pixel to each set of RGB phosphors. A Ne+Xe (4%) Penning mixture gas at the pressure of 600 Torr is used as the filling gas.

The barrier ribs for 20-inch diagonal PDP are produced by the thick-film screen printing method. Although thick-film printing technology has advanced, the production of barrier ribs is expected to be the technological hurdle in the production of PDPs of 40-inches or larger. In this environment, the sandblast method [2][3] and dry film method [4] are attracting attention as potential replacements for thick-film printing. The sandblast method is used in Fujitsu's 42-inch color PDPs. [5] This method is based on photoresist processing and can produce barrier ribs of 50 μm in width for the production of fine patterns.

Attempts have recently been made to incorporate photosensitivity into the insulating paste that forms the ribs themselves for discharge. In principle, the sandblast and dry film methods are advantageous for the production of fine patterns using photolithography. They, however, require a further process after the rib formation photoprocess. If the insulating material, which itself forms ribs, has photosensitivity, ribs can be formed by a single photoprocess.

One of the most advanced example is photolithographic technology to apply the fabrication color PDP with a performance for full-spec High-Definition specifications by *Panasonic*.

Color PDPs use the photoluminescence phenomenon induced by vacuum ultraviolet rays, as in the case of fluorescent lamps. Development has been advanced by improving the characteristics of the phosphors used in CRT for Red, Green, and Blue. (Y,Gd) BO₃:Eu³⁺ for Red, Zn₂SiO₄:Mn for Green, and BaMgAl₁₀O₂₃:Eu²⁺ for Blue, have been used. However, since Zn₂SiO₄:Mn has a long afterglow, BaAl₁₂O₁₉:Mn has recently been used for Green.

6. Systems for Achieving High Luminance and Luminous Efficiency and Future Issues

The most important issue to be tackled to promote the application of color PDPs in practical products is the improvement of luminance and luminous efficiency. In ac-PDPs that use the surface-discharge electrode configuration represented by *Fujitsu* products, the reflective structure is used. In this system, the light emitted from the phosphor surface of the rear substrate is obtained through the transparent electrodes formed on the surface substrate. This system has achieved twice the luminance of conventional transmissive formats in which light transmitted through phosphors is obtained. The application of phosphors deposited on the barrier rib sides also contributes to the improved luminance.

High luminance and high luminous efficiency have been achieved by adopting a surface-discharge electrode structure and phosphor reflection system. 21-inch diagonal PDPs with a life of more than 30,000 hours, and 200 cd/m² luminance and 0.7 lm/W luminous efficiency, have been achieved. [6]

A discharge cell of about 0.3 mm is used to form a pixel of 0.9-10 mm in 40-inch diagonal or larger PDP displays, and 42-inch diagonal models a luminance of 350 cd/m² and a luminous efficiency of 1.2 lm/W have been achieved using T shaped electrode structure with discharge cells of this size. [7] However, 17 to 20-inch diagonal models, which require smaller discharge cells, must be developed for workstations that accommodate multimedia applications.

In order to improve luminance and luminous efficiency of the surface-discharge ac color PDPs with a fine resolution,

Fujitsu proposed the ALIS (Alternate Lightning Surfaces) Method. ALIS is able to be operated almost two times finer resolution, that is SXGA, even the cell pitch of VGA. The basic operation mechanisms of ALIS is interlace operation in which pairs of row sustaining electrodes are addressed. From this reason, resolution increases two times finer with keeping the same resolution as VGA.

The 42-inch diagonal SXGA surface-discharge ac color PDP operated by ALIS accomplishes the remarkable achievements of luminance of 500 cd/m² and low power consumption of 250 W. These specification will be improved as luminance of 700 cd/m² and less than 200 W within a year. When these specifications will be accomplished, real home PDP TV will be commercialized in the near future.

7. Image Quality of Color PDPs for TV Monitor

Until recently, there was concern that the false contours generated by the use of the sub-flame modulation method for producing color PDP gradations may have become a bottleneck in the use of PDPs in TV display monitors. Technological advances in this field, however, have almost eliminated the problem of false contours, securing the future of color PDP TV monitors. [8]

It is important for color PDPs to increase luminance and luminous efficiency by new operation principle and electrode structure. *Panasonic*, however, shows that variable cell structure and new driving system called the Plasma AI (Adaptive brightness Intensifier)[9] are also very effective to improve performance of color purity and reducing power consumption, respectively.

8. Conclusions

There is a great deal of interest in color PDPs for use in TV or multimedia displays, and in particular, large ones that exhibit excellent characteristics. As a result, color PDPs have achieved superiority over other kinds of display in the field of 1m diagonal color displays.

On the basis of the achievements in the 1 m diagonal screen described in the present paper, further improvements are expected in basic structure, characteristics, device materials, driving systems, and manufacturing technology, targeting from 50 cm to over 1 m-diameter color PDPs that accommodate SXGA displays.

References

- [1] M.Sawa, H.Uchiike, S.Zhang, K.Yoshida: "Direct Observation of VUV rays for Surface-Discharge ac Plasma Displays by Using an Ultra-High Speed Electronic Camera," SID '98 Digest pp.361-364, 1998.
- [2] Y.Terao, R.Masuda, I.Koiwa, N.Higemoto, H.Sawai, and T.Kanamori: "Fabrication of Fine Barrier Ribs for Color Plasma Display Panels by Sandblasting," SID '92 Digest, pp. 724-727, 1992.
- [3] H.Fujii, H.Tanabe, H.Ishiga, M.Harayama and M.Oka: "A Sandblasting Process for Fabrication of Color PDP Phosphor Screens," SID '92 Digest, pp. 728-731, 1992.
- [4] H.Arimoto, S.Nagano, M.Kamisaki and K.Yoshikawa: "Production Technology for Large-Screen, High-Definition Plasma Display," IEICE Technical Report, EID 93-123, pp. 67-72, 1994.
- [5] T.Hirose, K.Kariya, M.Wakitani, A.Otsuka and T.Shinoda: "Performance Features of a 42-inch, Diagonal Color Plasma Display," SID '96 Digest, pp. 279-282, 1996.
- [6] T.Shinoda, K.Yoshikawa, Y.Kanazawa and M.Suzuki: "Study on the Basics of AC PDPs with Improved Gradation," IEICE, EID91-97, pp. 13-18, 1992.
- [7] K.Amemiya, T.Komaki, T.Nishio: "High Luminous Efficiency and High Definition Coplanar AC-PDP with "T" Shaped Electrodes," IDW '98 Proc. pp.527-730, 1998.
- [8] Y.-W.Zhu, K.Toda, T.Yamaguchi, T.Shiga, S.Mikoshiba, T.Ueda, K.Kariya, T.Shinoda: "A Motion-Dependent Equalizing-Pulse Technique for Reducing Gray-Scale Disturbances on PDPs," SID '97 Digest, pp.221-224, 1997.
- [9] M.Kasahara, M.Ishikawa, T.Morita, S.Inohara: "New Drive System for PDPs with Improved Image Quality: Plasma AI," SID '99 Digest, pp.158-161.

Gas discharge and experiments for plasma display panel

Po-Cheng Chen*, Yu-Ting Chien

Acer Display Technology Inc., Science-Based Industrial Park, Hsinchu, Taiwan, R.O.C.

ABSTRACT

Physical phenomena which take place in an AC Plasma Display Panel(PDP) cells are discussed in this paper.

Basic principles for gas discharge in PDP are presented. According to experiments in this paper, we can see PDP changes behaviors including memory margin, luminance, luminous efficiency, Penning effect and Paschen curve with varying gas composition and pressure. For pure helium and neon gas, helium has higher breakdown voltage than neon below 350Torr. Pure neon has higher memory margin than helium. The memory margins of both pure neon and helium decrease when their pressures are increased. In Ne-Xe gas mixture, the minimum breakdown voltage is located on $Xe = 0.1\sim 0.2\%$ due to Penning effect and then the voltage increases when Xe content is increased. The maximum memory margin for Ne-Xe gas mixture is located on $Xe = 4\sim 5\%$. The luminous efficiency increases when the gas pressure is increased. The spectrum of PDP with Ne-4%Xe at 500Torr from 400nm to 850nm is presented. Ne-Xe(up to 10%Xe) has lower luminous efficiency than pure Ne and the minimum value is located on 2~3%Xe. By SIPDP simulation model, we can see electrical and optical properties of PDP change with varying gas compositions.

Keywords : Gas Discharge, Plasma Display Panel.

1. INTRODUCTION

The gas discharge, that still suffers from a comprehensive understanding, is the predominant factor limiting the performance of the system.

PDP is a promising large size flat panel display for the next century. For the development of color plasma display panels, improvement of luminance and luminous efficiency is important. In color PDPs, vacuum ultraviolet(VUV) rays are produced by electrical discharges in a micro-cell which contain a mixture of gases including Xe. The VUV rays excite phosphors in each picture element and visible light is emitted from them.

An understanding of the discharge volume holds the key to improve VUV efficiency. Various discharge gas experiments and simulation are presented and discussed in this paper. We can also see how gas composition influence on electrical and optical behavior. From the simulation shown here, higher luminous efficiency can be achievable by increasing the xenon content in Ne-Xe gas mixture. Other ways to elevate the luminous efficiency are increasing the gas pressure and helium addition. But increasing the xenon content cause higher operation voltage and smaller margin. To increase the gas pressure limits the use of PDP at higher altitude area and has also the drawback of higher operation voltage. Helium addition pays for decreasing the luminance .

2. GAS DISCHARGE REACTIONS

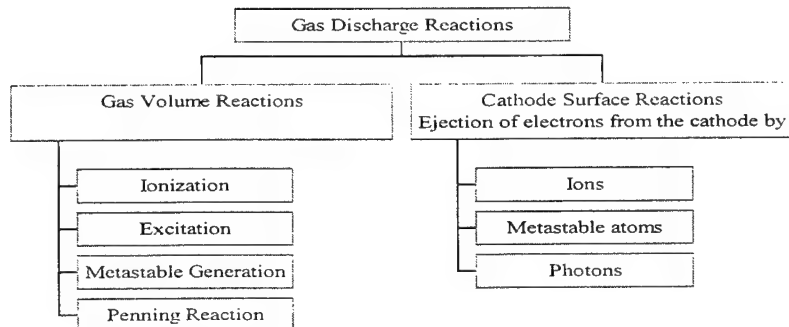
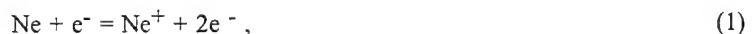


Table 1 Gas discharge reactions.

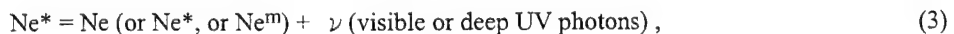
2.1. Gas Volume Reactions

Ionization : electron energy $> 21.6\text{eV}$



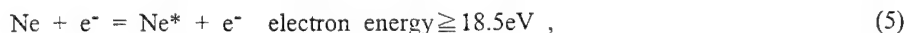
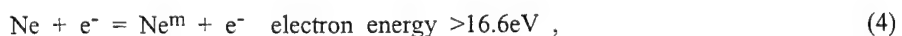
(The most important reaction of a gas discharge)

Excitation : $16.6\text{eV} < \text{electron energy} \leq 21.6\text{eV}$



(The excited atom can only remain excited for a relatively short time($\sim 10^{-8} \text{ s}$) before it radiates a photon and returns to the ground state.)

Metastable generation :



(Metastable atoms are simply excited atoms that do not radiate a photon and are not charged. In PDP, metastable lifetime's decay time constants are usually in the 1-to-10 microseconds range. Metastables usually do not decay naturally but are de-excited by a reaction with some other body, such as discharge chamber walls and by the Penning ionization process.)

Penning reaction :



(This reaction is of great importance to PDP because it generates additional ionization and allows PDP to operate at a lower voltage.)

Discharge Gas	Ionization Energy(eV)	Metastable Energy(eV)
He	24.6	19.8
Ne	21.6	16.6
Ar	15.8	11.53
Xe	12.1	8.28

Table 2 Ionization and metastable energy of various discharge gases.¹

2.2. Cathode Surface Reactions

The ejection of electrons is of critical importance to a gas discharge because these cathode electrons initiate the volume reactions and thus determines the firing voltage of the discharge.

The most important cathode surface reaction for PDP is the electron ejection due to positive *ions*. The neon ion has 21.6eV, and the argon ion has 15.8eV. During collision with the cathode, these ions capture an electron from the surface and they become neutralized. This energy is more than enough to allow an electron to escape the work-function energy of the cathode surface, which is usually in the 3-to-10eV range. This large amount of excess energy means that there is a high probability that an ion hitting the cathode will cause an electron ejection.

Since the work function of the cathode is generally greater than 3eV, only *UV photons* will have significant photoemission. But these photons have random directions and only a small fraction will be directed toward the cathode.

Although the *metastable* has about the same probability of ejecting an electron as an ion, the metastable is not nearly as important as the ion since the metastable diffuse in random direction at a very slow rate compared to the drift of the ions toward the cathode.²

3. CHARACTERISTIC VACUUM ULTRAVIOLET(VUV) WAVELENGTH AND XENON BEHAVIOR

3.1. VUV Wavelength

Gas	He	Ne	Ar	Kr	Xe
Characterized VUV Wavelength(nm)	58.4	74.4	107	124	147

Table 3 Characteristic vacuum ultraviolet wavelength of various discharge gases.

The discharge energy of a Xenon atom is easily eliminated by activated gases such as hydrogen.

Xenon has been the predominant noble gas dopant that has been used in generating vacuum UV radiation. Ar and Kr emit at much shorter wavelengths in the VUV(shadow penetration of the phosphor) and their lines are not as intense as those of Xe.

3.2. Xenon Behavior

*Xe** : *Xe* (3P_1 or 1S_0) resonance line(at 147nm)

The vacuum lifetime of a 3P_1 is naturally very short(3.7ns), but in dense gases, the emitted photons are quickly re-absorbed by ground state xenon atoms. These atoms are excited to a 3P_1 state, and re-emit 147nm photons. This resonant emission therefore occurs repeatedly through absorption and re-emission, and the effective lifetime becomes longer as photons "diffuse" relatively slowly toward the gas boundaries. This is called radiation trapping effect.³



Due to the self-absorbing phenomenon, the time when xenon atom becomes excited state is extended, so that the probability of collision between excited Xe^* and electrons becomes larger. Once the collision occurs, Xe^* is ionized and

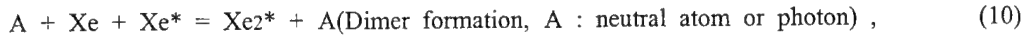
VUV photon is distinguished as :



It shows that the probability of collision between Xe^* and free electron becomes larger as the discharge current increases. This cause the lowering of luminance and luminous efficiency.⁴

Xe_2^* : *Xe molecular emission(at 173nm)(dimer or excimer radiation)*

The molecular excited states are produces by collisional interaction between the atoms of $Xe(^3P_1)$ excited state and other neutral atoms :



Since dimer radiative dissociation is a three body process involving two atoms and a photon, there are multiple solutions to the energy and momentum conservation equations. Consequently, each of these lines has rather broad spectra width, on the order of 40nm for the principal emission centered at 173nm.⁵

Figure 1 shows the memory margin with xenon percentage in Ne-Xe gas at 500Torr. As shown in the figure, the maximum memory margin appears at around 4~5%Xe and then decreases with higher xenon content. The luminous efficiency with xenon content in Ne-Xe gas at 500Torr is shown in figure 2. When the content of xenon in Ne-Xe mixture is increased, the xenon resonance line(147nm) decreased and the xenon excimer (173nm) increase. The response of phosphors to 173nm VUV is stronger than 147nm. From this, the luminous efficiency improves as the xenon content is increased.⁶ Although higher Xenon content has higher luminous efficiency, it's a flaw with higher operation voltage as shown in figure 3.

4. DISCHARGE GAS MIXTURE

Although xenon is an efficient UV emitter, the breakdown voltage in pure xenon is impractically large and mixtures of xenon with neon or helium are generally used in PDP.

Adding neon or helium to xenon decreases the breakdown voltage for two reasons

- 1) neon and helium ions are much more efficient than xenon at extracting secondary electrons from a MgO surface, and
- 2) the total ionization coefficient in some xenon-neon mixtures for example, can be larger than the ionization coefficient in pure xenon and in pure neon (this is because the momentum cross-section for electron-neutral collisions is much larger in xenon than in neon so that in a mixture containing a large concentration of neon, the electrons can gain energy more easily and reach the excitation and ionization thresholds of xenon for lower values of the reduced electric field).⁷

Figure 4 is the spectra emission from PDP cells with Ne-4%Xe gas at 500Torr. The intensity of the Xe 828nm emission is roughly proportional to that of the Xe 147nm vacuum ultraviolet. Figure 5 is the luminous efficiency with Ne-4%Xe gas pressure. Higher gas pressure has better luminous efficiency. It is because low electron temperature leads to high efficiency, in which the $Xe(^3P_1)$ excitation rate is larger than the ionization rate. The UV-light emission efficiency is determined by the ratio of dissipation energy due to $Xe(^3P_1)$ excited state to the Joule consumption energy of discharge current. As pressure increases, the ratio of $Xe(^3P_1)$ excitation rate to ionization rate increases, which results in highly efficient light emission.⁸ Figure 6 is the luminous efficiency in (He, Ne1-x)-4%Xe gas at 500Torr. He addition in Ne-4%Xe gas is helpful for

luminous efficiency improvement. In He-Ne-Xe gas mixture, XeI resonance line increases with Ne content and Xe^{2*} molecular emission increases with He content. The electron temperature decreases as He content increases. Thus the density of Xe^{*} decreases and that of Xe^{2*} increases as the He content increases due to the decreased electron impact reaction.

He-Xe mixture has a good color purity and fast response time, but its driving voltage is high and the lifetime of panel is short due to the high mobility of Xe ion in He gas.⁹

5. PENNING EFFECT

Penning effect does not play a significant role in mixtures of neon with more than a few percent of xenon because most of the electron energy in these mixtures is spent into xenon excitation and ionization. Penning effect starts to become much more important when the concentration of xenon is less than 1%. This is because for very low concentrations of xenon, most of the electron energy is deposited in excitation and ionization of neon. A lot of energy is stored in neon excited states and the ionization of a xenon atom by an excited neon atom becomes very probable. (Mixtures of neon with typically 0.1% argon have been used to lower the operating voltage in monochrome PDP.)⁹

Figure 7 is the breakdown voltage in Ne-Xe gas with Xe content. As shown in the figure, the breakdown voltage is minimum around 0.1~0.2%Xe due to Penning effect and then increases with higher xenon content.

Penning reaction is as follows for Ne-Xe gas :



6. BREAKDOWN VOLTAGE

In a coplanar geometry the breakdown voltage no longer depends on the pd product alone(p : gas pressure, d : discharge gap), because the electric field distribution in the cell also depends on the position of the address electrode. The breakdown curves can still be plotted as a function of pd, but different curves are found for different d and different h where d is the distance between the coplanar electrodes and h is the distance between the dielectric surface.

Figure 8 is the breakdown voltage for helium and neon at different gas pressure. We can see that Ne has lower breakdown voltage below about 350Torr but higher above it than helium. Figure 9 is the memory margins with pressures in helium, neon, and Ne-4%Xe gas. As shown in the figure, the memory margins increase with the gas pressure after the minimum around 200~300Torr.

7. TWO-DIMENSIONAL SIMULATIONS OF GAS DISCHARGE CHARACTERISTICS

The light-generating region starts close to the anode and rapidly moves towards the cathode. After the light generating region covers the whole cathode, the distribution remains unchanged but the intensity decreases fast.¹⁰

Luminance of the PDP is dominated by the intense N-type emission, which originates from the negative glow.¹¹ In the Ne-Xe gas, Ne-4%Xe gas has more Ne atoms and generates more secondary electrons. Its higher ionization rate(electron

density) and lower excitation rate lead to lower efficiency than Ne-10%Xe gas because the UV-light emission efficiency is determined by the ratio of dissipation energy due to Xe(3P_1) excited state to the Joule consumption energy of discharge current. Figure 10(a)~(d) are electron density, ion rate, excitation rate, and electric potential respectively for Ne-4%Xe and Ne-10%Xe.

REFERENCES

1. Nicholas C. Andreadakis, John R. Wullert II, "High frequency memory and gas mixture optimization in suspended electrode color plasma displays", SID 89 Dig., pp.347, 1989.
2. Lawrence E. Tannas, Jr., *Flat-Panel Display and CRTs*, pp. 332, NewYork : Van Nostrand Reinhold, , 1985.
3. Taichiro Tamida, Steven Jay Sanders, and Masaaki Tanaka, "Measurement and modeling of radiative transfer of Xe resonant emission in a PDP discharge", IDW 98, pp.571, 1998.
4. N. T. Nguyen, H. Nakahara, M. Wakitani, A. Otsuka, and T. Shinoda, "Optical characteristic of 42-inch diagonal color plasma display", IDW 96, pp.295, 1996.
5. Robert T. McGrath, Ramana Veerasingam, John A. Hunter, Paul D. Rockett, and Robert B. Campbell, "Measurements and simulations of VUV emissions from plasma flat panel display pixel microdischarges", *IEEE Trans. on Plasma Sci.*, vol. **26**, no. **5**, pp.1532, 1998.
6. T. Shinkai, T. Murata, Y. Okita, S. Kobayashi and K. Terai, "Improvement of luminous efficiency and phosphor lifetime in barrier discharge plasma display panel", IDW 98, pp.539, 1998.
7. J. P. Boeuf, C. Punset, A. Hirech, and H. Doyeux, "Physics and modeling of plasma display panels", *J. Phys. IV France* vol. **7**, pp.C4-3, 1997.
8. Shirun Ho, Miyuki Saji, Sigeo Ihara, Masatoshi Shiiki, Keizo Suzuki, Akitsuna Yuhara, Atsushi Yokoyama, Masaji Ishigaki, Ryohei Sato, Noriyuki Kouchi and Yoshihiko Hatano, "Numerical analysis of discharge voltage and light emission efficiency in AC-PDPs", IDW 98. pp.479, 1998.
9. H. Bechtel, P.J. Heijnen, A.H.M. Holtslag, M. Klein, R.Snijkers, and H.Tolner, "PDP Research in Philips", IDW 98, pp.527, 1998.
10. T. Shiga, K. Igarashi, and Mikoshiba, "Visualization of a PDP discharge growth and an interpretation of the growth mechanism", IDW 98, pp.487, 1998.
11. T. Shiga, K. Igarashi, and Mikoshiba, "Visualization of a PDP discharge growth and an interpretation of the growth mechanism", IDW 98, pp.487, 1998.

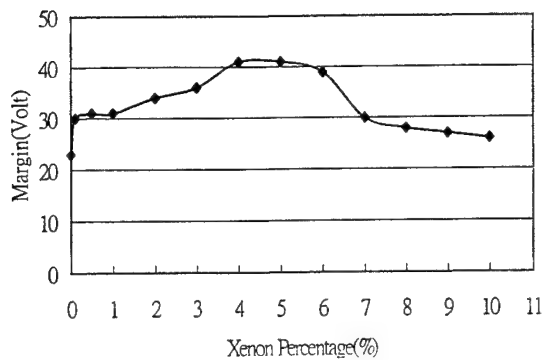


Fig. 1 The memory margin with Xenon percentage in Ne-Xe gas at 500Torr..

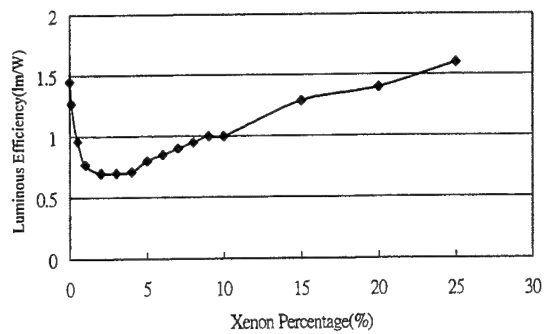


Fig. 2 The luminous efficiency with Xenon content in Ne-Xe gas at 500Torr.

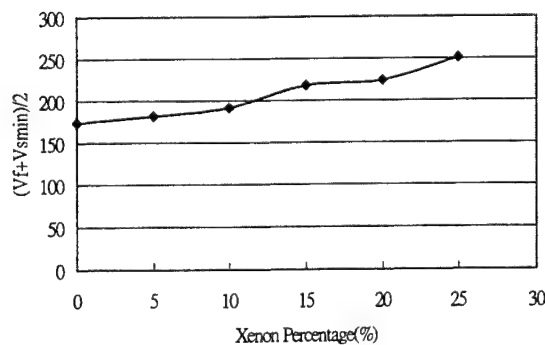


Fig. 3 The operation voltage with different Xenon content in Ne-Xe gas at 500Torr.

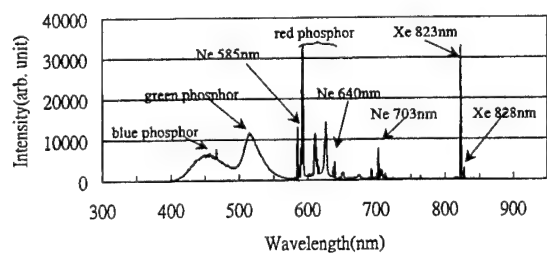


Fig. 4 The spectra emission from PDP cells with Ne-4%Xe gas at 500Torr.

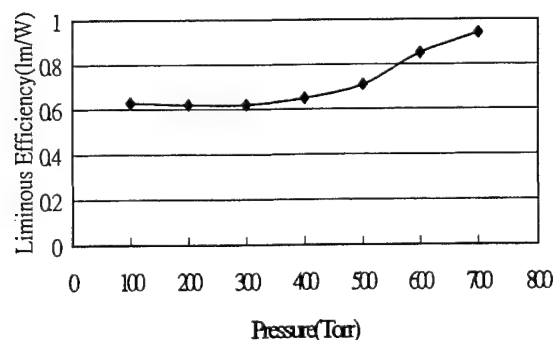


Fig. 5 The luminous efficiency with Ne-4%Xe gas pressure.

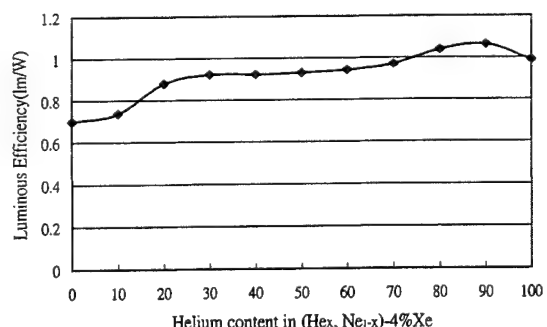


Fig. 6 The luminous efficiency in (He-X, Ne1-x)-4%Xe gas at 500Torr.

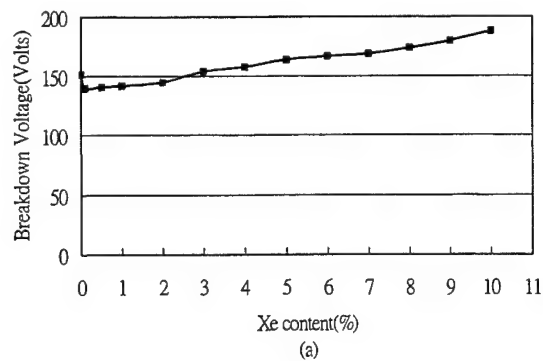


Fig.7(a) The breakdown voltage with Xenon percentage.

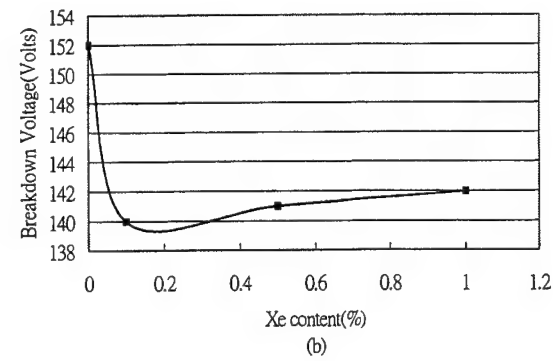


Fig. 7(b) The breakdown voltage with Xenon percentage.

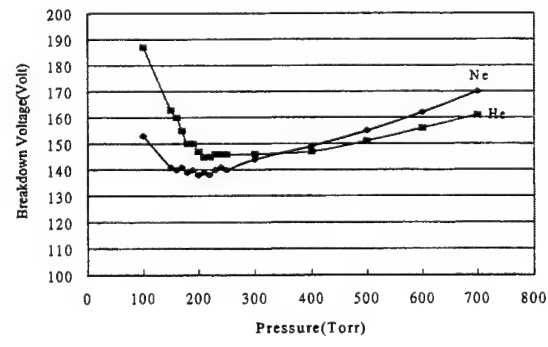


Fig. 8 The breakdown voltages for Helium and Neon at different gas pressure.

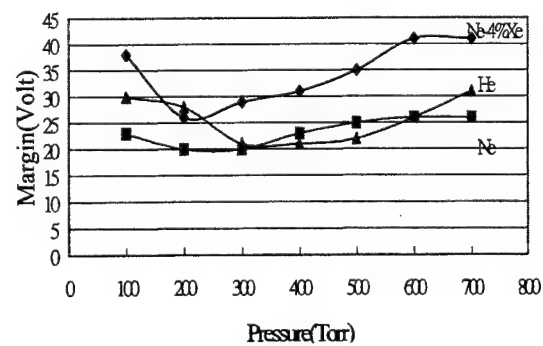
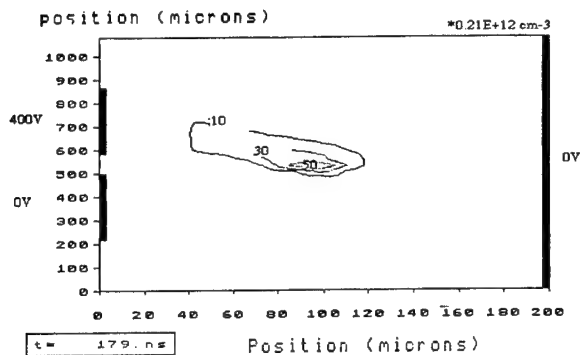


Fig. 9 The memory margins with pressures in different gas.

Electron density : Ne-4%Xe, 500Torr



Electron density : Ne-10%Xe, 500Torr

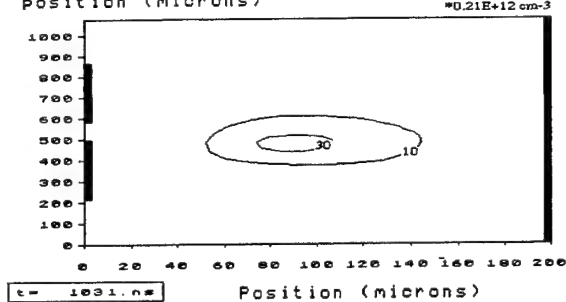
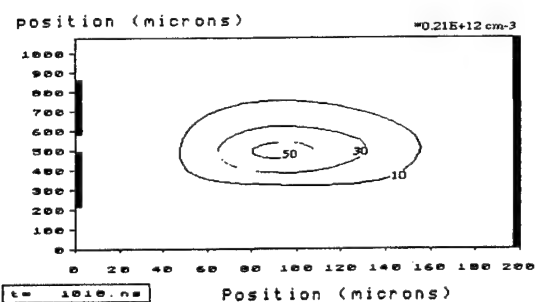
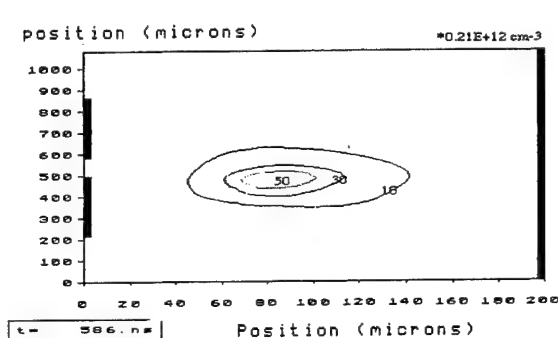
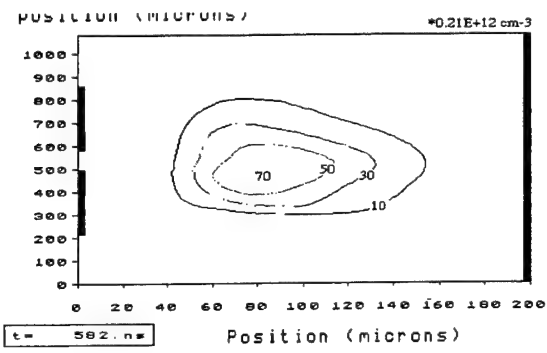
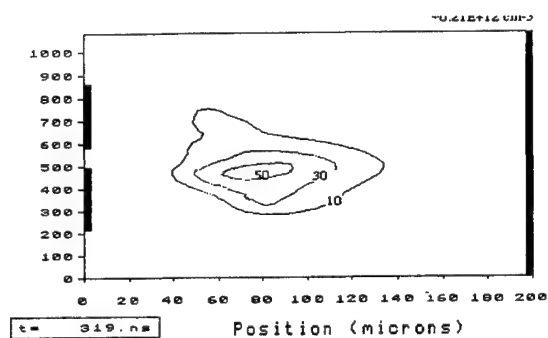
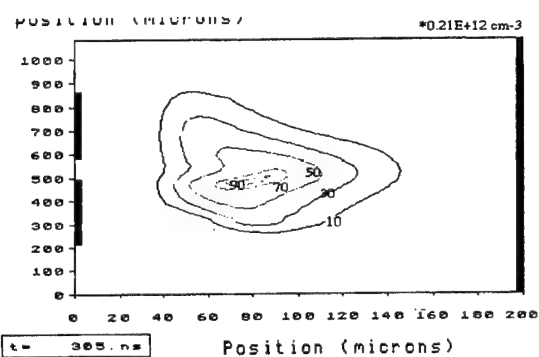
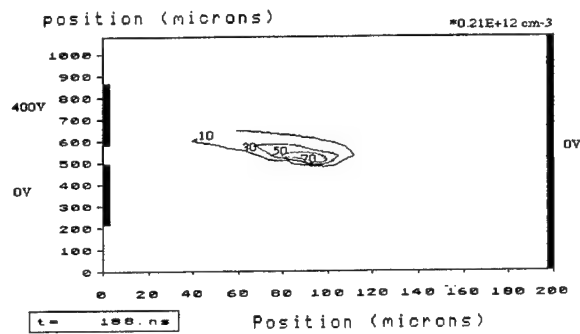
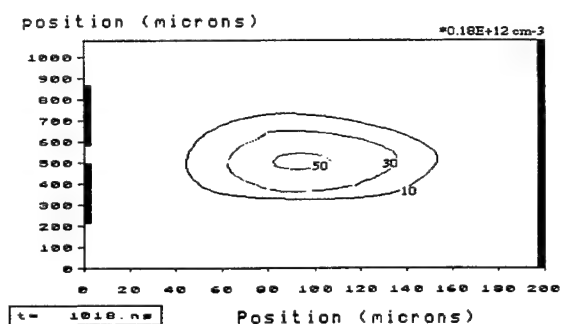
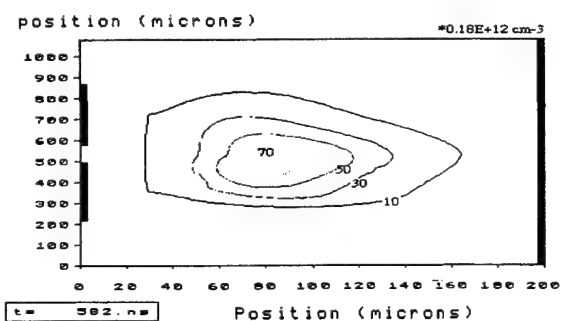
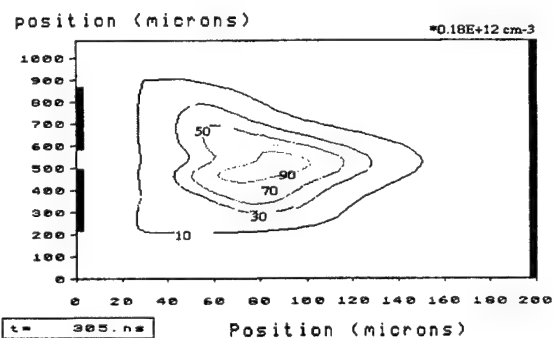
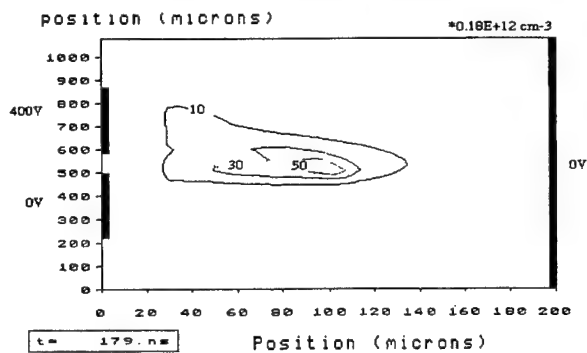


Fig. 10(a)-(d) Two-dimensional simulation of Ne4%Xe and Ne-10%Xe gas. Profiles of (a) electron density, (b) ion density, (c) excitation rate, (d) electric potential.

Ion density : Ne-4%Xe, 500Torr



Ion density : Ne-10%Xe, 500Torr

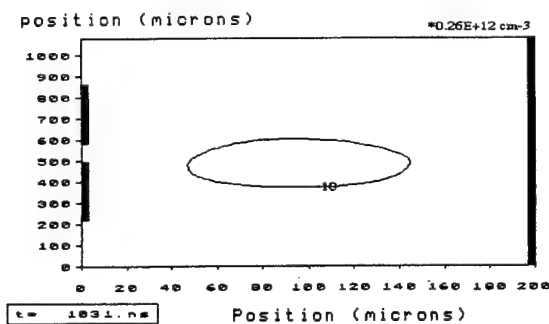
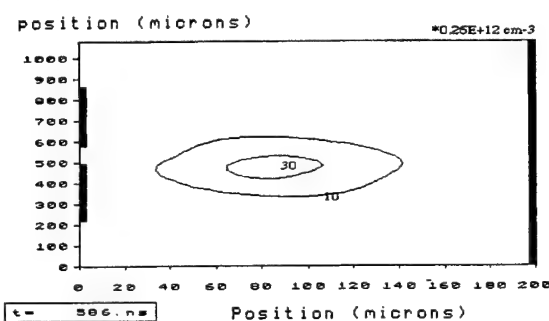
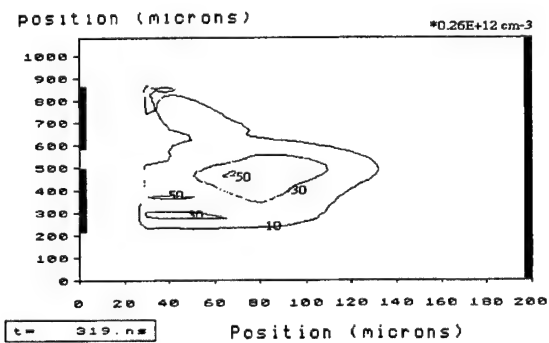
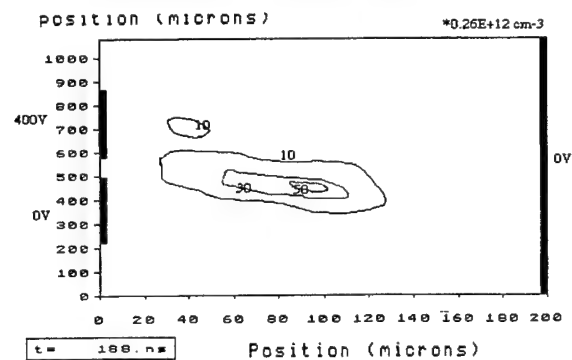
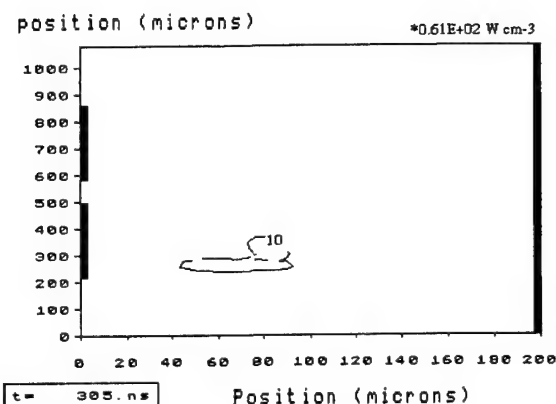
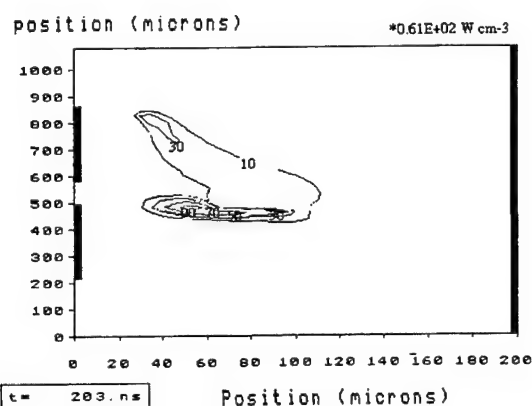
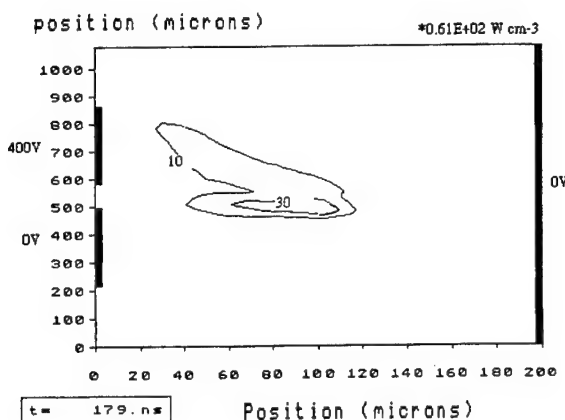


Fig. 10(b)

Excitation rate : Ne-4%Xe, 500Torr



Excitation rate : Ne-10%Xe, 500Torr

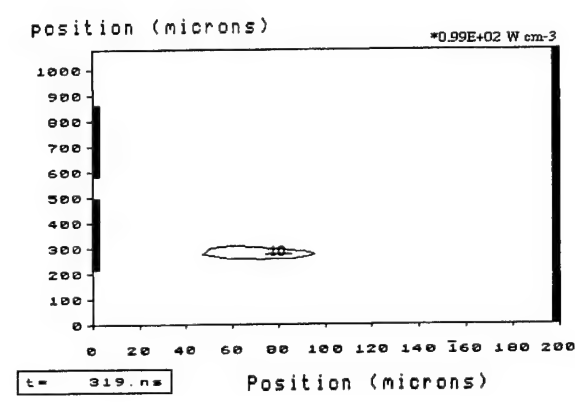
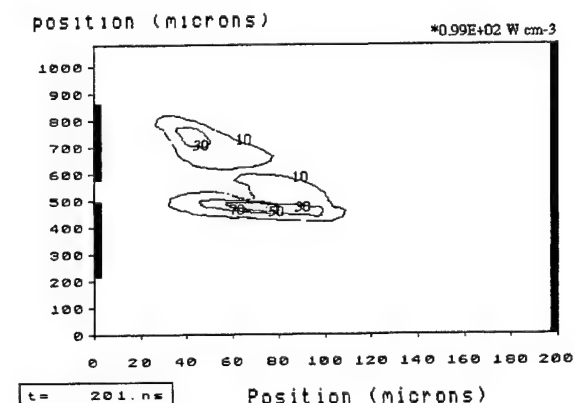
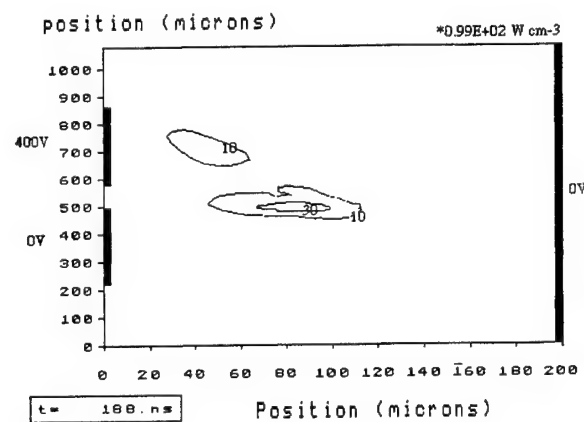
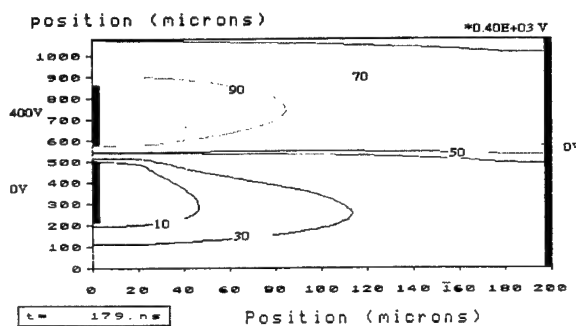


Fig. 10(c)

Electric potential : Ne-4%Xe, 500Tor



Electric potential : Ne-10%Xe, 500Tor

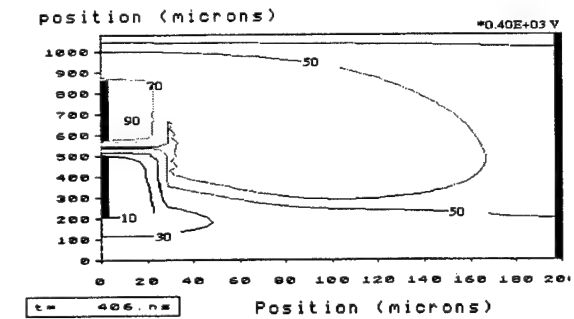
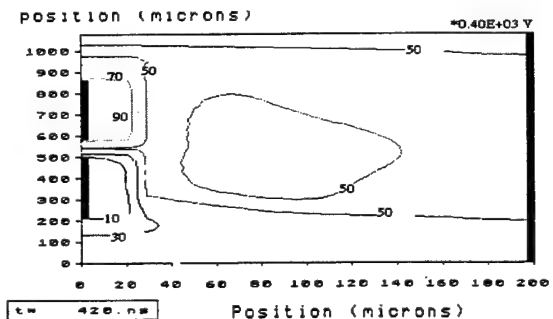
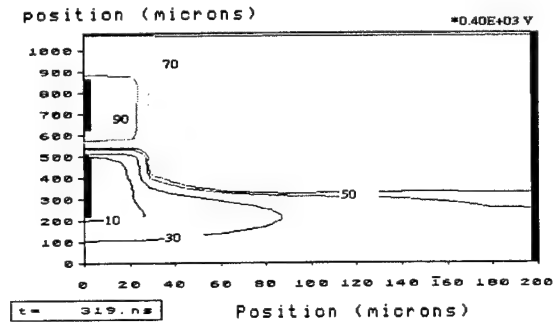
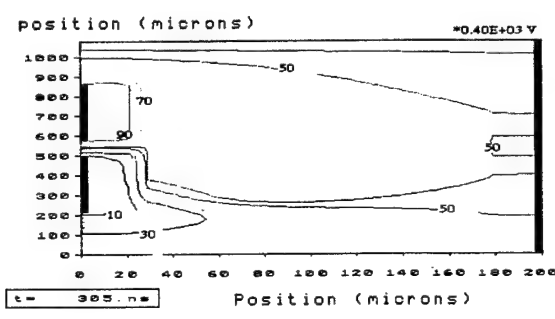
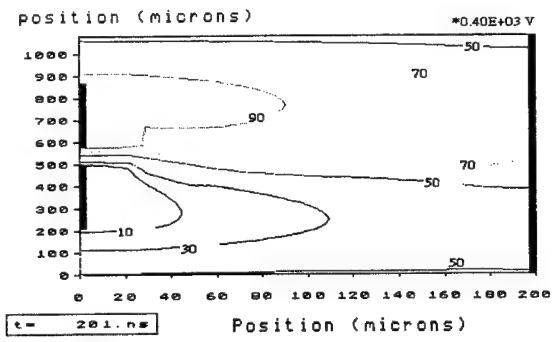
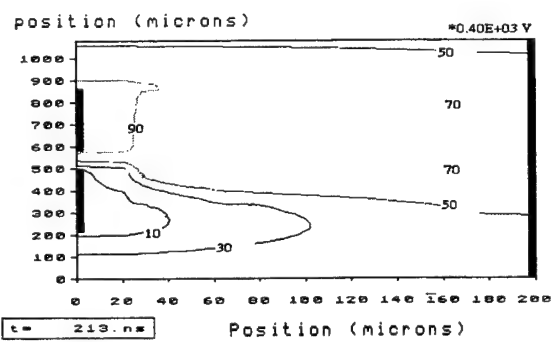
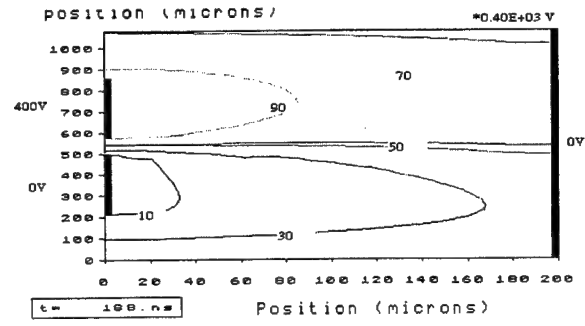


Fig. 10(d)

A Field Emission Display using Carbon Nanotubes as Emitters

Feng-Yu Chuang*, Cheng-Chung Lee, Jyung-Dong Lin, Jane-Hway Liao, Hua-Chi Cheng, Cheng-Xian Han, Jon-Lian Kwo¹⁾, Wen-Chun Wang
Electronic Research & Service Organization, Industrial Technology Research Institute, Hsinchu, Taiwan,
R.O.C.

¹⁾Department of Electrical Engineering, National Cheng Kung University, Tainan, Taiwan, 701, R.O.C.

ABSTRACT

A fully sealed field emission display (FED), indicator, using carbon nanotubes (CNTs) as emitters is examined. The CNTs chunk, synthesized by arc discharge, were crushed, mixed with conductive pastes and then screen-printed on glass for the cold cathode. And the anode plate, an ITO glass printed P15 phosphor, was separated from cathode using 90 μ m spacers. The indicator display performed a turn-on voltage as low as 250 V, and the emission current density 2.2 mA/cm² under 300 V with brightness of 500 nits. The pixels, driven by open drain IC with 5 V gate voltage, showed the clock image which indicated the application of CNTs-FED. No significant degradation of this performance was observed during 1000 mins testing. The influence of printing condition and surface treatment process on the emission characteristics will also be discussed in this letter.

Keywords: field emission display, indicator, carbon nanotubes, arc-discharge

Correspondence: Email: fychuang@itri.org.tw; Fax: 886-3-5826842

I. INTRODUCTION

Carbon nanotubes, grown on the cathode of arc discharge process, were first observed by Iijima in 1991 [1]. The needle-like tubes comprised coaxial tubes of graphite sheets and ranged in size from 4 to 30 nm in diameter and up to 1 μ m in length. The discovery of carbon nanotubes has been attracting considerable attention because of their own unique physical properties and their potential for a variety of applications [2~4]. Due to their high aspect ratios and small tip radii of curvature, the nanotubes (CNTs) exhibit excellent field emission characteristics. High field emission current density of 10 mA/cm² [5] and low turn-on electric field of 0.8 V/ μ m have been demonstrated [6,7]. Recently, Ise Electronic Corp. has demonstrated a CRT-lighting-element, which used MWNTs as the cold emitter source, with a lifetime of more than 5000 hours [8]. Further more, Samsung shows a matrix-addressable diode display using CNTs-emitters [9]. CNTs show potential in the application for vacuum fluorescent display (VFD) and field emission display (FED). Nowadays, CNTs can be synthesized by arc discharge [10,11], laser ablation [12], and chemical vapor deposition process [13,14], etc. Arc discharge is suitable for its throughput. In this work, we use DC arc discharge process to synthesize CNTs. The electron emission characteristics of CNTs films, which were patterned by printing process, will be investigated and a prototype of CNTs-FED will be demonstrated in this paper.

2. EXPERIMENTAL

The anode used in DC arc discharge process was a pure graphite rod with 15 cm in length, and the cathode was a graphite disc (18 mm in diameter) mounted into water-cool copper. The chamber was maintained in helium atmosphere (500mbar). Arc constant DC current (70~80 A) was applied to the anode and cathode separated with a gap about 2~3 mm, whereas the voltage across the gap was 20~24 V.

The morphology and structure of the CNT-bulks were examined using scanning electron microscopy (SEM). Field emission characteristics of the CNT-emitters were measured by a diode technique using an electrometer. Anode plate, a glass coated with ITO layer and P15 phosphor, was separated from the cathode by using 90 μ m spacers. The turn-on field (E_0) were designated as the field at which the Fowle-Nordheim plot, $\ln(I/V^2)-(1/V)$ deviates from the straight line.

To fabricate CNT emitters, silver paste was first printed on glass as bottom electrode. The tube was crushed using ball milling to reduce its length to 1~2 μ m. The slurry containing CNTs was then printed upon silver paste. The fully sealed CNTs-FED was fabricated using VFD-like vacuum sealing process. All the interfaces between the anode plate/spacer

bar/CNTs-emitter plate were sealed with glass frits, followed by thermal annealing to enable the reaction of the glass with glass frits.

3. RESULTS AND DISCUSSION

SEM micrographs of the bulk, shown in Fig. 1a and 1b, indicate that consists of multi-wall nanotubes embedded in fibrous bundles. Each bundle is approximately 50 μm in diameter. The nanotubes are about several tens of nm in diameter. The carbonaceous particles attached on the CNTs can easily be removed by post treatment at 600°C in air. The yields of nanotubes embedded in fibrous bundles are higher than 70% after thermal treatment. To reduce the length of nanotubes, ball milling was introduced to crush it for 2 hours.

To study the characteristics of CNTs emitters, the silver was first screen-printed in dot pattern on the glass as cathode. Each dot has $1 \times 1 \text{ mm}^2$ in area. The slurry containing CNTs and binders was then screen-printed upon silver paste, followed by oven curing. Figure 1c shows a cross-sectional SEM micrograph of CNTs-emitter. Most of CNTs are aligned perpendicularly to substrate after surface treatment process on the surface. The density of CNTs-emitters was markedly larger than the typical density of microtips in conventional Spindt-type FEDs. Further, the P15 phosphor was screen printed on another ITO glass plate as anode. The emission property of CNTs-emitter was measured using diode structure, as shown in Fig. 2. The CNTs-emitters turns on at a field as low as 1.45 V/ μm and the current rise to 0.5 mA under electric field of 5.5 V/ μm . The current significantly increased to 3.4 mA under 5.5 V/ μm applied field after surface treatment. The resultant fabrication process is shown in Fig. 3. The gap spacing between both plates, separated by the spacer bar, is 90 μm . All the interfaces between the anode/plate/sapcer bar/CNTs-emitter plate was sealed with glass frits, followed by thermal annealing to enable the reaction of the glass with glass frits. Exhaust process was performed with a conventional vacuum pump, which is almost the same as VFD vacuum sealing process.

To study the image and measure the characteristics of sealed FED device, the anode is applied with high voltage (300–350 V) and the cathode electrodes are switch-driven. Fig. 4 shows a sequence of the images of a counting clock. The images indicated that each dot could be controlled well using an MOSFET as a current switch. At the on-state, the voltage between gate and source was 5 V, i.e., turned on the channel. The voltage drop between the drain and source are neglected which compared to anode voltage. At the off-state, the voltage between gate and source was 0 V, thus there is no induced current in the channel due to floating.

Moreover, to demonstrate the driving of CNTs-FED, a seven-segment numerical indicator was designed using diode structure. Each segment has 1 mm wide and 5 mm long in size. The system of indicator consists of two components, control and driving circuits, as shown in Fig. 5. The control circuit, using FPGA, operated under duty cycle of 1/10~9/10. The high voltage driving circuit was n-channel open drain interface IC. Fig. 6 shows the emission image of seven-segment indicator. The brightness is as high as 500 nits when applied with 300 volts between anode and cathode. The voltages of 5 V and 12 V are applied to FPGA and driving IC, respectively. During 1000 min testing, the emission current decay is about 14% and saturated after 50 hours under 280 V applied anode voltage. It is still testing.

4. CONCLUSION

In summary, the seven-segment numerical indicator shows the excellent electron emission characteristics of CNTs-FED using diode structure. The brightness is as high as 500 nits when applied with 300 volts between anode and cathode, using open drain driver IC. Most of CNTs are aligned perpendicularly to substrate and its emission current density significant increase after surface treatment process on the surface. During 1000 min testing, the emission current decay is about 14% and saturated after 50 hours under 280 V applied anode voltage. It indicates that CNTs-FED is very promising for application of flat panel display.

REFERENCES

1. S. Iijima, "Helical microtubules of graphite carbon", Nature 354,pp56-58, 1991.
2. Saito,Susumu, Science ,V278,p77(1997).
3. P. G. Collins, A. Zettler, and R. E. Smalley, "Nanotube Nanodevice", Science, 278,p100(1997).
4. Walt A. De Heer, A. Chatelain , D. Ugarte , "A carbon nanotube field emission electron source", Science, 270, pp1179-1180, 1995.
5. J.M. Bonard, J.P. Salvetat, T. Stockli, "Field emission from single-wall carbon nanotube films", Appl. Phys. Lett. 73, pp918-920, 1998.
6. Q. H. Wang , T. D Corrigan , J. Y. Dai and R. P. H. Chang , "Field emission from nanotube bundle emitters at low fields", Appl. Phys. Lett., 70, p3308(1997).
7. P. G. Collins, and A. Zettl , "Unique characteristics of cold cathode carbon-nanotube-matrix field emitters", Phys. Rev.

- B55, pp9391-9399, 1997.
- 8. S. Uemura , T. Nagasako , J. Yotani ,T. Shimojo , SID 98 DIGEST,p1052(1998).
 - 9. W. B. Choi, D. S. Chung, S. H. Park, J. M. Kim, "Fully sealed high-brightness carbon-nanotube field emission display", Appl. Phys. Lett.75, pp3129-3131, 1999.
 - 10. J. M. Lauerhaas , J. Y. Dai , A. A. Setlur , and R. P. H. Chang, J.Mater. Res., 12 No.6, p1536(1997).
 - 11. P. M. Ajayan ,Ph. Redlich , and M. Ruhle, J.Mater. Res., 12 , No. 1, p244(1997).
 - 12. A. G. Rinzler, J. Liu, and R. E. Smalley, "Large scale purification of single wall carbon nanotubes", Appl. Phys. A, 67, pp29-37 1998.
 - 13. J. M. Mao, L. F. Sun, L. X. Qian, Z. W. Pan, B. H. Chang, W. Y. Zhou, G. Wang and S. S. Xie, "Growth of highly oriented carbon nanotubes by plasma-enhanced hot filament chemical vapor deposition", Appl. Phys. Lett. 72, p3297-3299, 1998.
 - 14. G. Che, B. B. Lakshmi, and E. R. Fisher, Chem. Mater, 10, p260 (1998).

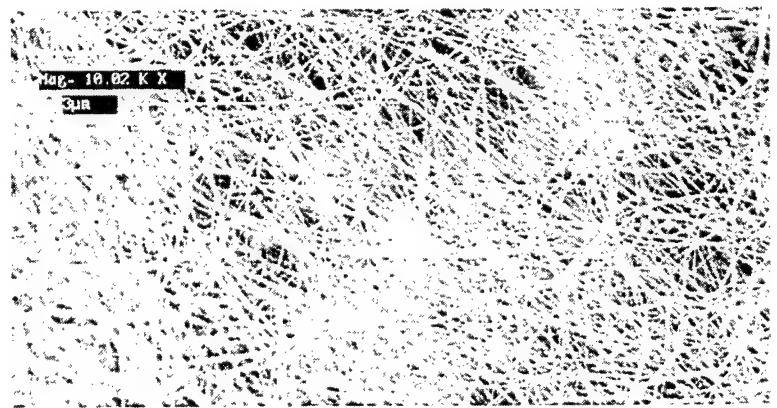
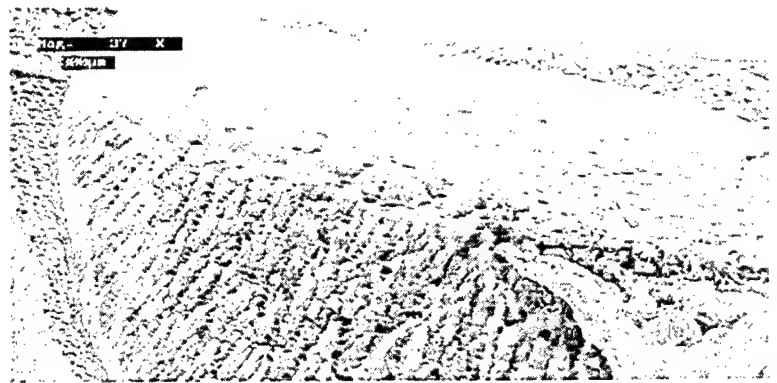


Fig.1 SEM micrographs show (a) as-grown bulk bundles, (b) multi-wall nanotubes embedded in bulk bundles, (c) cross-sectional image of screen-printed CNTs-emitters are perpendicular to substrate after surface treatment.

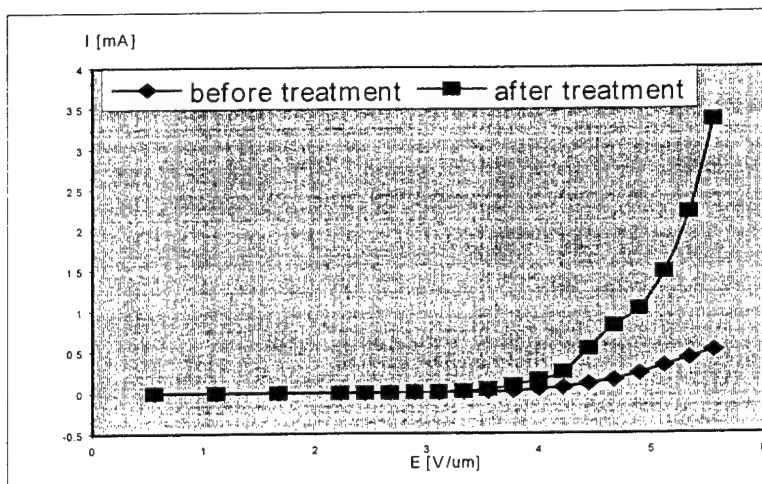


Fig. 2 Emission current of CNTs-emitter as a function of applied electric field, with and w/o surface treatment.

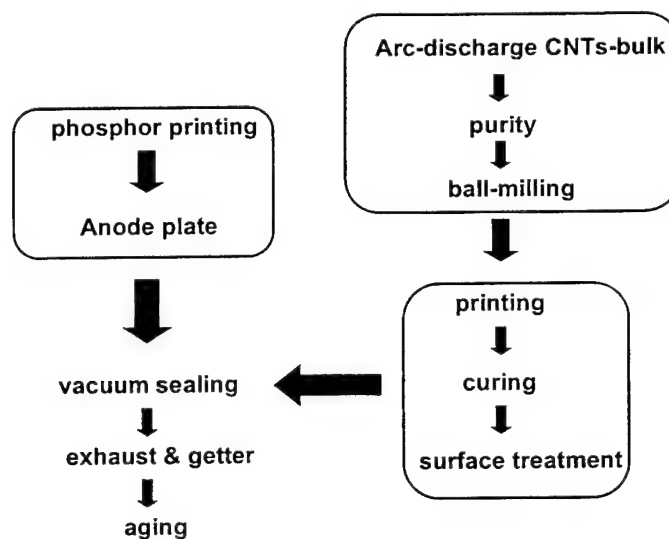


Fig.3 Fabrication process of CNTs-FED, using VFD-like vacuum sealing process.

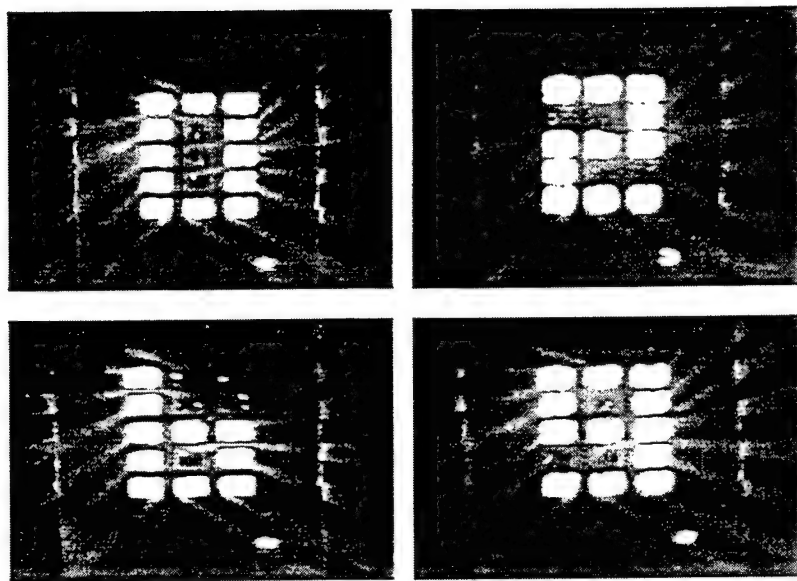


Fig. 4 Electron emission image of 15-pixels CNTs-emitter using diode structure, operated at 5 V/ μ m applied electric field.

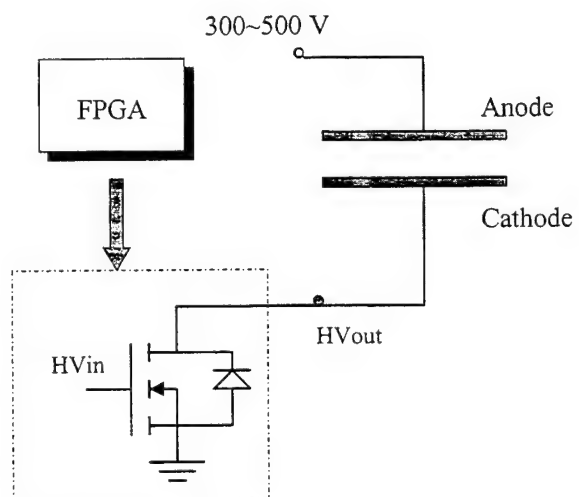


Fig. 5 Schematic diagram of driving circuit used in seven-segment CNTs-FED.

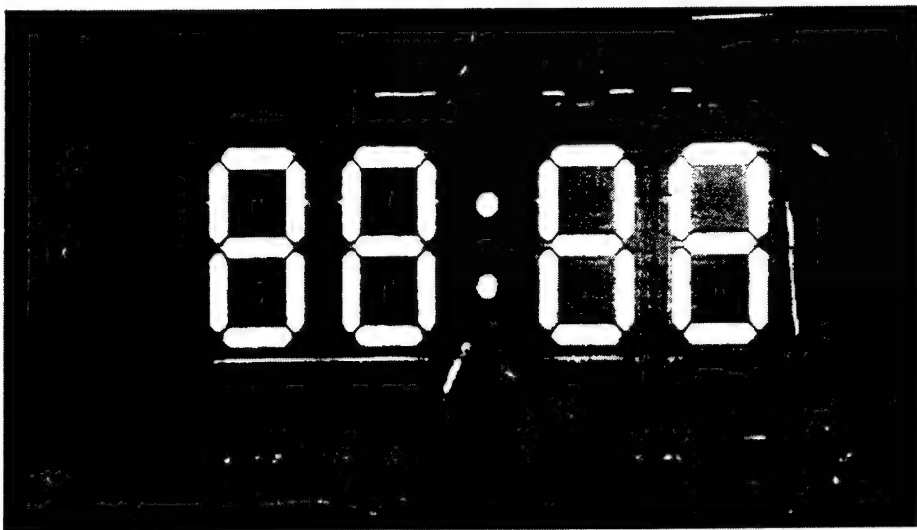


Fig. 6 Electron emission image of seven-segment numerical indicator using CNTs-emitter,
the applied electric field is 5 V/ μ m.

Field emission characteristics of carbon nanotube emitters using screen-printing technique

Cheng-Chung Lee*, Feng-Yu Chuang, Jyung-Dong Lin, Jane-Hway Liao, Hua-Chi Cheng, Jyh-Rong Sheu, Yu-Yang Chang, Chuan-Cheng Tsou, Wen-Chun Wang

Electronic Research & Service Organization (ERSO) / Industrial Technology Research Institute (ITRI)

* Correspondence: E-mail: leecc@itri.org.tw; Telephone: 886-3-5913384; Fax: 886-3-5826842

ABSTRACT

A carbon nanotube emitter with high uniformity, adhesion and emission current has been formed by screen printing. The raw carbon nanotubes (CNTs) chunk were crushed, purified, dispersed, mixed with organic additives and then screen-printed on Ag electrode. After burning out the organic additives under two thermal cycles, the surface of CNTs emitters were treated. The treated emitters showed a better emission characteristic than untreated emitters.

Keywords: carbon nanotubes, screen printing

1. INTRODUCTION

Carbon nanotubes have been attracting considerable attention because of their application potential for field emitters after the first observation by Iijima [1]. High chemical stability and high mechanical strength are advantageous for use in field emitters. Several results have been reported on the field emission not only from multi-walled nanotubes but also from single-walled nanotubes [2,3]. Recently, CRT-lighting element using MWNTs has been demonstrated by Ise Electronic Corporation [4] and Samsung showed a matrix addressable diode display [5]. From these typical papers, CNTs shows the potential in field emission display (FED).

The conventional FED formed by microtips. However, a major disadvantage of the microtip FED is the complicated processing steps such as a thin film deposition techniques and photolithographic methods which increase the manufacturing cost of FED. Therefore, utilizing CNTs emitters, the FED can be fabricated advantageously by a thick film printing technique at low fabrication cost and high fabrication efficiency.

In this paper, a screen printing process of fabricating CNTs emitters with high uniformity, high adhesion and high emission current has been studied.

2. EXPERIMENTS

The carbon nanotubes were fabricated by DC arc discharge. The chamber was maintained in He atmosphere with 500 mbar.

Arc constant DC current with 150 A and voltage with 20~24 V was applied to the anode and cathode separated with a gap about 2~3 mm.

To form the cathode plate, first, the cathode layer such as Ag was screen printed on a glass substrate. Secondary, on top of the cathode layer, CNTs layer was formed by a screen printing method. The homogeneous paste for screen printing was made by mixing organic components such as solvent, binder, plasticizer and dispersant with CNTs powders. Finally, the cathode and CNTs layer were heated to burn out the organic additives and melt the inorganic components such as frits and Ag.

The morphology and microstructures were observed by scanning electron microscopy (SEM). The particle size of CNTs powders were measured by Laser particle size analyzer. The decomposed temperature of CNTs and of organic additives of pastes were identified by thermalgravimetric analyzer (TGA). The field emission characteristics of CNTs layer by printing were measured by a diode technique using an electrometer. Anode plate with ITO layer and P22 or P15 phosphor was separated from cathode plate by 70 μm spacer.

3. RESULTS AND DISCUSSION

3.1. Purification and Dispersion

Usually, CNTs fabricated by arc discharge contains pure CNTs and other fillers. To increase the CNTs density of printed layer, the milled CNTs powders were purified by firing from 400°C to 600 °C in air atmosphere and the morphology of CNTs is shown in Fig. 1. From Fig. 1(b), the density of pure CNTs increase after the oxidation of other fillers. However, because of the physical and geometrical properties, the CNTs tend to form agglomeration. In Fig. 2, the weight loss of purified CNTs shows a drastically increase at 500 °C because of the decomposition of unstable fillers, and at 600 °C, few CNTs remain (about 6 wt%). From Fig. 1, whether purified CNTs or not, there are a lot of agglomeration. In order to improve the uniformity of emitters, the milled CNTs were treated by ultrasonics, acid solution or dispersants, and the particle size distribution is shown in Fig. 3. For ultrasonics treatment, the agglomerated CNTs (~20 μm) will be separated by screen to cause the non-homogeneous of paste. For acid solution and dispersants treatments, the negative ions adsorb on the open ends of CNTs and induce the electrostatic repulsion to make the CNTs powders dispersive well (~2 μm) in solution.

3.2 Firing and Microstructures

Fig. 4 shows the decomposed temperature of CNTs paste for screen printing. The first step of weight loss is solvent decomposition and the second step is binder, plasticizer and dispersant decomposition. From the results of Fig. 4, first, the CNTs layer was fired at 420°C in air to burn out clearly the organic and then fired at 450 °C to 550 °C to improve the adhesion between cathode layer (Ag) and CNTs layer.

Fig. 5 shows the microstructures in crosssection of CNTs and cathode layers. In Fig. 5(a), the green sample after drying shows the flatness upon CNTs layer resulted from the stress of blade, and a thin organic-rich film resulted from the evaporation of solvent. Because of above results in green, the surface of fired sample in Fig. 5(b) shows the poor outcrop of CNTs. From Fig. 5(a)(b), by the usual screen printing, it is not easy to produce a high density and perpendicular CNTs layer. Therefore, a surface treatment on CNTs layer is necessary and the result is shown in Fig. 5(c). The treatment such as sand blasting remove the stressed layer in surface of CNTs layer to disclose randomly arranged CNTs.

3.3 Characteristics of Field Emission

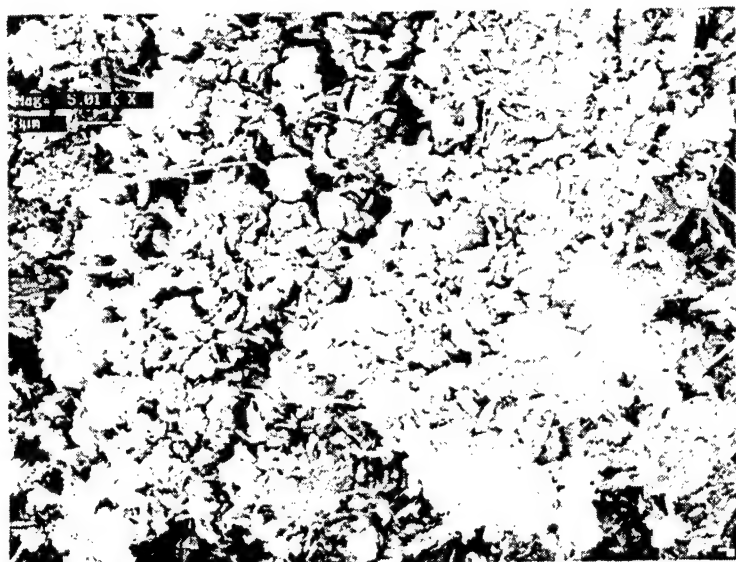
Fig. 6 shows the emission current density of CNTs layer with or without surface treatment. At the same electric field ($E=5$ V/ μm), current density is 0.6 mA/ cm^2 for untreated CNTs emitter and 12.5 mA/ cm^2 for treated CNTs emitter. The improvement of current density is consistent with the surface reformation of CNTs layer. The correlative emission images of Fig. 6 are demonstrated in Fig. 7 ($E=5$ V/ μm). From Fig. 7, surface treatment not only improves current density, but also increase the uniformity of emission.

4. CONCLUSION

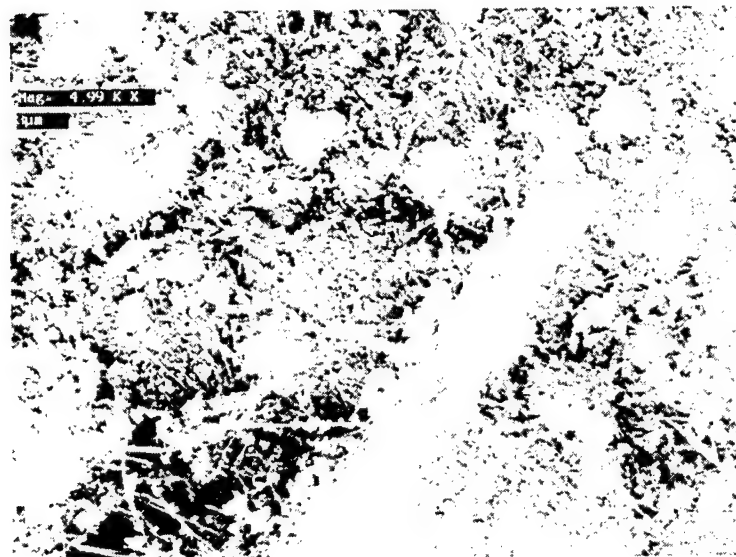
Purified CNTs powders were achieved by firing above 500 °C. Milled and purified CNTs powders was dispersive about 2 μm by acid solution and dispersant treatments. The firing process was two-cycles profile to made a high adhesion CNTs layer. After firing, a fine structure in CNTs surface was formed by surface treatment. Surface treatment not only improves current density, but also increases the uniformity of emission. At 5 V/ μm , current density is 12.5 mA/ cm^2 for treated CNTs emitter

REFERENCES

1. S. Iijima, *Nature*, 354, pp. 56, 1991.
2. Y. Saito et al., *Nature*, 389, pp. 554, 1997.
3. J. Bonard, J. Salvetat, T. Stockli, W. A. deHeer, L. Forro, A. Chatelain, *App. Phy. Lett.* Vol. 73, pp. 918, 1998.
4. S. Uemura, T. Nagasako, J. Yotani, T. Shimojo, *SID 98 DIGEST*, pp. 1052, 1998.
5. W. B. Choi, D. S. Chung, S. H. Park, J. M. Kim, *SID99 DIGEST*, pp. 1134, 1999.



(a)



(b)

Fig. 1 SEM micrographs of (a) milled, and (b) milled and purified at 600 °C CNTs powder.

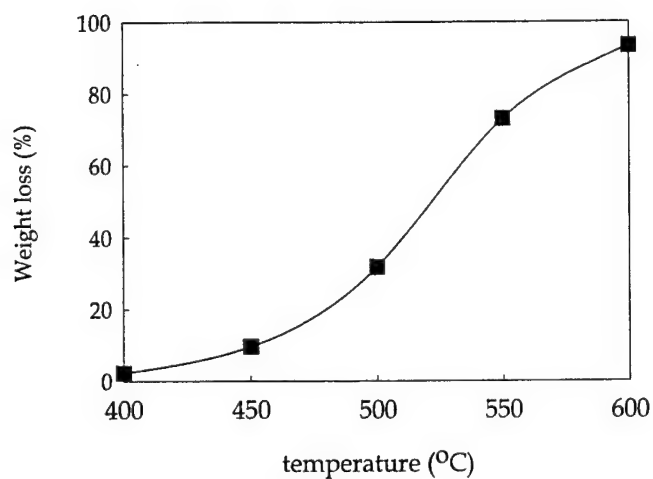


Fig. 2 Weight loss of purified CNTs powders from 400°C to 600 °C.

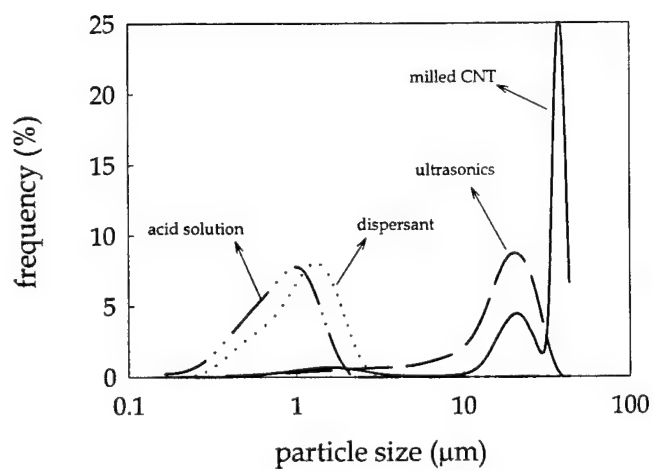


Fig. 3 Particle size distribution of milled and dispersed CNTs powders.

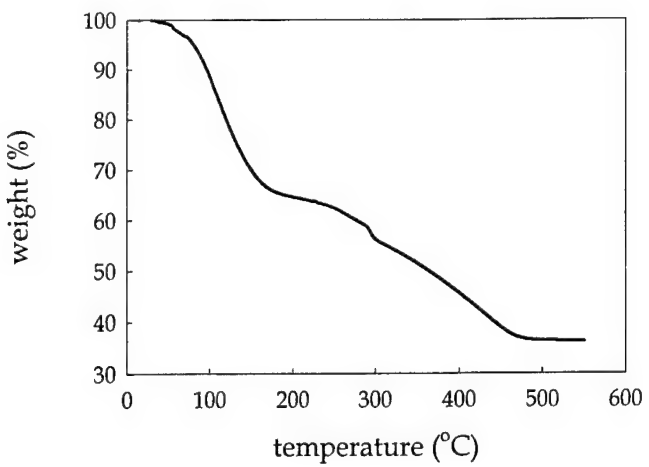
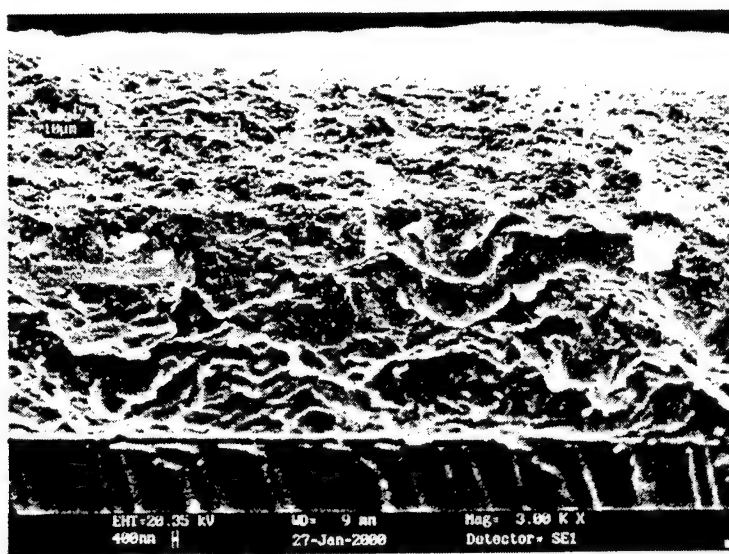
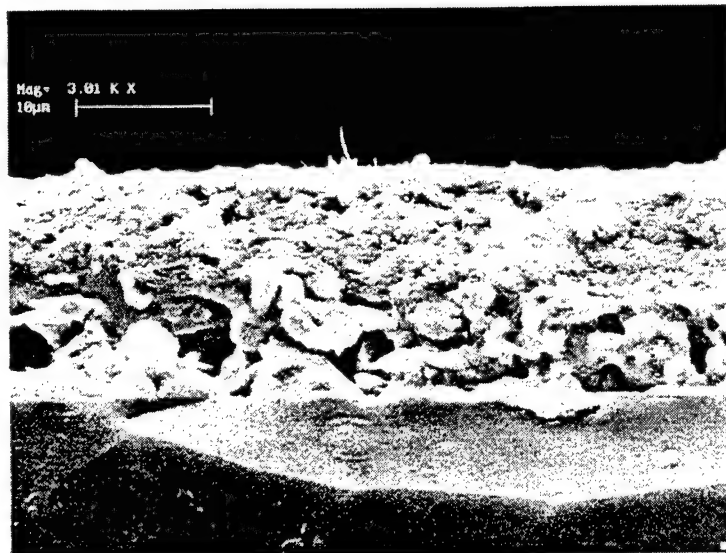


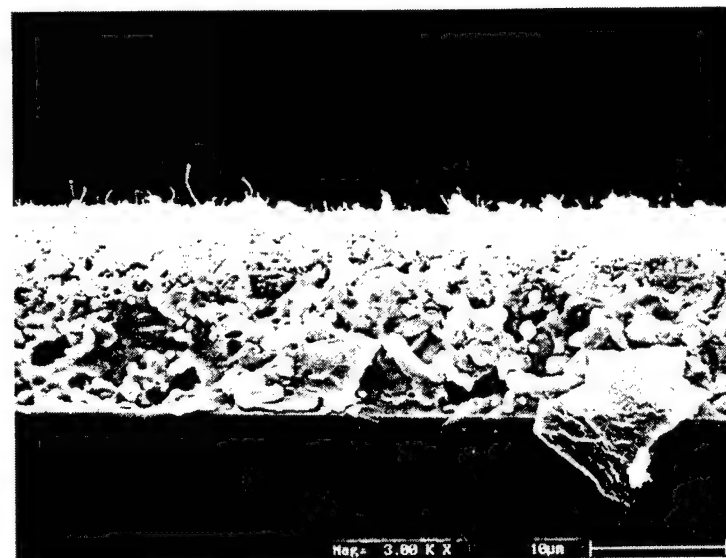
Fig. 4 TGA profile of CNTs paste.



(a)



(b)



(c)

Fig. 5 Microstructures of CNTs and cathode layers for (a) green, (b) fired, and (c) fired and treated samples.

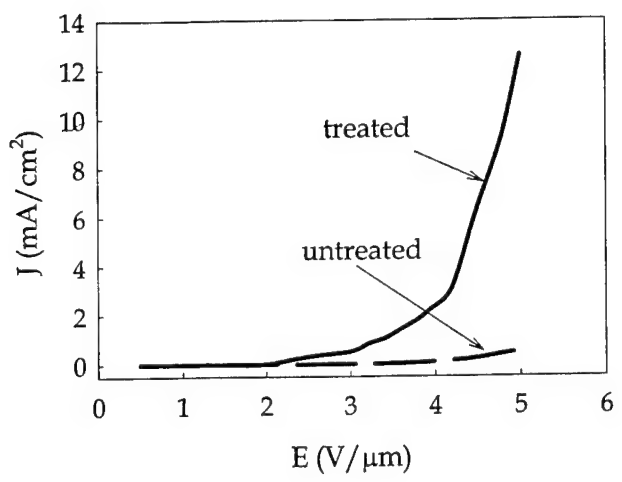
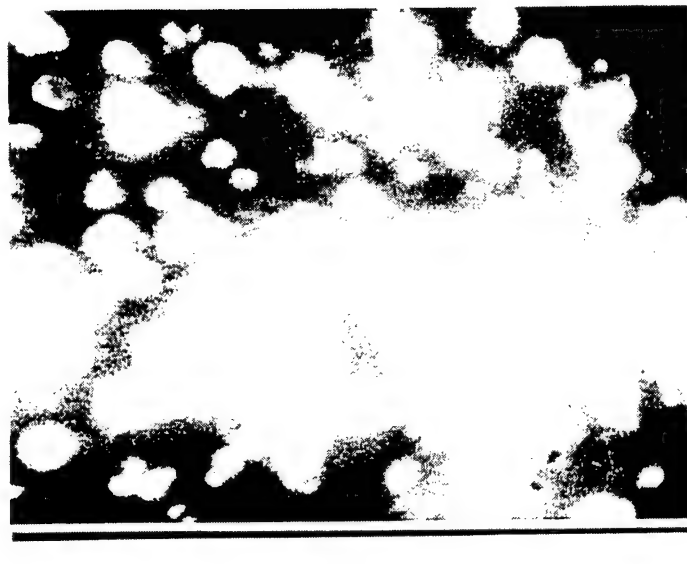
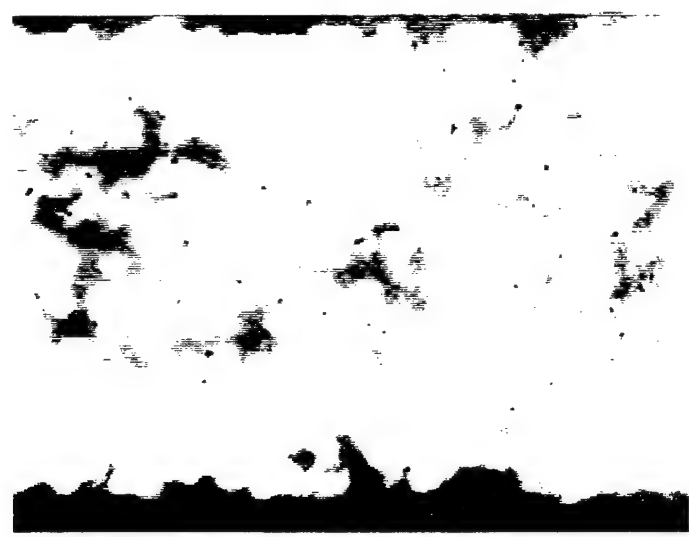


Fig. 6 Emission current density of CNTs layer before and after surface treatment.



(a)



(b)

Fig. 7 Emission images of CNTs layer (a) before, and (b) after surface treatment.

SESSION 4

LED/OLED

White illumination characteristics of ZnS-based phosphor materials excited by InGaN-based Ultraviolet Light-Emitting Diode

Kenji Murakami^a, Tsunemasa Taguchi^a and Masahiko Yoshino^b

^aDepartment of Electrical and Electronic Engineering, Faculty of Engineering, Yamaguchi University,
2-16-1 Tokiwadai, Ube, Yamaguchi 755-8611, Japan

^bKasei Optronics, Odawara, Kanagawa 250-0862, Japan

ABSTRACT

White illumination characteristics of ZnS-based phosphor materials excited by an $In_xGa_{1-x}N$ -based single quantum well (SQW) -structure ultraviolet (UV) light-emitting diode (LED) have extensively been investigated. In order to evaluate white luminescence, two kinds of ZnS-based white phosphors have been employed. When an UV LED was operated at a current of 10 mA, chromaticity (x, y), color temperature (T_c) and general color rendering index (R_a) of the white luminescence are obtained to be $(x, y)=(0.29, 0.33)$, $T_c=7700$ K and $R_a=70$, respectively, for $ZnS:Ag + (Zn,Cd)S:Cu,Al$ phosphors, whilst $(x, y)=(0.31, 0.34)$, $T_c=6900$ K and $R_a=83$, respectively, for white phosphor material including $ZnS:Cu,Al, Sr$ and Y materials. The value of chromaticity slightly changed with increasing forward current of the UV light source. As a result, it is possible to obtain stable white luminescence spectrum. The dependence of the luminescence brightness on the thickness of phosphor shows a tendency to saturate for reflection brightness, but for transmission brightness its dependence has a peak due to light scattering effect. The reflection brightness was higher than the transmission brightness. It is revealed that the white luminescence light of stable chromaticity and high brightness using reflection light can be obtained.

Keywords: $In_xGa_{1-x}N$ -based UV LED, ZnS-based white phosphor, chromaticity, general color rendering index, reflection brightness, white LED

1. INTRODUCTION

There is now intense interest in the development of high brightness visible and white light-emitting diodes (LEDs) because tremendous technological breakthroughs on the epitaxial growth and LED process of III-V compound semiconductors have been emerged.^{1,2,3,4} It is well-known that LEDs can offer advantageous properties such as high brightness, reliability, lower power consumption and long lifetime. The biggest potential application for LEDs will be general lighting.⁵ A national program underway in Japan has already suggested that white LEDs deserve to be considered as the general lighting technology of the 21st century owing to an electric power energy consumption.

During the last few years, the technology of white LEDs which is connected with the $In_xGa_{1-x}N$ blue LED coated with a

YAG:Ce phosphor, has improved the white LED efficiencies from 7.5 lm/W to approximately 30 lm/W. However, the brightness and color purity of InGaN-based white LEDs are dependent on the conditions of phosphor coating, showing "cool white light".

An alternative method of making a color conversion white LED is that a true white can be achieved using three colors from red, green, and blue phosphors excited by ultraviolet (UV) LEDs, similar to three colors based fluorescent lamp. At present, external quantum efficiencies are now as high as 7 % for the UV LED which is operated at about 370 nm. In the future, as the efficiency of blue and UV LEDs will be improved to be approximately 40 %, white LED lamps may replace conventional light bulbs or fluorescent lamps in many applications.

We are for the first time concerned in this paper with the fundamental white illumination characteristics of ZnS-based phosphor materials excited by InGaN-based ultraviolet LEDs. Particularly, two kinds of phosphor materials were used for the characterization of white emission.

2. EXPERIMENTAL PROCEDURES

2.1 Characteristics of an UV LED

Figure 1 illustrates the cross section of an $\text{In}_x\text{Ga}_{1-x}\text{N}$ -based UV LED structure used in the present study. Principally, the LED structure is composed of a single quantum well of $\text{In}_x\text{Ga}_{1-x}\text{N}$ whose thickness is estimated to be approximately 50 Å and also of a double heterostructure with a well thickness of 400 Å. The composition of In is nearly zero. The barrier layers are n-and p-type $\text{Al}_{0.2}\text{Ga}_{0.8}\text{N}$. All epitaxial layers were grown on (0001) sapphire substrate by two-flow metalorganic chemical vapor deposition (MOCVD).⁴ The typical properties of the UV LED are as follows: an emission wavelength of 370 nm, its linewidth of 11 nm, external quantum efficiencies between 3 and 7.5 % and light output powers between 2 and 5 mW at room temperature (RT).

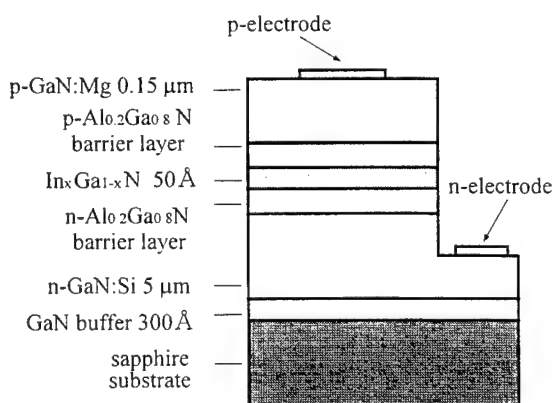


Fig.1 A schematically drawing of the cross section of InGaN/AlGaN

SQW UV LED having an active layer of $\text{In}_x\text{Ga}_{1-x}\text{N}$ ($x \neq 0$).

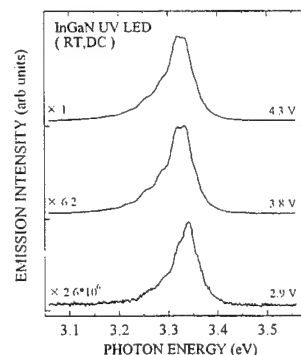


Fig.2 (a) Emission spectra obtained at RT

between 2.9 and 4.1 V.

Figure 2 (a) shows the electroluminescence spectra obtained at three different forward-biased voltages (2.9, 3.8 and 4.3 V) at RT. The 370 nm emission was observed around 2.9 V and with increasing bias its intensity was increased dramatically up to about 4V(as shown in Fig.2 (b)). Between 2.9 and 4.3 V, the emission peak does not shift with voltage.

2.2 Phosphor materials

Two kinds of phosphor materials based on ZnS were used; ① ZnS:Ag and (Zn,Cd)S:Cu,Al and ②ZnS:Cu,Al including Y- and Sr-components. Excitation spectrum for each phosphor was measured at RT using a CCD camera in conjunction with a 50 cm monochromator under the excitation condition by a Xe lamp (500 W). Excitation bands for each phosphor material were observed in the vicinity of 370 nm at RT.

2.3 Luminescence measurements

Current dependence of luminescence spectra of the phosphors excited by $In_xGa_{1-x}N$ SQW UV LED was measured using CCD camera. Chromatic points in the C.I.E chromaticity diagram and color temperature were evaluated by colorimeter using Si photodiode. Thickness dependence of the luminescence brightness of the phosphors at a current of 10 mA was measured using luminance meter.

3. Three methods for obtaining white lights

Table I shows three methods which can produce white light using LEDs. These technologies are likely to include: 1) RGB LED combinations, 2) binary complementary LED systems and 3) $In_xGa_{1-x}N$ -based blue and UV LED systems employing fluorescent phosphors. We need at least three LEDs which primary generate red, green and blue colors from each LED. However, since the different semiconductors are used, one of each primary color must be adjusted by individual supply circuit in order to control the intensity of each color. On the other hand, white LEDs by exciting phosphors have been fabricated using blue and UV LEDs with sufficiently high excitation energy. Using blue LED, the $YAG:Ce^{3+}$ phosphor is excited by 465 nm and then emits yellow fluorescence around 555 nm. The mixture of the blue light from the blue LED chip and the yellow from the phosphor results in a white emission. An alternative method is that a color conversion white LED is also fabricated using both RGB phosphors and UV LEDs.

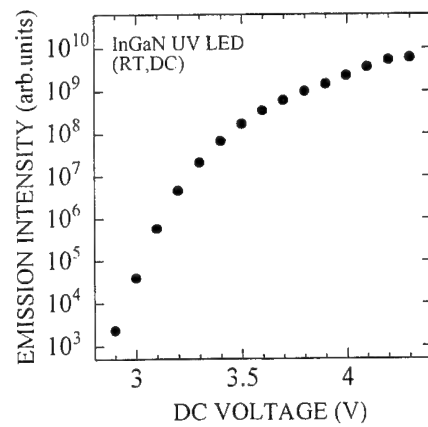


Fig.2 (b) Emission intensity of the 370 nm at RT as a function of forward-bias voltage

Table I . Three methods for obtaining white LEDs. Different LED sources, luminescent materials and how to get white light are shown.

Method	LED source	Luminescent materials	Emission mechanism
1 LED chip	Blue LED ^{6,7,8} .	In _x Ga _{1-x} N/YAG:Ce	Yellow emission from YAG:Ce excited by blue LED
	UV LED ^{9,10} .	In _x Ga _{1-x} N/R, G, B phosphors	White emission from R, G, B phosphors excited by UV LED
2 LED chips	Blue LED, Blue-green LED, Yellow LED, Amber LED	InGaN, GaP, AlInGaP	W = B + Y =B-G + Amber
3 LED chip	Blue LED, Green LED, Red LED	InGaN, AlInGaP	W = R + G + B

4. EXPERIMENTAL RESULTS AND DISCUSSION

4.1. White LED with ZnS:Ag and (Zn,Cd)S:Cu,Al phosphors

Figure3 shows the dependence of luminescence spectra on forward current: 1, 10 and 20 mA. There appear two emission peaks locating at 453 and 561 nm, respectively. We have obtained chromaticity (x, y), color temperature (Tc) and general color rendering index (Ra) to be (0.29, 0.33), 7700 K and 70, respectively, at a forward current of 10 mA. With increasing forward current, two peaks do not shift at all, but the 453 nm band is slightly increased in intensity.

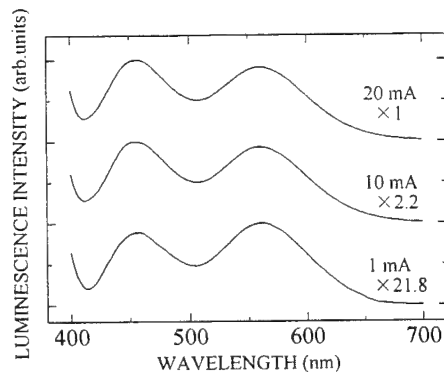


Fig.3 Emission spectra of ZnS:Cu,Al phosphor obtained at RT at three different forward-bias currents (1, 10 and 20 mA)

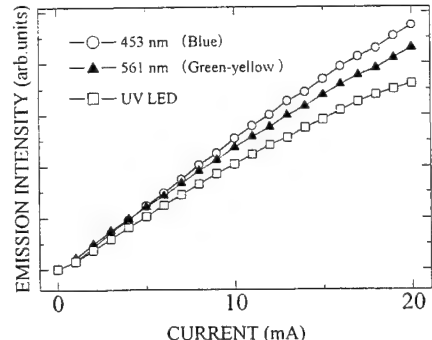


Fig.4 Emission intensities of the 453 nm blue and 561 nm green-yellow emission bands at RT as a function of forward-bias current. The 370 nm UV emission intensities are also plotted against current. The changes in the 453 nm and 561 nm emission intensity with current are normalized.

Figure 4 shows the relationship between the 453 nm blue band and 561 nm yellow band intensities, and forward current, where the normalized intensities for each emission band are plotted. This figure also shows the changes in the intensity of the 370 nm UV emission from the UV LED as a function of forward current. Over a forward current of 10 mA the UV emission is saturated in intensity. However, both the 453 nm and 561 nm emission bands are increased in intensities even over 20 mA.

4.2 White LED with RGB phosphors

Figure 5 shows the dependence of luminescence spectra on forward current: 1, 10 and 20 mA. There are at least three main peaks located at 447, 528 and 626 nm, respectively. The 447 nm blue emission, 528 nm green emission and 626 nm red emission bands are originated from fluorescent emission of ZnS:Cu,Al, Sr and Y materials. We have obtained chromaticity, color temperature and general color rendering index (R_a) to be (0.31, 0.34), 6900 K and 83, respectively, at a forward current of 10 mA. Compared to those of the ZnS:Cu,Al phosphor, illumination factors are much improved. The $R_a = 83$ is close to that of three-band emission fluorescent lamp, indicating the warm white light.

Figure 6 (a) shows the relationship between three (RGB) emission band intensities, and forward current, where the normalized intensities for each emission band are plotted. This figure also shows the forward-current dependence of the UV emission band at 370 nm of the UV LED source. Despite the fact that the UV emission is saturated in intensity, three RGB emission intensities are gradually increased up to a current of 20 mA.

The component of red emission is very important to improve the T_c and R_a values. However, the white light with a low R_a is possible to obtain using the blue and green-yellow components. Fig. 6 (b) shows the intensity ratio between the blue and green component as a function of forward current of the UV LED. Over a current of 10 mA, the ratio is maintained to be about 1.65, in which the blue component is always higher than that of the green component. Fig. 6 (b) also shows the intensity ratio between the red and green component as a function of forward current. Compared to the ratio between the blue and green component, this ratio (2.9-3.0)

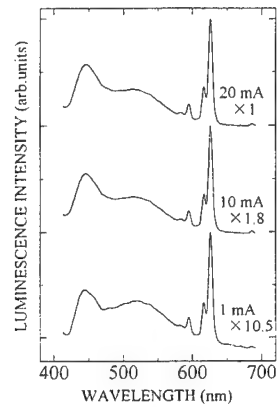


Fig.5 Emission spectra of ZnS-, Y- and Sr-based phosphor obtained at RT at three different forward-bias currents (1, 10 and 20 mA)

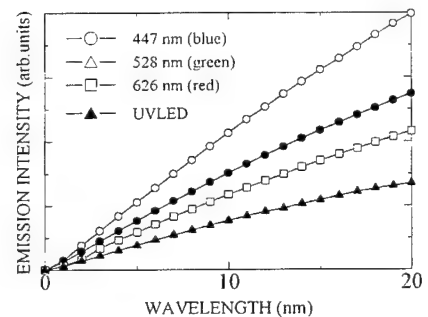


Fig.6 (a) Emission intensities of the 447 nm blue, 528 nm green and 626 nm red emission bands at RT as a function of forward-bias current. The 370 nm UV emission intensities are also plotted against current. The changes in the 447, 528 and 626 nm emission intensity with current are normalized.

of red emission to green emission is almost constant between 10 and 20 mA.

Figure 7 represents the forward current dependence of chromatic points of the RGB phosphor between 1 and 20 mA, where similar characteristics of $In_xGa_{1-x}N$ blue LED: YAG phosphor are plotted. As already seen in Figs. 5, 6 (a), and 6 (b), the changes in T_c values become small against the increase in the forward current. The use of the RGB phosphors for fabricating white LED is essential to produce stable color temperature and general color rendering index with increasing forward current. On the other hand, YAG phosphor-coated white LED indicates, that the changes in T_c values are decreased up to $(x, y) = (0.29, 0.28)$ in the chromaticity diagram at 20 mA.

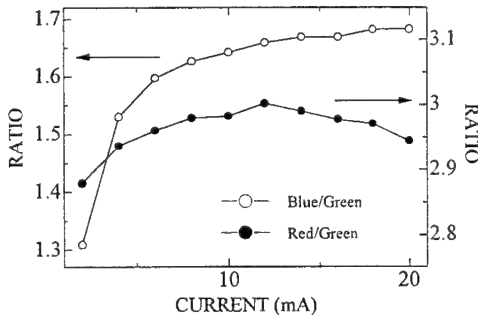


Fig.6 (b) Emission intensity ratios between blue and green component, red and green as a function of forward-bias current

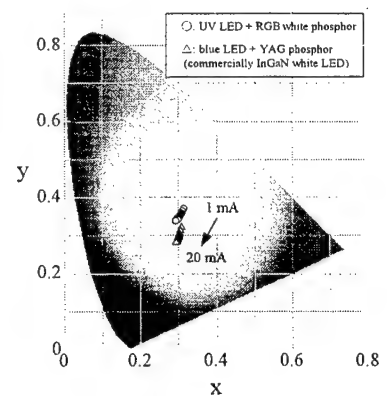


Fig.7 Changes (○) of chromaticity (x, y) coordinates in UV LED excited ZnS-, Y-, Sr-based RGB phosphor between 1 and 20 mA. Similar changes (\triangle) in the blue LED excited YAG phosphor are observed.

4.3 Phosphor thickness dependence of white light intensity under the transmission and reflection conditions

Figures 8 show the phosphor layer thickness of white brightness measured under the transmission and reflection conditions for two phosphors materials of $ZnS:Ag$ and $(Zn,Cd)S:Cu,Al$ (a) and $ZnS:Cu,Al$, Sr and Y system (b), respectively. In both cases, the vertical scale is plotted by luminous intensity. With increasing thickness, the white light intensity shows a tendency to saturate for reflection brightness in Figs. (a) and (b). On the other hand, the white light intensity has a maximum peak for transmission

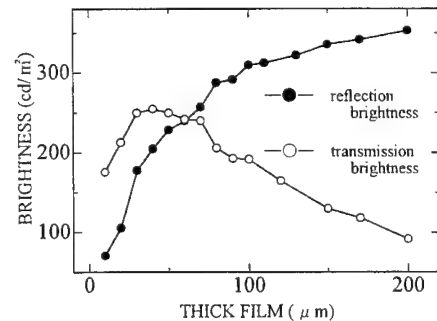


Fig.8 (a) Changes in white light intensity of $ZnS:Ag$ and $(Zn,Cd)S:Cu,Al$ phosphor as a function of phosphor layer thickness under

brightness because of the decrease in intensity due to light scattering with thickness. In the case of transmission brightness, the peak is located at about 30~50 μm and at a thickness of 200 μm the transmission intensity is two or three times of magnitude lower than the maximum intensity. On the other hand, in the case of reflection brightness, over the thickness of 100 μm , the intensity becomes saturated and is higher than the transmission maximum intensity.

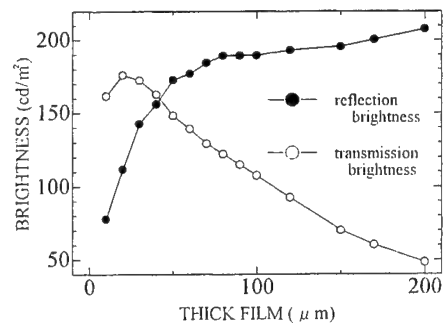


Fig.8 (b) Changes in white light intensity of ZnS-, Y-, Sr-based phosphor as a function of phosphor layer thickness under transmission

5. CONCLUSIONS

We have investigated the white illumination characteristics of two types of ZnS-based phosphor materials excited by an $\text{In}_x\text{Ga}_{1-x}\text{N}$ -based SQW UV LED. The chromaticity, color temperature and general color rendering index were obtained to be (0.31, 0.34), 6900 K and 83, respectively, in the ZnS-, Y- and Sr-based RGB phosphor. It is noted that the value of chromaticity slightly changes with increasing forward-bias current. The present experimental evidence suggests that the ZnS-based phosphor coating white LED can produce excellent spectral purity with forward current. The dependence of the white brightness on the phosphor thickness shows a tendency to saturate for reflection brightness, whilst for the transmission brightness its dependence has a maximum intensity around the thickness of 30~50 μm . It is indicated that the white light of stable chromaticity and high brightness can be obtained under the reflection condition.

ACKNOWLEDGEMENTS

We acknowledge Mr. H.Kudo for measuring the electrical and optical properties of UV LEDs. This work was supported by the Japanese National Project "The Light for the 21st Century" from MITI/NEDO/JRCM. One of the authors (T.T) expresses his sincere thanks to President E.Ogawa of Nichia Chemical Industries.

REFERENCES

1. T. Mukai and S. Nakamura, *White and UV LEDs*, Jpn. App. Phys. **68**, pp. 152, 1999 (in Japanese)
2. K. Miyazaki, *Development of Light Emitting Diode and Its Applications*, Jpn. J. Illum. Engng. Inst. Jpn. **81**, pp.558, 1997 (in Japanese)
3. T. Mukai and S. Nakamura, *Characteristics of InGaN-Based UV/Blue/Green/Amber/Red Light-Emitting Diodes*, Jpn. J. App. Phys. **38**, pp. 3976-3971, 1999
4. S. Nakamura, M. Senoh, T. Mukai, *P-GaN/N-InGaN/N-GaN Double-Heterostructure Blue-Light-Emitting Diodes*, Jpn. J. App. Phys. **32**, pp. L8-L11, 1993
5. S. Nakamura, NIKKEI ELECTRONICS. 602, pp. 93, 1994
6. S. Nakamura, *Present status and future prospects of GaN-based light emitting devices*, Jpn. App. Phys. **65**, pp. 676-685, 1996
7. H. C. Casey, J. Muth, S. Krishnankutty and J. M. Zavada, *Dominance of tunneling current and band filling in InGaN/AlGaN double heterostructure blue light-emitting diodes*, App. Phys. Lett. **68** pp. 2867-2869, 1996
8. NIKKEI ELECTRONICS. 674, pp. 79-100, 1996
9. NIKKEI ELECTRONICS. 743, pp. 41-48, 1999
10. T. Mukai and S. Nakamura, *Current and Temperature Dependence of Electroluminescence of InGaN-Based UV/Blue/Green Light-Emitting Diodes*, Jpn. J. App. Phys. **37**, pp. L1358-L1361, 1998

Email: taguchi@po.cc.yamaguchi-u.ac.jp; telephone: +81-836-85-9407; Fax: +81-836-85-9401

Characteristics of high-efficient InGaN-based white LED lighting

Yuji Uchida^a, Tatsumi Setomoto^a, Tsunemasa Taguchi^{a*}, Yoshinori Nakagawa^b and Kazuto Miyazaki^b

^a Department of Electrical and Electronic Engineering, Faculty of Engineering, Yamaguchi University,
2-16-1 Tokiwadai, Ube, Yamaguchi 755-8611, Japan

^b Nichia corporation, 491 Oka, Kaminaka-cho, Anan, Tokushima 774-8601, Japan

ABSTRACT

The basic illumination characteristics of an efficient white LEDs lighting source, which is composed of cannon-ball type 10 cd-class InGaN-based white LEDs, are described. It is noted that the temperature and forward-bias current dependence under full wave rectification of AC 100 V gives a significant effect to both electroluminescence properties and luminous efficacy. We have obtained a maximum luminous intensity of 95000 cd/m² and a luminous efficacy of about 27 lm/W at an electric power of 20 W (at a constant current of 10 mA). The developed white LEDs lighting source indicates two injection electroluminescence peaks at 465 and 555 nm, which are originated from a blue LED and a YAG:Ce³⁺ phosphor, respectively. The illuminance distribution of the LED lighting source was analyzed using our “multi sources of LED light” theory. We have performed the design of a street lighting as the practical application using the 700 LEDs array lighting source.

Keywords: InGaN, white LED lighting, YAG phosphor, luminous efficacy, LED lighting theory

1. INTRODUCTION

Visible and white light-emitting diodes (LEDs) are ideal for a large number of applications including illumination, displays and signage, with advantageous properties such as high-brightness, reliability, long lifetime and low power consumption.¹ Recently, there is a growing interest in shorter wavelength blue and ultraviolet LEDs for high-brightness white-light LEDs together with phosphor coating.² A 10 Cd class white LED composed of a multiple quantum well (MQW) InGaN blue LED and a YAG:Ce phosphor has been developed.^{3, 4} A structure of the white lighting source has been obtained by the integration of the blue InGaN LED die and the YAG phosphor into a single package. We have reported the improved luminous efficacy of about 40 lm/W using 700 LEDs lighting source at an electric power of 5 W.³ It has been expected that extremely high-brightness white LEDs can significantly replace standard incandescent bulbs usually used in hospitals, hotels and airplanes. We have already demonstrated an energy saving type street lamp linked with a photovoltaic solar cell, using a 10 cd-class white LEDs array lighting source.^{4, 5} These applications are extremely useful for saving electric power owing to lower energy consumption of LEDs.¹

In this paper, we will describe for the first time the basic illumination characteristics of high-efficient InGaN-based white LEDs array lighting source. The temperature and forward-bias current dependence which gives a significant effect to both electroluminescence properties and luminous efficacy has extensively been investigated. In spite of strong polar and linear radiation intensity profiles from a cannon-ball type LED, we will analyze the distribution of illumination intensities from the LEDs array using the “multi sources of LED light” theory which has recently been developed by our group.⁶

*Electric mail: taguchi@po.cc.yamaguchi-u.ac.jp

2. EXPERIMENTAL PROCEDURES

2. 1 White LED device

Table I shows the characteristics of the InGaN-based multiple quantum well (MQW) white LED together with YAG:Ce phosphor.⁵ The white LED structure in a cannon-ball type consists of InGaN/GaN MQW LED and YAG:Ce phosphor in a single package. An external quantum efficiency is over 20 %. A luminous efficacy for a chip is estimated to be approximately 20 lm/W at a forward-bias current of 20 mA at room temperature. The operation lifetime is expected to be over 20000 hrs. The white LED used in the present experiment has a luminous intensity of 10 candela.

Table I Basic properties of a InGaN-MQW white LED

Output Power	~10mW
External quantum efficiency	>20%
Luminous Efficacy	>20lm/W
Chromaticity coordinate	(0.31,0.32)
Color temperature	6500K
General color rendering index	Ra=85
Response time	120ns
Life time	>20000hr

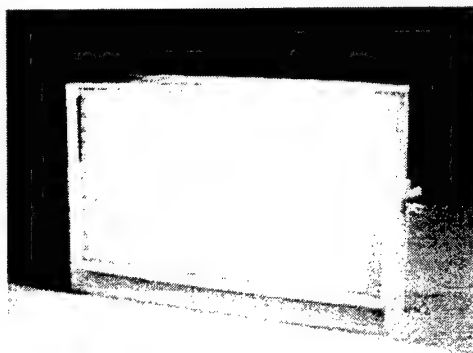


Fig. 1 A practical view of white LEDs lighting

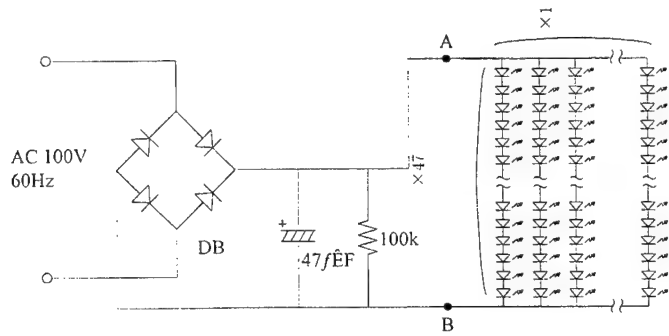


Fig. 2 A condenser-input type electric circuit

2. 2 White LEDs array lighting source and driving electric circuit

Figure 1 shows a typical example of a white LEDs array lighting source, where 705 pieces LEDs are composed by a 15 LEDs parallel connection with each 47 LEDs series connection block. Fig. 2 shows a typical driving electric circuit for the LEDs array lighting device, where a condenser-input type rectification circuit was used (AC 100 V supply and 60 Hz). A basic electric circuit consists of a diode bridge circuit, and a smoothing circuit with a 47 μ F condenser and a 100 k Ω resistance in order to obtain full wave rectification voltages between 143 and 126 V at 120 Hz. The maximum and minimum current was then about 17 and 3 mA, respectively. We obtained a maximum luminance of about 95000 cd/m² at electric power of about 20 W, and obtained a maximum illuminance as high as 10000 lx at a distance of 30 cm from the present LEDs array. The size of LEDs array has a 230 \times 180 mm² area.

2.3 Evaluation of lighting source

Temperature dependence of the emission spectra of a white LED under a forward bias DC or AC current of 20 mA was measured using a CCD camera in conjunction with a 50 cm single grating monochromator. A temperature variable cryostat was used for the measurement. A chromatic point in the CIE chromatocity diagram, luminous intensity and color temperature were evaluated by a luminance and illuminance meter using a Si photodiode.

3. RESULTS AND DISCUSSION

3. 1 Basic properties of a cannon-ball type white LED

Usually, a LED is operated under a forward-bias direct current (DC) and a cannon-ball type white LED has already been used as an indicator and displays in general. As mentioned in 2. 1, a white LED is made of a particular type of blue LED covered with a YAG:Ce phosphor. The white color is produced by a mixture of blue and yellow colors, which generate from an InGaN-MQW blue LED (465 nm) and a Ce³⁺ emission (555 nm), respectively. In spite of tremendous applications to optoelectronic devices using the white LEDs under the DC bias condition, there have been nothing reports on the characteristic of white LEDs under the AC and pulse-biased conditions.

3. 2 Temperature and forward-biased current dependence of illumination characteristics

Figure 3 shows the temperature dependence of the forward biased electroluminescence (EL) spectra of a cannon-ball type white LED between 20 and 160 °C. An emission peak at 465 nm at room temperature (RT) originates from a blue LED. An yellow emission at 555 nm with a bandwidth of about 150 nm is generated by an excitation of a Ce³⁺ center whose excitation wavelength exists near 460 nm. It is thought that energy from the 465 nm excitation band can be trapped at the Ce³⁺ ion and emits as cerium yellow emission at 555 nm. With increasing temperature, the 465 nm peak moves towards longer wavelength, which is similar to the temperature dependence of band gap energy of InGaN semiconductor.¹ On the other hand, the 555 nm peak position did not change with temperature. Due to the change in the emission peak wavelength of the blue LED with temperature, the effective excitation efficiency for YAG phosphor is decreased. As a result, the emission intensity of the 555 nm band becomes weak at 160 °C. It is therefore suggested that the emission properties of the InGaN white LED depends upon the temperature, and that an emission efficiency of the yellow band at 555 nm becomes weak above 50 °C.

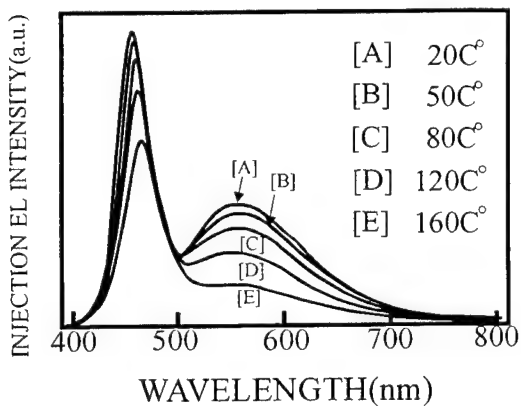


Fig. 3 Temperature dependence of EL spectra [A~D] of a white LED device between 20 and 160 °C.

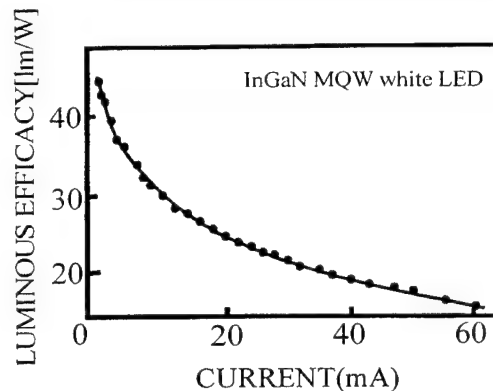


Fig. 4 Luminous efficacy of a white LED chip as a function of forward-bias current.

Figure 4 shows the characteristics of luminous efficacy of a 10 cd class white LED chip as a function of forward-bias current. The onset for the white emission starts from a forward-bias current of about 9×10^{-2} mA. At 1 mA, the luminous efficacy is estimated to be about 45 lm/W. However, the luminous efficacy is estimated to be about 27 and 23 lm/W at a constant forward-bias current of 10 and 20 mA, respectively. The evidence which indicates the high luminous efficacy at

low currents is related to an increase in the internal quantum of the blue LED itself. This behavior is quite different from that of AlGaAs red and AlInGaP amber LEDs.¹ However, the detailed physical process is still unknown at present.

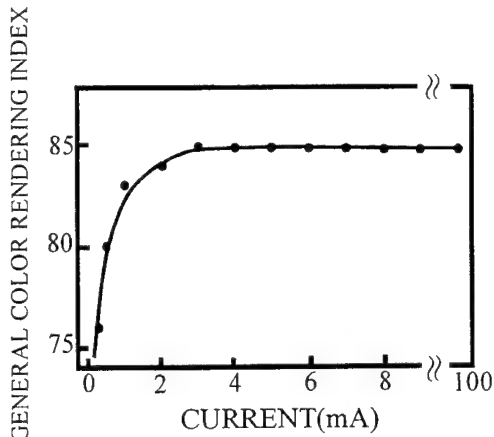


Fig. 5 General color rendering index of a white LED as a function of forward-bias current.

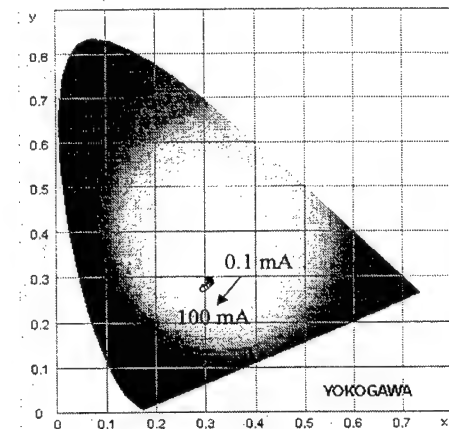


Fig. 6 Changes in (x,y) chromaticity coordinates of the chromaticity between 0.1 and 100 mA

Figure 5 shows the general color rendering index (Ra) of a white ED as a function of forward-bias current. Between 0.1 mA and 3 mA, the Ra gradually increases, but over 3 mA the Ra is nearly constant and kept to be 85, which is very good color index for all possible general lighting applications.

Figure 6 describes the experimental plots in (x,y) chromaticity coordinates of chromaticity between 0.1 and 100 mA. As seen in this figure, the changes in x- and y-coordinate lines are extremely small, so that the white LED indicates a good characteristic which is possible for high current operation.

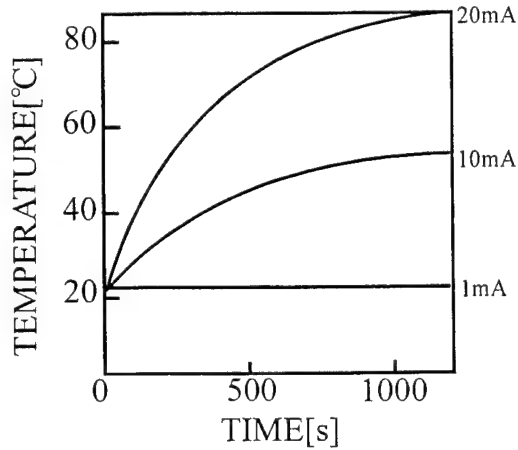


Fig. 7 Temperature rise of a 700 LEDs array lighting source at three different forward currents (1, 10 and 20 mA) as a function of driving time.

Figure 7 shows the temperature rise of a 700 LEDs lighting source at three different forward currents (1, 10 and 20 mA) as a function of driving time. At 1 mA, the temperature rise can not almost be observed with time. As has already been shown in Fig. 4, the luminous efficacy is high, so that the efficiency of the LED lighting device is extremely good. At 10 mA, the efficacy is decreased to be about 28 lm/W and the temperature rise gradually occurs with time. Finally, the temperature of the LED array rises up to 50 °C without cooling system after 3 hrs. When the forward current is 20 mA, the temperature rise

is significant and after 2 hr the temperature of the LED array is over 80 °C without cooling system. Such situation is extremely worse for operating the LED lighting array during a long time and as a result degradation of the LED array may occur. The luminous intensity of the LED array at 20 mA for about 3 hrs operation is decreased by 20 % of the initial value as shown in Fig.8.

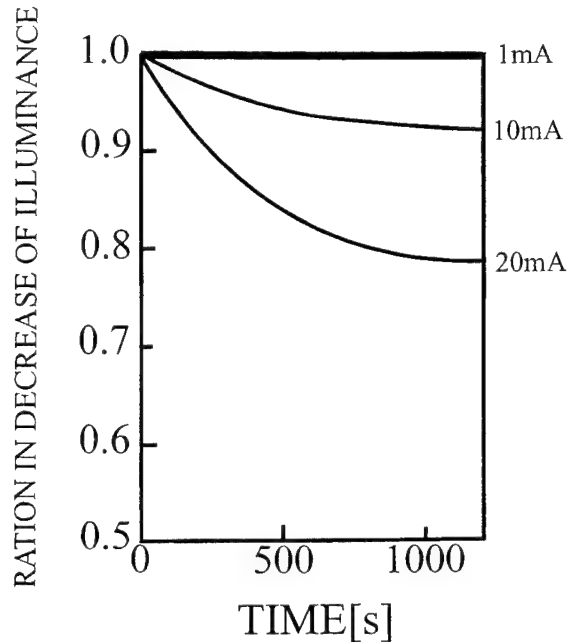


Fig. 8 Ratio in decrease of illuminance against the initial value as a function of time obtained at three different currents (1, 10 and 20 mA).

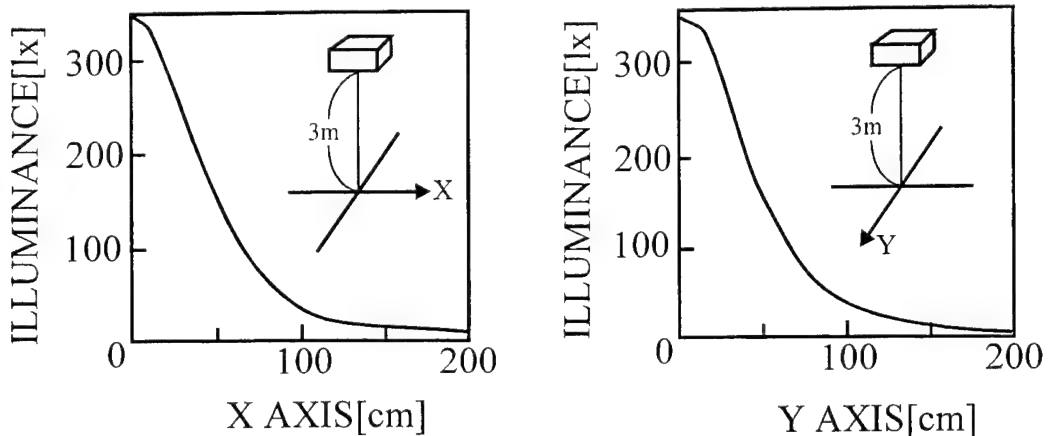


Fig. 9 Distribution of illuminance along x (a) and y (b) axial directions measured directly under a distance of 3 m from the white LED array source.

Figure 9 shows the distribution of illuminance along x (a) and y (b) axial directions measured directly under a distance of 3 m from the white LED array source (same as used in Fig. 7). This LED lighting device was operated at a constant current of 10 mA. At a center of (x, y) coordinates, the illuminance is estimated to be about 350 lx. At a 50 cm distance separated from the center, the luminous intensity is estimated to be 150 lx. The intensity distribution along x or y axis is equal and indicates the homogenous distribution character of the illumination intensity along x and y direction. This LEDs lighting source is applicable to the practical street lamp instead of white fluorescent lamp, and seems suitable for local lighting.

3. 3 A comparison between the experimental results and our theoretical LEDs lighting model

It is necessary to establish a new theory for calculating illuminance when an lighting array device constructed using many cannon-ball type LEDs is designed, because the LED is the exponential intensity source ($\cos^n \theta$ source).

As shown in Fig. 10, assuming that there are many LED light sources which are arranged by following the lattice- and circular-like configuration on the flat plate, the illumination at a search point of L in the (x, y, z) space can be calculated by the following equation,

$$E(x, y, z) = \sum_{i=1}^n \frac{I_i(\theta_i)}{r_i^2} \cos(\theta_i)$$

when i is a suffix for arbitrary position of LED light source and $r_i^2 = (x_i - x)^2 + (y_i - y)^2 + (z_i - z)^2$. We can calculate a polar and linear intensity profile of many LEDs by the inverse square (r^2) law, and the illuminance is expressed by a \cos component for a vertical direction. In order to understand how to arrange suitable LED light sources between 1 and n , we developed a basic algorithm for LEDs arrangement.⁶ Fig.11 shows a typical configuration for $n = 4$ including the lattice-and circular-like arrangement.

Fig. 12 shows the calculated result of illuminance of multi LED sources as a function of x and y distance from a center directly under a distance of 3 m from the LEDs lighting array used. The obtained results are in quantitatively good agreement with the experimental characteristics described in Figs. 8 (a) and (b).

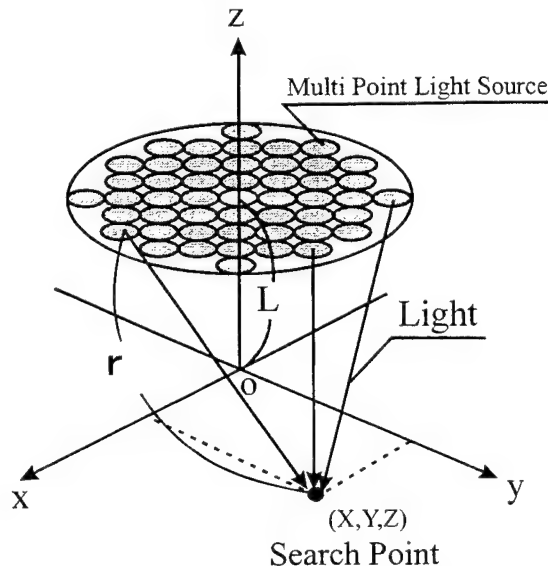


Fig. 10 A “multi source of LED light” model for the calculation.

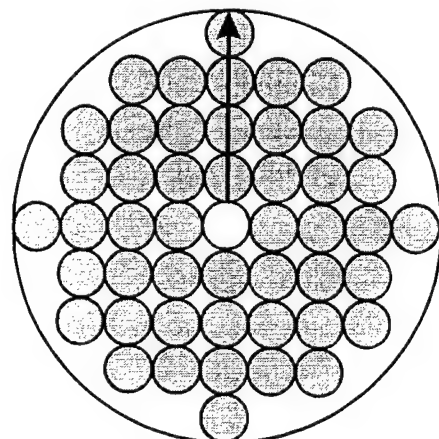


Fig. 11 A typical configuration of multi LED sources for $n = 4$

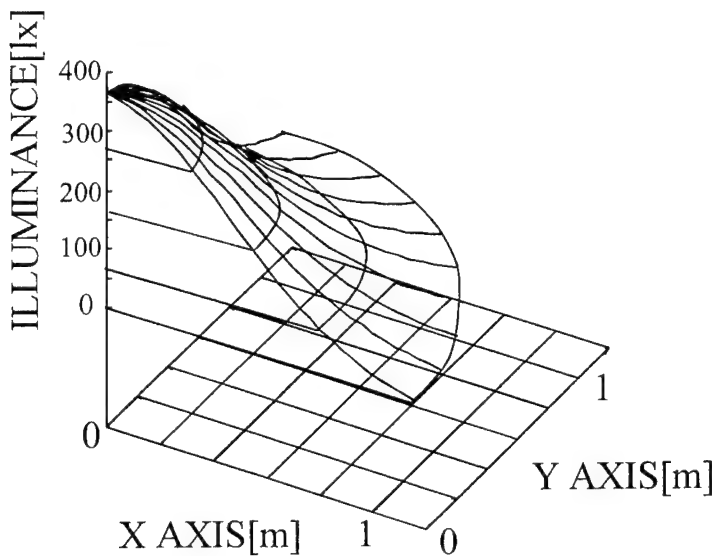


Fig.12 Calculated illuminance along x and y axial direction for a LEDs lighting source.

4. SUMMARY

The basic illumination characteristics of an efficient white LEDs lighting source, which is composed of cannon-ball type 10 cd-class InGaN-based white LEDs, have been extensively investigated. It is revealed that the temperature and forward-bias current dependence under full wave rectification of AC 100 V gives a significant effect to both electro luminescence properties and luminous efficacy. We have obtained a maximum luminous intensity of 95000 cd/m² and a luminous efficacy about 27 lm/W at an electric power of 20 W (at a constant current of 10 mA). The developed white LEDs lighting source indicates two injection electroluminescence peaks at 465 and 555 nm, which are originated from a blue LED and a YAG:Ce³⁺ phosphor, respectively. The illuminance distribution of the LED lighting source was analyzed using our theory on the basis of multi sources of LED light. We have constructed a street lamp as the practical application using the 700 LEDs array lighting source. The experimentally obtained illumination characteristics are well interpreted in terms of our LEDs lighting theory.

Acknowledgements

This work was supported by the Japan national project “The Light for the 21st century” from MITI/NEDO/JRCM. One of the authors (T.T) expresses his sincere thanks to president E. Ogawa of Nichia Chemical Industries.

REFERENCES

1. S. Nakamura and G. Fasol, “The Blue Laser Diode” (Springer) 1997.
2. S. Nishikawa, T. Tamura and M. Senoh, “Candela-class high-brightness InGaN/AlGaN double-heterostructure blue light-emitting diodes” Appl. Phys.lett., 64 (1994) 1687.
3. T. Tamura, T. Setomoto and T. Taguchi, “Fundamental characteristics of the illuminating light source using white light-emitting diodes based on InGaN semiconductors,” Trans IEE of Japan 120-A (2000) pp.244-249 (in Japanese).
4. T. Setomoto, Y. Uchida and T. Taguchi, “Energy-saving type white LED lighting source linked with a solar cell system” Proc. Int. Conf. on Electrical Engineering. (2000) to be published.
5. T. Tamura, T. Setomoto and T. Taguchi, “Illumination characteristics of lighting array using 10 candela-class white LEDs under AC 100 V operation,” J. of luminescence 23 (2000) pp. 201-203.
6. T. Taguchi, “White LED lighting project in Japan” presented as an invited talk in the “Strategies in Light” Conference held at San Francisco (2000, 9-10 Feb).
7. Y. Uchida and T. Taguchi, “The concept of multi sources of LED light” presented in the Spring meeting of Japan Society of Applied Physics held at Tokyo (2000, 27-30 March) (in Japanese).

Multicolor organic LEDs processed by integration of screen printing and thermal transfer printing

Hsin-hua Chang ^a, Chung-chih Wu ^b, Cheng-chung Yang ^b, Chieh-wei Chen ^b, and Cheng-chung Lee ^a

^a Institute of Optical Sciences, National Central University, Chung-Li, Taiwan, 32054

^b Graduate Institute of Electro-optical Engineering and Department of Electrical Engineering,
National Taiwan University, Taipei, Taiwan 10617

ABSTRACT

Color integration in organic LEDs (OLEDs) on a substrate has always been a challenge due to the incompatibility of OLED materials with the conventional photolithography. In this paper, we report a process for the fabrication of large-area multicolor OLEDs of arbitrary patterns by combination of thermal-transfer printing and screen-printing. Thermal transfer printing is used to introduce color-tuning dyes into a thermally stable OLED polymer layer from a dye-dispersed polymer layer on the donor plate. Such a process permits controllable and uniform doping of a polymer layer over large areas. By using a patterned color donor plate, color integration in OLEDs could be accomplished with a single thermal transfer step. In this work, the source plate containing multicolor patterns is fabricated by screen-printing. The RGB color patterns were printed sequentially by using RGB inks prepared by dispersing nile red, C6 and perylene into a commercial screen-printing paste. Based on these printing approaches, we have successfully fabricated multicolor single-layer and heterostructure OLEDs.

Keywords: Color integration, screen -printing, thermal-transfer printing

1. INTRODUCTION

In last decade, organic light emitting devices (OLEDs) based on small molecule organic materials or on polymer materials have been extensively studied because of their various advantages for flat panel display applications [1-2]. The capability of solution processing of polymers leads to manufacturing advantage for large-area coating. However, it is found difficult to integrate multicolor polymer materials or devices for full-color displays by conventional coating and sequential photolithography steps [3-4]. To resolve this issue, printing approaches have been aggressively pursued recently. For instance, ink-jet printing has been used to deposit directly patterned polymers or to introduce color-tuning dye patterns into/onto continuous buffer polymer layers [5-8]. However, ink-jet printing is in general a sequential process and might have a limit for substrate throughput [9]. Alternatively, a large-area thermal transfer process was recently proposed for color patterning of polymer layers in OLEDs [9]. Owing to a transfer mask inserted between the donor and the receiver films, this process involves several mechanisms: the sublimation of dye molecules from the heavily dispersed polymer film, travel of dye molecules to the surface of the receiver film, and the diffusion of dye molecules into the receiver film. Interaction of all these mechanisms has led to difficulty in controlling profiles of dye concentration and to complication of processing steps. For instance, long periods of annealing may be required to redistribute dye dopants in the receiver film after the transfer process.

In our previous paper [10], we report an effective transfer process for performing controllable doping of polymer films in OLEDs. In this process, the polymer receiver film is placed in direct contact with the dye-dispersed polymer donor film to permit direct dye-diffusion thermal transfer. We performed theoretical and experimental studies of this doping process and show that it can be modeled by Fick's diffusion theory under impermeable film-substrate boundary conditions. We have therefore named this process as finite-source dye-diffusion thermal transfer (FS-D2T2). We demonstrated doped-polymer OLEDs with device characteristics same as those made from the conventional blending process.

Using a source plate containing multicolor dye-dispersed polymer patterns, FS-D2T2 may be used to make multicolor OLEDs or color pixels in OLED displays. The color source plates may be fabricated with any patterning technique, ranging

from photolithography to printing, as long as the fabrication processing does not degrade the emission characteristics of dyes to be transferred. In this paper, we report the screen-printing process for the fabrication of color source plates for FS-D2T2. Screen-printing method is an additive and high-throughput patterning technique suitable for large areas. Using screen-printed source plates, we have been able to produce line width of $\sim 150 \mu\text{m}$ in the receiver film and have successfully fabricated multicolor single-layer and heterostructure OLEDs based on FS-D2T2.

2. EXPERIMENTAL RESULTS AND DISCUSSIONS

2.1 Thermal-Transfer Printing – Finite-Source Dye-Diffusion Thermal Transfer (FS-D2T2)

The arrangement for performing FS-D2T2 is shown in Fig. 1. A pressure is applied on top of the receiver plate to ensure intimate contact with the source film. At an elevated temperature, the dye dopants transfer thermally from source polymer layer to receiver polymer layer. In our previous paper [10], we showed that FS-D2T2 is a reliable and effective method of performing controllable doping of polymer films in OLEDs. The characteristics of FS-D2T2 include: (1) it is a self-limiting process. There would be no concern of over-doping or consequent concentration quenching even for elongated diffusion time as long as concentration of dye in the source polymer is chosen to match the desired final concentration in the receiver. (2) Doping level is controllable by concentration of dye in the source polymer. (4) Devices using the FS-D2T2 films exhibited characteristics same as those using conventional dye-blended films.

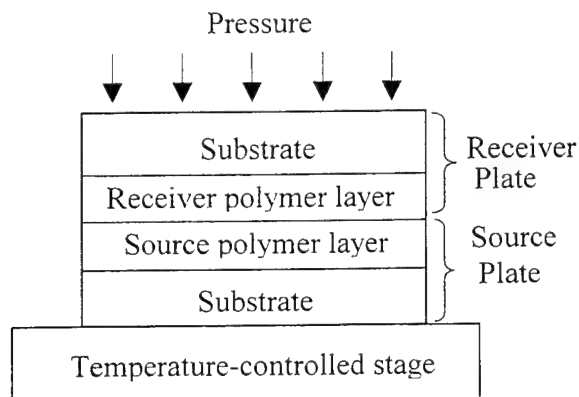


Fig.1. Arrangement for finite-source dye-diffusion thermal transfer.

2.2 Color Integration

Fig. 2 shows color integration process for OLEDs by FS-D2T2. Multicolor patterns are designed on the source plate. The source plate containing multicolor dye-dispersed polymer patterns may be fabricated with any patterning technique, from photolithography to screen-printing, as long as the fabrication processing does not degrade the emission characteristics of dyes to be transferred. By using a source plate containing color patterns, FS-D2T2 could be used to accomplish color integration for OLED devices or displays on a substrate in a single thermal transfer step.

One concern in this color integration process is the lateral diffusion of dyes. The edge definition of patterns will be influenced by the lateral diffusion effect. Since the diffusion length to get complete dye transfer is of the order of receiver

film thickness (~1000 Å) in the FS-D2T2 process for OLEDs, the lateral diffusion would not hinder the accomplishment of ~μm resolution eventually by reducing feature sizes on the source plates.

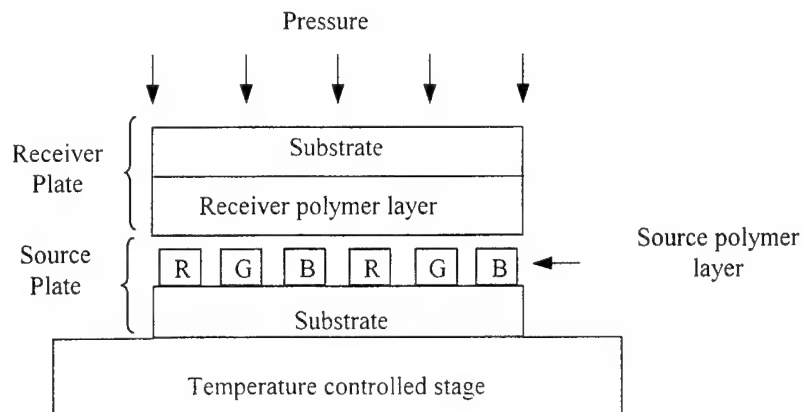


Fig. 2. Color integration of OLED by FS-D2T2

Another concern is the difference in the diffusion speed of different dyes used. For instance, Fig. 3 shows the diffusion coefficients of dyes C₆ and perylene vs. temperature in a bipolar polymer matrix PVK:PBD(100:40 wt%), where PVK is a hole transport polymer and PBD is an electron-transport molecule. The diffusion coefficient of perylene is larger than C₆ at the same temperature, indicating that perylene diffuses into PVK:PBD film more easily than C₆. Since the FS-D2T2 is a self-limiting process and the final dopant concentration in the receiver films is controlled by the initial concentration in the source films, the difference in the diffusion speeds of different dyes would not impose difficulties in controlling the concentrations of different dyes.

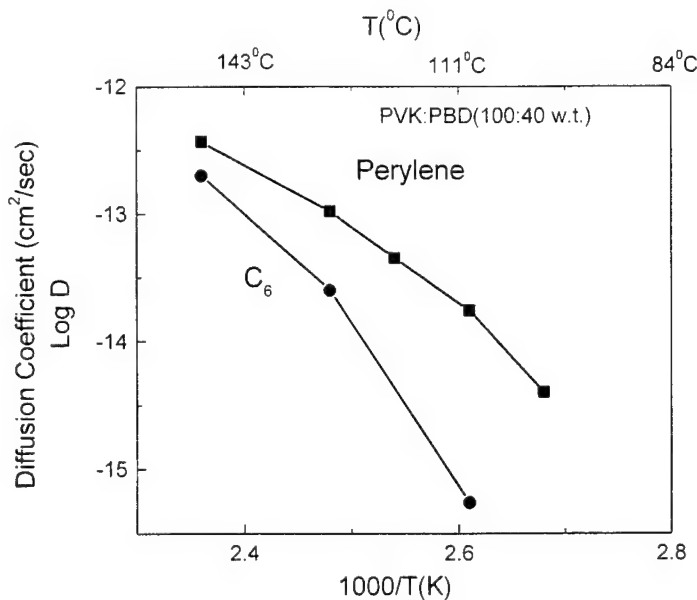


Fig. 3. Diffusion coefficients of C₆ and Perylene in bipolar polymer film PVK:PBD at different diffusion temperatures.

2.3 Multicolor Source Plate Prepared by Screen-Printing

Color source plate was fabricated by screen printing technique in this work. Screen-printing is a basic technology for thick film microcircuitry and inorganic electroluminescent devices. It is suitable for arbitrary large-area patterning. We applied this technology for the preparation of multicolor source plate needed in the FS-D2T2. The screen-printing process is illustrated in Fig. 4. Stainless-steel screen was chosen for better resolution and longer lifetimes than the polyester screen. The screen printer used in this work is manually aligned between sequential printings. Patterns on the stainless-steel screen are defined by photolithography of photoreactive emulsion over the screen surface. The screen printer applies the screen-printing paste evenly to the screen and rubbed it with a squeegee, which then pushes the paste onto the source plate substrate through the patterned openings in the screen. The screen printing paste is considered for a printable carrier of dye and is not thermally interactive with the receiver polyester film.

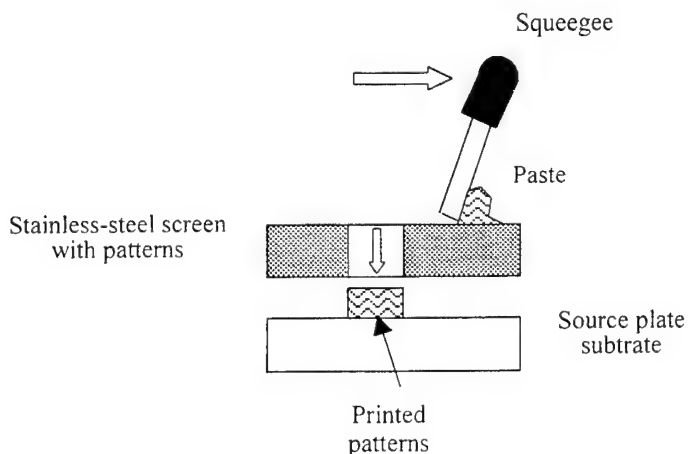
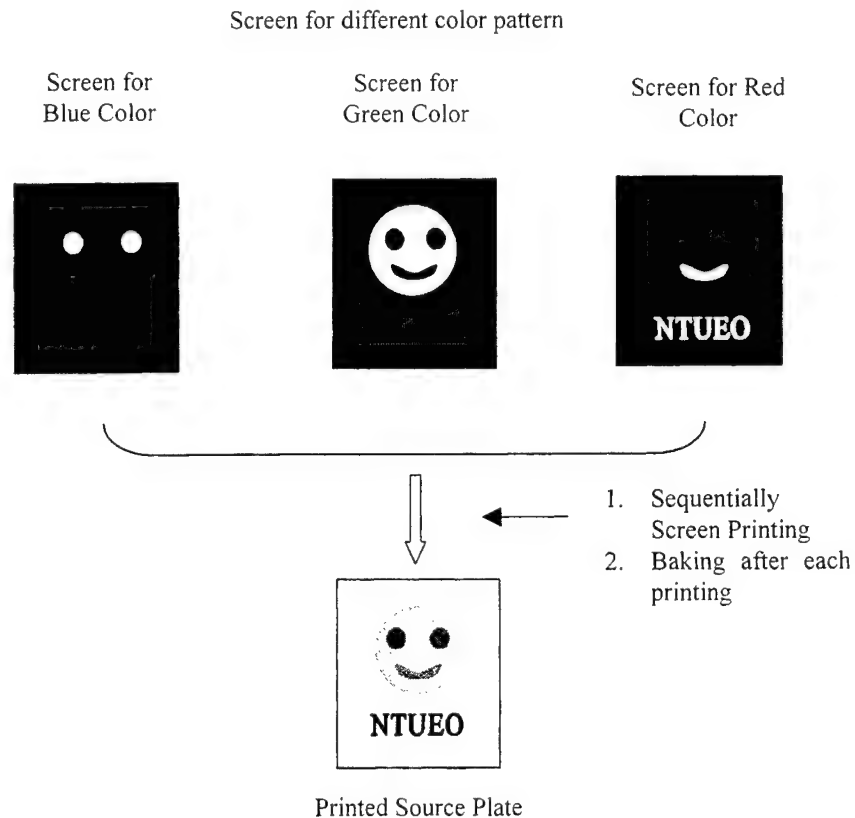


Fig. 4. Schematic representation of the screen printing process

Fig 5. shows how to prepare multicolor pattern source plates by sequentially screen sprinting. RGB inks were prepared by dispersing nile red (~0.006% wt.), Coumarine6 (~0.01% wt.) and perylene (~0.02% wt.) into a commercial screen-printing paste (DuPont 7155), respectively. Patterns of different colors are separated onto different screens, and are sequentially printed onto the substrate. The alignment of different colors was achieved by designed alignment marks on each screen. After each printing, the substrate was baked at the temperature-controlled stage (110 °C 6 minutes) to harden and fix the pastes. With the manually aligned screen printer, a linewidth of ~150 µm was achieved. However, a linewidth of tens of µm should be easily achieved by state-of-the-art semiautomatic or automatic screen printers..



Step 5 : Preparation of Multicolor Pattern Source Plate
by Sequentially Screen Printing

2.4 Multicolor Organic LEDs

By using a source plate containing color patterns, FS-D2T2 could be used to prepare multicolor organic polymer films for OLED devices or displays on a substrate in a single thermal transfer step. This multicolor layer may be the only active emissive layer in a single-layer OLED device structure, or it may be the emissive layer in a multi-layer OLED structure. In this paper, we demonstrated both types of multicolor OLED devices using the FS-D2T2 films.

The cross section of the device structure for the single-layer multicolor OLEDs is shown in Fig. 6. For this type of devices to work, the organic films must be able to conduct both holes and electrons. That is, the organic layer needs to be a bipolar layer. The hole-transport polymer PVK dispersed with ~25 wt.% of electron-transport molecules PBD has been used as the bipolar organic layer in this work. In addition, for regions of different colors in a same device to emit at the same time with comparable brightness, they all must have similar operation voltages and emission efficiency. Fortunately, for the RGB dyes, nile red, coumarin 6 and perylene used in this work, near their optimum concentrations, they all show similar electrical characteristics, permitting the realization of multicolor OLEDs. Such a multicolor OLED made from an FS-D2T2 film is shown in Fig. 7.

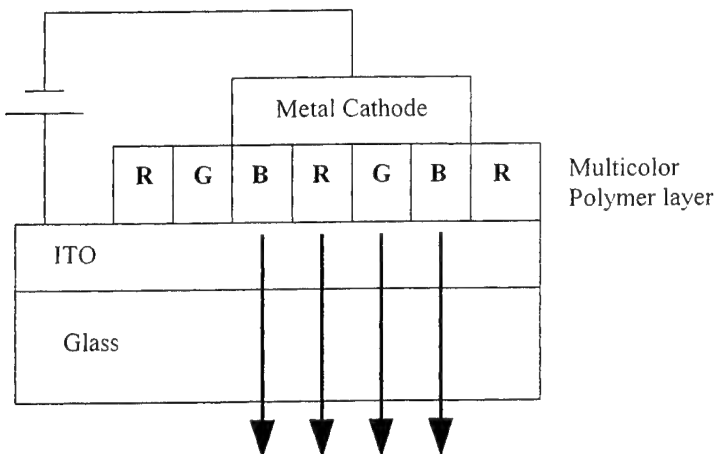


Fig. 6. Schematic illustration of operation of multicolor OLED device.

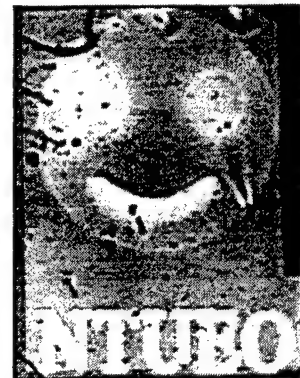


Fig. 7. EL Photograph of a Multicolor OLED from the FS-D2T2 film with single layer device structure.

The Cross section of a multicolor heterostructure device is shown in Fig. 8. The electron transport layer, Alq, and the metal cathode are vacuum evaporated after the FS-D2T2 process of the hole-transport polymer PVK. Fig. 9 shows EL spectra of the heterostructure OLED. Only emission from Alq₃ is observed in the PVK/Alq₃ structure, indicating that without dopants in the PVK excitons are formed and confined in the Alq layer. Compared with the PVK/ Alq₃ structure, we observed contribution from dopants in the doped-PVK/ Alq₃ structure. Since excitons are initially formed in the Alq layer, the emission contributions from dopants are through the interlayer energy transfer between Alq and dopants in PVK. This interlayer energy transfer is allowed since the Förster energy transfer mechanism is a long-range process. Making use of this interlayer energy transfer mechanism, a multicolor heterostructure OLED is thus achieved.

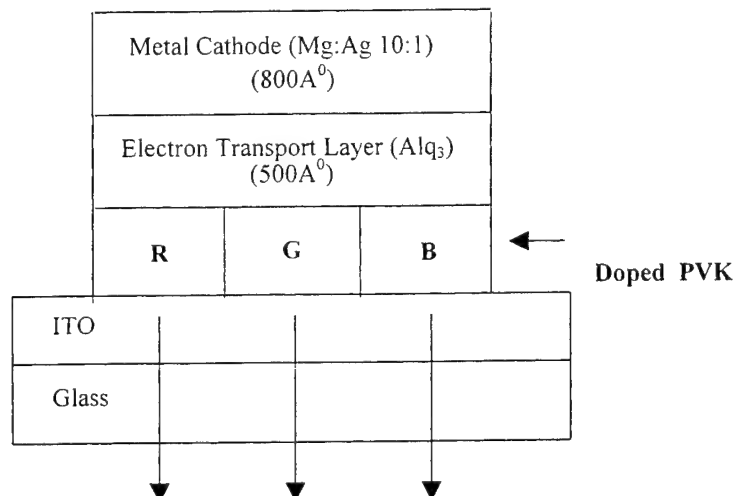


Fig. 8. Schematic cross section of multicolor heterostructure device.

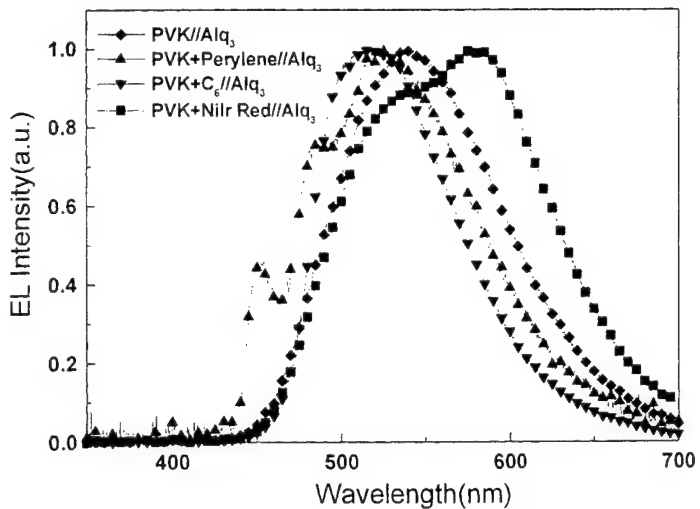


Fig. 9. EL spectra of multicolor heterostructure OLED from a FS-D2T2 film.

Although multicolors can be obtained from the above structure, the energy transfer is, however, incomplete through the interlayer energy transfer. In the future, a structure of introducing a hole-blocking and electron-transport layer between the electron-transport layer and the hole-transport layer may confine the formation of excitons within the PVK layer, ensuring complete energy transfer to the dopants and obtaining improved color purity.

3. CONCLUSION

We used FS-D2T2 to accomplish color integration for OLED devices or displays on a substrate in a single thermal transfer by using a source plate containing color patterns. Color source plate is prepared by screen-printing in this work. We have successfully fabricated multicolor single-layer and heterostructure OLEDs based on FS-D2T2 with screen- printing approaches.

4. ACKNOWLEDGE

The authors would like to express gratitude to Prof. T. Y. Luh, Prof. M. K. Leung, and Mr. Lien of Bayer Co. for stimulating discussions and for assistance in experiments. This work was supported by National Science Council of Republic of China (Grant no. NSC 88-2212-E-002-075).

5. REFERENCES

1. C. W. Tang and S. A. VanSlyke, Appl. Phys. Lett. **51**, 913 (1987)

2. J. H. Burroughes, D. D. C. Bradley, A. R. Brown, R. N. Marks, K. Mackay, R. H. Friend, P. L. Burns, and A. B. Holmes, *Nature* **347**, 539 (1990)
3. C. C. Wu, J. C. Sturm, R. A. Register and M. E. Thompson, *Appl. Phys. Lett.* **69**, 3117 (1996)
4. D. G. Lidzey, M. A. Pate, M. S. Weaver, T. A. Fisher, and D. D. C. Bradley, *Synth. Met.* **82**, 141 (1996)
5. T. R. Hebner, C. C. Wu, D. Marcy, M. H. Lu, and J. C. Sturm, *Appl. Phys. Lett.* **72**, 519 (1998)
6. T. R. Hebner and J. C. Sturm, *Appl. Phys. Lett.* **73**, 1775 (1998)
7. J. Bharathan and Y. Yang, *Appl. Phys. Lett.* **72**, 2660 (1998)
8. T. Shimoda, S. Kanbe, H. Kobayashi, S. Seki, H. Kiguchi, I. Yudasaka, M. Kimura, S. Miyashita, R. H. Friend, J. H. Burroughes and C. R. Towns, *Symposium proceeding of Society for Information Display*, 376, San Jose, California (1999)
9. F. Pschenitzka and J. C. Sturm, *Appl. Phys. Lett.* **74**, 1913 (1999)
10. Cheng-chung Yang, Chung-chih Wu, Hsin-hua Chang, Chieh-Wei Chen, Cheng-Chung Lee, in this proceeding

A Thermal Transfer Approach for the Doping of Organic LEDs

Cheng-chung Yang^a, Chung-chih Wu^a, Hsin-hua Chang^b, Chieh-Wei Chen^a

^a Department of Electrical Engineering and Graduate Institute of Electro-optical Engineering,
National Taiwan University, Taipei, Taiwan 10617

^b Institute of Optical Sciences, National Central University, Chung-Li, Taiwan, 32054

ABSTRACT

An effective process of performing controllable doping of polymer films in organic light-emitting devices is reported. In this approach, a film to be doped is brought into direct contact with a dye-dispersed polymer donor film to permit direct dye-diffusion thermal transfer. Theoretical and experimental studies indicate that this doping process can be modeled by Fick's diffusion theory and that a desired dopant distribution from shallow to flat profiles may be obtained in a single transfer step by adjusting the diffusion conditions. Doped-polymer light-emitting devices made by this process and the conventional blending process exhibited same device characteristics. Along with patterned color donor plates, we demonstrated multicolor OLEDs of arbitrary patterns over large areas with a single thermal transfer step.

Keywords: Organic Light Emitting Diodes; OLEDs; OLED Displays; Dye-Diffusion Thermal Transfer; Color Integration

1. INTRODUCTION

Organic light emitting devices (OLEDs) based on molecular organic materials or on polymer materials have been extensively studied because of their various merits suitable for flat panel display applications.^{1,2} The capability of solution processing of polymers leads to manufacturing advantage for large-area coating. However, it is found difficult to integrate multicolor polymer materials or devices for full-color displays by conventional coating and sequential photolithography steps.^{3,4} To resolve this issue, printing approaches have been aggressively pursued recently. For instance, ink-jet printing has been used to deposit directly patterned polymers or to introduce color-tuning dye patterns into/onto continuous buffer polymer layers.⁵⁻⁸ However, ink-jet printing is in general a sequential process and might have a limit for substrate throughput.⁹ Alternatively, a large-area thermal transfer process was recently proposed for color patterning of polymer layers in OLEDs.⁹ Owing to a transfer mask inserted between the donor and the receiver films, this process involves several mechanisms: the sublimation of dye molecules from the heavily dispersed polymer film, travel of dye molecules to the

surface of the receiver film, and the diffusion of dye molecules into the receiver film. Interaction of all these mechanisms has led to difficulty in controlling profiles of dye concentration and to complication of processing steps. For instance, long periods of annealing may be required to redistribute dye dopants in the receiver film after the transfer process.

In this paper, we report an effective transfer process for performing controllable doping of polymer films in OLEDs. In this process, the polymer receiver film is placed in direct contact with the dye-dispersed polymer donor film to permit direct dye-diffusion thermal transfer (Fig. 1). We performed theoretical and experimental studies of this doping process and show that it can be modeled by Fick's diffusion theory under impermeable film-substrate boundary conditions. We have therefore named this process as finite-source dye-diffusion thermal transfer (FS-D2T2). Using this process, we demonstrated doped-polymer OLEDs with device characteristics same as those made from the conventional blending process, and demonstrated multicolor OLEDs of arbitrary patterns using only a single thermal transfer step.

2. EXPERIMENTAL RESULTS

2.1. Finite-Source Dye-Diffusion Thermal Transfer (FS-D2T2)

We first explain the concept of finite-source dye-diffusion thermal transfer (FS-D2T2). The arrangement for performing FS-D2T2 is shown in Fig. 1. A pressure (typically $\sim 30 \text{ g/cm}^2$) is applied on top of the receiver plate to ensure intimate contact with the source film. Fig. 2 show the resulting layer geometry, in which the initial distribution of dye concentration is represented by a step from C_0 in the source to zero in the receiver. If the dye diffusion at an elevated temperature obeys Fick's diffusion theory, under the impermeable boundary conditions at two film-substrate interfaces, the spatial distribution of dye concentration $C(x,t)$ at time t is given by an infinite sum of error functions:¹⁰

$$C(x,t) = \frac{1}{2} C_0 \sum_{n=0}^{\infty} \left\{ \operatorname{erf} \left(\frac{-x - 2n(ds + dr)}{2\sqrt{Dt}} \right) + \operatorname{erf} \left(\frac{x + 2ds + 2n(ds + dr)}{2\sqrt{Dt}} \right) \right\} \\ + \frac{1}{2} C_0 \sum_{n=1}^{\infty} \left\{ \operatorname{erf} \left(\frac{-x + 2n(ds + dr)}{2\sqrt{Dt}} \right) + \operatorname{erf} \left(\frac{x + 2ds - 2n(ds + dr)}{2\sqrt{Dt}} \right) \right\}$$

, where x represents the space variable. d_S and d_R are the thickness' of the source and the receiver layers, and D denotes the diffusion coefficient of dyes in the matrix. Here for mathematical and analytical simplicity, we have assumed that the source and the receiver matrices are of the same composition and that the temperature and D are constant throughout both layers. (x,t) vs. normalized diffusion length ($\sqrt{Dt/dr^2}$) is shown in Fig. 2, which reveals that dyes originally in the source layer basically undergo a redistribution process. By choosing appropriate conditions (i.e. varying diffusion length), dye profiles into the receiver layer may be controlled from a shallow profile to a flat profile, a feature maybe useful in different designs

of devices. Since dye redistribution is a self-limiting process, there would be no concern of over-doping or consequent concentration quenching even for elongated diffusion time as long as C_0 is chosen to match the desired final concentration in the receiver.

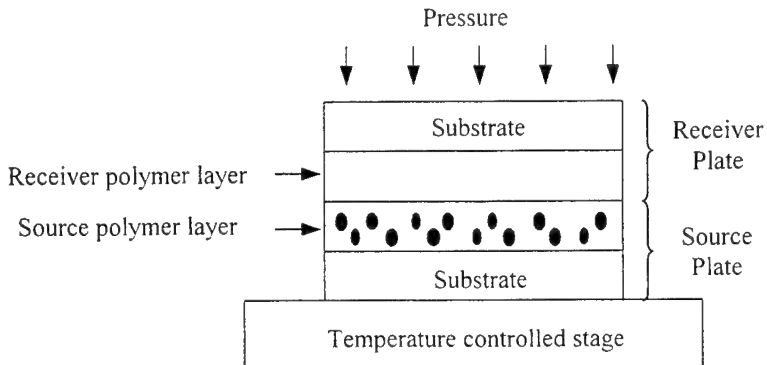


Fig. 1: Experimental arrangement for finite-source dye-diffusion thermal transfer.

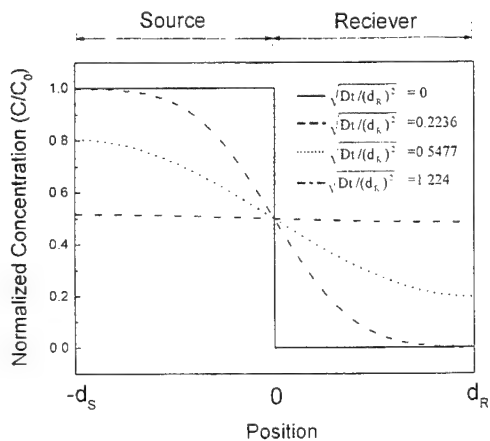


Fig. 2: Calculated normalized profiles of dye concentration $C(x, t)/C_0$ vs. normalized diffusion length $\sqrt{Dt / dR^2}$.

2.2. Experiment Results of Finite-Source Dye-Diffusion Thermal Transfer

To verify these concepts, we performed a series of dye-diffusion thermal transfer experiments based on the deep-blue-emitting polymer poly(N-vinylcarbazole) (PVK), shown in Fig. 3. Due to same reasons stated previously, results presented in this paper are for source and receiver layers of this same matrix composition and the same thickness ($\sim 1000 \text{ \AA}$), except that the source is initially charged with an additional small amount of dyes. Dyes such as perylene (blue), coumarin 6 (C_6 , green) and nile red (orange-red) were used in this study, shown in Fig. 3. Films were coated onto quartz substrates for photoluminescence (PL) and absorption measurements on the SLM-AMINCO AB2 luminescence spectrometer and the

Shimadzu UV-1601PC spectrophotometer, respectively. All the thermal transfer experiments and characterization were performed in air.

Fig. 4 show the growth with time of absorption spectra associated with the dye (C_6) diffused into the receiver layer for diffusion at 200 °C. Since the dye absorbance is proportional to the total amount of dyes inside the film (i.e. Beer's Law), the ratio of the amount of dyes diffusing into the receiver (M) to the initial amount of dyes in the source layer (M_0) can be obtained by dividing the associated absorbance peak intensities. Results of M/M_0 for different diffusion conditions are plotted in Fig. 5, in which the least-square fitting of experimental data from Fick's theory is also presented. Using diffusion coefficient D as the only parameter, the fitting reasonably follows the trend of experimental data. Fig. 6 shows the extracted diffusion coefficients of the dye at different diffusion temperatures. The extracted diffusion coefficient D is strongly dependent on the temperature and ranges from 10^{-12} to 10^{-17} cm²/sec within the temperature range (130 °C - 240°C) used, indicating that it is a highly thermally activated process. As can be seen in Fig.6, the temperature dependence of D shows different behaviors below and above the glass transition temperature (T_g) of PVK (~210°C). A rapid rise of D with temperature is observed around T_g , consistent with the rapid transfer of dyes around T_g . These diffusion characteristics are consistent with those found in previous study of dye diffusion in glassy polymer matrices around T_g .^{11, 12} Fig. 7 shows the PL spectra of the receiver layer vs. diffusion time at 220 °C for C_6 . It can be seen that, within a few minutes (or tens of seconds at even higher diffusion temperature), the diffused dye profile is deep enough to completely quench the luminescence from the host, consistent with the results of absorption experiments. The final PL intensity of the diffused film is basically the same as that of the dye-blended films with a similar dye concentration, showing no indication of degradation. All these results show that the FS-D2T2 is a relatively effective technique for doping the organic films.

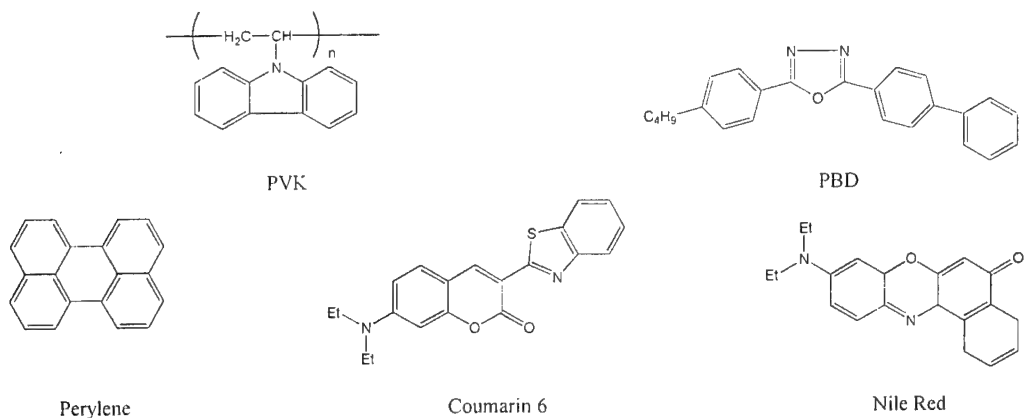


Fig. 3: Molecular structure of the organic compounds used in the present study. PVK is hole transport polymer. PBD is electron transport molecule. The perylene, coumarin 6, nile red are blue, green, orange-red dopants respectively.

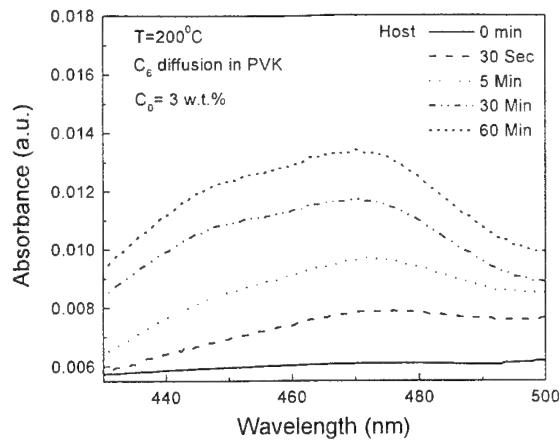


Fig. 4: Absorption spectra of C_6 -diffused PVK films vs. diffusion time at $T=200^\circ\text{C}$

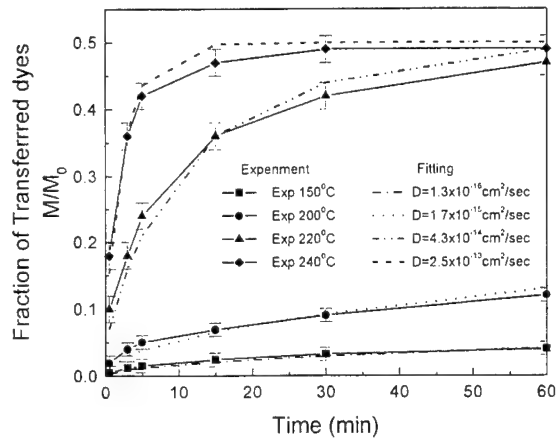


Fig. 5: Ratio of dyes transferred for different diffusion condition.

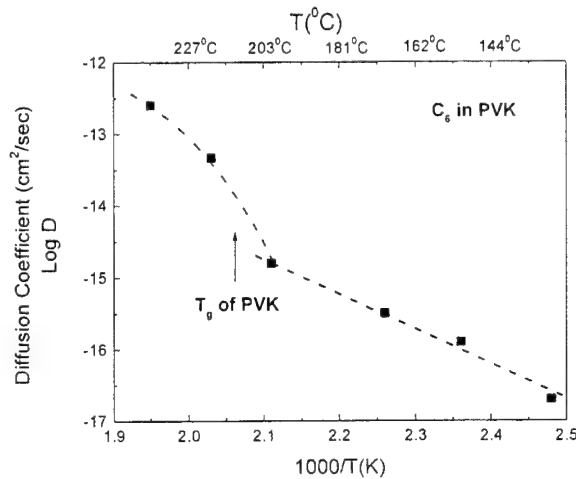


Fig. 6: Diffusion coefficients of C_6 in polymer PVK at different diffusion temperatures.

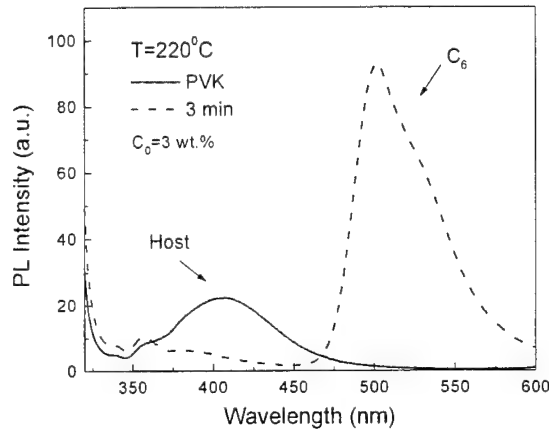


Fig. 7: Photoluminescence spectra of the receiver film vs. diffusion time.

2.3. Color tuning of OLED by Finite-Source Dye Diffusion Thermal Transfer

Since PVK is only hole-transport, in preparing films for OLED fabrication, ~25 wt.% of electron-transport molecules 2-(4-biphenyl)-5-(4-tert-butyl-phenyl)-1,3,4-oxadiazole (PBD), shown in Fig 3, is added to the PVK matrix by blending before spin coating. To investigate the effect of this doping process on OLED characteristics, we compared devices using

the dye-diffused films and "control" devices using conventional dye-blended films as the active emission layers. Both have the device structure of glass/ITO (indium tin oxide) anode/hole-injection layer (~300 Å)/active emission layer (~1000 Å)/Mg:Ag (10:1) cathode/Ag protection layer. The conducting polymer polyethylene dioxythiophene /polystyrene sulphonate (PEDT/PSS, Bayer Corp.) was used as the hole-injection layer. All the device processing were carried out in air. Fig. 8 compares the device characteristics of OLEDs using C₆-diffused and C₆-blended PVK:PBD films with similar dye concentrations. Within our experimental variation, both types of devices gave nearly the same characteristics with an external quantum efficiency of ~0.8%. By using different dyes in the source polymer layer, the colors of OLEDs made from the FS-D2T2 process can be tuned from blue to orange-red. Fig. 9 show the EL spectra of OLEDs doped with perylene, C₆ & nile red as the blue, green and orange-red emission dopants, all with similar device characteristics. Brightness over several thousand cd/m² can be obtained in these devices.

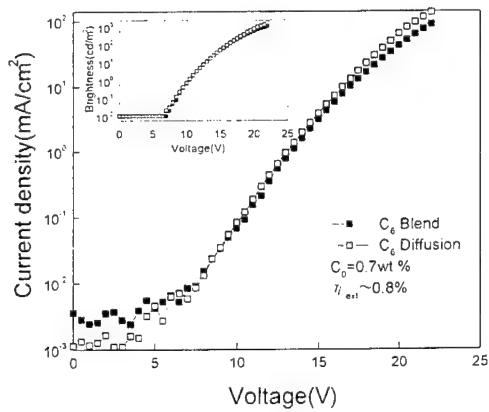


Fig. 8: Comparison of device characteristics of OLEDs using C₆-diffused films and C₆-blended films.

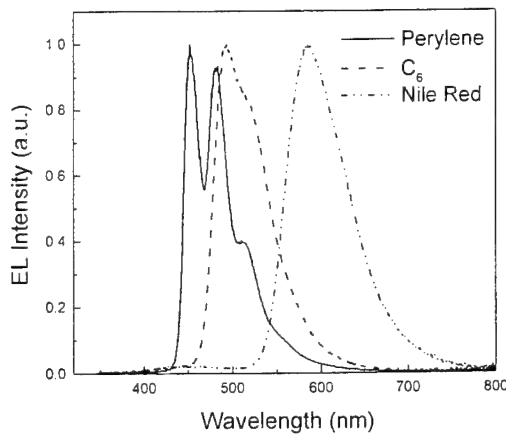


Fig. 9: EL spectra of OLEDs doped with perylene (blue), C₆ (green) and nile red (orange-red).

2.4. Color Integration

By using a source plate containing color patterns, FS-D2T2 could be used to accomplish color integration for OLED devices or displays on a substrate in a single thermal transfer step, as shown in Fig. 10. The source plate containing multicolor dye-dispersed polymer patterns may be fabricated with any patterning technique, ranging from photolithography to printing, as long as the fabrication processing does not degrade the emission characteristics of dyes to be transferred. Screen-printing, an additive and high-throughput patterning technique suitable for large areas, has been used as a demonstration to make the color source plates. The details will be discussed in another paper of this proceeding.¹³

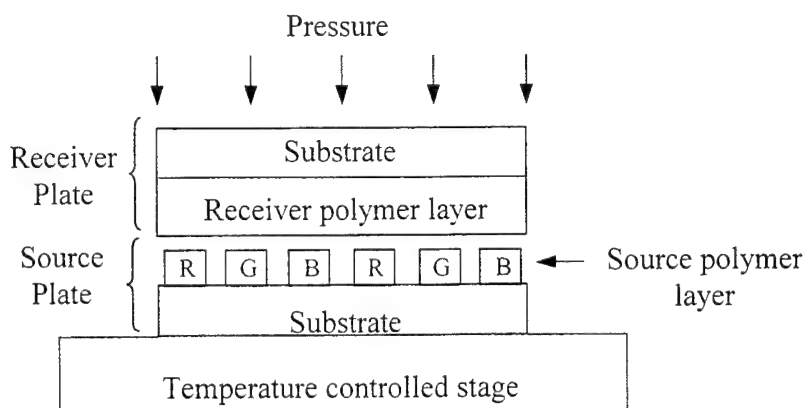


Fig. 10: Color integration of OLED by FS-D2T2 and color source plate.

3. CONCLUSION

We have introduced finite-source dye-diffusion thermal transfer as an effective method of performing controllable doping of polymer films in OLEDs. We show that this doping process can be modeled by Fick's diffusion theory under finite boundary conditions. We successfully applied this doping technique to color tuning of OLEDs without degrading device performance. Along with patterned color source plates, we can fabricate multicolor OLEDs of arbitrary patterns over large areas with a single thermal transfer step.

ACKNOWLEDGE

The authors would like to express gratitude to Prof. T. Y. Luh, Prof. M. K. Leung, Prof. G. J. Jan, Prof. L. A. Wang and Prof. H. C. Chang of NTU, and Mr. Lien of Bayer Co. for stimulating discussions and for assistance in experiments. This work was supported by National Science Council of Republic of China (Grant no. NSC 88-2212-E-002-075).

REFERENCE

1. C. W. Tang and S. A. VanSlyke, *Appl. Phys. Lett.* **51**, 913 (1987)
2. J. H. Burroughes, D. D. C. Bradley, A. R. Brown, R. N. Marks, K. Mackay, R. H. Friend, P. L. Burns, and A. B. Holmes, *Nature* **347**, 539 (1990)
3. C. C. Wu, J. C. Sturm, R. A. Register and M. E. Thompson, *Appl. Phys. Lett.* **69**, 3117 (1996)
4. D. G. Lidzey, M. A. Pate, M. S. Weaver, T. A. Fisher, and D. D. C. Bradley, *Synth. Met.* **82**, 141 (1996)
5. T. R. Hebner, C. C. Wu, D. Marcy, M. H. Lu, and J. C. Sturm, *Appl. Phys. Lett.* **72**, 519 (1998)
6. T. R. Hebner and J. C. Sturm, *Appl. Phys. Lett.* **73**, 1775 (1998)
7. J. Bharathan and Y. Yang, *Appl. Phys. Lett.* **72**, 2660 (1998)
8. T. Shimoda, S. Kanbe, H. Kobayashi, S. Seki, H. Kiguchi, I. Yudasaka, M. Kimura, S. Miyashita, R. H. Friend, J. H. Burroughes and C. R. Towns, Symposium proceeding of Society for Information Display, 376, San Jose, California (1999)
9. F. Pschenitzka and J. C. Sturm, *Appl. Phys. Lett.* **74**, 1913 (1999)
10. J. Crank, *The mathematics of Diffusion*, Oxford University Press, Oxford, UK (1975)
11. D. Ehlich and H. Sillescu, *Macromolecules* **23**, 1600 (1990)
12. P. F. Nealey, R. E. Cohen, and A. S. Argon, *Macromolecules* **26**, 1287 (1993)
13. Hsin-hua Chang et. al., " Multicolor Organic LEDs process by integration of screen-printing and thermal transfer printing ", in this proceeding

Luminescence of the InGaN/GaN blue light-emitting diodes

J. K. Sheu ^{a)}, T. W. Yeh and G. C. Chi

*Optical Sciences Center, National Central University
Chung-Li 32054, Taiwan*

M. J. Jou

Epistar Corporation, Hsinchu 300, Taiwan

Abstract

InGaN/GaN double heterostructure (DH) and multiple quantum wells(MQW) light-emitting diodes were grown by metalorganic vapor phase epitaxy(MOVPE). Band gap narrowing of the PL spectra for the InGaN/GaN MQW LEDs can be observed at room temperature. In addition, the emission wavelength of EL and PL spectra for the MQW blue LEDs exhibit a blue-shift phenomenon when increasing the injection current and laser power, respectively. This luminescence behavior can tentatively be understood as a competition between a spectral red-shift mechanism of piezoelectricity-induced quantum-confined Stark effect(PQCSE) and a blue-shift mechanism of band-filling and charge screening effects.

a):*e-mail: jksheu@joule.phy.ncu.edu.tw*

I. Introduction

In the past several years, the most studied of wide bandgap semiconductors have been the III-nitrides. Among them, GaN and its alloys with InN and AlN have attracted numerous attentions since the successful commercialization of bright blue/green light-emitting diodes followed latter by the demonstration of injection lasers[1-3]. GaN-based nitride semiconductors have several advantages over other wide bandgap semiconductors such as SiC and diamond. They can be doped both p- and n-type, have direct bandgaps, and can form heterostructures conducive to device applications. Blue/green laser diodes have been also achieved in ZnSe and related materials. However, the short lifetime prevent ZnSe-based devices from commercialization at present. It is considered that the short lifetime of these ZnSe-based devices is caused by crystal defects at a density of $10^3/\text{cm}^2$, because one crystal defect would cause the propagation of other defects leading to failure of the devices. By contrast the III-V nitrides are mechanically strong and chemically rather inert and do not have any gross reliability problems, at least judging from the preliminary studies of LED and LD operation.

II. Experiment

InGaN/GaN double heterostructure(DH) and multiple quantum well(MQW) light emitting diodes(LEDs) were grown by MOVPE system using a high-speed rotating disk in a vertical growth

chamber. Briefly, trimethylgallium (TMGa) and ammonia (NH_3) were used as Ga and N precursors, respectively. Biscyclopentadienyl magnesium (Cp_2Mg) and Si_2H_6 were employed as the p-type and n-type dopant, respectively. The trimethylindium (TMIn) was employed as the In precursors. The carrier gas was hydrogen, and the growth pressure was maintained at 100 torr for the growth of Si-doped GaN film. The carrier gas was nitrogen, and the growth pressure was maintained at 300 torr for the growth of InGaN layers. The typical growth procedures are described as follows: Before growing III-V nitride films, the substrates were treated by thermal baking at 1100°C in hydrogen to remove surface contamination. A low-temperature GaN nucleation layer, with thickness of about 300 Å, was grown at 560°C. After the growth of low-temperature GaN nucleation layer, the wafer temperature was raised to 1060°C to grow the Si-doped GaN buffer layer. Figure 1(a) and Fig. 1(b) shows the schematic structure of the MQW and DH blue LED, respectively, which consists of 300 Å-thick GaN nucleation layer grown at a low temperature of 560°C, a 3.5 μm-thick layer of Si-doped GaN(electron concentration of about $8 \times 10^{17}/\text{cm}^3$), 9 period of InGaN/GaN MQW structure consisting of 30 Å-thick $\text{In}_{0.3}\text{Ga}_{0.7}\text{N}$ well layers and 70 Å-thick GaN barrier layers (or 500 μm-thick bulk $\text{In}_{0.13}\text{Ga}_{0.87}\text{N}$ layer with Si and Zn coping)grown at a temperature of 780°C. Finally, a 0.3 μm-thick Mg-doped contact layer(hole concentration of about $3 \sim 5 \times 10^{17}/\text{cm}^3$) were grown. For fabrication of LED chips , the processing procedures were described as follows: (a) Ni was deposited onto the epi-wafer as the etching mask before ICP dry etching[4]. (b) the p-GaN layer was partially etched until the n-GaN was exposed. (c) An ultra thin Ni/Au(2 nm/6 nm) bi-layer was evaporated onto the p-GaN layer as the transparent p-type electrode[5]. (d) A Ti/Al(50 nm/2000 nm) bi-layer was deposited onto the n-GaN surface as the n-type electrode. (e) Wafer lapping was performed until the thickness down to 80 μm. Then the wafer was polished to remove the stress which results from the large roughness difference between the lapped surface and epitaxial surface. (f) The thin wafer was cut into a squared shape (350 μm × 350 μm) by diamond scribe and cutter.

III. Results and discussions

Figure 2 shows the electroluminescence (EL) spectra of the $\text{In}_x\text{Ga}_{1-x}\text{N}/\text{GaN}$ DH blue LED at forward dc currents of 5 mA, 20 mA and 60 mA. A typical peak wavelength and FWHM of the EL spectra were 468 nm and 76 nm, respectively, at current of 20 mA. The spectra exhibit blue shift as the injection current increases, as shown in Fig 2. The peak wavelength is 470 nm at 5 mA, 468 nm at 20 mA, and 462 nm at 40 mA. This blue shift of EL spectra suggests that the luminescence mechanism is donor-to-acceptor transition in the InGaN active layer codoped with both Zn, Si. At 60 mA, a shorter-wavelength peak emerges around 402 nm, as shown in Fig 2. In order to better understand the luminescence properties, the semilogarithmic EL spectra were performed for current ranging from 5 mA to 500 mA. At currents above 60 mA, 500 μs pulses at 1% duty cycle were used to prevent heating. At currents above 60 mA, the intensity of the shorter-wavelength peak at 402 nm related to blue band begins to increase more rapidly than the blue band, as shown in Fig 3. However, the position of the shorter-wavelength peak(402 nm) is fixed even though the injection current is further increased. In addition, the blue band exhibits blue shift as the injection current increases. Similar EL spectra have reported by Nakamura et al[6] and Lester et al[7] for the DH blue LEDs which with Zn, Si codoped InGaN active layer. But, as the active layers in InGaN/AlGaN DH LEDs with similar structure are not compensated, shifting peak spectra are not observed[3]. The shorter-wavelength peak could be attributed to the band-to-band transition in the InGaN active layer. In other words, the 402 nm emission peak

corresponds to the energy gap for $\text{In}_{0.13}\text{Ga}_{0.87}\text{N}$ and therefore is due to radiative recombination of electrons in the conduction band and holes in the valence band. This peak becomes resolved at higher injection levels where the impurity-related recombination is saturated. Electroluminescence with shifting peak spectra has been observed and analyzed for GaAs p-n junction[8]. In GaAs, the two mechanisms for shifting peak spectra are photon-assisted tunneling and band filling. In photon-assisted tunneling, the hole and electron tunnel into the depletion region where they recombine with the emission of a photon. As shown in Fig 3, for the $\text{In}_{0.13}\text{Ga}_{0.87}\text{N}/\text{GaN}$ DH blue LED, the emission intensity of the blue band does not saturate as the injection current is increased. Thus, the emission spectra shown in Fig 3. are consistent with the band filling mechanism. In band filling, the shift in the main peak results from the minority carriers(holes) filling the empty acceptor levels and valence band tails in the co-doped and therefore compensated active layer. The InGaN active layer of the blue LED is heavily doped with both the Si and Zn. Thus, the Zn acceptor level is expected to exhibit Gaussian broadening and both the valence band and the conduction band will have band tails[9-10].

For an $\text{In}_{0.3}\text{Ga}_{0.7}\text{N}/\text{GaN}$ MQW LED, the emission peak should be equal to or less than 450 nm. However, the emission peak of the $\text{In}_{0.3}\text{Ga}_{0.7}\text{N}/\text{GaN}$ MQW LED is around 465 nm. The energy difference between the strained-free band-edge emission peak of $\text{In}_{0.3}\text{Ga}_{0.7}\text{N}$ bulk layer, which the In content was determined by PL measurement, and the PL peak wavelength of the $\text{In}_{0.3}\text{Ga}_{0.7}\text{N}/\text{GaN}$ MQW LED is approximately 80 meV. Notice that the growth condition of $\text{In}_{0.3}\text{Ga}_{0.7}\text{N}$ bulk layer is the same as the active layers (well region) of the MQW LED. Plausible causes of such a band gap narrowing effect have been tentatively proposed by Nakamura but no quantitative explanations have been made[11]. The possible explanations of this band gap narrowing of $\text{In}_x\text{Ga}_{1-x}\text{N}/\text{GaN}$ quantum well can be attributed to the exciton effects(Coulomb effects correlated to the electron-hole pair) of the active layer or strain effects caused by the lattice mismatch and the thermal expansion coefficients difference between well layers and barrier layers. In the former case, it might be anticipated that radiative recombination in these devices is related to the presence of highly localized excitons , localized on fluctuations of indium contents in the active layer. In other words, a continuos density of states may be present within the band gap of the active layer. Perhaps, the emission mechanism of the $\text{In}_x\text{Ga}_{1-x}\text{N}/\text{GaN}$ multi-quantum well LEDs results from a competition between above-mentioned effects and quantum confinement.

In order to better understand the luminescence properties of the $\text{In}_x\text{Ga}_{1-x}\text{N}/\text{GaN}$ multi-quantum wells, the excitation power dependence of the PL spectra were performed at room temperature. Figure 4. shows the PL spectra of $\text{In}_{0.3}\text{Ga}_{0.7}\text{N}/\text{GaN}$ multi-quantum well LED measured at different excitation power. In the MQW blue LEDs, the well region of the active layer is $\text{In}_{0.3}\text{Ga}_{0.7}\text{N}$, and its band-edge emission peak is around 450 nm if there were strained-free in the QW structure. The emission peak of the MQW blue LED should be shorter than 450 nm when the quantum size effect is in action. However, our $\text{In}_{0.3}\text{Ga}_{0.7}\text{N}/\text{GaN}$ MQW LED exhibits the peak wavelength of around 465 nm. This unexpected observation may be caused by the piezoelectricity-induced quantum-confined Stark effect(PQCSE)[12-13]. In other words, it may tentatively be understood as an effect of the QW potential, which was severely distorted by the piezoelectric field . In addition, it is clear that the PL peak shifts toward shorter wavelength when the laser power is increased. Between $I=I_o$ and $I=I_o/20$ of excitation intensity, the shift can be as large as 8.5 nm (50 meV). Basically, the transition energy of the InGaN strained QWs was smaller than that of unstrained QWs since the band alignment of InGaN strained well layer was tilted by piezoelectric fields. When the samples were pumped with the excitation sources, the piezoelectric fields in the InGaN strained well layer were screened by generated carriers, thus weakening the PQCSE. Increasing the excitation intensity further weakened the PQCSE and increased the transition energy, that is , blueshift occurred.

To further explore the origin of the band gap shifting effect of $\text{In}_{0.3}\text{Ga}_{0.7}\text{N}/\text{GaN}$ quantum well, the EL measurements were performed at room temperature with various driving current. Figure 5 shows the EL spectra for current ranging from 1 mA to 500 mA. At currents above 60 mA, 500 μs pulses at 1% duty cycle were used to prevent heating. The EL peak energy of the MQW blue LED exhibits blueshift when the injection current is increased. The blueshifts are about 140 meV as the forward current are increased from 1 mA to 500 mA. In addition to the description mentioned-above, these blue shifts may also be due to a band-tail filling effect. According to the report of Narukawa et. al[14], the peak of the spontaneous emission shifts toward the high energy side with increasing excitation intensity. This emission behavior is only observed in the LED which have heavily doped and compensated active layer[14]. However, the active layer of the MQW blue LED which used in this study is undoped. The blueshifts could be attributed to a filling of band-tail states(i.e., localized states) where carrier or excitons are recombined for emission with increasing injection current. The localized states may be formed by indium composition fluctuation in the $\text{In}_{0.3}\text{Ga}_{0.7}\text{N}$ well layer due to a phase separation or indium segregation of the $\text{In}_{0.3}\text{Ga}_{0.7}\text{N}$ during growth. In other words, the radiative recombination may be attributed to excitons localized at deep traps which probably originate from the In-rich region in the well as quantum dots[14]. Recently, Peng et. al [13] reported that a spectral blueshift was observed as the injection current increases from 1mA to 1A. According to their repotrs, the emission spectrum of the InGaN QW is determined by a competition between a spectral redshifting mechanism of PQCSE and a blueshifting mechanism of band-filling and charge screening effects.

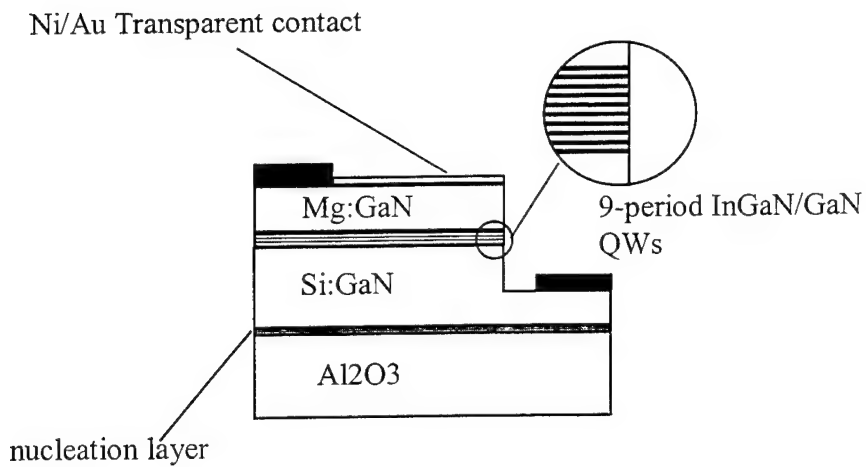
IV. Conclusions

In summary, the InGaN/GaN DH and MQW LEDs were fabricated. The peak wavelength of the typical EL spectra at 20 mA is about 465 nm. The FWHM of the typical EL spectra at 20 mA are about 70 nm and 30 nm for DH and MQW LEDs, respectively. The electroluminescence for the Si, Zn codoped InGaN active layers demonstrated spectra whose emission peak shifted to shorter wavelength as the injection current was increased which may be attributed to band filling. In addition, the blue shift and band gap narrowing of the EL and PL spectra for the InGaN/GaN MQW may tentatively be understood as a competition between a spectral redshifting mechanism of PQCSE and a blueshifting mechanism of band-filling and charge screening effects.

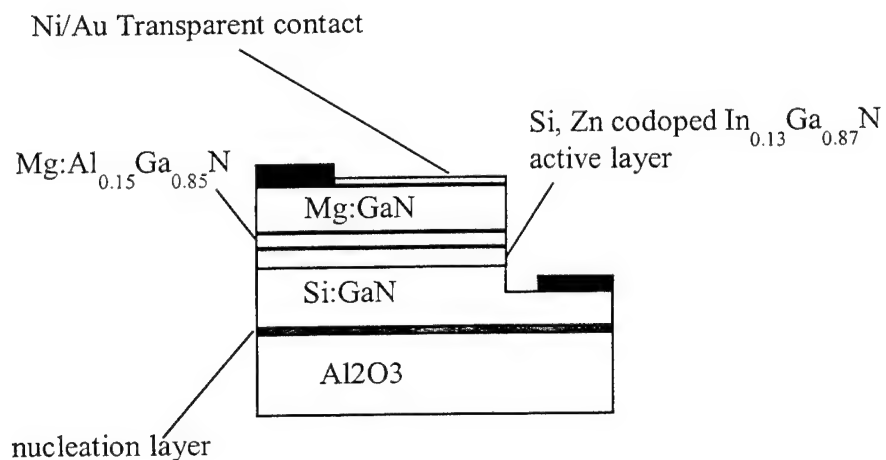
References

1. S. Nakamura, T. Mokai and M. Senoh, Jpn. J. Appl. Phys. Vol.**30**, 1998 (1991).
2. S. Nakamura, M. Senoh, S. Magahama, N. Iwasa, T. Yamada, T. Matsushita, H. Kiooku, and Y. Sugimoto, Jpn. J. Appl. Phys. Vol.**35**, L217 (1996).
3. S. Nakamura, T. Mokia and M. Senoh, Appl. Phys. Lett. Vol.**64**, 1687 (1994).
4. J. K. Sheu, Y. K. Su, G. C. Chi, M. J. Jou, C. M. Chang, C. C. Liu and W. C. Hung, J. Appl. Phys. Vol. Vol. **85**, 1970 (1999).
5. J. K. Sheu, Y. K. Su, G. C. Chi, M. J. Jou, C. M. Chang, C. C. Liu and W. C. Hung, Appl. Phys. Lett. Vol. **74**, 2340 (1999).
6. S. Nakamura, T. Mokia and M. Senoh, J. Appl. Phys. Vol.**76**, 8189 (1994).
7. S. D. Lester, F. A. Ponce, M. G. Crawford and D. A. Steigerwald, Appl. Phys. Lett. Vol.**66**, 1249

- (1995).
- 8. H. C. Casey, Jr. And R. Z. Bachrach, J. Appl. Phys. Vol.**40**, 241(1973).
 - 9. T. N. Morgan, Phys. Rev. **A 139**, 343(1965).
 - 10. B. I. Halperin and M. Lax, Phys. Rev. **A 148**, 722(1966).
 - 11. S. Nakamura, IEEE J. Sel. Top. Quantum Electron. Vol. **3**, 435 (1997).
 - 12. D. A. B. Miller, D. S. Chemla, T. C. Damen, A. C. Gossard, W. Wiegmann, T. H. Wood and C. A. Burrus, Phys. Rev. Vol. **53**, 2173 (1984).
 - 13. L. H. Peng, C. W. Chuang and L. H. Lou, Appl. Phys. Lett., Vol.**74**, 795 (1999).
 - 14. Y. Narukawa, Y. Kawakami, M. Funato, S. Fujita, S. Fujita and S. Nakamura, Appl. Phys. Lett., Vol. **70**, 981 (1997)



(a)



(b)

Figure 1. The schematic structures of the (a) MQW and (b) DH LED.

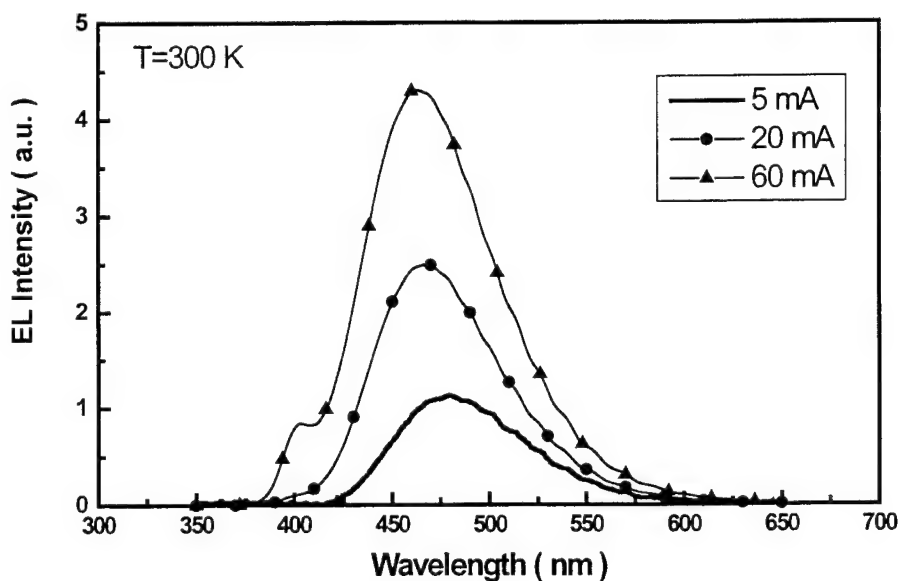


Figure 2. Electroluminescence spectra of the Si and Zn codoped InGaN/GaN DH blue LED at forward currents of 5 mA, 20 mA and 60 mA.

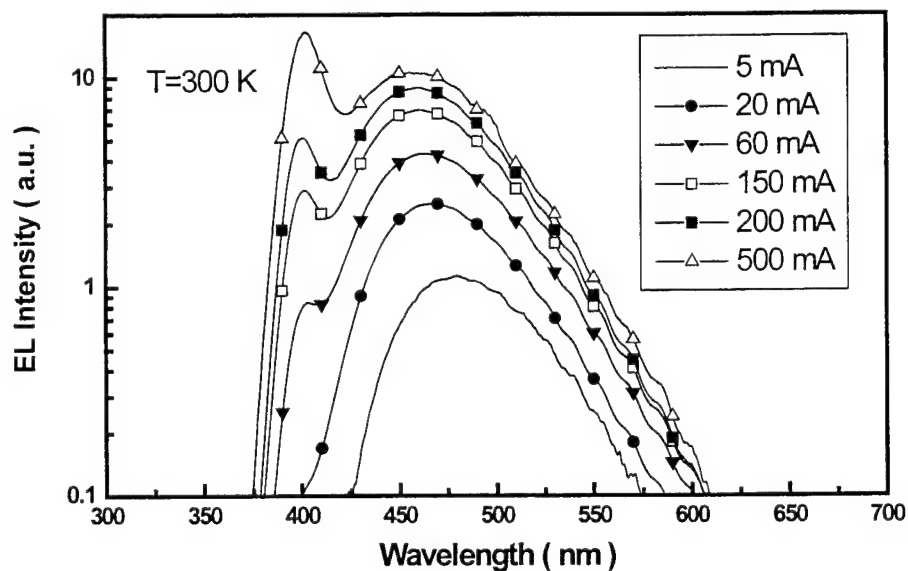


Figure 3. Semilogarithmic electroluminescence spectra of the Si and Zn codoped InGaN/GaN DH blue LED for current ranging from 5 mA to 500 mA.

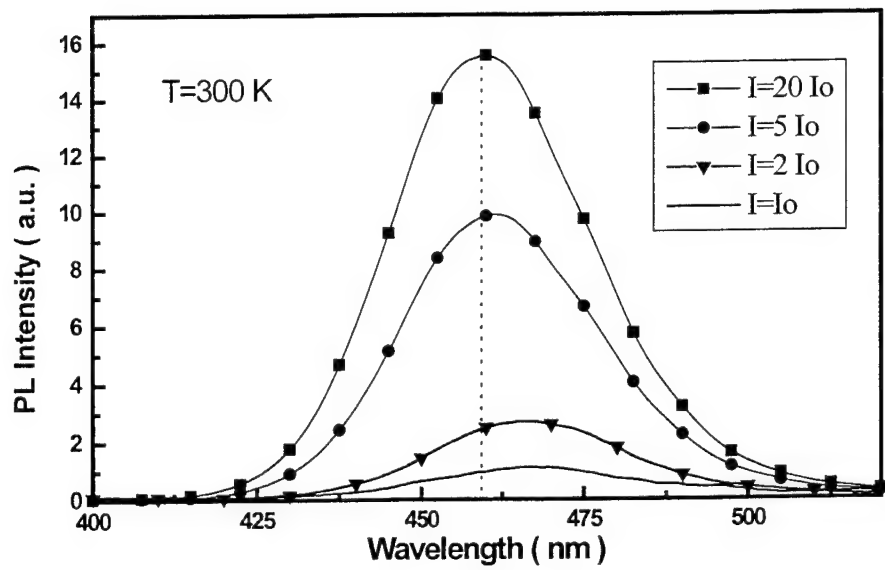


Figure 4. The PL spectra of $\text{In}_{0.3}\text{Ga}_{0.7}\text{N}/\text{GaN}$ multi-quantum well LED measured at different exciting intensity.

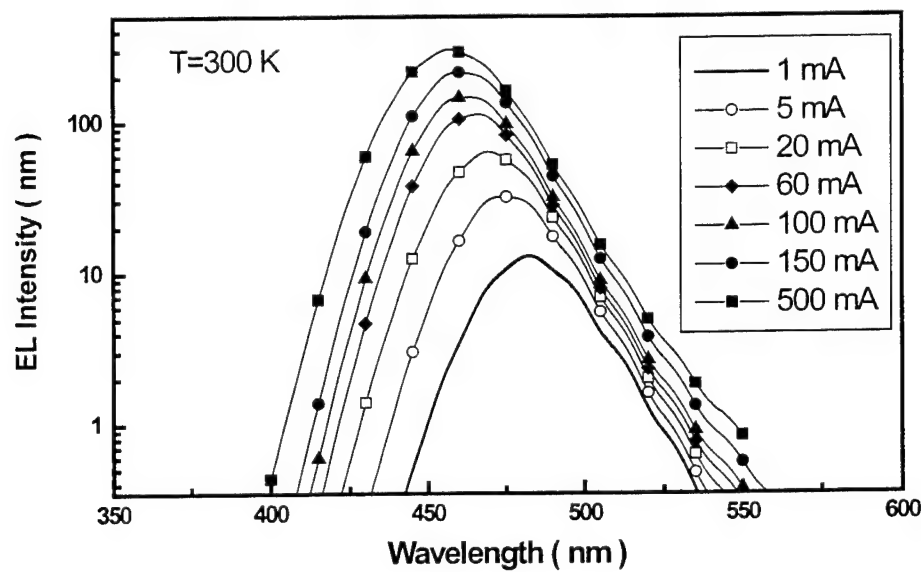


Figure 5. The EL spectra of InGaN/GaN MQW blue LED at different injection current.

SESSION 5

LCD

Recent trends on wide-viewing angle color TFT-LCDs

Yoshiharu Nagae

Displays, Hitachi, Ltd.

3300 Hayano, Mobera-shi, Chiba 297-8622, Japan

ABSTRACT

Many important innovations on LC display mode for wide-viewing angle color TFT-LCDs were reported within this several years, and recently the volume productions of LC monitors and LC TVs have been started using them. To realize good wide-viewing angle color TFT-LCDs, we have to design not only optical property of LC layer but also film polarizers and back lights. Typical wide-viewing angle LC display modes are classified into several categories and discuss their features.

Keywords: wide-viewing angle color TFT-LCD, film polarizers, back-light, TN, VA, OCB, IPS, AFLC, FLC

1. INTRODUCTION

With the progress of manufacturing technologies for TFT-LCDs, they can use rather large size mother-glass substrates and can product large size TFT-LCDs. Many users, therefore, will expect to have LC monitors and LC TVs with large size TFT-LCDs. For these applications, we have to solve the viewing angle problems that are not so serious items for smaller size TFT-LCDs used with notebook PCs. When the plural people are discussing using one LC monitor with conventional TFT-LCD designed for personal use, they may be watching different image, such as different color, different contrast ratio, on the LCD monitor. However, plural users are eager to discuss using a LC monitors in their office as shown in Fig. 1, and they are also eager to watch LC TVs with their family. An essential demand, therefore, on large size TFT-LCDs used for these applications should be a wide-viewing angle issue.

In order to solve the wide-viewing angle issue, many novel technologies are proposed within several years such as Wide View Film mode with conventional TN mode, In-Plane Switching mode, Vertical Alignment mode, and so on. Hitachi firstly proposed In-Plane Switching TFT-LCDs¹ using inter-digital electrodes scheme, and commercialized these LCDs and the desktop computers with wide-viewing angle TFT-LCDs.

Currently, many Asian LCD panel makers successfully product a lots of large size LCDs by using suitable type of wide-viewing angle LCD modes.

The purpose of this paper is to discuss the trends on these wide-viewing angle color TFT-LCDs. The other purpose is to discuss the optical characteristics of some components of the wide-viewing angle TFT-LCDs.



Fig. 1 Wide-Viewing Angle LCD

Correspondence: Email: nagaeyoshiharu@mobera.hitachi.co.jp

Telephone : +81-475-25-9062

Fax : +81-475-25-9168

2. NUMBER OF PAPERS ON WIDE-VIEWING ANGLE LCD MODES

Figure 2 shows the increase of the papers related to wide-viewing angle LCD modes. These data are corrected from major international display conferences which are SID, IDRC, IDW, and AM-LCD. The number of papers are rapidly increase from 1993, and still continue to increase.

In 1994 and 1995, the multi-domain mode seemed to be the major technology to realize wide-viewing angle TFT-LCDs. The manufacturing processes of the multi-domain mode, however, were rather difficult and their position was exchanged with the other modes after 1995. The In-Plane Switching mode (IPS) by using TFT with inter-digital electrodes was first reported in 1995. It had very good viewing angle characteristics, therefore, many people followed this mode after 1995. In 1998 Wide View Film mode (WVF)² and Vertical Alignment mode (VA)³ increased rapidly. Then, IPS, WVF and VA are widely used in the wide-viewing angle LCDs.

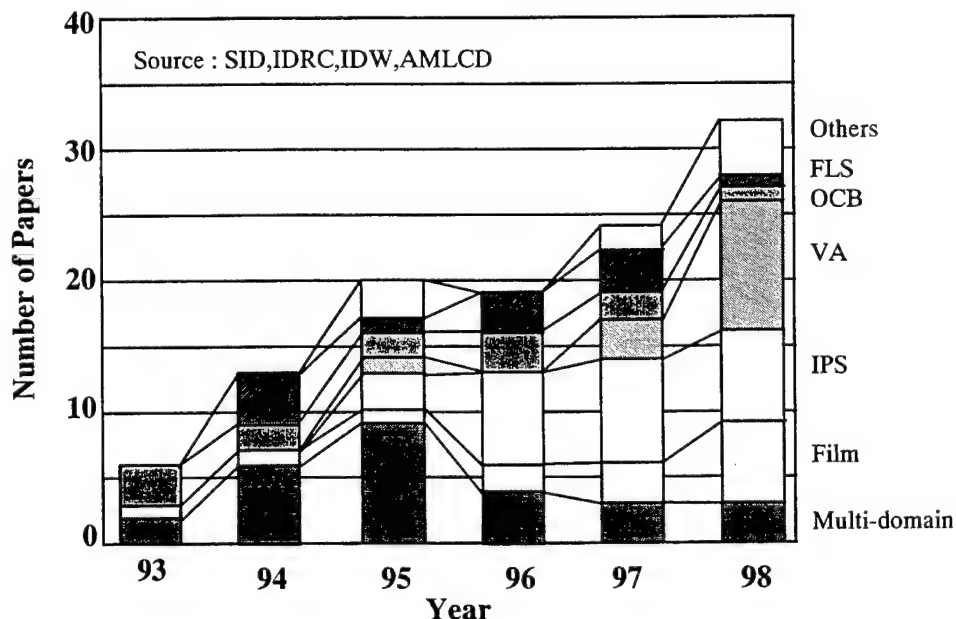


Fig. 2 Trend of papers for Wide-Viewing Angle LCDs

3. THREE MAJOR COMPONENTS IN WIDE-VIEWING ANGLE LCDS

When we discuss the optical properties of the wide-viewing angle LCDs, we have to consider following three components as shown in Fig.3.

- (1) Film Polarizers
- (2) LC Layer
- (3) Back Light

Even though an LC layer has no angular dependence on brightness and contrast ratio, an LCD should have large angular dependence because of the angular characteristics of a couple of film polarizers which is, for example, cross-nicol state.

When the back lights are used with wide-viewing angle

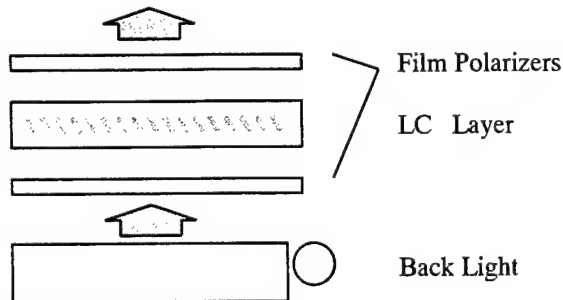


Fig. 3 Optical Components of LCDs

LCDs, the scattering angle of the back light should be wide as it can cover the viewing angle of the LCDs.

3.1. Angular dependence of film polarizers

Angular dependence is measured using the system shown in Fig. 4. A couple of film polarizers mounted on the case which can rotate in 3 directions as shown in this figure. The polarizing axes can change from cross-nicol state to parallel-nicol state.

The contrast ratio of the film polarizers, in this case, is defined as in the following formula at each angle.

$$CR = \frac{\text{Brightness of parallel-nicol state at right angle}}{\text{Brightness of cross-nicol state at each angle}}$$

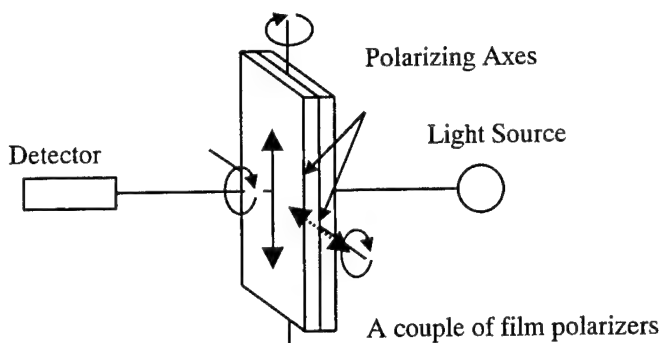


Fig.4 Measurement system on angular dependence for film polarizers

The measurement results are shown in Fig. 5. In the figure, maximum contrast ratio is 1150 at the center of the graph. This figure suggests that the film polarizers have serious angular dependence on their optical properties, so that, we must have much more interest in developing wide-viewing angle film polarizers.

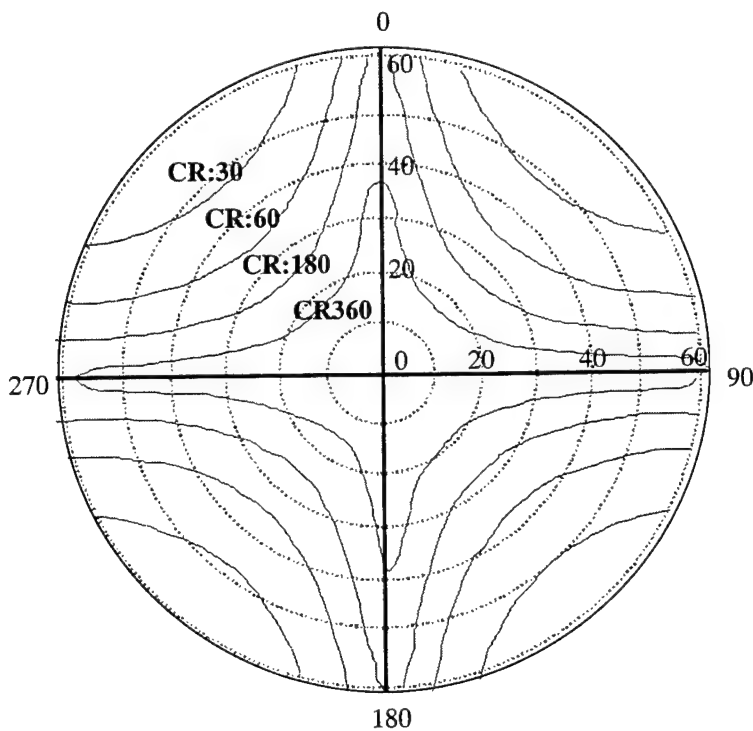


Fig. 5 Angular dependence on Contrast Ratio of film polarizers

3.2. Back light for wide-viewing angle LCDs

For the conventional LCDs used with notebook PCs, the major issue for the back lights is to get large brightness gain resulting narrow scattering angle property. However, recent demands for the back light are to achieve both large brightness gain and wide scattering property that can be work with wide-viewing angle LCDs.

The scattering properties of high gain and low gain back lights are shown in Fig.6. individually. As evident from Fig. 6, the brightness in the normal direction of high gain back light (a) is larger than that of low gain back light (b). But the uniformity of the brightness at different viewing angle of (a) is less than (b). It is evident that the low gain back light that has wide scattering angle is rather suitable for the wide-viewing angle LCDs.

In order to realize the suitable properties, many useful technologies are proposed and still use in the volume production.

For example, Fig. 7 shows the viewing angle dependence on brightness gain of the back light employed the 3M optical films.

- Curve (1) white PET film on the light guide
- Curve (2) (1)+DBEF
- Curve (3) (2)+BEF
- Curve (4) (3)+two BEFs (cross)

Among these curves, curve (2) or (3) are suitable for wide-viewing angle color LCDs, and curve (4) is suitable for personal use LCDs. Therefore the ratio of the brightness gain of curve (4) and (2) is approximately 1.7. When the wide-viewing angle LCD user wants to have same brightness as that of conventional LCDs, they need more electrical power 1.7 times as large as conventional LCDs. Thus, generally every wide-viewing angle LCD technologies have this essential trade-off relation between wide-viewing angle and power consumption.

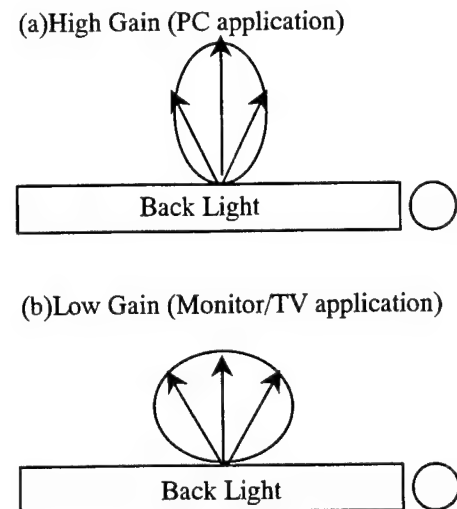


Fig. 6 Scattering properties of Back Lights

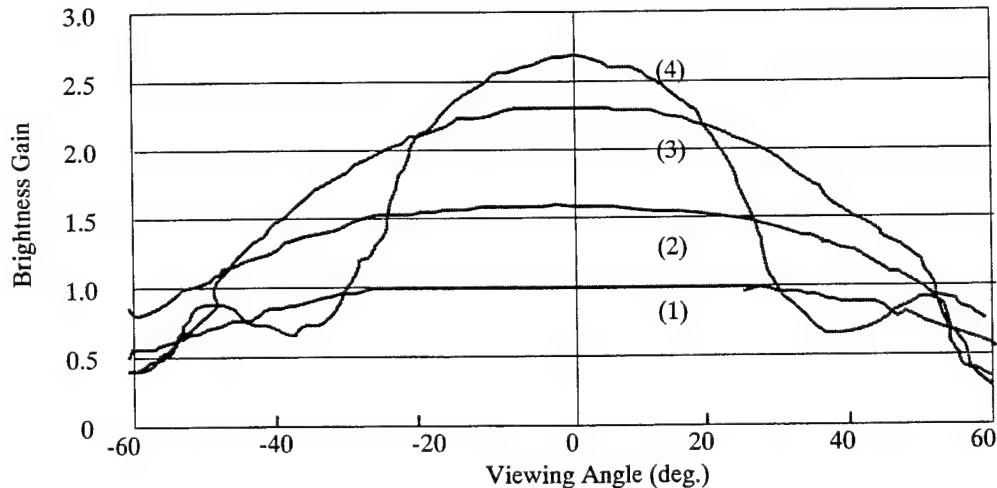


Fig. 7 Viewing Angle Dependence on Brightness Gain of Back Lights (Sumitomo 3M)

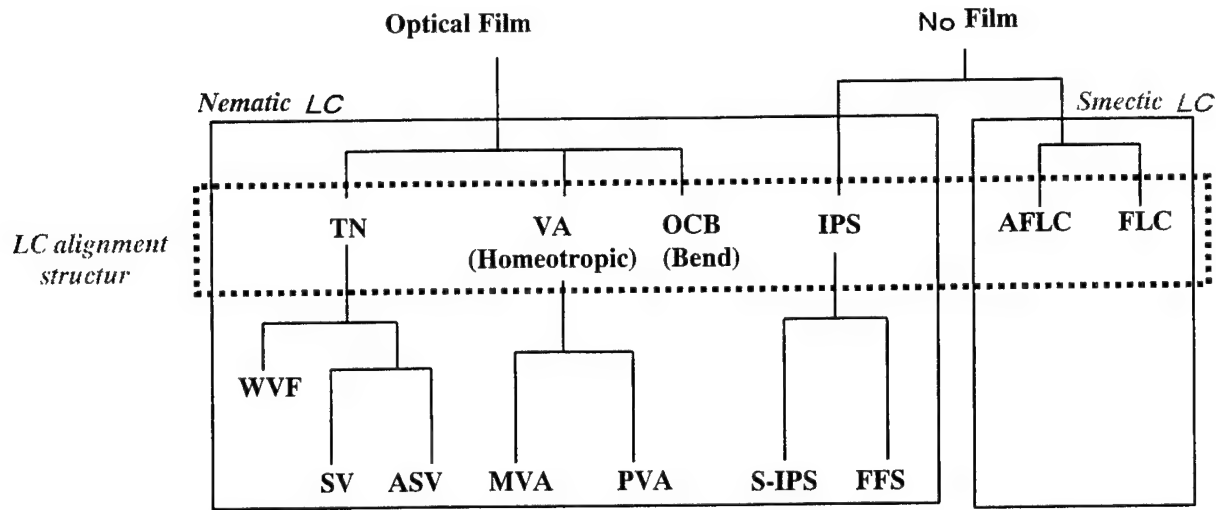


Fig. 8 Classification of Wide-Viewing Angle LCD Modes

3.3 LC layer for wide-viewing angle LCDs

Many wide-viewing angle LCD modes were proposed in this several years, and they are classified as in Fig. 8. The acronyms in Fig.8 are listed below.

TN	: Twisted Nematic mode
VA	: Vertical Alignment mode ³
OCB	: Optically Compensated Bend mode ⁴
IPS	: In-Plane Switching mode ¹
AFLC	: Anti-Ferroelectric Liquid Crystal mode ⁵
FLC	: Ferroelectric Liquid Crystal mode ⁶
WVF	: Wide Viewing Film mode ²
SV	: Super V mode ⁷
ASV	: Advanced Super V mode ⁸
MVA	: Multi-domain Vertical Alignment mode ⁹
PVA	: Patterned Vertical Alignment mode ¹⁰
S-IPS	: Super In-Plane Switching mode ¹¹
FFS	: Fringe Field Switching mode ¹²

Firstly they are divided into two groups. The feature of the first group is to use additional optical films except film polarizers, and that of the second groups is to use no additional optical films except film polarizers. Secondly, they can be classified by the LC materials such as nematic LCs and smectic LCs, then, each wide-viewing angle LCD modes can get their position by means of their LC alignment structures.

The wide-viewing angle property of WVF is not so excellent compare with the other modes. WVF, however, seems to get major market share about 80% because the production process is simple and completely same as the conventional TN LCDs. IPS (S-IPS) and MVA have the best properties in wide-viewing angle, e.g. color shift, contrast inversion. Therefore both modes should have big market share in the near future.

AFLC and FLC are still in development stage. Because of their high speed response and wide-viewing angle properties, users are eager to apply them especially in TV applications.

4. Properties of major wide-viewing angle LCDs

The features and R&D items for major wide-viewing angle LCD modes are listed in Table 1. The notable feature of WVF is that its cell structure is the same as that of conventional TN mode. Therefore, they can easily take WVF into volume production resulting low cost. And WVF has approximately 80% market share, even though, its wide viewing angle properties is inferior to other modes.

Concerning the response time, AFLC, OCB and ASV are superior to the others. Especially AFLCD has ultra fast response time less than microseconds.

It is evident that MVA and IPS have the best properties in the viewing angle characteristics such as color shift and contrast ratio. Both MVA and IPS, however, have some weak point. Small aperture ratio is the biggest weak point of IPS. In order to overcome this weak point, FFS is newly developed by using transparent inter-digital electrodes instead of metal inter-digital electrodes. S-IPS can improve, furthermore, wide viewing angle property of IPS by adopting multi-domain configuration.

Table 1 Features and R&D Items for each Wide-Viewing Angle LCD Modes

Mode	Features	Color stability	CR	R&D Items
Film	• The same cell structure as TN (mass productivity)	○	○	• Color shift less • Film cost
	• Total balance • Fast response	○	○	• Film cost
	• The best WVA • Fast on-off response (25ms)	◎	◎	• Nn LC material
	• Fast response (<several ms)	○	○	• Bend alignment stability
No Film	• The best WVA • Gray level response	◎	◎	• Transmittance (Aperture ratio)
	• Ultra fast response (<<ms)	○	△	• Alignment • Polarization

◎:Excellent, ○:Good, △:must be improved

5. IPS and S-IPS mode

In IPS mode, we use inter-digital electrodes on the TFT substrate to apply electric field parallel to the substrate. By this electric field, LC molecule can be switched their direction within the plane parallel to the substrate resulting extremely wide-viewing angle properties.

The schematic structures of the pixel are shown in Fig.9. The pixel of the conventional TFT-LCD is shown on the left hand side, and that of IPS TFT-LCD is shown on the right hand side. As you can find in the figure, the common electrode, that is inter-digital electrode, is engaged on the TFT substrate of IPS mode. By using the common electrode and pixel electrode, the electric field can switch LC molecular direction in the plane parallel to the substrate (in-plane switching). And there is no electrode on the upper substrate.

Because of the in-plane switching, there are no LC molecule that have opaque direction which induce angular dependence of the optical properties such as color shift, contrast degradation, contrast inversion.

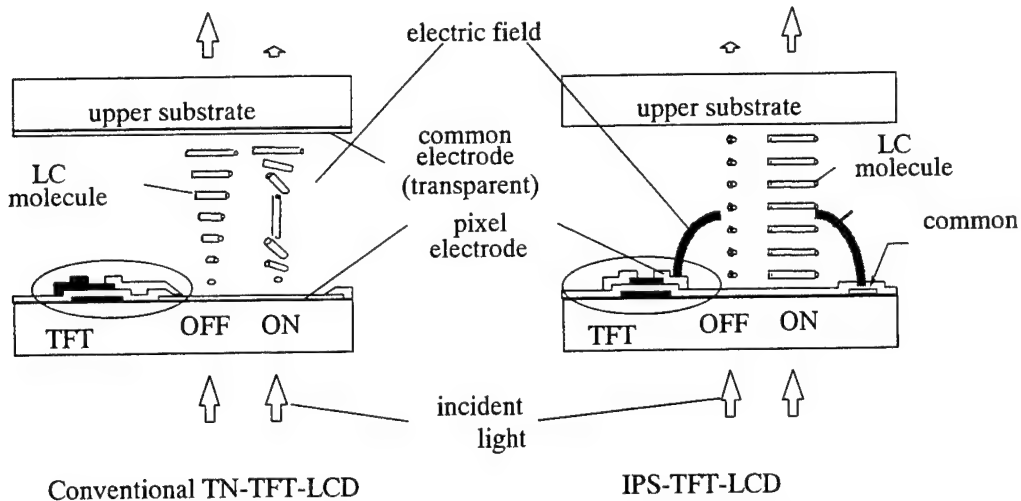


Fig 9. Schematic Structures of Pixel for Conventional TN-TFT-LCD and IPS-TFT-LCD

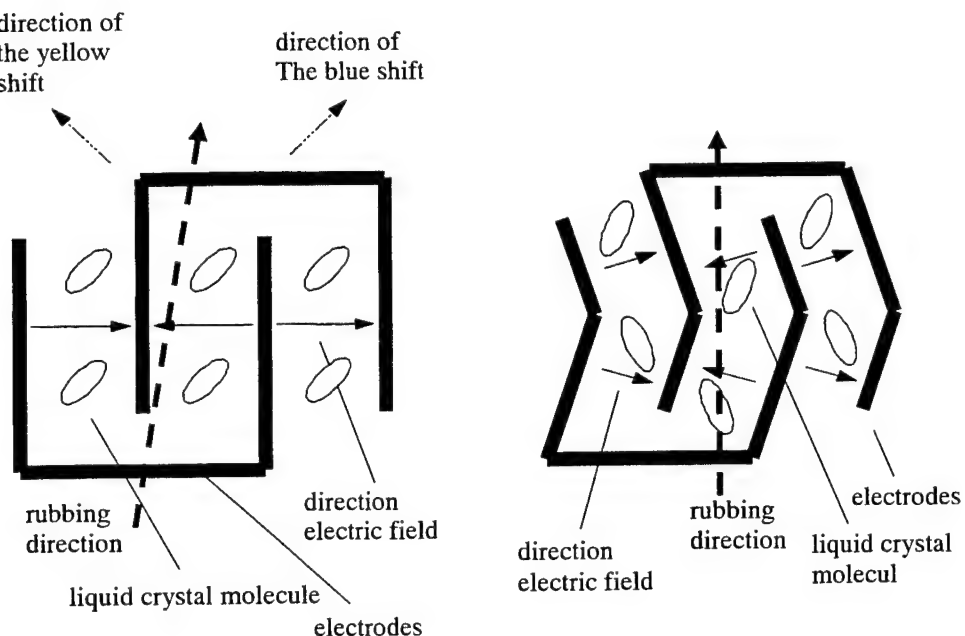


Fig. 10 Inter Digital Electrode Structures for IPS and S-IPS

Even though IPS has extremely good wide-viewing angle, there remains the small angular dependence. For example, there are small color change in white color, e.g. white changes to yellowish white or bluish white. In order to improve this white color shift, we introduced "Zigzag Electrode Pattern" as shown in Fig. 10. By this "Zigzag Electrode Pattern" direction of electric fields are different in the upper part of the pixel and in the lower part, therefore, multi-domain structure is builded up automatically. Thus we can easily achieve multi-domain structure with only one direction rubbing process.

Because of this multi-domain structure, the small white color shift remained in IPS are almost vanished. Then we named this mode as "Super IPS".

In 1999, we have succeeded to develop a 18.1-inch diagonal Super IPS SXGA Module introducing above technologies and more newly developed technologies such as new LC material, improved optical and electrical design. Table 2 shows the specifications of the Super IPS Module. This module has also better features such as 20ms response time with high brightness and mechanical small foot print of thinner thickness with narrower display frame.

REFERENCES

1. M.Oh-e, M.Ohta, S.Arata, and K.Kondo, "Principles and characteristics of electro-optical behaviour with In-Plane Switching mode," The 15th IDRC (Asia Display'95),pp557,1995- 580,1995.
2. H.Mori, Y.Itoh, Y.Nishiura, T.Nakamura, and Y.Shinagawa, "Optical performance of a novel compensation film for wide-viewing angle TN-LCDs,"AM-LCD'96/IDW'96, LCD2-1,pp.189-192,1996.
3. H.Koike, S.Kataoka, T.Sasaki, H.Chida, H.Tsuda, A.Takeda, and K.Ohmuro, "A vertical aligned LCD providing super-high image quality,"AM-LCD'97,pp25-28,1997
4. Y.Yamaguchi, T.Miyashita, and T.Uchida, "Wide-viewing angle display node for the active-matrix LCD using bend-alignment liquid-crystal cell," SID 93 DIGEST,pp.277-280,1993.
5. T.Saisyu, K.Takatoh, R.Ide, H.Nagata, and Y.Mori, "Voltage-holding properties of thresholdless antiferroelectric liquid crystals driven by active matrices," SID 96 DIGEST,pp.703-706,1993.
6. T.Tanaka, K.Sakamoto, K.Tada, and J.Ogura, "A full-color DHF-AMLCD with wide viewing angle," SID 94 DIGEST,pp.430-433,1994.
7. M.Hirata, N.Watanabe, T.Shimada, M.Okamoto, S.Mizushima, H. Take, and M.Hijikigawa, "Development of Super-V TFT-LCD,"AM-LCD'96,pp.193-195,1996.
8. S.Mizushima, N.Watanabe, M.Shiomi, M.Hirata, F.Shimoshikiryo, F.Funada, and M.Hijikigawa, "Development of novel high performance TFT-LCD; advanced Super-V LCD,"AM-LCD'99,pp177-180,1999.
9. T.Tanaka, Y.Taniguchi, T.Sasaki, A.Takeda, Y.Koibe, and K.Okamoto, "A new design to improve performance and productivity of high-quality MVA TFT-LCD panel," SID 99 DIGEST,p.206,1999.
10. K.H.Kim, and J.H.Souk, "Patterned vertical alignment (PVA) mode for high performance LCD monitors," Eoro Display'99,pp.137-140,1999.
11. S.Arata, H.Klausmann, M.Oh-e, M.Ohta, K.Ashizawa, K.Yanagawa, and K.Kondo, "Complete suppression of color shift in In-Plane Switching mode liquid crystal display with a multidomain structure obtained by unidirectional rubbing," Jpn. J. Appl. Phys. Vol.36,pp.L27-L29,1997.
12. S.H.Lee, S.L.Lee, H.Y.Kim, and T.Y.Eom, "A novel wide-viewing-angle technology; ultra-trans voewTM," SID 99 DIGEST,pp.202,1999.
13. S.Endoh, M.Ohta, N.Konishi, and K.Kondo, "18.1-inch diagonal Super-TFT-LCDs with mega wide viewing angle and fast response speed of 20ms," IDW'99,pp187-190,1999.

Table 2 Specifications of Super IPS Module

Item	Specifications
Resolution	SXGA
Number of pixel	H1280xV1024
Pixel Pitch (mm)	H0.2805xV0.2805
Number of Colors (Million)	16.7
Contrast Ratio	350
Brightness (cd/m ²)	350
Viewing Angle Range	Horizontal/Vertical Directions CR >10 Δ u'v < 0.0
	170 deg. 160 deg.
Response Time between White & Black Level	Rise Time (ms) Fall Time (ms) Total Time (ms)
	12 8 20
Color Position on CIE 1931	R(x,Y) G(x,y) B(x,y) W(x,y)
	(0.62,0.32) (0.28,0.60) (0.14,0.09) (0.29,0.30)
	Color gamut (%)
	65
Dimensions of Outline (mm)	H396xV31x124
Weight(g)	2000
Power Consumption (W)	50

New Two-Domain TN/LCD with Identical, Symmetrical and $\pm 80^\circ$ Viewing Cone in Left, Right, Up and Down Viewing Zones

Hiap L. Ong

Kopin Corporation. 125 North Drive. Westborough, MA 01581. USA.

Yung-Hsun Wu

Unipac Optoelectronics Corp

No. 5, Li-Hsin Rd 6, Science-Based Industrial Park, Hsinchu City, Taiwan.

ABSTRACT

We invented a new two-domain TN/LCD with excellent viewing performance with identical, symmetrical 160° ($\pm 80^\circ$) viewing cone in all four major viewing zones. The display also showed excellent color tracking and no gray scale reversal. Each sub-pixel is twisted nematic (TN) based with the LC alignments oriented in the horizontal and vertical directions. This is different from the conventional TN/LCD where the LC alignments are oriented in the two diagonal directions. In this special two-domain TN/LCD, the two sub-pixels show complementary asymmetrical horizontal and vertical viewing zones. Thus the combined two-domain effects show symmetrical and identical optical performances in the four major viewing zones. The viewing angle and display performances can be further improved by optical compensation films, in particular, the combination of types A and C films to enlarge the viewing angles in the diagonal viewing directions.

Keywords: LCDs, two-domain, viewing angle improvement, compensation film.

1. INTRODUCTION

The limited viewing angle cone and asymmetrical viewing angle are two of the major limitations of the present LCD's. [1] Various LCD structures have been developed to improve the LCD viewing angle cone and to change the asymmetrical viewing angle to symmetrical viewing angle. In general, the improvement results in lower yield, lower optical transmission, and higher cost. Major improvements methods include 2-domain and 4-domain LCDs, in-plane switching (IPS), optical compensation bend cell (OCB or Pi-cell), fringe field switching, multi-domain vertical aligned (MVA), and film compensation method.[1]

At present, IPS[2] and MVA[3] LCDs offered better viewing angle performance than the two-domain TN/LCDs. However, IPS and MVA have their own weakness and needed some major improvements to have visual performances comparable to CRT. Their optical transmissions are lower and the respond times are longer than those of the standard TN/LCDs.

Correspondence author: Hiap L. Ong. Chief LCD Technologist, Vice President and General Manager, Asia Division, Kopin Corporation. 125 North Drive. Westborough, MA 01581. USA. Tel: US 1-508-870-5959, Taiwan 886-3-577-2700 Ext 11350; Fax: US 1-508-870-0660, Taiwan 886-3-577-7941. Email: hiap_ong@kopin.com.

Multi-domain TN/LCD offered major advantages by a TN based LCD mode, in comparison to IPS and MVA.[1, 4] Thus the huge material technology, extensive device technology and manufacturing knowledge and know-how can be directly applied to this device fabrication and improvement. However, 2-domain TN/LCD viewing angle is still limited and inferior to the IPS and MVA. 4-domain TN/LCD offered a better viewing angle characteristics, but the cost is higher by the lower yield factor and much complex in the process, and optical aperture is further reduced and had not been used in actual production.

In this paper, we invented a new two-domain TN/LCVD with excellent optical performance, with identical symmetrical and $\pm 80^\circ$ viewing cone in left, right, up and down viewing zones. The display also showed no gray scale reversal and has excellent color tracking. For the standard TN/LCDs, the LC is oriented in two diagonal (135° and 45°) directions. In the standard 2-domain TN/LCDs, a pixel is divided into two sub-pixels, one with $135^\circ/45^\circ$ and the second with $315^\circ/225^\circ$. For this special two-domain TN/LCD, the LC is oriented in two horizontal and vertical (0° and 90°) directions; each pixel is divided into two sub-pixels; one with rubbing angle is 90° to 0° rotations, and the second sub-pixel with 270° to 180° . Each sub-pixel is a TN based with complementary asymmetrical horizontal and vertical viewing zone. The display performance can be further improved by optical compensation films, in particular, the combination of types A and C films to enlarge the viewing angles in the diagonal viewing directions. In this paper, we will present only the modeling results. The cell fabrication for this special two-domain TN/LCD is in progress and the experimental results will be reported when it is completed.

In the following discussion, we will review in Section 2 the optical performances for the standard one-domain and two-domain TN/LCDs. In Section 3, we discuss the optical performances for this new two-domain TN/LCD. We use two LC materials, one for the standard first minimum LC (Merck MLC-9000-100) with an operation cell gap of about 5um, and one high optical birefringence LC (Merck TL-203) with an operation cell gap of about 2um for fast response applications.

2. STANDARD ONE DOMAIN AND TWO DOMAIN TN/LCDs

2.1. Standard Single-Domain TN/LCDs

In the following discussion, we define the x-axis in the horizontal direction, and y-axis in the upper vertical direction. We use the standard spherical polar coordinate system where for the viewing azimuthal angle, 0° , 90° , 180° , and 270° are referred to as right, up, left and down viewing zones respectively.

For the standard TN/LCDs, LC is oriented in $135^\circ/45^\circ$ direction. Only the horizontal (left-right) viewing angle zone offers a symmetrical viewing angle, and all other viewing angle zones are asymmetrical. In particular, the vertical (up-down) is not symmetrical and the lower zone optical performance is better than that for the upper zone.

In the following discussion, we use two LCs for examples. First, we consider Merck TL-203 with an Δn (=ne-no) = 0.2013. The material parameters are as follows: $\epsilon_{\perp} = 4.2$, $\epsilon_{\parallel} = 15.2$, $k_{11} = 15.8 \text{ pN}$, $k_{33} = 17.9 \text{ pN}$, $V_{10} = 1.92 \text{ V}$ and $V_{90} = 2.62 \text{ V}$. By the operation voltage, k_{22} is estimated to be $k_{22} = 8.5 \text{ pN}$. TL-203 is an appropriate material for fast response and large viewing angle LCD applications. The optimal cell gap with a large viewing angle is about 2um, which offers a fast time response. Second, we consider Merck MLC-9000-100 with a standard $\Delta n = 0.1137$. The material parameters are as follows: $\epsilon_{\perp} = 4.2$, $\epsilon_{\parallel} = 12.4$, $k_{11} = 11.3 \text{ pN}$, $k_{22} = 6.1 \text{ pN}$, $k_{33} = 14.3 \text{ pN}$, $V_{10} = 1.42 \text{ V}$ and $V_{90} = 2.23 \text{ V}$. MLC-9000-100 is an appropriate material for low voltage and large viewing angle LCD applications. The optimal cell gap with a large viewing angle is about 4-5um.

The display performances for the TN/LCD with 2um TL-203 are shown in Figures 1-6. Figures 1-3 show the transmission vs. voltage and viewing angle in the horizontal and vertical viewing angle zones respectively. For

the horizontal viewing angle, left and right viewing angles are symmetrical where the optical response for a positive viewing angle $+\theta$ is the same for the optical response for the corresponding negative viewing angle $-\theta$. For the vertical viewing angle, the up and down viewing angles gave a different and asymmetrical viewing angle performances. Figures 4 and 5 show the standard TN/LCD transmission versus viewing angle and gray scale level for horizontal and vertical viewing zones with an 8-gray level operation. Good performances are shown in the horizontal viewing zone with a viewing cone of 100° ($\pm 50^\circ$) for contrast ratio CR=5, and 80° ($\pm 40^\circ$) for CR=10; and poor performances are shown in the vertical viewing zone with a viewing cone of 100° (+35 to -64°) for CR=5, and 90° (+27 to -54°) for CR=10. The viewing angle can be improved by Nitto C-plate with a vertically oriented optical axis and negative birefringence (ne-no<0) film, a FujiFilm, with an inhomogeneous oriented negative birefringence film, and also type A and O films, and ROLIC film.[1, 5, 6, 7] Figure 6 shows the standard TN CR contour plot at 5.0 volt, without any additional optical compensation film. The viewing angle cone is summary in Table 1.

Table 1. Comparison of TN/LCDs viewing angle cones.

o-mode TN/LCD	Horizontal zone (CR=5)	Horizontal zone (CR=5)	Vertical zone (CR=5)	Vertical zone (CR=5)
1-domain TN/LCD	$\pm 50^\circ$	$\pm 40^\circ$	$+35^\circ/-64^\circ$	$+27^\circ/-54^\circ$
Standard 2-domain TN/LCD	$\pm 50^\circ$	$\pm 40^\circ$	$\pm 43^\circ$	$\pm 34^\circ$
Special 2-domain TN/LCD	$>\pm 80^\circ$	$>\pm 80^\circ$	$>\pm 80^\circ$	$>\pm 80^\circ$

2.2. Standard Two-Domain TN/LCDs

In the standard 2-domain TN/LCDs, a pixel is divided into two sub-pixels, one with $135^\circ/45^\circ$ and the second with $315^\circ/225^\circ$ LC alignment. This geometry has the same left-right viewing zones in each sub-pixel, only the up and down are in the reverse. In the standard 2-domain TN/LCD, the left-right zone is the same as those for the single-domain TN/LCD, and the up-down becomes the averaged value of up and down in the single domain TN/LCD.

The display performances for the standard two-domain TN/LCD with 2um TL-203 are shown in Figures 1, 4, and 7-9. Figures 1 and 7 show the transmission versus voltage and viewing angle in the horizontal and vertical viewing angle zones respectively. For the horizontal viewing angle zone, one-domain and two-domain TN/LCD have the same performance, where left and right viewing angle are symmetrical. For the vertical viewing angle, as shown in Figure 7, for the two-domain, the up and down viewing zone show a symmetrical optical performance. Figures 4 and 8 show the standard two-domain TN/LCD transmission vs. viewing angle and gray scale level for horizontal and vertical viewing zones. Good performance is shown in the horizontal viewing zone with a viewing cone of 100° ($\pm 50^\circ$) for CR=5, and 80° ($\pm 40^\circ$) for CR=10. An improved symmetrical performance is shown in the vertical viewing zone with a viewing cone of 86° ($\pm 43^\circ$) for CR=5, and 68° ($\pm 34^\circ$) for CR=10. The viewing angle can be improved by Nitto C-plate with a negative birefringence film.[8] Figure 9 shows the standard two-domain TN CR contour plot at 5.0 volt. The viewing angle cone is summarized in Table 1.

Since these four viewing angle zones have a narrow viewing cone in the single domain TN/LCD, the resulting 2-domain TN have a limited viewing angle, and the vertical viewing zone is different with horizontal viewing zone. The results are summarized in Table 2.

Figure 1. Standard one-domain and two-domain TN/LCD transmission vs. voltage for normal incident, $\pm 15^\circ$, $\pm 30^\circ$, and $\pm 45^\circ$ in the horizontal viewing zone. LC: TL-203.

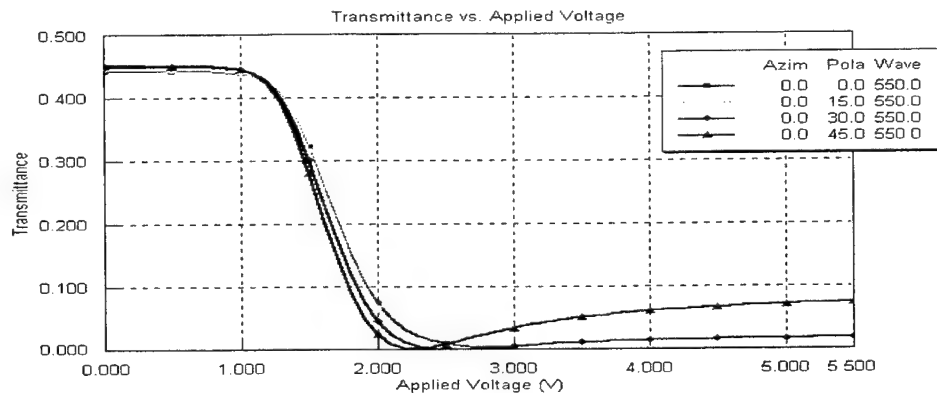


Figure 2. Standard one-domain TN/LCD transmission vs. voltage for normal incident, $+15^\circ$, $+30^\circ$, and $+45^\circ$ in the vertical viewing zone. LC: TL-203.

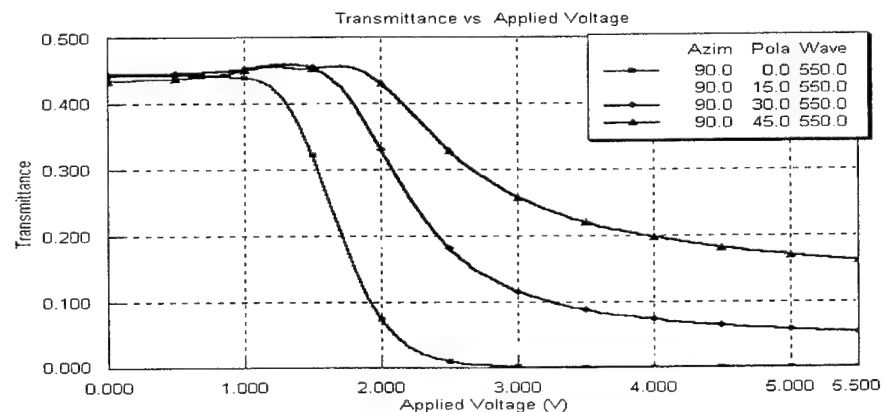


Figure 3. Standard one-domain TN/LCD transmission vs. voltage for normal incident, -15° , -30° , and -45° in the vertical viewing zone. LC: TL-203.

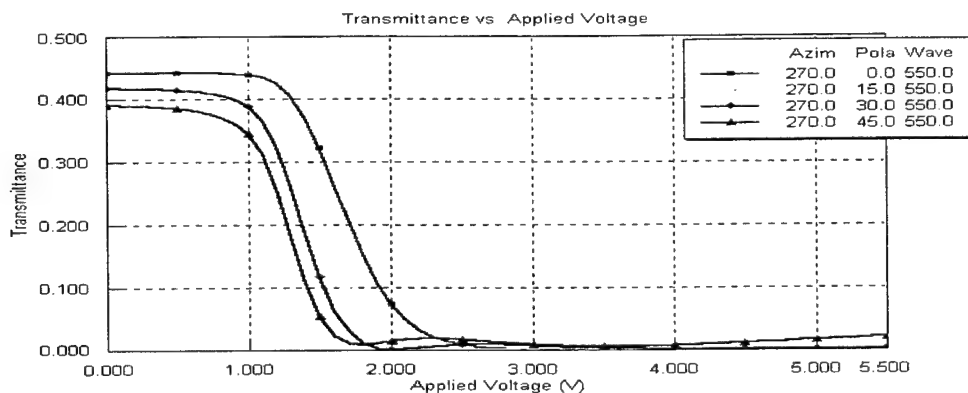


Figure 4. Standard one-domain and two-domain TN/LCD transmission vs. viewing angle and gray scale level for horizontal viewing zone. LC: TL-203.

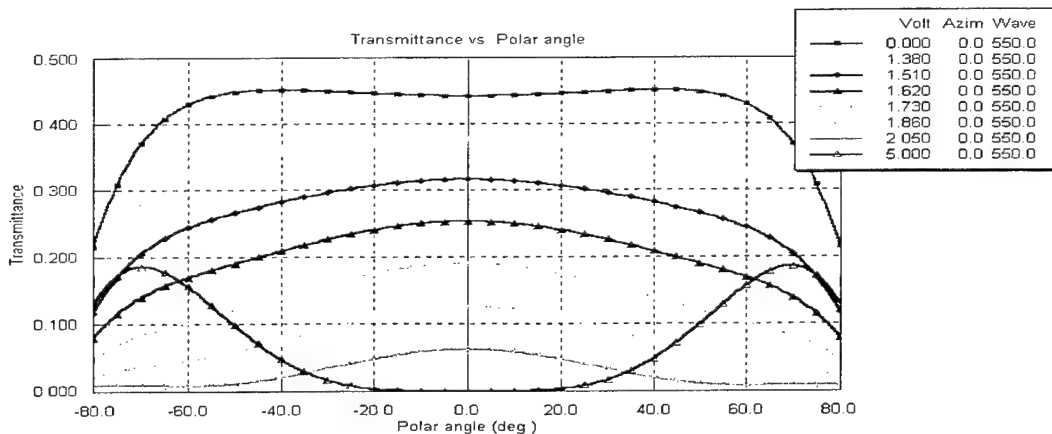


Figure 5. Standard one-domain TN/LCD transmission vs. viewing angle and gray scale level for vertical viewing zone. LC: TL-203.

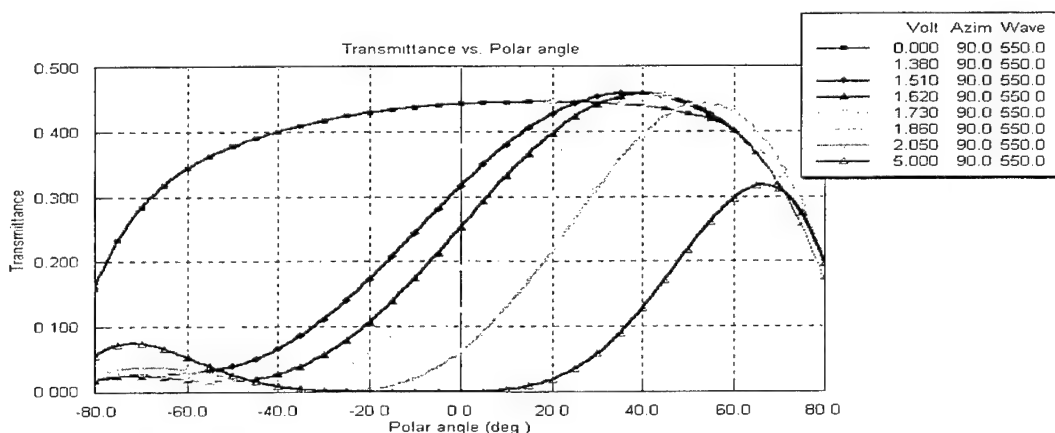


Figure 6. Standard TN CR contour plot at 5.0 volt. LC: TL-203.

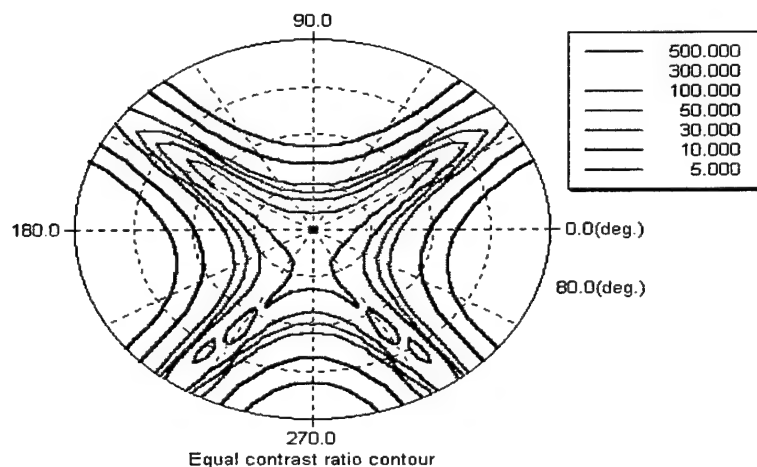


Figure 7. Standard two-domain TN/LCD transmission vs. voltage for normal incident, $\pm 15^\circ$, $\pm 30^\circ$, and $\pm 45^\circ$ in the vertical viewing zone. LC: TL-203.

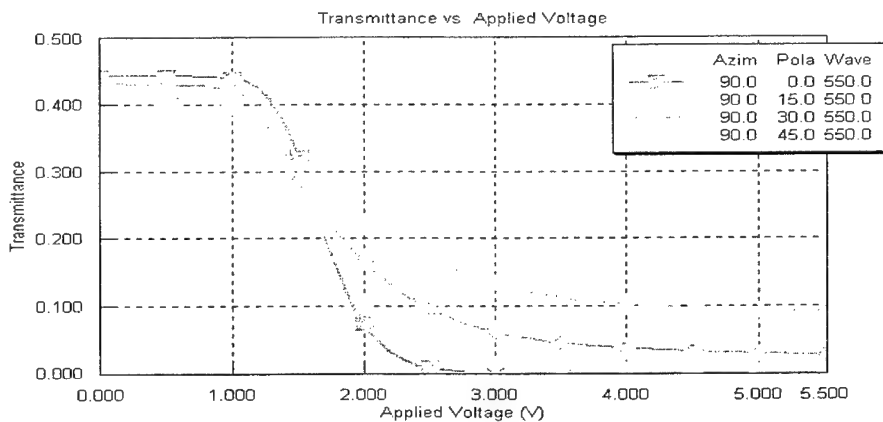


Figure 8. Standard two-domain TN/LCD transmission vs. viewing angle and gray scale level for vertical viewing zone. LC: TL-203.

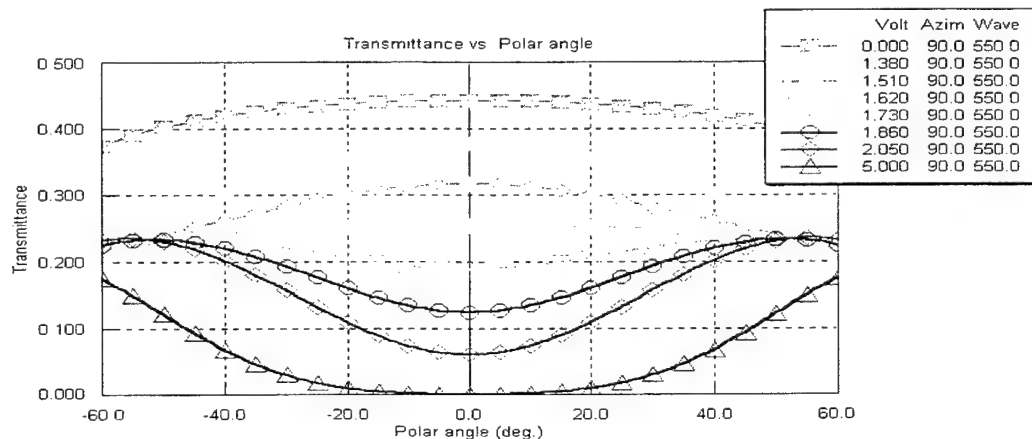


Figure 9. Standard two-domain TN/LCD CR contour plot at 5.0 volt. LC: TL-203.

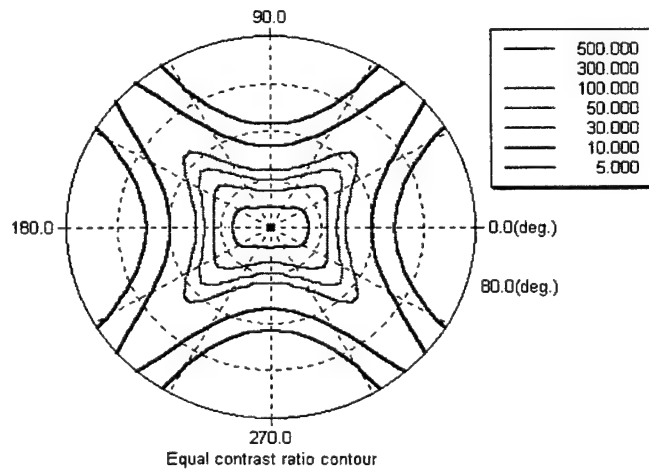


Table 2. Comparison of standard one-domain, 2-domain, 4-domain and the two-domain TN/LCDs.

	Standard 1-domain TN	Standard 2-domain TN	Standard 4-domain TN	New 2-domain TN
LC director	135°/45°	135°/45°, 315°/225°.	135°/45°, 315°/225°, 225°/135°, 45°/315°.	90°/0°, 270°/180°.
Left-right				
a. symmetrical	Yes	Yes	Yes	Yes
b. viewing cone (CR=5)	±50°	±50°	±45°	±80°
Up-Down				
a. symmetrical	No	Yes	Yes	Yes
b. viewing cone (CR=5)	+35° to -64°	±43°	±45°	±80°
c. = left-right	No	No	Yes	Yes
Aperture ratio	High	Medium	Low	Medium
Gray scale inversion	Yes	Small	No	No
Color tracking	Medium	Medium	Medium	No
Total performance	OK	Good	Good	Excellent

3. SPECIAL TWO DOMAIN TN/LCDs

3.1. Optical Performance for the Special 0/90 Single-Domain TN/LCDs

In the new two-domain TN/LCDs, a pixel is divided into two sub-pixels, one with rubbing along the 90° and 0° directions, the LC follows a 90°rotation from 90°axis to 0°axis, and the second sub-pixel with rubbing along the 270° and 180° directions, the LC follows a 90°rotation from 270°axis to 180°axis. Figures 10 and 11 show the viewing angle characteristics in each sub-pixel for the new two-domain TN/LCD where Figure 10 for 90°/0° direction and Figure 11 for 270°/180°. In each sub-pixel, both the horizontal (left-right) and vertical viewing angle zones are asymmetrical, but with the following important special features:

$$90^\circ/0^\circ \text{ right} = 90^\circ/0^\circ \text{ up} = 270^\circ/180^\circ \text{ left} = 270^\circ/180^\circ \text{ down}, \quad (1)$$

$$90^\circ/0^\circ \text{ left} = 90^\circ/0^\circ \text{ down} = 270^\circ/180^\circ \text{ right} = 270^\circ/180^\circ \text{ up}. \quad (2)$$

Thus this special features form a unique complementary asymmetrical viewing angle properties.

3.2. Optical Performance for the Special 0/90 Two-Domain TN/LCDs

In this special two-domain TN/LCD, we have the unique complementary optical proprieties given in Eqs. (1) and (2). Thus for this special two-domain TN, we have the following special identical symmetrical viewing in these four viewing zones property:

$$\text{right} = \text{up} = \text{left} = \text{down}. \quad (3)$$

The properties (3) offer a unique property in the two-domain TN/LCD where the display exhibits symmetrical and identical optical performances in the four major viewing zones. Also, we have a very large viewing cone of larger than 160° ($\pm 80^\circ$) with CR=10.

The display performances for this special two-domain TN/LCD with 2um TL-203 and not compensation film are shown in Figures 12-14. Figure 12 shows the transmission vs. voltage and viewing angle in the horizontal and vertical viewing angle zones, with not compensation films. Same identical optical performance is obtained in the horizontal and vertical viewing zones, with left, right, up and down symmetrical performances, where the optical response for a positive viewing angle $+\theta$ is the same for the optical response for a negative viewing angle $-\theta$, in both the vertical and horizontal viewing zones. Figure 13 shows the transmission vs. viewing angle and gray scale level for horizontal and vertical viewing zones. Good performance is shown in both viewing zones with a viewing cone of larger than 180° ($\pm 80^\circ$) for CR=5 and for CR=10. Figure 14 shows the special two-domain TN/LCD CR contour plot at 5.0 volt. The viewing angle cone is summarized in Table 1. The comparisons with other TN/LCDs are included in Table 2.

3.3. Improvement of the Optical Performance for the Special 0/90 Two-Domain TN/LCDs

The optical performances for this special two-domain TN/LCD can be further improved using film compensation method, including the types A, C, O films, FujiFilm, and ROLIC film. Special arrangement might be necessary for type O and Fuji Films, where the optical axes have tilted orientations. The improvements are mainly to improve the performance at the two diagonal directions (which are the horizontal and vertical directions for the standard 135/45 TN/LCDs).

Two types of optical films are used to improve the optical performances for this special two-domain TN/LCD. First, the C plate, in which the optical axis is homogeneous vertically oriented. Second, the A plate, in which the optical axis is homogeneous parallel oriented. In this study, the optical axis of the A plate is oriented parallel to the LC alignment direction of the adjacent surface. This orientation for the A plate is the same as those used by Yeh and Gu.[7] The optical birefringence of the A and C optical films is negative, where $\Delta n = n_e - n_o < 0$. For each plate, two identical films are used and placed between the entrance polarizer and exit analyzer and placed on both sides of the TN cell, to preserve the left-right viewing symmetry.[7, 9] In the Figure 15, we use A-plate with an optical birefringence thickness[($n_e - n_o$) $\times d$] of 120nm. In Figure 16, we use C-plate with an optical birefringence thickness of -160nm. In Figure 17, we use C-plate with an optical birefringence thickness of -80 nm and A-plate with an optical birefringence thickness of -120nm.

The optical films can be used to enlarge the viewing angle performances for this new two-domain TN/LCD. Figures 14-17 show the special two-domain TN CR contour plot at 5.0 volt, with and without optical compensation films. Super large viewing angle is demonstrated. In Figures 14, not optical film is used. The viewing angles along the two diagonal directions are small (these are the viewing angles for the standard two-domain in the horizontal and vertical directions). In Figure 15, we use an A-plate with an optical birefringence thickness of -120nm. In Figure 16, we use a C-plate with an optical birefringence thickness of -160nm. Figures 15 and 16 show that A and C-plates can separately used to enlarge the viewing angle. The combination of A and C plates are used in Figure 17 to further enlarge the viewing angle. In Figure 17, we use C-plate with an optical birefringence thickness of -80 nm and A-plate with an optical birefringence thickness of -120nm. The results showed that the viewing cone at the horizontal and vertical viewing zones are the same for all four cases, i.e., the viewing cones at the four major viewing zones are not affected by the A and C films. But A and C-plates can significantly improved the viewing cones in the two diagonal viewing axes.

Figure 10. Special one-domain TN/LCD with 90/0 LC alignment CR contour plot at 5.0 volt. LC: TL-203.

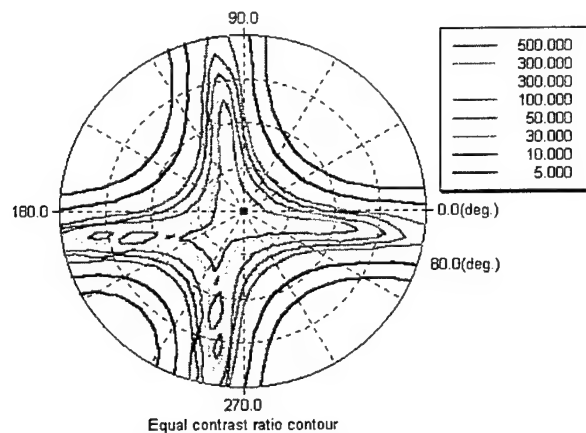


Figure 11. Special one-domain TN/LCD with 270/180 LC alignments CR contour plot at 5.0 volt. LC: TL-203.

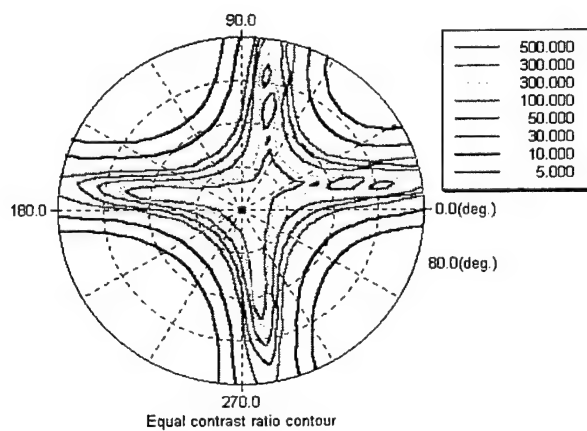


Figure 12. Special two-domain TN transmission vs. voltage for normal incident, $\pm 15^\circ$, $\pm 30^\circ$, and $\pm 45^\circ$ in the horizontal and vertical viewing zone with not film. LC: TL-203.

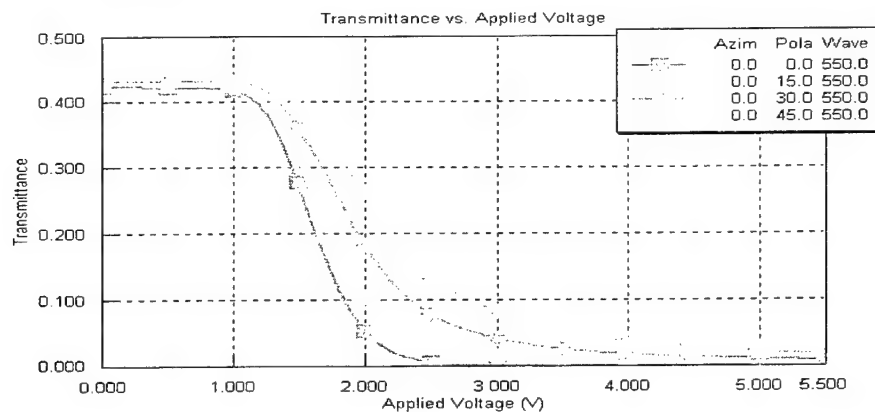


Figure 13. Special two-domain TN transmission vs. viewing angle and gray scale level for horizontal viewing zone with not film. LC: TL-203.

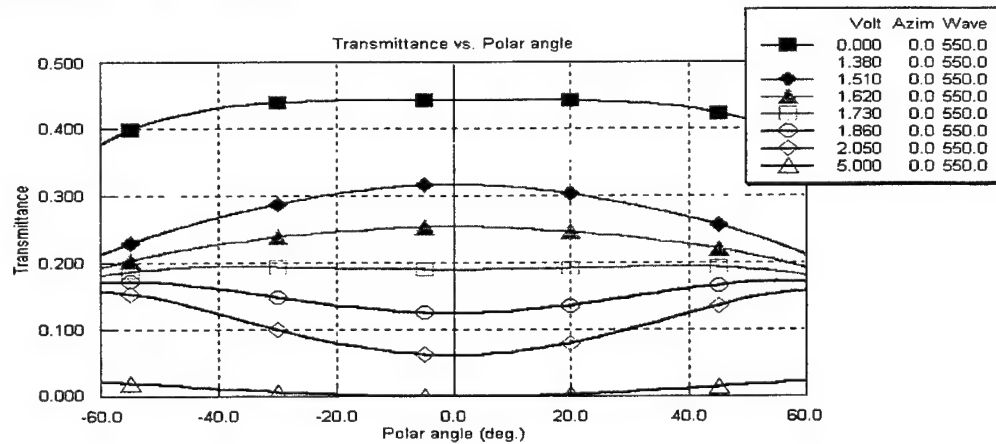


Figure 14. Special two-domain TN CR contour plot at 5.0 volt with not film. LC: TL-203.

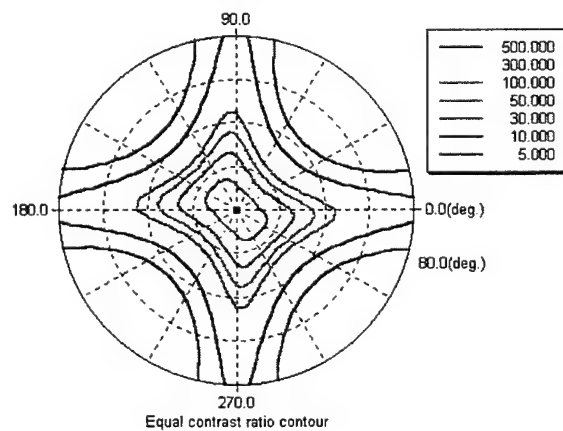


Figure 15. Special two-domain TN CR contour plot at 5.0 volt with A and not C-plates. LC: TL-203.

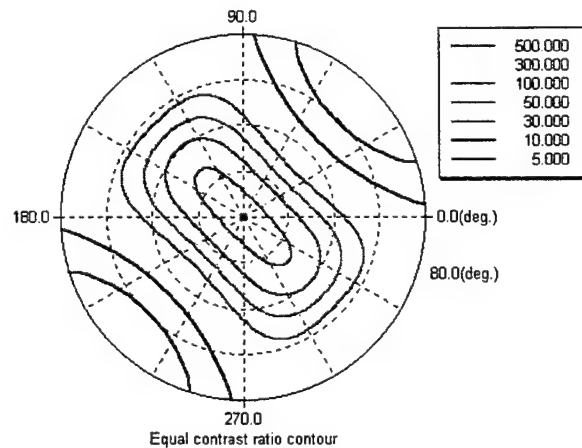


Figure 16. Special two-domain TN CR contour plot at 5.0 volt with C and not A-plates. LC: TL-203.

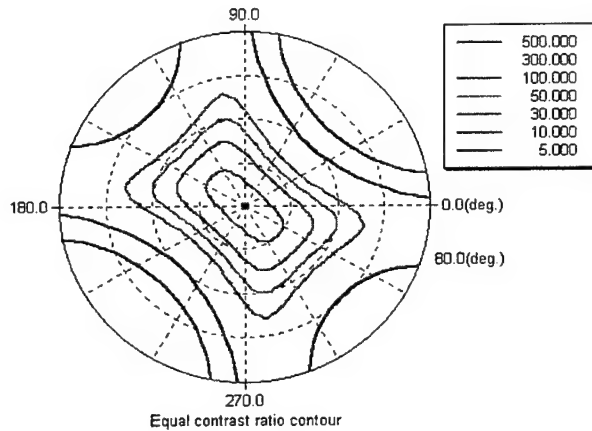
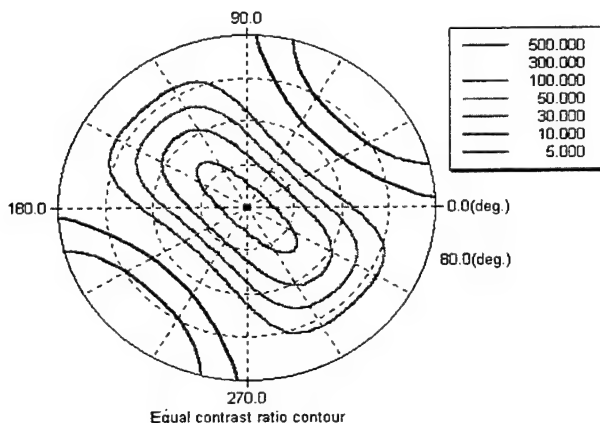


Figure 17. Special 0/90 two-domain TN CR contour plot at 5.0 volt with A and C plates. LC: TL-203.

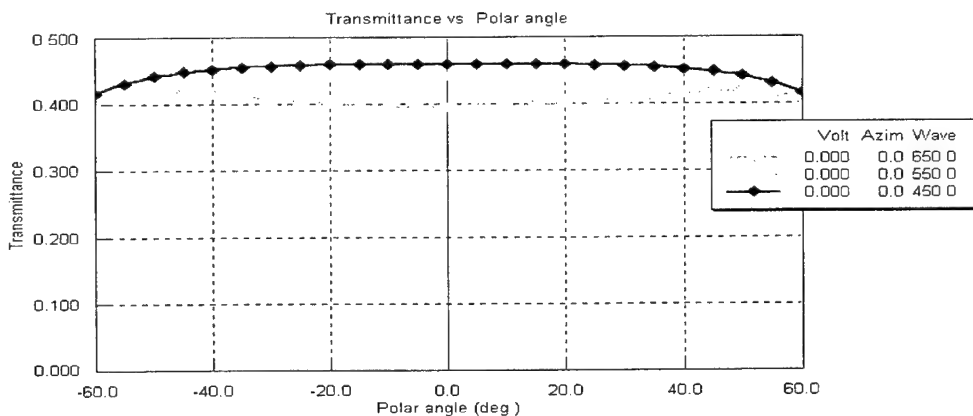


3.4. Improvement of the Color Tracking Performance for the Special 0/90 Two-Domain TN/LCDs

The special two-domain TN/LCDs also offer excellent color tracking. Figures 18-21 show the Red, Green, and Blue transmissions vs. viewing angle and gray scale levels 1 and 8 for horizontal and vertical viewing zones, for the standard one-domain and two-domain TN, and this special two-domain TN/LCD. In the standard one-domain and two-domain TN/LCDs, horizontal viewing zone shows a good color tracking, but poor color tracking appeared in the vertical viewing zone. In comparison to the normal one-domain and two-domain TN/LCDs, this new two-domain TN shows good color tracking.

Figure 18. Normal 135/45 1-domain TN/LCD Red/Green/Blue transmission vs. viewing angle, and gray scale levels No. 1 and 8, for horizontal viewing zone with no films. LC: TL-203.

18(a).



18(b)

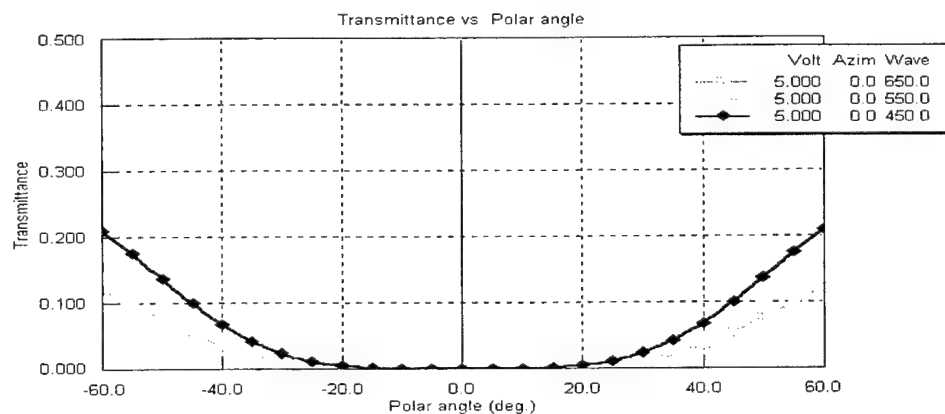
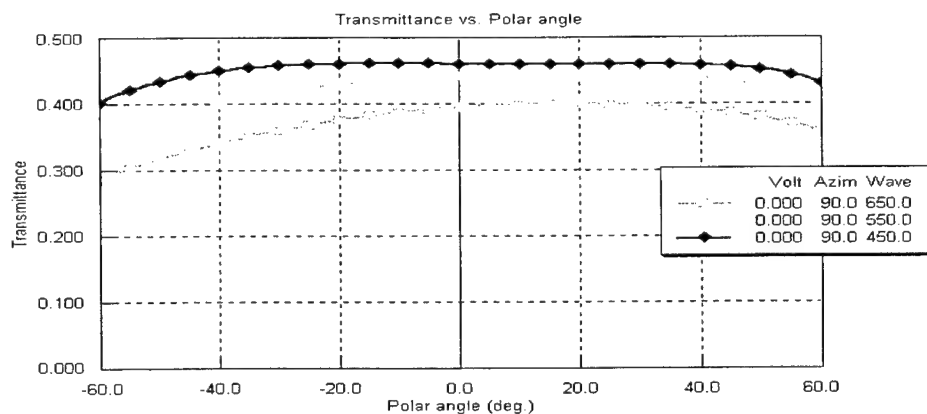


Figure 19. Normal 135/45 1-domain TN/LCD Red/Green/Blue transmission vs. viewing angle, and gray scale levels No. 1 and 8, for vertical viewing zone with no films. LC: TL-203.

19(a)



19(b)

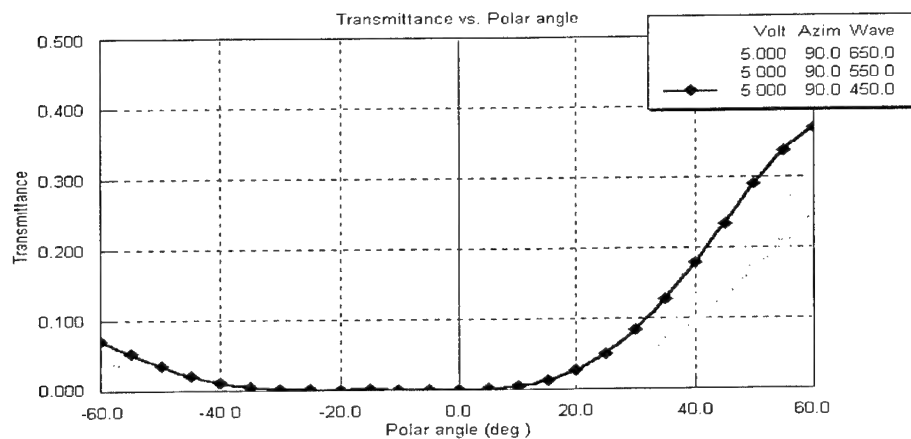
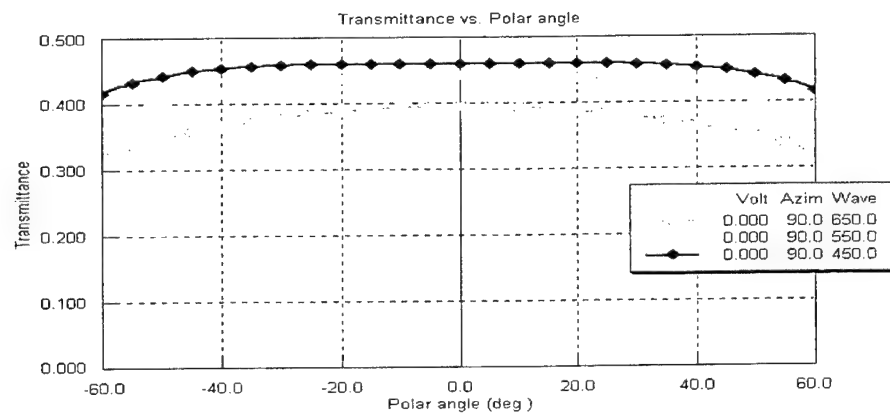


Figure 20. Normal 135/45 two-domain TN/LCD Red/Green/Blue transmission vs. viewing angle, and gray scale levels No. 1 and 8, for vertical viewing zone with no films. LC: TL-203.

20(a)



20(b)

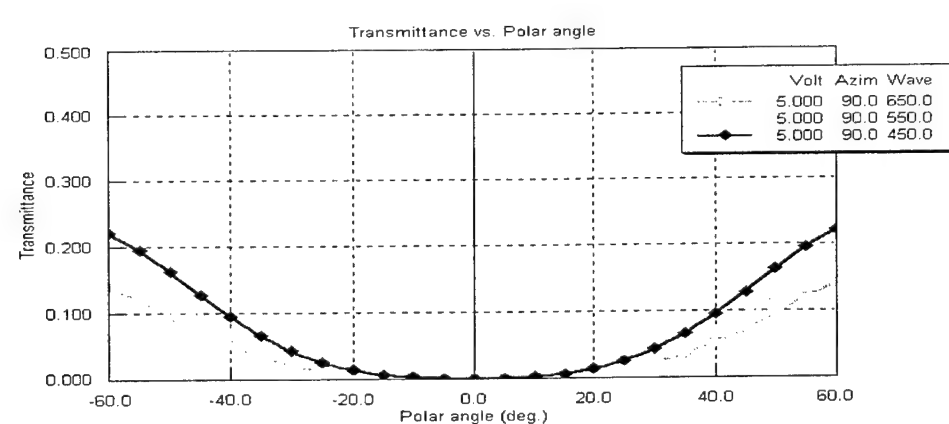
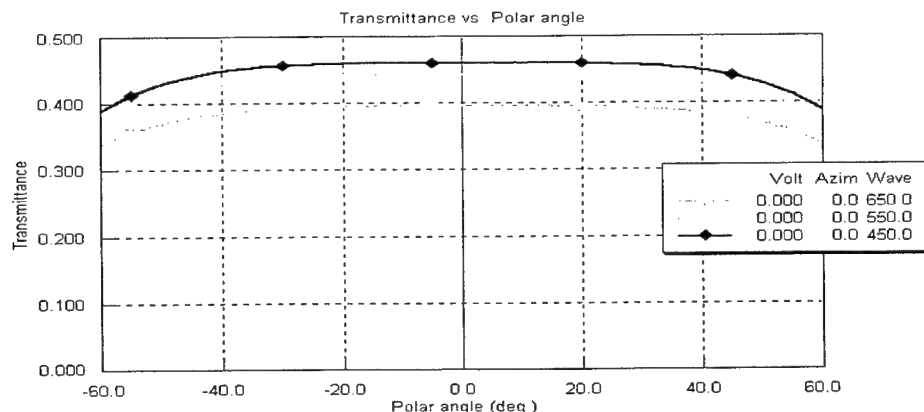
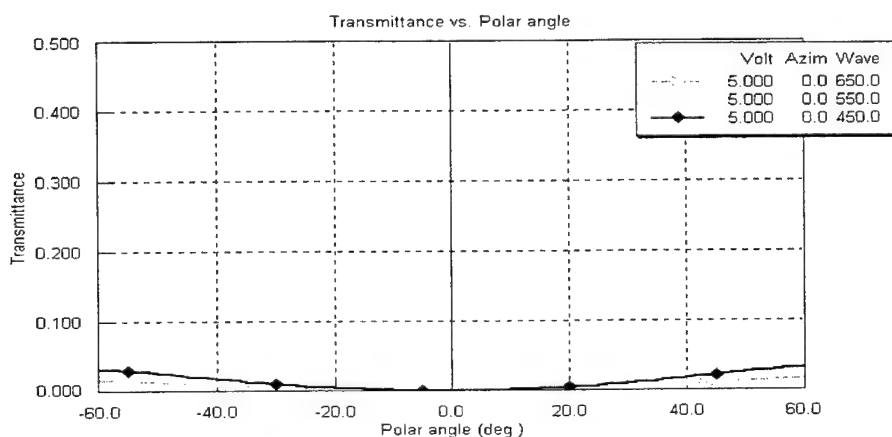


Figure 21. Special 0/90 two-domain TN/LCD Red/Green/Blue transmission vs. viewing angle, and gray scale levels No. 1 and 8, for horizontal viewing zone with A and C plates. LC: TL-203.

21(a)



21(b)



3.5. Improvement of the Optical Performance for the Special 0/90 Two-Domain TN/LCDs with Normal First minimum LC

The improvement of the optical performance for the special 0/90 two-domain TN/LCDs with a normal first minimum LC are shown in Figures 22-24 for MLC-9000-100. MLC-9000-100 is an appropriate material for low voltage and large viewing angle LCD applications. The optimal cell gap with a large viewing angle is about 4um. Again, the new two-domain TN/LCD show excellent viewing performance with identical, symmetrical 160° ($\pm 80^\circ$) viewing cone in all four major viewing zones. The display also showed excellent color tracking and no gray scale reversal.

4. CONCLUSION

We invented a new tow-domain TN/LCD with excellent viewing angle performances, where identical, symmetrical 160° ($\pm 80^\circ$) viewing cone appeared in all four major viewing zones. The new two-domain TN/LCD also offer no gray scale reversal and excellent color tracking.

The wide viewing TN/LCD should be important for the viewing angle LCDs, with major application for notebook PCs, monitor, and PFDA application. This result showed that with TN/LCDs, the viewing angle could be significantly improved and comparable to the advanced IPS and MVA LCDs viewing angle. This is a TN based LCD and make it attractive for AMLCDs having TN/LCDs as the standard LCD.

ACKNOWLEDGMENT

We thank Professors Pochi Yeh and Glaire Wu for useful discussion on the LCD modeling and viewing angle improvement, and Dr. Ronald Gale for his useful comments.

REFERENCES

1. For a review, see P. Bos, SID 99 Seminar Lecture Note, Vol. I, p. M-9 (1999).
2. For a review on IPS, see M. Ohata, et. al., SID'99, p. 86 (1999), S Endoh, et al. IDW'99, p. 187 (1999).
3. For a review on MVA, see Y. Tanaka, SID'99, p. 206 (1999).
4. K. H. Yang, IDRC'91, p. 68 (1991).
5. H. Ong, Japan Display'92, p. 247 (1992), SPIE Vol. 3421, p. 40 (1998).
6. H Mori and P. Bos, IDRC'97, p. 88 (1997).
7. P. Yeh and C. Gu, SPIE Vol. 3421, p. 224 (1998).
8. H. Ong, SID'93, p. 658 (1993).
9. H. Ong, SID'99, p. 673 (1999).

Figure 22. Standard one-domain TN/LCD CR contour plot at 5.5 volt. LC: MLC-9000-100.

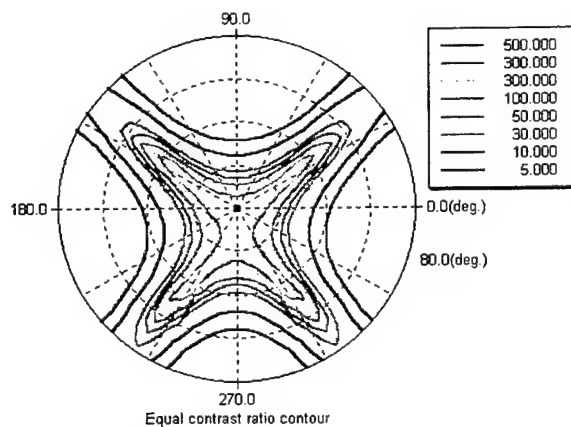


Figure 23. Standard two-domain TN/LCD CR contour plot at 5.5 volt. LC: MLC-9000-100.

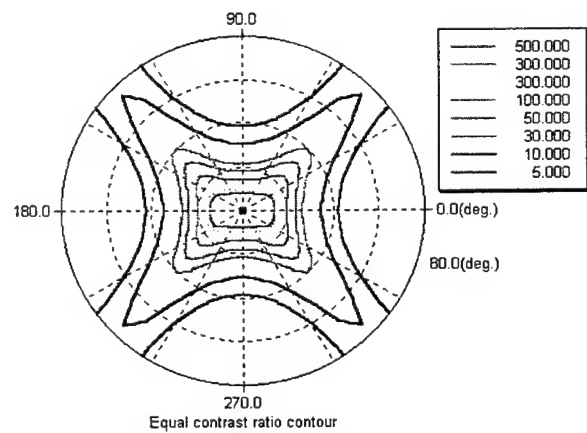
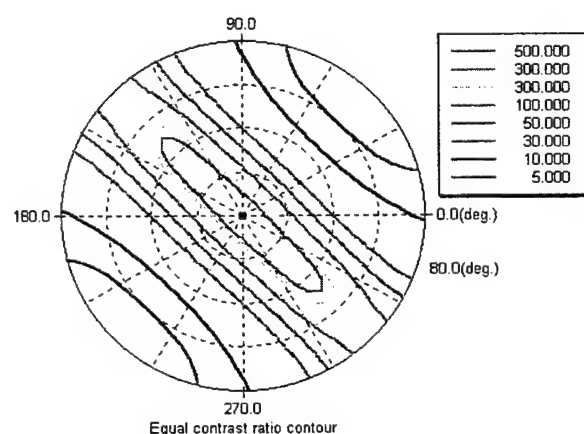


Figure 24. Special two-domain TN/LCD CR contour plot at 5.5 volt with A and C-plates. LC: MLC-9000-100.



An Overview of Wide-Viewing-Angle LCD Using Inter-Digital Electrodes

Lisen Chuang Wei-Fen Bair and Ching-Chao Chang,
Electronics Research and Service Organization, Industrial Technology Research Institute,
Hsinchu, Taiwan 310, ROC

1. ABSTRACT

We have compared the performance of wide-viewing angle technology using interdigital electrodes, which are in-plane switching (IPS), fringing field switching (FFS) and finger on plane (FOP). What we have found is that IPS has the fastest response, FOP has the largest process window, and FFS can provide the similar transmittance as FOP but with more difficult process. The basic properties of these technologies will be reviewed in this paper.

Keywords: wide-viewing angle; liquid crystal display; in-plane switching, fringing field switching, finger on plane

2. INTRODUCTION

Applications of LCDs to the huge potential market of desktop monitor and LCD TV have just been started. It is generally expected that there will be around 10% replacement of CRT in the monitor market in the year 2001. For these markets, large area LCD is necessary in which the development of wide viewing angle technology is one of key issues.

In these years, many techniques have been developed to overcome the above limitation. The most popular techniques are film-compensated TN-LCD, multi-domain vertically align (MVA) LCD, in-plane-switching (IPS) LCD, optically compensated bend (OCB) LCD. Each technique has its own advantages and drawbacks; however, it seems that none of them can dominate the LCD monitor market at this moment. Hitachi has done much effort and given many contributions on the IPS mode. However, according to the IPS structure, several different techniques are published such as Hyundai's fringe-field-switching (FFS) [1], comb-on-plane (COPS) [4] and ERSO's Finger-on-Plane (FOP) [5][6] which is similar to the second version of FFS [2]. In order to distinguish, we use FOP and FFS as the names of the structures shown in Fig. 1c and Fig. 1b, respectively. All of these techniques use the inter-digital electrodes. In this paper, we will have an overview of the wide-viewing-angle LCD using inter-digital electrode, especially focus on the comparison of IPS, FFS and FOP.

3. OVERVIEW OF IPS, FFS AND FOP

3.1 Structure description

Fig. 1a, 1b and 1c show the structures of the three technologies describing the difference in light transmitted area and electrode structure. In the IPS cell, the distance between electrodes is larger than the cell gap and the width of the electrode. Then the homogeneously aligned liquid crystal molecules do mainly twist deformation in horizontal plane by the horizontal electric field, giving rise to light transmittance. However, the molecules above electrodes do not go through twist deformation but tilt. As a result, the area that light can be transmitted is reduced. In the FFS and FOP cell, both the common and pixel electrodes are transparent. The distance between electrodes is very small around 0-1um in FFS cell, and is about 3-5um in FOP cell [1][2]. As a result, the electric field parallel to the substrate can not be formed but instead the fringing field is formed in the whole area. Because the pretilt angle of LC director is very low, only E_y has contribution to the dielectric torque when a negative LC is used. Almost in whole areas, the E_y exists such that the liquid crystal molecules do twist

deformation in plane and resulting in light transmission. In the IPS cell, both negative and positive liquid crystal material can be used, while in FFS and FOP, only negative type liquid crystal is suitable. Nowadays, the negative liquid crystal is more expensive and does not have many choices. Otherwise, the dielectric anisotropy of the negative LC is smaller compared to that of the positive LC, such that the driving voltage may get higher for FFS and Fop cells. This may be a disadvantage for FFS and FOP compared to IPS.

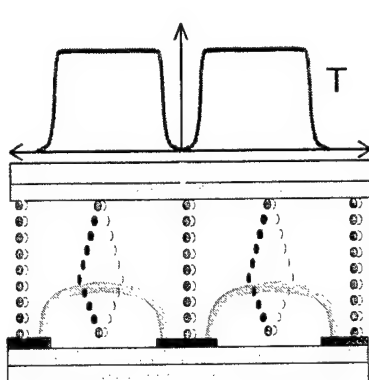


Fig. 1a IPS cell

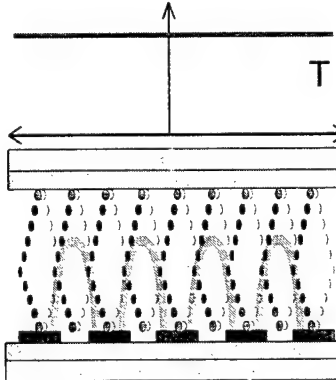


Fig. 1b FFS cell

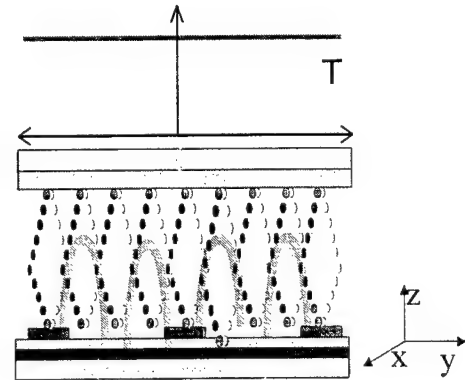


Fig. 1c FOP cell

For IPS cell, both the pixel and common electrodes are formed of metal and the pixel electrode can be built with the data bus at the same time; the common electrode can be built with the scan bus at the same time. Therefore, the number of the process is not large. Samsung has developed a 3-masks process in the IPS TFT process [23]. Compared to the IPS cell, both FFS and FOP need 2 or 3 more processes because the pixel and common electrodes in FOP and FFS are formed of ITO. For the FFS process, it is more difficult to control the very thin distance between electrodes. But for the FOP, the upper and lower electrodes have larger alignment tolerance. On the other hand, In the IPS cell, the pixel and counter electrodes are formed using data and scan bus metals that the thickness at least above 1000A, the LC molecules do not align so well in the dark state and may cause light leakage [3]. However in the FFS and FOP cell, the pixel and common electrodes are ITOs having a thickness about 400A, so good alignment of LC is obtained without extra process.

In order to avoid the current leakage due to the TFT off state and voltage drop due to the feed through of the scan line, we should have a capacitance as large as possible. In the traditional pixel design, the large storage capacitor gets better image quality but less light transmission. In Fig. 2a to 2c, the pixel structure of IPS, FFS and FOP are shown. For the IPS and FFS cell, both need additional area to form the storage capacitor. But for the FOP cell, it is very good that the overlap areas of the common and pixel electrodes can be treated as the storage capacitor and get a very high aperture ratio. Hyundai claimed that their design could achieve about 90% light efficiency of the TN mode [1][2]. And ERSO has developed a 12.4" SXGA FOP-TFT LCD in which a sub-pixel size is 64um*192um with 80% aperture ratio [6]. In IPS cell, the metal electrodes occupy additional aperture ratio such that IPS gets the lowest aperture ratio compared to the other two modes.

	IPS	FFS	FOP
Electrode distance	larger	Very small	zero
Field useful	Ey	Ey, Ez	Ey, Ez
Electrode	Metals or ITO	ITO	ITO
LC material	Positive and negative	negative	negative
Storage capacitor	Need additional area	Need additional area	Self-formed
Process number	few	larger	larger
Aperture	lowest	middle	Highest

Table 1

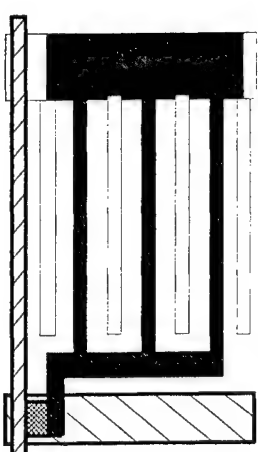


Fig. 2a IPS pixel structure

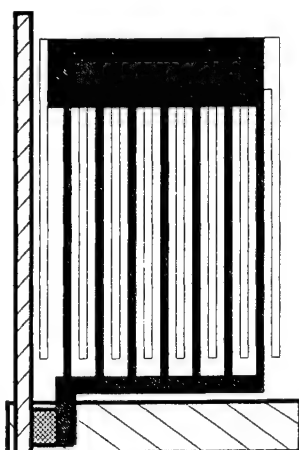


Fig. 2b FFS pixel structure

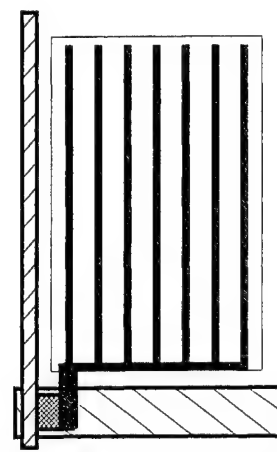


Fig. 2c FOP pixel structure

The brief comparison of the three structures is shown in Table 1.

3.2 Electro-optic characteristics

Fig. 3a and Fig. 3b show the light transmission along the y direction corresponding to IPS and FOP respectively. For the IPS mode, because the distance of the electrodes is larger, in the light transmission area, the horizontal electric field is almost the same for each y position. The LC molecules for each horizontal position twist similar angle as shown in Fig. 4a resulting in almost the same light transmission as Fig. 3a shows. For the FOP and FFS cell in which the fringe field dominate such that the electric field has larger difference in every horizontal position. For a given voltage, the LC molecules twist for different degree as shown in Fig. 4b resulting in different transmittance as shown in Fig. 3b. If we define the light efficiency as light detected (T) divided by the light transmission area (A) ($\text{Eff} = T/A$), the IPS cell gets the highest value although the FOP gets the highest light transmission due to the highest aperture.

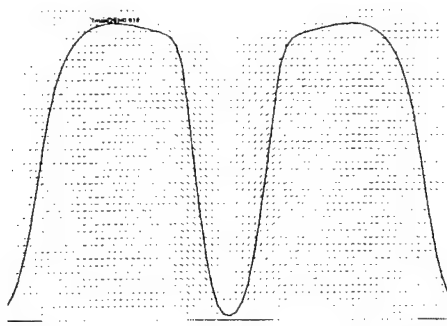


Fig. 3a Light transmission profile of IPS

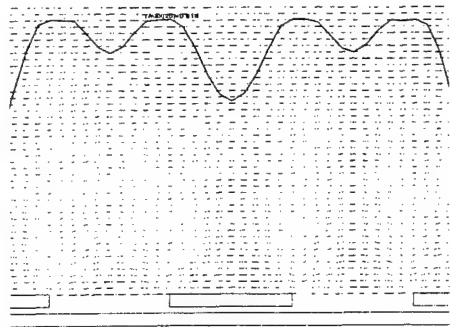


Fig. 3b Light transmission profile of FFS and FOP

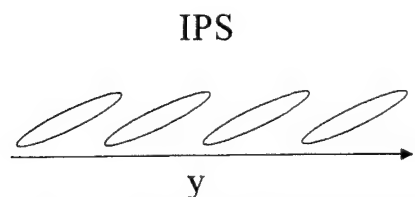


Fig. 4a Top view of LC distribution along the y direction

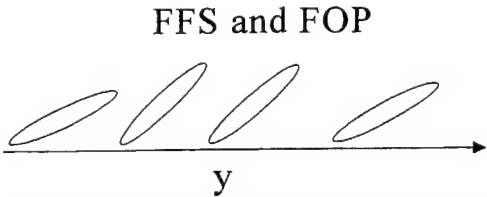


Fig. 4b Top view of LC distribution along the y direction

The color shift is very serious in the IPS mode while the viewing angle is large especially at the direction of 45 degree azimuthal angle (ϕ) from polarization axis of polarizer. The status is shown in Fig. 5a. While the viewing angle is parallel to the director, blue shift occurs due to the small Δn_d , and yellow shift occurs due to the large Δn_d when perpendicular to the director. In the FOP and FFS cell, the color shift is not so bad compared to the IPS cell because the LC director inhomogeneously distribute as shown in Fig. 5b. Fig. 6a and Fig. 6b show the experiment results of the color shift for white level near the maximum transmission of IPS cell and FOP cell respectively for polar angle (θ) range is less than 60 degree in all ϕ angles. One can find that the IPS cell gets the worse result but the FOP is not also good enough to eliminate the dispersion problem. People have used herring-bone shape electrode structure to form a two domain IPS [11] and can get good results. Actually, this structure can be applied to the FOP and FFS cell, too. However when a two-domain structure is used, the light transmission will decrease a little.

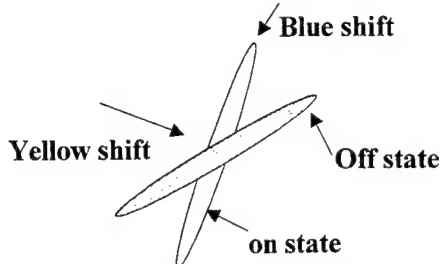


Fig. 5a Average effect for the LC distribution

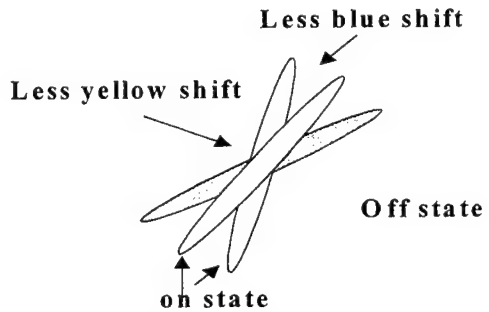


Fig. 5b Average effect for the LC distribution

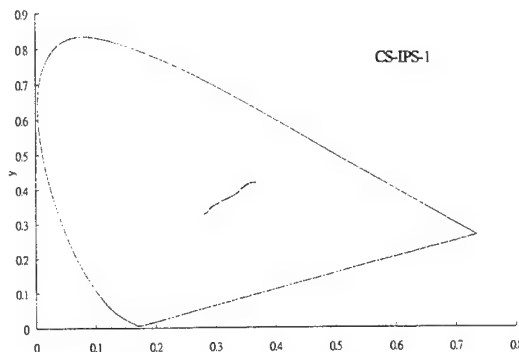


Fig. 6a Color shift for IPS

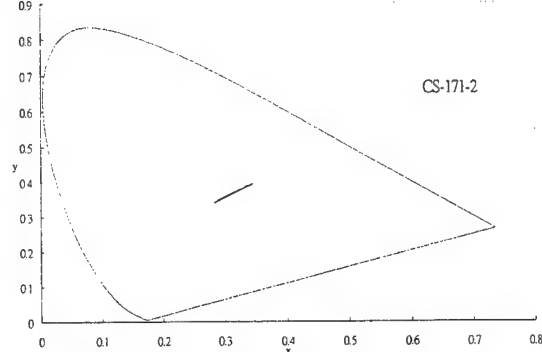


Fig. 6b Color shift for FFS and FOP

The gray level inversion is not a serious problem in the IPS, FOP, and FFS cell. As shown in Fig. 7a, the regions where no gray levels inversion of the IPS cell are very large [8]. The FOP and FFS cell have the same property according to our simulation results. Fig. 8a and 8b show the simulation results of the light transmission of 8 gray levels of IPS and FOP cells at the direction of 45 degree azimuthal angle (ϕ) from polarization axis of polarizer, respectively. From Fig. 8a and Fig. 8b, one can find that only the two darkest gray levels cross over at about 45 degree. In IPS and FOP, two-domain modes can obtain estimate the inversion of gray scale. Due to the perfect dark state, the IPS, FFS and FOP can get large region where the contrast ratio over 10. Fig. 7b shows the iso-contrast curves for the FOP cell [2]. We find that the IPS, FFS and FOP have the similar iso-contrast contours according to our simulation results.

Because the cell gap is shorter than the distance between electrodes, the black resin with high specific resistance but not metal is often used as the black matrix material in order to avoid disturbing the electric field in LC layer in the IPS cell [17]. However, in the FFS and FOP cell, the electrode distance is very small or zero, the field strength caused by Cr BM of upper substrate does not affect the field distribution much in modulated area.

Hyundai has checked that the influence of the Cr BM of FFS is very small [3]. On the other hand, ERSO has developed the ITO on top structure for FOP cell in which BM is not necessary because it uses the ITO to shield the fringe field caused from data and scan line [6]. Such structure can get very high aperture ratio.

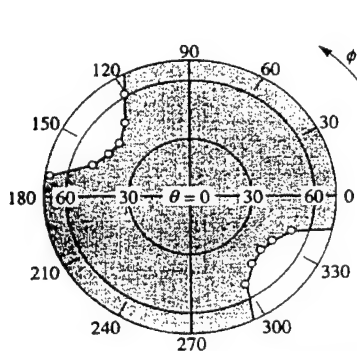


Fig. 7a Gray level inversion regions of IPS [8].

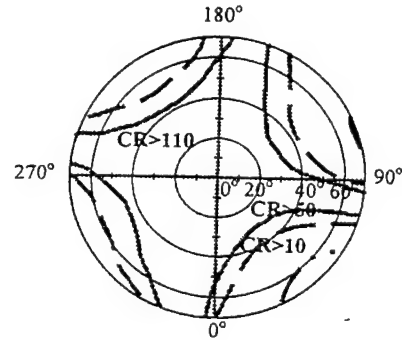


Fig. 7b Iso-contrast curve of the FFS cells [2].

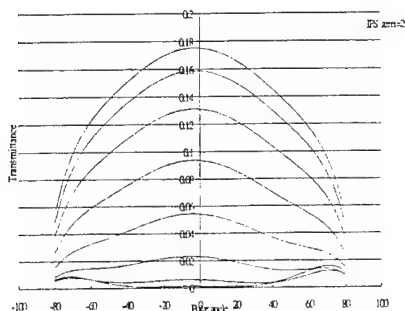


Fig. 8a 8 gray levels of IPS

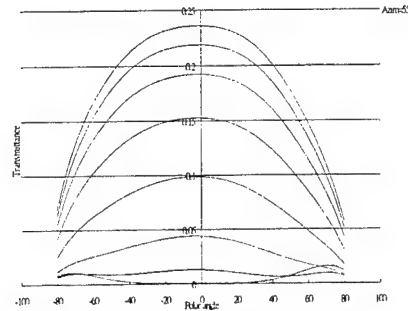


Fig. 8b 8 gray levels of FOP

Cross-talk caused by the source bus-line has two origins. One is capacitive coupling between the source bus-lines and the pixel electrodes. Fluctuation of the pixel electrode potential $\Delta V_p = (C_{sp}/C_t) \Delta V_s$, where the C_{sp} , C_t and ΔV_s are capacitance between the source bus line and a pixel electrode, and total capacitance of a pixel and variation of the source bus line potential, respectively. In the IPS cell, C_t is small because the capacitance of the LC is very small compared to traditional TN cell. But for the FOP cell, because the C_{st} is very large that the total capacitance is very large, too. Such that the FOP has less cross-talk issue than the FFS and IPS cells. The second origin is the leakage of the source bus line potential to the optical switching medium in a pixel between the two electrodes which are driving the LCs. This is especially serious in the IPS cell and some methods are published to shield the leakage field. But in these methods, not additional process is needed or the loading of the data bus increase causing a voltage wave distortion. According to this point, IPS suffers more problems than FFS.

For the IPS, FFS and FOP cell, it is one of the advantages that the driving waveform of the scan driver can be simplified. For a good quality of image, one has to consider the voltage coupling of the scan bus when the gate voltage turns off. C_t includes C_{lc} , C_{st} , and C_{gd} , where C_{lc} , C_{st} , and C_{gd} represent the capacitance of liquid crystal, storage capacitance and capacitance between gate and drain. When the voltage of scan line changes, it causes the pixel potential drop as $\Delta V_p = \{C_{gd}/(C_{gd} + C_{lc} + C_{st})\} \Delta V_g$. Unfortunately the value of C_{lc} is not constant and varies with voltage that will cause the pixel potential asymmetric. In most cases, we can not just change the common voltage level to compensate the voltage drop because the value of C_{lc} is not small compare to C_t and the flicker will occur. One can use a 3-level or 4 level driving wave form as shown in Fig. 9 to

compensate the voltage difference in the traditional TN cell. In the IPS, and FFS and FOP cell, the value of C_{LC} is much smaller than that of TN cell, we can get more symmetric pixel potential by just using a simpler 2-level driving wave-form as shown in Fig. 9.

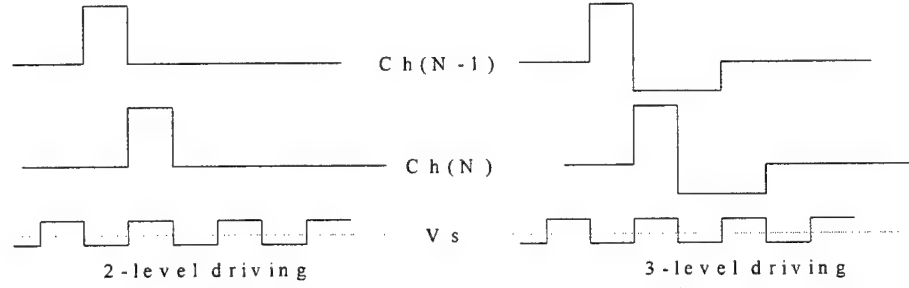


Fig. 9 The driving wave-form of the Scan bus

The IPS cell is critical to the cell gap [14]. Hitachi claimed a method based on enlargement of effective cell gap with the extrapolation length that generated with weak-anchoring effects at liquid crystal and alignment layer interface [15]. But a weak anchoring boundary may have the hysteresis phenomenon. We have compared the cell gap tolerance of IPS and FOP [6]. V-T curves shown in Fig. 10b correspond to cell gap d1-d4 of FOP LCD and those in Fig. 10a to cell gap D1-D3 of IPS LCD. The two V-T curves of d2 and d4, with cell gap deviation of $\pm 5\%$ from d3, almost coincide with curve of d3. For curve d1 with larger cell gap deviation $\sim 11\%$ from d3, the 6V transmittance ($T(6V)$) is 97% of on-state (6V) transmittance of cell gap d3. For IPS LCD with similar cell gap deviation (D1 and D3 with $\pm 12.5\%$ deviated from D2), differences in Von and on-state transmittance are larger as shown in Fig. 9a. From the comparison, it is obvious that FOP LCD have smaller cell gap dependence in terms of on-state voltages.

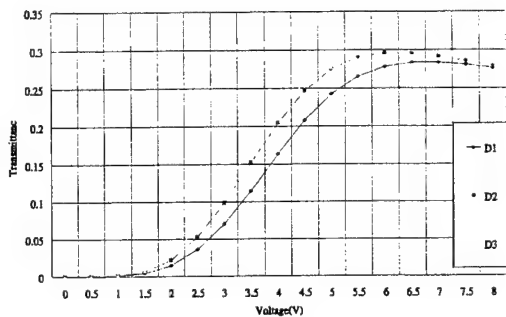


Fig. 10a Simulation results of the cell gap variations in IPS LCD.

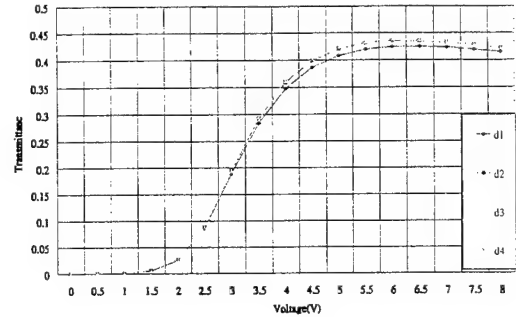


Fig. 10b Simulation results of the cell gap variations in FOP LCD

The response time of the IPS cell has the relation as follows:

$$T_{on} = \gamma / \varepsilon_0 \Delta \varepsilon (E^2 - E_c^2), \quad T_{off} = \gamma d^2 / K_2 \pi^2.$$

Where γ , d , K_2 and $\Delta \varepsilon$ are the rational viscosity cell gap, elastic constant of twist deformation and dielectric anisotropy of liquid crystal, respectively. Due to that the value of K_{22} is smaller than K_{11} and K_{33} , the response time of IPS, FOP and FFS is slower than traditional TN cell. But for the switching times between gray levels of IPS cell are fast than that of TN and MVA cells [11][19]. Some methods to increase the response time are published. Hitachi used proper LC material, smaller cell gap and high voltage (15V) to improve the response time to 20 ms [11]. IBM Japan improved the switching speed by adding a chiral agent to negative $\Delta \varepsilon$ nematic liquid crystal [20]. FFS and FOP cell use the negative type liquid crystal which has the higher value of γ and lower value of $\Delta \varepsilon$ such that the response time of these two modes is slower than IPS mode.

It is well known that the IPS mode has high value for the voltage holding ratio (VHR) [21][22]. The VHR has relation with time constant ($R*C$) and discharge path. Fig. 11a, b, c and d show the equivalent circuits for IPS, FFS, FOP and TN cell respectively. Due to the discharge path, IPS gets higher VHR than TN. The equivalent circuit of FFS is the same with IPS, but the value of capacitance is larger than that of IPS and the value of resistance is smaller than that of IPS because the electrode distance in FFS is smaller than that in IPS. For the FOP cell, the value of the storage capacitance is very large such that it has perfect property for VHR. The residual DC can be divided into two reasons. One is the ion absorption in the PI and liquid crystal interface and the other one is the discharge capacity for each layer. The first reason has relation with the material and we will not discuss here. The second one has relation with the equivalent circuit, too. With the same behavior with VHR, FOP will get the highest value of R_{dc} , FFS and IPS are the next, and TN is the smallest one. But if we consider both reasons together, it is hard to distinguish between IPS and FFS and FOP.

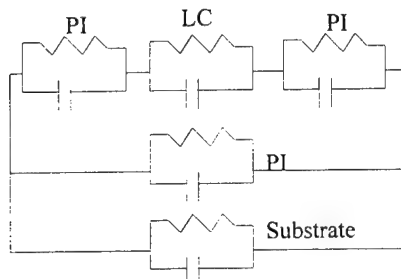


Fig. 11a The equivalent circuit of IPS

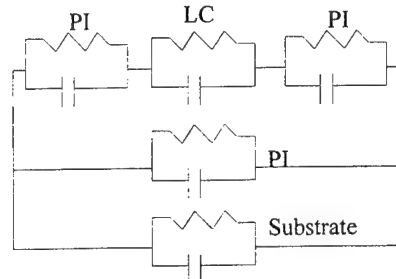


Fig. 11b The equivalent circuit of FFS

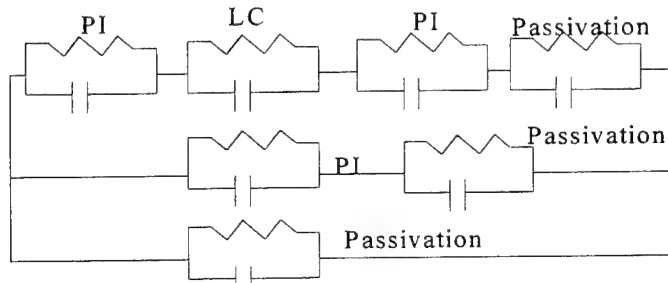


Fig. 11c The equivalent circuit of FOP.

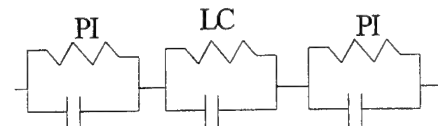


Fig. 11d The equivalent circuit of TN

The brief comparison of the three structures mentioned above is shown in Table 2 as follows.

	IPS	FFS	FOP
Color shift	worse	Less worse	Less worse
Response	faster	slow	slow
Light efficiency (T/A)	higher	high	high
Light transmission	lowest	high	highest
Gray-level inversion	good	good	good
VHR	good	good	perfect
R_{dc}	bad	bad	bad
Viewing angle	perfect	perfect	perfect
Cell gap tolerance	bad	good	good
BM material	limited	flexible	flexible
Cross-talk	Not good	better	Best

Table 2

4. CONCLUSION

In the paper, we have compared the structures and the electro-optics properties between the IPS, FFS and FOP cells. The three modes are very good in viewing angle, VHR and gray level inversion. The IPS cell has the simpler process and faster response but lowest light transmission. FOP has the largest aperture and less cross-talk, but 2-3 more process are needed. FFS is not so good compared to the FOP cell. Otherwise, the residual DC property of the FFS and FOP are not investigated much, one can put more effort on it.

5. REFERENCE

1. S. H. Lee, et. al., "High-Transmittance, Wide-Viewing-Angle Nematic Liquid Crystal display Controlled by Fringe-Field Switching", Asia Display, pp. 371-374, 1998.
2. S. H. Lee, et. al., "A Novel Wide-Viewing-Angle Technology: Ultra-Trans View", SID, pp. 202-205, 1999.
3. S. H. Lee, et. al., "A High Quality AM-LCD using Fringe-Field Switching Technology", IDW, pp. 191-194, 1999.
4. Zhiguo Meng, et. al., "Liquid Crystal Switching Using Comb-on-Plane Electrodes", IDW, pp. 125-128, 1999.
5. I-W. Wu, et. al., "Advancement in Wide-Viewing-Angle LCDS", IDW, pp. 383-386, 1999.
6. L-S. Chuang, et. al., "Study of Cell Gap Tolerance in Finger-on-Plane (FOP) LCD", SID, p-78, 2000.
7. Masahito Oh-E and Katsumi Kondo, "The in-plane switching of homogeneously aligned nematic liquid crystals", Liquid Crystals, vol. 22. No. 4, 379-390, 1997.
8. K. Kondo, "Wide-Viewing-Angle Displays with In-Plane Switching Mode of Nematic LCs Addressed by 13.3-in XGA TFTs", SID, p81-84, 1996.
9. M. Olita, et. al., "Electric Field Analysis in TFT-LCDs with In-Plane Switching Mode of Nematic LCs", Euro Display, pp49-52, 1996.
10. K. Kondo et. al., "Pixel Design concept for super TFT-LCDs", SID, PPM15-18, 1997.
11. S. Endoh et. at., "Advanced 18.1-inch Diagonal Super-TFT-LCDs with Mega Wide Viewing Angle and Fast Response Speed of 20ms", IDW, p187-190, 1999.
12. Hagen H. H. Klausmann et. al., "Optical characterization of the in-plane switching effect utilizing multi-domain structures", Amer Insti of Phys, vol 83, No 4, pp1854-1862, 1998.
13. Y. Masutani, et. al., "Novel TFT-Array Structure for LCD Monitors with In-Plane-Switching Mode", SID, p 15-18, 1997.
14. Masahito Oh-E et. al., "Quantitative Analysis of Cell Gap Margin for Uniform Optical Properties Using In-Plane Switching of Liquid Crystals", Jpn. J. Appl. Phys. Vol. 36 pp. 6798-6803, 1997.
15. M. Yoneya et. al., "Enlargement of Cell Gap Margin for Brightness Uniformity of In-Plane Switching Mode Liquid Crystal Display", AM-LCD, p 39-42, 1998.
16. S. Matsumoto et. al., "Display Characteristics of In-Plane-Switching (IPS) LCDs and a Wide-Viewing-Angle 14.5-in. IPS TFT-LCD", Euro Display, p 445-448, 1996.
17. H. Wakemoto et. al., "An Advanced In-Plane-Switching Mode TFT-LCD", SID, p929-932, 1997.
18. H. Asuma et. al., "Electrical Characteristics of Black Matrix for Super-TFT-LCDs", IDW, pp167-170, 1997.
19. H. Kagawa et. al., "Advantageous Response Characteristics of Gray Levels in the In-Plane-Switching (IPS) Mode", Euro Display, p137-140, 1999.
20. M. Hasegawa, "Response-Time Improvement of the In-Plane-Switching Mode", SID, p699-702, 1997.
21. Masahito Oh-e et. al., "Unusual Voltage-Holding Ratio Characteristics Using In-Plane Switching of Nematic Liquid Crystals", Jpn. J. Appl. Phys. Vol. 36 pp L1025-L1028, 1997.
22. Masahito Oh-e et. al., "Advantageous Voltage-Holding Ratio Characteristics Using In-Plane Switching of Nematic Liquid Crystals", IDW, p171-174, 1997.
23. D. G. Kim et. al., "Methods of forming active matrix display devices with reduced susceptibility to image-sticking and device formed thereby", U. S. Patent, 5917564, 1999.

Studies of Polymer-Stabilized Cholesteric texture films

Andy Ying-Guey Fuh^{a)}, Chi-Yen Hung, Chi-Huang Lin, and Tsung-Chih Ko

Tainan, Taiwan 701, ROC

Department of Physics, National Cheng Kung University

ABSTRACT

We report the results obtained from the studies of polymer-stabilized cholesteric texture films. Two sets of samples were fabricated. The first set were fabricated by adding various ferroelectric liquid crystal (SmC*) dopant concentrations in the mixtures. The second were fabricated using a dual-frequency liquid crystal. The experimental results obtained from the first set show that adding a small amount of SmC* could significantly improve the cells' electro-optical (E-O) characteristics. Both the driving threshold voltage and the rise time were decreased, while the hysteresis width was increased. The result from the second set shows there exists a pronounced hysteresis effect in the transmission versus frequency curve at a given applied voltage. The hysteresis width is increasing as the applied voltage is increasing. A display mode is proposed based on this bistable feature.

Keywords : Cholesteric liquid crystal, ferroelectric liquid crystal, dual-frequency liquid crystal

1. INTRODUCTION

Liquid crystal polymer dispersions have been studied intensively owing to their fundamental importance and potential use as displays and light modulating devices.¹⁻⁹ There are basically two types of liquid crystal polymer dispersions which have been reported so far. They are polymer-dispersed liquid crystal (PDLC) and polymer-stabilized cholesteric texture (PSCT) films. The polymer concentration is usually greater than 20% in the former system to confine LC's. In addition to its use in displays and light modulating devices, it can also be used as a Gaussian filter,¹⁰ switchable gratings (both electrically¹¹ and optically¹²). The polymer concentration in PSCT films is usually below 10% for use in stabilizing the cholesteric texture LC structure in the cell. Because of its high polymer content, a PDLC film has an index-matching problem, which results in a limited view angle. This index-matching problem is eliminated in PSCT films, since the polymer concentration is low. As a result, PSCT films are haze-free at wide view angles in the clear mode, and are suitable for display applications.⁶

Depending on the surface treatment of the glass substrates and on the pitch length of the cholesteric LC, we can fabricate three types of display devices for the PSCT films. Based on the mode of operation, they are classified into normal-mode (opaque in a field-off condition and clear in a field-on condition), reverse mode (clear in a field-off condition and opaque in a field-on condition) and color-reflective bistable mode.^{6,13-14}

Usually, PSCT films are fabricated using a cholesteric LC, which is a mixture of a nematic LC and a chiral dopant. In this paper, we report the results obtained from the studies of two sets of PSCT normal-mode devices. One set was fabricated by adding various ferroelectric liquid crystal (SmC*) dopant concentrations. The other set was fabricated using a dual-frequency nematic mixed with a chiral dopant. We then measured their electro-optical (E-O) characteristics. It was found in the first set samples that adding a small amount of SmC* could improve the films' E-O characteristics significantly,

^a Author to whom correspondence should be addressed
(e-mail: andyfuh@mail.ncku.edu.tw).

such as the reduction of both the threshold driving voltage and rise-time, and the increase of the hysteresis width. The causes of such improvements were found to be due to the modification of the cells' polymer networks and the increase of fills' dielectric anisotropy with the addition of SmC* in the mixture. For the second set, there exists a pronounced hysteresis effect in the transmission versus frequency curve at a given applied voltage. The hysteresis width is increasing as the driving voltage is increasing. A display mode is proposed using a dual-frequency PSCT device based on its bistable feature of the transmission versus frequency of the driving voltage.

2. EXPERIMENTAL

Two sets of PSCT films were prepared in this experiment. The first set was fabricated as follows. The cholesteric LC used was a mixture of a nematic E48 (from E. Merck) with a chiral CB15 (E. Merck) by a weight ratio of 92.0:8.0%. A laboratory-synthesized monomer Bis[6-(acryloyloxy)hexyloxy]-1,1'biphenylene (BAB-6) ~2.7wt% and a photoinitiator BME (~10wt% of the monomer) were then added in the cholesteric LC mixture. In a separated experiment, we have studied the dependence of this PSCT system on the monomer concentration. The result showed that the addition of ~2.7wt% of monomer gives the best E-O characteristic. The final mixture was then used to fabricate the first set PSCT cells with the addition of 0, 0.5, 1.0 and 1.5 times of SmC* (CS-2003; from Chisso) as much as CB15. In the following, we are referring these set samples as the PSCT cells having y-times SmC* in the mixture with y=0, 0.5, 1.0 and 1.5.

The second set PSCT films were fabricated identically to the sample having 0-times SmC* in the first set except for the nematic in the mixture (i.e. no SmC* was added in the second set samples). In this set, the cholesteric LC used was a mixture of a dual-frequency nematic DF-02XX (Chisso) with CB15. Its dielectric anisotropy $\Delta \epsilon = \epsilon_{\parallel} - \epsilon_{\perp}$ as a function of frequency is plotted in Fig. 1. Notably, $\Delta \epsilon$ is positive for $f < f_c$, and becomes negative for $f > f_c$. The crossover frequency f_c at $T=25^\circ\text{C}$ is ~1.1 KHz. It is also noted that no SmC* was added in the second set samples.

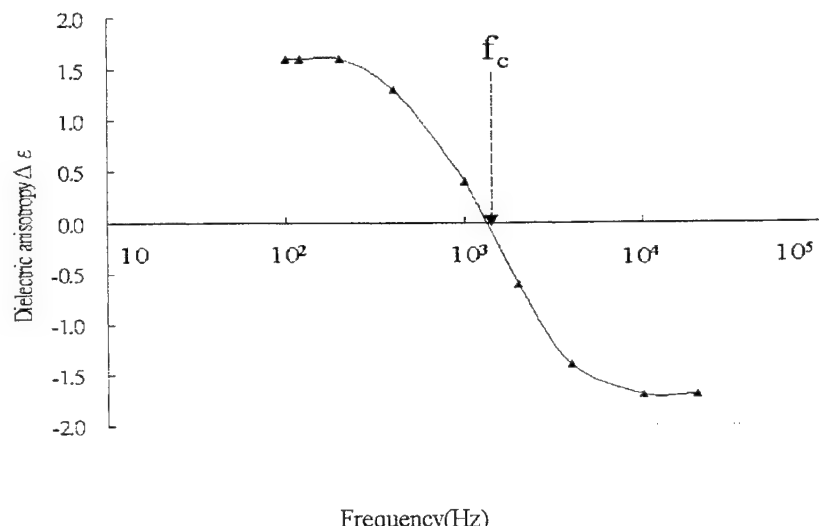


Fig. 1: Variation of the dielectric anisotropy of the dual-frequency nematic liquid crystal (DF-07XX) with respect to frequency (at room temperature). f_c is the crossover frequency.

The sample cell used in this experiment was fabricated with two indium-tin-oxide (ITO) coated glass slides, separated by a $12 \mu\text{m}$ plastic spacer. The surface of these glass substrates was cleaned without being further treated. The final mixture prepared as described above was vacuum filled into an empty cell. The filled cell was cured using a UV lamp provided by a Philips model 400/300s' metal halide lamp ~30minutes to form a sample. The UV intensity was about 3mw/cm^2 . During

curing, the LCs in a cell were aligned homeotropically with the application of a 300 Hz square-wave voltage across the ITO electrodes (~ 40 V, 65V for the first and second sets, respectively).

Details of apparatus used to perform the electro-optical measurements can be found in Ref. 15. For scanning electron microscope (SEM) study of the film's polymer network, details on how to prepare the sample can be found in Ref. 16. To measure the pitch length, cholesteric planar cells having a thickness of $12 \mu\text{m}$ were employed using a FTIR spectroscopy. Finally, an Impedance Analyzer was used to measure the dielectric constant of LC mixtures.

3. RESULTS AND DISCUSSION

The measured E-O characteristics of the first set samples are shown in Figs. 2 and 3. Let the hysteresis width ΔV be defined as the voltage difference at the mid-point of the ramp-up curve (voltage increase) and the ramp-down curve (voltage decrease) between the maximum and minimum transmission in Fig. 2. And, the threshold (driving) voltage V_{th} is defined as the voltage of the light transmission to increase 10% from the minimum in the ramp-up curve. Notably, Fig. 2 shows that V_{th} is decreasing, but ΔV is increasing with an increasing SmC* concentration in the mixture. It is also noted from Fig. 3 that the rise-time (10-90%) and the fall-time (90-10%) are decreasing and increasing, respectively, with an increasing SmC* concentration. Based on the driving scheme designed for PSCT normal-mode displays^{6,7}, it is desired to have a lower V_{th} , but a larger ΔV .

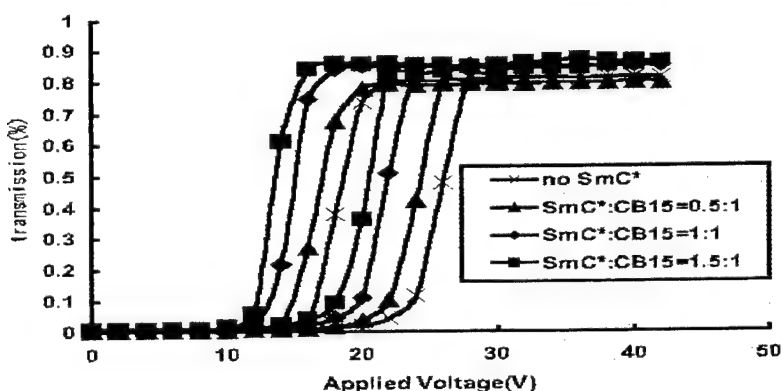


Fig. 2: Measured transmissions of the PSCT cells having y -times SmC* concentrations ($y = \text{SmC}^*/\text{CB15}$).

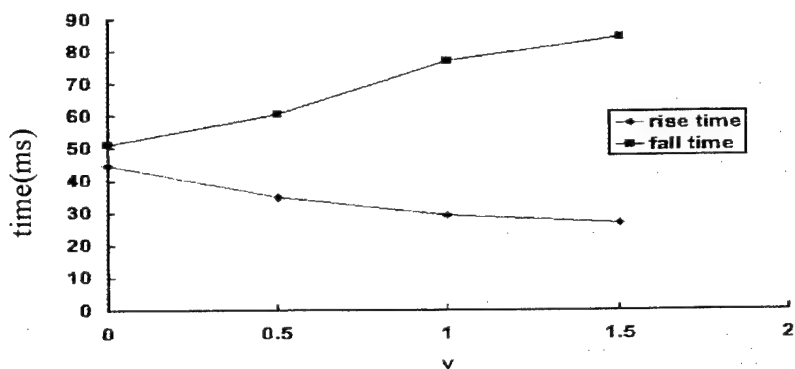


Fig. 3: The measured response times of the PSCT cells having y -times SmC* concentration ($y = \text{SmC}^*/\text{CB15}$).

In order to understand the causes that give rise to the results shown in Figs. 2 and 3. We then studied the polymer network

morphologies of these cells. The pitch length of the cholesteric LC mixtures with various SmC* concentrations was also measured. It was found that, regardless of the SmC* concentration, the cholesteric LC mixtures have about the same pitch length for the first set samples. The top-view SEM images of the cells' polymer network are depicted in Fig. 4. It is clear to see that adding a small amount of SmC* in the cell modifies the cells' polymer network morphology significantly. As the added SmC* concentration increased, more polymers were phase-separated out to form the polymer network. As a result, the formed polymer network became denser. For PSCT normal-mode cells, the polymer fibers align perpendicularly to the cells' surface. The formed polymer networks induce an alignment force on LC molecules that helps a PSCT cell to transit from its off-state (focal-conic state) to on-state (homeotropic alignment). We would expect that the denser polymer network resulting from the increasing SmC* concentration in the cell gives a stronger alignment force. The decrease of V_{th} , rise-time and the increase of ΔV and the fall-time shown in Fig. 2 and 3 are, thus, reasonable.

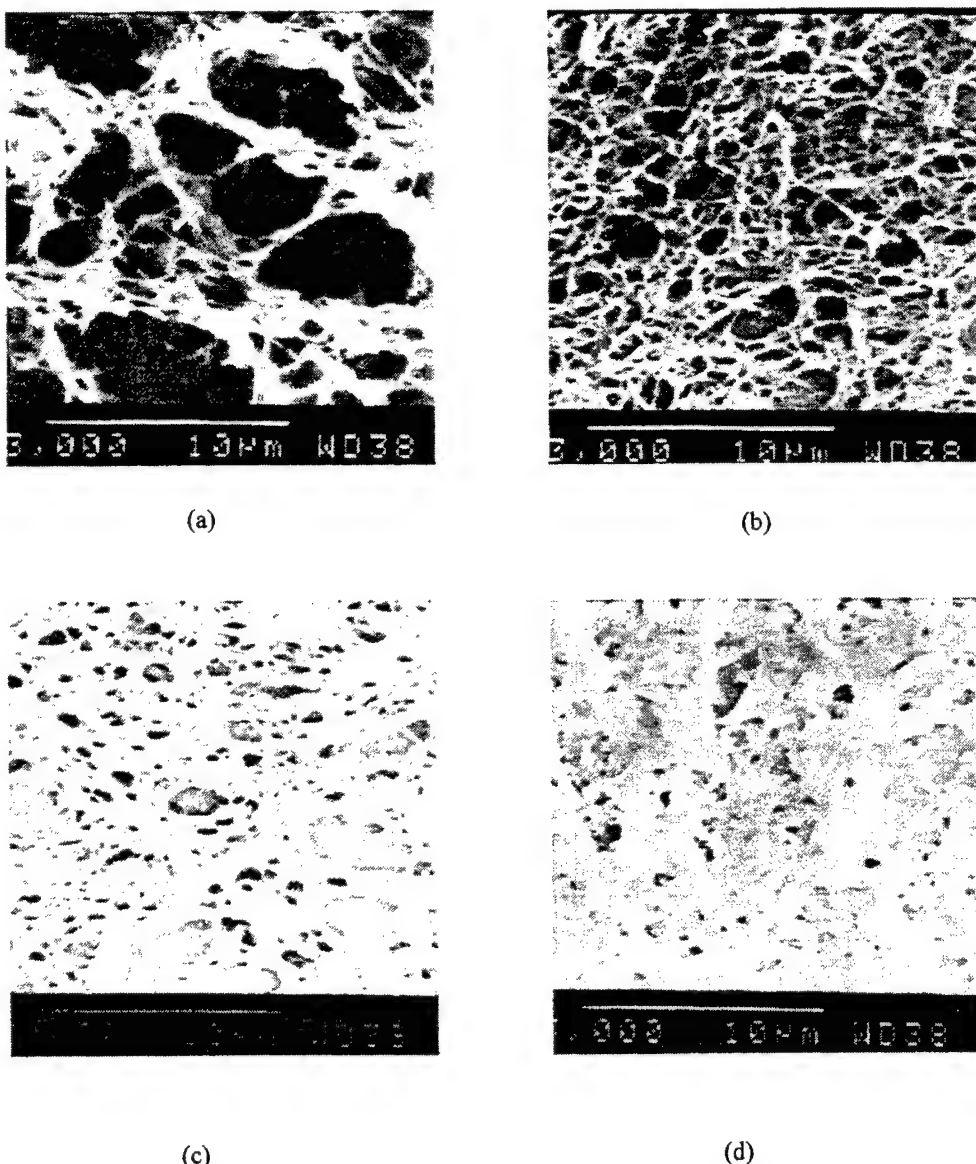


Fig. 4: Top-view SEM images of the polymer network formed in PSCT cells having y -times SmC* concentrations ($y = \text{SmC}^*/\text{CB15}$), (a) $y=0$, (b) $y=0.5$, (c) $y=1.0$, (d) $y=1.5$.

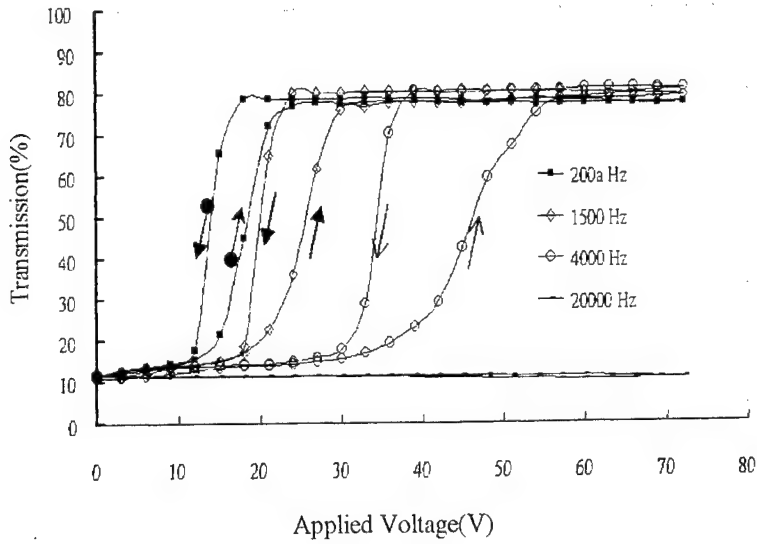


Fig. 5: Measured transmissions of a dual-frequency PSCT cell as a function of the applied voltage at four different frequencies.

Figure 5 shows the variations of the measured transmission of a dual-frequency PSCT cell with respect to the applied voltage driven at four different frequencies. Notably, both V_{th} and ΔV are increasing with an increasing frequency for the lower three frequencies. At $f=20,000$ Hz, it is not switchable. With the application of an electric field, a PSCT normal-mode cell transits from a focal-conic (helical structure) state to a homeotropic state. The V_{th} is known to be¹⁷

$$V_{th} = \frac{2\pi d}{p} \sqrt{\frac{\pi K_{22}}{|\Delta \epsilon|}}, \quad (1)$$

where p is the pitch length, $\Delta \epsilon$ is the dielectric anisotropy, K_{22} is the twist elastic constant and d is the cell's thickness. Since $\Delta \epsilon$ of a dual-frequency LC is decreasing with an increasing frequency for $f < f_c$, the increase of V_{th} with an increasing frequency shown in Fig. 5 is consistent with Eq. (1). At $f=20,000$ Hz, $|\Delta \epsilon|$ is believed to be very small, so the device is not switchable. It is noted from Fig. 1 that the device should be unable to be switched by an applied voltage at a frequency $f=f_c$. A much higher unswitchable frequency observed in Fig. 5 is believed to be due to the impurities such as CB15, BAB-6 monomer dissolved in LC. Furthermore, the decrease of ΔV with a decreasing frequency is believed to be due to the decrease of the field strength by the polarization charges. As the frequency is increasing, the liquid crystal is driven initially in the conduction regime, and then approaching to the dielectric one. The compensation effect is thus smaller as the frequency is increasing.

Figure 6 gives the variations of the measured transmissions with respect to the frequency at three driving voltages. The data points were taken every ten seconds at a given applied voltage. At low frequencies, $\Delta \epsilon$ is positive and relatively large, the cell is transparent due to its homeotropic alignment. At higher frequencies, $|\Delta \epsilon|$ becomes so small that the cell remains in the focal-conic (opaque) state. The cell transits from the homeotropic alignment (clear) to the focal-conic state (opaque) at a higher frequency when driven with a larger voltage. It is reasonable since a higher voltage could maintain the cell aligned in the homeotropic state with a relatively lower value of $|\Delta \epsilon|$ (i.e. higher frequency). It is noted from Fig. 6 that the curves trace back at different routes with lowering the frequency. There exists a pronounced "hysteresis" effect. The cause of such a "hysteresis" effect may be associated with the smaller polarization field in the higher frequency. As mentioned above, the polarization field is stronger in the low frequency (conductive) regime. The "hysteresis" width is larger when the cell is driven with a larger voltage.

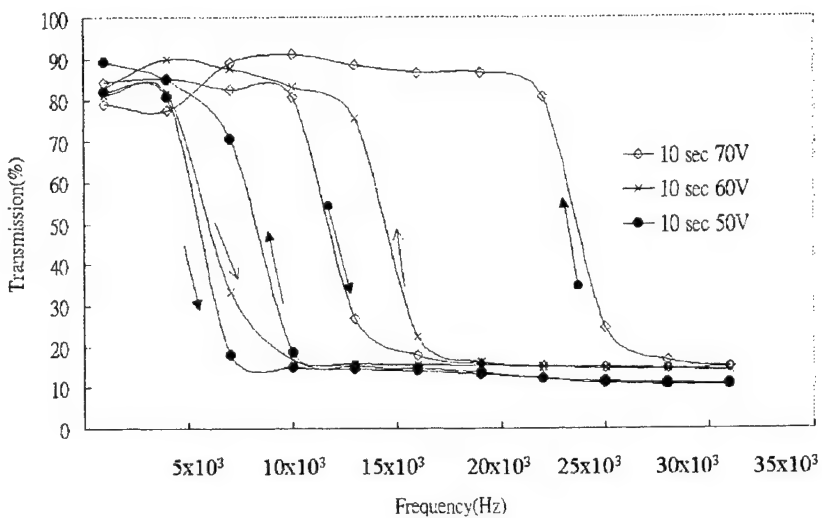


Fig. 6: Variations of the measured transmissions with respect to the frequency (T-f curve) at three driving voltages, $V_{rms} = 50V, 60V$ and $70V$. The data points were taken every ten seconds under a driven voltage

Using the bistable feature shown in Fig. 6, we propose a driving scheme for a PSCT display. Referring to Fig. 7, which is a simplified drawing representing one of curves shown in Fig. 6, the display is initially driven with an applied voltage at a frequency f_2 at C point. It is in a focal-conic (off) state. It can be switched on (homeotropic state) by increasing the frequency to f_3 ($\Delta f = f_3 - f_2$) and decreasing back to f_2 . Similarly, it can be switched off by decreasing the frequency from f_2 to f_1 ($\Delta f = f_2 - f_1$), and increasing back to f_2 .

In conclusion, we have studied two sets of PSCT samples. It is found that adding a small amount of SmC* in the mixture could result in a lower threshold voltage, a faster rise-time and a larger hysteresis width of the device. From the perspective of PSCT display applications⁷, these features are desired. In addition, a PSCT based on a dual-frequency nematic LC exhibits a pronounced “hysteresis” effect in its electrooptical curve. A display mode is proposed using this bistable feature.

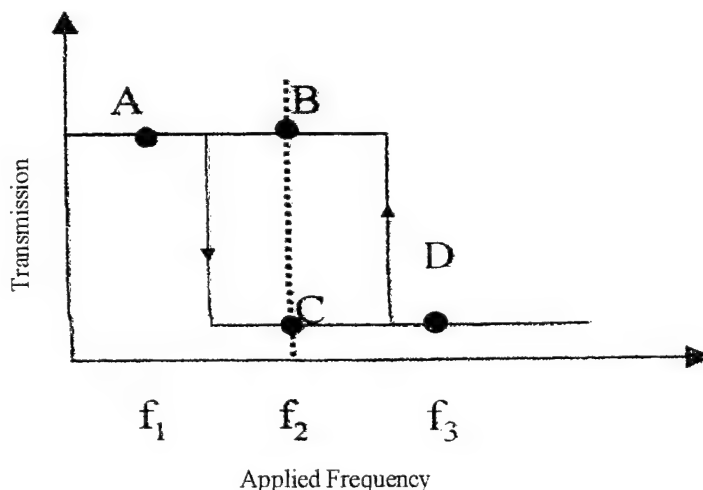


Fig. 7: A simplified T-f curve of a dual-frequency PSCT cell illustrated in Fig. 6. The cell driven by an AC voltage of frequency f_2 can be either at homeotropic (on) state or at focal-conic (off) state, depending on the change of the frequency from f_3 to f_2 or f_1 to f_2 .

ACKNOWLEDGEMENTS

The author would like to thank the National Science Council (NSC) of the Republic of China for financially supporting this research under Contract No. NSC-88-2622-E006-005.

REFERENCES

1. J. W. Fergason: SID Int. Symp. Dig. Tech. Paper **16**, (1985) 68.
2. J. W. Doane, N.A. Vaz, B. -W. Wu and S. Zumer: Appl. Phys. Lett. **48** (1986) 269.
3. P. S. Draic: J. Appl. Phys. **60** (1986) 2142.
4. S. Zumer and J. W. Doane: Phys. Rev. **A43** (1986) 3373.
5. A. Y. -G. Fuh, T. -C. Ko, Y. -N. Chyr, C. -Y. Huang, B. -W. Tzen and C. -R. Sheu: Jpn. J. Appl. Phys. **32** (1993) 3526.
6. D. -K. Yang, L. -C. Chien and J. W. Doane: Appl. Phys. Lett. **60** (1992) 3102.
7. A. Y. -G. Fuh, C. -Y. Huang, M. -S. Tsai and G.-L. Lin: Chin. J. Phys. **33** (1995) 291.
8. J. W. Doane, D. -K. Yang and Z. Yaniv: Proc. SID, Japan Display 1992, p-73.
9. Y. Fung, D. -K. Yang, J. W. Doane and Z. Yaniv: Research conf. Euro Display 1993, p-157.
10. A. Y. -G. Fuh, C. -Y. Huang, B. -W. Tzen: Jpn. J. Appl. Phys., part I **33** (1994) 1088.
11. A. Y. -G. Fuh, M. -S. Tsai, C. -Y. Huang, T. -C. Ko, and L. -C. Chien: Opt. Quantum Electron **28** (1996) 1535.
12. A. Y. -G. Fuh, M. -S. Tsai, L. -J. Huang and T. -C. Liu: Appl. Phys. Lett. **74** (1999) 2572.
13. D. -K. Yang, L. -C. Chien, and J. W. Doane: SID 1991 Int. Symp. Dig. (1991) p.49.
14. D. -K. Yang, L. -C. Chien and J. W. Doane: SID 1992 Int. Symp. Dig. (1992) 759.
15. A. Y. -G. Fuh, T. -C. Ko and M. -H. Li: Jpn. J. Appl. Phys. **31** (1992) 3366.
16. A. Y. -G. Fuh, C. -Y. Huang and C. -W. Lau: Jpn. J. Appl. Phys. **36** (1997) 2754.
17. P. G. deGennes: Solid State Comm. **6** (1968) 168..

Comparison between Reflective LCDs with Diffusive Micro Slant Reflector (DMSR) and Bump Reflector

C.-J. Wen, D.-L. Ting, C.-Y. Chen, L.-S. Chuang, C.-C. Chang, and Y.-J. Wong

Electronics Research and Service Organization, Industrial Technology Research Institute,
Hsinchu, Taiwan 310, ROC

ABSTRACT

A reflective TFT-LCD with an internal asymmetric diffusive micro slant reflector (DMSR) is developed to enhance the light efficiency¹⁻³. The DMSR structure is optimized to obtain a desired light distribution cone with asymmetric characteristics. In this paper, we will compare the optical properties of a reflective TFT-LCD panel with a DMSR structure and those of a reflective LCD with symmetric bump structure reflector. Since the light intensity distribution of a reflective LCD depends strongly on the behavior of the incident light source, we used two different incident light sources for illumination. One is collimated light, and other is diffused light. The conoscope is then used to understand the light distribution of the panels in all directions. When the collimated light source is used for illuminating the reflective LCD panel, the brightness of a LCD panel with DMSR is about 2 times of that of a LC cell with a symmetric bump type reflector. If the incident light is the diffusive type, the reflectance of a bump reflector will be independent of the viewing angles. However, the diffusive property of the new DMSR design will redistribute the reflected light so that an asymmetric viewing cone can be generated to increase the brightness in this area. The asymmetric property of the cone is a result of the slant structure. The experimental results demonstrate that the DMSR structure can redirect the collimated light in a designated area. Due to the effect of DMSR, the peak of reflected light is shifted away from the surface specular reflection and the light distribution is wider. Normal environment contains both the collimated and diffusive light. With the DMSR structure, we can utilize both light sources and make our panel much brighter, suitable for many information applications.

1. INTRODUCTION

The increasing demands of portable information tools with high information content, such as personal digital assistants, hand-held personal computers, and digital still cameras, have created a new market for high quality and low power consumption flat panel displays. Full-color reflective LCDs (RLCD) with merits of low power consumption, light weight, compact size and good legibility under the sunlight are the most suitable devices for such market requirements. Several types of reflective LCD mode have been proposed such as PCGH mode, PDLC mode, ECB mode, MTN mode and R-OCB mode. However, it is obviously that most of them did not show favorable performance when compare with a transmissive LCD or CRT. Among these LCD modes, MTN mode has shown high contrast ratio and high brightness. ERSO/ITRI has spent a great amount of effort in the development of single-polarizer MTN-RLCD⁴⁻⁷ due to its advantages of high contrast, high brightness and high productivity. MTN mode also has some other attractive features, such as low operation voltage, wavelength insensitivity, wide viewing angle, and fast response. Recently, we have developed an internal diffusive micro slant reflector (DMSR) structure. It is well to change the diffusive property of the reflector and to improve the

light efficiency of a reflective LCD. In this paper, we will compare the optical properties of a 6.4" reflective TFT-LCD panel with a DMSR structure and that of a reflective LCD with a symmetric bump reflector. The 6.4" reflective LCD panel with DMSR structure has a VGA resolution and an aperture ratio of 59%. It shows 2~4 times brightness enhancement compared with that of a mirror reflector. In addition, the contrast ratio is over 20:1 in the angles from 0 to 30 degrees. When combined with color filters, this structure shows reflectivity of 42% (~ 75% of newspaper) relative to a Lambertian white standard, measured at display's normal direction under -30° collimated illumination condition. This configuration provides a much brighter image, compared with those with internal micro bump-diffusive structures⁸⁻⁹ in the designated area. However, the internal symmetric bump reflector can have a more uniform light distribution when the panel is illuminated by a diffusive light source. When collimated light source is used to illuminate the panel, bump reflector also can obtain a uniform light distribution in a larger area than that with a DMSR structure.

2. DEVICE CONFIGURATIONS

To obtain a reflective LCD with high resolution and no parallax, a diffusing reflector with rough surface must be placed inside the panel. Therefore, the design of the surface structure of the internal diffusing reflector will dominate the optical properties of a reflective LCD panel. As we know, the internal reflector used in conventional reflective LCD is a flat mirror type or a symmetric bump structure type. In those structures, the brightest portion of a reflected image is severely affected by the specular reflection of the top surface of the LCD panel. In such instance, the distribution of the reflected image close to the specular reflection is wasted because it does not have enough contrast ratio in these directions. Thus, the overall brightness and contrast is not satisfactory enough. Recently, we have developed a diffusive micro slant reflector (DMSR) structure. The DMSR structure can scatter the ambient light into a desired light distribution cone with asymmetric characteristics. When the DMSR structure is used in a LCD panel, the brightest portion of the reflected image is shifted to the normal observer's direction, away from the specular reflection of the top surface. Therefore, the ambient illuminating light could be used more efficiently to increase the brightness and contrast in the designed viewing direction. The normally white mixed-mode TN (MTN) mode⁵⁻⁷ is adopted because of its large tolerance to cell-gap variation caused by the DMSR structure.

The basic configuration of reflective LCD with MTN LC mode and DMSR structure is shown in Figure 1. This device is composed of a polarizer, a quarter-wave retardation film, a MTN liquid crystal cell, a set of micro color filters and an asymmetric diffusive micro slant reflector. The DMSR is coated with a metallic thin film, such as aluminum or silver, on the inner side of the bottom substrate of the LC cell. The other reflective LCD panel that we used to compare with this new reflective LCD with DMSR structure is composed of a polarizer, a quarter-wave retardation film, a MTN LC and a symmetric bump structure reflector. The bump structure is also deposited with a metallic thin film on the inner side of the bottom substrate of the LC cell. Figure 2 illustrates the configuration of reflective LCD with bump reflector. This bump reflector is more suitable to be used in a diffusing illuminating condition.

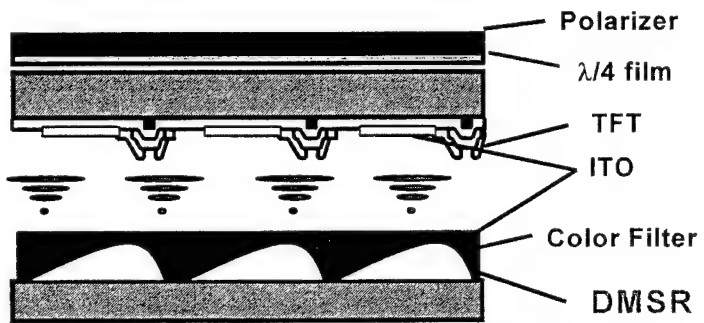


Fig. 1 The basic configuration of a color reflective TFT-LCD with the internal DMSR structure.

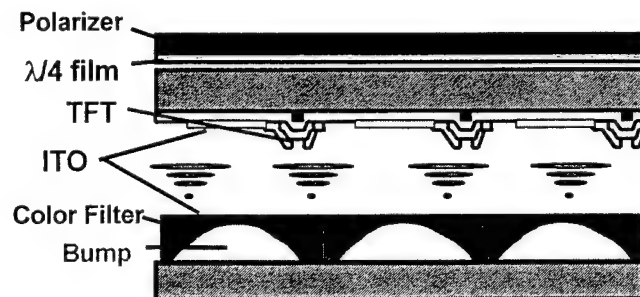


Fig. 2 The basic configuration of a color reflective TFT-LCD with a internal Bump structure reflector.

3. THE DMSR AND BUMP REFLECTOR FABRICATION PROCESSES

The photolithographic method is applied to generate the diffusive micro slant structure. First, the photoresist is coated on the raw glass substrate. Then the photoresist is exposed by a multi-step exposure method to create the MSR structure. After that, a second exposure is applied to obtain a bump structure on the MSR surface. Finally, appropriate control of the developing and baking condition will result in a well slant-bump structure. The slant-bump structure could achieve an intelligent asymmetric scattering property. The diffusive property is strongly influenced by the detail procedure of the exposure processes, since the photoresist used here is very sensitive to the photolithography processes. In order to using this slant-bump structure in a reflective LCD, aluminum is then deposited onto the diffusive micro slant surface to complete the DMSR process. Figure 3 shows the profile of the proposed DMSR structure measured by an atomic force microscope.

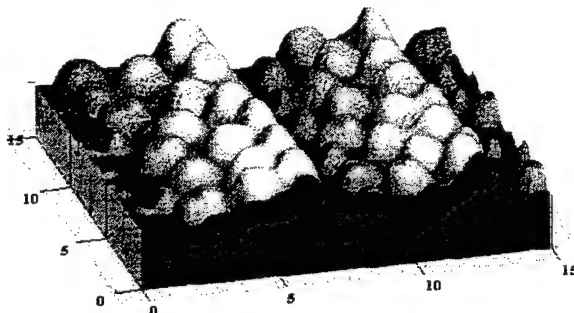


Fig. 3 DMSR profile measured by an atomic force microscope.

The bump structure is also obtained by the photolithography method. The photoresist used for generating bump structure is different from that for preparing DMSR structure. We have developed a single-step exposure method for generating bump structure. In this new method, we don't need an additional overcoating process. And, the shape of bump structure is very sensitive to the developing condition. The shape of bump structure will strongly influence the light scattering properties. The profile of this new bump structure reflector measured by an atomic force microscope is shown in Figure 4.

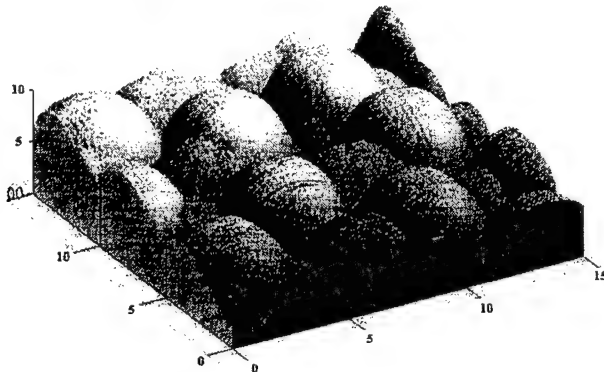


Fig. 4 Bump structure profile measured by an atomic force microscope.

4. OPTICAL PROPERTIES OF TFT-LCD WITH DMSR AND BUMP REFLECTOR

In our reflective LCD panels, the normally white MTN mode is adopted. The liquid crystal used is for low driving voltage and was provided by Chisso Corp.. We used two different optical measurement system to understand the optical performance of these 6.4" reflective TFT-LCDs. One is the Goniometric measurement system, the other is the Conoscopic measurement system.

4.1 Goniometric Measurements

Some of the characteristics of LCD panels are just measured by Goniometric system. The V-R curve of our 6.4" reflective TFT-LCD is shown in Figure 5.

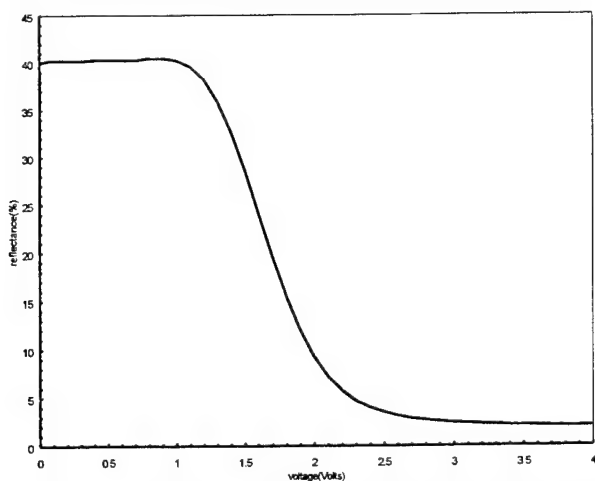


Fig. 5 The V-R curve of ERSO's 6.4" full-color reflective LCD with DMSR.

The V-R curve for both DMSR and bump reflector is almost the same. In this measurement, the incident light was illuminated from -30° relative to the normal direction of the panel and the detector was at the normal direction. Based on the liquid crystal material that we used, the threshold voltage is about 1 volt and the saturation voltage can be as low as 3 volts. Fig. 6 shows the reflectivity and contrast ratio as a function of viewing angles. The viewing angles vary from 0° to 60° in the plane of incidence. Due to the effect of DMSR, the peak of reflected light is shifted away from the surface specular reflection and the light distribution is wider. The reflectance at 0° is about 42% ($\sim 70\%$ of newspaper) relative to a Lambertian white standard. The contrast ratio is about 20:1.

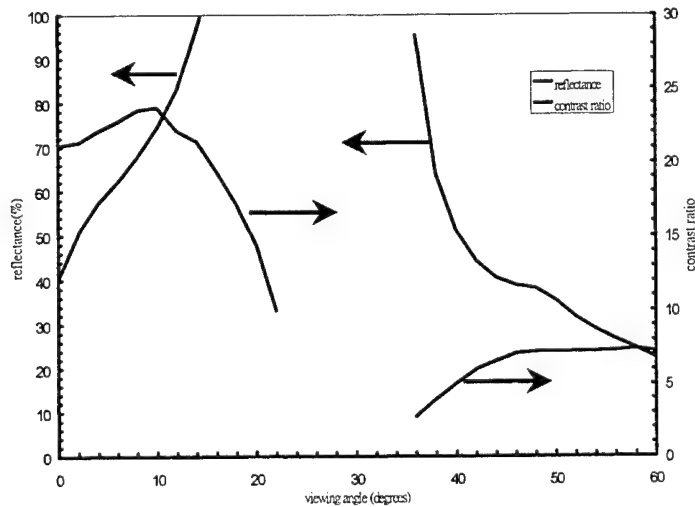


Fig. 6 Reflectance and contrast ratio of reflective LCD with DMSR.

The brightness of reflective LCD with DMSR is about 4 times when compared with that of a LC cell with a mirror type reflector as shown in Figure 7.

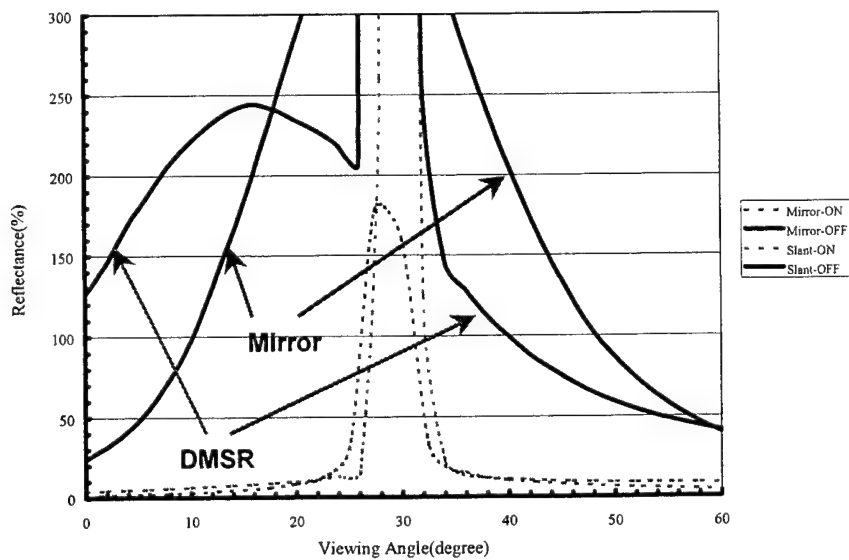


Fig. 7 Light scattering property of DMSR and Mirror reflector+Diffuser

The CIE chromatic behavior of the 6.4" reflective TFT-LCD is shown in Figure 8. Without using a polarizer, the white balance point is very close to the C light source. Because the transmission spectrum of the polarizer suppresses the blue color, the white balance point shifts away from the C light source after the polarizer is used. The reflection spectrum of our 6.4" reflective LCD is shown in Fig. 9. In the figure we can see that the reflective spectrum is very uniform from 380nm to 780nm in the normal viewing direction ($B=0$). The color becomes yellowish when the viewing angle is increased.

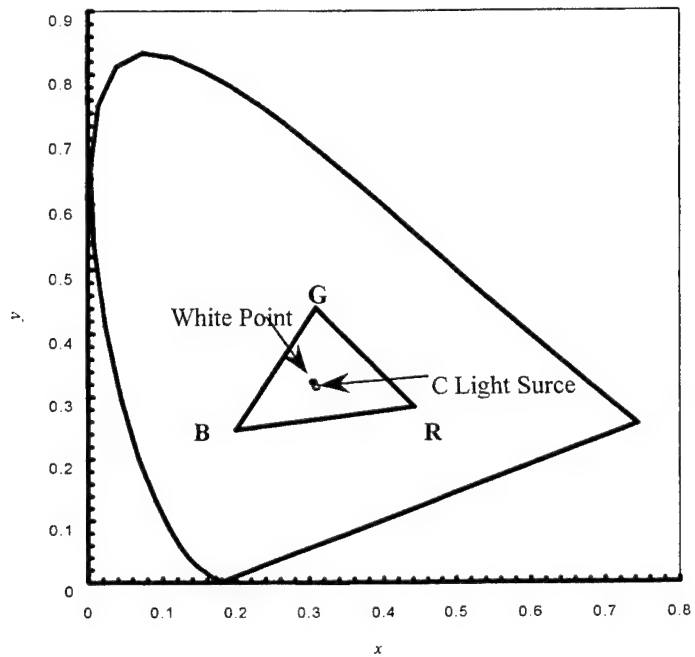


Fig. 8 The Color gamut of 6.4" TFT-LCD with DMSR.

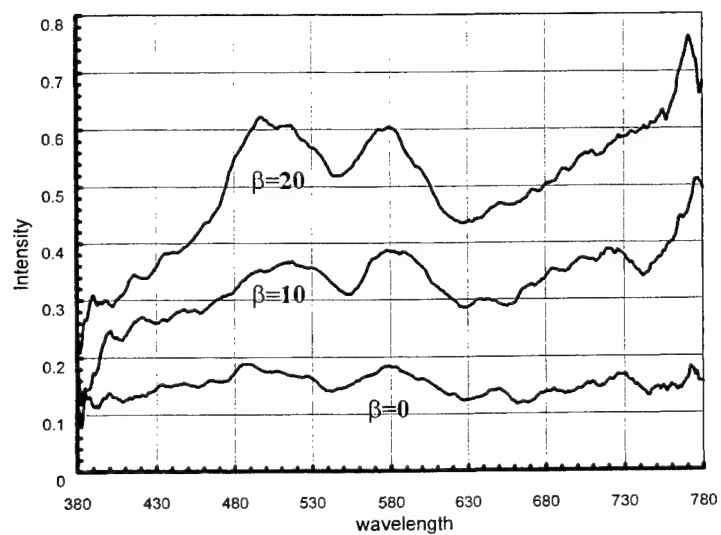


Fig. 9 The reflection spectrum of 6.4" full-color reflective TFT-LCD with DMSR.

When we compare the light distribution of DMSR, bump reflector and GameBoy in the plane of incident. We can find that the brightness of DMSR is about 3 times of that of bump reflector or Gameboy. The measurement is shown in Figure 10.

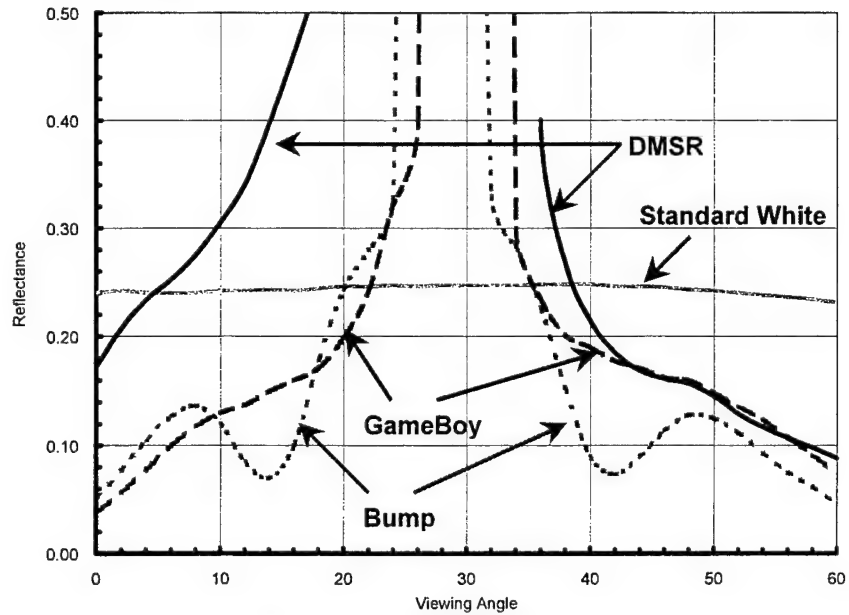


Fig. 10 Light scattering distribution of DMSR, bump and GameBoy.

The other important issue that must be considered is that the influence of DMSR asymmetric structure when illuminate from different direction with respect to the arrangement of DMSR structure. Figure 11 illustrates that when the illuminating light is rotated to 70°, the bightness of DMSR in most portions of the viewing angle is smaller than that of bump reflector(GameBoy).

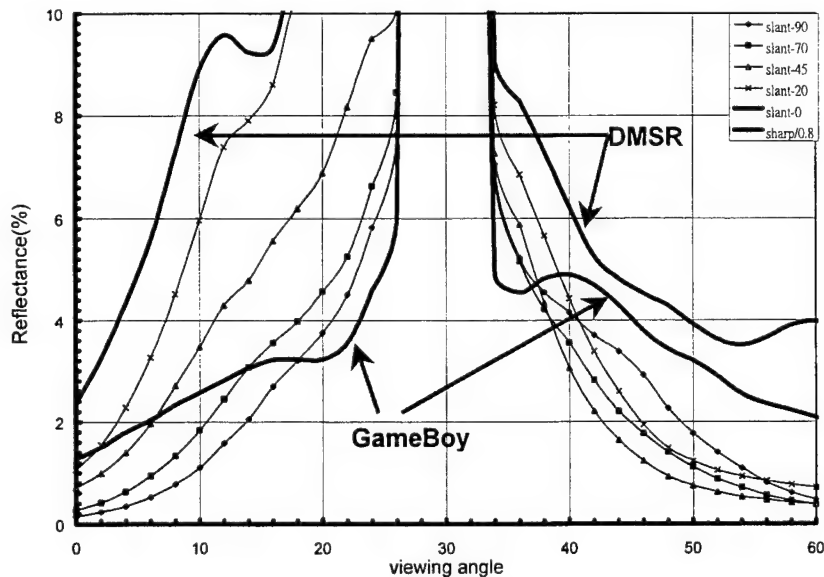


Fig. 11 Light scattering distribution for several different light incident conditions with respect to the direction of DMSR.

4.2 Conoscopic Measurements

In order to compare the light distribution in the whole space. We then used the conoscope to understand the optical distribution of our panel in all directions. CONOSCOPE (autronic-Melchers) and EZcontrast (ELDIM) are used to measure the light distribution of reflective LCD with DMSR and bump reflector. The light intensity distribution of reflective LCD depends strongly on the behavior of the incident light source. First, we used the collimated light as the incident light source. Fig. 12a shows the distribution of the reflected light intensity. Here the collimated light was located at an angle of 30 degrees relative to the normal axis of the panel. We then observed the light distribution at the cross section passing through the light source. The reflective intensity as a function of the viewing angles is shown in Fig. 12b. It clearly shows that there is a strong specular peak at -30 degrees. Besides that, some light is reflected in the region between 0 and 20 degrees. This demonstrates that the DMSR structure can only redirect the collimated light in a designated area. In general, the reflector with bump structure is optimized to obtain a light scattering distribution with symmetric characteristics. The reflective TFT-LCD with a bump reflector shows well uniform reflectance over a wide range of viewing angle symmetrically. This measurement result is shown in Figure 13.

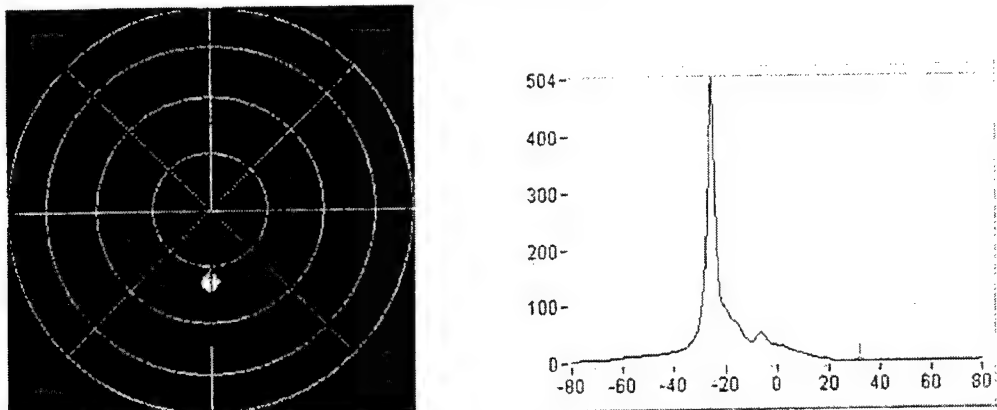


Fig. 12 (a) Reflected light intensity distribution for collimated light source. (b) One cross section.

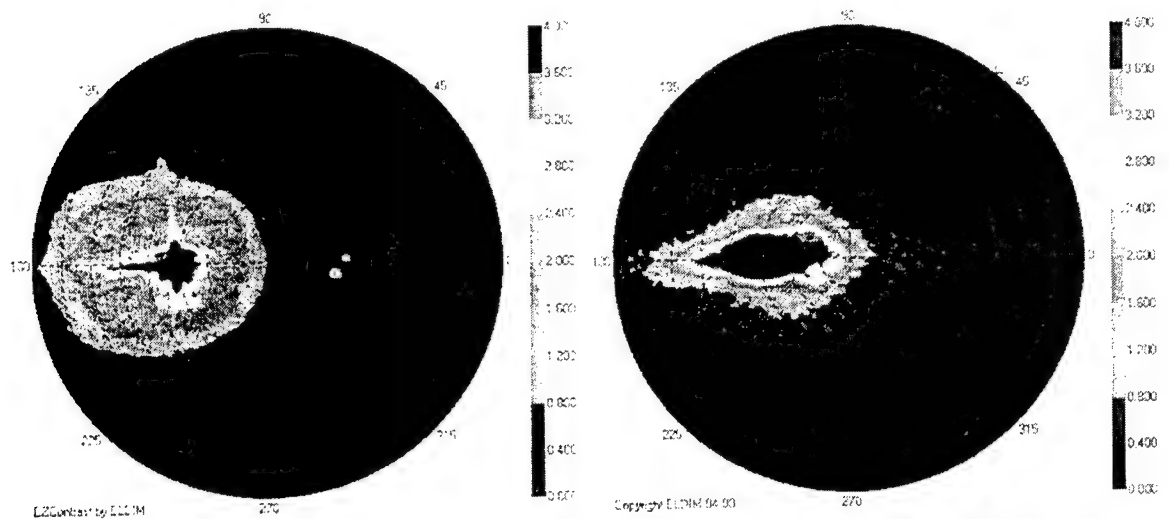


Fig. 13 Illuminating by collimated light source, reflected light distribution of (a)bump reflector (b) DMSR

If the incident light is the diffusive type, the light intensity distribution is shown in Fig. 14. The diffusive light source is generated by using the collimated light at the normal direction, so a specular peak can still be observed at 0 degree in Fig. 14b. In the conoscopic measurement, the reflectance will be independent of the viewing angles for both the bump reflector and a Lambertian white standard. The diffusive property of our DMSR design will redistribute the reflected light at larger angles so that a viewing cone can be generated to increase the brightness. This cone is from -60 degrees to 40 degrees. The asymmetric property of the cone is a result of the DMSR structure. That also causes the reflectance in the region of the negative angles greater than that in the other direction. Fig. 14a is the ISO-luminance contour of our panel. It clearly shows that the bottom-right part will be the best viewing region. Normal environment contains both the collimated and diffusive light. With the DMSR structure, we can utilize both light sources and make our panel much brighter, suitable for many applications mentioned above.

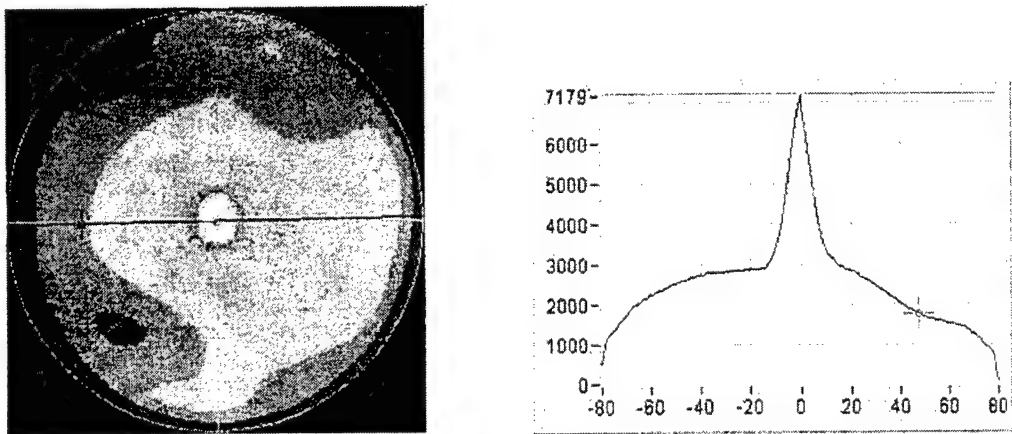


Fig. 14 (a) Reflected light intensity distribution for diffusive light source. (b) One cross section.

5. CONCLUSION

We have compared the optical properties of reflective LCDs with an asymmetric DMSR and that with a symmetric bump reflector. A reflective TFT-LCD with an internal asymmetric diffusive micro slant reflector (DMSR) is developed to enhance the light efficiency. The DMSR structure is optimized to obtain a desired light scattering distribution cone with asymmetric characteristics. The reflective TFT-LCD with a DMSR exhibits high reflectance and high contrast ratio over a wide range of viewing angle. In general, the reflector with bump structure is optimized to obtain a light scattering distribution with symmetric characteristics. The reflective TFT-LCD with a bump reflector shows well uniform reflectance over a wide range of viewing angle symmetrically. If the incident light is the diffusive type, the reflectance of a bump reflector will be independent of the viewing angles. However, the diffusive property of the new DMSR design can redistribute the reflected light so that an asymmetric viewing cone can be generated to increase the brightness in this area. The asymmetric property of the cone is a result of the DMSR structure. Normal environment contains both the collimated and diffusive light. With the DMSR structure, we can utilize both light sources and make our panel much brighter, suitable for many information applications. The DMSR structure can get better performance than the bump reflector in the viewing angle range from normal direction to 60 degrees.

ACKNOWLEDGMENT

We would like to thank Dr. I-Wei Wu, Deputy Director of ERSO, for his encouragement and support. We would like to thank Chisso Corp. and autronic-Melchers GmbH for providing us the LC materials and the conoscopic measurements, respectively. This work is supported by the Ministry of Economic Affairs of R.O.C. government through ERSO/ITRI.

REFERENCES

1. C.-J. Wen, D.-L. Ting, C.-Y. Chen, L.-S. Chuang and C.-C. Chang, "Optical Properties of Reflective LCD with Diffusive Micro Slant Reflectors (DMSR)," SID'00, to be published (2000).
2. W.-C. Chang, C.-J. Wen, D.-L. Ting, J.-W. Shiu, L.-S. Chuang and C.-C. Chang, "A Novel Reflective LCD with Diffusive Micro Slant Reflector," EuroDisplay '99 Late-News, pp.49-52 (1999).
3. D.-L. Ting, W.-C. Chang, C.-Y. Liu, J.-W. Shiu, C.-J. Wen, C.-H. Chao, L.-S. Chuang and C.-C. Chang, "A High Brightness and High Contrast Reflective LCD with Micro Slant Reflector(MSR)," SID '99, pp.954-957 (1999).
4. S.-T. Wu and C.-S. Wu, "Mixed-mode twisted nematic liquid crystal cells for reflective displays", Appl. Phys. Lett., 68, p.1455 (1996).
5. C.-L. Kuo, C.-K. Wei, S.-T. Wu, et al, "Reflectivedirect-view display using a mixed-mode twisted nematic cell," Jpn. J. Appl. Phys. Vol.36, p.1077, (1997)
6. S.-T. Wu, C.-S Wu, and C.-L.Kuo, "Reflective direct-view and projection displays using twisted-nematic liquid crystal cells," Jpn. J. Appl. Phys. Vol.36, p.2721, (1997)
7. C.-L. Kuo, C.-L. Chen, D.-L. Ting, C.-K. Wei, C.-K. Hsu, B.-J. Liao, B.-D. Liu, C.-W. Hao, and S.-T. Wu, "A 10.4-in. Reflective MTN-Mode TFT-LCD with Video-Rate and Full-Color Capability," SID'97, pp.79-82, (1997).
8. D.-L. Ting, C.-Y. Liu, C.-W. Shiu, W.-C. Chang, H.-T. Wei and C.-J. Wen, "A High-Contrast and High Brightness Reflective LCD with an Internal Diffusive Reflector", ASID '99, pp. 41-44 (1999).
9. Y. Ishii and M. Hijikigawa, "Development of Highly Reflective Color TFT-LCDs", Asia Display 98 Digest, pp. 119-122 (1998).

Intensive Optical Field Improves the Photopolymerization-induced Alignment Quality of Liquid Crystals

Sun Li^a and Wang Shumei^b

^aDepartment of Biochemistry, Yantai University, Yantai, 264005, P. R. China

^bLab Of Excited State Processes, Changchun Institute of Physics, Changchun 130021, P. R. China

E-mail: sunwangl@public.ytptt.sd.cn

Abstract

Based on a novel concept that intensive optical field may improve alignment of polymer films photopolymerized by linearly polarized laser light, we investigated effects of instantaneous intensity of the laser light and viscosity of the films on alignment of liquid crystals on the photopolymerization-induced anisotropic films. The intensity and the viscosity are the two essential factors related intimately to magnitude and relaxation time of the reorientation Kerr effect. The experiments demonstrated that the increase in the intensity and the decrease of the viscosity improved the photopolymerization-induced orientation of the films. Based on the photochemical points, we discussed causes of the improvement.

Key words: Kerr Effect; Photo-induced Alignment; Photopolymerization; Liquid Crystals

1. Introduction

Recently photo-induced alignment of liquid crystals (LCs) on thin layers of polymers has been attracting many researchers owing to its great potential for replacing the conventional rubbing techniques. The rubbing techniques often causes electric and mechanical damage to the polymer films, such as the generation of static charge, dusts and grooves in the process. The photo-induced LC-aligning techniques extensively reported¹⁻¹¹ are established mainly on the bases of either anisotropic photoisomerization of dichroic dyes doped in polymer films¹⁻⁴ or anisotropic photopolymerization of actinic polymer films⁵⁻¹⁰ under linearly polarized light. For both of the techniques, the orientation quality of the polymer films, on which LCs anisotropically align, depends directly upon the efficiency of the anisotropically induced photoreactions in the path of the acting light, because the orientation originates from the photoreaction products of the actinic molecules in the films whose transition dipolar moments are parallel to the polarization direction of the acting light and from the steric interaction exerted by the products on their adjacent molecules.

Paparo et al¹¹ reported that the optical Kerr effect associated with light-induced molecular orientation largely enhances the alignment of anisotropic molecules in a transparent liquid doped with a small amount of dye. They ascribed the enhancement to two processes: electronic excitation of molecules induced by light absorption that generates oriented populations of excited and ground-state molecules and intermolecular interactions originated from photo-induced molecular transition dipole that generates an anisotropic intermolecular force field; the orienting actions add to the direct optical field action¹¹. In accordance with the concept of reorientational Kerr effect, intensive optical fields of laser pulses can distort electron distribution of a molecule and lead to generating an instantaneous dipolar moment in it. Driven by the optical field, the induced dipolar moment may rotate and strive to be parallel to the field direction. Consequently, structural parts of the molecule related to the range of the distorted electron distribution reaching may reorientate with the induced moment. Under specified conditions, the reorientational Kerr effect is a main contributor of third-order optical nonlinearity, and it can be evaluated by magnitude of third-order refraction. Moreover, the relaxation time of the Kerr effect is intimately related to viscosity coefficient of liquid systems and to excited-state lifetime of molecules when wavelengths of laser pulses are within absorption bands of the molecules.

Here we present an approach of photopolymerization-induced LC orientation based on the concept that the intensive optical field of linearly polarized laser light may enhance the photopolymerized-induced anisotropic alignment of polymer films. A coumarin derivative was used as the actinic prepolymer; in it the coumarin structure, equivalent to dichroic dyes, is the part that responds to the active light field of high intensity and reorientates with the direction of the light field. The reactive bond of (2+2)-cycloaddition lies in the coumarin part, and its excited-state dipolar moment is parallel to polarization of the coumarin structure. This feature favors the anisotropic polymerization induced by the laser light. The obtained results demonstrate that reorientational Kerr effect can improve anisotropic alignment of the polymerized spin-coated polymer films.

2. Material and methods

Actinic prepolymers of spin-coated polymer films are coumarin derivatives (Fig. 1). They can polymerize by (2+2)-cycloaddition under 355nm linearly polarized light⁵. The polymer films were made with the actinic prepolymer spin-coated on ITO glass substrates. The films were used to polymerize immediately after they were made in unsolidified state, or after solidified at 130°C for 2h.

Anisotropic photopolymerization of the spin-coated polymer film, either fresh or solid, was performed for 10min under linearly polarized 355nm laser pulses, third harmonic of Q-switched mode-locked Nd:YAG laser, of 35ns (FWHM) and 250ps (FWHM) pulse train with 7 pico-pulses whose intervals are 7.5ns. Fig.2 shows the set-up for the experiment. Both of the active lights had same energy. Three kinds of the photopolymerized films were used to fabricate LC cells of conventional sandwich type.

Third-order nonlinearity of the used actinic prepolymers was measured by Z-scan technique¹². The prepolymers dissolved in N,N-Dimethylformamide at a weight ratio of ~0.1% was filled in a 1.0mm thick curette. The Z-scan was performed with the third harmonic of Q-switched mode-locked Nd:YAG laser in the TEM₀₀ mode. The 250ps (FWHM) pulse train with 7 pico-pulses whose intervals are 7.5ns were focused to a beam radius of 12.3μm (HW 1/e² M), and $I_0 = 24.8 \text{ MW/cm}^2$

3. Results and Discussions

We experimentally investigated effects of two essential factors on photopolymerization-induced orientation of the polymer films in order to study the influence of reorientational Kerr effect, an intensive optical field effect, on photo-induced alignment of liquid crystals. One is intensity of acting light, and the other is viscosity of the polymer films. In evaluating the intensity effect, we anisotropically photopolymerized the solidified polymer films by exposing them respectively to the 355nm 250ps(FWHM) pulse trains and the 355nm 35ns(FWHM) pulses. The single pulse train has the same energy as the single 35ns pulse; however, the ratio of their intensities (I_{ps}/I_{ns}) is 35 for the same irradiation area supposed that average energy per pulse in the pulse train is 0.25E. The intensities are calculated from formula of the peak irradiance $I=E/S\tau$, where E is pulse energy, S is irradiation area and τ is pulse duration. Instead of single picosecond pulses, We used picosecond pulse trains to induce anisotropic photopolymerization of the polymer films to ensure that the films get enough illumination for the photoreaction, which was the reason that the picosecond pulse trains were used in the Z-scan. In investigating the viscosity effect, we substituted the fresh spin-coated polymer films not solidified by baking for the baked films; but they were heated at 70°C meanwhile exposed to the 250ps pulse trains. As shown in Fig.3, (b) presents the LC alignment better than (a), and (c) is the best one. These results exhibit that the increase in the laser intensity and the decrease of the polymer film viscosity improve the reorientation of the photopolymerization-induced films.

The peak-valley configuration obtained from the normalized Z-scan curve (not shown) indicated that the nonlinearity of the prepolymer was negative. Its nonlinear refractive index under these conditions was determined to be $n_2=2.37 \times 10^{-9}$ esu. The rise-time of a thermal lens in a liquid is determined by the acoustic transit time $\tau=\omega/v_s$, where v_s is the velocity of sound in the liquid and ω_0 beam waist radius. In the present experiment, $\omega_0=12.3\mu\text{m}$ and $v_s=10^5\text{cm/s}$, we obtained a risetime of 12.3ns. Obviously, owing to accumulating effect at the end of several pulses electrostrictive and thermal effects may produce. Because the picosecond laser pulse trains have only seven pico-pulses and 7.5ns pulse interval¹³, they are not major origins of the nonlinearity. Therefore, the major origination of the third-order nonlinearity is reorientational Kerr effect. In contrast, the electrostrictive and thermal effects are major origins of the prepolymer nonlinearity under the optical pulse with 35ns (FWHM) duration. That means the prepolymer molecules can be reorientated when the optical intensity is high enough to result in the Kerr effect.

When the two kinds of acting light have the same energy at 355nm, the photopolymerization probability of the films is equivalent in the range of linearity. When the intensity of acting light increases higher enough, optical nonlinearities occur. There are several origins of third-order optical nonlinearity in isotropic media, such as thermal effect, electrostriction and reorientational Kerr effect. Of them only the reorientaional Kerr effect is anisotropic. Obviously, the reorientaional Kerr effect may enhance the anisotropic alignment of the pepolymers in the films; therefore, it gives its contribution to the improvement of the quality of the anisotropic photopolymerization in the films in our experiments.

The reorientational Kerr effect leads to the increase in the number of the pairs of the actinic molecules that couple in spatial positions for the anisotropic photopolymerization, so that the probability of the reaction is increased. Consequently, it improves the anisotropic alignment of the polymer films. In addition, the low viscosity of the unsolidified films may make the Kerr effect come into full play to the anisotropic photopolymerization; and it may be favorable to the steric interaction to enhance the anisotropic reorientation of the films. Furthermore, the gradual evaporation of solvent in the films may contribute to fixing the orientated alignment in them. In the solidified polymer films, only the molecules the angles of whose transition dipolar moments with respect to wave vector directions of acting lights are within the range from 0° to 45° are easily photopolymerized no matter what directions of the acting-light wave vector are with respect to the film plane. Therefore, pretilt angles of the photopolymerization-induced film alignment can not be changed identically with

the wave vector directions of the acting lights changing, unless the polymer molecules may reorientate along with the optical fields before they are photopolymerized. Reorientation Kerr effect may efficiently cause the polymer molecules employed to make spin-coated films to reorientate adequately with the field direction changing¹⁴ if in intensive optical fields, electron distribution distortion of them covers most part of their structures, such as molecules with large conjugated electron systems. Such being the case, pretilt angles of the film alignments may be satisfactorily controlled by adjustment of optical field direction of acting lights.

Probability of anisotropic photo-reactions, on the photochemical points of view, are critically decided by the directional identity of transition dipolar moments of reactive molecules with polarization direction of the acting light and by correct coupling of spacial positions between two reactive polymers. However, the increase in the photo-reactions which the actinic polymers whose transition dipolar moments are somewhat unparallel to the polarization direction of the acting light participate in may decrease the established anisotropy of the polymer films^{6, 9}. Therefore the number of molecules contributing to generating high qualitative anisotropy of the polymer films are pretty limited because all the molecules of the films are isotropically distributed. Furthermore, the anisotropic reorientation originated from the steric interaction between the photochemical products and their adjacent molecules, as well as that of the prepolymers, is also pretty restricted by the viscosity of the films in solid state^{3, 5, 8}. Therefore, either increasing the efficiency of the anisotropic photo-reactions or decreasing the viscosity restriction of polymer films may improve the reorientational quality of the films and that of the adjacent LC molecules.

Reference

1. P. J. Shannon, W. M. Gibbons, and S. T. Sun, "Patterned optical properties in photopolymerized surface-aligned liquid-crystal films," *Nature* **368**, pp. 532-533, 1994.
2. W. M. Gibbons, P. J. Shannon, S. T. Sun, and B. J. Swetlin, "Surface-mediated alignment of nematic liquid crystals with polarized laser light," *Nature* **351**, pp. 49-50, 1991.
3. Y. Iimura, J. Kusano, S. Kobayashi, Y. Aoyagi, and T. Sugano, "Alignment control of a liquid crystal on a photosensitive polyvinylalcohol film," *Jpn. J. Appl. Phys.* **32**, pp. L93-L96, 1993.
4. K. Ichimura, Y. Hayashi, H. Akiyama, T. Ikeda, N. Ishizuki, "Photo-optical liquid crystal cell driven by molecular rotors," *Appl. Phys. Lett.* **63**, pp. 449-451 1993.
5. M. Schadt, H. Seiberle, and A. Schuater, "Optical patterning of multidomain liquid-crystal displays with wide viewing angles," *Nature* **381**, pp. 212-215, 1996.

6. M. Schadt, H. Seiberle, A. Schuater, and S. M. Kelly, "Photo-generation of linearly polymerized liquid crystal aligning layers comprising novel, intergrated optically patterned retarders and color filters," *Jpn. J. Appl. Phys.* **34**, pp. 3240-3249, 1995.
7. M. Schadt, H. Seiberle, A. Schuater, and S. M. Kelly, "Photo-induced alignment and patterning of hybrid liquid crystalline polymer films on single substrates," *Jpn. J. Appl. Phys.* **34**, pp. L764-L767, 1995.
8. M. Schadt, K. Schmitt, V. Kozinkov, and V. chigrinov, "Surface-induced parallel alignment of liquid crystals by linearly polymerized photopolymers," *Jpn. J. Appl. Phys.* **31**, pp. 2155-2164, 1992.
9. T. Hashimoto, T.Sugiyama, K. Katoh, T. Saitoh, H. Suzuki, and Y. Iimura, "TN-LCD with quartered subpixels using polarized UV-light-irradiated polymer orientation films," *SID95 Digest*, pp. 877-880, 1995.
10. H. Endo, T. Shinozaki, H. Fukuro, Y. Iimura, and S. Kobayashi, "Optically-controlled alignment of nematic liquid crystals on photo-sensitive polyimide films," *AM-LCD '96/IDW'96*, pp. 341-344, 1996.
11. D. Paparo, L. Marrucci, G. Abbate, and E. Santamato, "Molecular-field-enhanced optical Kerr effect in absorbing liquids," *Phys. Rev. Lett.* **78**, pp. 38-41, 1997.
12. M. Sheik-bahae. A.A Said, Tai-huei Wei, D. J. Hagan, and E. W. Van Stryland, "Sensitive measurement of optical nonlinearities using a single beam," *IEEE J. Quantum Electron.* **26**, pp. 760-769, 1990.
13. E. L. Kerr, "Electrostrictive Self-focusing of picosecond laser pulse trains," *IEEE J. Quantum Electron.* **7**, pp. 532-533, 1971 and E. L. Kerr, "Transient and steady-state electrostrictive laser beam trapping," *IEEE J. Quantum Electron.* **6**, pp. 616-621, 1970.
14. D. J. McGraw, A. E. Siegman, G. M. Wallraff, R. D. Miller, "Resolution of the nuclear and electronic contributions to the optical nonlinearity in polysilanes," *Appl. Phys. Lett.* **54**, pp. 1713-1715, 1989.

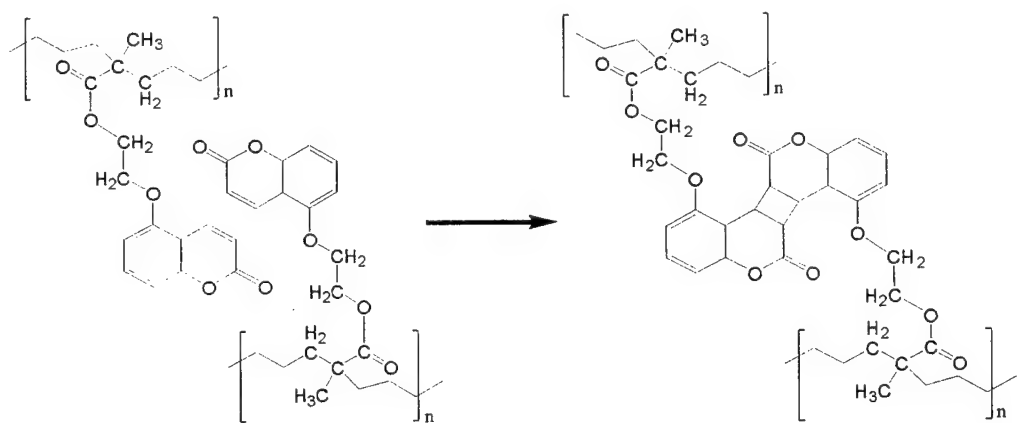


Fig.1 The structure of two actinic repolymers (left) and their dimerization (right) by intermolecular photo-induced (2+2) cycloaddition

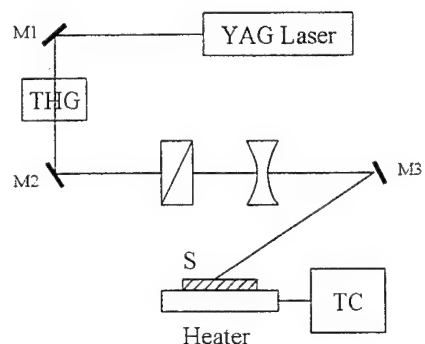


Fig.2 A new experimental setup used for unsolidified polymer films to be photopolymerized under illumination of linearly polarized laser light. S, sample; TC, temperature controller.

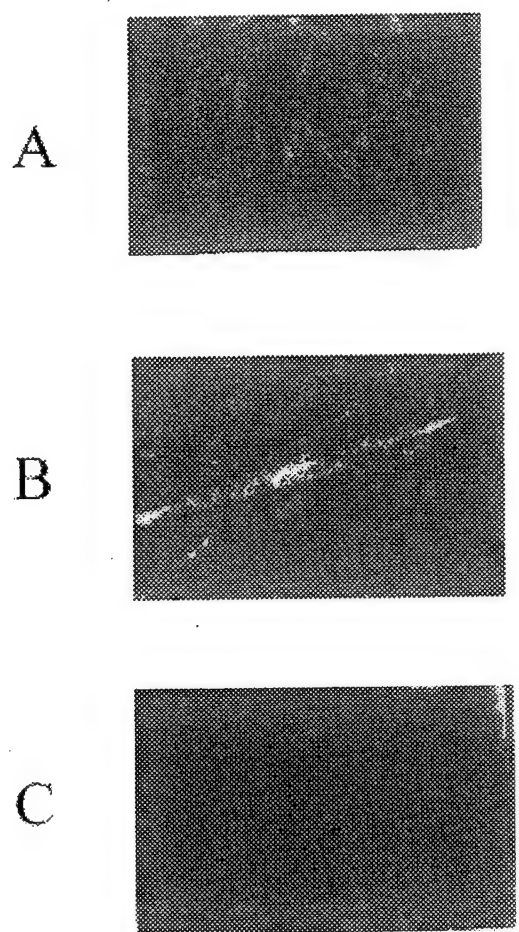


Fig.3 Polarized microscopic photographs of the LC cells fabricated with three differently photopolymerized polymer films: (a) the baked films photopolymerized by exposition to 355nm 35ns laser pulses; (b) the baked films by exposition to 355nm 250ps pulse trains; (c) the unsolidified films by exposition to 355nm 250ps pulse trains.

SESSION 6

TFT/LCM

Study of 5-Mask TFT Array Process with Low Cost, High Yield and High Performance Characteristics

Jr-Hong Chen^a, Ting-Hui Huang^b, I-Min Lu^a, Pi-Fu Chen^a and Dou-I Chen^a

^aElectronics Research and Service Organization / Industrial Technology Research Institute (ERSO/ITRI), 195-4, Sec. 4, Chung Hsing Rd., Hsinchu, Taiwan, R.O.C.

^bQuanta Display Inc., 3F, No.361, Fu-Shin 1 Rd., Kuei-Shan Hsiang, Tao Yuan Shien, Taiwan, R.O.C

ABSTRACT

Three types of 5-mask TFT array process have been compared and analyzed their characteristics including TFT performance, process window, etc. Results showing here indicate that a 5-mask TFT manufacturing process can be optimized with low cost, high production yield and high performance. These properties let the reduced mask TFT array process reveal a much higher potential in mass production.

Keywords: 5-mask process, TFT array,

1. INTRODUCTION

Since the hydrogenated amorphous silicon (a-Si:H) thin-film transistor (TFT) has been considered as a good driving and switching device for the active matrix liquid crystal display (AMLCD)[1] and the other large area electronics, the TFT-LCD industry has been grown up to the mass production area. So many researches have been focused not only on the physics but also on the improvement of image quality of the large area AMLCD with low manufacturing cost and high production yield.

In order to reduce the cost and improve productivity and yield, the number of masks which are used in manufacturing process has to be reduced. It is also important that the reduction of the number of the masks has to be compromised with the improvement of performance of the TFTs and TFT-LCD panels. Typically, there are two kinds of structure in inverted-staggered TFT, back channel etched (BCE) type and etch stopper (E/S) type. Many literatures [2-8] have been proposed the ways to reduce the mask of TFT process. However, most of the proposed reduced mask TFT process only stopped in ideal level. There are many difficulties to overcome and then can reach the realistic mass production level.

In this paper, three types of 5-mask TFT manufacturing process were proposed and studied. Results showing here indicate that a 5-mask TFT manufacturing process can be optimized with low cost, high production yield and high performance.

2. PROCESS DESCRIPTIONS AND ANALYSIS

Figure 1 shows the comparison of TFT and their Cst structural cross-sections for three types 5-mask TFT manufacturing process in ERSO/ITRI. The detailed process descriptions are shown in **Figure 2(a),(b),(c)** for process A, B, C, respectively. **Figure 3** reveals the illustration of top view unit pixel, a-a' for TFT cross-section, b-b' for Cst cross-section.

Process A (**Figure 2a**) is detailed described as follow: Firstly, 200nm-thick chromium film was deposited by DC magnetron sputtering to serve as the M1 gate electrode. Next, a silicon nitride (SiNx:H) film, an intrinsic amorphous silicon (a-Si:H) film, and a P-doped amorphous silicon (n⁺ a-Si:H) film were continuously deposited using PECVD apparatus. A

busline M2 layer Cr/Al/Cr was then sputtered immediately. The -thickness of SiNx:H, a-Si:H, n⁺ a-Si:H and Cr/Al/Cr are 370nm, 150nm, 30nm and 50/600/100nm, respectively. And the RF power densities for SiNx:H, a-Si:H and n⁺ a-Si:H are 120, 10 and 20 mW/cm², respectively. During the PECVD process, substrate temperature was kept at 280°C. The source-drain and busline metals Cr/Al/Cr layers were patterned. Then the n⁺ a-Si:H and a-Si:H layers were in both TFT and Cst area.

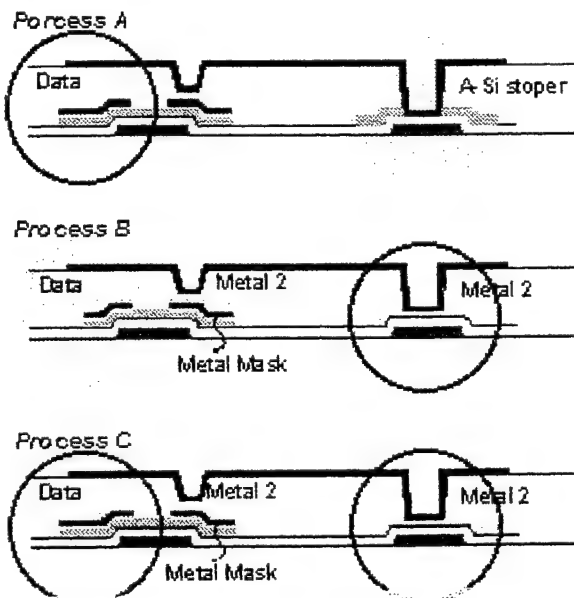


Figure 1. The comparison of three types of 5-mask TFT manufacturing process.

The purpose of Cst a-Si layer is to be an etching stopper. It is in order to avoid the etching through the gate SiNx and damaging the Cst in the next etching process. If it uses the metal as the etching stopper, the Cst structure will be the metal/n+a-Si:H/a-Si:H/SiNx/metal. It is hard to control the variation of storage capacitance when the gate pulse driving in the Cs on gate mode. After the n⁺ a-Si:H channel etched, the passivation layer was then deposited and patterned. The pattern areas locate not only in the TFT 's source area for pixel electrode conducting, but also in the Cst area for ITO/gate SiNx/M1 structure. Accordingly, a complicated etching recipe was needed for high selectivity for passivation materials to a-Si:H and then a recipe with high selectivity of a-Si:H to gate SiNx. Finally, the pixel electrode was then sputtered and patterned for top-ITO structure to finish the TFT process.

It was found there are some advantages in this process. (1) Mask numbers were reduced to 5; (2) Buslines, source-drain metal (M2) layer was the 2nd mask. It could improve significantly the open-line defects issue due to the reduction of particles coming from the photolithography process when compare to the conventional process. (3) Continuously sputtered the metal after PECVD deposition of active layers gate SiNx, a-Si:H and n+a-Si:H. It can improve the source-drain metal to n+a-Si:H contact resistance.[9] In the conventional process, the TFT is usually dipped in BOE solution before drain metal sputtering to exclude the native oxide on the n⁺ a-Si:H surface and thus ensure a good contact between n+a-Si:H and the drain metal. However, the interface of n+a-Si:H/drain metal is hardly well controlled due to the limitation of BOE solution. (4) It don't need island taper for M2 to island step coverage due to the M2/island stack structure (no step coverage in M2/island). Hence,

the open-line defects probability also can be lowered. However, there are some drawbacks, including: (1) It needs complicated etching process in making Cst structure. (2) The storage capacitance of Cst area completely depends on the area of passivation etching hole. It will reduce the aperture ratio due to enlarge the M1 area for keeping the same capacitance value.

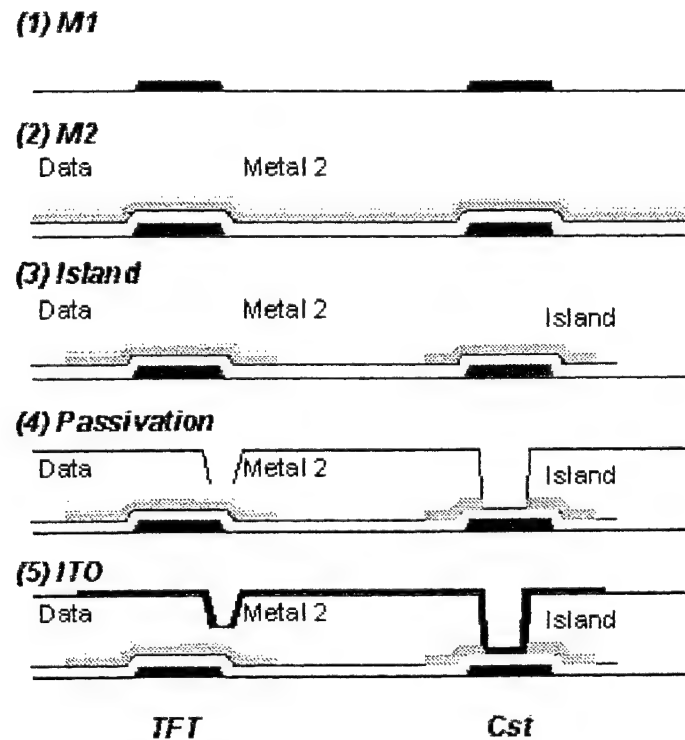


Figure 2a. The process flow of *Process A*

Process B possesses an island metal masking structure [10] is shown in **Figure 2b**. This process can be compromised with the same mask in Process A and accomplished in rearrangement of the process sequence: M1, I/metal making, M2, Passivation, and ITO.

In this process, the protected channel metal was etched in S/D metal mask patterning simultaneously. This metal masking structure will serve an extra advantage, e.g., the plasma damage free in the dry etching or oxygen ashing process. It also provides a same S/D metal to n+a-Si:H contact resistance like Process A. Accordingly, the TFT performance will be good as Process A. Moreover, Process B will give a wider process window of controlling TFT characteristics than Process A due to the prevention of plasma damage. On the other hand, the different process sequence of M2 and I will provide a better Cst structure: metal/gate SiNx/metal than Process B (see **Figure 1**). Unfortunately, although it can solve the drawbacks of Cst problems and possess the same TFT performance of Process A, it can not avoid the M2 to metal masking/island high step coverage. This phenomenon will seriously cause the increasing of buslines open-line defects.

From the discussion mentioned above, it can be seen the comparison of two types of Process A and Process B in **Figure 1**. How to get the all advantages of two processes? A total solution is shown in Process C.

The process C sequence follows the Process B as M1, I/metal masking, M2, Passivation, ITO to solve the Cst process issue and keep the excellent TFT performance. But it needs a modification in I/metal masking layout to achieve the M2 open-line defect free like the Process A type's advantage in TFT and M2. The concept is presented in **Figure 4**. The final Process C could possess not only an excellent TFT quality (from better S/D metal contact resistance) and uniformity (from reduction of plasma damage in TFT). Moreover this process could possess a better Cst structure (metal/SiNx/metal) for etching process window and driving capability. On the other hand, it also provides a good process window for busline open-line defects controlling (due to two times of metal sputtering in island metal masking structure and M2, see **Figure 4**). This property will be much better than the M2 process in Process A. It is believed that the process C will be a low cost, high yield and high performance properties good process in mass production.

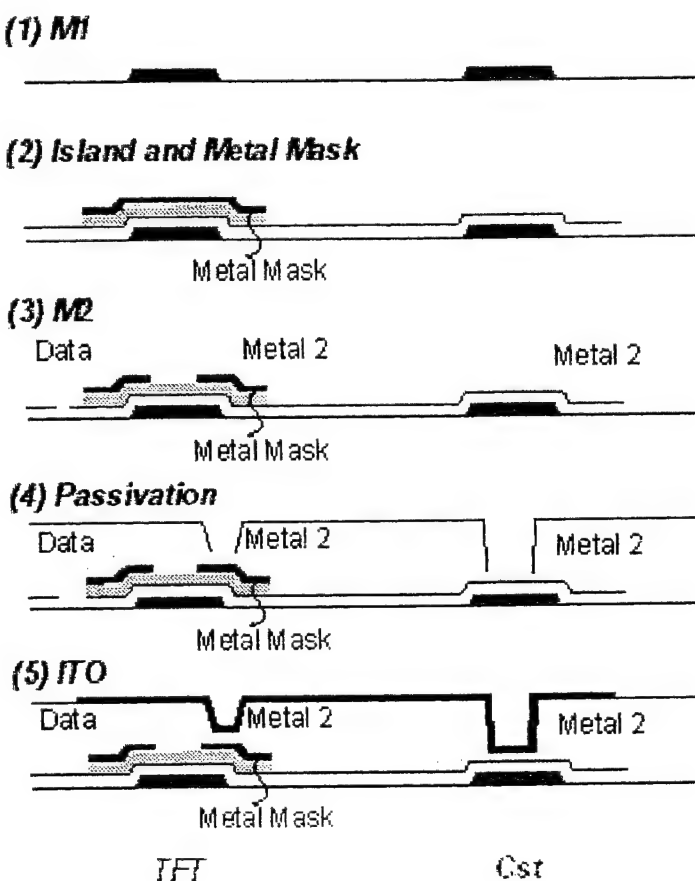


Figure 2b. The process flow of *Process B*

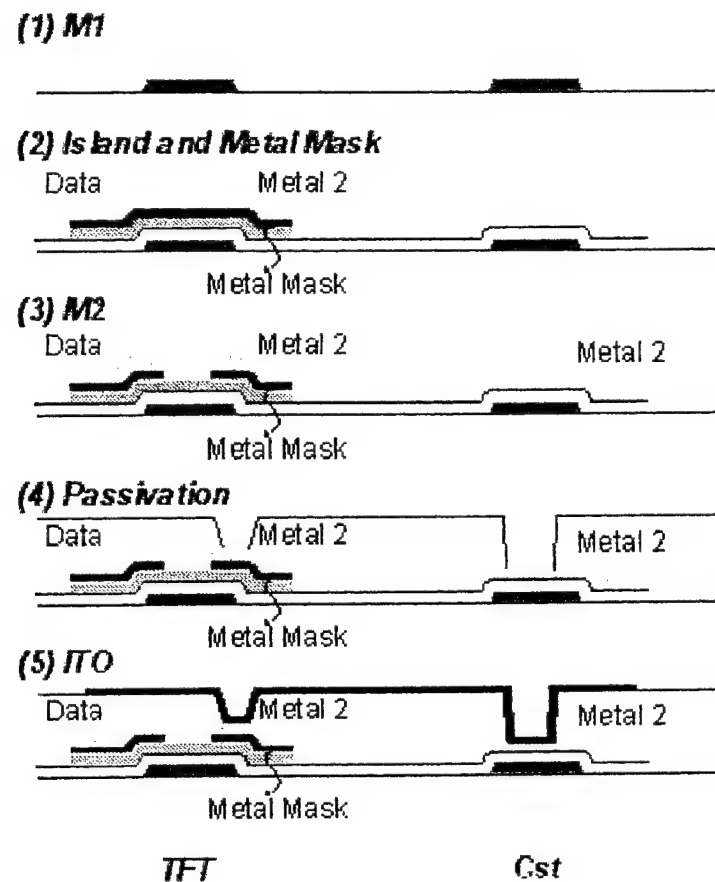


Figure 2c. The process flow of *Process C*

3. CONCLUSION

In this paper, three types of 5-mask TFT array process have been compared and analyzed their characteristics. These characteristics include TFT structure, performance, and process window, etc. Results showed here indicate that a 5-mask TFT manufacturing process (process C) can be optimized with low cost, high production yield and high performance. These properties let the reduced mask TFT array process (process C) reveal a much higher potential in mass production.

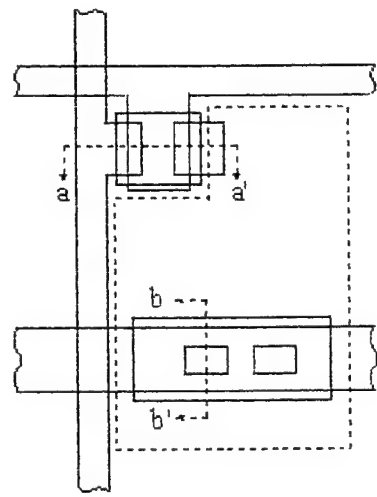


Figure 3. The illustrated top view unit pixel, a-a' for TFT cross-section, b-b' for Cst cross-section, related to Figure 1 and Figure 2.

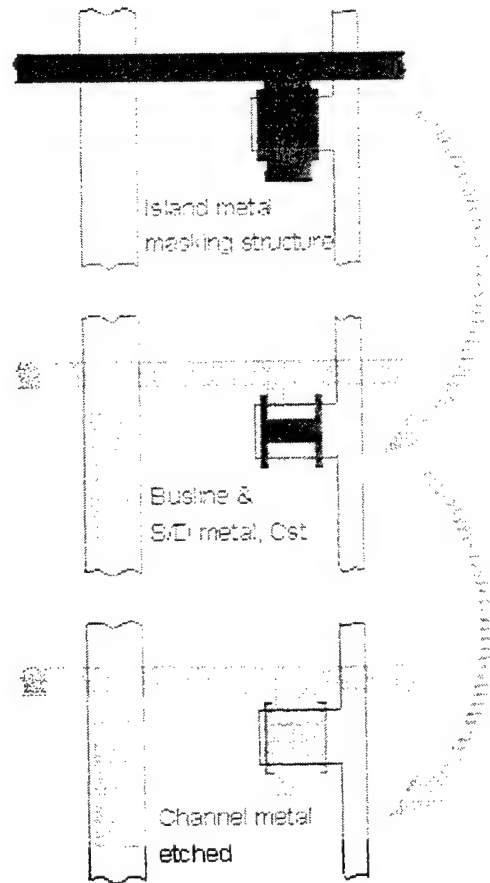


Figure 4. The Process C layout illustration

ACKNOWLEDGMENTS

The author would like to thank the financial support of MOEA for flat panel display project.

REFERENCES

1. I. Magarino, *Appl. Phys. A*, **41**, 297(1986).
2. H. Watanabe et al., *Jpn. J. Appl. Phys.* Vol 33 (1994) Pt. 1, No. 8, pp. 4491-4498.
3. S. D. Brotherton, et al., *J. Appl. Phys.* **82** (8), 1997, pp. 4086-4094.
4. K. Sera, et al., *IEEE Transactions on Electron Devices*, Vol. 36, No. 12, 1989, pp. 2868-2872.
5. J. S. Im, et al., *Appl. Phys. Lett.* **63** (14), 1993, pp. 1969-1971.
6. K. Yoneda, *IDW '97*, pp. 231-234.
7. D. Pribat, et al., *Flat Panel Display Materials II. MRS Vol. 424*, p. 127.
8. S.C. Chang, et.al, "Low Parasitic Resistance Process in Laser Crystallized Low-Temperature Poly-Si TFTs", *IDW '99*.
9. J. H. Chen et al., *ASID '99*, pp. 293-296.

Amorphous-Silicon Thin-Film Transistor with Two-Step Exposure Process

Pi-Fu Chen, Jr-Hong Chen, Dou-I Chen, Hsioxg-Ju Sung, June-Wei Hwang,
and I-Min Lu

Electronics Research and Service Organization / Industrial Technology
Research Institute (ERSO/ITRI) Taiwan R.O.C

ABSTRACT

The two-step-exposure (TSE) technology has been developed in application for combination the active layer with metal II layer. And this TSE technology has been applied in our Reduced-Mask process (five-mask) for cost reduction. The result shows that this amorphous-silicon thin-film transistor with four-photolithography process has great potential in mass production.

Keywords: Two-step exposure technology, a-Si thin-film transistor

1. INTRODUCTION

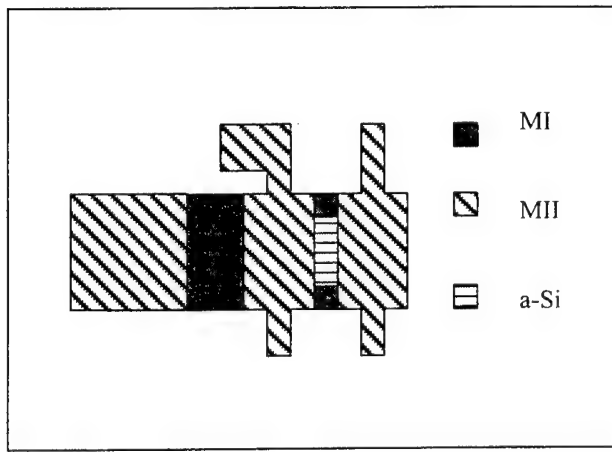
Amorphous-silicon thin-film transistor displays have already entered the market and are used in notebook PC, desktop type monitor and so on. As far as the a-Si TFT manufactures are concerned, there are two factors to keep them in a better position for competition. One is the process yield another is the process cost. At present, mass production for a-Si thin film transistors (TFT) usually take six or seven (even more) photolithography processes¹⁻⁵. It's believed that reduction of the photolithography process will put it in a better position for competition.

The a-Si TFT process flow of the conventional six-mask BCE (back-channel-etched) type is Metal I (gate electrode), Island (active layer), Contact, ITO, Metal II (source/drain electrode), Passivation. In ERSO, we have already developed the Reduced Mask (five-mask) process. Its process flow is Metal I (gate electrode), Island (active layer)/Metal Mask, Metal II (source/drain electrode), Passivation, ITO. Based on this experiment, we developed the **two-step-exposure** (TSE) technology to combine Island layer with MII layer in one photolithography process. In this paper, we will discuss the TSE technology and the TFT characteristic of this a-Si TFT with four-photolithography process.

2. EXPERIMENT

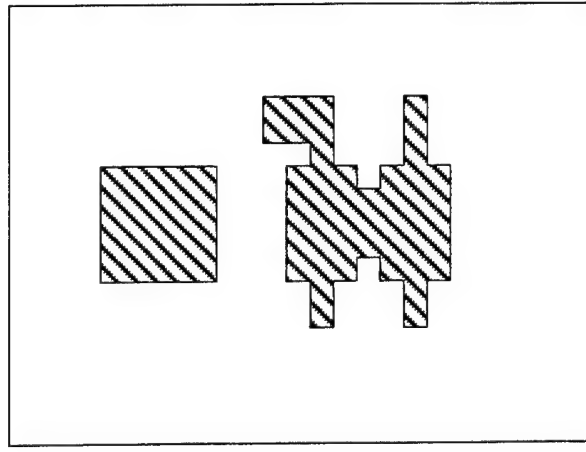
TFT's were fabricated with the combination of standard BCE type Reduced Mask (5-mask) process and **TSE** technology. This four- photolithography process flow is listed as below, **Figure 1** shows the schematic diagram of our TFT pixel. **1:** MoW was sputtered and patterned as gate electrode. **2:** SiNx (gate insulator), intrinsic a-Si, n+ a-Si were deposited and Cr/Al/Cr were sputtered as the MII source-drain electrode. Following is the **two-step-exposure (TSE)** process, the photoresist was coated and exposed pattern A with higher light intensity – complete exposure (**Figure 2**), exposed pattern B with lower intensity – incomplete exposure (**Figure 3**). Then developed the TSE pattern, so there was still some photoresist on pattern B (channel region). The next step, MII wet etching and n+ a-Si, a-Si, SiNx dry etching. After patterning TSE pattern, the photoresist on pattern B (channel region) was etched with O2 plasma ashing. Because the photoresist on pattern B was thinner than that on the other region, the photoresist on pattern B could be etched completely and remain about 7000~8000 Å thickness on the other part if O2 plasma ashing uniformity、rate/time were well controlled. Next, MII on the channel region was wet etched and then stripped off the photoresist. Then used MII as the mask to dry etch n+ a-Si. **3:** Passivation layers. **4:** ITO layer. Step 3and 4 were completed by using conventional 5-mask Top ITO process method.

Email: ansel@itri.org.tw; Telephone: 886 3 5917144; Fax: 883 3 5820052



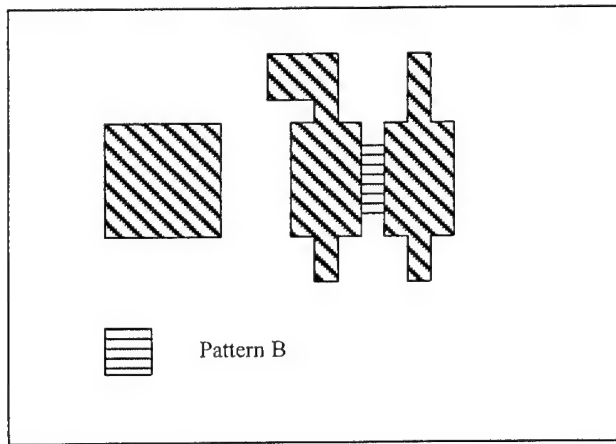
TFT pixel top view

Figure 1



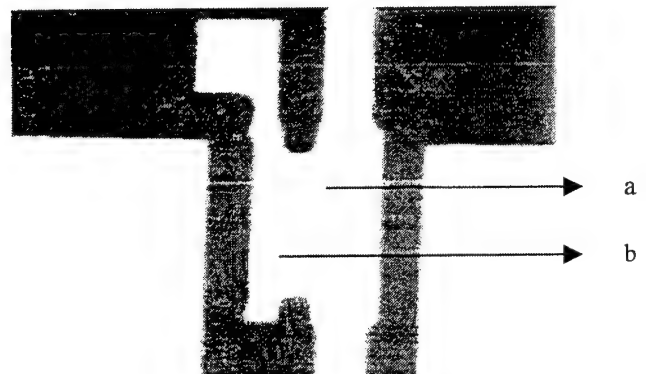
TSE pattern A

Figure 2



TSE pattern B

Figure 3



Photograph of TFT pixel top view

Figure 4

3. PROCESS CHARACTERISTIC

It is considered there are two critical steps in this four-photolithography process. One is TSE process another is O₂ plasma ashing.

3.1. Two-Step-Exposure (TSE) Process

The general issues in this process are the photoresist thickness and thickness uniformity of pattern B. Those are not easy to control because the photoresist of not being completely developed usually creates a large deviation on thickness. Besides, if the photoresist thickness difference between pattern A and pattern B (incomplete exposure) is not larger than 3000 Å, there will be a very narrow process window in the O₂ plasma ashing and the n+a-Si etching. Furthermore, photoresist pattern of incomplete exposure usually produces very dull edge. In Figure 4 there is the dull edge in point A and B. If the edge is too smooth, the PR of these side walls will connect on the top and bottom area of the channel region. This will cause some residue in following channel MII etching process and fail in n+a-Si etching.

The effect of the etching process on photoresist thickness is another factor that should be considered. In island etching process (after first MII wet etching) photoresist was etched about 300 Å and O₂ plasma etching rate was about 3000 Å. Because of this two etching factor, the photoresist thickness on the channel region can't be too thin. In other words, increase the photoresist thickness will widen the process window.

In this study, we coated 1.5 μm SHIPLEY photoresist and tried many exposure intensity. The best condition we've found was listed as below: Eth of complete exposure is 70mj/cm², Eth of incomplete exposure is 35mj/cm² and remained photoresist with the thickness of 8000 Å~9000 Å in the channel region. The thickness of photoresist remained in the channel region is very safe for the following n+ a-Si /a-Si dry etching and O₂ etching process.

3.2. O₂ plasma ashing

In this work, two mode of O₂ plasma ashing process were studied: PE mode and RIE mode. Table 1 shows the etching recipe of two different etchers that we used. When using RIE mode O₂ plasma ashing to remove photoresist on the channel region, the following MII wet etching failed. The MII on the channel region could not be removed by wet etching even with a long period of overetching which only produced serious lateral etching, and led to source-drain MII broken. By using PE mode O₂ plasma ashing to remove photoresist on the channel region, no process issue of this kind was occurred. The cause of this process issue might be the surface of the top MII layer Cr formed CrO_x in RIE mode O₂ plasma ashing process and this is reasonable. In PE mode, chemical reaction dominates the etching process, and less energy (momentum) will be transfer to the film. There for, it's harder to surmount activation energy to form CrO_x.

Cl₂ plasma treatment before MII wet etching is one method that we've tried to solved this issue. It was effective but the uniformity was not easy to control. In addition, change the MII material or etch the channel MII with dry etching process may be another solution to this issue.

RF mode	RIE	PE
O ₂ (sccm)	400	400
power(W)	800	500
cooler temp	20	40
pressure(m Torr)	100	375
result	MII residue	no residue

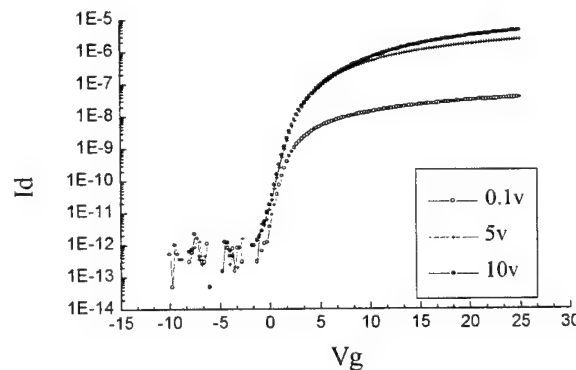


Table 1

FIGURE 5

4. TFT CHARACTERISTIC

The drain-source current I_{ds} vs. the gate-source voltage V_{gs} characteristic at room temperature is plotted in **Figure 5**. The threshold voltage V_{th} is about 2.63 v, field effect mobility μ_{FE} is about 0.74 cm²/v-sec, subthreshold swing is about 0.72v/dec. The result shows that the TFT characteristic won't be obviously affected by the series etching process.

5. SUMMARY

In general, the process issue of TFT mass production line partly comes from the photoresist residue or particle contamination, which will cause the MII open or MI/MII short. To advance MII process earlier can reduce the probability of such occurrence. And this is the spirit of the a-Si TFT array with four-photolithography process. Besides, this process also has the characteristic of island metal masking structure⁶, which can protect the active layer from plasma damage in plasma etching process. In addition to the benefits of process reduction and those listed above, better contact condition between MII and island layer is also another benefit of this process.

Studies in this paper conclude that four-photolithography a-Si TFT is highly potential in mass production.

6. REFERENCE

1. Patent Number:4601097, 1986. Seiko Instruments & Electronics Ltd.
2. Patent Number: 4778560, 1988. Matsushita Electric Industrial Co., Ltd.
3. Patent Number: 5478766, 1995. Samaung Electronics Co., Ltd.
4. Patent Number:5719078, 1998. Samsung Electronics Co., Ltd.
5. Patent Number: 5736436 (5545576), 1998. Casio Computer Co., Ltd.
6. J.H.Chen, T.H.Huang , and Y.E.Chen, *ASID '99*, p277

Mismatch Analysis of TAB-on-Glass Connection with ACF

Wei-Fun Hou^a, Tai-Yan Kam^{*a}

Adam Hsieh^b, Jian-Cheng Chen^b and Shyh-Ming Chang^b

^a Mechanical Engineering Department, National Chiao Tung University,
Hsin Chu, Taiwan, R. O. C.

^b Electronics Research Laboratories, Industrial Technology Research Institute,
Chu Tung, Taiwan, R. O. C.

ABSTRACT

Mismatch between outer lead bonds (OLBs) of a tape automated bonding (TAB) and a glass panel during fabrication is studied using the finite element method. A two-dimensional finite element model for the TAB-on Glass (TOG) connector is presented for determining the deformation of the connector. The deformation of the TOG connector induced by residual thermal stresses are determined via a two-stage approach. At the first stage, the TOG connector is under heat and pressure. The anisotropic conductive film (ACF) in-between the TAB and glass panel is assumed to be in a melting condition so that both TAB and glass panel can expand freely. At the second stage, the connector is cooled down to room temperature and the ACF becomes solidified. The deformations of the connector at the two stages are determined in the finite element analysis in which the temperature dependence of material properties is considered. Effects of particular parameters on the mismatch between the OLBS are studied by means of a number of numerical examples. A method for compensation design of the lead locations of the OLBS is proposed. It has been shown that the compensation design can produce results that will avoid the occurrence of unwanted mismatch.

1. INTRODUCTION

Liquid crystal display (LCD) has become an important display device in the electronic industry in recent years. In the fabrication of LCDs, Tape Automated bonding (TAB) technology by which fine pitch interconnections between LCD panels and driver-IC TAB are made possible using an anisotropic conductive film (ACF) has been adopted for packaging the components of LCDs [1-7]. When compared with the conventional packaging methods, the use of TAB package technique can provide many advantages such as having smaller and lighter packaging, reducing chip size, increasing I/O pins on the chip, facilitating space reduction in LCD devices et al. Due to the advance in packaging technology, the finest interconnection pitch for LCD can be as narrow as 70 μm . As the interconnection pitch gets finer, the probability of having LCD failure induced by the mismatch between the outer lead bonds (OLBs) of the TAB and glass panel will be higher. The OLB mismatch is mainly caused by the thermally induced residual stresses in the cured ACF. Although some research work has been devoted to the thermal stress analysis of TOG connection, the failure of LCD induced by mismatch of OLBS is still a problem to be tackled. In this study, methods for mismatch analysis of TOG connection and compensation design of interconnection pitch are presented. The feasibility and applications of the proposed methods are demonstrated by means of a number of examples.

2. DESCRIPTION OF THE PROBLEM

The two-dimensional configuration of a TOG connection is shown in Fig. 1. Figs. 1a and 1b show, respectively, the connection with or without mismatch. Basically, the connection consists of three components, namely, a tape with outer leads, an ACF, and a glass panel with outer leads. The ACF is placed in-between the tape and glass panel and the three components are bonded together under heat and pressure. The curing cycle for the assembly is shown in Fig. 2. During heating, the ACF melts down and both the tape and glass panel expand freely in the lateral directions. When the assembly cools down, the ACF is solidified and the three components become an integral part. The material properties of the components are available in the literature and also listed in Table 1.

* Correspondence: Email: tykam@cc.nctu.edu.tw; Telephone: 886-3-5725634; Fax: 886-3-5728504

3. MISMATCH ANALYSIS

The seriousness of mismatch developed in the TOG connection depends on the deformations of the three components. In the deformation analysis of the connection, the outer leads of the TAB and glass panel are not included in the formulation and their effects on the deformations of the components are neglected. Herein, the deformation analysis of the TOG connection is formulated on the basis of a two-dimensional model coupled with a two-stage deformational approach. At the first stage, the connector is under heat and pressure. The ACF is assumed to be in a melting condition and the TAB and glass panel can expand freely. The elongation of the TAB is calculated as

$$\delta_p = \alpha_p L_p \Delta T \quad (1)$$

where δ , α , L denote elongation, coefficient of thermal expansion, and length, respectively; ΔT is temperature rise; subscript P denotes TAB. The elongation of the glass panel is determined in a heat transfer analysis of the panel. At the second stage, the connector cools down to room temperature under no pressure and the ACF is transformed to a solid bar with temperature dependent material properties. The final deformations of the components of the connector are then analyzed using the two-dimensional finite element model shown in Fig. 3. It is noted that due to symmetry only one half of the TOG connector is used to establish the finite element model. The deformation analysis is then accomplished using the commercial finite element code NASTRAN [8]. Once the final deformation of the connector is determined in the above analysis, the mismatches between the outer leads of the TAB and those of the glass panel can be calculated as

$$s_i = \tilde{x}_{ip} - \tilde{x}_{ig} \quad (2)$$

where s_i is the mismatch between the i th outer lead of the TAB and that of the glass panel; \tilde{x}_{ip} , \tilde{x}_{ig} are the coordinates of the i th outer leads of the TAB and glass panel after deformation, respectively.

4. NUMERICAL EXAMPLES

The feasibility and applications of the aforementioned method are demonstrated by means of several examples. The material properties in Table 1 and the curing cycle of Fig. 2 are used to analyze the mismatch of the TOG connector in Fig. 1. At the first stage, the assembly is heated up from room temperature to 280°C. In the heat transfer analysis of the assembly, it has been found that the temperature rise in the TAB is 172°C. The temperatures at the top and bottom surfaces of the glass panel are 172°C and 60°C, respectively. The elongations of the TAB and glass panel are 12.98mm and 13.629mm, respectively. At the second stage, the assembly cools down to room temperature. The ACF is solidified and considered in the finite element analysis of the connector. The deformed shape of the assembly is shown in Fig. 4. The distribution of OLB mismatch across the span of the connector can be determined using Eqn. (2) and the result is shown in Fig. 5. It is noted that except for a few outer leads close to the free edge of the TAB, the OLB mismatch basically varies linearly across the span of the connector. The maximum mismatch of the connector is 13.37 μm which is relatively close to the value observed in practical applications. Maximum mismatches for cases with some changes in material constants or curing parameters are also computed and the results are listed in Table 2 for comparison. It is noted that among the parameters considered, the thermal expansion coefficient of the tape may have significant effects on the OLB mismatch of the connector.

5. COMPENSATION DESIGN OF MISMATCH

Mismatch of OLBs will be inevitable if a uniform interconnection pitch is adopted in designing the TOG connection. Excessive OLB mismatch will be likely to cause early failure of the LCD panel. Therefore, methods for alleviating the adverse effects induced by OLB mismatch should be pursued. Herein, a nonuniform interconnection pitch approach is adopted to design the locations of the outer leads on the TAB and glass panel. The coordinates of the outer leads on the glass panel remain unchanged while those of the outer leads on the TAB are determined as

$$x'_{ip} = x_{ig} (1 + \zeta_g) - x_{ip} \zeta_p \quad (3)$$

where x_{ip} , x'_{ip} are coordinates of outer leads on tape before and after modification, respectively; x_{ig} are the original coordinates of the outer leads on glass panel; ζ_p , ζ_g are slopes of displacements of tape and glass panel determined at the first stage. The mismatch of the same TOG connector but with modified locations of outer leads on the TAB is also studied and the result is shown in Fig. 6. The comparison of the results in Figs. 5 and 6 shows that the adoption of the present compensation design can significantly reduce the magnitude of OLB mismatch.

6. CONCLUSIONS

Mismatch between the OLBs of the TAB and glass panel for a LCD panel has been studied using a two-dimensional finite element model. Reasonable results on OLB mismatch have been obtained. The results have also revealed that the thermal expansion coefficient of TAB may have significant effects on the OLB mismatch. A compensation method for mismatch design of TOG connections has been proposed. It has been shown that the proposed compensation method can greatly reduce the magnitude of the OLB mismatch induced in the connection. It is suggested that a three-dimensional finite element model be used in the mismatch analysis if a more accurate prediction of OLB mismatch is desired.

REFERENCES

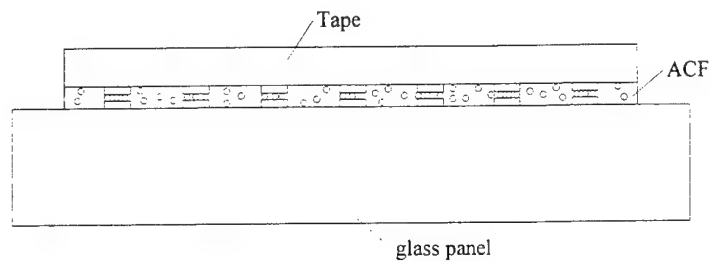
1. H. Atarashi, N. Kakimoto, H. Matsubara, K. Yamamura, T. Mukai, and H. Matsui, "Chip-on-Glass technology using conductive particles and light-setting adhesives," Proceedings of 1990 Japan International Electronic Manufacturing Technology Symposium, June 9-11, 1990, Tokyo, Japan, pp. 190-195.
2. H. Matsubara, H. Atarashi, K. Yamamura, N. Kakimoto, K. Naitoh, and T. Nukii, "Bare-chip face-down bonding technology using conductive particles and lightsetting adhesives:ELASTIC method," IMC 1992 Proceeding, Yokohama, pp. 81-87, 1992.
3. H. Yoshida, et al, "Packaging method of liquid crystal driver LSIs by Tape-On-Panel technology," ISHM '88 proceeding, pp. 307-313.
4. F. Juskey, "Heat seal connector: a new high density SMT interconnection system," IEEE/CHMT '89 IEMT symposium, pp. 121-125.
5. J. C. Hwang, "Advanced Low-Cost Bare-Die Packaging Technology for Liquid Crystal Displays," IEEE/CPMT Int'1 Electronics Manufacturing Technology Symposium, 1994, pp. 199-202.
6. N. R. Basavanhally, D. D. Chang, B. H. Cranston, "Direct Chip Interconnect with Adhesive-Connector Films," Proceeding of Electronic of Electronic Components and Technology Conference, 1992, pp.498-491.
7. R. Ascenbrenner, A. Ostrmann, G. Motulla, E. Zakel, H. Reichl, "Flip Chip Attachment Using Anisotropic Conductive Adhesives and Electronic Nickel Bumps," IEEE Transactions on Components, Packaging and Manufacturing Technology – Part C, Vol. **20**, No. 2, April 1997, pp.95-100.
8. "MSC/NASTRAN Version 66," MacNeal-Schwendler Corp., Los Angels, CA, Dec 1990.

Table 1. Material constants for components of TOG connection

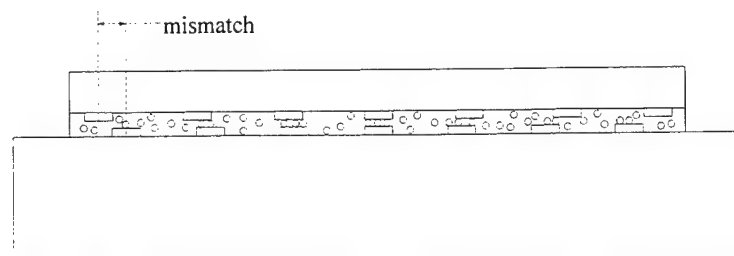
Component Constant	Tape	ACF		Glass
E(MPa)	8826	0 °C	2548	70000
		40 °C	2548	
		121 °C	1500	
		200 °C	1500	
v	0.3	0.3		0.2
$\alpha(\times 10^{-6} / ^\circ C)$	0 °C	8	0 °C	52.2
	99 °C	8	110 °C	52.2
	100 °C	9	111 °C	177.6
	101 °C	10	112 °C	303
	300 °C	10	300 °C	303

Table 2. Maximum mismatches for TOG connectors with different parameters

Modified parameter	Maximum mismatch (μm)
$\alpha_G = 3.8 \times 10^{-6} / ^\circ C$	14.43
$\alpha_p = 5 \times 10^{-6} / ^\circ C$	5.90
$T_p = 165^\circ C$	12.65



(a)



(b)

Fig. 1. 2-D view of TOG connection

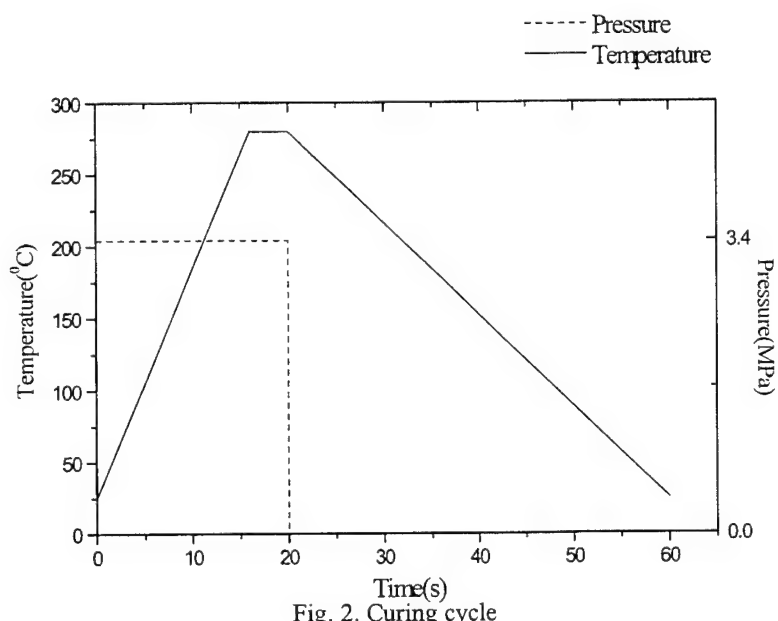


Fig. 2. Curing cycle

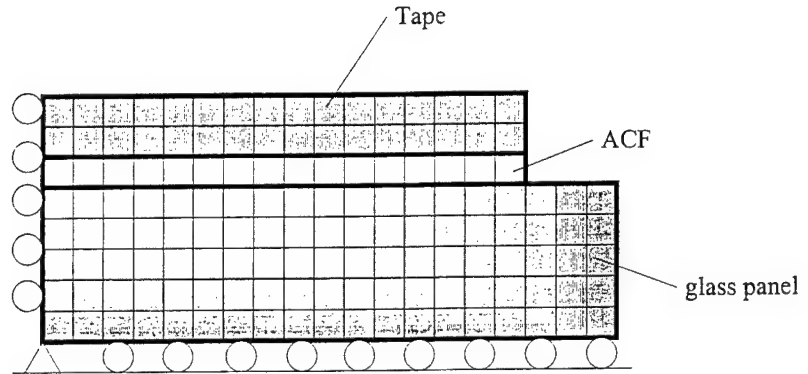


Fig. 3 Finite element model of connector

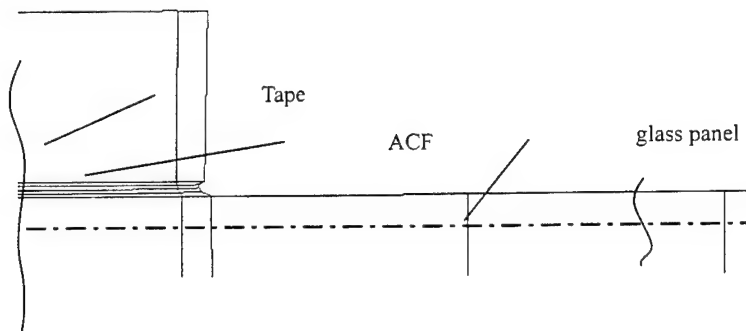


Fig. 4. Deformed shape of TOG connector

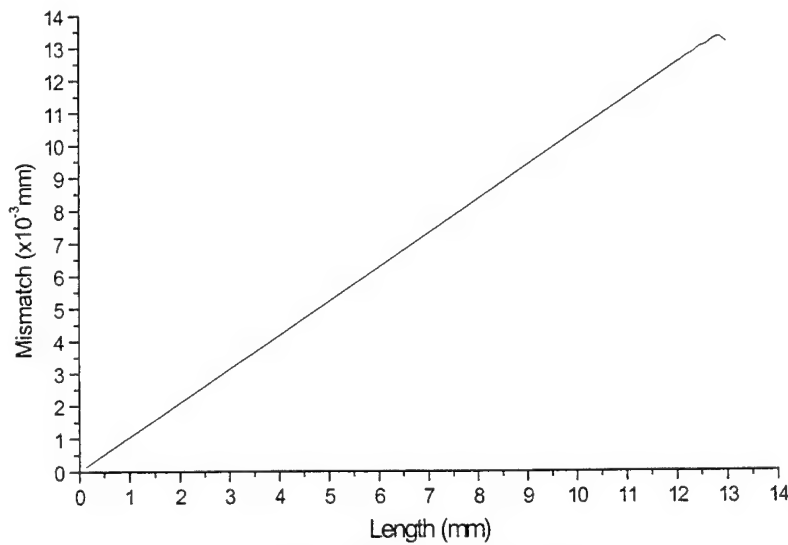


Fig. 5. Distribution of mismatch

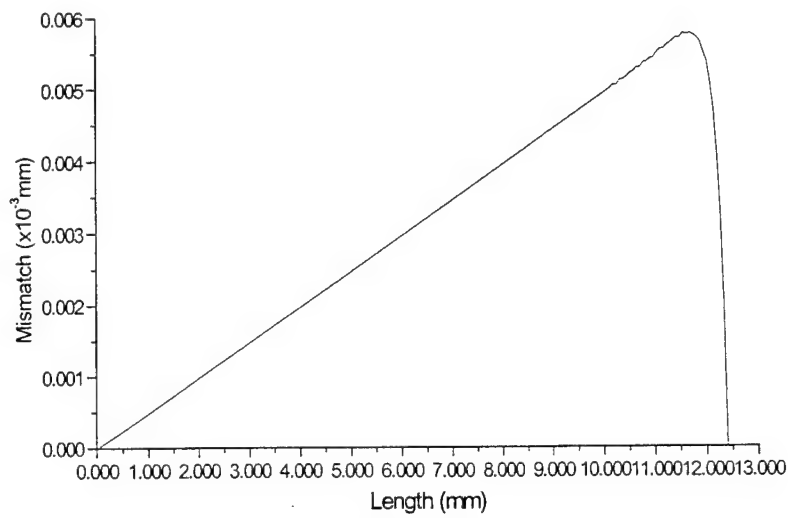


Fig. 6. Mismatch of TOG connection with compensation design

Characteristic Study of Chip-on-Film Interconnection

Shyh-Ming Chang^{*a,b}, Jwo-Huei Jou^b, Adam Hsieh^a, Tai-Hong Chen^a, Ching-Yun Chang^c, Yung-Hao Wang^c, Hong-Yu Lin^a, Chun-Ming Huang^c

^a Electronics Research and Service Organization / ITRI, Chu-Tung, Hsin-Chu, TAIWAN 310, ROC

^b National Tsing-Hua University, Hsin-Chu, TAIWAN300, ROC

^c Wintek Corporation, Tepz Tantzu,Taichung, TAIWAN 427, ROC

ABSTRACT

Chip-on-film (COF) is a new technology after tape-automated-bonding (TAB) and chip-on-glass (COG) in the interconnection of liquid crystal module (LCM). The thickness of the film, which is more flexible than TAB, can be as thin as 44 μm . It has pre-test capability, while COG hasn't. It possesses great potential in many product fabrication applications.

In this study, we used anisotropic conductive film (ACF) as the adhesive to bind the desired IC chip and polyimide (PI) film. The electric path was formed by connecting the bump on the IC and the electrode on the PI film via the conductive particles in the ACF. In the COF bonding process experimental-design-method was applied basing on the parameters, such as bonding temperature, bonding pressure and bonding time. After reliability tests of (1) 60°C/95%RH/100Hr and (2) -20°C ~70°C/ 30 cycles, contact resistance was measured and used as the quality inspection parameter. Correlation between the contact resistance and the three parameters was established and optimal processing condition was obtained. The COF samples analyzed were fabricated accordingly. The contact resistance of the COF samples was measured at varying temperature using the 4 points test method. The result helped us to realize the relationship between the contact resistance and the operation temperature of the COF technology. This yielded important information for circuit design.

Key words: Chip-on-Film (COF), Anisotropic Conductive Film (ACF), Polyimide (PI), Tape Automated Bonding (TAB), Chip-on-Glass (COG)

1. INTRODUCTION

COF (Chip-on-Film or Chip-on-Flex), as shown in figure 1, is the fabrication technology that currently applied in LCM (Liquid Crystal Module) of small panel. COF is developed after the Surface Mount Technology (SMT), TAB (Tape Automated Bonding), and COG (Chip On Glass) technology as shown in figure 2. The geometry of the COF is similar to that of TAB, but due to its substrate is of two-layer structure (Cu and polyimide), it is thinner, of higher density, better flexibility and high-temperature durable; not like TAB which is normally three-layer structure (Cu, adhesive, and polyimide). Compared with COG, COF has the features of lower contact resistance and available pre-test capability. This technique has

grown quickly and been applied on high-density, multi-functional LCM fabrication, such as mobile phone, PDA (Personal Digital Assistance). In addition, it is also applied to CSP (Chip Scale Package) [1]-[3] and multi-chip module [2]. Typical examples are the mobile phone products by Wintek Corporation as shown in figure 3. The corresponding pitches of ILB (Inner Lead Bonding) are $120 \mu\text{m}$ and $80 \mu\text{m}$, respectively. Numerous local makers are developing this technology and are setting up production lines after Japan.

This study first searched for the optimal process parameters according to the results from reliability test. The COF samples were then fabricated accordingly. The contact resistance was measured under various different temperatures to understand the influence of the environmental temperature on the COF contact resistance.

2. BONDING METHODS OF CHIP-ON-FLEX

COF is one of the Flip Chip Bonding technologies, and it uses flexible printed circuit board as the substrate. The COF bonding can be processed with ACF bonding, eutectic bonding, or soldering connection.

2.1 ACF process

As presented in figure 4, ACF bonding is one of the main stream processes, and this method is based on the conductive particle which makes electrode connection between IC bump and electrode on flex. The binder not only can be used as an adhesive but also provides the necessary contractility to maintain the contact between the electrodes. In order to achieve the minimum contractility required for the conductivity of the contact provided by the binder, An Au coated polymer particle was chosen as the conductive particle instead of a pure metal one. This causes lower contractility which is needed for ACF binder. Furthermore, the TCE (Thermal Coefficient of Expansion) of polymer particle is similar to that of the ACF binder. As a result, under different temperature environments, the variation of the contractility is moderately minor as well as the variation of contact resistance. Because COF process is similar to COG and TAB-on-Glass processes, many LCM fabricators have developed in accordance with this trend.

2.2 Eutectic bonding [1]

This process is achieved by heating the joints of IC chip and flex to form the eutectic bonding between Au and Sn, then protecting the joints by underfill. In the past, TCP (Tape Carrier Package) used eutectic process. However, due to the mid layer (adhesive) in this three-layer structure is not high temperature durable, punching a window for bonding area is unavoidable and the bonding lead's support substrate (PI) is removed. Finally, the ILB joints are protected by encapsulation. On the other hand, COF's substrate (flex) is two-layer structure without adhesive layer. Hence, it can endure high-temperature process like eutectic bonding. Since the COF process is similar to TCP process, many manufactures with TCP fabrication lines move towards this direction. This technology becomes another mainstream manufacturing procedure of COF.

2.3 Soldering [2]-[3]

This is based on solder reflow. Connection is achieved by melting the joints on the electrodes of IC Solder bump and flex, and then fills the underfill. The disadvantage of this process is easy to form shortage resulted from melting connection so that it is not suitable for high-density connection.

3. EXPERIMENT

This experiment adopted the most commonly used ACF process in the LCM field.

3.1 Materials preparation

Driver IC :

Chip Size: X=11.49 mm, Y=2.44 mm

Chip Thickness: $400 \mu\text{m} \pm 30 \mu\text{m}$

Bump Size: $50 \mu\text{m} \times 110 \mu\text{m}$

Bump Pitch: $80 \mu\text{m}$

Bump Height: $25 \mu\text{m}$

Bump Material: Au

Flex Substrate:

-Base film (Polyimide): $22 \mu\text{m}$ thick

-Conductor(Copper): $12 \mu\text{m}$ thick, coated with gold

-Insulator (Solder resistor): $10 \mu\text{m}$ thick

ACF:

-Binder: $25 \mu\text{m}$ thick, thermal set

-Conductive particle (Resin coated with gold): $5 \mu\text{m}$

3.2 ACF properties measurement

In order to improve the quality of connection and further investigate the characteristics of the connection; besides having the bonding parameters suggested by ACF maker, we measured the curing temperature and Tg value from DSC (Differential Scanning Calorimeter) and TMA (Thermomechanical Analyzer) to fully understand the characteristics of the ACF.

The ACF's DSC analysis is shown in figure 5. The curing reaction was started when temperature was higher than 124°C . Bonding time had to be long enough for fully curing. Generally, the bonding temperature was set at $180^\circ\text{C} \sim 210^\circ\text{C}$ to increase the throughput.

The ACF's TMA analysis is shown in figure 6. The curing condition was set at 180°C for 5 sec. The resultant Tg was 131°C . Some ACF samples were cured at various temperatures, i.e. 160°C , 170°C , 180°C , 190°C , 200°C and 210°C . The Tg results are shown in figure 7. When curing temperature was higher than 180°C , the Tg achieved a stable value which was around 130°C . This means that bonding temperature needs to be set at temperature higher than 180°C to ensure enough curing degree. It is also discovered that the COF product under an environmental temperature higher than Tg shows

significant variation on its contact resistance.

3.3 Bonding accuracy measurement

Bonding accuracy affects the contact resistance of high-density connection. Poor accuracy causes random data and serious experimental deviation. It is difficult to check the accuracy due to poor transparency of the flex. Thus, X-ray or ultrasound measurement must be applied to check the connection. Figure 8 shows the X-ray photograph of the bonding result of the COF sample from the backside. It is clear to see that the leads of the flex have been accurately bonded to the bumps of the chip.

3.4 Bonding procedure

The process of COF bonding material by ACF is listed below:

Cleaning: Cleaning the surface of flex by IPA (isopropyl alcohol) or acetone

Lamination (Temporary bonding): Attaching ACF to Flex by proper temperature and pressure.

Removal of the separator: Peel off the separator of ACF

Alignment: CCD camera with image processor is used to capture and align the image of IC and flex.

Apply heat and pressure (Bonding): Impose high temperature and pressure on IC to cure ACF.

Remove pressure: The COF process is done after removing the thermode.

3.5 Experimental design

The parameters in this experiment included bonding temperature, bonding pressure and bonding time. The temperature was set at 170°C, 190°C, and 210°C, respectively. The pressure was set at 30 g/bump, 50 g/bump, and 70g/bump. The time was set at 5 sec, 10 sec, and 15 sec. 27 combinations were obtained by all-factor experimental method. 6 samples were made for each parameter set. These samples were tested to realize their reliability upon thermal cycling from -20 to 70°C for 30 cycles and high temperature humidity at 60°C, 95%RH for 100Hr. All these reliability tests follow IEC 60068-2-3 standards. According to these optimal parameters, several COF samples were made and the contact resistance of each sample was measured under different temperature environments. The relationship between the contact resistance and the temperature variation had been established. In the meantime, the I-V curve of the joints was determined

3.6 contact resistance measurement

Figure 9 shows the COF's circuit design for electrical measurement and the equivalent circuit. Since I_{sense} is negligible, one has

$$V/I = R_2$$

where R_2 is the contact resistance from bump-2 to the electrode of flex through ACF. The electrical resistance of the copper electrode is relatively small when compared to the ACF contact resistance, so it can be neglected.

4. RESULT AND DISCUSSION

4.1 Contact resistance after COF bonding

Figure 10 shows bonding force effect on the contact resistance of the COF samples cured at various temperatures before reliability test. The respective curing conditions are (a) 170°C, (b) 190°C, and (c) 210°C. As can be seen the contact resistance is lower when the bonding force is larger, the bonding temperature higher, and the bonding time longer.

Figure 11 shows SEM photographs of the COF samples cured under three different conditions (a) 170°C/5sec/(30g/bump), (b) 210°C/5sec/(30g/bump), and (c) 210°C/15sec/(70g/bump). The photographs obviously indicate the gap between the leads of flex and the bumps of IC chip to be the largest for condition (a), second largest for condition (b), and the smallest for condition (c). The corresponding contact resistance of the sample shown in figure 11(a) is the largest, followed by (b), and (c) is the lowest. Comparing figure 11 (a) with 11 (b), it is learned that higher bonding temperature results to higher curing extent for the binder, the binder hence becomes stiffer. After the bonding process, the conductive particle only recoils a little, the gap is small, and then the contact resistance is relatively low. As learned from figures 11(a), (b), and (c), the gap is smaller and the contact resistance lowers, when the bonding force is larger, bonding temperature higher, and bonding time longer.

4.2 Contact resistance after thermal cycling test

Figure 12 shows bonding force effect on the contact resistance of the COF samples cured at various temperatures after thermal cycling test (-20°C~70°C / 30 cycles). The respective curing conditions are (a) 170°C, (b) 190°C, and (c) 210°C. As can be seen the contact resistance is lower when the bonding force is larger, bonding temperature higher, and bonding time longer. The variation of contact resistance is relatively small after the thermal cycling when comparing figure 10 against figure 12. This indicates that the ACF bonding has been barely affected by thermal cycling.

4.3 Contact resistance after high temperature humidity test

Figure 13 shows bonding force effect on the contact resistance of the COF samples cured at various temperatures after the high temperature humidity test (60°C/95%RH/100Hr). The respective curing conditions were (a) 170°C, (b) 190°C, and (c) 210°C. As shown in figures 13, those samples cured at the higher temperatures or longer curing time, the contact resistance decreased with the increase of bonding force, except for the sample bonded at 170°C for 5 sec as shown in figure 13(a), the contact resistance increases with the increase of the bonding force. This sample which bonded at 170°C for 5 sec may be due to poor curing of the binder that results to weak structure and poor adhesion. Since larger bonding force induces larger bouncing force, larger gap could then be resulted after the high temperature humidity test. This in turn results to higher contact resistance.

Comparing figure 13 against 10, it can be seen that the contact resistance of all the COF samples became higher after the high temperature humidity test. This was especially true for that cured at 170°C for 5 sec. This clearly indicates high temperature humidity test to have great impact on the ACF bonding, especially when the resin is not fully cured.

According to the 27 sets of experiment, it was realized that the COF sample fabricated at 210°C for 15 sec with a bonding force of 70g/bump exhibited the lowest contact resistance. Its contact resistance had been barely affected after the reliability test. Its fabrication condition was then decided to be optimal. The subsequent COF samples were then prepared under this chosen condition. Their interconnection characteristics were investigated and given in the following section.

4.4 Contact resistance at various temperatures

Figure 14 shows the contact resistance of the COF samples at different environmental temperatures. As seen in figure 14, the contact resistance increased with the increase of temperature. This may be attributed to the fact that the CTE of the ACF binder is smaller than that of the Au bump and conductive particle. This CTE mismatch caused reduction of the contact area between the IC bump and particles or between the electrode and particles, which would increase the contact resistance.

When the temperature was higher than 130°C, the contact resistance increased with the increase of temperature at a higher rate. This is because the binder was softened at temperature above its T_g. The softened structure would be more difficult to hold the conducting parts in good contact. Furthermore, the CTE value of the binder increased with the increase of temperature at a higher rate. Larger thermal mismatch for the binder with the conducting parts caused more serious reduction in their contact area. This, in turn, resulted to a rapid increase in the contact resistance.

4.5 IV curve measurement

Figure 15 shows the I-V curve result of the COF joints. The I-V curve shows a linear relationship as the current is smaller than 0.09A, indicating that the joint is an ohmic contact.

5. CONCLUSION

The impact of thermal cycling test was quite small on the contact resistance of COF joint. Whilst, the impact of high temperature humidity was significantly large.

Optimal process parameters were determined according to the results from high temperature humidity test. When bonding temperature($\geq 180^{\circ}\text{C}$) and bonding time(≥ 5 sec) were fixed, the contact resistance become smaller when the bonding force increased. Either higher bonding-temperature or longer bonding time can result to higher degree of curing for the resin. In order to have a high throughput, bonding temperature can be increased to shorten the bonding time. To prevent resin damage, bonding time can be increased to improve the desired extent of curing even at lower bonding temperature.

The contact resistance of the COF sample obtained according to the optimal process parameters was quite low (around 0.1Ω) and it was ohmic contact. The variation of the contact resistance after reliability test was quite small (below 0.02Ω). Even when the operation temperature is as high as 140°C , the contact resistance is still small (around 0.18Ω). The electrical characteristics of the COF samples were stable and excellent.

References

- [1] Janto Tjandra, CL Wong, James How, and Stefan Peana, "Au-Sn Microsoldering on Flexible Circuit", 1997 IEEE/CPMT Electronic Packaging Technology Conference, pp. 52-57
- [2] Christine Kallmayer, Hermann Oppermann, Sabine Anhock, Ramin Azadeh, Rolf Aschenbrenner, and Herbert Reichl, "Reliability Investigation for Flip-Chip on Flex Using Different Solder Materials", 1998 Electronic Components and Technology Conference, pp. 303-310
- [3] Ray Fillion, Bill Burdick, Pat Piacente, Len Douglas, and Dave Shaddock, "Reliability Evaluation of Chip-on-Flex CSP Devices", 1998 International Conference on Multichip Modules and High Density Packaging, pp. 242-246.

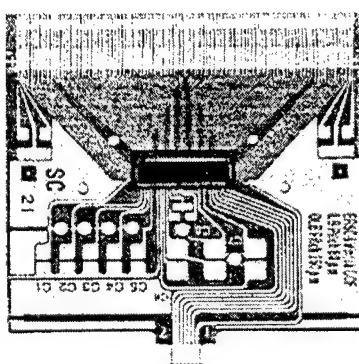
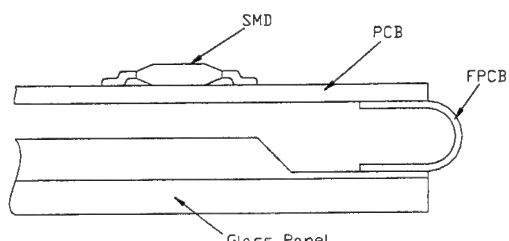
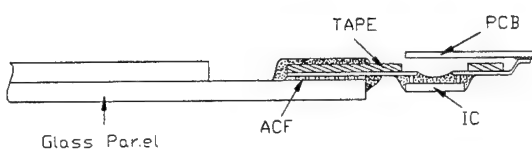


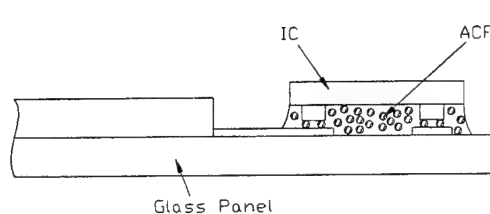
Figure 1. COF sample developed by Wintek and ITRI ERSO. The pitch is $80 \mu\text{m}$ and film thickness is $44 \mu\text{m}$.



(a)



(b)



(c)

Figure 3. COF mobile phones by Wintek. The pitches are $120 \mu\text{m}$ (left) and $80 \mu\text{m}$ (right).

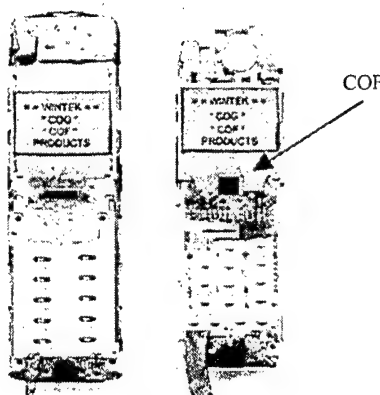


Figure 2. Three kinds of LCM packaging technology: (a) Surface Mount Technology (SMT), (b) Tape Automated Bonding (TAB), and (c) Chip on Glass (COG).

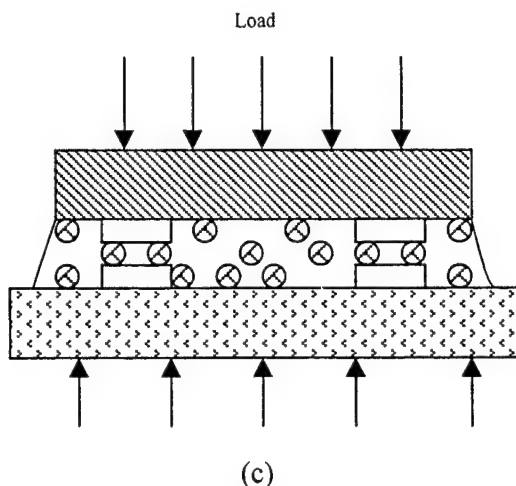
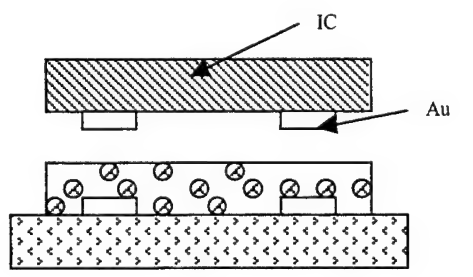
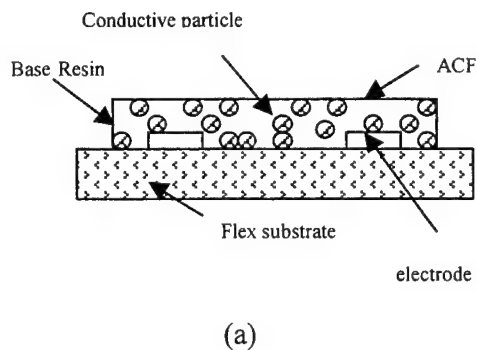


Figure 4. ACF process:

(a) Lamination (Temporary bonding): Impose enough pressure and temperature to attach ACF on flex substrate,
 (b) Alignment: Align between IC and flex substrate, and
 (c) Bonding: Apply high temperature and pressure through IC to cure the ACF.

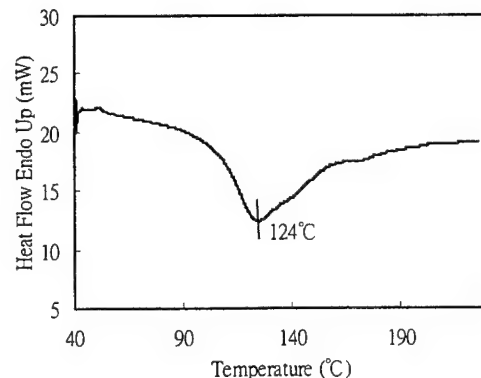


Figure 5. DSC result of the ACF. The ramp rate is 10°C/min.

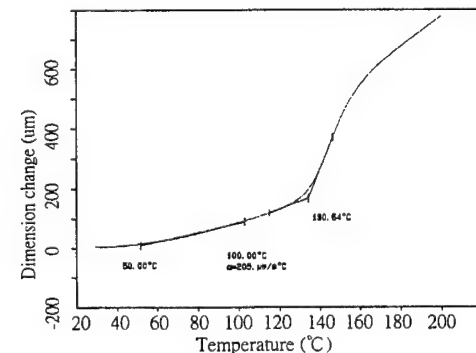


Figure 6. TMA analysis of the ACF, which had been cured at 180°C for 5sec.

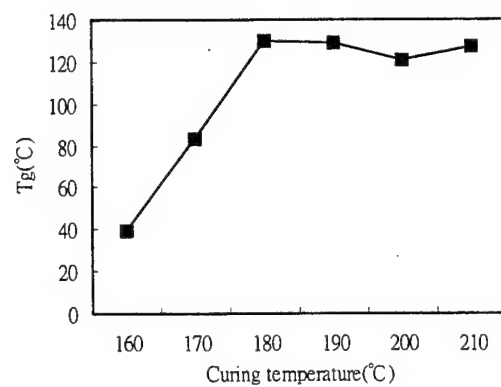


Figure 7. Effect of curing temperature on the Tg of the studied ACF.

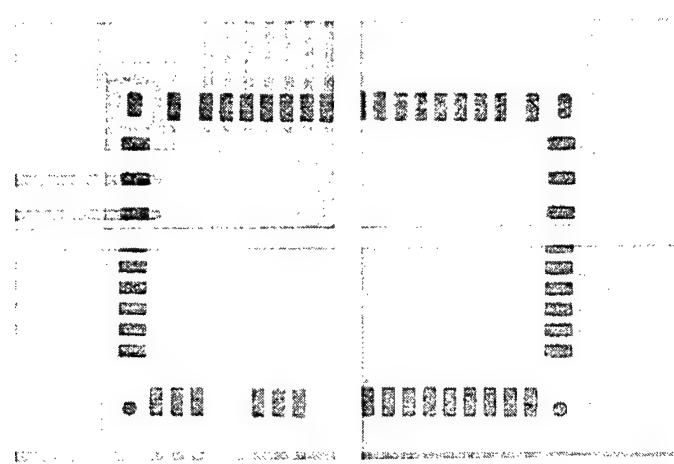


Figure 8. X-ray inspection of the backside of COF sample.

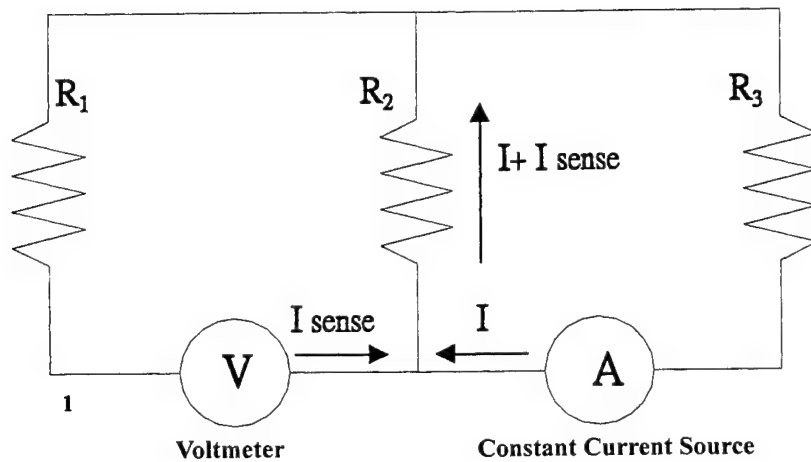
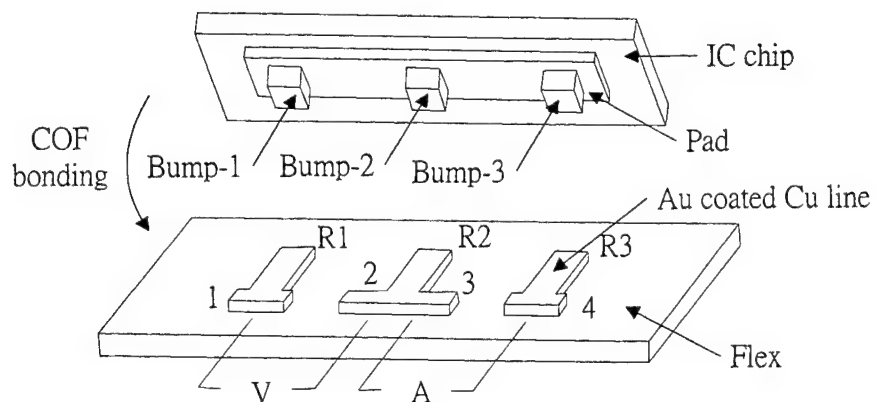
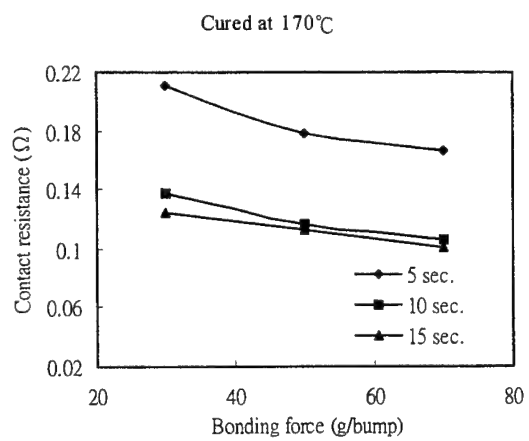
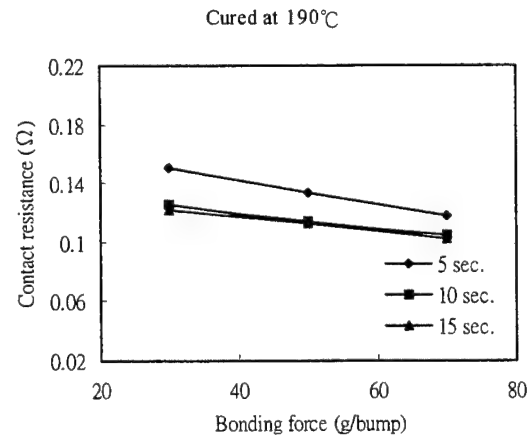


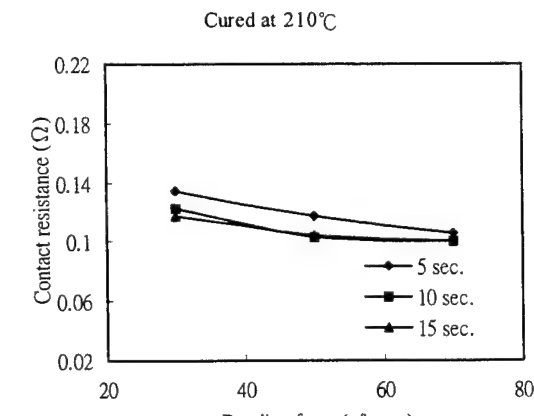
Figure 9. Schematic illustration of the R_2 contact resistance measurement by using the 4 points test method and its corresponding circuitry.



(a)



(b)



(c)

Figure 10. Bonding force effect on the contact resistance of the COF samples cured at various different temperatures before the reliability test.

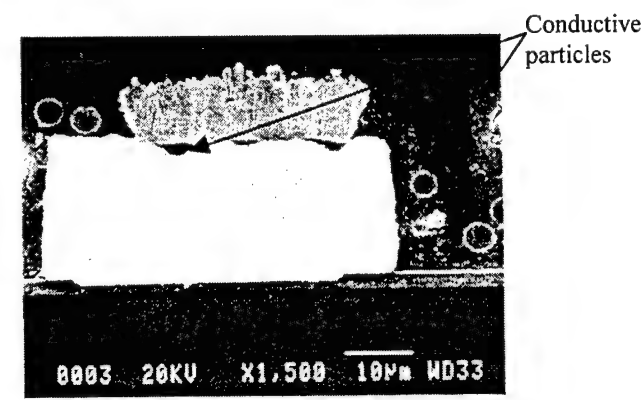
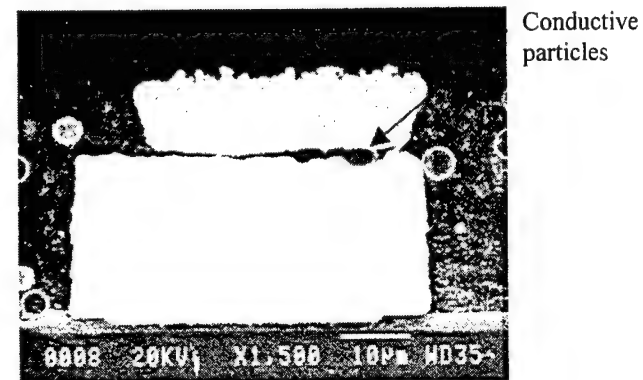
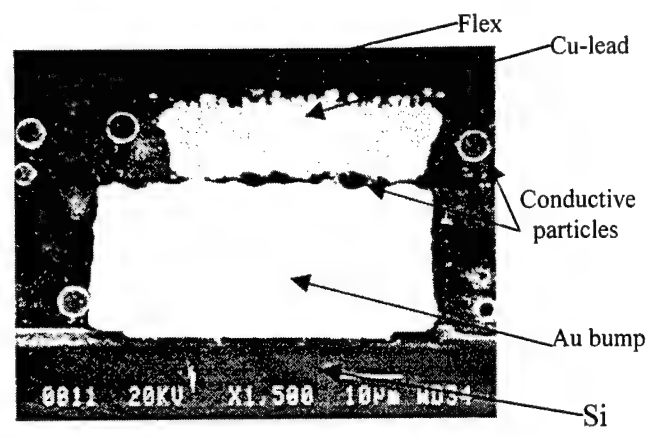
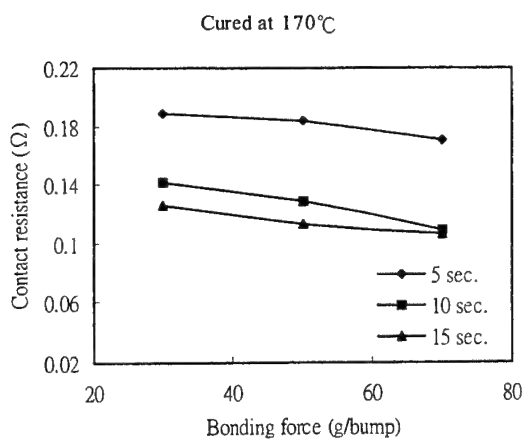
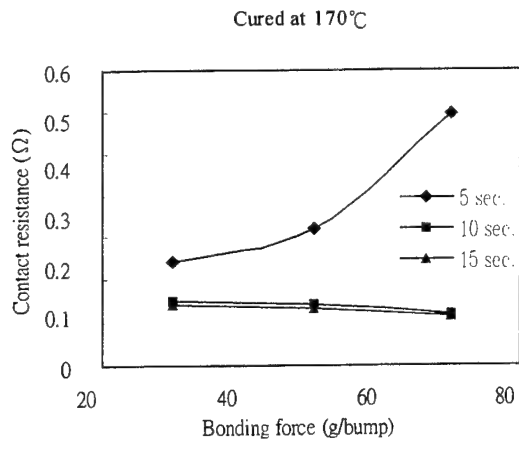


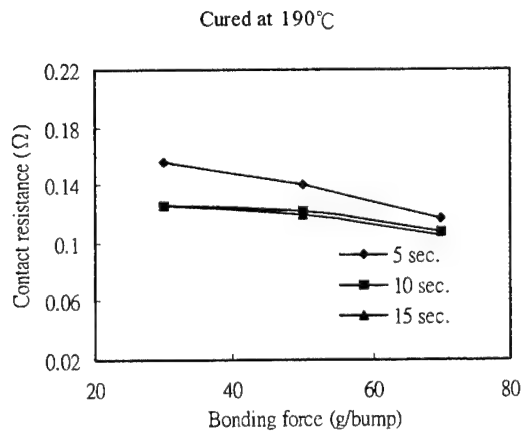
Figure 11. SEM photographs of the COF samples cured under these different condition (a) 170°C/5sec/(30g/bump), (b) 210°C/5sec/(30g/bump) and (c) 210°C/15sec/(70g/bump)



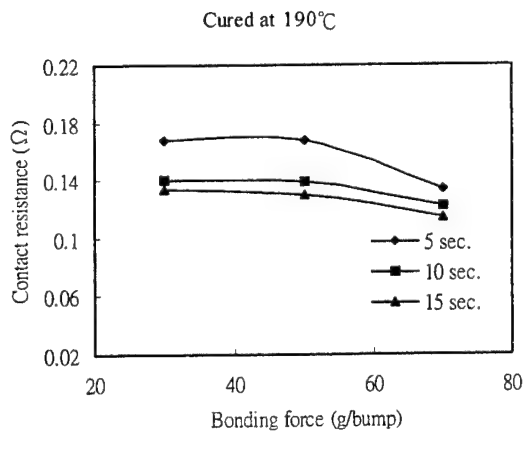
(a)



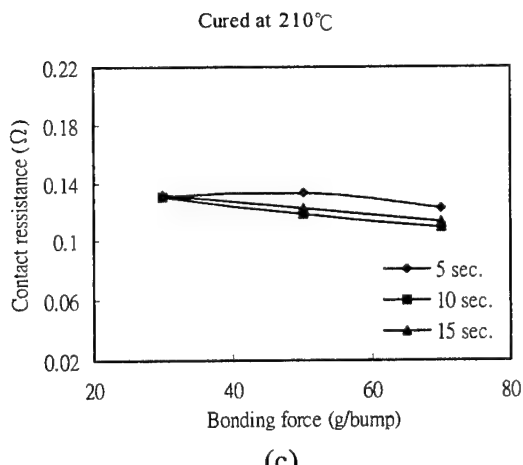
(a)



(b)

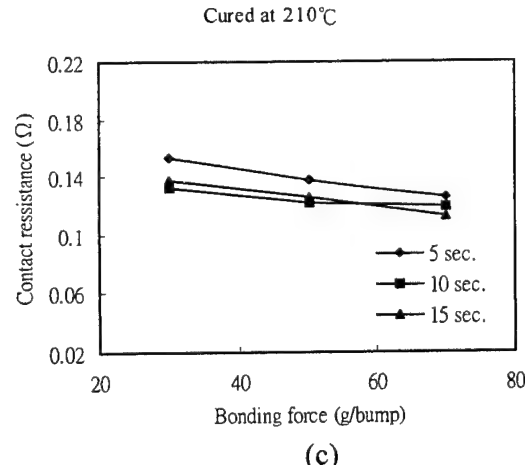


(b)



(c)

Figure 12. Bonding force effect on the contact resistance of the COF samples cured at various different temperatures after the thermal cycling test from -20°C~70°C for 30 cycles.



(c)

Figure 13. Bonding force effect on the contact resistance of the COF samples cured at various different temperatures after the high temperature humidity test at 60°C, 95%RH for 100hrs.

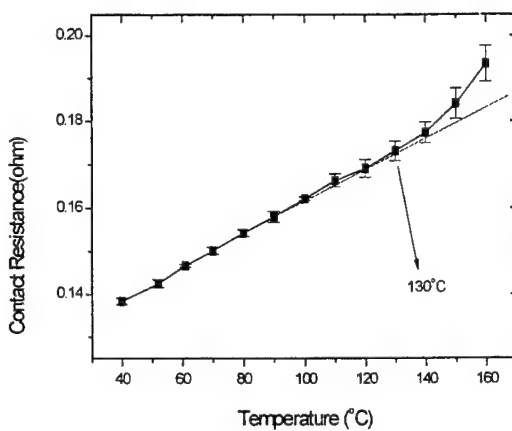


Figure 14. Contact resistance measured at various different temperatures.

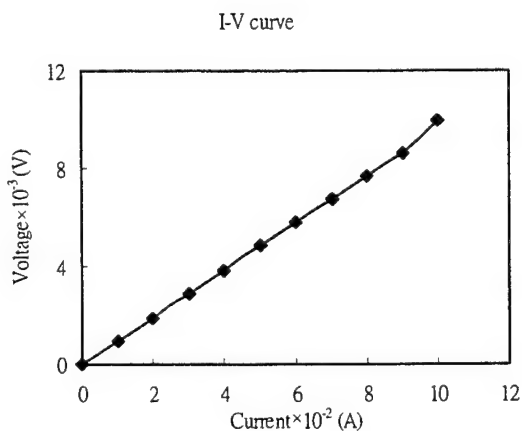


Figure 15. I-V curve of the resultant COF sample. The nearly straight line clearly indicates its ohmic contact characteristic

Poster Session

Multibubble sonofluorescence display

Hua-Mao Li*

Scientific Research Managerial Office, JI-AN Teachers College, JI-AN 343009, China

ABSTRACT

Based on the multibubble sonofluorescence display principle of the aqueous luminol-alkaline solution, two experimental applications, displaying the ultrasonic cavitation field and confirming the temperature distribution characteristic of the ultrasonic fountain are introduced.

Keywords: Multibubble, sonofluorescence, display, jetting cavitation field, luminol-alkaline solution, ultrasonic fountain, cavitation concentrating effect , temperature.

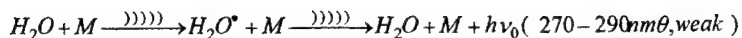
1.INTRODUCTION

In this time, more and more scientists think highly of the ultrasonic cavitation, especially its physical, chemical and biological effects. But many of them feel perplexed because of the difficulties they meet with in duplicating some effects. One of the reasons is lack in the understanding for the whole cavitation field. Actually the cavitation field consists of a great number of cavitating bubbles at micron and microsecond dimensions and their bulky host "liquid". In the past half century, many scientists researched the cavitation field by means of different methods and knew some important characteristics of it, but still the interactions among the bubbles and their impacts on the transmission, absorption and reflection of the ultrasound haven't been understood^{1,2}. The author refers specially to the works of Katsuo Negeshi in 1962 and V. Rauandin et al. in 1994. A common technology adapted by them was to use the sonoluminescence (SL) of aqueous luminol – alkaline solution (luminol C₈H₇N₃O₂, a chemiluminescence substance) for real-timely displaying the cavitation field. However, the ultrasounds with some frequencies lower than one megahertz were used, also the sonochemical reactors were alone symmetric in shape^{3,4}, and even nobody has so far detected the temperature distribution of the field which is very important for the most of the ultrasonic effects as mentioned above^{1,2}. Based on the multibubble sonofluorescence (Abbreviated to MBSF) display principle proposed by the author, this paper introduces the MBSF display of the cavitation field in space which generated by the ultrasound with a frequency of 1.45MHz and intensity of 5W/cm² in both the symmetric reactor and non-symmetric reactor, and the MBSF confirmation of the temperature distribution characteristic of the ultrasonic fountain(a jetting cavitation field) produced by the ultrasound with a frequency of 1.7MHz and intensity of 18W/cm².

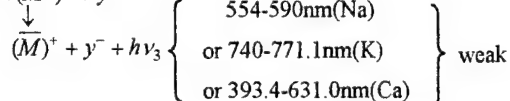
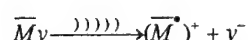
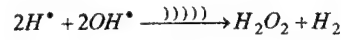
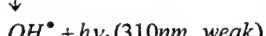
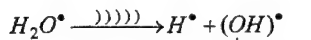
2.PRINCIPLE

In the ultrasonic cavitation field, the excited water molecule (H₂O') is divided into the hydrogen free radical (H') and hydroxyl free radical (OH'), and they quickly reform to hydrogen peroxide (H₂O₂), an intermediate product when the two free radicals combine again. It is the hydrogen peroxide that serves as an oxidation substance for clear chemical fluorescence of luminol in the aqueous alkaline solution. From the point of view of the exciting source, such the oxidation goes the name of cavitation oxidation and the chemical fluorescence by name MBSF The sonophysical and sonochemical process of it would be indicated in the following reactions^{5,6}:

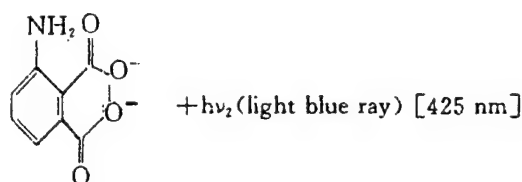
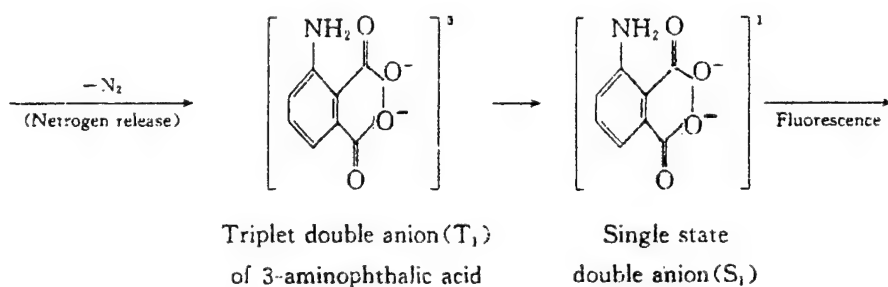
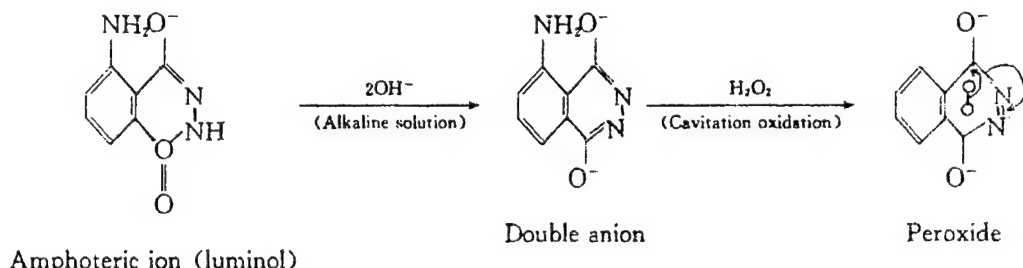
Correspondence: Mail: c/o P. O. Box 903, JI-AN City, JIANG-XI province, 343005, China;
E-mail: lihm @ public1.japtt.jx.cn ; Telephone: 796-8211526; Fax: 796-8103283



M: dissolved gas molecule or atom)))): cavitation field



$\overline{M}y$: alkaline compound, Na_2CO_3 , NaOH , KOH or Ca(OH)_2



Ground state
double anion (S_0)

Based on the above-stated views, the author has detected the MBSF spectra of the above-described aqueous solutions. The main emission of the solutions is about 375~750nm, a fluorescence range of luminol⁵. One of them is shown as in Fig.1. Apparently the emission region is sensitive to the naked eyes and the color film, and the intensiver the cavitation field is, the more the cavitation oxidation is, and the brighter the MBSF is.

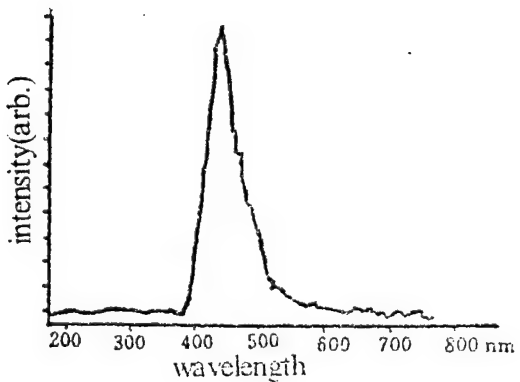


Fig.1 MBSF spectrum of $C_8H_7N_3O_2 \cdot H_2O \cdot Na_2CO_3$ (Used by SPEX 1403 monochrometer , USA)
Ultrasonic frequency: 1.45MHz, acoustic intensity: $5W/cm^2$

3.APPLIED EXPERIMENTS AND RESULTS

3.1 Displaying the Cavitation Field

In doing the experiments, the display set-ups and processes must be conducted in the dark room, the ultrasound applied is equal to that in Fig.1. The exposition time of the color film is about 15 minutes. Figs.2-3 represents the display set-ups with a symmetric reactor or non-symmetric reactor, and the MBSF pictures of the cavitation fields induced in the reactors

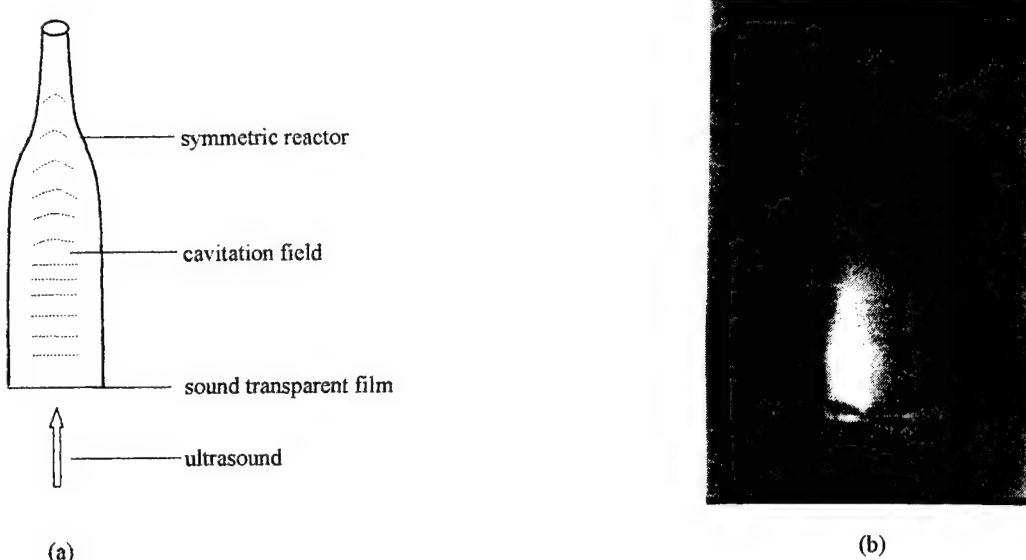


Fig.2 (a) set-up for display; (b) MBSF picture of the cavitation field induced in the symmetric reactor with the aqueous luminol - NaOH solution

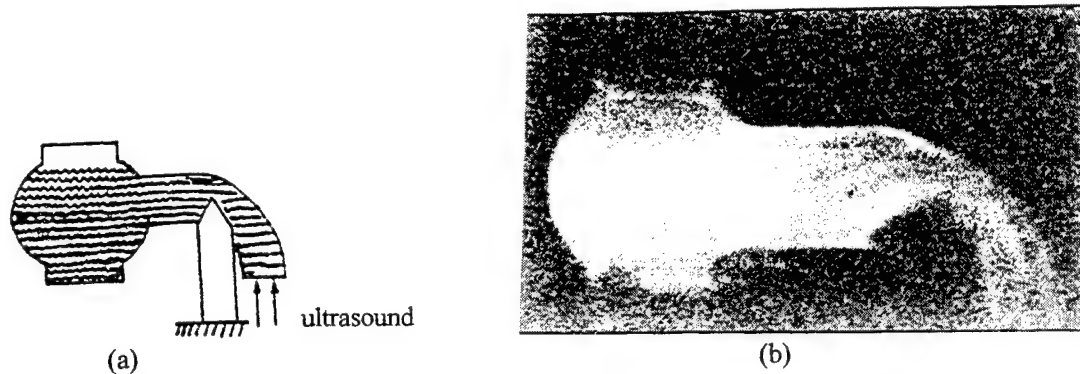


Fig.3 (a) set-up for display; (b) MBSF picture of the cavitation field induced in the non-symmetric reactor with the aqueous luminol-KOH solution.

Figs.2-3 shows that all the cavitation fields are clearly non-uniform in space no matter what sonochemical reactors used in shape, and the cavitation intensity of any point in the field changes with its space position in the field.

3.2 Confirming the Temperature Distribution of the Ultrasonic Fountain

According the heating phenomenon by the ultrasonic fountain, the authors made a point that the fountain, a cavitating water, should be considered as a jetting ultrasonic cavitation field, and the heat would result from the cavitation concentrating effect in the field^{7,8}. Based on the physical concepts of the fountain, it is easy to get the rough and relative temperature distribution along with the axis of the fountain produced by an ultrasound with a frequency of 1.7 MHz and intensity of 18W/cm^2 in the reactor with the aqueous luminol- Na_2CO_3 solution even with the tap water (Fig.4). In order to confirm the characteristic of the temperature distribution, in a similar way, the space picture of the fountain can be taken by using the MBSF display as mention above.

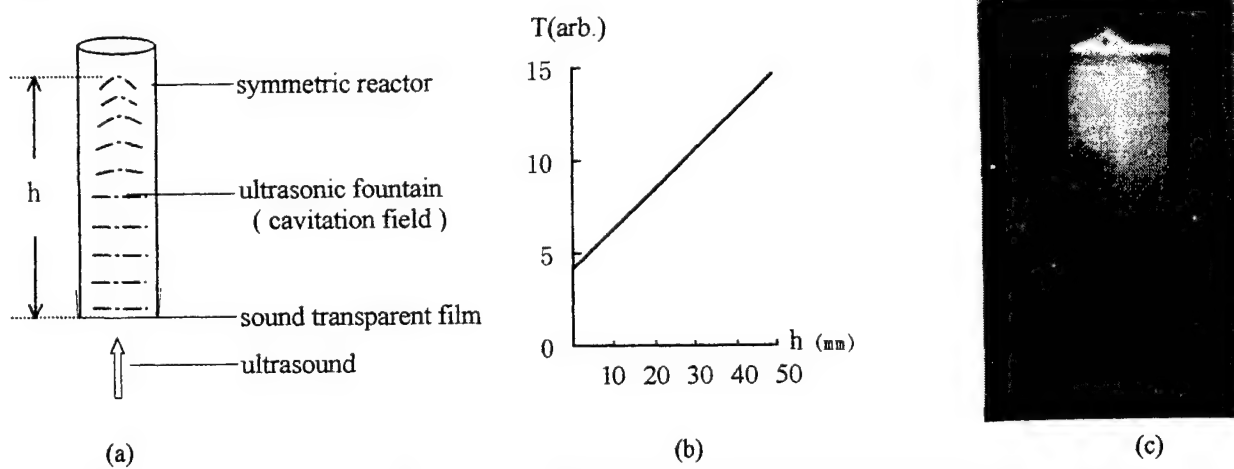


Fig.4 (a) ultrasonic fountain and its display set-up; (b) Rough temperature distribution along with the axis of the ultrasonic fountain (h : height of the fountain; T : reading in one minute when the thermometer is set into the fountain); (c) MBSF picture of the ultrasonic fountain.

The result shows that the stronger the cavitation region is, the brighter the region is, so the higher the temperature is in the region and that the cavitation effect is upward concentrated in the jetting cavitation field.

4. CONCLUSIONS AND DISCUSSIONS

The MBSF can be used to display the whole ultrasonic cavitation field directly and real-timely. In the mean time, used to confirm the rough temperature distribution characteristics of the jetting cavitation field. As a simple method, it might be used to improve the ultrasonic reactor, and to explain the some effects in the cavitation fields.

ACKNOWLEDGEMENTS

The project supported by the Natural Science Foundation of JIANGXI province, NANCHANG and the National Lab. of Acoustic Field and Information, Beijing.

REFERENCES

1. E. A. Neppiras, "Acoustic cavitation," Physics Reports **61**, pp.232-242, 1980.
2. K.S.Suslick, ULTRASOUND: Its Chemical, Physical, and Biological Effects, VCH publishers, Inc., New York, 1988.
3. K. Negishi, "Experimental studies on sonoluminescence and ultrasonic cavitation," Journal of the Physical Society of Japan, **16**, pp.1450-1464, 1961.
4. V. Renaudin, N. Gondrexon, P. Boldo, C. Petrier, A. Bernis and Y. Gonthier, "Method for determining the chemically active zones in a high-frequency ultrasonic reactor," Ultrasonics Sonochemistry, **1**, S81-S85, 1994.
5. H. Li, F. Zhong, A. Xi, R. Feng and Z. Chen. "Sonoluminescence enhanced by luminol," Proceedings of the World Congress on Ultrasonics (Sept.3-7,1995, Humboldt-University, Berlin, Germany), Part2, pp. 627-630, 1995.
6. H. Li, "Sonofluorescence method," Acousto-Optics and Applications III (May 18-22,1998,Gdansk-Jurata, Poland), SPIE Vol.3581, pp. 371-373, 1998.
7. H. Li,Y. Li and Z. Li, "The heating phenomenon produced by an ultrasonic fountain," Ultrasonics Sonochemistry, **4**, pp.217-218, 1997.
8. H. Li, "Cavitation concentration," Proceedings of the International Symposium on Hydroacoustics and Ultrasonics (May 12-16,1997, Juratsa, Poland), pp.151-152,1997.

THE METHOD AND THEORY OF TURN BACK POINT ERROR

Ya-Nan Liu,^a Jian-Kang Zeng,^a Jun-Qi Liu,^a Tong Wu^b

^aXi'an Institute of optics & precision Mechanics (XIOPM), Xi'an, Shaanxi 710068, The People's Republic of China;

^bNorthwestern Polytechnical University, Xi'an, Shaanxi 710072, The People's Republic of China.

ABSTRACT

This paper described the theoretical basis of extreme Value orientation in detail, which is used to examine the dimension of hole and axle with double point one coordinate measure instrument, and it's quality and feature and calculation method of survey error on dimension, which is caused by turn back point error, The paper also provide a practical chart, which is used to revise at the same time also introduced the study method which is designed by author;

Key words: Two point and one coordinate measure instrument, turn back point error; Orientation.

1. GENERALIZATION

Double measuring points and single coordinates instruments of geometric element gauge is the most common used precision instrument. The design of measuring method of these instruments is fundamentally based on orientation by extreme value criterion, that is, in measuring direction, there exists extreme on the size-line of measured parameter, because of this orientation method, all these instruments assemble universal bed. When measured parts was fitted on the universal bed, they have five freedoms, so can move to and fro, left and right, up and down, horizontal and vertical so on. Which makes it convenient to find the extreme value on the transversal and axial of measured parts. The whole process of finding extreme value is completed under surveillance of reading meter of the instrument. Find turn back point from the reading meter is label of finding extreme value.

It is analyzed in this text that theoretical base of extreme value existence and its nature, also it describes turn back point error which was created by transfer mechanism error of the bed, reading error from reading meter, and surface roughness of measured parts, and also it relates size measuring error by positional error of turn back point. Experimental research method of turn back point error designed by the author is also included in the text.

2. THEORETICAL BASE OF TURN BACK POINT

If there exists residual deviant ΔC in the cross section of measured aperture, the following formula is given(shows in fig 1):

$$(R_X - \delta)^2 = \left(\frac{\delta}{2}\right)^2 + \Delta C^2$$

$$\frac{s^2}{[2(R_x - \delta)]^2} + \frac{\Delta C^2}{(R_x - \delta)^2} = 1$$

(1)

This formula is probability equation (shows in fig.3), so we can get the following conclusions:

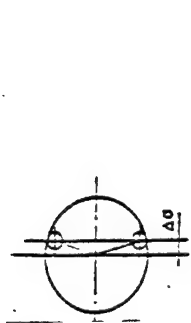


fig.1

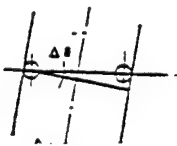


fig.2

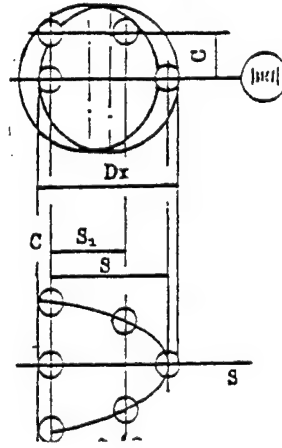


fig.3

1. Vertex of major axis $[2(R_x - r), 0]$, we get the maximal value of size s . So this point is called turn back point at which point the detection error of measured aperture is 0. ($\delta_{DX}=0$)
2. When offset the turn back point ($C \neq 0$), the detection error of measured aperture is :

$$\delta_{DX} = 2\sqrt{(R_x - r)^2 - Dc^2} - 2(R_x - r) \quad (2)$$

3. When $\Delta C \ll D_x$

THE FORMULA:

$$\delta_{DX} = 2(R_x - r) \left[1 - \frac{\Delta C^2}{2(R_x - r)^2} - 1 \right] = \frac{-\Delta C^2}{R_x - r} \quad (3)$$

The formula express that detection error is proportional to the deviant δ_c^2 and inverse proportional to aperture ratio of the measured to the probe.

4. At vertex of major axis $[2(R_x - r), 0]$, the radius of curvature is given as:

$$\rho = \frac{R_x - r}{2} \quad (4)$$

So the sensitivity of extreme value method is limited in searching of turn back point.

5. When $\delta=0$, formula 3 can be simple as:

$$\delta_{DX} = \frac{\Delta C^2}{R_x} \quad (5)$$

In the axial section of measured aperture, and the residual deviant of inclination being as: $\Delta \theta$, the following formula is given.(fig.2 can be seen)

$$\delta = \frac{2(R_X - r)}{\cos \theta} \quad (6)$$

The formula above is a periodic curve.(fig.5)

Conclusions

1. At curvilinear vertex, we get the maximal value of size s. So this point is called turn back point at which point the detection error of measured aperture is 0.(/ $\delta_{DX}=0$)

(7)

2. When offset the turn back point ($\Delta C \neq 0$), the detection error of measured aperture is :

$$\delta_{DX} = 2(R_X - r) \left(\frac{1}{\cos \Delta \theta} - 1 \right) \quad (8)$$

3. When $\Delta \theta = 0$

$$\delta_{DX} = (R_X - r) \cdot \Delta \theta^2 \quad (9)$$

THE FORMULA:

The formula express that detection error δ_{DX} is proportional to the inclination deviant $\Delta \theta^2$ and proportional to deviation between measured aperture and diameter of the probe.

4. At curvilinear vertex($R_X, 0$) the radius of curvature is given as:

$$\rho = \frac{1}{2(R_X - r)} \quad (10)$$

So the sensitivity of extreme value method is limited in searching of turn back point.

5. When $\delta = 0$ formula 8 can be simple as:

$$\delta_{DX} = R_X \cdot \Delta \theta^2 \quad (11)$$

The things listed above is all about components of pore, to components of shaft generally use probe with axe formation (fig.4)

Width of its cutting edge is r.

Length is L.

In the transversal section of shaft, $L=8$. So it is easy to make $\Delta C=0$. In the axial section, since $h=1.5mm$, inclination deviant is $\Delta \theta$. Size detection error is:

$$\delta_{DX} = R_X \cdot \Delta \theta^2 + h \cdot \Delta \theta \quad (12)$$

For there exists an item of $h \Delta \theta$, the sensitivity in searching for turn back point is greatly improved.

3. CORECTION METHOD OF TURN BACK POINT ERROR

When the radius of probe $r=0$, detection error of the measured aperture created by residual deviant ΔC can be calculated through formula 5.

Fig.6 gives the detection error δ_{DX} when $r=0$ $\Delta C=0.01\sim 0.1\text{mm}$ $D_x=10\sim 100\text{mm}$
 Fig.7 gives the detection error δ_{DX} when $r=0$ $\Delta \theta=0.1\sim 1^\circ$ $D_x=10\sim 100\text{mm}$

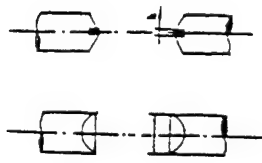


fig. 4

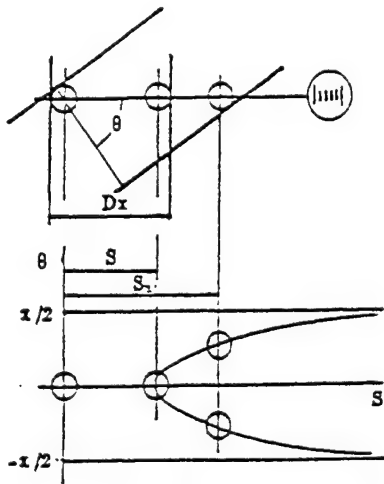


fig. 5

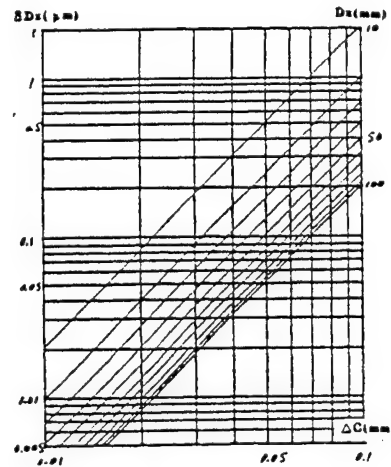


fig. 6

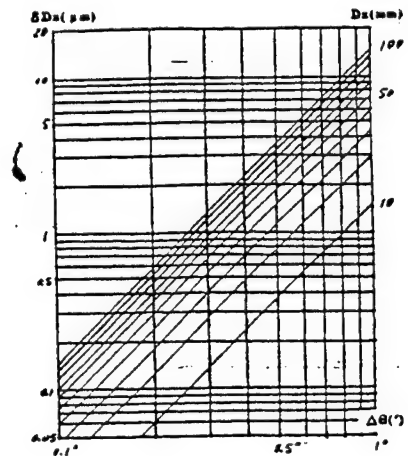


fig. 7

The partial plane level of terrace and its test

Ya-Nan Liu,^a Jian-Kang Zeng,^a Jun-Qi Liu,^a Tong Wu^b

^aThe Xi'an Institute of optics and precision Mechanics (XIOPM), Department of optics-Electronics Engineering, Xi'an, Shaanxi 710068, The People's Republic of China;

^bNorthwestern Polytechnical University, Xi'an, Shaanxi 710072, The People's Republic of China.

ABSTRACT

At present, the way to test plane level of terrace are all indirect survey methods at first, author choose some survey sections and get dates from these sections according to stipulation with survey method and then proceeding the dates, through which can strive the plane level error. The plane level dates Calculated with these dates can't make an overall plane level assessment to the terrace, especially to the partial position so, it can't be describe in detail on all terrace because of not been survived usually. Author all the error and plane level in the partial range the partial plane level, its assessment is very important to control the microcosmic quality.

The paper also discuss the theory issue on speckle method and plane fluctuate capacity method with exist for a long term;

Key words: terrace partial plane level, assessment.

0. INTRODUCTION

Now the detection method of plate flatness are all indirect in and out of the country. It is let light selects definite detection cross section on which according to the specified check point we get the datum and by treating them, the value of flatness is known. Since the method is limited by technical conditions Such as the way of detection and of datum treating, there is some local position (shows as area on large plate)left undetected, then it is impossible to make an elaborate describe about the working site of detected plate.

Usually, local error on the local range of plate and flat of small plate is called local flatness, and detection on which is greatly important on controlling microscopic quality of the plate, so it is absolutely necessary to test the local flatness of plate to make the detection result according to some test point of certain section honestly reflect condition of integrate plate flatness error.

The text described often used method to detect local flatness of plate, items to be cared, and disputing problems long-term existed such as form of detection instrument, how to evaluate the plate quality showed by touched spots and so on.

1. GRINDING TOUCHED SPOTS OF PLATE AND ITS DETECTION

For scraped cast iron plate, in addition to test its geometry error ,still there is a need to test the colored spots .Doing this has two purpose one is to detect microscopic quality of plate working area ,that is ,to detect height of peak and valley .the other is to prevent plate working area from local distortion in small ranges .when detect the flat of plate working area by existed instrument ,pitch method is the most often used way which detect according to certain sections and definite spans ,so the test spots is limited .In all , colored spots detection must be done.

In JJG117-91 verification code of plate measurement ,it clearly specified the touched spots data of new-made and repaired scraped cast iron plate, and stipulate the data deviation between any two positions should coincident to the Table1.

Table 1

Detection item	precision grade			
	00	0	1	2
Touched spots datum in 25mm*25mmarea	≥25	≥20	≥12	
Data deviation between any two square(25mm*25mm)		≤5		

Use the verification instrument which coincident to table 1 and table 3 to make the colored detection.(coating thickness should be 0.002 to 0.004mm)

Table 2

Precision grade	Verification instrument
00	00 grade of plate
0.1	0 grade of plate and flat ruler
1.2	1 grade of plate and flat ruler

Table 3

The specification of detected plate	Verification tools	
	Specification of plate	Flat ruler specification
<400×400	<400×400	>500
>400×400~1000×1000	≥400×400	>500~1500
>1000×1000~1600×1600	≥630×630	>1500~2500
>1600×1600	≥1000×1000	>2500

When verification tools and detected plate touch each other, we can not apply loads along vertical direction. When the verification tools is smaller than plate, the tools must not be dragged away from the working area of detected plate. When sizes of the two is same, the tools can be dragged out but up to one fifth of its own area.

It can not afford accurate error value, so it is difficult to evaluate the plate grade by it, and this method needs a lot of energy. On the other hand, distortion is inevitable. With the development of detection skill, the effect of this method has been reduced. But the method has been used for years and it is beneficiary to keep the plate quality especially to high precision plate, the method is still a kind of important useful detection method at least to the plate which has high accuracy and small size.

2.THE RATIO EVALUATION OF TOUCHED SPOTS TO AREA

When the verification on the data of touched spots create disputes, it is necessary to add the verification of the ratio of touched spots to area and take it as the last evaluation result .the ratio should coincident to the table 4.

Table 4

Verification item	precision grade			
	00	0	1	2
The ratio of touched spots to area on unit area	≥ 25	$\geq 16\%$	$\geq 10\%$	
The ratio deviation between any two unit area	$\leq 5\%$			

Specific ratio of touched spots to area is evaluated by the following way. place a piece of glass plate with the 500mm*500mm area on which engraved 400 small quadrates which area is 2.5*2.5mm,in sequence observe and estimate the fraction of touched spots to area on each quadrate, record the results .the detected plate ratio of touched spots to area is reached by add all fractions and multiply by 1/400.

The reason to refill the additional specification(specific ratio of touched spots to area)is that the stipulation on touched spots data prompt that: needs a lot of time and energy to make the bigger point dispersed, or the spots datum is not qualified. But use for a while, many spots joint together to be an area, which is beneficiary to improve wear resistance .in fact, the most parts of energy spend on precision ground is ineffective. So the detection of touched spots data is displaced by detection of special ratio of touched spots to area in some foreign countries.

3.PLANE FLUCTUATION VALUE OF WORKING AREA

Local flatness error of plate is specified as flatness of straight line in any position and certain length in most countries. The norm of China is SL flatness in 200mm length, and it stipulate to check by using fluctuation instrument showing in fig.1, which was used by English plate norm. Chinese norm is also stipulate: if it is inconvenient to check touched spots such as cast iron plate and stone plate, plane fluctuation value of working area should be detected, the value of it must be up to the specification of table 5.

Table 5

Precision degree	00	0	1	2	3
Fluctuation value of working area	4	8	16	32	80

Verification: place the plane fluctuation instrument on the working area of plate , and drag it along a SL .the dragging distance is one half of the diagonal length of the plate and must larger than 200mm .during the dragging ,read the maximal and minimal value from the dial indicator on the fluctuation instrument .absolute value of the deviation between the two listed value is plane fluctuation value.

This verification result only reflect the action under the dial indicator, and have no data value exchanging relationship with SL flatness error in 200mm and the plane height changes created by three fixed supporting point, so in the table 5 intuitively specify tolerant variance value of the instrument. It is convenient to measure and check the local flatness error of working area by using this method. And the method is required for stone plate. It is very easy for the plate in use to find abrasion condition and scratches on surface by using this detection method , and from this we can conclude if it is necessary to repair.

4. THE FLATNESS OF WORKING AREA IN ANY LOCAL REGION

International norm ISO/DP 8512/1984 specified the flatness of working area in any local region of plate. 250mm*250mm local area is called local region, and the norm clearly express the detection method of flatness tolerance in any local region of working area is as same as the detection of overall flatness of plate with the area of 250*250mm. Detection by this method, smooth and integrity of the working region appearance should be first searched. Then research and analysis the measurement results of overall flatness error to determine which parts produce sudden and big configuration degree changes. Draw the maximum deviation region then make verification on them, if in that region the flatness is acceptable, then it is certain that local flatness of overall plate is reasonable. The plate which diagonal length is less than 354mm can not have a region with 250mm*250mm area, under this condition, check the overall flatness to express local flatness.

5. CONCLUSIONS

1. Since local flatness of working area of plate is an important parameter to show its surface microscopic quality, it must be detected.
2. To scraper, touched spots data and specific ratio of touched spots to area can be checked. To stone plate, it is necessary to make verification on plane fluctuation value.
3. To plate which is not made by scraping such as ground plate and stone plate, it is recommend to check the plate local flatness by using the detection method of testing flatness of any local region on working area.
4. Since detect local error of plate working area by plane fluctuation instrument has many distinct advantages, it is necessary to take research on the relationship between its detection value and flatness error of SL which length is 200mm also and local flatness error to improve the method applied extensively.

Simulation of Geometric Effects on Double-Gate Field Emission Devices

Ching-Wu Wang, Chih-Liang Chen^{a)}, Yuan-Hsiu Yang and Tsung-Yu Yang

Department of Electronic Engineering

I-Shou University

Ta-Hsu Hsiang, Kaohsiung County,

Taiwan, R.O.C.

ABSTRACT

We report a study of the circular-shaped and rectangular-shaped focus-gate Field Emission Devices (FED) structure. In this work, we have developed a simulator of FED based on the Finite Difference Method (FDM). The major element of this simulator is a modified Fowler-Nordheim (F-N) field emission model. We evaluate the performances of the circular-shaped and rectangular-shaped focus-gate FED structures by using this simulator. Results reveal that the circular-shaped focus-gate FED structure has more collector current. Also, the focusing characteristics of electron beam are improved.

Keywords: circular-shaped, rectangular-shaped, focus-gate, Field Emission Devices, simulator, Finite Difference Method, Finite Difference Method, Fowler-Nordheim, electron beam

1. INTRODUCTION

Field Emission Devices (FED) have many potential applications in Flat Panel Display (FPD)¹⁻³. Field emission displays are increasingly becoming one of the significantly emerging candidates for the next generation technology of display due to lightweight, small volume, wide view-angle and low power. They are highly predicted to be commercially available in the near future. Nonetheless, there are many drawbacks of the FED, such as the phosphor power of exceptional materials, small collector current and low brightness. Many investigators have tried to improve these defects.

To improve the collector current and beam-focusing characteristics of FED and to obtain an optimized device structure, many investigators simulated the performances of FED⁴. Most investigators used Finite Element Method (FEM)⁵ and Fowler-Nordheim (F-N) field emission model to simulate FED. However, the FEM consumes computation time of CPU. Therefore, we utilized Finite Difference Method (FDM) to compute the current—voltage relationships to accelerate computation time of CPU than FEM. Besides, the major elements of our simulator are a modified Fowler-Nordheim field emission model, electron-trajectory simulation in vacuum space (considering space charge effects) and the characteristic simulation of electrical performances. The procedure steps of the FED simulation include: (1) solving the two-dimensional Poisson equation, (2) calculation of the emitter-tips electric field (3) obtain the current density⁶⁻⁸ by using the remarkable Fowler-Nordheim (F-N) tunneling formula. In addition, space charge effect⁹⁻¹¹ and emitter heating effect¹² have been considered in the simulation.

In this work, simulated electrical performances based on the geometric effects of different focus-gate structures have been systematically investigated. In addition, we will evaluate the performances of the circular-shaped and rectangular-shaped focus-gate FED structures by using this simulator. Finally, we will show the results of collector current and electron beam in vacuum space.

* Correspondence: E-mail: cwwang@isu.edu.tw; Telephone: 886-7-6577711 ext. 6668; Fax: 886-7-6577056

2. NUMERICAL MODEL AND SIMULATION METHODS

When an external electric field is applied to the surface of a metal, the potential barrier is lowered due to the Schottky effect. If the electric field exceeds the order of 1×10^7 V/cm, field emission takes place.

A Fowler-Nordheim emission module was developed to model electron field emission from the surface. Emited current density is determined from the Fowler-Nordheim equation, which has been expressed as:

$$J = \frac{AE^2}{\phi \cdot t^2} \exp\left(-\frac{B \cdot v(y) \cdot \phi^{3/2}}{E}\right) \quad \text{Eq. (1)}$$

where $A = 1.5414 \times 10^{-6}$, E = the normal component of the electric field at the emitter surface, ϕ = work function of the emitter, taken as 4.35eV for Mo, $B = 6.8308 \times 10^9$, $t^2 \approx 1.1$, an approximation, and $v(y) = 0.95 - y^2$ with $y = 3.79 \times 10^{-5} \times E^{1/2} / \phi$ in SI unit. Initially, the Green's function solutions of the Laplace equation are computed for the given geometry. The electric field along the emitter surface was determined by superposition of the contribution from each conductor.

After the emission current is evaluated, we perform the electron trajectory simulation. The reason is this simulation paves the way for the determination of the electron density distribution in vacuum.

Electron trajectory simulation is in the following. First, no scattering event occurs during the electron transport in vacuum. Second, the non-diversity property of electron motion in space is suggested. The electron distribution function drops rapidly with an increase of the transverse-part of electron energy if the longitudinal-part of electron energy is kept the same due to the Fermi-Dirac statistics. Only a small portion of the tunneling electrons has an extra velocity component in the transverse direction. So, the assumption of the non-diversity effect of the electron tunneling through the barrier can easily be justified. Eventually, the magnetic effect is neglected.

From the classical Newtonian mechanics, the equation for the motion of electrons in the vacuum region can be expressed as:

$$\frac{d\vec{r}}{dt} = \vec{v} \quad \text{Eq. (2)}$$

$$m \frac{d\vec{v}}{dt} = e \nabla V \quad \text{Eq. (3)}$$

where \vec{r} and \vec{v} are the position and the velocity of the electron, respectively, t are the time, e and m are the electron charge and mass, respectively.

The initial conditions imposed on this assumption are:

$$\overline{\vec{r}(0)} = \frac{\int_{E_f}^{\phi} [r_o(W_l)N(W_l)T(W_l)]dW_l}{\int_{E_f}^{\phi} [N(W_l)T(W_l)]dW_l} \hat{n} \quad \text{Eq. (4)}$$

$$\overline{\vec{v}(0)} = \vec{0} \quad \text{Eq. (5)}$$

where $r_o(W_l)$ is the tunneling distance of electron with the longitudinal-part of electron energy equal to W_l and \hat{n} represents the unit vector which is normal to the emitter surface at that emission site. In addition, two kinds of boundary conditions, i.e., gate and collector, are employed. The total emitter-to-electrode current is computed by summing up all the

current elements, which are absorbed by the electrode. If the electrons arrive at a dielectric or vacuum boundary, the reflective boundary condition is applied for the same reason as we used in solving the 3D Poisson equation. Eq. (4) and Eq. (5) are then decomposed into six first order differential equation in the 3D Cartesian coordinate system. With the initial and boundary conditions, the fourth order Runge-Kutta method is applied to solve these six equations simultaneously. The position \vec{r} and the velocity \vec{v} of the emitted electrons can be easily obtained.

3. SIMULATION RESULTS AND DISCUSSION

The FED structures which includes a pyramid-like emitter, a control-gate electrode, an additional gate electrode (we call focus-gate), and a collector electrode is shown in Fig. 1. The control-gate controls the major current of tip emission¹⁶. Furthermore, the focus-gate is needed for focusing and accelerating emitted electrons.

We evaluated the performances of various focus-gate FED structures by using our simulator. Then, we will gain a physical insight into these devices by way of a series of analysis. Firstly, we discuss the results of current-voltage characteristic curves of the circular-shaped and rectangular-shaped focus-gate FED structure. Secondly, we will compare their electron trajectories. The effects of the focus-gate structure will be studied systematically. Finally, the dependence of collector current of the aperture of focus-gate will be investigated.

Fig. 2 shows the Current-Voltage characteristics curve of the circular-shaped and rectangular-shaped focus-gate FED structure. The collector and control-gate voltage are 1000V and 100V, respectively. As shown, the collector current of the circular-shaped focus-gate FED structure is larger than the rectangular-shaped focus-gate FED structure. Also, raising focus-gate bias of both FED structure can increase more collector current.

Fig. 3 (a)~(b) show the electron-trajectory simulation of different focus-gate structures. The applied biases of collector, control-gate and focus-gate are 1000V, 100V, and 10V, respectively. According to the simulation results of electron trajectory, we took advantage of circular-shaped focus-gate to control the electron trajectory of emitter, because it can significantly improve the focusing characteristics of electron beam.

Final, the dependence of collector current on the aperture of the circular-shaped and rectangular-shaped focus-gate FED structure is shown in Fig. 4. The biases of the control-gate, focus-gate and collector are 100V, 10V and 1000V respectively. The collector-electrode current increases with the aperture. Also, the collector current of the circular-shaped focus-gate FED structure is larger than that of the rectangular-shaped one.

4. CONCLUSIONS

We have applied our simulator to study the electrical performances of the circular-shaped and rectangular-shaped focus-gate FED structures. The dependence of the focus-gate characteristics of FED structures was investigated extensively. Results of the circular-shaped focus-gate FED structure are able to emit larger collector current than the rectangular-shaped one. By using circular-shaped focus-gate FED structure, the focusing characteristics of electron beam can be significantly improved.

ACKNOWLEDGMENT

Two of the authors (Ching-Wu Wang and Chih-Liang Chen) wish to thank National Science Council (NSC) in Taiwan for receipt of financial assistance (contract number: NSC89-2213-E-214-033) to undertake this work.

REFERENCES

1. Charles A. Spindt, Christopher E. Holland, Ivor Brodie, John B. Mooney, and Eugene R. Westerberg, IEEE Trans. Electron Devices, **36**, no. 1, pp. 225, 1989.
2. Boris Georfinkel and Jong Min Kim, J. Van. Sci. Technol. B, **15**, no. 2, pp. 254, 1997.
3. Chi-Chang Wang, Jiin-Chuan, Chin-Ming Huang, IVMC'96, pp. 557, 1996.
4. Xieqing Zhu and Eric Munro, J. Van. Sci. Technol. B, **7**, no 6, pp.1862, 1989.

5. A. Khursheed and A. R. Dinnis, High zaccuracy, J. Van. Sci. Technol. B, **7(6)**, pp.1882, 1989.
6. Forbes, R.G., J. Van. Sci. Technol. B, **17**, no. 2, pp.534, 1999.
7. Forbes, R.G., J. Van. Sci. Technol. B, **17**, no 2, pp.526, 1999.
8. Ashihara, K. Nakane, H. and Adachi, H., "Experimental confirmation of the Fowler Nordheim plot at several micro-meters emitter to anode distance", IVMC'95, pp. 93, 1995.
9. Zheng Chi and Linsu Tong, IEEE Trans. Electronic Devices, **40(2)**, pp. 448, 1993.
10. Nagaitsev, S. Ellison, T. Ball, M. Derenchuk, V. East, G.; Ellison, M. Hamilton, and B; Schwandt, P., Proceedings of Particle Accelerator Conference, **5**, pp. 2937. 1995.
11. Tron, A. and Merinov, Proceedings of Particle Accelerator Conference, **2**, pp. 2247, 1998.
12. Hao Ming, Tian Lilin and Yu Zhiping, Solid-State and Integrated Circuit Technology, pp. 472, 1998.
13. Richard True, in IEDM Tech. Dig., pp 379, 1992.
14. Richard M. Mobley and Jack E. Boers, IEEE Trans. Electron Devices, **38(10)**, pp. 2383, 1991.
15. Chen Wang, Baoping Wang, Hongwei Zhao, Johnny K. O. Sin and M. C. Poon, J. Van. Sci. Technol. B, **15(2)**, pp.394, 1997.
16. Chih-Wen Lu and Chung Len Lee, IEEE Trans. Electron Devices, **45(10)**, pp. 2238, 1998.

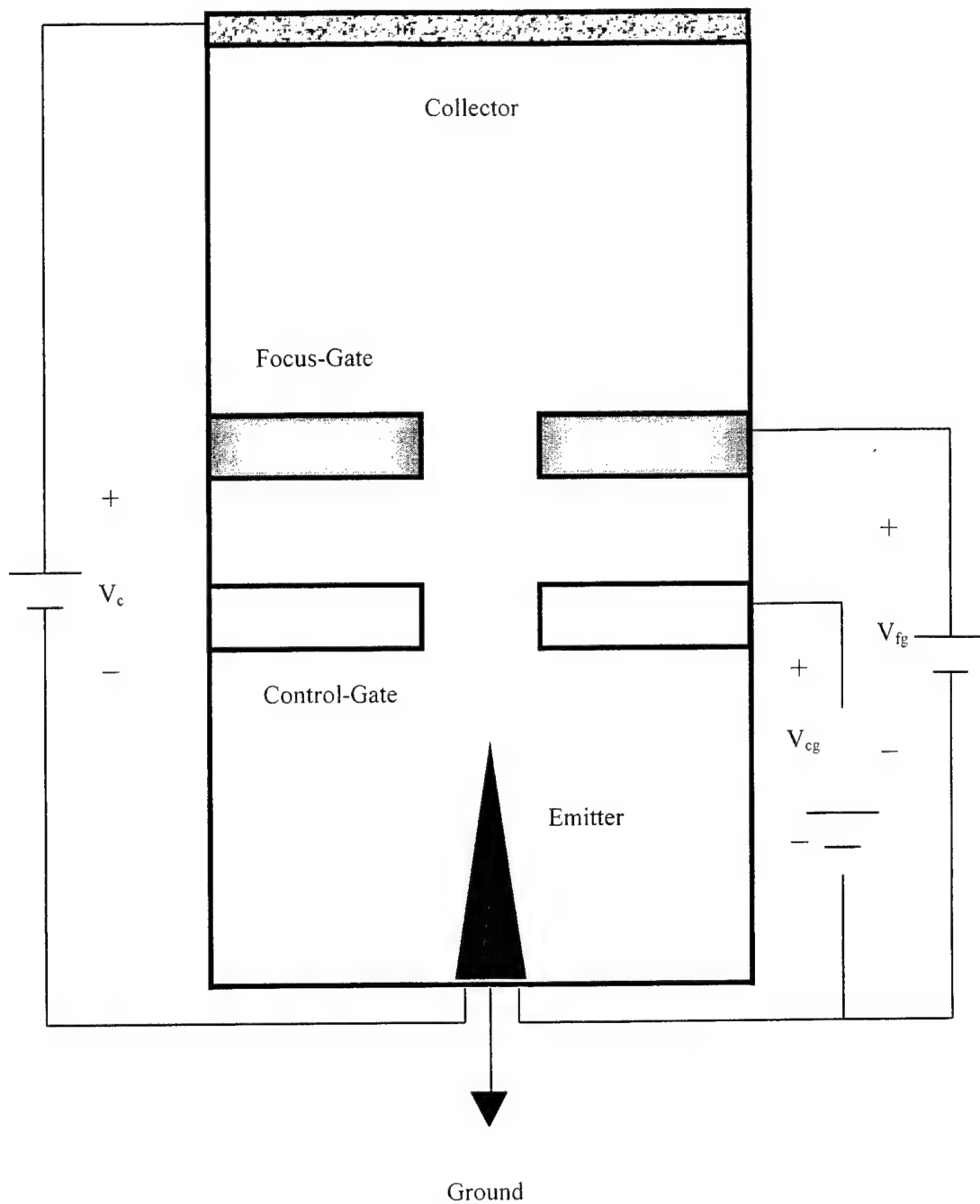


Fig. 1. Schematic diagram of the typical double-gate FED structure used in this article.

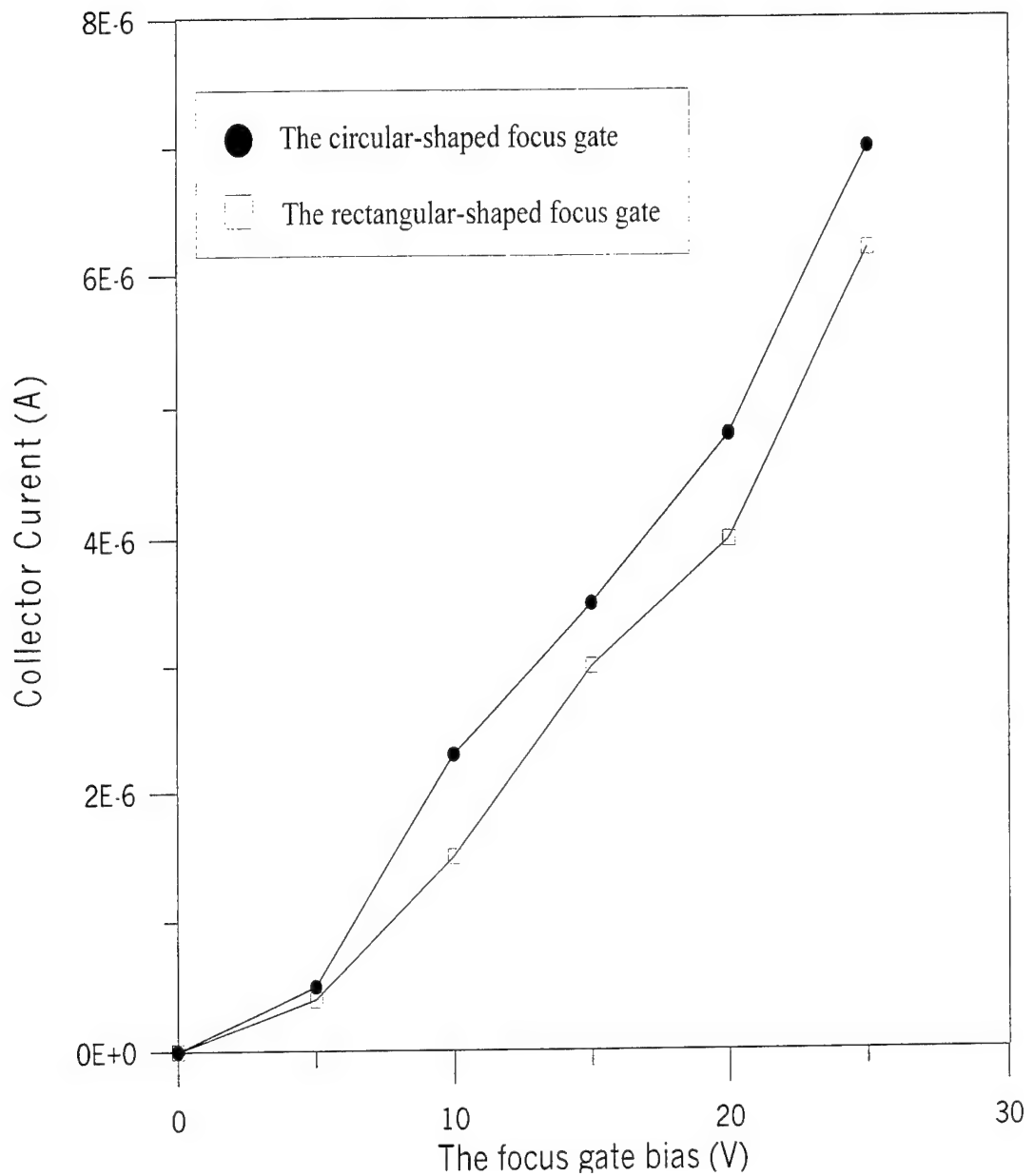


Fig. 2. The collector currents of the circular-shaped and rectangular-shaped focus-gate FED structures with different focus-gate bias. Where, the identical applied biases are $V_{cg}=100V$ and $V_c=1000V$.

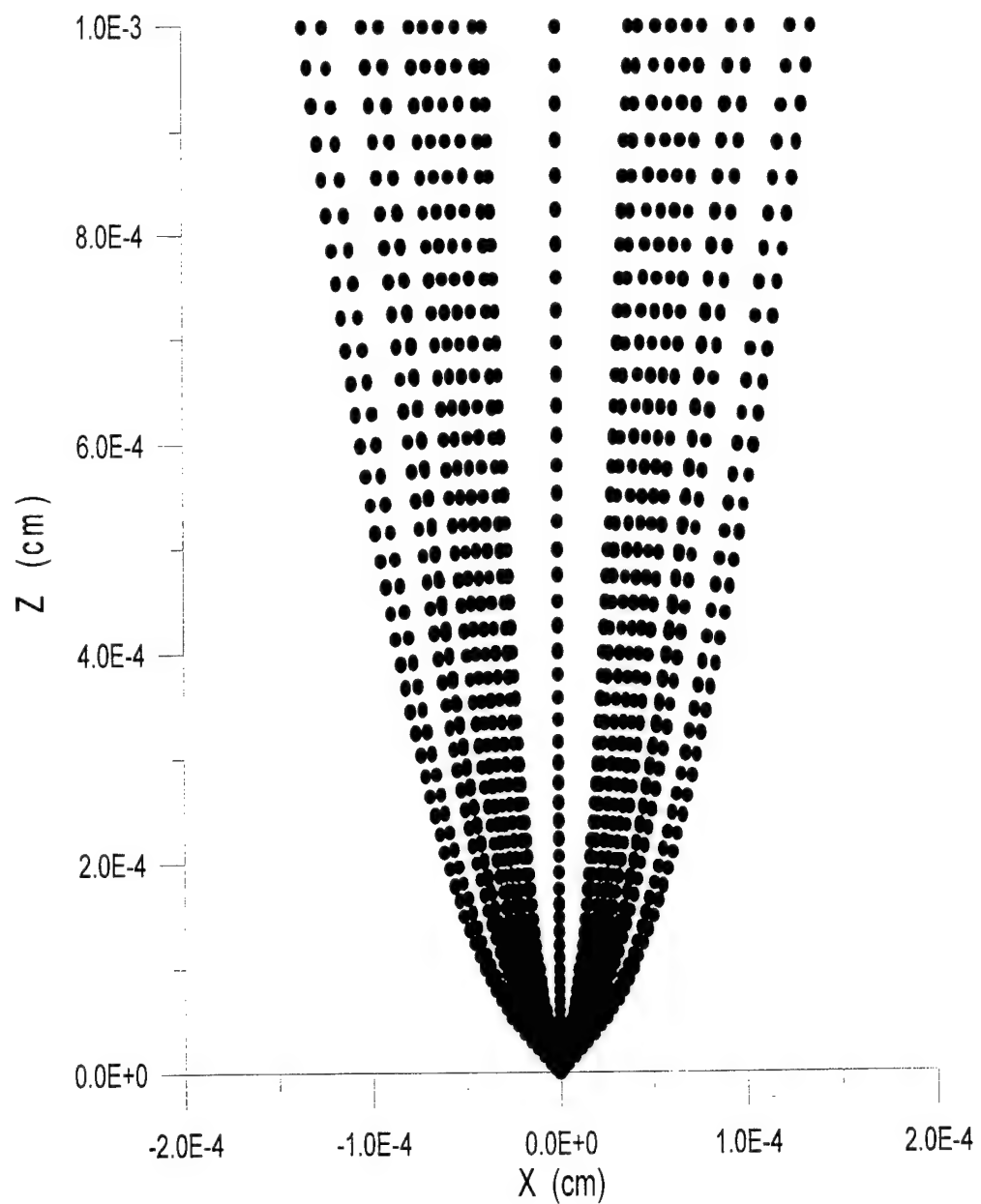


Fig. 3. (a) The simulated electron-trajectory results of the circular-shaped focus-gate of double-gate FED structure. Where, the applied biases are $V_{cg}=100V$, $V_{fg}=30V$, and $V_c=1000V$.

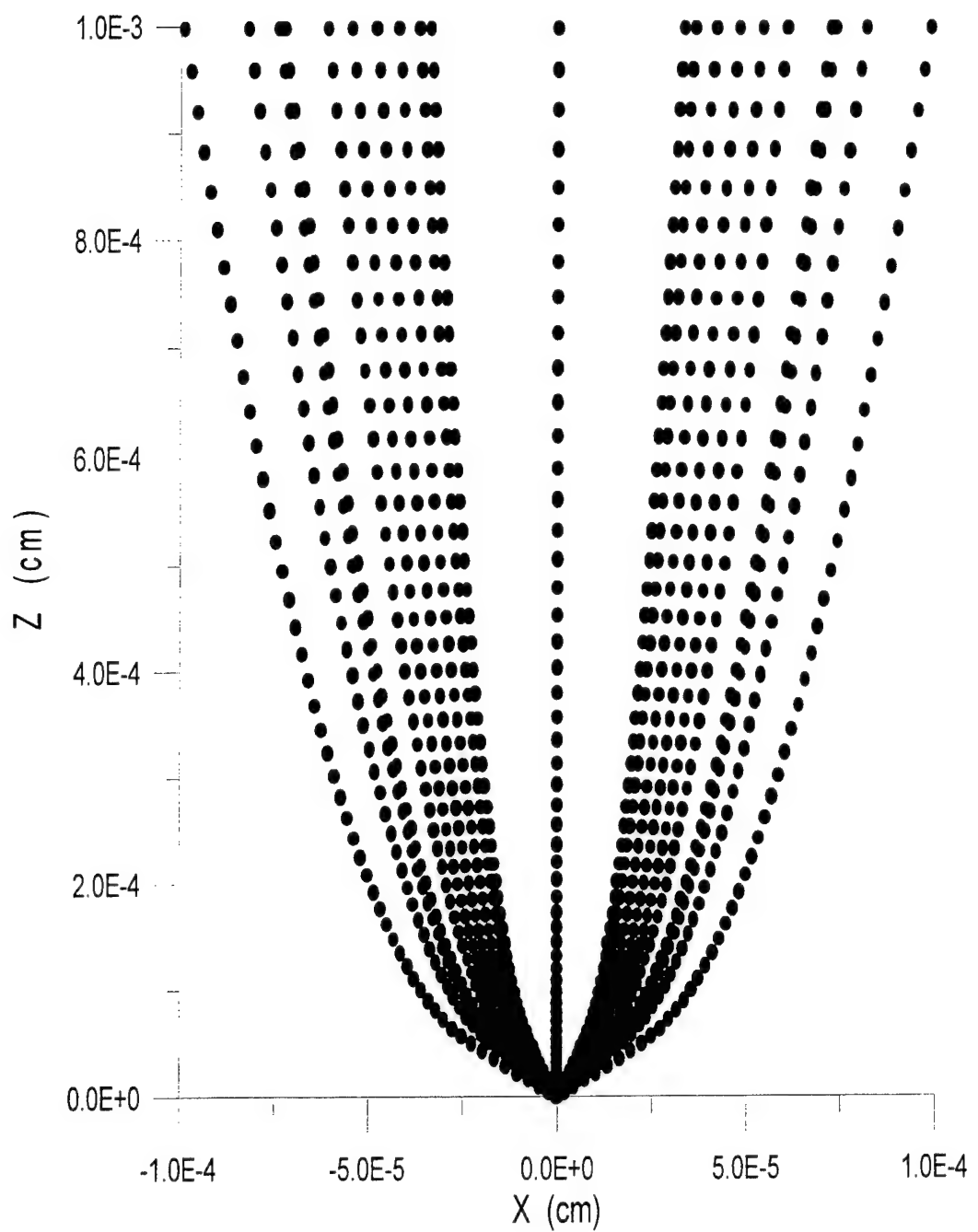


Fig. 3. (b) The simulated electron-trajectory results of the rectangular-shaped focus-gate of double-gate FED structure. Where, the applied biases are $V_{cg}=100V$, $V_{fg}=30V$, and $V_c=1000V$.

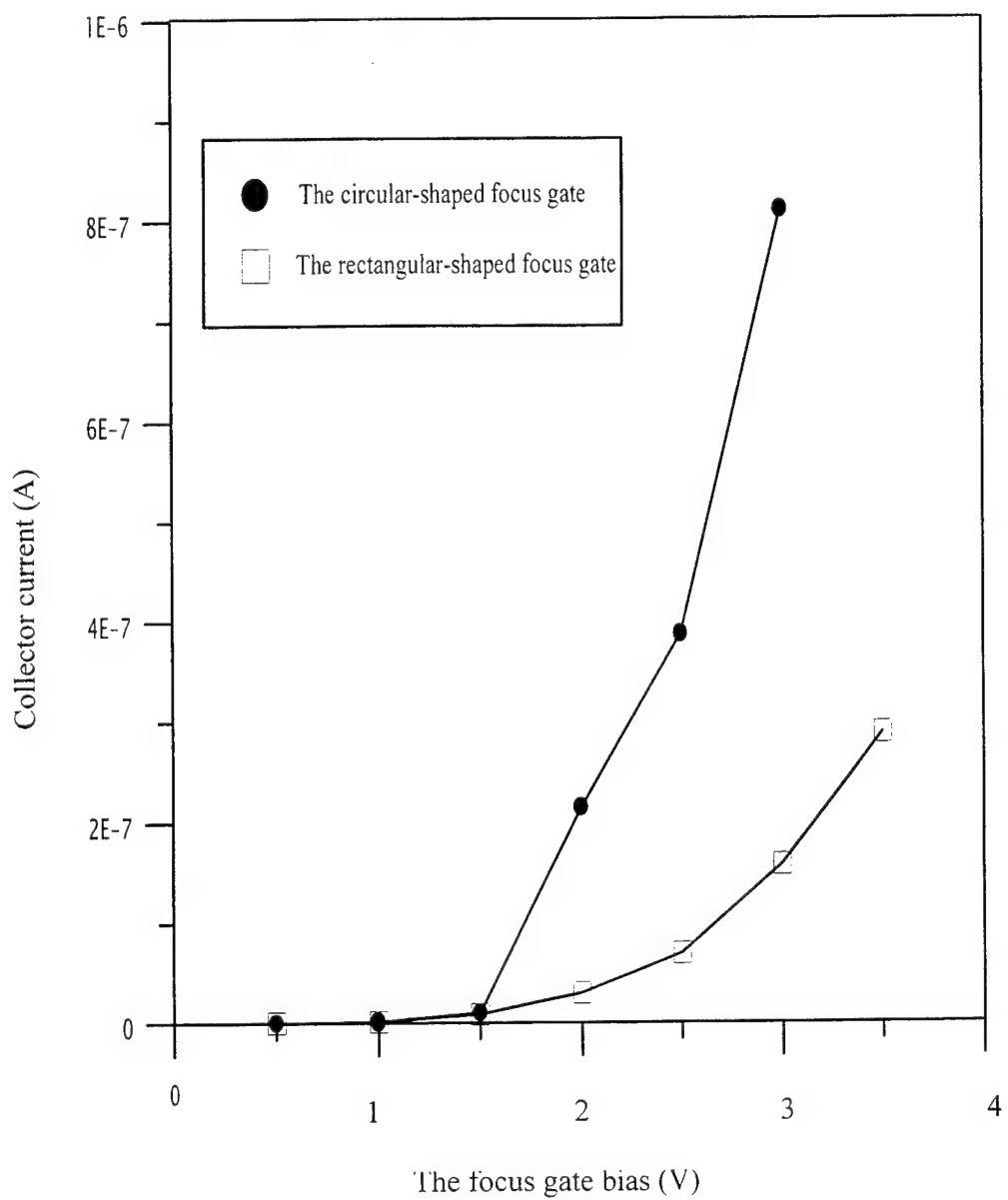


Fig. 4. The collector currents of the circular-shaped and rectangular-shaped focus-gate FED structure with different focus-gate aperture, where the identical applied biases are $V_{cg}=100V$, $V_{fg}=10V$, and $V_c=1000V$.

Improve product aperture ratio by controlling magnitude of reverse tilt domain

W.H.Ho, C.J.Pan, H.H.Wu**

Prime View International Co., Ltd., HsinChu, Taiwan, R.O.C.

Keywords: aperture ratio, reverse tilt domain, pre-tilt angle, rubbing density, pile impression, disclination, black matrix

ABSTRACT

In thin-film-transistor LCD, aperture ratio is an important parameter of transmittance. In this paper, we describe the relation between aperture ratio and reverse tilt domain. We conclude that we can control the magnitude of reverse tilt domain by changing rubbing density, pile impression, cell gap and altitude of TFT. Consequently, relatively large aperture ratio could be obtained by decreasing the area of black matrix.

PREFACE

In TFT-LCD, tilt direction of liquid molecule is opposite between reverse tilt domain and tilt domain⁽¹⁾. Consequently, the light leakage is observed at this boundary, especially in black picture. Furthermore, shade and contrast of reverse tilt domain are different to normally domain. In order to improve contrast and quality of picture, black matrix of color filter is used to cover reverse tilt domain. Aperture ratio depends on the area of black matrix, so we must reduce this area. The mechanism of reverse tilt domain is that voltage difference between pixel electrode and neighbor electrode change corner of liquid molecule tilt direction. Its position depends on rubbing direction, design of circuit and position of TFT. And its magnitude depends on cell gap, rubbing density, pile impression, and so on. Figure.1 Show the relation between electric field distribution and occurrence of reverse tilt domain⁽²⁾. According to this relation, we can increase pre-tilt angle to restrain reverse tilt domain, or decrease influence of voltage difference between pixel electrode and neighbor electrode.

EXPERIMENT

To focus on 6.4'''s product of PVI, we experimented with different conditions to measure reverse tilt domain, as follows:

First, to change roller revolution and moving velocity of rubbing machine to get different rubbing density⁽³⁾.

Second, to change clearance between roller and stage of rubbing machine to get different pile impression.

Third, to change density of spacer and end sealing pressure to get different cell gap.

Fourth, to change array process to get different altitude of TFT.

Fifth, to change rubbing direction.

The above-mentioned conditions are show in Table 1.

Table 1. Different experimental condition

Rubbing density	50, 100, 150
Pile impression	0.25, 0.35, 0.45mm
Spacer density	60, 100 piece/mm ²
End Sealing Pressure	0.5, 0.7 kgf/cm ²
Cell gap	4.8 ~ 5.8 μm
Passivation layer	2000, 6000 Å
Conduction layer	2000, 6000 Å
Rubbing direction	↖ ↗

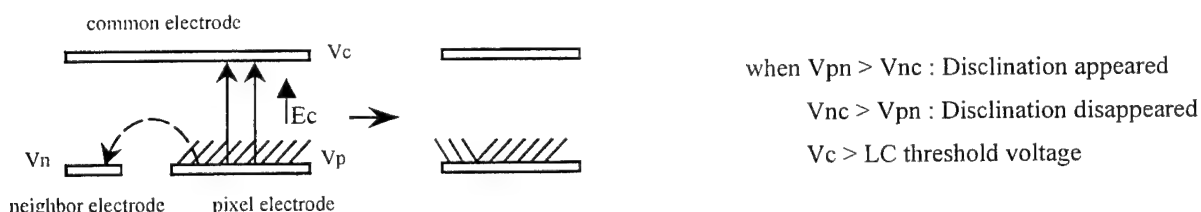


Figure 1. The mechanism of reverse tilt domain

RESULTS

Disclination line of 6.4", 1.8", 6.4"VGA production are shown in figure 2.

Pile impression

To decrease pile impression to increase pre-tilt angle, reverse tilt domain would be restrained effectively. The relation is shown in figure 3.

Rubbing density

Figure 4 shows the relation of rubbing density and reverse tilt domain. We find no regular relation among them. The reason is that rubbing density changes pre-tilt angle lightly (about 0.8°), when rubbing density is from 100 to 200.

Cell gap

Figure 5 shows that cell gap decreasing would restrain reverse tilt domain. When cell gap decrease, electric field intensity E_c and electric force F_c would increase, and reverse tilt domain would decrease.

Altitude of TFT

Altitude of TFT decrease, alignment would be improved at corner and reverse tilt domain would decrease.

Rubbing direction

Figure 6 shows that position of reverse tilt domain depends on direction of rubbing.

Spacer

Figure 7 shows that spacer would effect reverse tilt domain clearly, especially small size pixel.

Different Pixel Size

Table 2 shows that reverse tilt domain do not depend on pixel size, it is decided by driving signal and circuit layout.

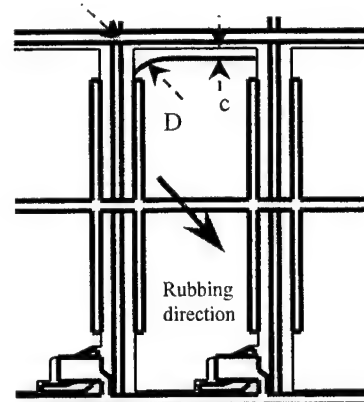


Figure 2.2 Structure of 6.4" pixel

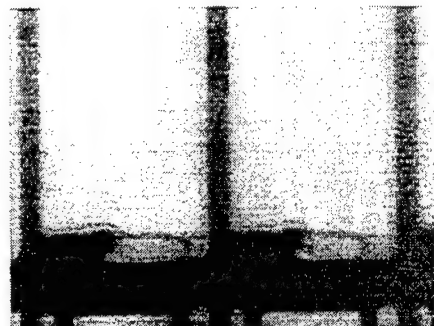


Figure 2.3 Disclination of 6.4"VGA product

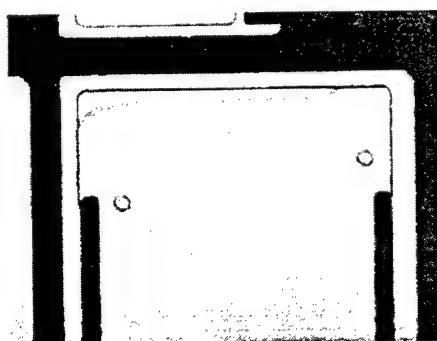


Figure 2.1 Disclination of 6.4" product

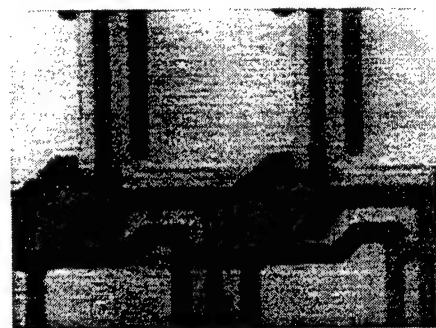


Figure 2.4 Disclination of 1.8" product

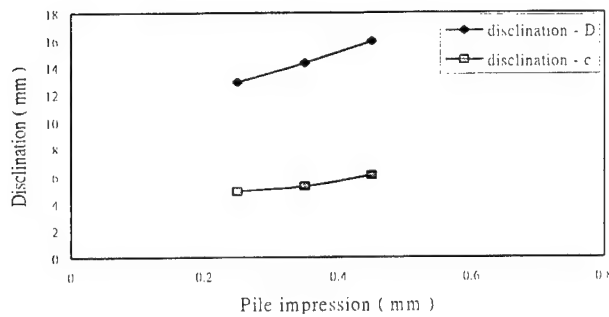


Figure 3.The relation of pile impression and disclination

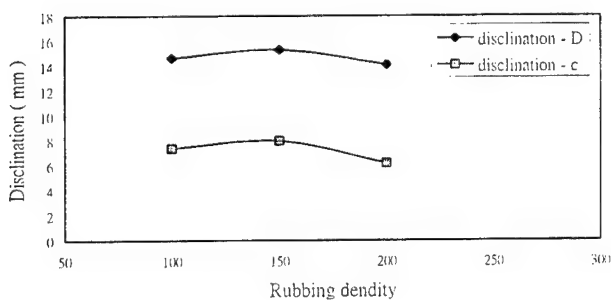


Figure 4.The relation of rubbing density and disclination

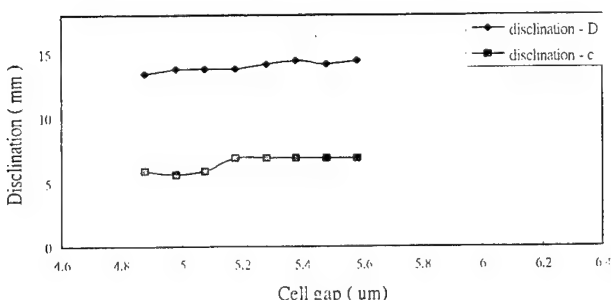


Figure 5.The relation of cell gap and disclination

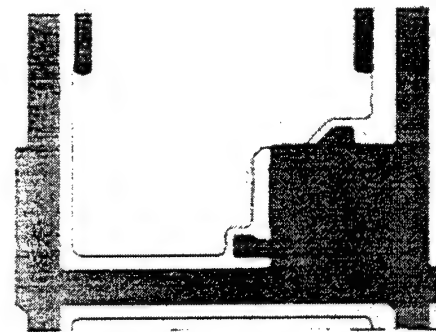


Figure 6.Disclination appears opposite direction after changing rubbing direction

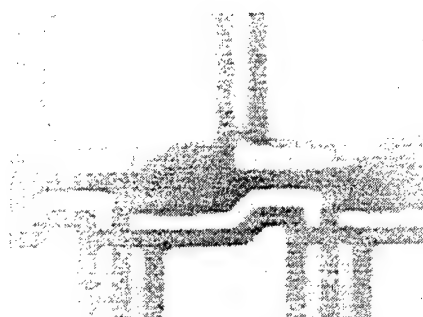


Figure 7.Effect of spacer

Table 2. Disclination of different pixel size

Size	1.8"	6.4"	6.4"VGA
Disclination - c	7.05	7.2	7.94

DISCUSSION

We conclude that we can change the magnitude of reverse tilt domain. and that if we according to actual range of reverse tilt domain to re-design black matrix of color filter in present products, we can increase 4~5% aperture ratio to improve transmittance.

REFERENCE

1. Shinji Shimada, Takao Nomura et.al., Jpn.J.Appl.phys.,30,pp.3308-3312(1991)
2. N. Takahashi, Y. Hirai, S. Kaneko., SID'93 Digest,pp.610-613
3. Yumiko Sato, Kazutoshi Sato and Tatsuo Uchida., Jpn.J.Appl.phys.,31,pp.579-581(1992)

To evaluate the LC pretilt angles of the alignment layer polyamide using the Taguchi method

C.J.Pan^a, H.R.Lin, H.H.Wu*

Prime View International Co., Ltd., HsinChu, Taiwan, R.O.C.

ABSTRACT

Alignment of liquid crystal induced by rubbing is not only interesting in physical chemistry but also important as a fundamental technology of mass production of liquid crystal devices. A detailed investigation on the influences of various rubbing parameters and temperature on the polyamide film has been carried out to study the temporal behavior of the pretilt angle. We also use the Taguchi Method of the Quality Engineering to prove the evaluated value and experimental value of the pretilt angle. The possibility of using the method as in-line control parameters of the alignment process in an actual LCD production facility is considered.

Keywords: Taguchi method , pretilt angle , rubbing density

1.PREFACE

It is well known that uniform alignment of liquid crystals over a large area is a prerequisite for the optimal performance of various types of liquid crystal display devices¹. Therefore a polymer, like polyamide, has been used as a liquid crystal alignment layer². In order to obtain an excellent alignment, the polymer film is rubbed with a roller covered with a cloth, and consequently the outer layer of the rubbed film is oriented³. One of the important parameters of liquid crystal alignment is the pre-tilt angle that influences the viewing angle characteristics and electrooptics properties of the LCDs⁴. The pre-tilt angle is a critical parameter to control the optical properties of liquid crystal display, like creation of reverse-tilt domain , steepness of voltage-transmission curve and response time. However, the pre-tilt angle will be affect by the curing temperature⁵ , rubbing density and pile impression in alignment process ^{6,7}. Since materials have its own characteristic, different pre-tilt angle may be got even using the same process condition. This experiment focuses on the material of SE-7492 only. It is challenging to find out the condition of process for expected pre-tilt angle, it maybe have to try many times. Taguchi method⁸ is widely used in design of experiment to get the sufficient data with limited experiments and to compare sensitivity of these parameters. In this paper, we present results of deviation between measured data and evaluated data by the Taguchi method.

2.EXPERIMENT

The polyamide (PA), SE-7492, is obtained from Nissan. The PA films were performed by curing the samples at 280°C for 30 minutes after prebake at 70 °C, 90 °C or 110 °C for 5 minutes. Thickness of PA films were controlled in the range of 95~105nm. The rubbing conditions were as follows: rubbing density=100 °C, 200, pile impression=0.2 °C, 0.4 and 0.6mm. The cells were filled with the Merck's liquid crystal in a vacuum chamber under 200torr at room temperature, and the cells were sealed with the UV glue. Thickness of cells were controlled in the range of 40~50μm. In these experiments the filled antiparallel cells were annealed at 95°C for 90min. The pretilt angles at two different spots in a uniform area of each anti-parallel cell were measured at room temperature by the crystal rotation method⁹, and the average value is reported. In these experiments, variable parameters were prebake temperature (70 °C, 90 °C and 110 °C) , rubbing density (100 °C, 200) and pile impression (0.2 °C, 0.4 and 0.6mm) . The definition of the rubbing density was taken from reference¹⁰. If we shall try all condition, we have to do eighteen times. Since we use the Taguchi method, we can calculate the freedom is 5 from the variable amount of parameters. It is suitable for use L₆ design of experiment⁸. Each experiment tests twice and experiment orders were as follows:

	Prebake	Pile impression	Rubbing density
1	70°C	0.2	100
2	70°C	0.4	200
3	90°C	0.6	100
4	90°C	0.2	200
5	110°C	0.4	100
6	110°C	0.6	200

3.RESULTS

We assume prebake temperature 70°C、90°C and 110°C as A1、A2 and A3 respectively ; pile impression 0.2、0.4 and 0.6mm as B1、B2 and B3 respectively ; rubbing density 100 and 200 as C1 and C2 respectively. These results were listed as follow :

	Prebake	Pile impression	Rubbing density	Result 1	Result 2	Average
1	A1	B1	C1	9.96	9.85	9.91
2	A1	B2	C2	7.62	7.22	7.42
3	A2	B3	C1	7.45	7.09	7.27
4	A2	B1	C2	9.83	9.74	9.79
5	A3	B2	C1	8.74	8.49	8.62
6	A3	B3	C2	5.86	5.84	5.50

$$\text{Average } T = (9.91 + 7.42 + 7.27 + 9.79 + 8.62 + 5.5) / 6 = 8.14$$

$$\bar{A} = (9.91 + 7.42) / 2 = 8.67$$

$$\bar{B} = (9.91 + 9.79) / 2 = 9.85$$

$$\bar{C} = (9.91 + 7.27 + 8.62) / 3 = 8.6$$

$$\text{And so on } \bar{A} = 8.53, \bar{B} = 8.02, \bar{C} = 7.69$$

$$\bar{A} = 7.23, \bar{B} = 6.56$$

Evaluated equation by Taguchi method:

$$\mu = T + (\bar{A} - T) + (\bar{B} - T) + (\bar{C} - T)$$

Ex. experiment No 1.

Prebake : 70 (°C) , Pile impression : 0.2 (mm)

Rubbing density : 200

The evaluated value :

$$\mu = 8.14 + (8.67 - 8.14) + (9.85 - 8.14) + (7.69 - 8.14) = 9.93$$

Table 1.Evaluated data by the Taguchi method

and measured data from experiments

No	A	B	C	Evaluated data	Measured data
1	1	1	2	9.93	9.82
2	1	2	2	8.09	7.59
3	1	3	2	6.63	6.26
4	1	1	1	10.82	10.18
5	1	2	1	9.00	8.78
6	1	3	1	7.54	7.48
7	2	1	2	9.79	9.93
8	2	2	2	7.96	7.94
9	2	3	2	6.50	6.59
10	2	1	1	10.70	10.24
11	2	2	1	8.87	9.00
12	2	3	1	7.41	7.51
13	3	1	2	8.49	9.42
14	3	2	2	6.66	7.31
15	3	3	2	5.20	5.93
16	3	1	1	8.94	9.70
17	3	2	1	7.57	8.64
18	3	3	1	6.11	7.25

**The gray areas are indicated those are conditions

by the Taguchi method.

4.DISCUSSION

The deviations between measured data and evaluated data by the Taguchi method are showed in Fig 1,there are very good correspondence. At prebake 90°C, the deviations are lower than our expectation. However, there are large deviations at 110°C (the maximum is 1.14°), these results are acceptable for us.

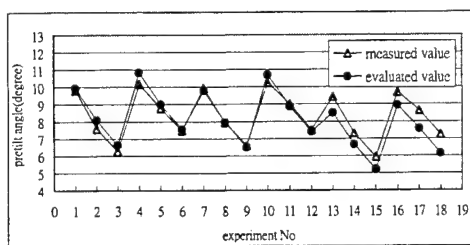


Figure 1. The deviations between measured data and evaluated data by The Taguchi method.

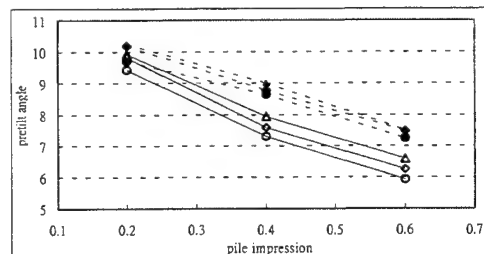


Figure 2,Effects of pretilt angle (measured data) with variable of each parameter.

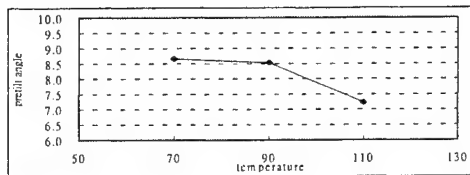


Figure 3. Temperature dependence of pretilt angle by The Taguchi method.

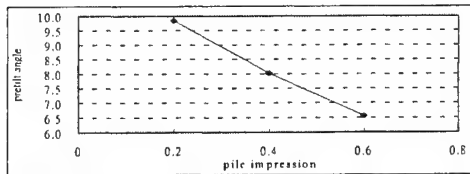


Figure 4. Pile impression dependence of pretilt angle by The Taguchi method.

(◇ : prebake 70°C , rubbing density 200)
 (△ : prebake 90°C , rubbing density 200)
 (○ : prebake 110°C , rubbing density 200)
 (◆ : prebake 70°C , rubbing density 100)
 (▲ : prebake 90°C , rubbing density 100)
 (● : prebake 110°C , rubbing density 100)

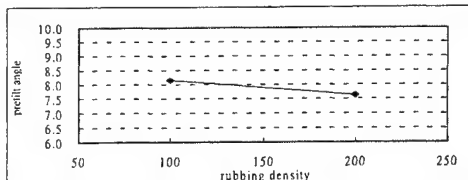


Figure 5. Rubbing density dependence of pretilt angle by The Taguchi method

Fig 2 shows the effects of pretilt angle with each parameter. It is known that pretilt angle becomes lower according to increase of the pile impression (in conditions of moderately large pile impression) [11] and rubbing density. However, temperature dependence of pretilt angle has seen different tendency. At 90°C, pretilt angle is higher than others in the same rubbing condition. Figure 4~6 show dependence of pretilt angles, that are evaluated by the Taguchi method, on variable parameters. Figure 4~5 show their tendency are the same as Figure 2. Nevertheless, in Figure 3, the pretilt angle does not vary much with the rubbing process for low-temperature processing. It is seen correspondence to Figure 2 about temperature dependence of pretilt angle. In Figure 5, the slope of line is very small than others. This probably indicates that pretilt angles are more affected sensitively by pile impression and prebake temperature, even if the variable amounts are not identical. Using the Taguchi method, we can get very good results to compare with measured data. So this method will be helpful in process control and experiment design.

REFERENCE

1. J. Cognard, Mol. Cryst. Liq. Cryst., Suppl.,1,p.1,1982
2. B. O. Myrvold, Liq. Cryst.,3,p.1255,1988
3. M. Nishikawa et.al., Proc. Japan Display, 92,p.819,1992
4. A. Lien, R. A. John, M. Angelopoulos et.al., Appl. Phys. Lett.,67,p.3108,1995
5. I. Hirosawa, N. Sasaki et.al., IDW,p.133,1997
6. D. S. Seo, S. Kobayashi, M. Nishikawa, and Y.Yabe, Liq. Cryst.,19,p.289,1995
7. B. O. Myrold, Y. Iwakabe, S.Oh-Hara, and K. Kondo, Jpn. J. Appl. phys.,32,p.5052,1993
8. G. I. Taguchi, "Introduction to design of experiment, 3rd ",1993
9. T. J. Scheffer and J. Nehring, J. Appl. Phys.,48,p.1783,1997
10. D. S. Seo, H. Matsuda, T.Oh-Ide and S. Kobayashi., Mol. Cryst. Liq. Cryst, 224,p.13,1993
11. K. W. Lee, A. Lien, H. Fukuro., Euro Display ,p.319,1996

Are the Color Gamuts of CRT and LCD Triangular? An Experimental Study

Guan-wei Lee^a and Chao-hua Wen^b

^aDepartment of Industrial Engineering, National Tsing Hua University
Hsin-chu, Taiwan, ROC

^bOpto-Electronics & Systems Laboratories, Industrial Technology Research Institute
Hsin-chu, Taiwan, ROC

ABSTRACT

Color LCD (Liquid Crystal Display) has been widely used for personal computers (PC) and video monitors because of its light weight, small volume, low power consumption and so on. Color reproductions for LCD panels are different from that of CRT (Cathode Ray Tube) display. This study describes the difference of color gamuts in different luminance level and the accuracy of color between CRT and LCD. In the present study, the reproduction color gamuts on the chromaticity diagram are measured in three types of displays, including two CRT types (BARCO Reference Calibrator Plus and ViewSonic PT775) and one LCD type (NEC MultiSync LCD 200). In the experiment, the tristimulus values XYZ for the combinations of three primary colors R(red), G(green), B(blue) were measured by varying the input digital levels. The digital levels which varied from 0 to 255 in every primary color were equally divided into 17 stages, including 0 and 255, and thus the tristimulus values of 4913 colors at each display were measured. Size and shape of color gamuts varied with the luminance, sampling distribution and color difference of LCD and CRT will be discussed. The higher the value of Y, the smaller the area of the color gamut, no matter which display type performed. The area of the color gamut of LCD is smaller than that of CRT in most levels of luminance. This paper discovered that some special patterns exist in color gamut diagrams. Final, relationships among patterns have been clarified for characterizing the color gamuts of displays.

1. INTRODUCTION

Color LCDs are more and more popular in the computer market. If the price of LCDs can drop down, LCD will substitute CRT which are the mainstream of the display market at the present time, because of its light weight, small volume, low power consumption and so on. And the display panels of notebooks are all used LCDs. Color reproduction for LCD panels are different from that for CRTs, so this makes the differences of the gamut, color difference and sampling distribution between different type displays. These differences will influence legibility, color matching, user's task performance and feeling, and so on. In contrast to CRTs, LCDs have sharp edged pixels being therefore more suitable to produce sharp edged horizontal and vertical lines. Moreover, pixels of LCD are not subject to spatial instabilities such as jitter. Uncontrolled external electromagnetic radiation may induce jitter at a CRT reducing legibility of characters displayed. Visibility of flicker may be less at LCD because of a more favorable time-course of single pixel luminance. Most CRT displays are equipped with phosphors with a short persistence-time¹. Yukio² indicated that the color gamut and correlated color temperatures for a LCD panel change according to the input digital level. Hence, the CRT does not change its color gamut and corrected color temperature. It is shown that the LCD reveals the bluish color reproductions. Wright³ compared the resolution and legibility of TFT-LCDs and that of CRTs. Although there are some researches about comparing LCD and CRT, there are few researches advertising to the comparisons of color gamuts between LCD and CRT. This paper will focus on measuring color gamuts with field study, not computing.

Pointer⁴ indicated that the gamut of chromaticities of standardized set of color-television receiver phosphors was a triangle. Up to present, many manufacturers use primary color phosphor (RGB) to depict the triangular color gamuts of displays on 2-D plots. There is no need to emphasize that method does not consider about the lightness. Theoretically, transection of color gamut is not always triangular from dark to white. In this paper, we measured the color gamuts of three different type displays, one LCD type display and two CRT type displays. The color reproduction characteristics for a LCD

* Correspondence: Chao-hua Wen; OES/ITRI, S010, B51, 195-8, Sec. 4, Chung-Hsing Rd., Chu-tung, Hsin-chu 310, Taiwan, R.O.C.; Email: h880021@itri.org.tw; Telephone: 886-3-5913714; Fax: 886-3-5829781.

and CRTs have been analyzed. It is found that the color gamuts are changed with the change of luminance, and there is a special relationship between RGB color space and CIE ($Lu'v'$) color space. This relationship will be useful of color correction. The color difference of CRT and LCD is analyzed, too.

2. METHOD

The gamuts of three types display, including two CRT types and one LCD type, were measured by the colorimeter, PR650. Two CRT displays, BARCO Reference Calibrator Plus and ViewSonic PT775, and one LCD display, NEC MultiSync LCD 200, were examined. The BARCO display has been calibrated with calibrator talk. The display card used in the experiment is Matrox Millennium G400-DH.

The resolution of display is 1204*768. The color is set as 24 bits true color. The background is MS Windows98 desktop. A color specimen, which is an 800*600 pixel rectangle, is shown in the center on the display. The specimen fixed for 3 seconds before measured in all dark room. The measured distance between the display and the colorimeter is 40 cm, and the diameter of measured dot is 4 mm. The tristimulus values (X, Y, Z) for the combinations of three primary colors are measured by varying the input digital levels. The digital levels changed from 0 to 255 in every primary color are equally divided into 17 stages, including 0 and 255, and thus the tristimulus values of 4913 ($17 \times 17 \times 17$) colors at each display are measured.

3. RESULTS

3.1. Color gamuts

The tristimulus values (X, Y, Z) are transformed to CIE 1976 (u', v'). The gamuts of three displays are shown in Figure 1. The gamut of LCD is the smallest in the three displays, and its shape is not a typical triangle. LCD's gamut in blue area is smaller than that in CRTs, but LCD's gamut is wider than CRT in cyan to blue part.

Figure 1 is a 2-D projection of gamut, and it does not illustrate the difference of gamut in a variety of luminance. For observing the variation of gamut at different luminance, this study divided luminance into five levels ($0 < Y \leq 20, 20 < Y \leq 40, 40 < Y \leq 60, 60 < Y \leq 80, 80 < Y \leq 100$). The results are shown in Figure 2, Figure 3 and Figure 4. According to these figures, the color gamuts are triangular only at $0 < Y \leq 20$.

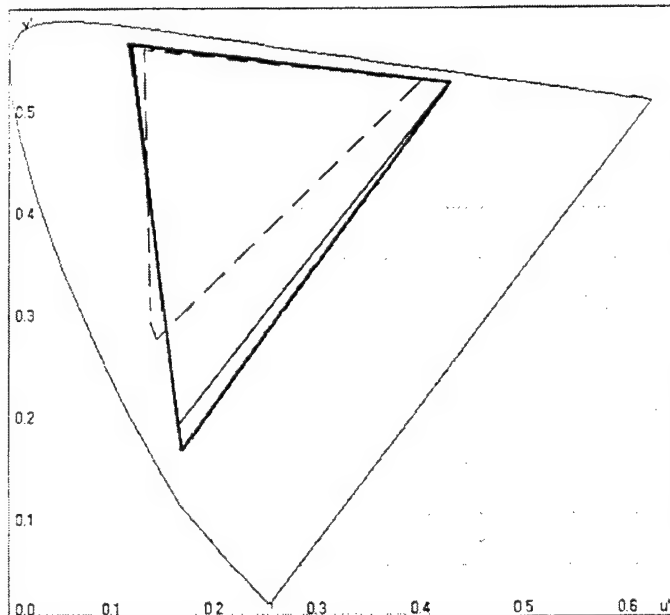


Figure 1. The gamuts of the three displays: Ruggedness-BARCO, Hairline-ViewSonic PT775, Leader- NEC MultiSync LCD 200.

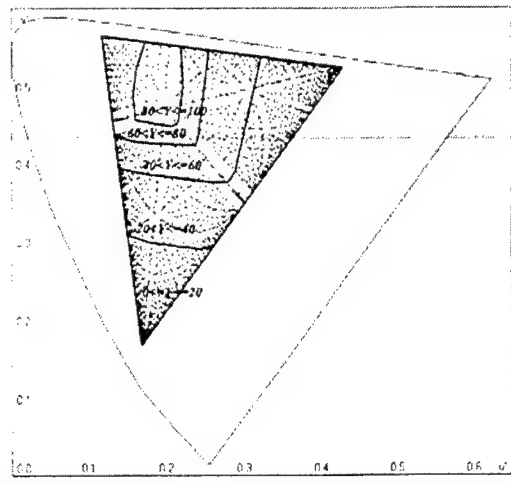


Figure 2. Boundaries of color gamuts of BARCO at different luminance levels.

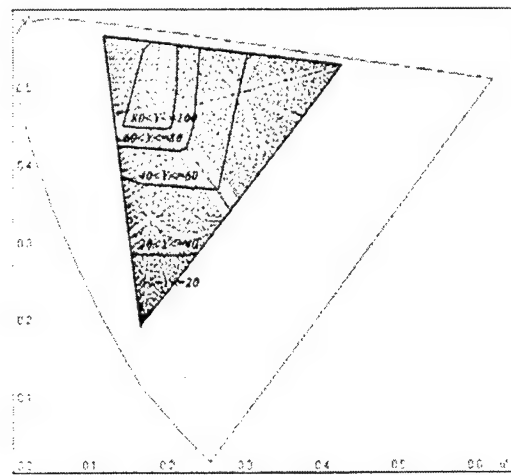


Figure 3. Boundaries of color gamuts of ViewSonic PT775 at different luminance levels.

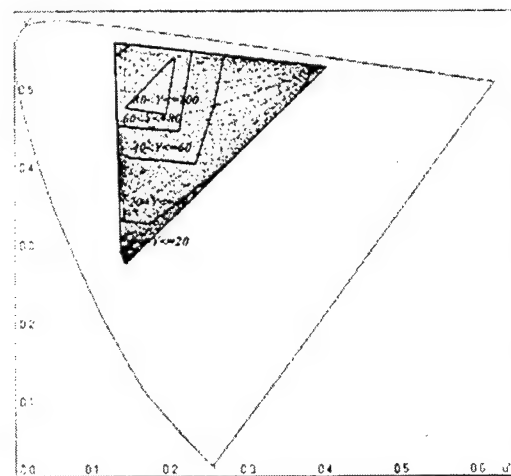


Figure 4. Boundaries of color gamuts of NEC MultiSync LCD 200 at different luminance levels.

3.2. Sampling distribution

As Figure 2 and Figure 3 shown, the sampling distribution performs in regular form on CRT displays. There are several characteristic patterns of CRTs, and to find these patterns can help us to understand CRTs more. To take BARCO as an example, there are thirteen points selected as the characteristic patterns of BARCO. These points are shown in Figure 5.

According to these characteristic patterns, we analyzed their (u', v') values and determined the values of (u', v') \pm 0.005 as ranges. Next, We tried to search for measured specimens matching the condition. The results listed in Table 1. Surprisingly, those measured data fitted to a characteristic pattern were colinear. It revealed that every characteristic pattern represented a line in RGB color space.

Table 1. The RGB values of BARCO characteristic patterns

Characteristic pattern	Color	u'	v'	R	G	B
R	Red	0.425	0.52375	X>=96	0	0
G	Green	0.12	0.56375	0	X>=64	0
B	Blue	0.17125	0.17125	0	0	X>=128
O	White	0.20875	0.55125	X	X	X
D	Magenta	0.30125	0.45127	X	0	X
E	Cyan	0.13375	0.45125	0	X	X
F	Yellow	0.20875	0.55125	X	X	0
H	Light Green	0.145	0.5325	X/2	X>=64	X/2
I	Rose	0.305	0.49375	X>=96	X/2	X/2
J	Light blue	0.185	0.335	X/2	X/2	X>=96
M	Mauve	0.625	0.395	X	X/2	X
N	Aqua	0.15125	0.45625	X/2	X	X
P	Cream	0.20625	0.53125	X	X	X/2

X is the integer between 0 and 255.

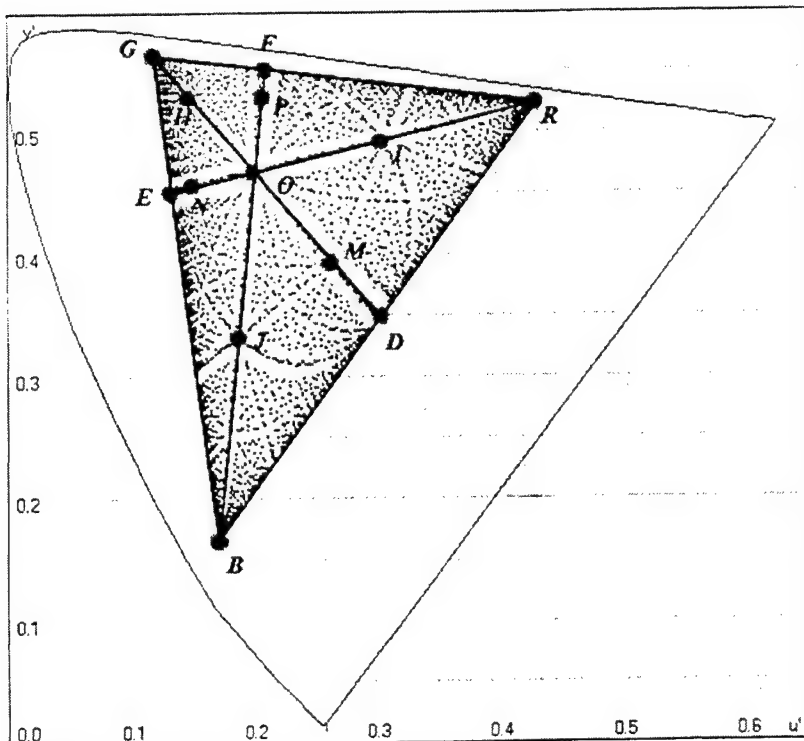


Figure 5. The characteristic patterns of BARCO's color gamut.

3.3. Color difference

To know which type of the three displays, BARCO, ViewSonic PT775 and NEC MultiSync LCD 200, presented the most accurate color, $\Delta E_{CIE}(L^*u^*v^*)$ of them was used to compare their color difference. The formulas that were used is shown below. In Addition, sRGB color space was as reference and D65 was the reference white.

$$L^* = 116(Y/Y_u)^{1/3} - 16 \quad Y/Y_u > 0.01$$

$$u^* = 13L^*(u' - u'_u)$$

$$v^* = 13L^*(v' - v'_u)$$

and

$$u' = \frac{4X}{X + 15Y + 3Z}$$

$$v' = \frac{9Y}{X + 15Y + 3Z}$$

$$u'_u = \frac{4X_u}{X_u + 15Y_u + 3Z_u}$$

$$v'_u = \frac{9Y_u}{X_u + 15Y_u + 3Z_u}$$

X_u, Y_u, Z_u are the tri-stimulus values of D₆₅.

$$\Delta E_{CIE}(L^*u^*v^*) = [(\Delta L^*)^2 + (\Delta u^*)^2 + (\Delta v^*)^2]^{1/2}$$

After computing, results revealed that NEC MultiSync LCD 200 had the largest color difference, and BARCO had the smallest color difference among these three types of display, listed in Table 2. Even ViewSonic PT775 was much better than NEC MultiSync LCD 200. CRT type displays were better than LCD type displays in the field of color difference.

Figure 6, Figure 7 and Figure 8 illustrate that the spots were the least color difference among the three displays in individual display. BARCO has the most spots (75.03%) with the least color difference. The spots in ViewSonic PT775 (23.06%) distributed over yellow, green, Cyan and Magenta. In addition, the spots in NEC MultiSync LCD 200 (3.51%) distributed over several lowest lightness and aquamarine were the worst. These results were reasonable. BARCO has been calibrated as a reference display or was used in the professional field of colors. It had good accuracy in color reproduction.

Table 2. Mean and standard error of ΔE

	NEC MultiSync LCD 200	ViewSonic PT775	BARCO
Mean ΔE	27.68	9.94	6.37
Standard Errors ΔE	15.59	4.47	3.68

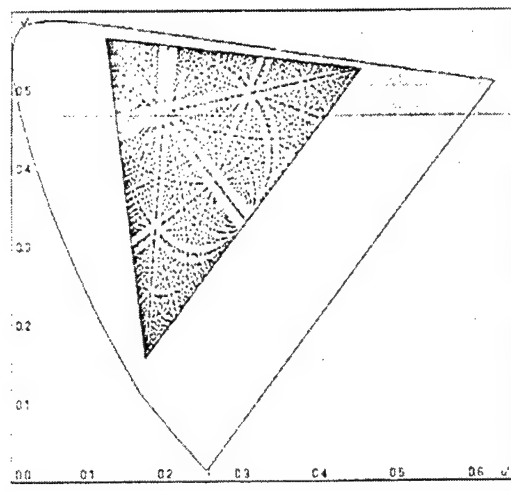


Figure 6. The spots were the least color difference among the three displays (BARCO)

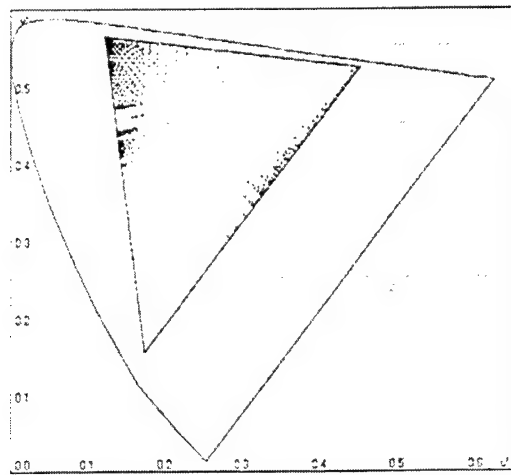


Figure 7. The spots were the least color difference among the three displays (ViewSonic PT775)

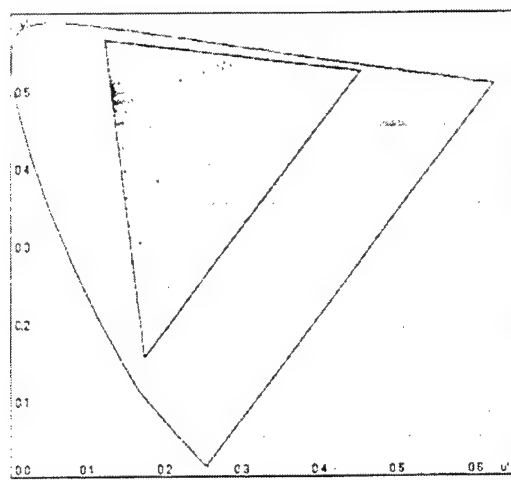


Figure 8. The spots were the least color difference among the three displays (NEC MultiSync LCD 200)

4. DISCUSSION

As Figure 1 depicts, the gamut in LCD was smaller than that in CRT, and LCD could not reproduce more saturate color in blue and red than CRT could. According to Figure 2, Figure 3 and Figure 4, the higher the luminance, the smaller the gamut area. But, is this always true? The gamut of the value of Y between 0 and 20 was analyzed fine. Take BARCO as an example. The biggest area of gamut appears when the value of Y was between 2 and 8. If the value of Y reduced from 2 to 0, the area of gamut reduced rapidly. It could be found that saturate green and yellow could be reproduced in high lightness ($Y_{yellow} > 80$, $Y_{green} > 60$), but red and blue could not. The most saturate red could be reproduced when the value of Y was smaller than 40, and the most saturate blue could be reproduced when the value of Y was smaller than 20. In most lightness, the size of gamut in CRT was bigger than that in LCD, and the green reproduction in CRT was better than that in LCD.

Traditionally, three apexes (RGB) represent the color gamuts of displays, and they formed a triangle. But it can't represent the gamut in a specific lightness. The results of this experiment revealed that the gamut was not triangular in a specific lightness. Is this really a truth? As shown in Figure 4, the shape of gamut was similar with a triangle when the value of Y was 80, but the apexes were not at the positions of R, G and B. They were at the positions of C, M and Y (cyan, magenta and yellow). This is because magenta, yellow and cyan are combined by two of primary colors, and the lightness of them can be gained by adding the lightness of two of primary colors. The shapes of gamut in most lightness were not triangular. Because the size of the gamut was out of the range that the display could reproduce with primary colors, and the part that exceeded would be cut. That is why the shapes of gamut in most lightness looked like quadrangles. The shape of gamut in the LCD varied rapidly with the lightness.

According to Figure 5 and Table 1, the five points (G, H, O, M and D) were on a straight line, and the line could be limned by a formula. Every line through one of the three apexes can be limned by a formula which contains three variables, R, G, B. For example, $LINE_{G,H,O,M,D}$ is evaluated by the following formula,

$$R=B.$$

In addition, $CURVE_{F,I,D}$ can be limned as the following formula,

$$R=G+B.$$

$LINE_{G,N,J}$ can be limned as the following formula,

$$B=2R.$$

The relationship between (L,u',v') and sRGB has been clarified, and it will be useful in color correction of CRT. Why is it only useful in CRT, and would it be useful in LCD too? Figure 4 displays that the sampling distribution of LCD is not as regular as that of CRT, and there was no curve that can be seen clearly. The possible reasons why LCD is worse than CRT is color reproduction by different ways, or color reproduction of LCD is not easily controlled.

5. CONCLUSION

There are some conclusions in this paper.

1. The higher the lightness, the smaller the size of gamut. But if the lightness is under a specific low value, the size of gamut will reduce rapidly when the lightness is minified.
2. The size of gamut in LCDs is smaller than that in CRTs. It means that CRTs can reproduce more colors than LCDs can.
3. The shape of gamut in a specific lightness is similar with a triangle, but this shape may be slashed by the capability that the display can reproduce.
4. A plane in RGB color space can form a line or a curve in the CIE (L,u',v') color space map, and this relationship will be useful in color correction. Moreover, these characteristic patterns can evaluate the quality of display, because they involved more information than the primary color.
5. The color difference of CRT is smaller than that of LCD in most color area. It means that there is still plenty of room for improvement of LCD.

REFERENCES

1. Marino Menozzi, Urs Näpflin and Helmut Krueger, "CRT versus LCD: A pilot study on visual performance and suitability of two display technologies for use in office work", *Displays*, 20, 3-10, 1999.
2. YuKio Okano, "Color Reproductions Varying the Input Level on a Liquid Crystal Display Panel", *The Seventh Color Imaging Conference: Color Science, Systems, and Applications*, 233-236, 1999.
3. Wright, S. L., "Resolution and Legibility: A Comparison of TFT-LCDs and CRTs", *SID 99 DIGEST*, 346-349, 1999.
4. Pointer, M. R., "The Gamut of Real Surface Colors", *Col Res Appl*, 5, 145-155, 1980.

Field emission performances of diamond complex ceramic thin film

Weibiao Wang, Jingqiu Liang, Guang Yuan, Haifeng Zhao, Chuiping Zhang, Xiuhua Yin,
Changchun Institute of Physics, Chinese Academy of Sciences, Changchun 130021, China

ABSTRACT

Diamond maybe is an ideal electron emission material for field emission display because of its low work function and better chemistry stability. In this research, complex diamond conduct ceramic thin film is fabricated by using Ag-Bi-Pb-B-O base in organic conduct paste and diamond grains. The research aim is to find a method for making large area diamond-base electron emission material. Field emission performances of complex diamond ceramic are studied, too. The turn-on voltage and maximum stable emission current of material are 300V and 760 μ A, respectively. The material also shows better emission stability at low vacuum pressure. The emitting center view is employed to explain the electron emission from diamond ceramic thin film.

Keywords: Field emission, Complex diamond ceramic

1, INTRODUCTION

Field emission display (FED) is evolving as one of the promising techniques for the future generation of flat panel display. In making a successful FED, one of the critical issues is the fabrication of the cold cathode, which not only generates a high emitting current at relatively low operating voltages but also is stable and reliable to the operating conditions. The key of cold cathode fabrication is selection of electron emission material. Diamond material may be ideal electron emission material for vacuum microelectron devices and field emission display because of its low emission work function, high hardness, high thermal conductivity and better chemistry stability. These desirable properties come from the sp^3 structure of carbon atoms in diamond. The field emission characteristics of chemical vapour deposition (CVD) diamond thin film have been universally studied by lots of authors^[1,2,3]. Many theories have been employed to explain the electron emitting mechanism because of its complex structure and component. Most of authors considered that the sp^2 -bonded carbon (in graphite or amorphous forms) as well as many structures' defects plays the important rules in electron emission. Especially the sp^2 -bonded carbon (in graphite or amorphous forms) has an important action in transferring electrons. Synthetic high-pressure diamond has also been studied by some authors^[4,5], and shown the better electron emission performances. The result shows that the good electric contact between diamond grains and substrate is necessary for better electron emission.

In this research, complex diamond conduct ceramics are fabricated, and its field emission performances are studied, too. The purpose of research is to find a better method solving the diamond grains' application in FED. This kind of complex diamond ceramics may be used in fabrication of large area micro-emitter.

2, EXPERIMENT

Complex diamond ceramics thin films are made from diamond grains powder synthesized and inorganic paste. Synthetic high-pressure diamond powder grains size is about 0.7 μ m on average. Diamond grains are treated with Cs-salt and annealed in H₂ firstly and then mixed with Ag-Bi-Pb-B-O base inorganic conduct paste. The Mixture of diamond and inorganic conduct paste are coated onto silicon substrate. The mixture become the complex ceramics after heated over 300 °C. The ceramic's resistivity is about 0.03 $\Omega \cdot cm$. Because the diamond grains' surface is covered by paste in mix process, the ceramic on diamond grains' surface must be removed by using acid treatment and let diamond surface expose. Complex

diamond conduct ceramic (diamond ceramic) is formed after treatment. Exposure diamond grains' surface must be cleaned carefully and treated again with Cs-salt. As a comparable, some samples are made from diamond grins in Cs-salt solution by using electrolyte deposition. The diamond surface was checked by Raman spectrum. Field emission performances are measured in high vacuum chamber at pressure of 10^{-5} Pa. Indium-tin-oxide coated glass is as anode. The distance between anode and cathode are about $100\text{ }\mu\text{m}$. The circuit of field emission performance measurement is shown in Fig. 1. Applied voltage on anode is 0-5KV.

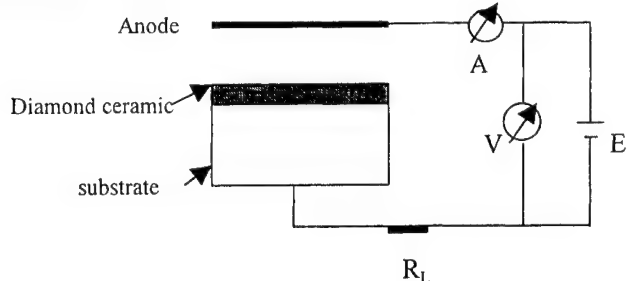


Fig. 1 The circuit diagram of field emission performances measurement

3, RESULTS AND DISCUSSION

3.1, Surface Morphology Photographs of Complex Diamond Conduct Ceramic

The seep electron microscope (SEM) photograph of the surface morphology of complex ceramic, as shown in fig.2(a). From the photograph, it could be known that the surface of diamond grains in complex ceramic is covered by ceramic. Fig. 2(b) shows the surface morphology of complex ceramic thin film after treated with acid solution for 3min. Diamond grains is exposure after treatment. The Raman spectrums confirm that the diamond grains' surface is exposure. As shown in fig.3(b). Fig.2(c) shows the surface morphology of diamond grains film deposited onto silicon substrate by electrolyte in Cs-salt solution. Diamond grains and the vacancy could be seen clearly in fig.2(c).

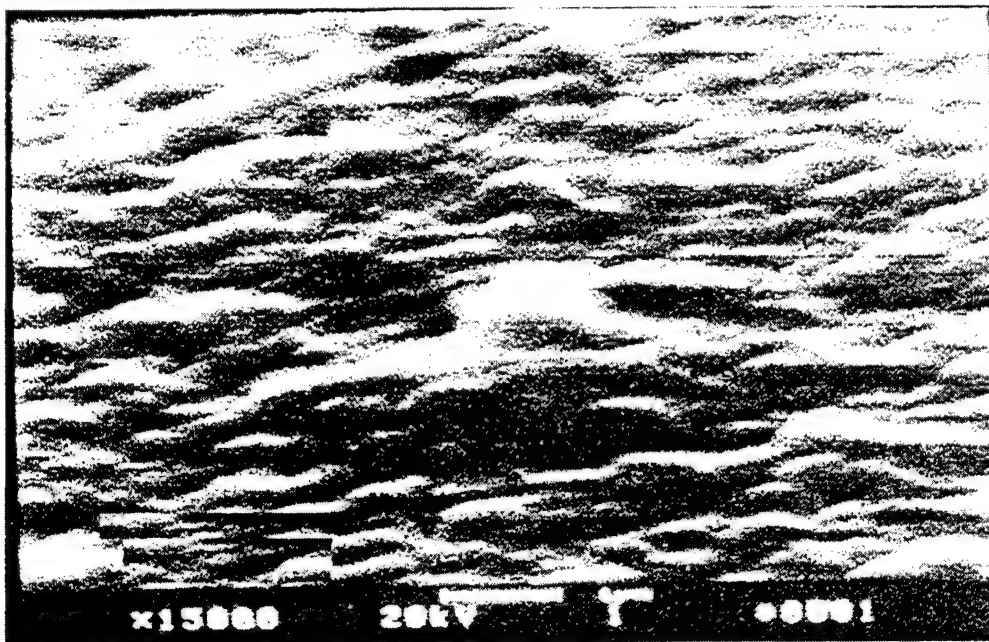


Fig.2(a) SEM photograph of complex ceramic thin film with no surface treatment.

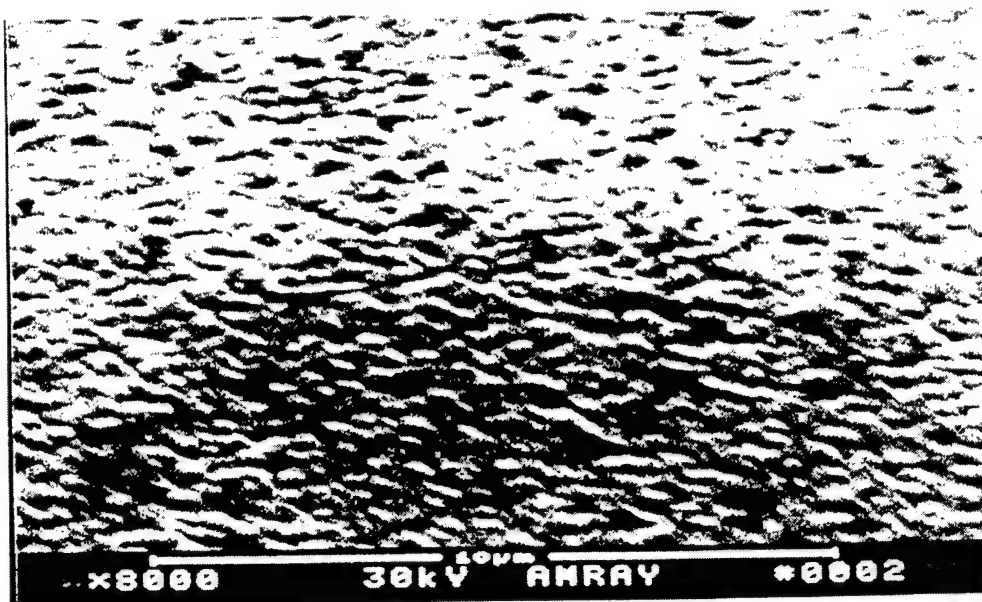


Fig.2(b) The surface morphology photograph of diamond ceramic after treated by acid solution.
The diamond grains' surface is exposure, and vacancies are filled with ceramic.

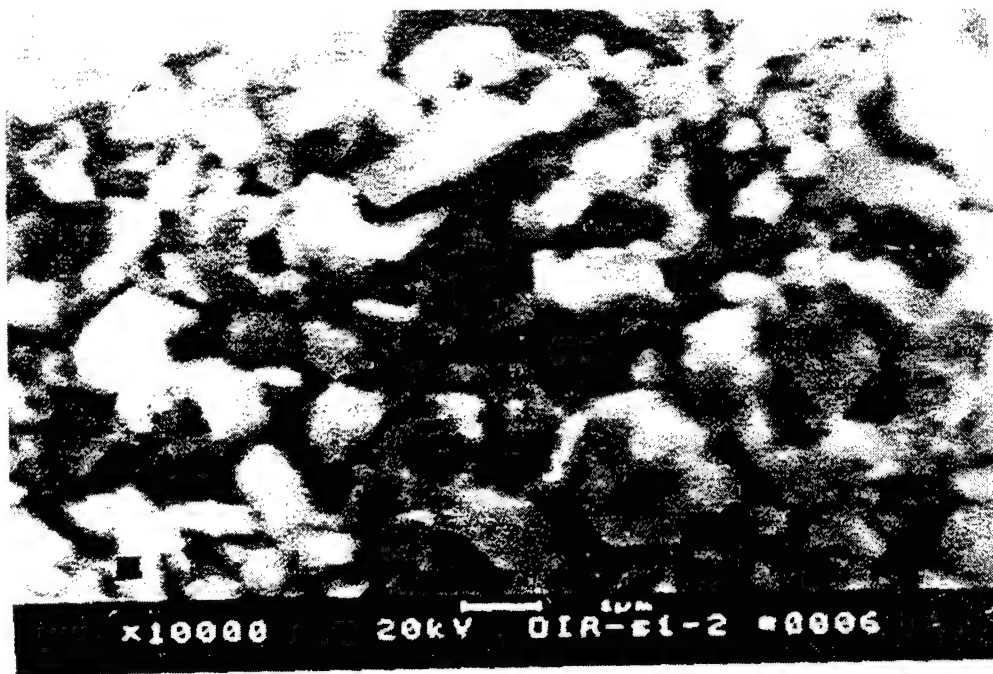


Fig.2(c) The surface morphology photograph of diamond grains deposited by electrolyte in Cs-solution.

3.2, Raman Spectrum of Diamond Grains

Diamond grains is checked by Raman spectrum. The Raman peak of diamond grains is at 1332.6cm^{-1} . Fig.3(a) shows the Raman spectrum of complex diamond conduct ceramic thin film with no treatment. Due to covered of ceramic, no

Raman peak of diamond grains is observed in spectrum. Fig.3 (b) shows Raman spectrum of diamond grains in complex diamond conduct ceramic film after treated with acid solution for 3min.. The sharp Raman peak at 1332.6cm^{-1} shows that diamond grains' surface is exposure. Fig.3(c) shows the Raman spectrum of diamond grains film. From these Raman spectra, acid treatment affect the half-peak -width ($\Delta \lambda$) of diamond grains Raman peak.

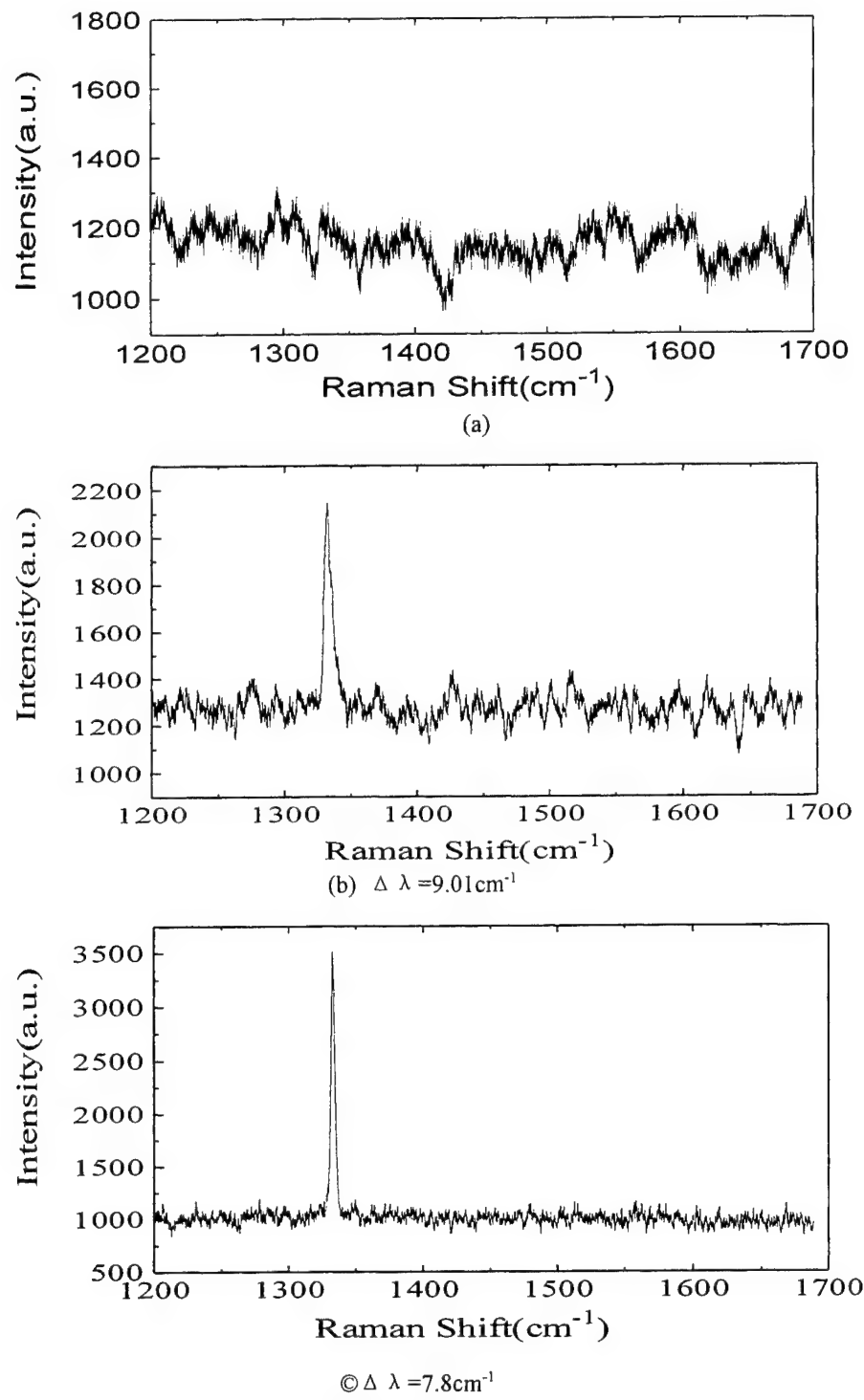


Fig.3 Raman spectra of different samples

3.3, Field Emission Performances

The field emission of diamond maybe described by Fowler-Nordheim equation, as follow:

$$a = (A \times 1.5 \times 10^{-6} \beta^2 / 1.1\phi^2) \exp\left(\frac{10.4}{\sqrt{\phi}}\right) \dots \quad (2)$$

Parameter A is emitting area. β is the field enhancement factor at sharp geometry. ϕ is effective work function of material.

Parameter a and b could be used to describe electrons emitting feature. In the experiment, a and b is got from experiment data, which determine the work function.

3.3.1 Field emission performances of samples

Fig.4(a) shows the field emission performance of complex ceramic (ceramic). Because diamond grains' surface is covered by Ag-Bi-Pb-B-O conduct ceramic, as shown in fig.2(a), the most of electron emission come from ceramic. The turn-on voltage V_{cer} is about 850V. $\phi_{cer} = 0.006$ eV (calculated according to equation (3)) for $\beta = 1$.

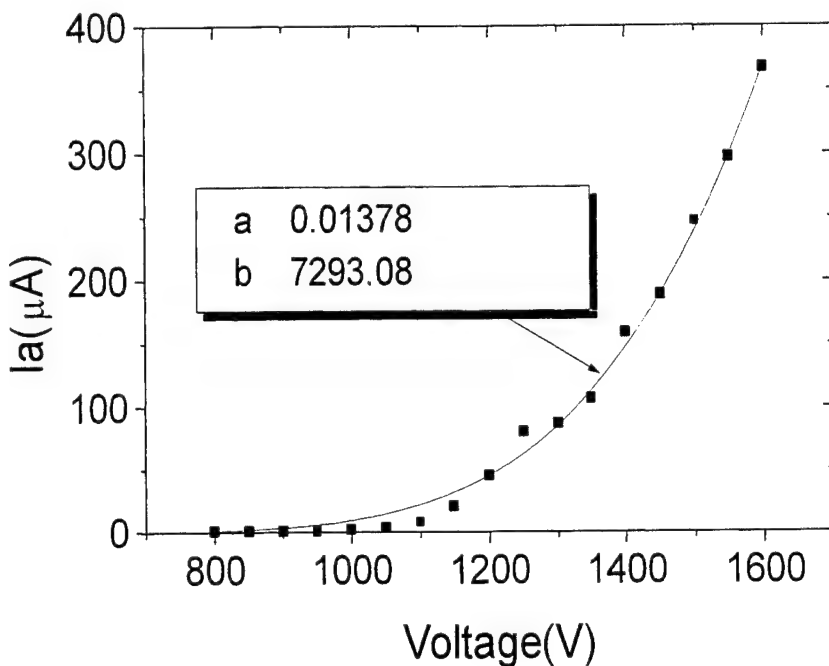


Fig.4(a) Field emission performance of diamond complex conduct ceramic thin film with no acid treatment

The solid line in figure is fitting curve by using Folower-Nordheim equation.

Fig.4 (b) shows field emission performance of diamond ceramic thin film. Diamond grains' surface is exposure after with acid treatment, as shown in fig.2(b). The turn-on voltage $V_{dia-cer}$ is about 300V. According to equation (3), Effective work function $\Phi_{dia-cer}$ is calculated , and equal to 0.0025eV for $\beta=1$, The turn-on voltage is lower than V_{cer} . The reasons will be discussed later.

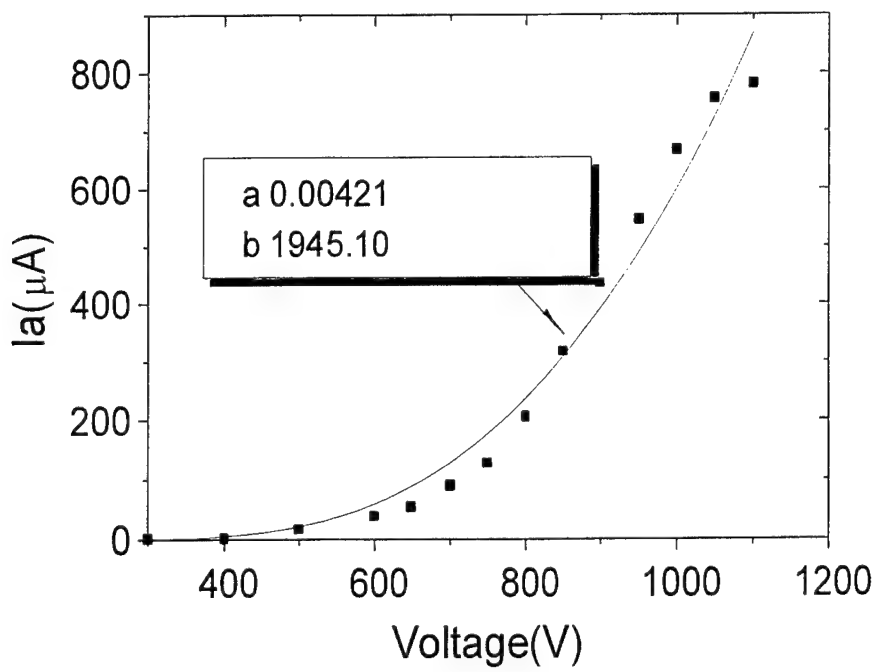


Fig.4(b) field emission performance of complex diamond conduct ceramic thin film after acid treatment
The solid line in figure is fitting curve by using Folower-Nordheim equation.

Fig.4(c) shows field emission performance of diamond grains deposited on silicon by using electrolyte. The turn-on voltage is about 300V. emitting current is about $120 \mu\text{A}$ at maximum. Φ_{dia} is 0.002eV for $\beta=1$.

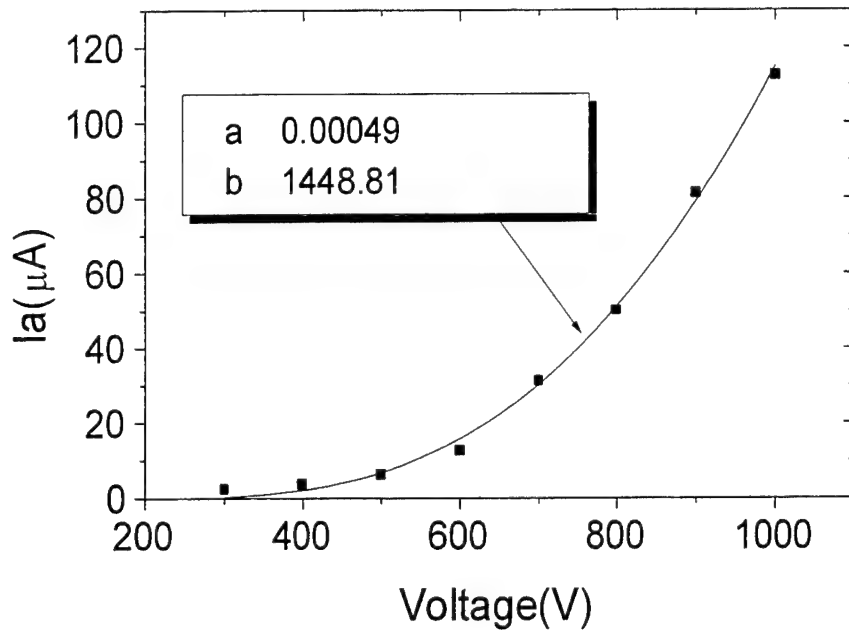


Fig.4© Field emission performance of diamond grains deposited on silicon by electrolyte
According to experiment data, effective work function ratio of ceramic and diamond grains $\phi_{\text{cer}}/\phi_{\text{dia}}$ is equal to 3.

It shows that diamond grains have lower effective work function than ceramic, and means that electron emission of diamond ceramic mainly comes from diamond grains. But the effective work function ratio ϕ_{dia} of diamond grains film deposited by electrolyte onto silicon is equal to 0.002eV, $\phi_{dia-cer}/\phi_{dia}$ is equal to 1.25, only small difference. Emission current of diamond ceramic is higher than that of diamond grains film, although its effective work function is almost equal to diamond grains. The result shows that good electric contact is important to transfer electrons.

3.3.2 Field emission stability

The stability of electron emitting is important for material application in FED. so the emission stability with time and pressure is researched in experiment.

Fig.5(a) shows the emission stability of diamond ceramic at 900V and 650V, emission current is about 400 μA , and 50 μA . Fluctuation of emission current is recorded. Emission current is unstable at high emission level, but it is stable at low emission level.

Fig.5(b) shows emission stability with pressure at 650V and 800V. The emission current is unstable at high emission level and stable at low emission level.

Fig.6 (a) shows the emission stability of ceramic film with time. The emission stability is worse.

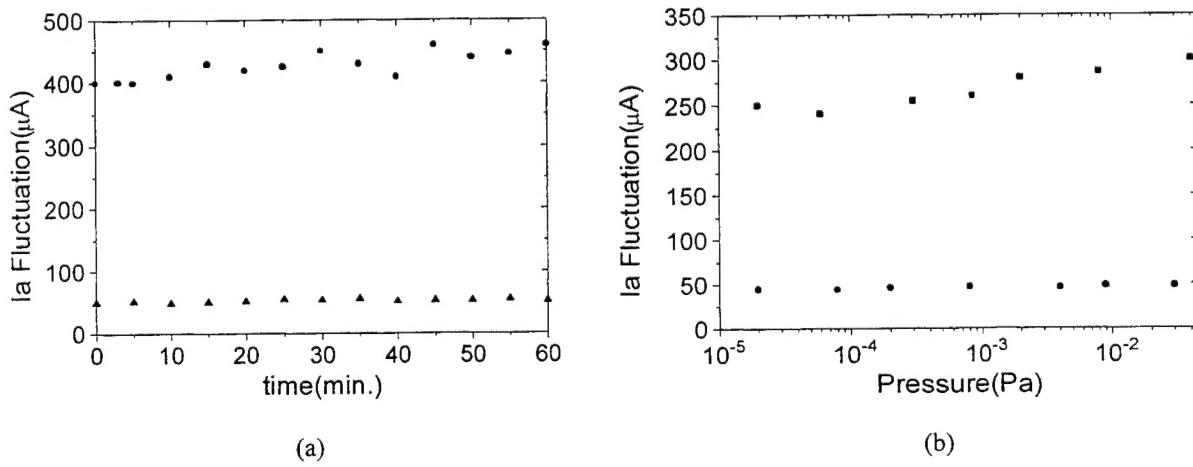


Fig.5 Field emission stability of diamond ceramic with (a) time, (b) pressure

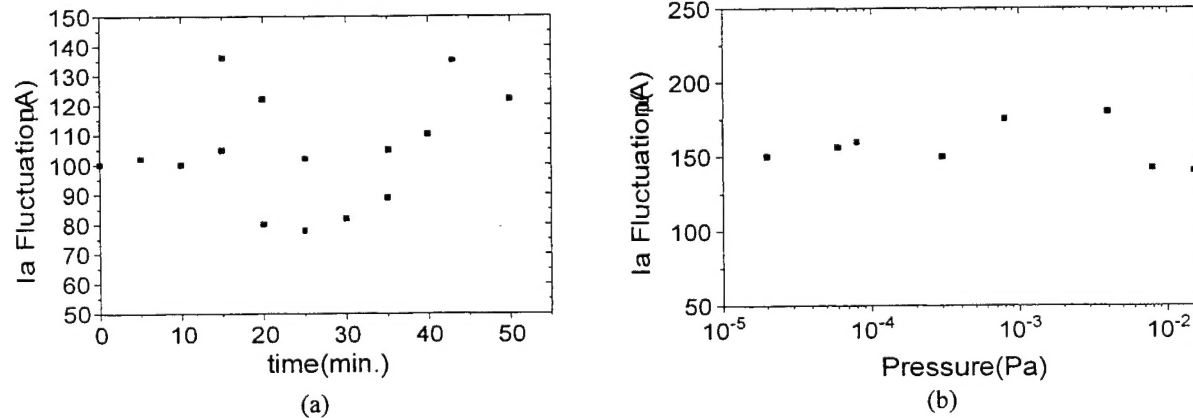
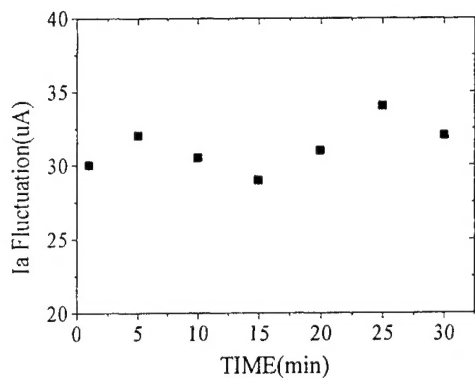
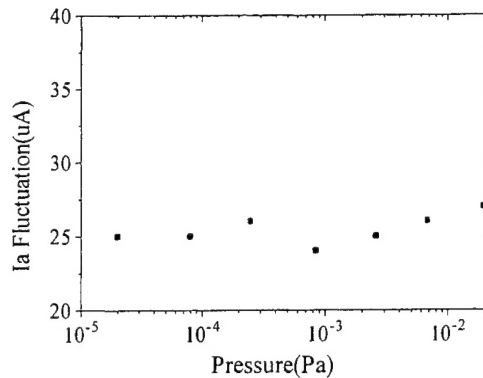


Fig.6 emission current fluctuation of ceramic with (a) time and (b) pressure

Fig.6(b) shows that emission current fluctuation of ceramic change with vacuum pressure. The current fluctuation is unstable at a high level. Fig.7(a) and (b) shows that the emission current of diamond grains film at constant applied voltage change with time and vacuum pressure, respectively. Emission stability of diamond grains film is not very well, too.



(a)



(b)

Fig. 7 emission current fluctuation of diamond grains film with (a) time and (b) pressure

3.4, Electrons Emitting Mechanism

Although diamond is a wide band-gap material, it is an insulator, the free carrier concentration electrons density is very low in perfect diamond due to the high energy band-gap. Diamond has been shown to have a negative electron affinity and a low work function. Fig. 8 shows the band diagram for diamond. Note in this diagram that the band-gap is about 5.5eV and conduct band (E_c) is above the vacuum level E_{vac} . Generally, the emitting current predicted by this band diagram is not very high because the free carrier concentration in diamond is very low. the primary source of free carrier in CVD diamond comes from non-diamond phase such as graphitic phase, so the emission current of perfect diamond grains is not high. If want to get high emission current, it must has a better electrons transfer passage to maintain the electron source for constant electron emission. Generally, it is not easy to form the good Ohmic contact between diamond and substrate. In our research, hard ceramic has better conductivity. It can form good contact between diamond and substrate, and plays an important role in carrier transfer.

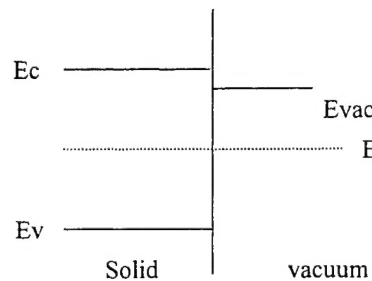


Fig. 8 Band diagram of diamond at vacuum interface

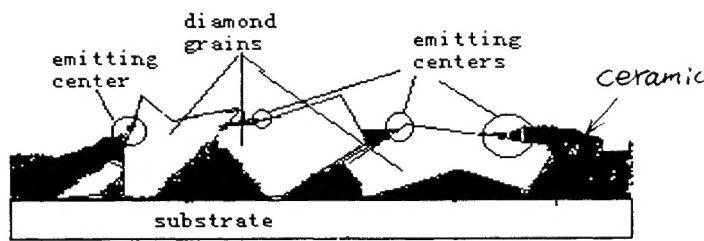


Fig. 9 The sketch diagram of electron emission centers on diamond ceramic's surface.

From above experiment results, the effective work function of diamond ceramic $\phi_{dia-cer}$ is lower than that of ceramic

ϕ_{cer} and almost equal to ϕ_{dia} , also the turn-on voltage is same with that of diamond grains film, but is lower than that of ceramic. In principle, electrons emit more easily from diamond surface than from ceramic surface due to their work function difference. In fact, it is confirmed by experiment results. According to these experiment results, we consider that emitting centers are formed on surface of diamond ceramic. These emitting centers locate at the contact micro-area between diamond surface and conduct ceramic. The Electron emission comes from these emitting centers. The diagrammatic sketch of emitting center is shown in fig. 9. Electrons transfer from conduct ceramic to diamond surface near tightly ceramic, and then emit into vacuum from diamond surface because of its low effective work function. High emission current of diamond ceramic than that of diamond grains film is due to good electric contact between diamond and substrate. Current fluctuation at high emission level maybe is relation with hot carrier transfer and unstable surface. This view is used to explain the result of low turn-on voltage and high emission level of diamond ceramic than that of pure diamond grains film.

4, CONCLUSION

Diamond complex conduct ceramic field emitter is fabricated from diamond grains and Ag-Bi-Pb-B-O base conduct paste. This material is easily fabricated, and has better field emission performances. It suits to use in large area plate display. It needs to improve the emission stability of diamond ceramic at high emission level in further research work.

ACKNOWLEDGE

The authors wash to thank the supports of National Nature Sciences Foundation Council, and the High Technology Research and Development Program of P. R. China.

REFERENCES

1. W. Zhu, G. P. Kochanski, S. Jin, and L. Seibles, "Electron field emission from Chemical vapor deposited diamond," J. Vac. Sci. Technol. B14(3), pp2011-2019, 1996.
2. C. Wang, A. Garcia, D. C. Ingram, M. Lake, M. E. Kordesch, "Cold field emission from CVD diamond films observed in emission electron microscopy", Electronics Letters, Vol.27(16), pp1459-1460, 1991.
3. K. Okano, S. Koizumi, S. Ravi, P. Silva, and Gehan A. J. Amaralunga, "Low-threshold cold cathodes made of nitrogen-doped chemical vapor deposited diamond", Nature, 381, pp140-141, 1996.
4. M. W. Geis, J. G. Twichell, and T. M. Lyszczarz, "Diamond emitter fabrication and theory," J. Vac. Sci. Technol. B14(3), pp2060-2067, 1996.
5. W. B. Choi, J. J. Cuomo, V. V. Zhimov, A. F. Mayer, and J. J. Hren, "Field emission from silicon and molybdenum tips coated with diamond powder by dielectrophoresis", Appl. Phys. Lett., 68(5), pp720-722, 1996

Correspondence: Email: jincc@public.cc.jl.cn; Telephone: 86-431-5952215-125; Fax: 86-431-5955378

Author Index

- Bair, Wei-Fen, 176
Betsui, Keiichi, 70
Chang, Ching-Chao, 176, 191
Chang, Ching-Yun, 228
Chang, Hsin-hua, 127, 135
Chang, Shih-Chang, 43, 47
Chang, Shyh-Ming, 221, 228
Chang, Ting-Kuo, 51
Chang, Yu-Yang, 101
Chen, Chi-Yi, 191
Chen, Chieh-Wei, 127, 135
Chen, Chih-Liang, 255
Chen, Dou-I, 210, 217
Chen, Jian-Cheng, 221
Chen, Jr-Hong, 210, 217
Chen, Pi-Fu, 210, 217
Chen, Po-Cheng, 82
Chen, Shang-Li, 59
Chen, Tai-Hong, 228
Cheng, Hua-Chi, 94, 101
Cheng, Huang-Chung, 51
Cheng, Li-Jing, 51
Cheng, Po Wing, 17
Chi, Gou Chung, 143
Chien, Yu-Ting, 82
Cho, Kyu Sik, 8
Chuang, Feng-Yu, 94, 101
Chuang, Lisen, 176, 191
Fuh, Andy Ying-Guey, 184
Han, Cheng-Xian, 94
Hiruma, Teruo, 2
Ho, Wei Hsuan, 264
Hou, Wei-Fun, 221
Hsieh, Adam, 221, 228
Huang, Chi-Yen, 184
Huang, Chun-Ming, 228
Huang, Ho Chi, 17
Huang, Ting-Hui, 210
Hwang, June-Wei, 217
Jang, Jin, 8
Jou, Jwo-Huei, 228
Jou, M. J., 143
Kam, Tai-Yan, 221
Ko, Tsung-Chih, 184
Kwo, Jon-Lian, 94
Kwok, Hoi Sing, 17
Lee, Cheng-Chung, 94, 101
Lee, Cheng-chung, 127
Lee, Gwan-wei, 271
Li, Hua-Mao, 242
Liang, Jingqiu, 279
Liao, Jane-Hway, 94, 101
Lin, Chi-Huang, 184
Lin, Ching-Wei, 51
Lin, Hong-Yu, 228
Lin, Hung Ru, 268
Lin, Jyung-Dong, 94, 101
Liu, Jun-Qi, 247, 251
Liu, Ya-Nan, 247, 251
Lu, I-Min, 43, 47, 55, 210, 217
Lu, Yin-Lung, 51
Miyazaki, Kazuto, 120
Murakami, Kenji, 112
Nagae, Yoshiharu, 152
Nakagawa, Yoshinori, 120
Ong, Hiap L., 160
Pan, Chih Jui, 264, 268
Ryu, Jai Il, 8
Setomoto, Tatsumi, 120
Sheu, J. K., 143
Sheu, Jyh-Rong, 101
Shih, Chu-Jung, 43, 47
Shih, Jun-Ren, 59
Sun, Li, 201
Sung, Hsioxg-Ju, 55, 217
Taguchi, Tsunemasa, 112, 120
Ting, Dai-Liang, 191
Tsou, Chuan-Cheng, 101
Uchida, Yuji, 120
Uchiike, Heiju, 79
Wang, Bowen, 59
Wang, Ching-Wu, 255
Wang, Li-Ming, 47, 55
Wang, Shumei, 201
Wang, Weibiao, 279
Wang, Wen-Chun, 94, 101
Wang, Yung-Hao, 228
Wen, Chao-hua, 271
Wen, Chi-Jain, 191
Wong, Man, 28
Wong, Y.-J., 191
Wu, Chung-chih, 127, 135
Wu, H. H., 264, 268
Wu, I-Wei, 43, 47, 55
Wu, Tong, 247, 251
Wu, Yung-Hsun, 160
Yang, Cheng-chung, 127, 135
Yang, Tsung-Yu, 255
Yang, Yuan-Hsiu, 255
Yeh, Ting Wei, 143
Yin, Xiuhua, 279
Yoshino, Masahiko, 112
Yuan, Guang, 279
Zeng, Jian-Kang, 247, 251
Zhang, Chuanping, 279
Zhao, Haifeng, 279